

Synthesis and Photophysical Properties of Ferrocene and Dithienylethene Based Multi-responsive Organic Materials

A THESIS

Submitted by

MANISHA KARMAKAR

for the award of the degree

DOCTOR OF PHILOSOPHY (SCIENCE)



Department of Chemistry

Jadavpur University

Kolkata-700032, India

May, 2023



CERTIFICATE FROM THE SUPERVISOR

This is to certify that the thesis entitled "**Synthesis and Photophysical Properties of Ferrocene and Dithienylethene Based Multi-responsive Organic Materials**" submitted by **Smt. Manisha Karmakar**, who got her name registered on 20.09.2018. for the award of Ph.D. (Science). Degree of Jadavpur University, is absolutely based upon her own work under the supervision of **Dr. Arunabha Thakur** and that neither this thesis nor any part of it has been submitted for any degree/diploma or any other academic award anywhere before.

Thakur 26/05/23

(**Dr. Arunabha Thakur**)

Signature of Supervisor and date with seal

Dr. Arunabha Thakur

Assistant Professor

Department of Chemistry

Jadavpur University

Kolkata-700032, India

*Dedicated to my parents and
respected teachers...*



*“Arise! Awake! and stop
not till the goal is
reached”*

DECLARATION

I hereby declare that the research work embodied in the present thesis entitled "**Synthesis and Photophysical Properties of Ferrocene and Dithienylethene Based Multi-responsive Organic Materials**" being submitted to Jadavpur University, Kolkata, has been carried out at the Jadavpur University under the supervision of Dr. Arunabha Thakur, Assistant Professor, Jadavpur University. This work is original and has not been submitted in part or in full, for any degree whatsoever.

Manisha Karmakar . 26/05/23

(Manisha Karmakar)

Signature of Scholar with date

Contents

	<i>Page</i>
Preface	[XXIX-XXX]
Certificate of Supervisor.....	[II]
Declaration.....	[V]
Acknowledgement.....	[XXXI-XXXIII]
Abstract	[XXXIV-XXXV]
List of Figures.....	[XI-XXV]
List of Scheme.....	[XXV-XXVI]
List of Tables.....	[XXVI-XXVIII]
Abbreviations.....	[XXXVI-XXXIX]

Table of Contents

Chapter || 1 *Introduction and literature survey*

1.1. General Introduction.....	[2-6]
1.2. What is DAE/DTE?.....	[7]
1.3. Theoretical background	
Diarylethene photoswitches.....	[7-8]
1.4. Structural versatility of photochromic DAE molecules.....	[8]
1.4.1. Role of bridging moiety.....	[8-9]
1.4.2. Role of the heteroaryl rings.....	[9-10]
1.4.3. Role of substituents R ¹ at the ring-closing carbon atoms	[10]
1.4.4. Role of substituents R ² at reactive carbon atoms....	[11]
1.5. Why DTE over other DAE molecules?.....	[11-12]

1.6. Synthetic development of dithienylperfluorocyclopentene.....	[12-17]
1.7. General structure-property relationships of DTE	
Conformational isomers.....	[18]
1.8. Photophysical and Chemical characterisation of DAE/DTE molecules	[19]
1.8.1. Photochromism.....	[19]
1.8.2. NMR.....	[19-20]
1.8.3. HPLC.....	[20]
1.8.4. UV/vis absorption spectra.....	[20]
1.8.5. Electrochemical properties.....	[20-21]
1.8.6. Fluorescence.....	[21-22]
1.8.7. Dual change in Electrochemistry/Photochemistry.....	[22]
1.8.8. Fatigue resistance.....	[22]
1.8.9. Thermal Stability.....	[23]
1.9. Functionalisation of DAE/ DTE molecules.....	[24]
1.9.1. Lithiation Reactions.....	[24]
1.9.2. Cross-Coupling Reactions.....	[25]
1.9.2.1. Sonogashira Coupling.....	[25]
1.9.2.2. Suzuki Coupling.....	[25]
1.9.2.3. Alkyne-alkyne coupling.....	[26]
1.10. Applications of Dithienylethene (DTE) derivatives.....	[27-31]
1.10.1. Optoelectronic devices.....	[28]
1.10.2. Memory device.....	[27-28]
1.10.3. In security technology.....	[28]
1.10.4. Organic light-emitting diodes (OLED).....	[29]
1.10.5. NLO (Non-linear optical) switches.....	[30-31]
1.10.6. Drug delivery.....	[31]
1.11. Benefits for the incorporation of organometallic unit....	[32]
1.11.1. Speciality of Ferrocene- as an organometallic compound.....	[32-33]
1.11.2. Functionalisation of ferrocene.....	[33-34]
1.11.3. Application of ferrocene and its derivatives.....	[35]
1.11.3.A. Application of ferrocenyl systems in material science.....	[35-36]

1.12. Judicious design of DTE derivatives for my research.....	[36-40]
1.13. References.....	[40-49]

Chapter || 2 *Light-Triggered Metal Coordination Dynamics in Photoswitchable Dithienylethene–Ferrocene System*

2.1. Introduction.....	[51-52]
2.2. Results and Discussion.....	[53-56]
2.2.1. Synthesis and Characterization.....	[53-55]
2.2.2. UV-vis Absorption Study.....	[56-62]
2.2.3. Electrochemical Studies.....	[63-66]
2.2.4. Comparative ¹ H NMR and IR Studies.....	[66-68]
2.3. Theoretical (DFT) Studies.....	[68-74]
2.4. Conclusions.....	[75]
2.5. Experimental Sections.....	[75-76]
2.5.1. Materials and Measurements.....	[75-76]
2.5.2. Instrumentation.....	[76]
2.5.3. Preparation of sample for IR and elemental analysis of [30·Hg ²⁺] complex.....	[76-77]
2.5.4. Synthesis of Compound 3.....	[77]
2.5.5. X-ray crystallographic analysis.....	[77-78]
2.6. Computational Details.....	[78]
2.7. References.....	[78-82]

Chapter || 3 *A Conjugated Photoresponsive Dithienylethene-Ferrocene System: Application in Secret Writing and Decoding Information*

3.1. Introduction.....	[107-109]
3.2. Results and Discussion.....	[109]
3.2.1. Synthesis and Characterization.....	[109-110]
3.2.2. Photophysical studies	[110-122]
3.2.3. Electrochemical Studies.....	[122-123]

3.3. Application.....	[124-125]
3.4. Theoretical (DFT) Studies.....	[125-129]
3.5. Conclusions.. ..	[130]
3.6. Experimental Sections.....	[130]
3.6.1. Materials and Measurements.....	[130-131]
3.6.2. Instrumentation.....	[131]
3.6.3.A. Synthesis of Compound 1	[132]
3.6.3.B. Synthesis of Compound 2	[132-133]
3.6.3.C. Synthesis of Compound 4o	[133]
3.7. Computational Details.....	[133-134]
3.8.1. Preparation of DTE-Fc containing photochromic ink for generation of QR/bar code.	[134]
3.8.2. Preparation of DTE-Fc containing PMMA film. .	[134]
3.9. References.....	[135-140]

Chapter || 4 *Peptide Bridged Napthalimide-Dithienylethene
Diad with Aggregation Induced Emission Activity:
Application in Forensic Fingerprint Technology*

4.1. Introduction	[192-194]
4.2. Results and Discussion.....	[194]
4.2.1. Synthesis and Characterization.....	[194-196]
4.2.2. Photophysical studies.....	[196-204]
4.2.3. AIE Property studies.....	[204-206]
4.2.4. Organogelation Study.....	[206-208]
4.3. Applications	[208]
4.3.1. Fingerprint technology.....	[208-209]
4.3.2. Light controlled security technology.....	[210]
4.4. Conclusion.....	[211]
4.5. Experimental Sections.....	[211]
4.5.1. Materials and Measurements.....	[211-212]
4.5.2. Instrumentation.....	[212]
4.5.3. Synthesis and Characterization.....	[212]
4.5.3.1. General procedure for synthesis of compound	

3C₂ and 3C₈	[212]
4.5.3.1.A. Synthesis of compound 3C₂	[213]
4.5.3.1.B. Synthesis of compound 3C₈	[213-214]
4.5.3.2. General procedure for synthesis of compound 4C₂ and 4C₈	[214]
4.5.3.2.A. Synthesis of compound 4C₂	[214]
4.5.3.2.B. Synthesis of compound 4C₈	[215]
4.5.3.3. General procedure for synthesis of compound 6 and 7	[215]
4.5.3.3.A. Synthesis of compound 6	[215-216]
4.5.3.3.B. Synthesis of compound 7	[216-217]
4.6. References.....	[217-222]

Chapter || 5 *Oxidation Induced Differentially Selective Turn-On
Fluorescence via PET Based on Ferrocene Appended
Coumarin-Quinolin Platform: Application in Cascaded
Molecular Logic*

5.1. Introduction	[244-247]
5.2. Results and Discussion.....	[247]
5.2.1. Synthesis and Characterization.....	[247-250]
5.2.2. UV-vis Absorption Study.....	[250-252]
5.2.3. Fluorescence Study.....	[252-257]
5.2.4. Electrochemical Study.....	[257-259]
5.2.5. Reversibility Test.....	[260]
5.2.6. Binary Logic Gates	[261-262]
5.2.7. Colorimetric Detection by Naked Eye.....	[263-264]
5.2.8. Competitive Experiment	[263-264]
5.2.9. ¹ H NMR and FT-IR Titration.....	[265-266]
5.3. Theoretical (DFT) Studies.....	[266-273]
5.4. Conclusions.....	[273-274]
5.5. Experimental Sections.....	[274]

5.5.1. Materials and Measurements.....	[274]
5.5.2. Instrumentation.....	[275]
5.5.3.A. Synthesis of Compound 3	[275-276]
5.5.3.B. Synthesis of Compound 5	[276]
5.6. Computational Details.....	[276]
5.7. References.....	[277]
Overall conclusion and outlook	[290-293]
List of publications	[294-295]
Scientific poster presentations	[296]

List of Figures

CHAPTER | 1

Figure 1.1. Typical examples of different classes photochromic organic molecules and their photoisomerization process.....	[4]
Figure 1.2. Typical examples of different classes photochromic organic molecules and their photoisomerization process.....	[5]
Figure 1.3. Molecular structures of diarylethene derivatives.....	[6]
Figure 1.4. The reversible structural transformation of diarylethene under irradiation.....	[7]
Figure 1.5. Structural versatility of photochromic DAE scaffold..	[8]
Figure 1.6. Retrosynthetic analysis of photochromic DAE molecules by different pathways.....	[14]
Figure 1.7. Synthetic procedure of DTE core (46 and 48).....	[17]
Figure 1.8. Parallel, anti-parallel conformers open and closed isomer of dithienylethene (DTE).....	[18]
Figure 1.9. Photophysical and electrochemical characterisation for photoisomerization reaction of DTE molecules..	[21]
Figure 1.10. (a) Fatigue recyclability and (b) thermal stability	

of DTE molecules.....	[24]
Figure 1.11. Functionalisation of DAE derivatives by various coupling reaction.....	[26]
Figure 1.12. Applications of DAE/DTE molecules.....	[27]
Figure 1.13. Photochromic (DAE based) materials application in opto-electronic devices.....	[28]
Figure 1.14. DAE based photochromic switches and their application in memory media.....	[29]
Figure 1.15. Chemical structure of diarylethene derivatives and their application in security technology.....	[29]
Figure 1.16. DAE functionalised molecules application for organic light-emitting diodes (OLED).....	[30]
Figure 1.17. Metal co-ordinated DTE based NLO switches.....	[31]
Figure 1.18. DAE based biologically active molecules.....	[31]
Figure 1.19. Chemical structure of ferrocene.....	[33]
Figure 1.20. Various methods for functionalization of ferrocene.....	[34]
Figure 1.21. Application of ferrocene derivatives in material science.....	[36]
Figure 1.22. Schematic representation of DTE molecules for the investigation of metal co-ordination dynamics...	[37]
Figure 1.23. Schematic representation of DTE molecules with highly conjugated π -system for abnormal fluorescence behavior.....	[38]
Figure 1.24. Schematic representation of self-assembly behavior.	[39]
Figure 1.25. Schematic diagram for application of photoswitchable DTE molecules.....	[40]

CHAPTER | 2

Figure 2.1. Synthetic route of compound 3	[54]
Figure 2.2. (a) X-ray structure of 3o drawn with thermal ellipsoids at the 50% probability level;	

(b) porous 2D hydrogen bonded network structure; (c) parallel packing of the 2D networks sustained by van der Waals interactions..... [55]

Figure 2.3. Visual color changes observed for free (a) **3o** and (b) **1** after addition of several metal ions in 10^{-4} (M) CH_3CN solution. Visible color changes of (c) **1** (open and closed) and (d) **3** (open and closed) in presence of $\text{Hg}(\text{ClO}_4)_2$ in 10^{-3} M CH_3CN solution..... [56]

Figure 2.4. (a) Changes in the absorption spectra of **3o** by gradual irradiation at 365 nm UV light in CH_3CN (inset: variation of absorption intensity at 581 nm against irradiation time, upon transforming from **3o** to **3c**); (b) Changes of absorption spectra of **3o** (5×10^{-5} M) upon gradual addition of Hg^{2+} ion up to 1 equiv in CH_3CN solvent (inset: zoomed portion representing the isosbestic point at 259 nm); (c) Changes of absorption spectra of **3c** upon gradual addition of Hg^{2+} up to 1 equiv (inset: variation of absorption intensity of **3c** at 581 nm with $[\text{Hg}^{2+}]$ and its comparison with **3o** for the same); (d) Changes of absorption spectra of $[\mathbf{3o} \cdot \text{Hg}^{2+}]$ upon irradiation with 365 nm UV light (inset: zoomed portion representing the emergence of peak at 581 nm)..... [58]

Figure 2.5. Schematic representation of the photoresponsive switching process of **3o** and **3c** in presence of $\text{Hg}(\text{ClO}_4)_2$ and lights of different wavelengths..... [59]

Figure 2.6. Changes of absorption intensities of (a) **3o** and (b) **3c** with Hg^{2+} addition. Job's plot for compound **3** (c) open form and (d) closed form with Hg^{2+} (5×10^{-5} M) in CH_3CN solution indicating the formation of 1:1 complex. Binding constant for compound **3** (e) open

- form and (f) closed form with Hg^{2+} (5×10^{-5} M) in CH_3CN solution..... [60]
- Figure 2.7.** $\ln[(A_0 - A_\infty)/(A_t - A_\infty)]$ vs irradiation time plot for (a) free **3o** to **3c** (b) [**3o**· Hg^{2+}] to [**3c**· Hg^{2+}] for determination of respective rate constants of conversion;(c) comparison of the two linear plots for better comparison of the rates of cyclization. Reversibility test of (d) **3o** and (e)**3c** with Hg^{2+} (5×10^{-5} M, CH_3CN) and EDTA (5×10^{-5} M, H_2O) for 1:1 binding stoichiometry..... [61]
- Figure 2.8.** (a) UV-vis spectral changes of **3o** upon addition of several metal ions. UV-vis spectral changes of **3o** upon gradual addition of (b) Fe^{3+} and (c) Cu^{2+} in CH_3CN (5×10^{-5} M). UV-vis spectral changes at 630 nm peak of **3o** in CH_3CN (5×10^{-5} M) upon gradual addition of (d) Fe^{3+} /LAS and (e) Cu^{2+} /LAS. (f) Schematic representation of photoisomerization process for **3o** to **3c**..... [62]
- Figure 2.9.** (a) Cyclic voltammetry (CV) and (b) differential pulse voltammetry (DPV) of open form (**3o**) to closed form (**3c**) upon irradiation of UV ($\lambda = 365$ nm); (c) Cyclic voltammetry (CV) and (d) differential pulse voltammetry (DPV) of **3o** (open form) upon addition of Hg^{2+} up to 1 equiv in CH_3CN solution with $[(n\text{-Bu})_4\text{N}]\text{ClO}_4$ as supporting electrolyte at 0.06 Vs^{-1} scan rate..... [64]
- Figure 2.10.** (a) Cyclic voltammetry (CV) and (b) differential pulse voltammetry (DPV) of **3c** (closed form) upon addition of Hg^{2+} up to 1 equiv; (c) Cyclic voltammetry (CV) and (d) differential pulse voltammetry (DPV) of [**3o**· Hg^{2+}] upon irradiation of UV ($\lambda = 365$ nm) in CH_3CN solution with $[(n\text{-Bu})_4\text{N}]\text{ClO}_4$ as supporting electrolyte at 0.06 Vs^{-1} scan rate..... [65]

Figure 2.11. (a) Tabular representation of photophysical and electrochemical data for free 3 and [3 ·Hg ²⁺] in both open and closed forms in CH ₃ CN. Normalized (b) absorption intensity (5×10 ⁻⁵ M) and (c) electrochemical changes of compound 3 after Hg ²⁺ (1.25×10 ⁻⁴ M) binding and after UV irradiation (365 nm) in CH ₃ CN solution.	[66]
Figure 2.12. Comparative ¹ H NMR spectra of 3o in presence of 1 equiv Hg ²⁺ in CD ₃ CN as a solvent.....	[67]
Figure 2.13. (a) Comparative IR spectra of 3o in presence of 1 equiv Hg ²⁺ in solid state at room temperature, (b) zoomed image of IR stretching of alkyne (–C≡C–) peak of 3o before and after addition of Hg(ClO ₄) ₂	[68]
Figure 2.14. Energy minimized structures of 3o [(a) anti-parallel and (b) parallel], (c) 3c , (d) [3o ·Hg(ClO ₄) ₂], (e) [3c ·Hg(ClO ₄) ₂].....	[69]
Figure 2.15. Geometry comparison between the starting (red) and optimized (green) geometries.....	[70]
Figure 2.16. (a) Tabular representation of computed energy of the reactions (b) Energy diagram of the reaction of 3c/3o with Hg ²⁺ , calculated at the B3LYP/6-31(d,p)LANL2DZ level of theory.....	[71]
Figure 2.17. Calculated absorption spectra of (a) 3o , (b) [3o ·Hg(ClO ₄) ₂], (c) 3c , (d) [3c ·Hg(ClO ₄) ₂].....	[72]
Figure 2.18. FMOs of (a) 3o (mo cutoff 0.05); (b) 3c (mo cutoff 0.05)...	[73]
Figure 2.19. FMOs of (a) [3o ·Hg(ClO ₄) ₂] (mo cutoff 0.05); (b) [3c ·Hg(ClO ₄) ₂] (mo cutoff 0.05).....	[74]
Figure 2.20. ¹ H NMR spectra of compound 3o in DMSO-d ₆ as a solvent...	[84]
Figure 2.21. ¹³ C NMR spectra of compound 3o in CDCl ₃ as a solvent.....	[85]
Figure 2.22. ¹⁹ F NMR spectra of compound 3o in CDCl ₃ as a solvent.....	[86]
Figure 2.23. HRMS spectrum of compound 3	[87]
Figure 2.24. FT-IR spectra of compound 3o	[88]
Crystallographic data for 3o	[89]

Figure 2.25. ^1H NMR spectra of compound **3c** in CD_3CN as a solvent.... [90]

CHAPTER | 3

Figure 3.1. Synthetic route of compounds **1**, **2**, and **4o**..... [110]

Figure 3.2. Absorption spectral changes of (a) **4o** by gradual irradiation of 365 nm UV light (inset: variation of absorption intensities of **4o** with irradiation time); (b) **4c** by gradual irradiation of >450 nm visible light (inset: variation of absorption intensities of **4c** with irradiation time) in CH_3CN (5×10^{-5} M) solvent..... [111]

Figure 3.3. Plot of Absorbance vs irradiation time (s) for the (a) cyclization (**4o** to **4c**), (b) cycloreversion (**4c** to **4o**) for the calculations of respective quantum yields..... [113]

Figure 3.4. Plot of $\ln[(A_0 - A_\infty)/(A_t - A_\infty)]$ vs irradiation time (s) for determination of rate constant (K) for conversion of (a) free **4o** to **4c**, and (b) free **4c** to **4o** in CH_3CN solution..... [115]

Figure 3.5. (a) HPLC chromatograms of **4o** and **4c**; (b) reversible color changes of **4o** and **4c** with UV and visible light irradiation respectively in CH_3CN solution..... [116]

Figure 3.6. Changes of fluorescence emission spectra upon gradual irradiation of (a) UV light (365 nm) ($\lambda_{\text{ex}} = 550$ nm) for **4o**; (b) Linear plot of fluorescence emission intensity vs irradiation time (s) of compound **4o** CH_3CN solution. Changes of fluorescence emission spectra upon gradual irradiation of (c) visible light (>450 nm) ($\lambda_{\text{ex}} = 630$ nm) for **4c** in CH_3CN (1.5×10^{-7} M) solution; (d) Linear plot of fluorescence emission intensity vs irradiation time (s) of compound **4c** CH_3CN solution. (e) 10 consecutive photoswitching cycles of fluorescence intensity of **4o** and **4c** ($\lambda_{\text{em}} = 595$ nm)

- upon alternating irradiation of UV and visible light;
 (f) fluorescence lifetime spectra of **4o** (1.5×10^{-7} M)
 and **4c** (1.5×10^{-7} M) at room temperature..... [117]
- Figure 3.7.** Changes in the (a,b) absorption spectra of **4o** and **4c**
 by gradual irradiation of UV light (365 nm) and
 visible light (>450 nm) in solid state respectively.
 Plot of $\ln[(A_0 - A_\infty)/(A_t - A_\infty)]$ vs irradiation time (s)
 for determination of rate constant of (c) free **4o** to **4c**,
 (d) free **4c** to **4o** in solid state..... [118]
- Figure 3.8.** Changes in the (a,c) absorption spectra of **4o** and **4c**
 by gradual irradiation of UV light (365 nm) and visible
 light (>450 nm) in solid state respectively. Linear plot
 of fluorescence emission intensity vs irradiation time (s)
 of compound (b) **4o** and (d) **4c** state..... [119]
- Figure 3.9.** Changes in the (a,b) absorption spectra and (c,d)
 fluorescence emission spectra of **4o** and **4c** by gradual
 irradiation of UV light (365 nm) and visible light
 (>450 nm) in PMMA film respectively..... [120]
- Figure 3.10.** (a) Solid state color change of DTE-Fc and (b) color
 change in PMMA thin film with embedded DTE-Fc,
 (c) HRTEM images of DTE-Fc upon irradiation with
 UV (365 nm) and visible (>450 nm) light respectively... [121]
- Figure 3.11.** SAED image of **4o**..... [121]
- Figure 3.12.** (a) Schematic representation of the photo-responsive
 fluorescent switching process of **4o** and **4c** in presence
 of UV and visible light respectively; colorimetric
 picture of (b) **4o** and **4c** in different solvents;
 normalized fluorescence emission spectra of (c)
4o and (d) **4c** ($\lambda_{ex} = 550-583$ nm) in different
 solvents..... [122]
- Figure 3.13.** Cyclic voltammetry for (a) open to closed (**4o** to **4c**);
 (b) closed to open (**4c** to **4o**) conversion; differential
 pulse voltammetry (DPV) for (c) open (**4o**) to closed

(4c) and (d) closed (4c) to open (4o) by irradiation of UV ($\lambda = 365$ nm) and visible light (>450 nm) Respectively.....	[123]
Figure 3.14. (a) Writing patterns obtained by masking of 4o (2 mg in 3 ml CH ₃ CN) as photochromic ink on white coated paper; (b) QR code with visible/invisible transformation behavior was achieved by using 4o; (c) decoding information <i>via</i> bar code scanning through a smartphone.	[125]
Figure 3.15. Ground state DFT optimized structure of 4o and 4c.....	[126]
Figure 3.16. FMOs of open (4o) B3LYP/6-31G*/LANL2DZ (Solvent: Acetonitrile) (mo cutoff 0.03).....	[126]
Figure 3.17. FMOs of closed (4c) B3LYP/6-31G*/LANL2DZ (Solvent: Acetonitrile) (mo cutoff 0.03).....	[127]
Figure 3.18. (a) Illustration of the probable fluorescence “turn-on” mechanism for 4o/4c before and after UV light exposure; molecular electrostatic potential (ESP) energy (kJ/mol) map of (b) 4o and (c) 4c calculated at B3LYP/6-31g*/LANL2DZ (isovalues = 0.002).....	[128]
Figure 3.19. TD CAM-B3LYP computed absorption spectrum of (a) 4o and (b) 4c.....	[129]
Figure 3.20. Ground state (S ₀) and Excited state (S ₁) geometries of 4o (left) and 4c (right) with energies and dipole moments.	[129]
Figure 3.21. ¹ H NMR spectrum of compound P1 in CDCl ₃ as a solvent.....	[142]
Figure 3.22. ¹³ C NMR spectrum of compound P1 in CDCl ₃ as a solvent.....	[143]
Figure 3.23. ¹ H NMR spectrum of compound 1 in CDCl ₃ as a solvent.....	[144]
Figure 3.24. ¹³ C NMR spectrum of compound 1 in CDCl ₃ as a solvent.....	[145]
Figure 3.25. HRMS spectra of compound 1.....	[146]
Figure 3.26. ¹ H NMR spectrum of compound 2 in CDCl ₃ as a	

solvent.....	[147]
Figure 3.27. ^{13}C NMR spectrum of compound 2 in CDCl_3 as a solvent.....	[148]
Figure 3.28. HRMS spectra of compound 2	[149]
Figure 3.29. ORTEP representation of the molecular structure of 2 with thermal ellipsoids drawn at the 50% probability level.....	[150]
Figure 3.30. ^1H NMR spectrum of compound 4o in CDCl_3 as a solvent.....	[151]
Figure 3.31. ^{13}C NMR spectrum of compound 4o in CDCl_3 as a solvent.....	[152]
Figure 3.32. ^{19}F NMR spectrum of compound 4o in CDCl_3 as a solvent.....	[153]
Figure 3.33. HRMS spectra of compound 4o	[154]
Figure 3.34. FT-IR spectra of compound 4o at room temperature in solid state.....	[155]
Figure 3.35. ^1H NMR spectrum of compound 4c in CDCl_3 as a solvent.....	[156]
Procedure of HPLC study.....	[157]

CHAPTER | 4

Figure 4.1. Stepwise synthesis of precursor compounds P1 , 1C_n , 2 and 5	[195]
Figure 4.2. Synthetic procedure of compounds 3C₂ , 3C₈ , 4C₂ , 4C₈ , 6 and 7	[196]
Figure 4.3. The absorption spectra of (a) 6o (inset: absorbance at 550 nm vs exposure time); (b) 7o (inset: absorbance at 550 nm vs exposure time) upon gradual irradiation of 254 nm UV ($310 \mu\text{W}/\text{cm}^2$); (c) 6c (inset: absorbance at 550 nm vs exposure time); (d) 7c (inset: absorbance at 550 nm vs exposure time) upon gradual irradiation of >450 nm visible light in CH_3CN ($1.25 \times 10^{-5} \text{ M}$) solution respectively. Fatigue resistance (at least 45 cycles) for (e)	

- 6 and (f) 7 measured at 550 nm monitored by alternating irradiation of UV ($\lambda = 254$ nm) and visible ($\lambda = >450$ nm) light respectively..... [197]
- Figure 4.4.** Naked eye color changes of open and closed isomer for (a) 6 and (b) 7 in CH₃CN (10⁻³ M) under UV light/visible light; HPLC chromatogram of (c) 6 and (d) 7 before and after UV light irradiation (310 μ W/cm²) (eluted with CH₃CN: H₂O = 90:10)..... [198]
- Figure 4.5.** Calculation of photoreaction quantum yields for cyclization ($\Phi_{o \rightarrow c}$) and cycloreversion ($\Phi_{c \rightarrow o}$) of (a) 6o and (b) 7o by 254 nm UV light and (c) 6c and (d) 7c by >450 nm visible light irradiation..... [199]
- Figure 4.6.** Plot of $\ln[(A_0 - A_\infty)/(A_t - A_\infty)]$ vs irradiation time (s) for determination of rate constant (K) of (a) 6o to 6c, (b) 6c to 6o and (c) 7o to 7c, (b) 7c to 7o in CH₃CN solution.. [200]
- Figure 4.7.** Fluorescence emission spectra ($\lambda_{ex} = 330$ nm) of (a) 6o (inset: fluorescence intensities vs exposure time); (b) 7o (inset: fluorescence intensities vs exposure time) upon gradual irradiation of 254 nm UV (310 μ W/cm²); (c) 6c (inset: fluorescence intensities vs exposure time); (d) 7c (inset: fluorescence intensities vs exposure time) upon gradual irradiation of >450 nm visible light in acetonitrile (7.8 \times 10⁻⁷ M) solution respectively; (e) spectral overlap of normalised absorption and emission spectra of 7 for FRET process; (f) schematic representation of 7 for reversible fluorescence switching (OFF-ON) via FRET process..... [202]
- Figure 4.8.** Absorption spectra of (a) 6o (b) 6c by gradual irradiation of 254 nm UV light and (c) 7o (d) 7c by gradual irradiation of >450 nm visible light respectively. Fluorescence emission spectra of (e) 6o (f) 6c by gradual irradiation of 254 nm UV light and (g) 7o (h) 7c by gradual irradiation of >450

nm visible light respectively in PMMA embedded thin film..... [204]

Figure 4.9. Changes in the absorption spectra of (a) **7o** and (b) **7c** in THF/water binary solvents with increasing water fractions ranging from 0 to 90%. Fluorescence emission spectra of (c) **7o** and (d) **7c** in THF/water binary solvents with increasing water fractions ranging from 0 to 90%..... [205]

Figure 4.10. Bar plot from fluorescence emission spectra of (a) **7o** and (b) **7c** with different percentage of water (0 and 90% H₂O) in THF. Fluorescence photograph of (c) **7o** and (d) **7c** at different water contents (0 and 90% H₂O) under illumination of 365 nm UV light. FESEM images of **7o** in (e) 0% THF, (f) aggregated state (THF: H₂O=30:70); FESEM images of **7c** in (g) 0% THF, (h) aggregated state (THF: H₂O=30:70) [206]

Figure 4.11. (a) Optimization table for gelation experiment; (b) preparation of the organogel from **7o** (sol) to **7o** (gel) and photoisomeration; (c) strain sweep tests for **7** (gel). Absorption spectra of **7** (gel) for (d) cyclization and (e) cycloreversion; Fluorescence emission spectra of **7** (gel) for (f) cyclization and (g) cycloreversion..... [208]

Figure 4.12. Schematic representation of the overall methodology used for the generation of latent fingerprints using compound **7**..... [209]

Figure 4.13. Schematic representation of the overall methodology (developed in laboratory) used for the generation of (a) QR code and (b) erasable writing pattern using compound **7**..... [210]

Figure 4.14. ¹H NMR spectra of compound **3C₂** in CDCl₃ as a solvent..... [222]

Figure 4.15. ¹³C NMR spectra of compound **3C₂** in CDCl₃ as

a solvent.....	[223]
Figure 4.16. ^{13}C NMR spectra of compound 3C₂ in CDCl_3 as a solvent.....	[224]
Figure 4.17. ^1H NMR spectra of compound 3C₈ in CDCl_3 as a solvent.....	[225]
Figure 4.18. ^{13}C NMR spectra of compound 3C₈ in CDCl_3 as a solvent.....	[226]
Figure 4.19. HRMS spectra of compound 3C₈	[227]
Figure 4.20. ^1H NMR spectra of compound 4C₂ in DMSO-d_6 as a solvent.....	[228]
Figure 4.21. ^{13}C NMR spectra of compound 4C₂ in DMSO-d_6 as a solvent.....	[229]
Figure 4.22. HRMS spectra of compound 4C₂	[230]
Figure 4.23. ^1H NMR spectra of compound 4C₈ in CDCl_3 as a solvent.....	[231]
Figure 4.24. ^{13}C NMR spectra of compound 4C₈ in DMSO-d_6 as a solvent.....	[232]
Figure 4.25. HRMS spectra of compound 4C₈	[233]
Figure 4.26. ^1H NMR spectra of compound 6 in CDCl_3 as a solvent.....	[234]
Figure 4.27. ^{13}C NMR spectra of compound 6	[235]
Figure 4.28. ^{19}F NMR spectra of compound 6 in CDCl_3 as a solvent.....	[236]
Figure 4.29. HRMS spectra of compound 6	[237]
Figure 4.30. ^1H NMR spectra of compound 7 in CDCl_3 as a solvent.....	[238]
Figure 4.31. ^{13}C NMR spectra of compound 7	[239]
Figure 4.32. ^{19}F NMR spectra of compound 7 in CDCl_3 as a solvent.....	[240]
Figure 4.33. HRMS of compound 7	[241]
Figure 4.34. FT-IR spectra of compound 7	[242]

CHAPTER | 5

- Figure 5.1.** Single crystal structure of compound **3**..... [249]
- Figure 5.2.** HRMS of compound [**5**·Cu⁺]..... [250]
- Figure 5.3.** (a) Changes in the absorption spectra of **5** (10⁻⁵ M) in CH₃CN upon addition of several cations. Variation in absorption spectra of **5** in CH₃CN (2.5 × 10⁻⁵ M) upon addition of increasing amount of (b) Fe³⁺, (c) Cu²⁺, (d) Cu⁺ up to 1.5 equiv; The inset in (d): Job's plot of receptor **5** with Cu⁺..... [251]
- Figure 5.4.** Effect of addition of various metal ions in fluorescence emission spectra of **5** (10⁻⁶ M)..... [252]
- Figure 5.5.** Fluorescence emission spectra ($\lambda_{\text{ex}} = 318 \text{ nm}$) of compound **5** (1 × 10⁻⁶ M) upon addition of various concentrations of (a) Fe³⁺ ion up to 1.5 equiv, (b) back reduction by LAS, (c) Cu²⁺ and (d) Cu⁺ ions up to 1.5 equiv in CH₃CN solution..... [254]
- Figure 5.6.** (a) Schematic representation of active and inactive mode due to interaction of different metal ions *via* PET process, (b) color changes of receptor **5** with Cu²⁺, Fe³⁺ and Cu⁺ ions under illumination of light 365 nm..... [255]
- Figure 5.7.** (a) Limit of Detection (LOD) calculation for **5** with Cu⁺ ion by 3.3 σ /S method; (b) Quantitative binding data (Benesi-Hildebrand plot) for **5** with Cu⁺ ion. (b) Quantitative binding data (Benesi-Hildebrand plot) for **5** with Cu⁺ ion..... [261]
- Figure 5.8.** Evolution of Electrochemical study (CV) observed for **5** in CH₃CN (10⁻⁴ M) after addition of 1 equiv of several metal cations..... [258]
- Figure 5.9.** Cyclic voltammetry (CV) and (b) differential pulse voltammetry (DPV) of **5** (1.25 × 10⁻⁴ M) upon addition of (a) Fe³⁺, (b) Cu²⁺, (c) Cu⁺ up to 1.5 equiv in CH₃CN solution with [*n*-Bu₄N]ClO₄ as supporting electrolyte in the presence of ferrocene(Fc/Fc⁺) as an internal

standard. Differential pulse voltammetry (DPV) of 5 (1.25×10^{-4} M) upon addition of (d) Fe^{3+} , (e) Cu^{2+} , (f) Cu^+ up to 1.5 equiv in CH_3CN solution with $[n\text{-Bu}_4\text{N}]\text{ClO}_4$ as supporting electrolyte in the presence of ferrocene (Fc/Fc^+) as an internal standard.....	[259]
Figure 5.10. Reversible interaction of 5 with Cu^+ , introduction of to the system; Inset: Stepwise complexation/decomplexation cycles carried out in CH_3CN	[260]
Figure 5.11. Truth table, logic circuit and bar diagram representation of (a) INHIBIT logic gate constructed with Fe^{3+} and LAS as inputs;(b) OR logic gate constructed with Fe^{3+} and Cu^{2+} as inputs and (c) combinational logic gate (red bar indicates input 0; yellow bar indicates input 1 and green bar is for output) constructed with Cu^{2+} , Fe^{3+} and LAS as inputs respectively.....	[262]
Figure 5.12. Visual color changes observed for receptor 5 in CH_3CN (1.25×10^{-4} M) after addition of 1 equiv of several metal cations.....	[262]
Figure 5.13. Bar plot representation of the fluorescence emission intensity of 5 upon the addition of (a) Fe^{3+} , (b) Cu^{2+} , (c) Cu^+ upon several competitive metal cations in CH_3CN medium and (d) fluorescence emission spectra upon addition of Fe^{3+} , Cu^{2+} , Cu^+ up to 1 equiv.....	[263]
Figure 5.14. ^1H NMR spectral changes of probes 5 upon the addition of 1 equiv of Cu^+ ion in CDCl_3 as a solvent.....	[265]
Figure 5.15. FT-IR spectra of receptor 5 and its binding effect on addition of Cu^+ metal ion.....	[266]
Figure 5.16. (a) The most stable optimized structure of receptor 5 and (b) after oxidation of ligand, calculated at the CAM-B3LYP/LanL2DZ/CPCM (acetonitrile) level....	[267]
Figure 5.17. The most stable optimized geometry of $[\mathbf{5}\cdot\text{Cu}^+]$	

calculated at the CAM-B3LYP/LanL2DZ/CPCM (acetonitrile) level (Cu–O = 1.93 Å, Cu–N = 2.72 Å and Cu–NH = 3.20 Å distances).....	[267]
Figure 5.18. Frontier Molecular Orbitals of free ligand with energy calculated at the CAM-B3LYP/LanL2DZ/CPCM (acetonitrile) level.....	[268]
Figure 5.19. Frontier molecular orbitals of oxidized ligand with energy calculated at the CAM-B3LYP/LanL2DZ/CPCM (acetonitrile) level.....	[269]
Figure 5.20. Frontier Molecular Orbitals of [5·Cu ⁺] with energy calculated at the CAM-B3LYP/LanL2DZ/CPCM (acetonitrile) level.....	[270]
Figure 5.21. ¹ H NMR spectrum of compound 3 in CDCl ₃ as a solvent.....	[283]
Figure 5.22. ¹³ C NMR spectrum of compound 3 in CDCl ₃ as a solvent.....	[284]
Figure 5.23. ¹ H NMR spectrum of compound 5 in CDCl ₃ as a solvent.....	[285]
Figure 5.24. Expanded ¹ H NMR spectrum of compound 5 in CDCl ₃ as a solvent.....	[286]
Figure 5.25. FT-IR spectrum of Compound 5	[287]
Figure 5.26. HRMS of compound 3	[288]
Figure 5.27. HRMS of compound 5	[289]

List of Schemes

Scheme 2.1. Photoisomerization in DAE/ DTE systems.....	[51]
Scheme 3.1. Strategies for designing UV-light triggered “turn-on” mode fluorescent DAEs.....	[109]
Scheme 4.1. Schematic illustration for designing of peptide Based photoswitchable dithienylethene molecule..	[193]
Scheme 5.1. Schematic representation of chemosensor towards interaction with an analyte unit.....	[245]
Scheme 5.2. Synthesis of ligands 3 and 5	[249]

Scheme 5.3. Illustration of probable PET based mechanism for 5 , (a) before oxidation (b) after oxidation at the CAM-B3LYP/LanL2DZ/CPCM (acetonitrile) level...	[272]
Scheme 5.4. Schematic representation of fluorescence quenching for [5 ·Cu ⁺] complex calculated at the CAM-B3LYP/ LanL2DZ/CPCM(acetonitrile) level.....	[273]

List of Tables

Table 2.1. Quantum yields of cyclization ($\Phi_{o \rightarrow c}$) and cycloreversion ($\Phi_{c \rightarrow o}$) for free 3 and its metal chelated form [30 ·Hg ²⁺] upon irradiation by 365 nm UV light.....	[61]
Table 2.2. TD-DFT calculated photophysical data for 30 , 3c , [30 ·Hg(ClO ₄) ₂] and [3c ·Hg(ClO ₄) ₂].....	[91]
Table 2.3. Energy, wavelength, oscillator strength and major contributions for each of the 15 mono-excitations calculated by TD-DFT methods at cam-B3LYP/6-31g(d)/LANL2DZ// B3LYP/6-31g(d)/LANL2DZ for 30 . ^a	[92-94]
Table 2.4. Energy, wavelength, oscillator strength and major contributions for each of the 15 mono-excitations calculated by TD-DFT methods at cam-B3LYP/6-31g(d)/LANL2DZ// B3LYP/6-31g(d)/LANL2DZ for 3c . ^a	[94-96]
Table 2.5. Energy, wavelength, oscillator strength and major contributions for each of the 15 mono-excitations calculated by TD-DFT methods at cam-B3LYP/6-31g(d)/LANL2DZ// B3LYP/6-31g(d)/LANL2DZ for [30 ·Hg(ClO ₄) ₂]. ^a	[96-97]
Table 2.6. Energy, wavelength, oscillator strength and major contributions for each of the 15	

mono-excitations calculated by TD-DFT methods at cam-B3LYP/6-31g(d)/LANL2DZ// B3LYP/6-31g(d)/LANL2DZ for [3o·Hg(ClO₄)₂] . ^a	[97-99]
Table 2.7. Cartesian coordinates (Å) of 3o	[98-99]
Table 2.8. Cartesian coordinates (Å) of 3c	[101-102]
Table 2.9. Cartesian coordinates (Å) of [3o·Hg(ClO₄)₂]	[102-104]
Table 2.10. Cartesian coordinates (Å) of [3c·Hg(ClO₄)₂]	[104-105]
Table 3.1. Quantum yields of cyclization ($\Phi_{o\rightarrow c}$) and cycloreversion ($\Phi_{c\rightarrow o}$) for 4o and 4c upon irradiation by 365 nm UV light and visible light (>450 nm) respectively.....	[112]
Table 3.2. Comparative quantum yield values for photocyclization and cycloreversion.....	[113-115]
Table 3.3. Fluorescence quantum yields of open (4o) and closed (4c) isomers.....	[117]
Table 3.4. HPLC data for 4o and 4c at PSS.....	[157]
Table 3.5. Energy, wavelength, oscillator strength and major contributions for each of the 30 mono-excitations calculated by TD-DFT methods at CAM-B3LYP/ 6-31g(d)/LANL2DZ// B3LYP/6-31g(d)/LANL2DZ for Open-Solvent-opt (4o). ^a	[158-163]
Table 3.6. Energy, wavelength, oscillator strength and major contributions for each of the 60 mono-excitations calculated by TD-DFT methods at WB97XD/cc-pVDZ//B3LYP/6-31g(d)/LANL2DZ for Open-Solvent-opt (4o). ^a	[163-168]
Table 3.7. Energy, wavelength, oscillator strength and major contributions for each of the 30 mono-excitations calculated by TD-DFT methods at CAM-B3LYP/ 6-31g(d)/LANL2DZ// B3LYP/6-31g(d)/LANL2DZ for Open-Solvent-opt (4c). ^a	[169-175]
Table 3.8. Energy, wavelength, oscillator strength and major contributions for each of the 60 mono-excitations	

calculated by TD-DFT methods at WB97XD/cc-pVDZ//B3LYP/6-31g(d)/LANL2DZ for Open-Solvent-opt (4c). ^a	[176-182]
Table 4.1. Summary of photoreaction quantum yields [$(\Phi_{o \rightarrow c})$ and $(\Phi_{c \rightarrow o})$] and rate constants (K) data for 6 and 7 upon exposure of UV light (254 nm) and visible light (>450 nm) respectively.....	[262]
Table 4.2. Data for fluorescence quantum yields for open (7o) and closed (7c) isomers in normal and aggregated state.	[207]
Table 5.1. Comparison of LOD of present probe with various other reported Cu ⁺ ion sensors.....	[257]
Table 5.2. The major transitions with Osc. strength and λ_{ex} of free ligand.....	[270]
Table 5.3. The major transitions with Osc. strength and λ_{ex} of oxidized ligand.....	[271]
Table 5.4. The major transitions with Osc.strength and λ_{ex} of [5 ·Cu ⁺]....	[271]

Preface

The research embodied in the present thesis entitled “**Synthesis and Photophysical Properties of Ferrocene and Dithienylethene Based Multi-responsive Organic Materials**” deals with the synthesis and characterization of molecules based on dithienylethene and redox active ferrocene conjugates and their various applications in material sciences.

Investigations described in this thesis have been carried out by the author in the Jadavpur University, Jadavpur, Kolkata-700032, India during the time of February, 2018 to April, 2023 under the supervision of Dr. Arunabha Thakur. The entire work has been described and summarized within the five chapters of this thesis.

Chapter 1 is the general introduction which provides the comprehensive literature survey on dithienylethene (DTE), a special class of organic photochromic molecule and ferrocene, a redox active molecule. This chapter highlights structural features of DTE derivatives and their different applications. At the end of this chapter, the idea for judicious designing of DTE derivatives are summarised and their applications in different fields of material science have been surveyed briefly.

Chapter 2 describes the synthesis of C_2 -symmetric photochromic molecule, containing dithienylethene (DTE) and ferrocene units connected by an alkyne bridge, represents a unique probe where the coordination strength of a metal ion can discriminate the photoswitchable states of a DTE unit. The metal co-ordination dynamics of DTE core has been explored by photophysical, electrochemical studies and quantum chemical calculations.

Chapter 3 describes a ferrocene appended dithienylethene (DTE-Fc) bridged π -conjugated photochromic material, with high photoreaction quantum yield and fatigue resistance property, was rationally designed. It is a unique example of a “turn-on” mode fluorescent DAE without a traditionally known fluorophore or S,S-dioxide moiety. Furthermore, DTE-Fc is proven to be highly efficient in lithographic technique (erasable ink) and deciphering secret codes.

Chapter 4 describes the gelation phenomenon of a photochromic fluorescent molecules, which contain a photochromic dithienylethene (DTE) moiety attached with a

peptide unit and a fluorescent naphthalimide (NI) unit, covalently connected with shorter and longer length alkyl chain respectively, in an unsymmetrical manner. For the first time, we developed a fluorescent photochromic material based on DTE that generates latent finger prints (LFPs) in powder form and exhibits dual activities (photochromic and fluorescent) without losing the legibility of the pattern. Additionally, it also conferred the most promising practical application like information encryption in quick response (QR) patterns and invisible writing on security documents.

Chapter 5 presents, little different kind of work, which does not include any photochromic organic molecules based on dithienylethene molecule rather, it is comprised of redox active ferrocene and two fluorophores (quinoline and coumarin) and applied in cascaded molecular logic gates. Therefore, this chapter of thesis deals with the manufacture of ferrocene based organometallic chemosensor molecule, which shows differential selectivity (either as oxidizing agent or binding agent) towards different metal ions.

Each chapter (**chapter 2 to 5**) begins with a short 'Introduction' followed by 'Experimental Section', 'Results and discussion' and 'Conclusion'. For convenience, 'References' are given at the end of each chapter. Overall conclusions and outlook, list of publications, list of poster presentation has been appended at the end of the thesis.

Acknowledgement

As I approach towards the end of my doctoral research journey, there are so many wonderful people to whom I owe a debt of gratitude, for their contribution, support, and guidance towards my Ph.D. dissertation.

At this moment of accomplishment, first and foremost, I would like to express my sincere gratitude to my Ph. D. supervisor, *Dr. Arunabha Thakur*, Asst. Professor, Department of Chemistry, Jadavpur University, for providing me the opportunity to pursue Ph.D. in his research group. I am much obliged to him for leading me into the world of research with his constant guidance, valuable suggestions, and encouragement throughout the progression of my research. He provides me with enough academic liberty in his lab to conduct research work of my interest, that enables me to explore the fascinating field of photochromic organic materials. I am deeply beholden for his untiring determination and patience, which helps to channelize my performance in right perspective. His own zeal for excellence has always inspired me and set a good example for me in my career.

I am also given my sincere thanks to **Head of the Department, Section-in-Charge**, Organic Chemistry Section and all the faculty members of our department, Jadavpur University.

I gratefully acknowledge for taking care of **STATE** for financial support during my doctoral research tenure.

I do not have words to express my thanks to two internet giants Google and Wikipedia, as I cannot dream of compiling my research work without them. It is because of them that the knowledge in several disciplines related to my research is just a fingertip away from me. They are the door and window to the entire outside world as I work in my lab day in and day out.

The laboratory and other instrumental facilities along with the friendly and cordial atmosphere rank Jadavpur University given me the opportunity to work at this institute as a Ph. D. scholar. I would also like to convey my special thanks to Mr. Raju Biswas (NMR operator), Baby di, and other research scholars (acting as instrument handling) of department of Chemistry, Jadavpur University, for kind instrumental support in my research career.

I convey my special acknowledge to IACS and IICB for instrumental facilities and also convey my special thankfulness to department of Physics and material science for providing instrumental facilities.

I consider myself lucky enough to have experienced such a friendly lab environment with cooperative labmates during my Ph.D. tenure. It is because of them that I have never felt alone or depressed during my struggles in this once in a lifetime journey to become the doctor of philosophy. It is from the bottom of my heart that I acknowledge all the wonderful souls that I met in the lab since I joined. Senior labmate Dr. Sushil Ranjan Bhatta and all my juniors Mr. Krishna Mohan Das, Ms. Adwitiya Pal, Mr. Sayan Kumar Bag, helped me immensely in my lab work. I am also happy to get such labmates for keeping my social life alive during these 5 years and decorating my Ph.D. life with many beautiful memories. Without such huge supports from past and present labmates it would have been almost impossible for me to complete my work smoothly.

I am also very much thankful to former M.Sc. and project students of our lab, Mr. Arnab Goswami, Mr. Abhisheek Chakraborty, Mr. Subradeep Ghosh, Mr. Sreejit Ghosh, Ms. Bolaka Ghosh, Mr. Subhajit bhuia and Ms. Tulsi Dhar for their kind cooperation.

It is my pleasure to thank the neighbouring lab members from our department for their help in both academic and non-academic matters. Thanks to Dr. Mohabiul Alam Mondal and his group helped me in HPLC studies and Biswajit Pabi, S. N. Bose National Centre for Basic Sciences for his cordial help in TEM measurements. I greatly appreciate and acknowledge the support received from other laboratories of Jadavpur University outside our lab for providing their facilities.

Collaborators played a big role in my doctoral research projects. Thus, my sincere gratitude goes with Dr. Santanab Giri (School of Applied Sciences and Humanities, Haldia Institute of Technology), Dr. Bijan Mondal (Universitat Regensburg), Dr. Nayarassery N. Adarsh (School of Chemical Sciences, Mahatma Gandhi University), Dr. Saikat Dutta (Department of Chemistry, National Institute of Technology Karnataka).

The motivation for pursuing higher studies in scientific research came right from the school days. Therefore, it will be a grave mistake if I do not acknowledge their efforts of teaching a relatively mediocre student like me. Thus, I take this platform to thank all of my teachers. The Chemistry Department of Visva Bharati boosted my motivation of doing Ph. D. So, contribution from my teachers Prof. Pranab Sarkar, Prof. Goutam Brahmachari, Dr. Alakananda Hazra, Dr. Adinath Majee, and Dr. Najnin Ara Begum is deeply acknowledged in this regard.

I also take this opportunity to tender my special thanks to my dearest friend Bishwanath for his unconditional support during the happy and hard moments, and to motivate me throughout my Ph.D. tenure.

Finally, it is time to mention the names of the two most important persons in my life, my parents and Didi for showing faith in me and giving me the liberty to choose what I have desired. I salute you for all the selfless love, care, and sacrifices of yours which shaped my life. You are the architect of whatever I am today, you are the light to whichever path I choose to walk, and you are the reason behind my independent self. Thank you, Maa, for all your patience and tolerance, and fulfilling all my legitimate and in some case a bit illegitimate demands since childhood. Thank you, Bapi, for always encouraging me for higher education and teaching me to face difficult situations with calmness instead of running away from them. It is because of their unconditional love and prayers; I have been able to complete this thesis.

Finally, I want to thank everyone who helped me finish my thesis and apologise for not naming everyone.

Manisha Karmakar 26/05/2023

Manisha Karmakar

Jadavpur University

Department of Chemistry

Kolkata, 700032

India.

Date:

Abstract

Index No: 195/18/Chem./26

Thesis title: “Synthesis and Photophysical Properties of Ferrocene and Dithienylethene Based Multi-responsive Organic Materials.”

The main aim of the research work is to synthesize photochromic dithienylethene (DTE) and redox active ferrocene based molecules, describing their photophysical and electrochemical properties and to study their various applications in material science. In order to accomplish this goal, a variety of photochromic molecules based on DTE have been designed and successfully synthesised by using several types of organic transformations. In every instance, the reactive position of the photoswitching DTE unit is connected either by redox active ferrocene molecules or by a wide variety of fluorophore molecules, such as quinoline, coumarin, naphthalimide, and so on. The structural architecture has been designed in such a way that their properties of isomerization process can be regulated in presence of light as a stimulus to make them an excellent candidate as an efficient photoswitch.

In **first work**, A C_2 -symmetric photochromic molecule, containing dithienylethene (DTE) and ferrocene unit, represents the first probe where a metal (Hg^{2+}) binds with the central DTE moiety. Remarkably, the inherent photo-isomerization property of DTE core remains unperturbed upon Hg^{2+} coordination, however with slower kinetics. The dynamic metal coordination between photoisomerized states was confirmed by experimental as well as quantum chemical calculations. Further, we have designed another ferrocene appended dithienylethene (DTE-Fc) in **second work**. The ferrocene appended dithienylethene (DTE-Fc) is highly π -conjugated photochromic material which displayed high photoreaction quantum yield and fatigue resistance property. It is a unique example of a “turn-on” mode fluorescent DAE without a traditionally known fluorophore or S,S-dioxide moiety. Furthermore, DTE-Fc is proven to be highly efficient in lithographic technique (erasable ink) and deciphering secret (QR/ Bar) codes. However, the extended conjugation at the reactive position of DTE restricts its optimum capability to show fast photoswitching. Therefore, to obtain good photoswitching speed, further development of photochromic fluorescent molecule was performed keeping the connection of DTE and fluorophore in a non-conjugated manner. In **third work**, demonstrated

DTE exhibits fluorescence photoswitching performance in solution, solid state, as well as in gel form through FRET mechanism. Taking advantage of high fluorescence photoswitching performance in solution as well as in solid state along with AIE, the developed DTE based material was applied in latent fingerprints (LFPs) and in anti-counterfeiting technology.

The work described in the 5th Chapter of thesis does not include any photochromic organic molecules and their specific applications in security technology (photochromic ink or photo-erasable writing of confidential information, light triggered generation of QR/bar code, latent fingerprint generator, and so on), rather, it is comprised of ferrocene and two fluorophores (quinoline and coumarin) and applied in cascaded molecular logic gates. In this work, a novel differentially selective electrochemical and fluorescent chemosensor, based on a ferrocene-appended coumarin-quinoline platform has been designed and synthesized. The probe is very specific toward Fe^{3+} via a reversible redox process, whereas it detects Cu^{2+} via irreversible oxidation. Interestingly, it exhibits differential affinity toward the Cu^+ ion via complexation. HRMS, ^1H NMR titration, and IR spectral studies revealed the formation of a bidentate Cu^+ complex involving an O atom of the amide group attached to the quinoline ring and a N atom of imine unit, and this observation was further supported by quantum-chemical calculations. Upon the addition of Fe^{3+} and Cu^{2+} ions, the fluorescence emission of the probe shows a “turn-on” signal due to inhibition of the photoinduced electron transfer (PET) process. The addition of sodium L-ascorbate (LAS) as a reducing agent causes fluorescence “turn off” for the Fe^{3+} ion but not for the Cu^{2+} ion because it oxidizes the ferrocene unit to a ferrocenium ion with its concomitant reduction to Cu^+ , which further complexes with the probe. A unique combination of Fe^{3+} , LAS, and Cu^{2+} ions has been used to produce a molecular system demonstrating combinational “AND-OR” logic operation.

Dr. Arunabha Thakur
Assistant Professor
Department of Chemistry
Jadavpur University
Kolkata-700032, India

Arunabha Thakur 26/05/23

.....
(Signature of the Supervisor date with official seal)

Mamisha Karmakar 26/05/2023

.....
(Signature of the Candidate with date)

Abbreviations

AU	Absorbance units
AIE	Aggregation induced emission
ACQ	Aggregation caused quenching
a.u.	Arbitrary units
α	alpha
β	Beta
Boc	Tertiary butyloxycarbonyl
Bz	Benzyl
Cp	Cyclopentadienyl ligand
CV	Cyclic voltammetry
CH ₃ CN	Acetonitrile
CCDC	Cambridge crystallographic data centre
δ	Chemical shift
d	Doublet
DAE	Diarylethene
DCC	N,N'-dicyclohexylcarbodiimide
DCU	N,N'-dicyclohexylurea
deg	degree
DFT	Density functional theory
DMF	Dimethylformamide
DPV	Differential pulse voltammetry
DMF	Dimethyl formamide

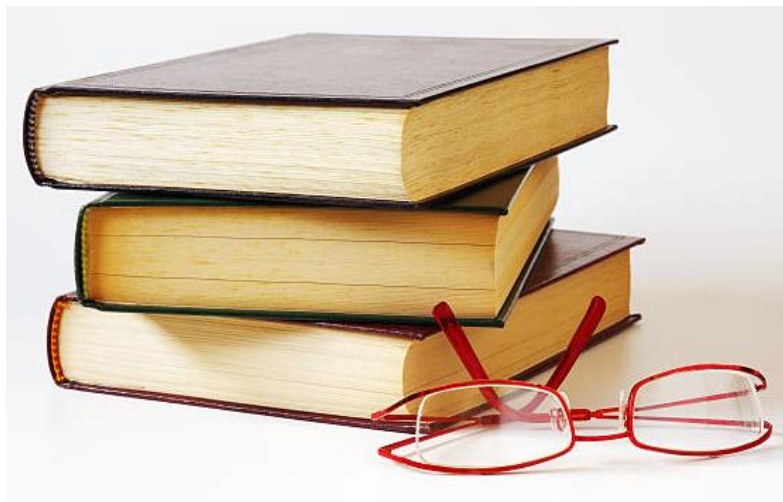
DMSO	Dimethyl sulfoxide
ESI	Electro spray ionization
ESI-MS	Electrospray ionization- mass spectrometry
DTE	Dithienylethene
EDTA	Ethylenediaminetetraacetic acid
Fc	Ferrocene
Fc ⁺	Ferrocenium ion
FE-SEM	Field emission scanning electron microscope
FL	Fluorescence
FRET	Förster resonance energy transfer
FT-IR	Fourier transform-Infra red
GOF	Goodness of fit
h	Hours
HOMO	Highest occupied molecular orbital
HR	High resolution
HRMS	High resolution mass spectrometry
HR-TEM	High resolution transmission electron microscope
HPLC	High performance liquid chromatography
IR	Infra-red
<i>J</i>	Coupling constant
<i>k</i>	Rate constant
<i>K</i>	Binding constant
LEP	Latent fingerprint
LAS	Sodium L-ascorbate
LOD	Limit of detection
LUMO	Lowest unoccupied molecular orbital
M	Molar
m	Multiplate

Me	Methyl
MeOH	Methanol
m/z	Mass/charge
MHz	Megahertz
MS	Mass spectrometry
<i>n</i> -BuLi	<i>n</i> -butyl lithium
Nm	Nanometer
NMR	Nuclear magnetic resonance
NI	Napthalimide
NLO	Non-linear optical material
ORTEP	Oak ridge thermal ellipsoidal plot
PMMA	Poly methylmethacrylate
PET	Photoinduced electron transfer
Ppm	Parts per million
Ph	Phenyl
Phe	Phenyl alanine
PSS	Photostationary state
Φ	Quantum yield
r. t.	Room temperature
s	Singlet (in NMR)
s	Seconds
t	Triplet
TD-DFT	Time-dependent Density Functional Theory
TBAP	Tetrabutylammonium perchlorate
TFA	Trifluoroacetic acid
THF	Tetrahydrofuran
TLC	Thin layer chromatography

TMS	Tetramethylsilane
UV/Vis	Ultraviolet/visible spectroscopy
V	Volt
XRD	X-ray diffraction
TMEDA	Tetramethylethylenediamine
DIPEA	N,N-Diisopropylethylamine
DCC	N,N'-Dicyclohexylcarbodiimide
HBTU	Hexafluorophosphate Benzotriazole Tetramethyl Uronium
(BOC) ₂ O	Di-tert-butyl dicarbonate

Chapter: 1

Introduction and Literature survey



1.1. General Introduction

Beginning with the development of recent organic chemistry, the primary responsibility as a synthetic chemist is to design and manufacture molecules, like reagents, catalysts, or organic frameworks, which serve the specific functions. These functions are mostly determined by macroscopic physical features such as color, or charge transport capabilities, morphology as well as chemical properties that includes reactivity or binding affinity. Currently, the complexity and particularity of these functions are growing more interest which cannot be provided by conventional molecules or materials interacting passively with their environment. However, the molecule or material responsiveness to external stimuli allows them to dynamically modify their characteristics in response to changing environmental conditions or to perform their function on-demand and in a highly regulated manner. Temperature, pressure, the presence of chemicals like protons or metal ions, or an electrochemical potential are all act a stimulus that may be utilised to control such "smart" systems. In addition, light is a very interesting external stimulus due to several advantages: it is non-invasive, may be applied across long distances, and can be easily modified based on their intensity and photon energy.

To develop "smart" light triggered material molecular interface is required that dynamically interact with photons and produce the necessary property change.¹ For this, conventional chromophores may be taken into consideration, in which case the alternating features of states are used, like in photoredox catalysis. However, the excited states often have very short life time, when it is irradiated by light it is preferable for the ground state to undergo a change in its properties. Nevertheless, in order to develop the phototunable fully dynamic molecular system, the interaction of molecules with photons must be reversible. For these purpose, photochromic molecules with two or more reversibly switchable photochromic states with distinct physical and chemical properties, must be utilised.²

Photochromism is a phenomenon that can be explained as the reversible transformation of a chemical species into two isomeric forms, which is triggered by the absorption of electromagnetic radiation and produces color change. The process of photo-isomerization of organic molecules involves variable chemical reaction that includes: pericyclic reactions, cis-trans isomerization, electron, and intramolecular hydrogen transfers, and photodimerization. Due to their fundamental characteristics and prospective uses in stimuli-responsive materials, photochromic molecules have recently received a great attention. Particularly, light is regarded as one of the most appealing stimuli for regulating stimuli-responsive materials due to its ability to provide precise spatial and temporal remote control.

In response to an external stimulus, photochromic materials exhibit a variety of properties on both the microscopic and macroscopic levels. The method through which photochromic materials exhibit their photoresponses may involve several photons and molecules. With the structural diversity photochromic organic materials have strong fatigue resistant properties with no loss of any sensitivity. The excellent anti-fatigue capability of this molecules has been intensively investigated for its prospective applications in security markings, optical shutters, ions, and liquids probing, photo-switchable molecular devices, optical memory storage systems, and topographical change materials. The photochromic features can be activated or controlled by various physical or chemical processes, including temperature, acidity, hydrogen bonding, ion binding, chemical reactions, and oxidation/reduction. Photochromic organic molecules can belong to different classes, such as hydrazones, fulgides, oxazones, disulfoxides, anils, quinones, semicarbazones, spiro-oxazines, stilbene derivatives, succinic anhydrides, spiro compounds and so on (1-6, as shown in Figure 1.1). Photochemistry has been exploring this phenomenon since the early 20th century, although new techniques have just been introduced like temperature dependent reflectance spectroscopy, picosecond time resolved spectroscopy, X-ray along with other spectroscopic techniques. Due to their versatility, photochromic compounds are used in a variety of natural science disciplines. They are used to precisely regulate chemical reactions by remote-controlling molecular processes like catalysis and reactivity.³⁻⁵ Even the single molecule fluorescent photochromic system is used in sensing and super resolution microscopy⁶⁻⁸ or specific binding interactions are favoured by the photocontrol of biological systems and self-assembling materials.⁹ Furthermore, novel light sensitive functions originating from molecular ensembles comprising photochromes can be accomplished, such as photo activation and -mechanics,^{10,11} optical memory devices, and organic optoelectronic devices.^{12,13} To obtain technologically relevant functional systems, it is necessary to optimize the utilized photochromic materials in terms of the desirable characteristic change. This characteristic change, or the degradation of the photochromic compound over numerous switching cycles, is incorporated into their photoswitching efficiency which is not advantageous for all photochromic compounds. As a result, the synthesis and photophysical characterization of photochromic organic compounds with quick responsiveness, robust fatigue resistance, thermal irreversibility, and large quantum yields are extremely demanding.

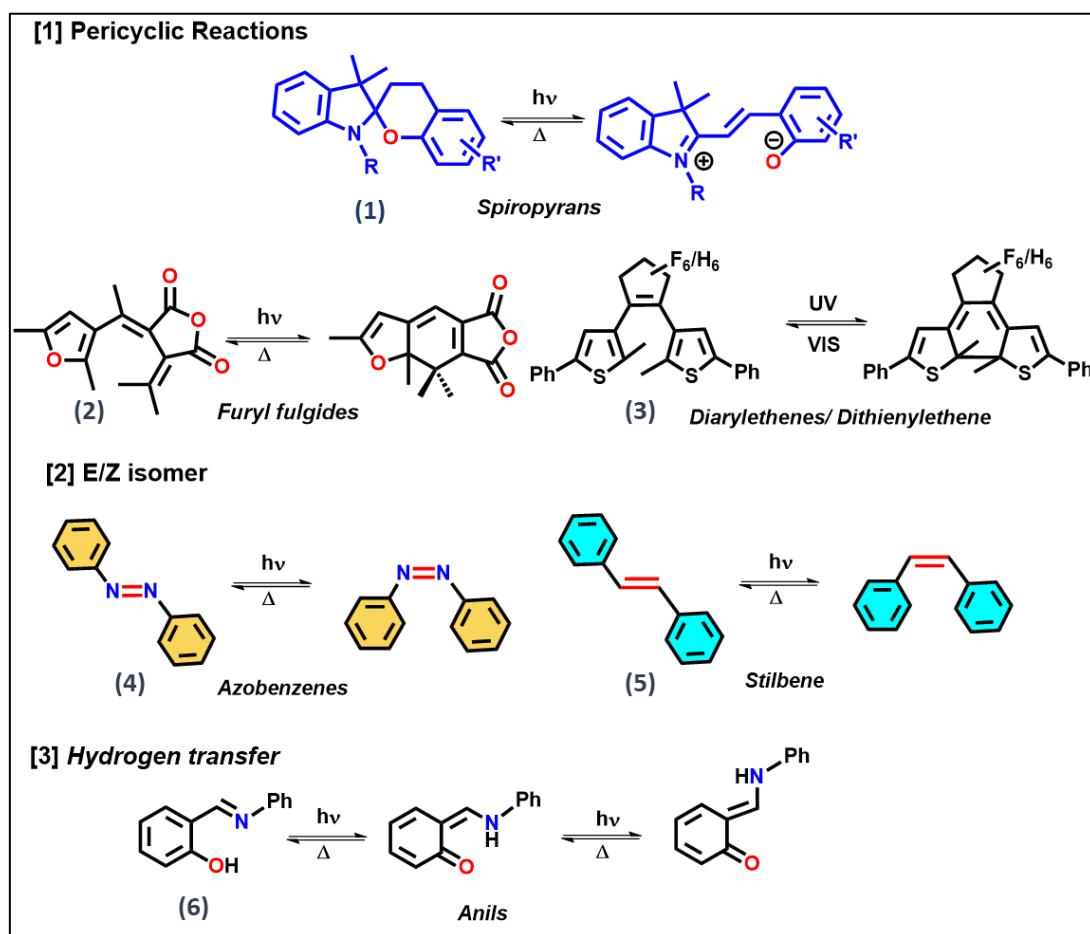


Figure 1.1. Typical examples of different classes photochromic organic molecules and their photoisomerization process.

Further, a new category of photochromic families has been discovered, which has been systematically explored over the last few decades.¹⁴ Due to their excellent photochromic properties, fast response times, robust fatigue resistance, good quantum yields, thermal irreversibility, high levels of reactivity in solid states, and notable differences in the absorbance profiles of the two isomers, diarylethenes are the most promising classes of compounds for use as switching components.¹⁵⁻¹⁷

Since, the discovery of thermally irreversible photochromic molecules diarylethenes (DAE) in the mid-1980s, numerous types of diarylethenes have been synthesised to increase their photochromic performance. Figure 1.2 depicts the structural development of DAE derivatives (7-16) over time.

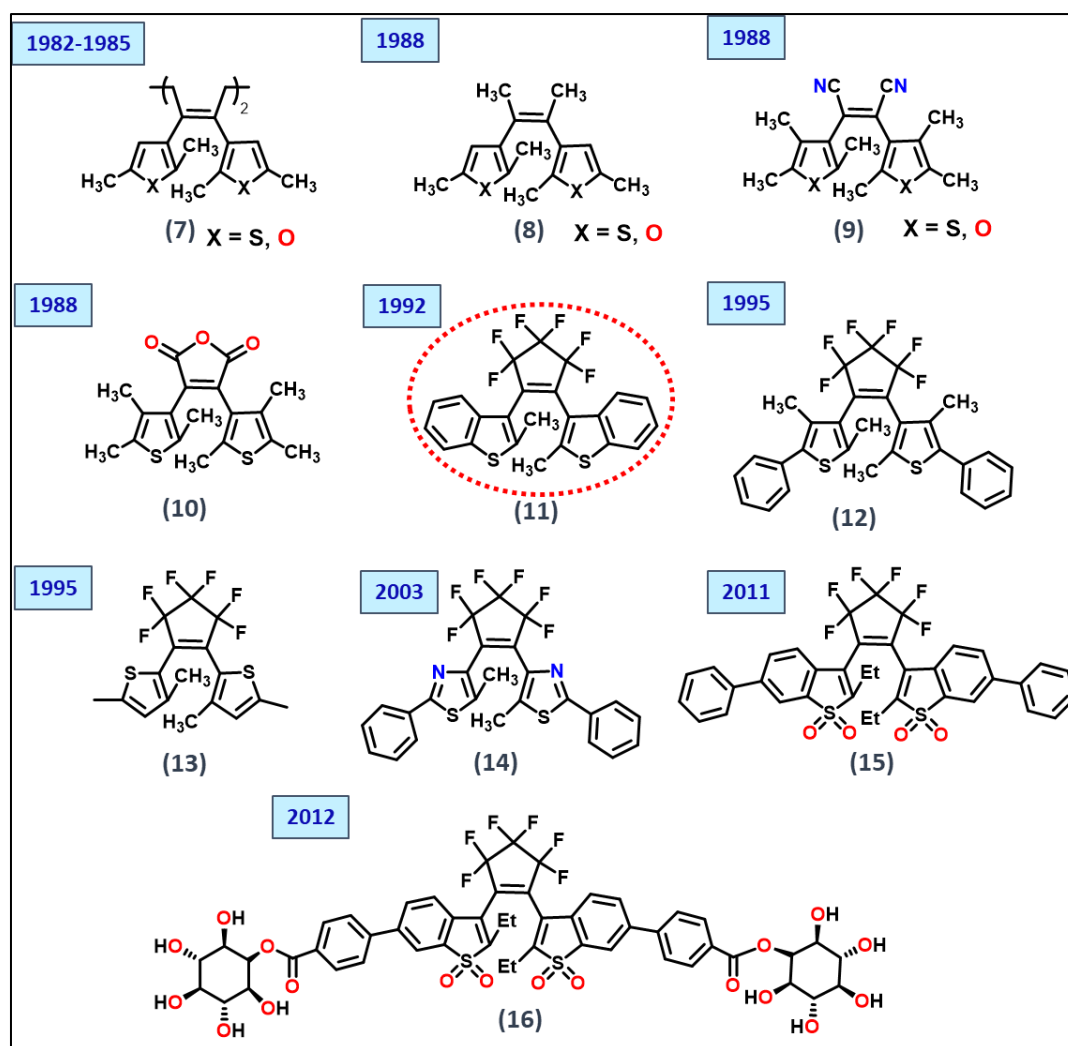


Figure 1.2. Typical examples of different classes photochromic organic molecules and their photoisomerization process.

Dithienylethene (DTE) is one of the photochromic organic molecules among all the DAE family that can switch structurally from its open isomer to its closed isomer and vice versa via electrochemical and photochemical processes. Such photo/electro-switching behaviour can be induced either by electrical or optical features accompanied by the change in UV-vis absorption, luminescence, FT-IR, and redox potentials.

Photochromic molecular switches are molecules that may switch between two isomers (open and closed) with distinctly different absorption spectra when exposed to light in a reversible manner.¹⁸ The open ring isomer transforms into the closed ring isomer upon exposure to monochromatic wavelengths of light *via* photocyclisation. In addition to the UV-vis absorption spectra, other physical and chemical characteristics of the switch, including the refractive index, redox potential, polarity, fluorescence, etc., may also changes.¹⁹ Owing to

their reversible photoswitchability, rapid response, adjustable energy supply, and capacity for transforming optical input into a range of useful output signals, photochromic switches are of great interest. These characteristics can lead to several applications, including non-destructive optical data capture and storage,^{20,21} molecule wires,²² molecular switches,²³ wave guide,²⁴ polarizers and so on. Figure 1.3 depicts the most widely used diarylethene derivatives are diarylmaleicanhydrides, diarylmaleimides, and diarylperfluorocyclopentenes (17-28).^{25,26}

To explore how enhancing the π -conjugation influences the optically and electrically induced cyclization/cycloreversion processes, 3-ethynylthiophene and its derivatives were attached to perfluoro analogues. The thermal stability and high fatigue resistance capacity of dithienylethene derivatives were encouraged to further explore their applications in everyday life and their photo-luminescent activity was examined in both open and closed-ring forms in a non-destructive read-out manner.

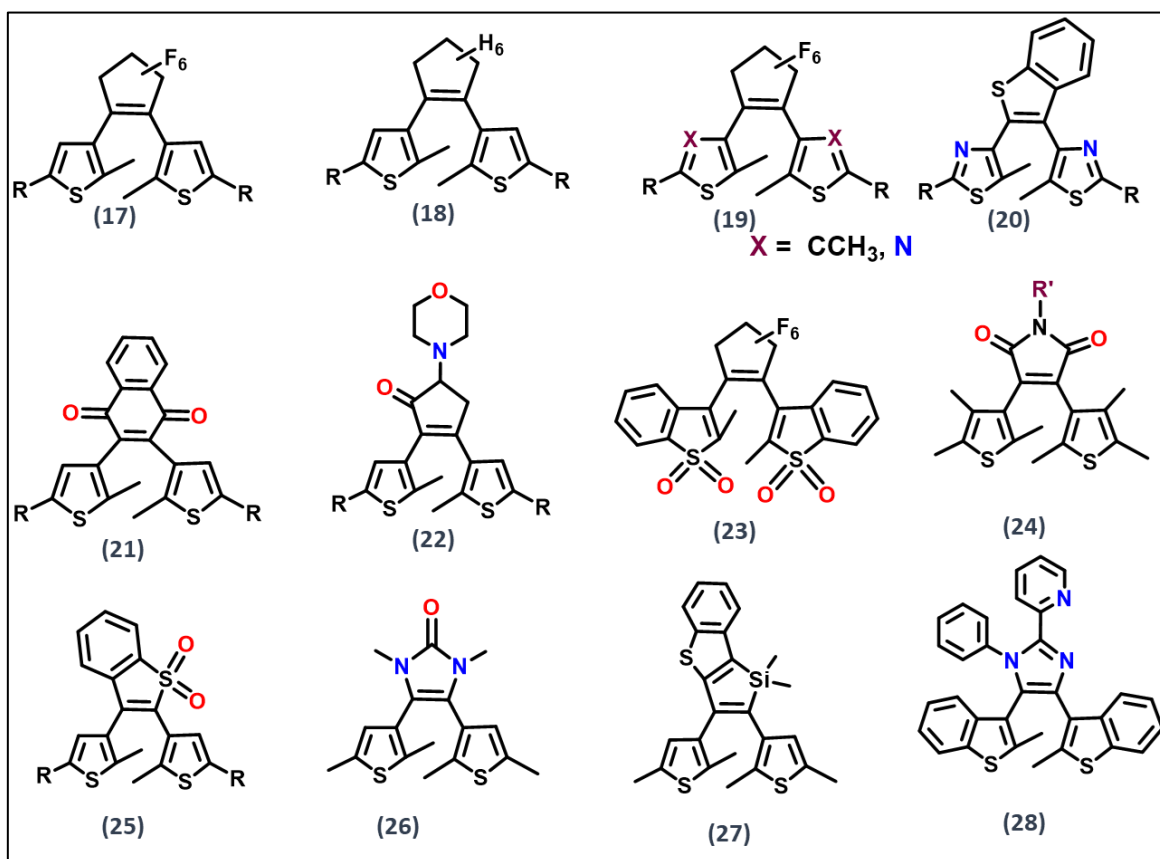


Figure 1.3. Molecular structures of diarylethene derivatives.

1.2. What is DAE/DTE?

The dithienylethene (DTE) is the most attractive class of organic molecules among diarylethene (DAE) family (29) which are capable of 6π electrocyclization reaction with the conversion of ring-closed isomer from their open-ring to their closed-ring isomers, and vice versa in presence of external stimuli like light or heat. Scientist M. Irie discovered this field in the late 90th century.²⁷ In the ring open form of DTE molecules, the conjugation is confined to the thiophene ring, whereas the π -conjugation delocalizes throughout the molecule in the ring-closed form, leading to changes in the electrical and geometrical properties of the molecule (30), as shown in Figure 1.4.

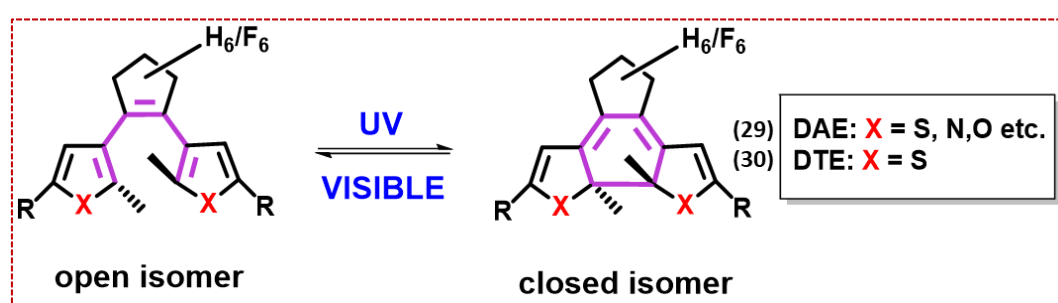


Figure 1.4. The reversible structural transformation of diarylethene under irradiation.

1.3. Theoretical background

Diarylethene photoswitches

The photochromism of DAE/DTE occurs through 6π -electrocyclisation reaction of 1,3,5-hexatriene unit and cycloreversion reaction of 1,3-cyclohexadiene core respectively. As cyclisation reaction that leads to the formation of ring closed isomer is a thermally endergonic process because the hexatriene core is a component of a tricyclic structure, which normally comprises of two heteroaromatic moieties. This implies that only the photochemical reaction pathway is possible.

Theoretically, it can be considered that, the ring open isomer can exist in two energetically comparable conformers (parallel and antiparallel).²⁸⁻³⁰ Among them, only 50% of the optically excited molecules were able to undergo the cyclisation reaction and such theoretical value has the potential to significantly improve preference for the antiparallel conformer in the ground state.³¹ Both isomers are thermally stable because the activation energy barrier for cyclisation and cycloreversion is quite large.³² Typically, the ring-open isomer shows absorption bands in the UV region due to cross-conjugated aryl moieties. Upon

excitation, the conjugated system of the closed isomer is extended across the full backbone of the molecule, producing a sharp, defining a visible region absorption band. The light-triggered photoisomerization process leads to generation of photostationary state (PSS) which strongly influences the photoreaction quantum yields value for both forward and backward processes. The DAE core frequently exhibits cyclisation yields that are one order greater in magnitude than cycloreversions, leading to conversions up to 90% in response to UV exposure.^{33,34}

1.4. Structural versatility of photochromic DAE molecules

The most fundamental structure of DAEs was discovered in the mid-1960s from detailed photochemical surveys of stilbenes and heteroaryl stilbenes leading to the formation of dihydrophenanthrene derivatives³⁵ and in the late 1980s Irie and co-workers discovered 1,2-dihetarylethenes as thermally stable photochromic switches.³⁶ The structural versatility of photochromic core DAEs is outlined in Figure 1.5, which is assembled by four building blocks: (i) a bridging moiety, (ii) hetero-aryl rings, (iii) substituents R_1 at the ring-closing carbon atoms of the DAEs, and (iv) substituents R_2 attached to the reactive carbon centre of the DAE unit.

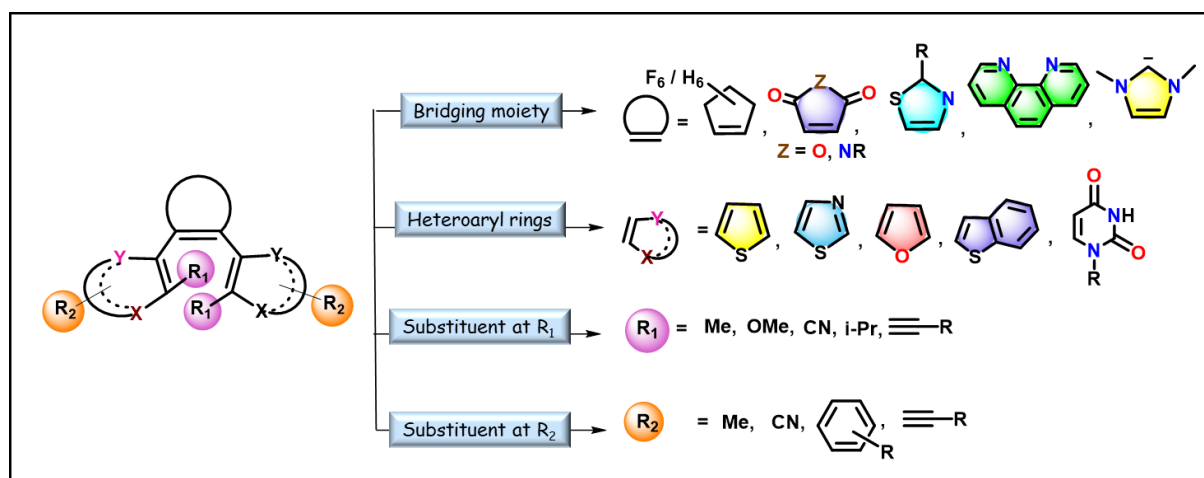


Figure 1.5. Structural versatility of photochromic DAE scaffolds.

1.4.1. Role of bridging moiety

The inclusion of central double bond into the hexatriene core mainly induces the photoisomerization reaction *via* the formation of ring open isomer and closed ring isomer. Cyclic structure prevents photochemical E/Z isomerization where the DAE derivatives were functionalised by various substituted such as maleicanhydride,³⁷ malimide,³⁸

perhydrocyclopentene, perfluorocyclopentene³⁹ and so on (as shown in Figure 1.5). Among all the DAE community perfluorocyclopentene bridge still get huge attention because of its high photoswitching efficiency and thermal stability.^{25,26,40} However, the electron densities of the core cyclopentene moieties that include perhydro and perfluoro units are surprisingly similar. This is due to the fact that these moieties experience very minor shifts in the effects of substituents and solvatochromism. It is also important to note that both types of switches had outstanding quantum yields (0.6) and high levels of photoconversion (>0.85). The key distinction is that perhydrocyclopentene molecular switches have lower photochemical and thermal stability. Due to the presence of high fatigue resistance and thermal stability of perfluorocyclopentenenes may be more appropriate for applications like data storage and memory media. Therefore, perfluorocyclopentenenes can be considered a great alternative to perhydrocyclopentenenes in general.

1.4.2. Role of the heteroaryl rings

A variety of diarylethene have been designed and synthesised by altering heteroaryl moiety on either one side or both side of ethylene bridge giving diarylethene molecules a variety of characteristics. The presence of two double bonds in the hexatriene system facilitates the disrotatory cyclisation reaction by the formation of 5-membered heteroaryl rings which is endergonic in nature. Simultaneously, it provides an absorption band for π -electronic system by absorbing light of monochromatic wavelength. To keep the photochromic reaction thermally irreversible, heteroaromatics with relatively low aromatic stabilisation energy must be used.³⁶ However, thiophene or benzothiophene rings are present in the majority of DAE compounds in the literature, additional heteroaryl structures like pyrrole, furan, imidazole, thiazole, and their benzannulated equivalents can also be employed (as presented in Figure 1.5). Interestingly, the use of an unsymmetrical substitution pattern at reactive C atoms allows the several interesting structural alterations. However, the two different heteroaryl ring at two “arms” of DAE have no effect on their photoswitchability and thermal stability. Several unsymmetrical DAEs with highly aromatic benzene and naphthalene rings or nucleosides have been reported, which are easily functionalized with DNA nucleosides.⁴¹⁻⁴³

The photochemical characteristics of DAEs are significantly influenced by the mode of attachment between bridging unit and the heteroaryl rings. When the thiophene ring is coupled with β -positions of heteroarene, specifically X = S and Y = CH, the so-called "normal type"

DAEs are produced (as shown in Figure 1.5). On the other hand, a connection *via* the α -positions ($X = \text{CH}$ and $Y = \text{S}$) produces "inverse type" DAEs with significantly differing photochemical properties.²⁷ Due to cross-conjugation between the bridging unit and two heteraryl moieties, there is no direct conjugation in the ring-open isomer of normal type DAEs. On the other hand, inverse type DAEs exhibit a substantial bathochromic shift in absorption spectra because π -electron density is highly delocalized. After cyclisation, the conjugation process is stopped, so the absorbance of the ring-closed isomer is shifted hypsochromically compared to normal DAEs.

Besides from the differentiation between normal and inverse type DAEs, no systematic studies on the dependence of quantum yields and other photochemical parameters on the basic structure of the heteroaryl moieties have been documented.

1.4.3. Role of substituents R¹ at the ring-closing carbon atoms

To prevent oxidation of the ring-closed isomer into phenanthrene analogues, substitution at the ring-closing carbon atoms is necessary.^{35a} Thus, methyl protons on the inner α -positions of heteroaryl rings in most DAEs documented in the literature. However, altering this substituent results in compounds with changing properties: because there is more antiparallel conformer in the ground state, adding a bulky substituent, like an isopropyl group, increases the quantum yield for ring closure.^{31a} As well as, thermal reversibility can also be caused by the increased steric strain, which weakens the created C-C bond.^{28-30, 44,45} or fluorine⁴⁶ on the reactive carbon atoms, which have the +M effect, considerably stabilise the ring-closed isomer, which causes a significant drop in the quantum yield for ring opening. Attaching electron withdrawing cyano (-CN) groups, on the other hand, has been demonstrated to accelerate photochemical cycloreversion.^{47,48} Thermal reversibility can also be caused by the increased steric strain, which weakens the created C-C bond.²⁸ Other derivatives show that substituents with a +M effect on the reactive carbon atoms, such as methoxy groups^{28,29,45} or fluorine,⁴⁶ considerably reinforce the ring-closed isomer, resulting in a large decrease in the quantum yield for ring opening. In contrast, it has been demonstrated that attaching electron-withdrawing cyano groups accelerates photochemical cycloreversion.^{47,48}

1.4.4. Role of substituents R² at reactive carbon atoms

A significant influence on the photochemical characteristics and thermal reversibility of DAE structures can be achieved by substitution at the periphery of these structures. In the case of DAEs of the normal type, a wide range of substituents have been added to α -positions of heterocyclic rings, which are located opposite the reactive carbons. These substituents range from straight forward methyl groups to substituted phenyl groups to nearly any type of functional group, such as chlorine, aldehydes, carboxylic acids, dicyanoethylene, or alkyne moieties.

Generally, two types of modifications can be noticed. Firstly, it has been found that strong electron accepting moieties (dicyanoethylene, N-methylpyridinium, or protonated amine groups) are present at the reactive carbon atoms that significantly reduce the thermal stability of the ring-closed isomer.⁴⁹ Secondly, as the substituent increases in the π -conjugation of the DAE backbone, the absorbance of both the ring-open and ring-closed isomers shifts to longer wavelengths, eventually allowing DAEs to operate purely with visible light.⁵⁰ However, as the ring-closed isomer stabilises by more electron delocalization the quantum yield value decreases for cycloreversion until it effectively becomes zero.^{51,52} The decreased quantum yield values is also beneficial to enhance the significant transformation from open to closed isomer. Thus, in most of the cases, DAE structures contain phenyl rings that is utilised as substituents R² in DAE structures, resulting in a one-order-of-magnitude drop in the cycloreversion quantum yield.³⁴

In addition to the precise tuning of the photochromic characteristics, the peripheral substituents typically act as an anchoring point for the enactment of a variety of chemical functions that are intended to be remotely controlled by the operation of the switch (see Section 2.2).

1.5. Why DTE over other DAE molecules?

- Dithienylethenes (DTEs) are a unique type of light responsive organic molecules, among the other photochromic molecules that are capable of rapid electrocycloisatation reaction which is reversible in nature.
- Dithienylethenes are potential candidates since they are thermally reversible in nature even at temperatures higher than 100°C and have low cycloreversion quantum yields.

Furthermore, the addition of bulky alkoxy substituents at the 2- and 2'-positions of the thiophene rings reduces the cycloreversion quantum yields.

- The thermal stability of diarylethene molecules as photo-switching units is one of their major benefits.^{32, 53-58} After performing theoretical studies, Irie et al.^{41,59} stated the factors influencing the thermal stability of diarylethene switches. They observed that when diarylethene derivatives with heterocyclic rings are exposed to light, they undergo cyclisation and cycloreversion processes between open and closed forms, but not when heat is applied.
- The photoswitching characteristics of DTE molecules also produce electrical and optical behavioral changes. These changes include UV-vis absorption, fluorescence emission, FT-IR, oxidative/reductive potentials, etc. Due to their fatigue resistance and thermal stability these switches have a wide range of potential applications in the development of optoelectronic devices like read/write memory devices with non-destructive read-out capabilities.
- The perhydro dithienylethene switches and their perfluoro analogous were attached to the 3-ethynylthiophene and phenyl-3-ethynylthiophene moiety in order to investigate the effect of increasing the π -conjugation on the optically and electrically induced cyclisation/cycloreversion processes. In addition, the thermal stability and fatigue resistance of these switches are analysed because these properties are crucial to the development of practical uses. As a potential non-destructive readout approach, their luminescent behaviour in open and closed ring forms was investigated. The incorporation of organometallic complexes onto molecular switches can result in distinctive excited state reactivity, thereby substantially influencing the photochromic and electrochromic properties of such switches.

1.6. Synthetic development of dithienylperfluorocyclopentene

There are four established strategies are documented in the literature for the synthesis of DAE's (Figure 1.6). Irie and co-workers first described the "classic" synthetic strategy for DAEs with the perfluorocyclopentene bridge, involves reacting a lithiated heterocyclic precursor with octafluorocyclopentene *via* an addition elimination mechanism (strategy A in Figure 1.6). They have synthesised halo derivative of dithienylethene (perfluoro and perhydro)

either by introducing of directly or by the incorporation of octafluorocyclopentene unit (31) to thiophene (39). As a result, the symmetric photochromic core is constructed in a single step, or the reaction is carried out in stages to access unsymmetrically substituted DAEs, *i.e.* those with varied substitution patterns on the left and right "arm." Because there are inadequate yields, the reaction can only take place with substitution patterns that are not sensitive to lithium organyls. In addition, the heterocyclic building blocks must be preassembled before the synthesis begins, which makes the process rigid. As a result, strategy A was not implemented in this piece of work (Figure 1.6).

Lucas et al.^{60,61} reported the synthesis process above, which focused mainly on the creation of dithienylethene derivatives with chlorine substituents. They created halo derivatives of dithienylethene (perfluoro and perhydro) either directly or by incorporating an octafluorocyclopentene unit into thiophene. However, similar procedures are applicable to bromo derivatives of dithienylethene with a little variation from the synthesis of DTE Br₂, requiring just substituting 5-dimethylthiophene for compound 39. However, the latter can be achieved by incorporating Mg into the final step of McMurry ring-closing reaction, as it is a stronger reducing agent due to the generation of thienyl group dechlorination products.^{60,61} The synthesis of the dithienylcyclopentenes (perfluoro and perhydro) with chlorine atoms at the 5-position of the thienyl groups is the preferred method, as it enables the switches to be functionalized in a variety of relatively straightforward ways, as described below:

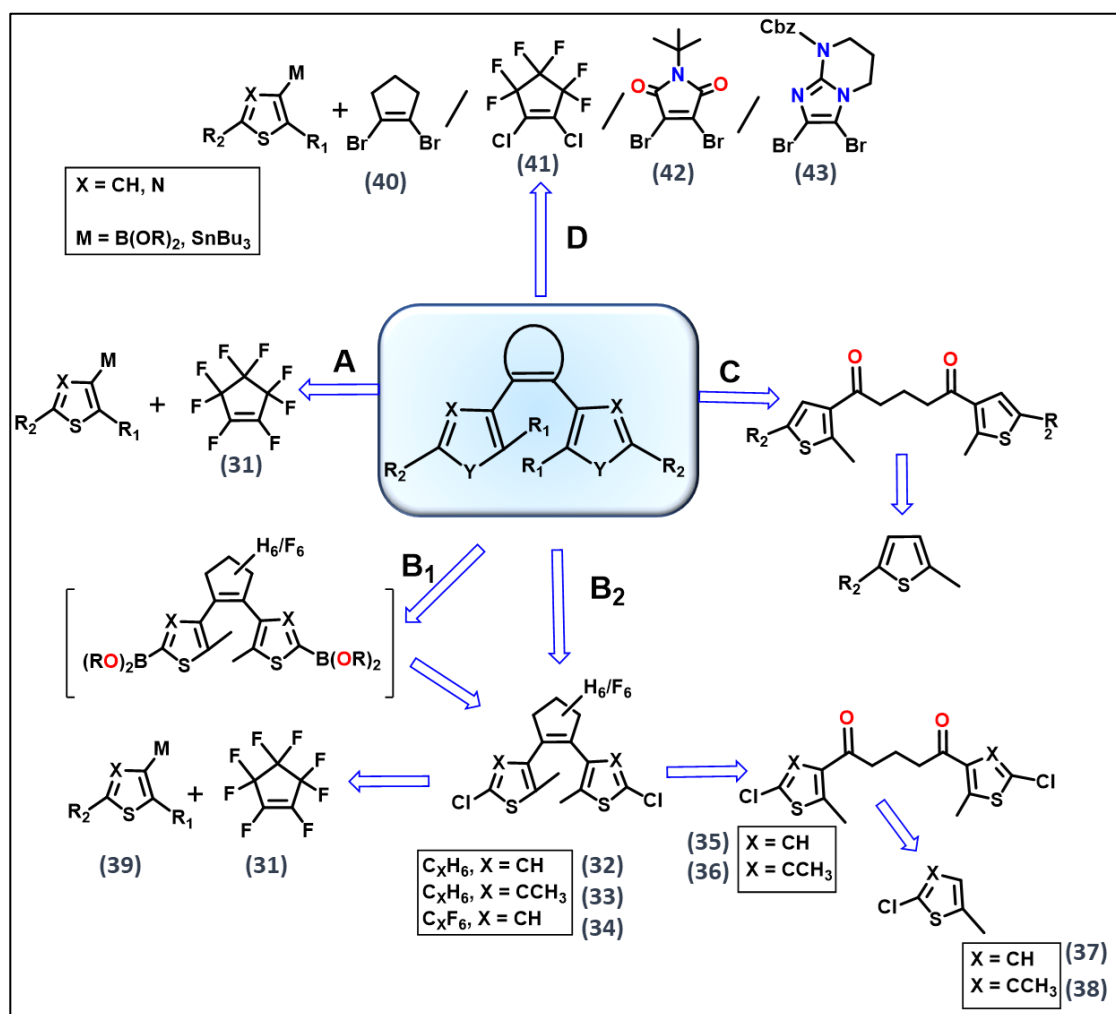


Figure 1.6. Retrosynthetic analysis of photochromic DAE molecules by different pathways.

On the other hand, Ferring's group initially proposed versatile synthetic route where 1,2-bisthiencylcyclopentene or 1,2-bisthiencylperfluorocyclopentene act as a building block and it also contains a chlorine atom at the α -position of thiophene rings (32,33,34). Further, this synthetic intermediate can be functionalised easily by the peripheral changes like chlorine-lithium exchange, transformation to boronic ester under conventional Suzuki coupling conditions, and cross coupling reaction (strategy B₁ in Figure 1.6). The unsymmetrically substituted DAEs can also be synthesised by the same procedure as described before. However, the cross-coupling step exhibits polarity reversal when α -chlorinated thiophene and an aryl boronic acid are employed as active partners. Strategy B₂ displayed the formation of bis-chlorinated perhydrocyclopentene intermediates by Friedel-Crafts acylation and subsequent McMurry coupling reaction to the formation of 1,4-diketone. One of the major drawbacks of strategies B₁ and B₂ is that this method is only applicable to thiophene ring due

to difficulties in the lithiation step. The second issue is that these methods do not allow for the inclusion of CF_3 groups at the inner α -position of thiophene rings because they would significantly reduce regioselectivity and reactivity in the Friedel-Crafts acylation. The synthesis of halogenated, CF_3 decorated heterocycles with low molecular mass proved to be challenging (see Figure 1.6).

As a modification, the Friedel-Crafts acylation and concomitant McMurry coupling were carried out on a thiophene building block to synthesise the corresponding DAE derivative (method C), which is a variation of techniques B₁ and B₂. While technique C generally cannot be employed because substituted thiophenes have weak Friedel-Crafts acylation regioselectivity, it has been done in the instance to take advantage of the high yielding oxidative cross coupling between 2-methylthiophene and pentafluorobenzene.

In order to modify the bridging unit as well as in situations where strategies A-C cannot be used, the cross-coupling reaction between a dihalogenated bridging moiety and hetaryl boronic esters or Sn derivatives must be used (strategy D). It is altered by the addition of sensitive functional groups, the use of thiazoles as heterocycles, or the substitution of CF_3 at the ring-closing carbons. Cross couplings have been performed on 1,2-dibromocyclopentene (40),⁴³ 1,2-dichloroperfluorocyclopentene (41),^{62,63} 3,4-dibromo-N-tert-butylmaleimide (42),⁶² Cbz protected 8,9-dibromo-1,5,7-triazabicyclo[4.3.0],⁶⁴ and 8,9-dibromo-1,5,7-triazabicyclo[4.3.0]-nona-6,8-diene (43). Lithiation reactions can be used to create the precursors of the heteroaromatic organoboron and organotin. When accessible organolithium intermediates are not available, the Pd catalysed Miyaura borylation can alternatively be employed to produce boronic esters.^{65,66}

For the synthesis of DTE derivatives, several methods have been reported; a few of them are briefly addressed in the section below.

Method 1

M. Irie, the pioneer of organic photochromic molecule DTE, described the synthetic procedure of dithienylperfluorocyclopentene derivatives by a lithiation reaction using *n*-Buli under cold conditions (0°C to -78°C), followed by a substitution reaction with octafluorocyclopentene (Figure 1.7).

- At first, to synthesize bromo derivative of thiophene *via* a bromination reaction, an acetic acid solution of 2-methylthiophene was treated with bromine at 0°C.

- Then, at -60°C , 44 was lithiated by dissolving in ether and stirring overnight by adding *n*-butyllithium. At room temperature, water was added consequently to replace the lithium at the 5-position, resulting 45.

- Finally, 45 was then subjected to another lithiation reaction under the same conditions in THF medium, followed by a reaction with perfluorocyclopentene and yielding 1,2-bis(2,4-dimethylthiophen-3-yl) perfluorocyclopentene (46).

Method 2

There are certain drawbacks with the **method 1** of synthesising dithienylperfluorocyclopentene.

- The yields are moderate since a considerable proportion of the monosubstituted product is formed.
- Owing to its high volatility (bp. $26-28^{\circ}\text{C}$), octaperfluorocyclopentene is difficult to handle effectively.
- Also, octafluorocyclopentene is very expensive.

As a result, Lucas et al^{60,61} established a different synthetic approach with less expensive starting materials which are economically controlled and also produce greater yields.

In order to get the photochromic molecule DTE in a different pathway, first, they tried the Friedel-Crafts acylation reaction of 2-methyl-5-chlorothiophene using hexafluoroglutaryl dichloride and AlCl_3 in benzene or toluene following the previously documented procedure, however, the acylium intermediate was not successfully formed, which was most probably due to the presence of electron withdrawing fluorine atomsinterfered with the formation of the acylium intermediate. Therefore, in order to achieve the appropriate diketone second approach was developed by using an acid-catalysed esterification procedure (as illustrated in Figure 1.7).

There were several factors that are needed to be considered. Acylation reaction takes place at 3-position of thiophene ring, though, the 2-and 5-positions are more reactive (as described in Figure 1.7). Therefore, it is crucial to use only a thiophene ring which is already substituted at 2 and 5 positions. In order to use additional derivatization, it is also crucial that the final dithienylcyclopentene molecule have functionality. The halogen group on methyl substituted thiophene compound may play a function, when, bromothiophenes are used, acylation occurs at the 2-position and the bromine substituent is transferred to the 3-position.

Since iodine and chlorine are known to react similarly, Lucas and co-workers⁶⁰ employed a chlorine substituent. By reacting 2-methylthiophene with N-chlorosuccinimide in benzene and acetic acid, 2-methyl-5-chlorothiophene was produced.^{60,61} Using Br₂ in chloroform, 5-chloro-2-methylthiophene underwent a bromination process at the 3-position to produce 5-chloro-3-bromo-2-methylthiophene, which was then used to create the dithienyl-1,5-diketone. It was created to make sure that the bromine at the 3-position, rather than the chlorine at the 2-position, would exchange with the lithium during the subsequent lithiation reaction using *n*-BuLi in diethyl ether at -78°C. Diethyl hexafluoroglutarate was added to the reaction mixture after step 5 was lithiated at the same temperature, producing 1,5-bis(5-chloro-2-methyl-3-thienyl) pentafluorodione (47). The McMurry coupling reaction was then performed to close the ring by adding 6 to a 40 °C solution of THF containing zinc and TiCl₃ (THF)₃. 1,5-bis(5-chloro-2-methyl-3-thienyl)cyclopentene (48) was produced *via* column chromatography-based purification.

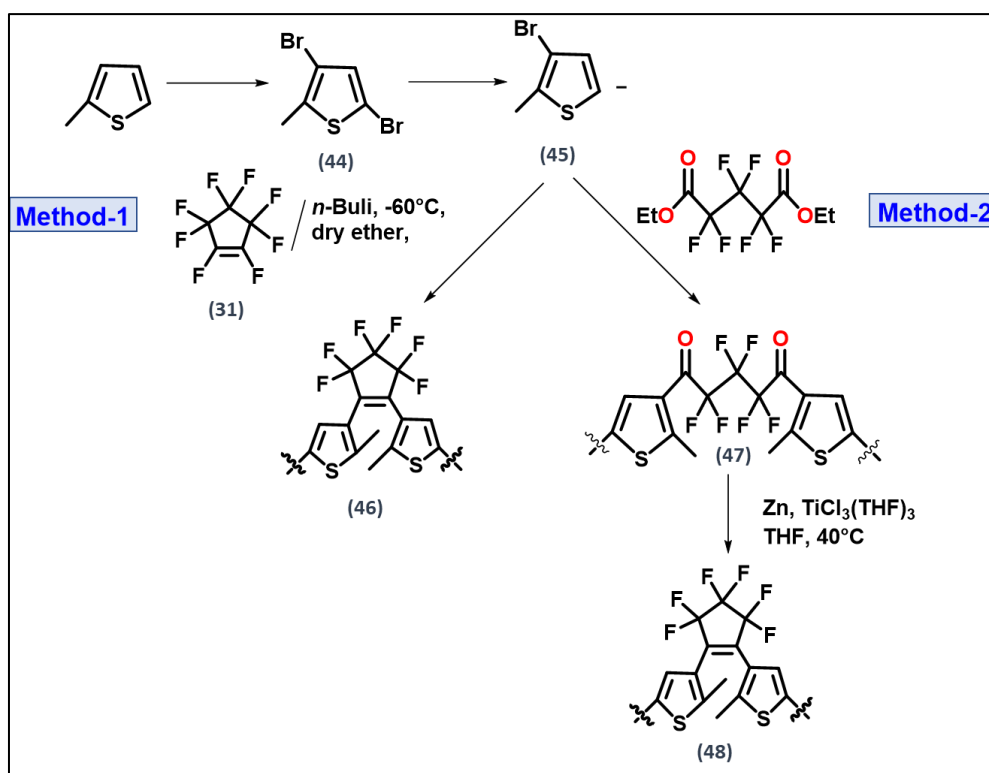


Figure 1.7. Synthetic procedure of DTE core (46 and 48).

1.7. General structure-property relationships of DTE

Conformational isomers

The open isomeric form of dithienylethene exists in two conformations: a parallel (inactive) $(49_{\text{open}})_{\text{parallel}}$ and an anti-parallel (active) $(49_{\text{open}})_{\text{anti parallel}}$ conformation. Diarylethenes undergo photoisomerization between a 1,3,5-hexatriene and a 1,3-cyclohexadiene core primarily through the 6-electrocyclisation and cycloreversion reaction, which proceeds disrotatorily when carried out thermally and conrotatory manner after photochemical excitation in accordance with the Woodward-Hoffmann rules for the conservation of orbital symmetry.⁶⁷ Since the thermal cyclisation of the hexatriene core to the disrotatory ring-closed isomer (49_{closed}) is an endergonic process due to the tricyclic structure typically containing two (hetero) aromatic moieties, only the photochemical reaction path is available (Figure 1.8). The cyclisation reaction can only take place in an anti-parallel conformer. The predicted quantum yield for the cyclised product is typically 0.5 due to the quick interconversion between these two conformers.^{33,34} However, it has been discovered that when bulky metal complexes are added to the dithienylethene structure, the anti-parallel conformation is preferred because of steric repulsion between the substituents.³¹ As a result, the quantum yield for the cyclisation reaction increases.

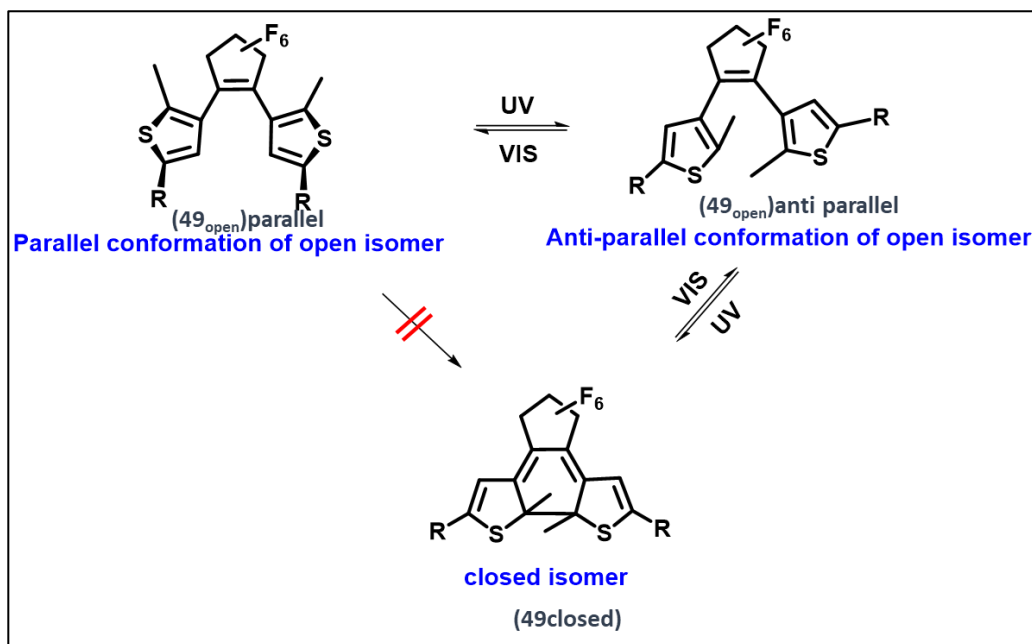


Figure 1.8. Parallel, anti-parallel conformers open and closed isomer of dithienylethene (DTE).

1.8. Photophysical and Chemical characterisation of DAE/DTE molecules

Photochromic organic molecules DAE/DTE are intelligent molecular systems that are designed to bring about the appropriate functions in response to environmental changes; they are crucial for the development of smart materials. Photophysical and photochemical studies are crucial for defining the photochromic state of DAE/DTE molecules. The well-known method for determining their photochromic states is briefly described here:

1.8.1. Photochromism

Photochromism is a phenomenon that is mainly used to describe the reversible switching of a molecule triggered by light.³² As a photochromic molecule, DAE undergoes a photoisomerization process, changing from their colorless open-ring isomer to their colored closed-ring isomer when exposed to monochromatic UV/visible light or vice versa (described in Figure 1.8). Therefore, researchers have synthesised a novel class of organic photochromic compounds (open and closed isomer) that are distinguished by different ways based on this intriguing photoswitching phenomenon of DAE derivatives. It is also established that, photoconversion is more facile in solution state as compared to solid or aggregated form.

1.8.2. NMR

Theoretically, two conformers of the open-ring isomers were distinguished by ¹H NMR which is first proposed by Nakamura et al.⁵⁶ The methyl protons connected at the 2-position of thiophene rings have a strong effect on chemical shift. In the anti-parallel conformer, the two methyl groups face the ring; therefore, the ring current imparts a strong magnetic field onto the methyl protons, leading to a peak in range 1.70-2.20 ppm in the ¹H NMR spectrum. Whereas, in the case of parallel conformer, this magnetic field effect is not applied, and the peak of methyl protons is moved to downfield range from 2.16-2.25 ppm,⁵⁶ however, the parallel and anti-parallel isomers are fluxional in nature. Therefore, both conformers (parallel and antiparallel) transform to each other within very fast time-scale, even at -90°C, and shows only one ¹H NMR signals. In contrast, the sterically hindered substituents are affixed to the dithienylethene moiety, which inhibits the rotation of the thienyl groups, resulting in two distinct sets of ¹H NMR signals for the two open-ring conformers. On the other hand, during photocyclisation the chemical shift values for thiophene proton at the 4-position are shifted

upfield (~0.4 - 0.8 ppm) and the methyl group protons are shifted downfield (~0.03 -0.27 ppm) due to loss of aromaticity (Figure 1.9a).

1.8.3. HPLC

For elucidating the photodynamic behaviours of open and closed isomers of DAE derivatives, HPLC analysis is crucial. Upon illumination with light, an HPLC chromatogram was recorded, and isomers can be easily isolated. At photostationary state (PSS), HPLC showed the conversion ratio, as determined by irradiation with monochromatic (UV/Visible) light (Figure 1.9b).

1.8.4. UV-vis absorption Spectra

The ring open isomers of DAE are normally colourless, however the ring closed isomer can exhibit a variety of colors, including yellow, violet, blue, red, and others, depending on how the molecules of the diarylethene switch are put together.^{54,58} The absorption bands of the open rings generally emerge in the UV region at wavelengths ranging from 240-350 nm. On the other hand, the brightly colored closed isomers result in the appearance of new absorption bands in the visible range. Therefore, absorption spectral change from UV to visible region indicates that both ring-opening and ring closing takes place by photoirradiation and reached saturation point at PSS state.^{60,68} However, it can be predicted that at PSS state the quantum yields value for diarylethenes revealed that cyclisation (ring-closing) is a more effective process than cycloreversion (ring-opening).⁶⁰

Furthermore, when ring-open diarylethene derivatives are changed to the closed state after being exposed to UV light, the subsequent changes in the UV-vis spectra can be exploited as the "read-out" purpose in memory media. Diarylethene derivatives are an excellent candidate for its photo-switching application with noticeable changes in the UV-vis absorption spectra and color. Therefore, the photoactive samples in the vicinity of these absorption bands induces cyclisation/cycloreversion processes and erased the stored data.^{40,54}

1.8.5. Electrochemical properties

Electrochemical investigations utilising cyclic voltammetry demonstrate that the DAE-based electronic system undergoes a strong alternation during isomerization, from isolated

aromatic cores containing ring-open isomer to highly conjugated molecular backbone of ring-closed isomer. The ring-open isomer is often oxidised and reduced at substantially greater positive or negative potentials than the ring-closed isomer, due to lowering of the HOMO-LUMO gap during cyclisation (Figure 1.9c).³⁴ An interesting feature of most of the DAE structures is that the photoisomerization process not only triggered by light but also there is a possibility of electrochemical transformation *via* oxidation/reduction.

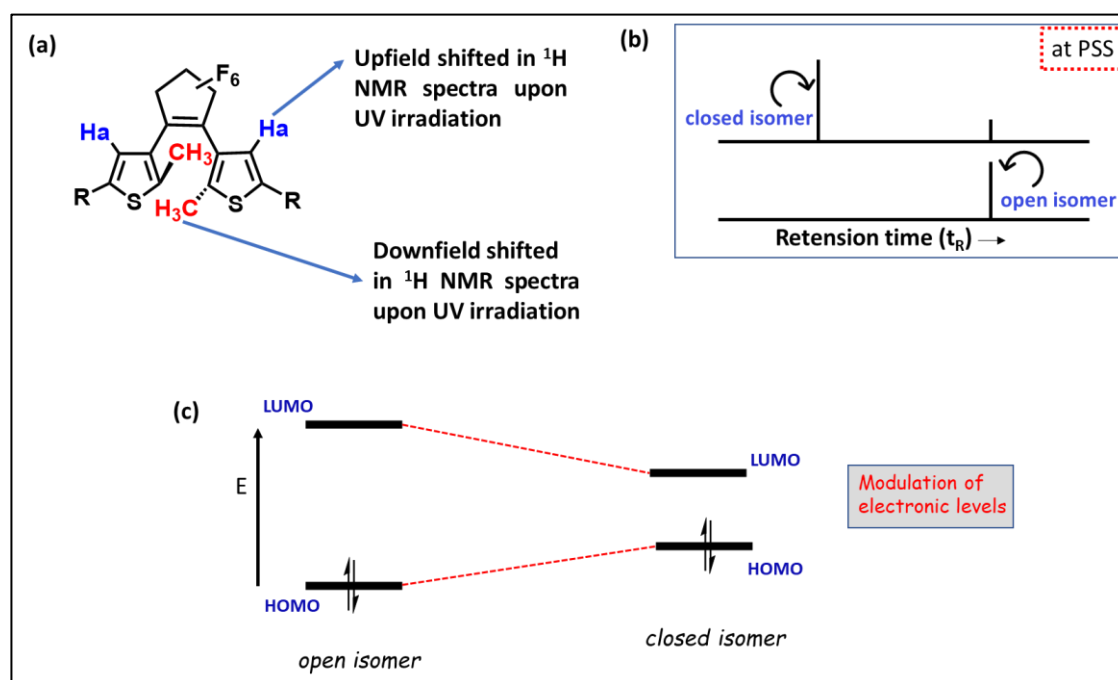


Figure 1.9. Photophysical and electrochemical characterisation for photoisomerization reaction of DTE molecules.

1.8.6. Fluorescence

Most of the diarylethene-based molecules were in the open-ring form and they emitted a lot of fluorescence. However, it has been observed that when exposed to UV light, the fluorescence intensity tends to diminish.^{58,69,70} The fluorescence intensity difference between open and closed forms is reversible, as once the closed ring form is exposed with visible light, the ring open form is regenerated. Therefore, it may conclude that the open-ring isomer is in the "ON" state while the closed-ring isomer is in the "OFF" state and this "OFF" state is further reverse back to "ON" state. The benefit of this method is that fluorescence behavior may be induced using monochromatic UV/visible light irradiation, which limits the occurrence of cyclisation and cycloreversion processes and reduces the recorded information. Due to their

sensitivity, resolution, and high contrast, reversible changes in luminescence are highly beneficial for non-destructive optical read-out devices.^{40,54}

1.8.7. Dual change in Electrochemistry/Photochemistry

Dual combination of electrochemical and photochemical switching processes of open and closed form of diarylethene switches can be employed for write, read, and erase data in memory systems. In the beginning, the information can be "written," and this information can be "readout" by either photochemically or electrochemically changing the open-ring isomer into the closed isomer. The information can be "readout" in a way that is not destructive by monitoring the first reversible oxidation of the closed form at a voltage at which the open form is electrochemically inert. This is the only condition under which this is possible. After that, the information that was stored can be removed from memory by photochemically or electrochemically converting the closed-ring isomer back to its open-form counterpart.⁷¹

Beside the characterisation of open and closed isomeric form of DAE in various way like NMR, HPLC, UV-visible absorption spectra, electrochemically and so on, DAE derivatives have several photophysical properties (such as Fatigue resistance, thermal stability, etc) which are briefly discussed below.

1.8.8. Fatigue resistance

According to Irie,⁷² these switches have a limited photostability and the main way for decomposition processes is happen from the excited state of the closed form. Based on investigations, the perhydro-based switch has strong fatigue resistance after several successive photocyclisation and photocycloreversion operations, but the perfluoro-based molecules' photostability was discovered to be 2-3 times higher (Figure 1.10a).^{60,68} Diarylethene (DAE) and its derivatives undergo photochemical redox reactions when exposed to the light of a specific wavelength, changing from their colorless open-ring to their corresponding closed-ring isomers. The photogenerated closed-ring isomeric form is thermally stable at ambient temperature, however the reverse process occurs only when exposed to visible light; both isomers have high fatigue resistance.

1.8.9. Thermal Stability

As previously stated, one of the major benefits of utilizing diarylethene molecules as photo-switching units is their temperature stability.^{32,40,54,55,56} After conducting theoretical research, Irie et al^{72,73} elucidated the factors affecting the thermally stable characteristics of diarylethene switches. They observed that diarylethene derivatives with heterocyclic rings can only change between their open and closed forms through cyclisation and cycloreversion when they are exposed to light and not when heat is used (Figure 1.10b). When phenyl rings are used instead of heterocyclic rings, however, the cycloreversion process can be started by both heat and light. This shows that the six-membered ring's closed form is less stable than the five-membered ring's closed form. In order to find out more about the result, they performed some theoretical calculations to look at how the ground states of the open and closed ring isomers differ in energy. A correlation diagram showed that the difference between the open and closed ground states is related to the energy barrier of the cycloreversion reaction. This means that the lower the energy barrier for cycloreversion, the larger the difference between the open and closed ground states. Since the phenyl ring transition has a substantial ground-state energy difference and a tiny reaction energy barrier, cycloreversion is anticipated to happen readily. However, when the phenyl groups were substituted to furyl or thienyl ones, the diarylethene moiety's ground-state energy difference dropped. This decrease was followed by a rising reaction energy-barrier. The closed-ring isomer of DAE derivatives are therefore more stable than their open-ring isomer, and a thermally induced cycloreversion reaction is not anticipated to happen frequently.⁷³ The aromatic nature of the substituent can be used to explain the variations in thermal stability between these diarylethene derivatives. The highly aromatic phenyl group produced the largest difference in ground-state energy. As a result of conjugated electron migration, this energy difference decreased when five-membered rings with less aromatic character supplanted the phenyl groups. When the closed-ring isomer is made by cyclisation, the aromatic ring is destroyed, which makes the system less stable and raises the ground-state energy. So, adding aryl groups that have low aromatic stabilisation energy can make diarylethene switches more stable at high temperatures.^{72,73}

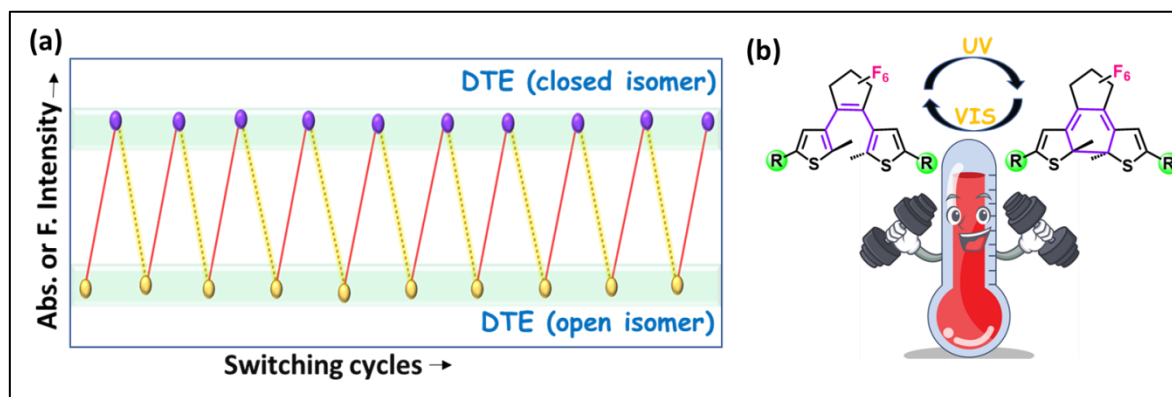


Figure 1.10. (a) Fatigue recyclability and (b) thermal stability of DTE molecules.

1.9. Functionalisation of DAE/ DTE molecules

The above-mentioned synthetic techniques by Lucas et al.^{60,61} concentrated on the production of dithienylethene switches with chlorine substituents, however, these procedures can be slightly modified to produce 1,2-bis(2,5-dimethylthien-3-yl)cyclopentene or 1,2-bis(2-methylthien-3-yl)cyclopentene. The synthetic protocol for functionalisation of DAE/ DTE (perfluoro and perhydro) molecules with chlorine atoms at the 5-position of the thienyl groups is described below and it can be functionalized in several different ways by several different processes.

1.9.1. Lithiation Reactions

The chloro derivative of DAE/DTE can undergo lithiation reaction easily, where chlorine/lithium exchange takes place in presence of *n*-BuLi. This highly reactive lithiated intermediate further reacts with several readily available reagent and formed various functionalised products, as illustrated in Figure1.11.

- ✓ The reactive lithiated intermediate reacts with DMF, a dialdehyde derivative of DAE/DTE is formed (50).^{60,61}
- ✓ The DAE/DTE diacid derivatives are formed when CO₂ (solid or gas) is added to the lithiated DAE/DTE (51).⁶⁰
- ✓ Lithium/iodine exchange is produced when iodine is added to a molecule that has been doubly lithiated, resulting in an iodine substituent being placed at the 5-position on each thienyl group (52).²⁹

1.9.2. Cross-Coupling Reactions

Irie and co-workers also synthesised various DAE/DTE functionalised molecules (50-57) by the cross-coupling reaction upon interaction of substituted diarylethene with the modified substrates. Increasing the aromaticity of dithienylcyclopentene switches is a subject of considerable interest. For this purpose, a variety of cross-coupling processes, including Sonogashira coupling, Suzuki coupling, and Negishi coupling, can be used (Figure 1.11).⁷⁴⁻⁷⁸ The following literary results are reported using such methods:

1.9.2.1. Sonogashira Coupling

The addition of alkyne substituents to the 5-position of the DAE/DTE thiophenes led to the sonogashira reaction. Standard sonogashira conditions were followed, which included the addition of alkyne derivative to a mixture of THF, diisopropylamine, CuI (act as a co-catalyst), Pd(PPh₃)₂Cl₂ and amine (as a base).⁷⁹⁻⁸² After stirring the reaction mixture at room temperature to 65°C, the pure TMS protected product was obtained which readily deprotected upon addition of NaOH in MeOH/THF to form alkyne derivative of DAE/DTE (55).

1.9.2.2. Suzuki Coupling

The carbon-carbon bonds are formed by Suzuki cross-coupling reactions where, organohalides are used as a reactant that reacts with organometallic compounds of transition metal.⁷⁴ Tsivgoulis and co-workers⁸³ reported the functionalization of a diarylcyclopentene by modifying the conditions of the Suzuki coupling reaction. In most the cases the Suzuki coupling reactions progress *via* three important steps: (i) oxidative addition, (ii) transmetalation, and (iii) reductive elimination.^{74,76,77} By dissolving DTE(H)₂ in diethyl ether, adding n-butyllithium, and then adding B(nOBu)₃, boronic acid derivative was produced. In the presence of Pd(PPh₃)₄, ethylene glycol, and aqueous Na₂CO₃, in THF, under reflux, the resultant boronic acid derivative further loses boron and continues to react with 2-bromothiophene. The DTE functionalised Suzuki coupling product (54) was successfully synthesised using this synthetic approach.

1.9.2.3. Alkyne-alkyne coupling

The reaction of two terminal alkynes in the presence of Cu(I) catalyst and TMEDA has resulted in the alkyne-alkyne coupling reaction. The reaction mixture was stirred at room temperature for 1h, and the product (56) was successfully formed.

In addition to the coupling reactions mentioned above for functionalizing DAE/DTE derivatives, several other techniques to synthesise symmetrical or unsymmetrical DAE/DTE derivatives have also been reported (57). These includes Friedel-Crafts alkylation, Knoevenagel condensation, Wittig reaction, amidation reaction, click reaction, and others.

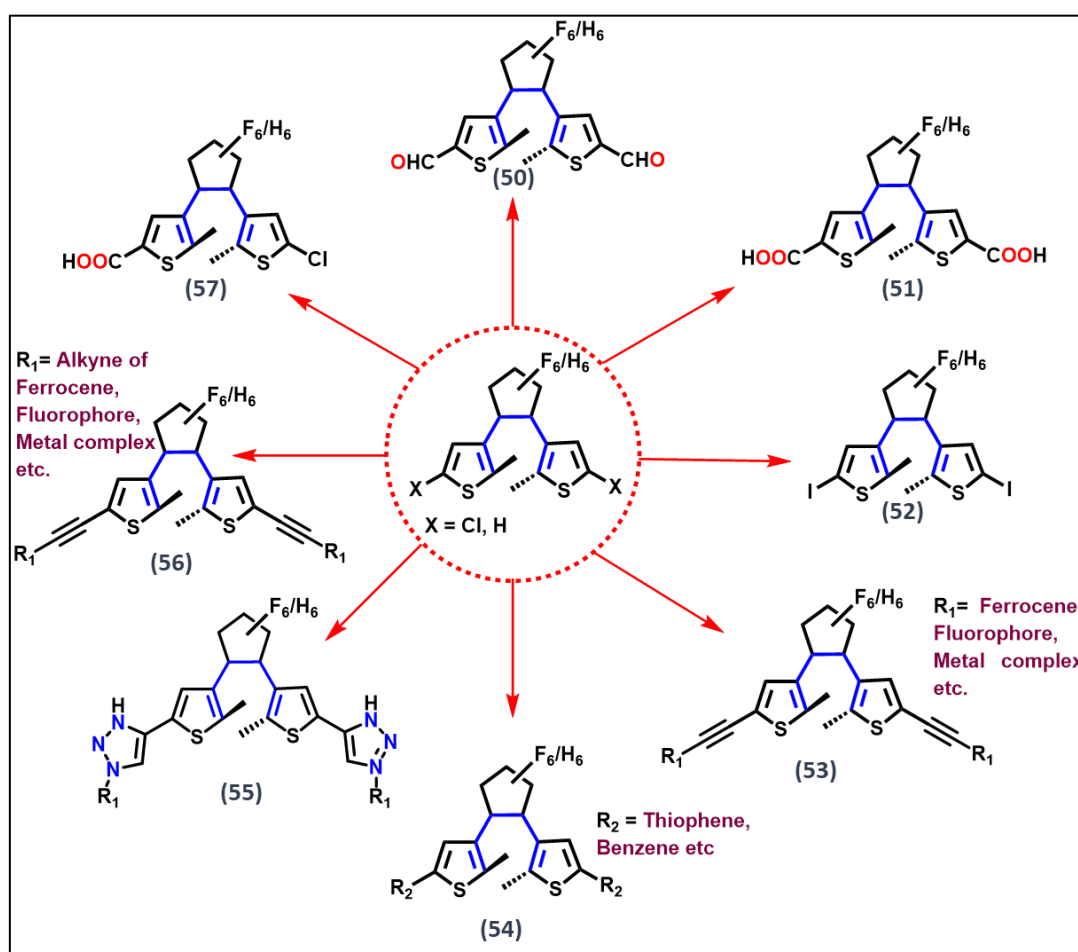


Figure 1.11. Functionalisation of DAE derivatives by various coupling reaction.

1.10. Applications of Dithienylethene (DTE) derivatives

Dithienylethene compounds have a switching behavior that is promising for application in molecular switches, single-molecule fluorescence, molecular wires, and non-destructive high density data storage devices because it is fatigue resistant, and thermally stable with a rapid response time.^{40,54,56, 69, 61, 68,84} The major alterations in the data produced from the following analytical techniques like UV-vis absorption, fluorescence emission, infra-red spectroscopy and electrochemistry, can be used to track the switching properties of dithienylethene.

In the past few decades, several diarylethene based photochromic families are developed, their photoswitching performance and photo-physical properties are monitored either in solution or solid state, by above-described techniques. Apart from this, the photochromic molecules have attracted great interest to scientific community for their potential application ranging from material chemistry to biological science.⁸⁵⁻⁸⁸ It also played an important role for the fabrication of optoelectronic devices (e.g., wave guide, sensors, memory device, energy storage), security technology and many more (Figure 1.12).⁸⁹⁻⁹³ Here, the application of diarylethene based photochromic molecules in various fields have been briefly discussed.

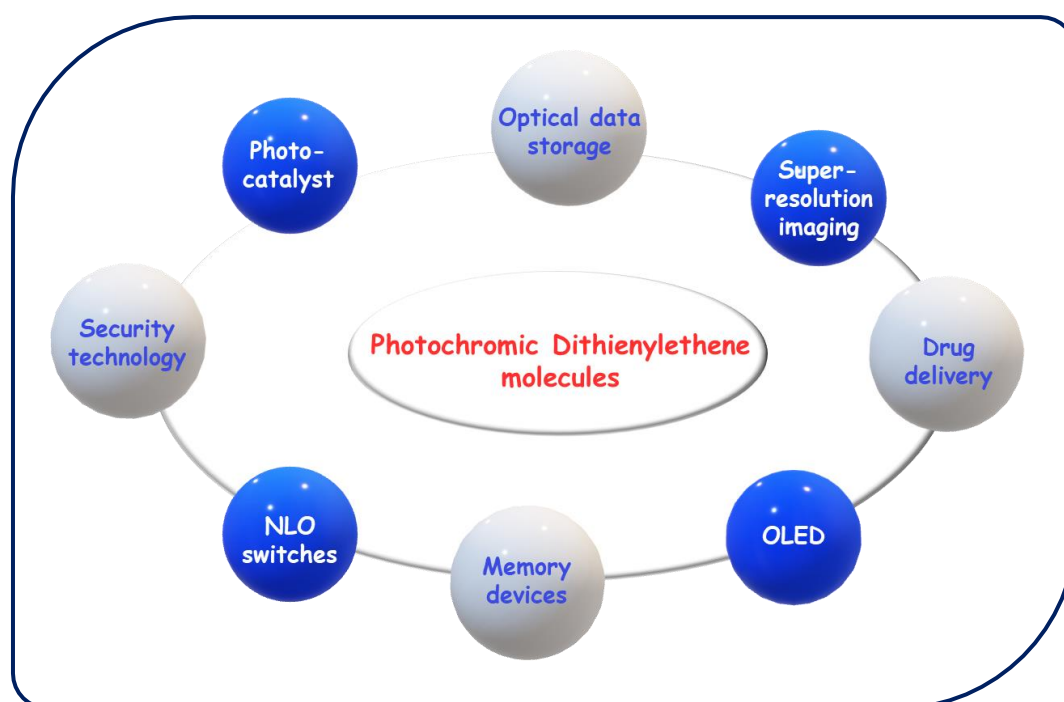


Figure 1.12. Applications of DAE/DTE molecules.

1.10.1. Optoelectronic devices

Photochromic materials are special class of molecules that undergo photoreversible isomerization between a pair of isomers with distinct properties, and they serve as excellent tool for application in opto-electronic devices because it permits remote control of their properties *via* exposure to monochromatic light and/or other external stimuli.⁹⁴ Several diarylethene-based molecules (58-60) have been used to promote the construction of optoelectronic devices, as shown in Figure 1.13.⁹⁵⁻⁹⁷

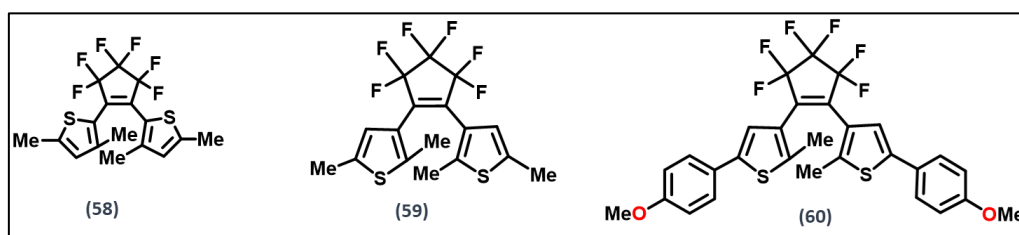


Figure 1.13. Photochromic (DAE based) materials application in opto-electronic devices.

1.10.2. Memory device

The photochromic switches are used in erasable memory media, where both photochromic states may be identified in a read-out event easily and non-invasive manner. Typically, UV/vis absorption spectroscopy is used to record the spectral variations near the absorption bands corresponding to the two photochromic states during the read-out process. Therefore, sampling around these photoactive absorption bands invariably results in partial switching of the photochromic compound and wipes out the recorded data. Over the past few years, a significant effort has been made to discover novel molecular systems and to achieve non-destructive read-out capabilities (61-63). Recently, a novel photochromic molecule bis(thienyl)ethene–phthalocyanine hybrids (63) has been reported by Tian et al, which has received more attention because it acts as a promising candidate for direct non-destructive read-out memory devices (Figure 1.14).^{98,99}

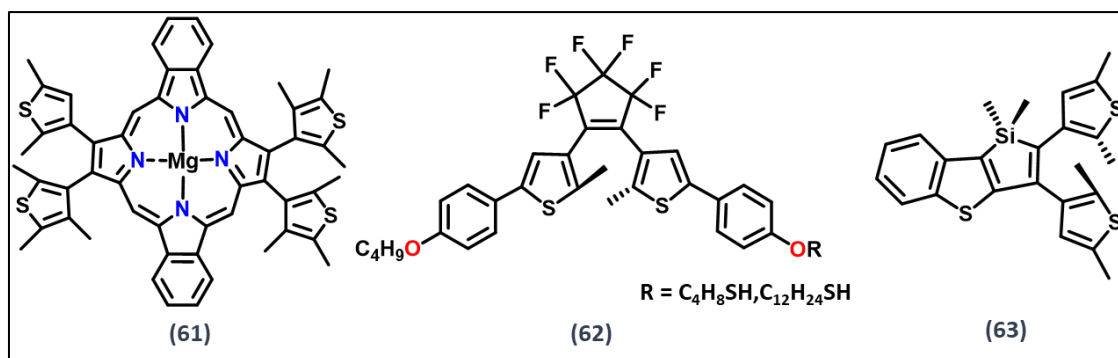


Figure 1.14. DAE based photochromic switches and their application in memory media.

1.10.3. In security technology

Counterfeiting and copying security papers including money, passports, banknotes, diplomas, and certificates is a global problem that costs corporations, governments, and billions of customers. Therefore, one of the major concerns is that DAE derivatives have potential for applications in high security authentication systems. As depicted in Figure 1.15, the distinct chemical structures (64-67) of the synthesised diarylethene derivatives resulted in various electron resonances in a conjugated colored closed isomer under UV illumination. The prepared erasable ink was used to print on cellulosic paper to produce one-color and the color completely erased after the irradiation of visible light (Figure 1.15). The ability of the recently developed anti-counterfeiting inks to repeat printing and erasing cycles repeatedly is their most significant advantage.^{100,101}

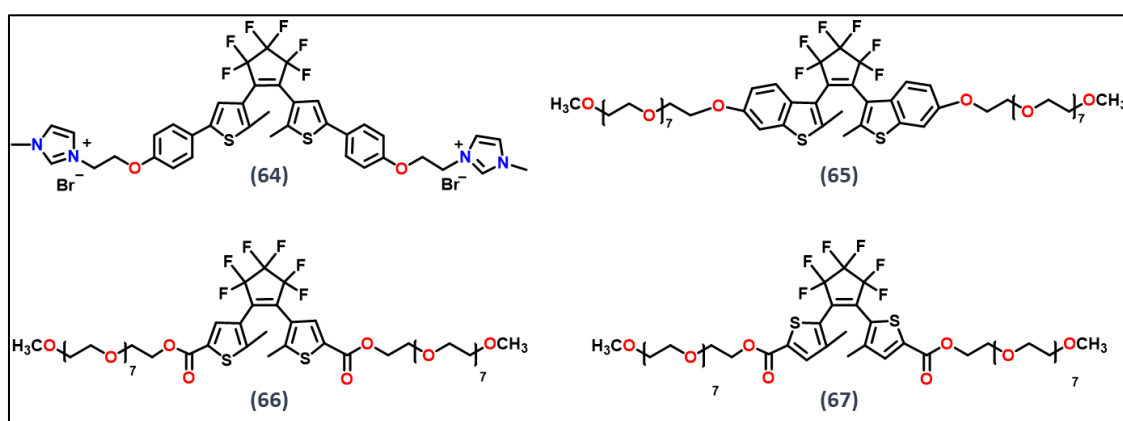


Figure 1.15. Chemical structure of diarylethene derivatives and their application in security technology.

1.10.4. Organic light-emitting diodes (OLED)

The DAE based π -conjugated molecules and polymers offer tremendous functional and financial potential toward high performance in electronic and optoelectronic devices. These include organic light-emitting diodes (OLEDs), which can be produced in an economical and energy-efficient manner. Recently, OLEDs with a DAE-functionalized ITO electrode were developed (68-71) (Figure 1.16) and then their I–V electrical characteristics were studied after several alternating illumination cycles by UV and visible light (71).¹⁰²⁻¹⁰⁴

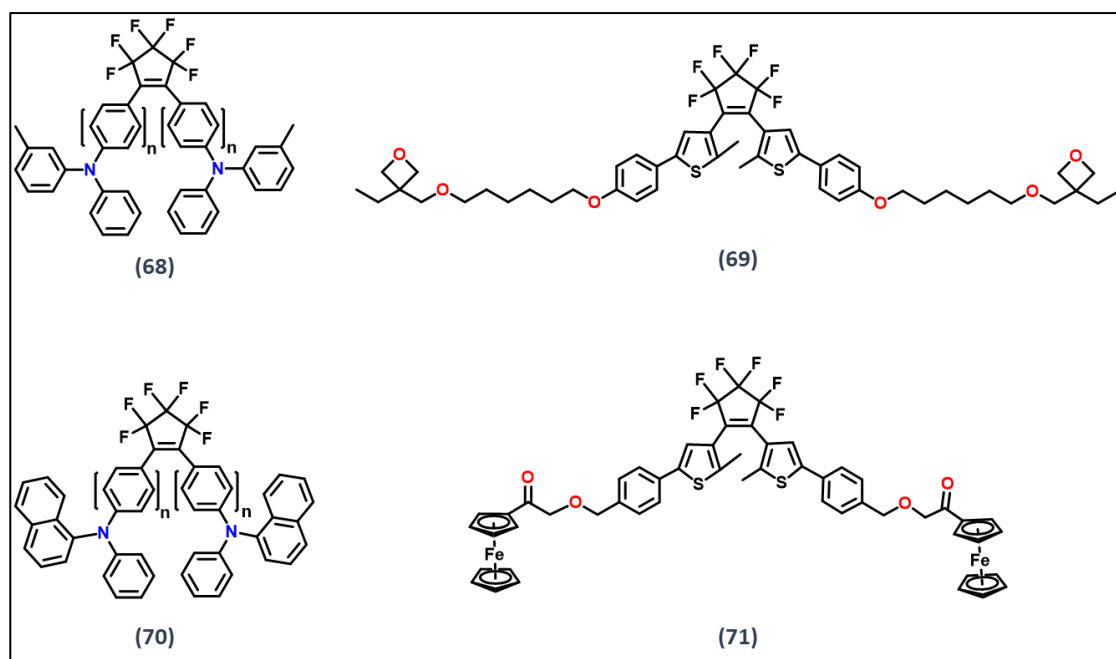


Figure 1.16. DAE functionalised molecules application for organic light-emitting diodes (OLED).

1.10.5. NLO (Non-linear optical) switches

Metal-coordinated dithienylethene (DTE) backbone has attracted the attention due to wide range of applications. The reversible switching of an NLO response has been achieved by a Zn^{2+} bipyridyl complex bound to a DTE core (72). On the other hand, the monitoring of the quadratic NLO properties has been carried out using a Cu^+ bipyridyl complex (73) with an appended DTE moiety (Figure 1.17). Furthermore, the use of light for controlling the second-

order NLO properties of molecules is intriguing since it leads to all-optical molecular materials where light is utilised to read, write, and store information.^{105,106}

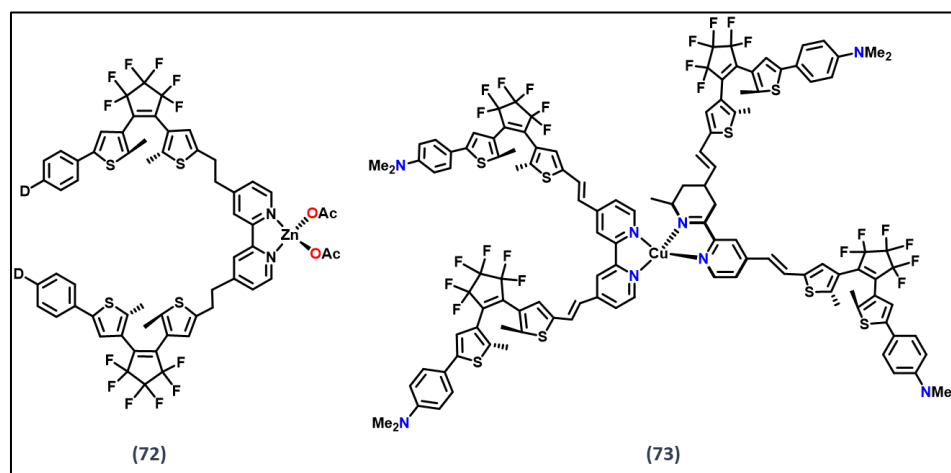


Figure 1.17. Metal co-ordinated DTE based NLO switches.

1.10.6. Drug delivery

Several peptides with DAE derivatives have been developed recently and are being used as therapeutics. In photopharmacology, developing peptides with photoswitch modifications (peptidomimetics) is a promising strategy. Target selectivity, favourable pharmacokinetics, low immunogenicity, and relatively inexpensive production costs are all advantageously combined by peptides (Figure 1.18). They are easily accessible through solution and solid phase peptide synthesis and can be developed to mimic naturally occurring peptidic ligands or to prevent crucial protein-protein interactions (74,75). Therefore, light sensitive peptides molecules contain photoisomerisable fragments which seem to be connected via covalent modification.¹⁰⁷⁻¹⁰⁹

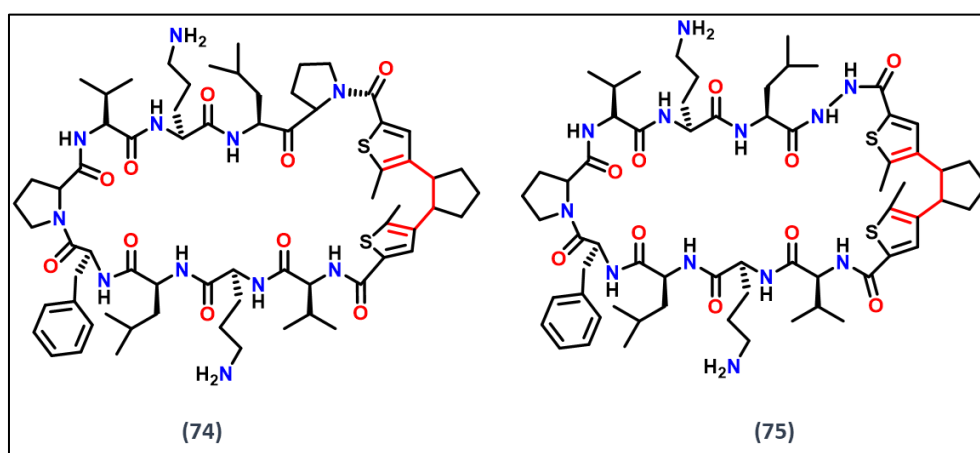


Figure 1.18. DAE based biologically active molecules.

1.11. Benefits for the incorporation of organometallic unit

The organometallic substituents are attached to thiophene rings of dithienylethene compounds can have a significant impact on the electrochemical and photophysical behavior of photochromic molecules. Therefore, by modifying the metal centres, it is possible to tune these characteristics, which has several benefits for the applications of dithienylethene switches.^{110,111}

Among various organometallic compounds, ferrocene is one of the well-known organometallic compounds. Because of its reversible oxidation process, the organometallic substance ferrocene has excellent electrochemical characteristics and is useful for quenching excited states.¹¹² Ethynyl ferrocene and phenyl-ethynylferrocene moieties are substituted into the perfluoro- and perhydro-derivatives of the dithienylcyclopentene switches to further investigate the major impact of the ferrocene units on the photochemical and electrochemical capabilities of the switches.^{56,58,61}

1.11.1. Speciality of Ferrocene- as an organometallic compound

In the year of 1951, Kealy, Pauson, and Miller independently discovered ferrocene and this pioneering work had a huge impact.¹¹³ The simplest and most stable organometallic compound is ferrocene, in which the iron is confined between two delocalised π -system (cyclopentadienyl rings) in an eclipsed or staggered shape.^{114,115} It was known as “dicyclopentadienyliron” and has a molecular formula $[\text{Fe}(-\text{C}_5\text{H}_5)_2]$ (Figure 1.19). However, among all metallocenes, ferrocene is the most employed due to two rotatory coplanar cyclopentadienyl (Cp) rings and reversible redox characteristics. Ferrocene appears as an orange solid, has a camphor-like odour, and is soluble in a wide variety of organic solvents. It is highly stable in air, since it does not change when exposed to air, water, strong bases, or even heat up to the temperature 400°C, although under an oxidising environment, it generates ferrocenium ion (Fc^+) upon reaction with strong acid.^{116,117} Based on its unique structural feature, bonding, and reactivity, it opened the way for the growing field of organometallic chemistry. Therefore, the synthesis of this sandwich system in all its varieties, as well as its varied reaction chemistry, structural characteristics, accompanying mechanistic and theoretical research, make ferrocene and ferrocene-based molecules more than just simple organometallic

compound. Also, this family of compounds has grown rapidly due to its application in homogeneous catalysis, particularly stereoselective and asymmetric transformations, electrochemistry, especially electron-transfer processes, new materials, including fuel additives, bioorganometallic chemistry, polymer chemistry, anticancer reagents and so on.¹¹⁸

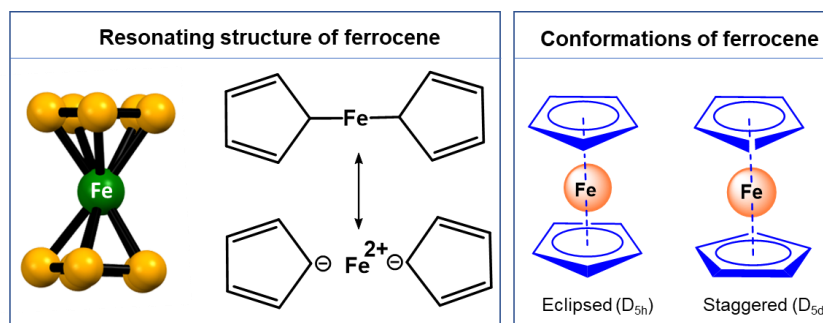


Figure 1.19. Chemical structure of ferrocene.

Ferrocene has been extensively employed as a crucial redox probe to better understand the kinetics of electrochemical charge transfer in a wide platform, from solution-based systems and molecule thin-films to solid-state molecular electronics and spintronic devices.¹¹⁹ When the redox behaviour of ferrocene was examined, it was discovered that the only typical redox product was the blue ferrocenium ion and that ferrocenium could be reduced back to ferrocene.

On the other hand, the interesting optical and excellent electrochemical detection properties of ferrocene and its derivatives have led to their widespread acceptance as a fundamental and extraordinarily potent building block for the development of multi-responsive chemosensors.¹²⁰⁻¹²³ Considering its excellent redox characteristics, a significant portion of the commitments is devoted to the transfer of electrons between ferrocene centres or among other redox centres, both intramolecularly and intermolecularly, and for utilisation in switchable architectures.¹²⁴⁻¹²⁷

1.11.2. Functionalisation of ferrocene

The present cyclopentadienyl rings in ferrocene moiety have a partial negative charge which demonstrates a significant attraction for electrophiles as comparable to other aromatic frameworks (Figure 1.20). For instance, it rapidly undergoes aromatic electrophilic substitution

reaction like halogenation or nitration at Cp ring.¹²⁸ The mono- and disubstituted ferrocenes that are produced as a result of an alkylation or acylation reaction of the Cp-rings by means of electrophilic aromatic substitution processes (for example, the Friedel-Crafts reaction) are very simple to separate using chromatographic techniques (79). However, because electron-withdrawing functional groups firmly deactivate the second Cp ring through an electrical effect, formylation (80)^{129,130} and carboxylation (84)^{131,132} procedures only control the cost of the mono-functionalized ferrocene (76-85). It is interesting to note that metalation reactions can also be performed in a sequential fashion using *n*-butyl-lithium, which results in the formation of 1,1'-disubstituted derivatives.¹³³

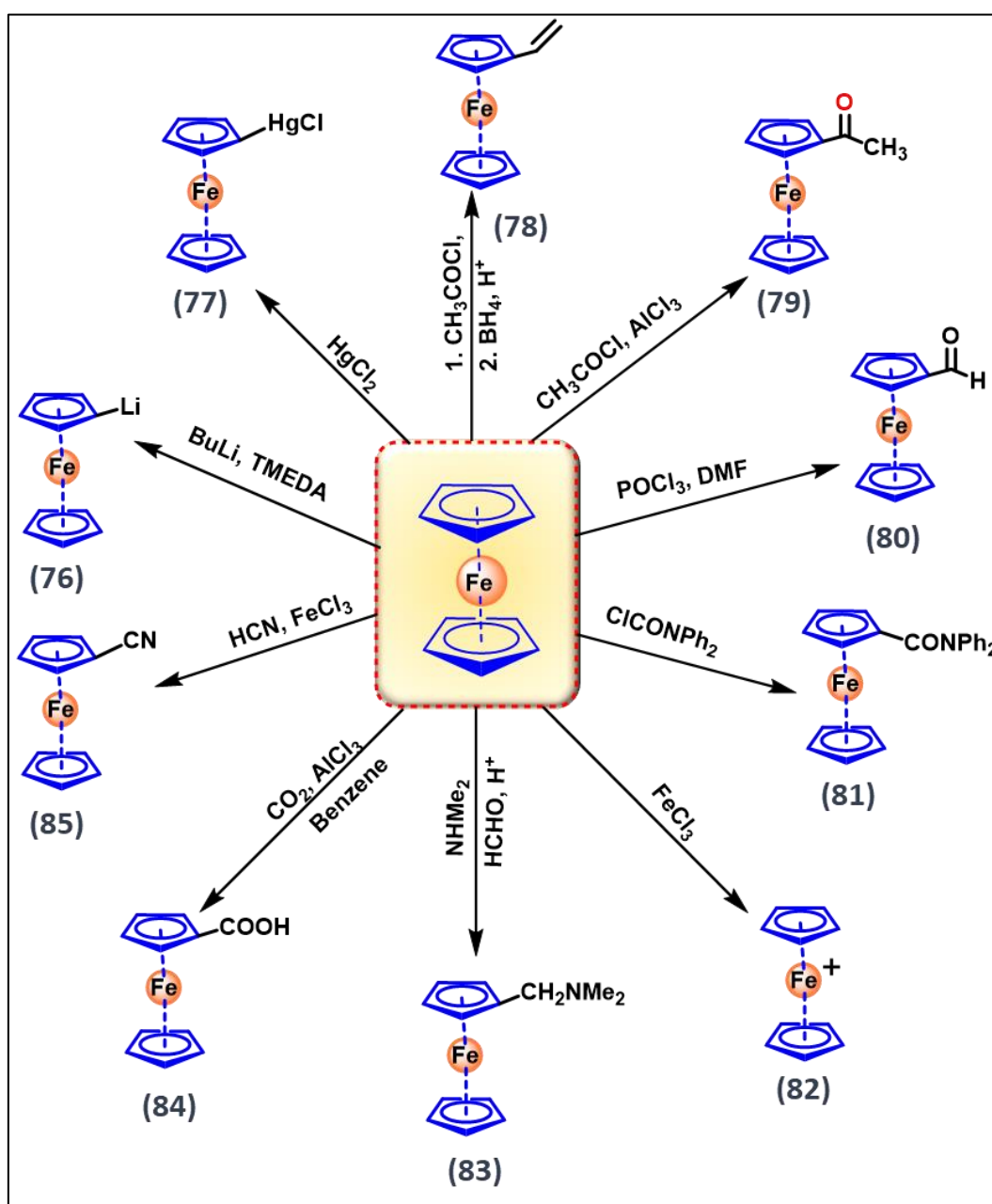


Figure 1.20. Various methods for functionalization of ferrocene.

1.11.3. Application of ferrocene and its derivatives

Ferrocene's robustness in aqueous and aerobic mediums, as well as the availability of a large range of derivatives and advantageous electrochemical features, have made it an especially fascinating molecule for biological uses.¹³⁴⁻¹⁴⁰ Ferrocene is being investigated for potential use in the field of medicine which is a very active study area. There have been several studies that have demonstrated that some ferrocene derivatives have a high level of activity in vivo and vitro against several diseases, such as fungal and bacterial infections, human immunodeficiency virus (HI), cancer,¹³⁴⁻¹⁴⁰ and malaria.^{138,141-143} As a result, numerous kinds of ferrocene-based compounds have been synthesised and utilised in various fields ranging from medicinal chemistry to material science which are here briefly discussed:

1.11.3.A. Application of ferrocenyl systems in material science

Transition metal complexes, especially those with redox-active parts like the ferrocenyl group, are still a big area of research.¹⁴⁴⁻¹⁴⁸ They are mainly investigated for a number of potential applications, such as improving novel materials¹⁴⁹⁻¹⁵² and producing materials for nonlinear optics.¹⁵³⁻¹⁵⁵ Ferrocenyl and multiferrocenyl complexes have been applied as polymer building blocks, redox sensors for chemical recognition, coatings to alter electrode surfaces, and mediators in biosensors.¹⁵⁶⁻¹⁵⁹ Furthermore, ferrocene based molecules have potential applications in material science (86-91), with few examples including bio-electrochemical systems (87), rechargeable battery cathodes (88, 91) and so on. Modular electrochemical biosensor systems are created employing ferrocene-avidin and ferrocene-streptavidin conjugates to enable effective electron transfer (87) (Figure 1.21). It is also important to note that ferrocene has frequently been utilised as a reagent in the manufacture of nanotubes, including those containing iron.¹⁶⁰

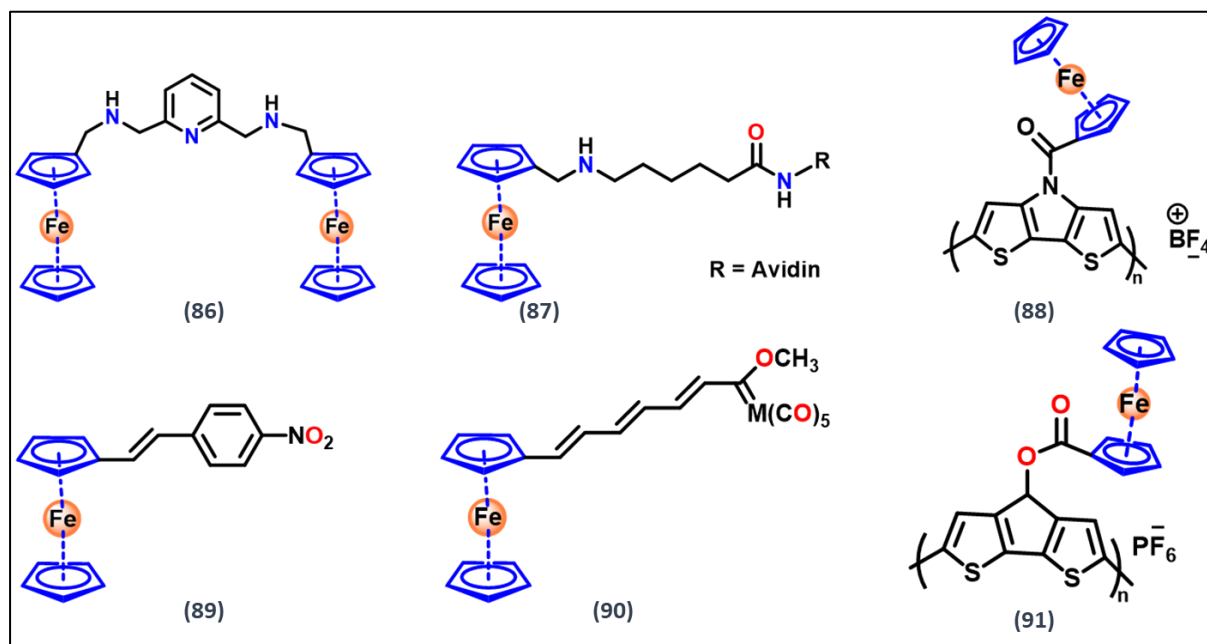


Figure 1.21. Application of ferrocene derivatives in material science.

1.12. Judicious design of DTE derivatives for my research

From literature survey the following conclusive outcome may be drawn:

❖ In 21st century, researchers have focused their attention in developing the DTE based photochromic molecules co-ordinated with different metal and studied their photophysical and photochemical properties for various application in different fields. However, majority of research group have focused on incorporation of metal complex either in diethynylethene bridge or in reactive carbon atoms which permits light irradiation to modulate guest incorporation and release. Furthermore, there are many examples of chemosensor of DTE derivatives conjugated with fluorophores which exhibited excellent metal coordination phenomena with DTE.^{95,161} All of these probes are made so that the metal ions do not attach to the sulphur atoms of the DTE core, so they don't directly affect the photoisomerization process. Instead, they bind with a remote binding unit that is attached to the DTE core. A highly selective ratiometric fluorescent chemosensor for Hg²⁺ based on a new diarylethene All of these probes are engineered in such a manner that the metal ions do not directly participate in the photoisomerization process because they do not connect to the sulphur atoms of the DTE core; instead, they form a bond with a remote binding unit that is coupled to the DTE core.¹⁶² So far,

they have functionalised the DTE molecule by introducing metal binding site at reactive carbon atoms. Clever and co-workers have shown Pd(II) metal ion containing coordination cages based on DTE unit which permit regulation of guest uptake and release under light irradiation at different wavelengths.^{163,164} Therefore, it can be concluded that the synthesis of DTE molecule having metal coordinating capability at DTE core is highly demanding which still not reported (Figure 1.22). The metal co-ordination at the core position of DTE may offer different kind of photophysical, photochemical and photoswitching properties which can be applied in new field.

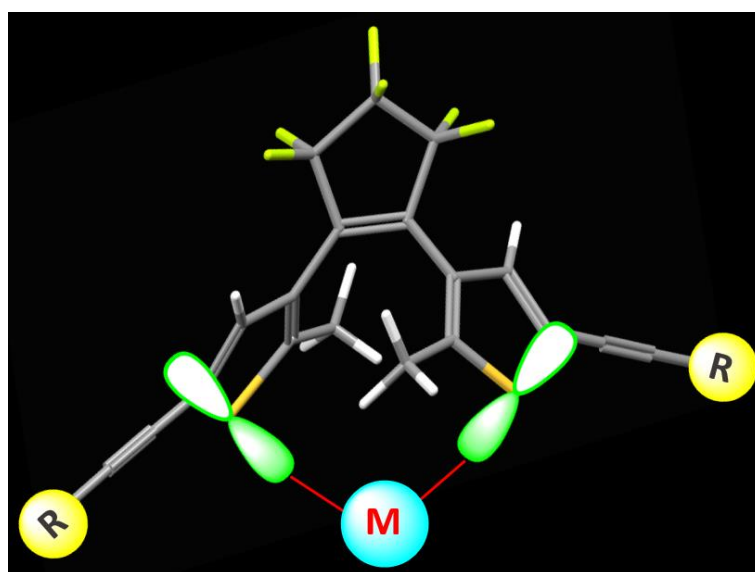


Figure 1.22. Schematic representation of DTE molecules for the investigation of metal co-ordination dynamics.

❖ On the hand, the properties of DTE can be tuned by introducing a long range π -conjugating functional unit which is positioned at the reactive carbon atom of diarylethene. It should also be noted that conjugation is an advantageous property that increased the color intensity of photochromic molecules. As a result, the photoisomerization features are expected to be significant with remarkable change in color. From another point of view, this phenomenon also improves communication *via* long-range π -conjugation between the photochromic (DTE/DAE) unit and the fluorophore/redox active unit. Furthermore, the photochromic system may generate fluorescence property solely for π -conjugation and long-range electronic communication (without any inclusion of fluorophore or sulfoxide unit). The switching behaviour can be linked to a shift in the π -conjugation in the molecules; specifically, the π -conjugation is no longer present in the open-ring isomer, whereas it is present in the

closed-ring isomer. In closed isomer the π -conjugation is distributed across the entire molecule. Because of the long-range electronic communication, the photoisomerisation speed of highly conjugated DTE molecules is slow. From literature survey it can be conclude that, the non-conjugated DTE molecule displayed rapid photoisomerization reaction.¹⁶⁵ Therefore, the synthesis of DTE molecules, where no such π -conjugation is present, is highly demanding (Figure 1.23). The hexafluorocyclopentene ring containing DTE provides additional benefits to photochromic systems: Photoirradiation provides good fatigue resistance.

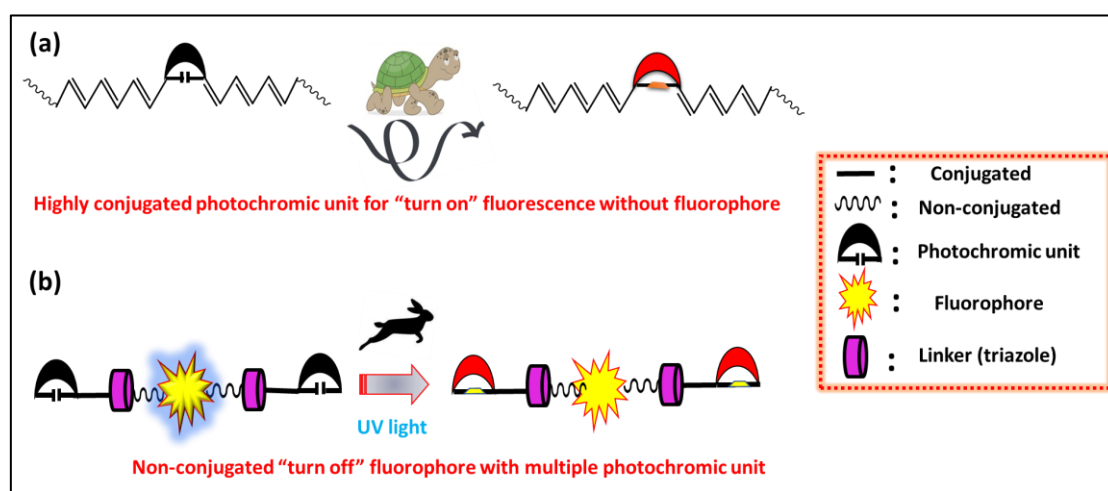


Figure 1.23. Schematic representation of DTE molecules with highly conjugated π -system for abnormal fluorescence behavior.

❖ Based on DTE molecules and its derivatives have been explored in various fields including material science to medicinal chemistry. However, another imported field depending on DTE derivatives is self-assembly and formation of organogel as well as hydrogel that can be applied in congealing oil spills, nano medicine and so on. Gels are a very interesting type of soft condensed materials that, as they combine the elastic behavior of solids with the viscous behaviour of fluids, are well adapted to act as responsive materials.^{166,167} Chemical or polymer gels are the most commonly used gels, in which covalent cross-links maintain a three-dimensional network. Because of the covalent cross-links, these gels are strong and resistant to physical deformation. Chemical gels have been developed that may change their size, shape, optical, dielectric, or viscoelastic properties in response to physical or chemical stimuli. These gels have applications in valves, motors, muscles, security technology, smart drug release systems, and more.¹⁶⁸⁻¹⁷⁰ Chemical gels respond to changes in the physical or chemical

environment through interactions between their viscoelastic characteristics, viscoelastic network filament interaction potential, and/or filament-liquid interactions.

Low molecular weight gelators (LMWG) or low molecular mass organogel substances (LMOGs), which have the potential to gelate liquids at concentrations considerably below 1 mass%, represent a separate class of physical gels. Despite the structural variety among LMOGs, they all share the property that these compounds efficiently self-assemble into fibres in solution. The networks formed by these fibres in turn cause the liquid (sol) to solidify into a gel (Figure 1.24). Most of the recent research has focused on structural aspects of organogelation, organogelators that are specifically designed for liquids, and functional organic gelators. This has led to the effective design of a novel gelator molecules that form various architectures, including sheets, cylinders, fibres, and tapes.

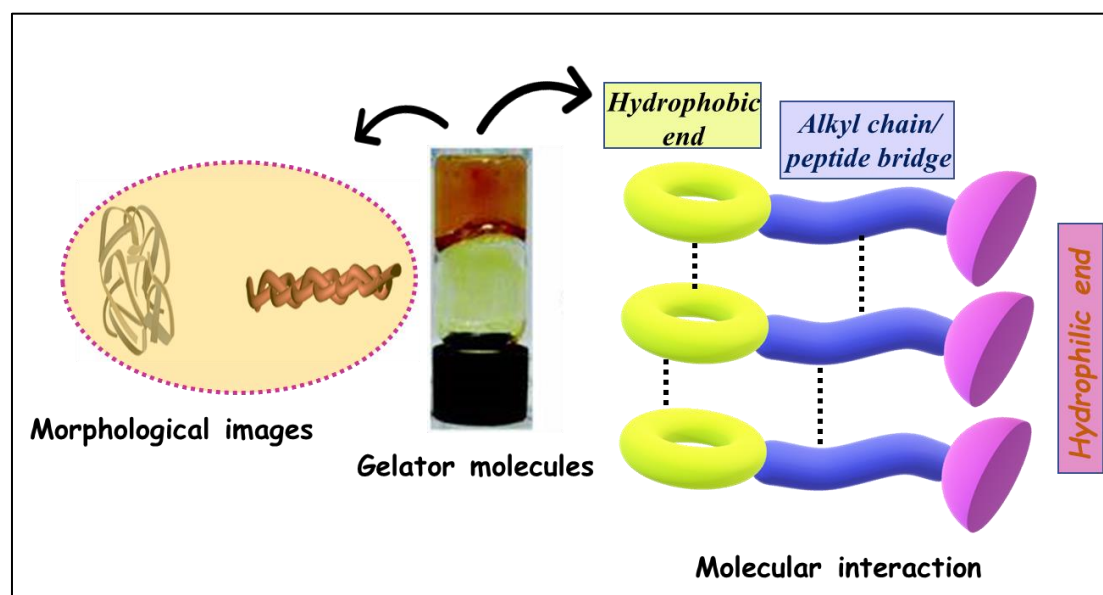


Figure 1.24. Schematic representation of self-assembly behavior.

The main goal of this thesis is to investigate the effect and corresponding properties of the substituents linked to the thiophene units and the central per-fluorocyclopentene unit on the photochemical and electrochemical properties of dithienylcyclopentene switches. Additionally, the impact of adding organometallic moieties like ferrocene on the reactive carbon centre of DTE switches is investigated. The purpose of this thesis is to investigate the effects of modification of DAE by introducing perfluorocyclopentene, which have high fatigue resistance behaviour and thermal stability, and surveyed their photophysical properties to apply in different fields. Further, these molecules can be used to develop read/write security systems,

revealed a smart technique for latent fingerprint (LFP) identification with non-destructive read-out capabilities and other optoelectronic devices because of their high fatigue recyclability and quality of thermal stability. The fields include metal co-ordination dynamics, security technology, erasable ink formulation, latent fingerprint generation and so on (Figure 1.25).

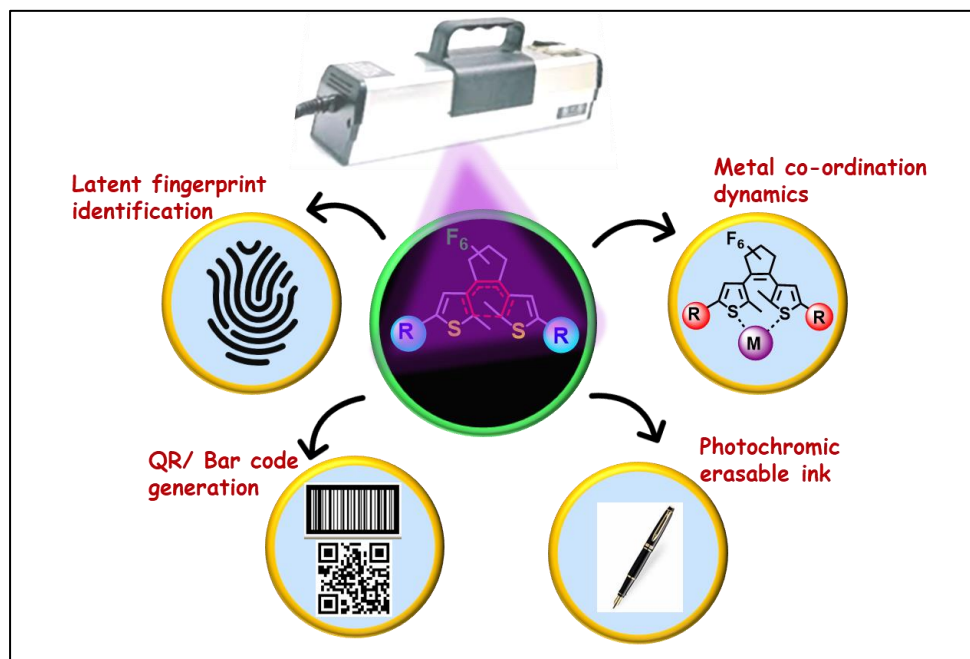


Figure 1.25. Schematic diagram for application of photoswitchable DTE molecules.

1.13. References

1. Stoll, R.S.; Hecht, S. *Angew. Chem. Int. Ed.* **2010**, *49*, 5054-5075.
2. Bouas-Laurent, H.; Dürr, H. *Pure Appl. Chem.* **2001**, *73*, 639-665.
3. Neilson, B.M.; Bielawski, C.W. *ACS Catalysis* **2013**, *3*, 1874-1885.
4. Göstl, R.; Senf, A.; Hecht, S. *Chem. Soc. Rev.* **2014**, *43*, 1982-1996.
5. Samachetty, H.D.; Branda, N.R.; *Pure Appl. Chem.* **2006**, *78*, 2351-2359.
6. (a) Raymo, F.M. *Phys. Chem. Chem. Phys.* **2013**, *15*, 14840-14850; (b) Fukaminato, T. *J. Photochem. Photobiol. C* **2011**, *12*, 177-208.

7. (a) Cusido, J.; Deniz, E.; Raymo, F.M. *Eur. J. Org. Chem.* **2009**, 2009, 2031-2045; (b) Heilemann, M.; Dedecker, P.; Hofkens, J.; Sauer, M. *Laser & Photon. Rev.* **2009**, 3, 180-202.
8. Raymo, F.M.; Tomasulo, M.; *Chem. Soc. Rev.* **2005**, 34, 327- 336.
9. (a) Szymański, W.; Beierle, J.M.; Kistemaker, H.A.V.; Velema, W.A.; Feringa, B.L. *Chem. Rev.* **2013**, 113, 6114-6178; (b) Natali, M.; Giordani, S. *Chem. Soc. Rev.* **2012**, 41, 4010-4029; (c) Yagai, S.; Kitamura, A. *Chem. Soc. Rev.* **2008**, 37, 1520-1529.
10. Kim, T.; Zhu, L.; Al-Kaysi, R.O.; Bardeen, C.J. *ChemPhysChem* **2014**, 15, 400-414.
11. Bleger, D.; Yu, Z.; Hecht, S. *Chem. Commun.* **2011**, 47, 12260-12266.
12. Orgiu, E.; Samorì, P. *Adv. Mater.* **2014**, 26, 1827-1845.
13. Tsujioka, T.; Irie, M. *J. Photochem. Photobiol. C* **2010**, 11, 1-14.
14. Cheng, H.-B.; Zhang, S.; Bai, E.; Cao, X.; Wang, J.; Qi, J.; Liu, J.; Zhao, J.; Zhang, L.; Yoon, J. *Adv. Mater.* **2022**, 34, 210828.
15. (a) Matsuda, K.; Irie, M. *J. Photochem. Photobiol. C.* **2004**, 5, 169-182; (b) Zheng, C.; Pu, S.; Xu, J.; Luo, M.; Huang, D.; Shen, L. *Tetrahedron* **2007**, 63, 5437-5449; (c) Nakamura, S.; Yokojima, S.; Uchida, K.; Tsujioka, T.; Goldberg, A.; Murakami, A.; Shinoda, K.; Mikami, M.; Kobayashi, T.; Kobatake, S.; Matsuda, K.; Irie, M. *J. Photochem. Photobiol. A.* **2008**, 200, 10-18.
16. Yang, T.; Pu, S.; Fan, C.; Liu, G. *Spectrochim. Acta A.* **2008**, 70, 1065-1072.
17. Kobatake, S.; Irie, M. *Tetrahedron* **2003**, 59, 8359-8364.
18. Zhang, J.; Zou, Q.; Tian, H. *Adv.Mater.* **2013**, 25, 378-399.
19. Chen, J.; Zhang, P.; Fang, G.; Yi, P.; Zeng, F.; Wu, S. *J. Phys. Chem. B* **2012**, 116, 4354-4362.
20. (a) Tian, H. *Angew. Chem. Int. Ed.* **2010**, 49, 4710; (b) Kawata, S.; Kawata, Y. *Chem. Rev.* **2000**, 100, 1777; (c) Pardo, R. Zayat, M.; Levy, D. *Chem. Soc. Rev.* **2011**, 40, 672.
21. (a) Dong, H.; Zhu, H.; Meng, Q.; Gong, X.; Hu, W. *Chem. Soc. Rev.*, **2012**, 41, 1754; (b) Bruder, F. K.; Hagen, R.; Rölle, T.; Weiser, M. S.; Fäcke, T. *Angew. Chem. Int. Ed.* **2011**, 50, 4552.
22. Tanaka, Y.; Ishisaka, T.; Inagaki, A.; Koike, T.; Lapinte, C.; Akita, M. *Chem. Eur. J.* **2010**, 16, 4762-4776.
23. Motoyama, K.; Li, H.; Koike, T.; Hatakeyama, M.; Yokojima, S.; Nakamura, S.; Akita, M. *Dalton Trans.* **2011**, 40, 10643-10657.
24. *J. Phys. D: Appl. Phys.* 55 (2022) 044002 (10pp)

25. Lucas, L. N.; de Jong, J. J. D.; van Esch, J. H.; Kellogg, R. M.; Feringa, B. L. *Eur. J. Org. Chem.* **2003**, 155-166.
26. Lucas, L. N.; van Esch, J.; Kellogg, R. M.; Feringa, B. L. *Chem. Commun.* **1998**, 2313-2314.
27. Irie, M.; Yokoyama, Y.; Seki, T.; Editors, ISBN 978-4-431-54290-2 DOI 10.1007/978-4-431-54291-9.
28. Kobatake, S.; Irie, M. *Chem. Lett.* **2003**, 32, 1078-1079.
29. Morimitsu, K.; Shibata, K.; Kobatake, S.; Irie, M. *J. Org. Chem.* **2002**, 67, 4574-4578.
30. Kobatake, S.; Uchida, K.; Tsuchida, E.; Irie, M. *Chem. Lett.* **2000**, 29, 1340-1341.
31. (a) Li, W.; Jiao, C.; Li, X.; Xie, Y.; Nakatani, K.; Tian, H.; Zhu, W. *Angew. Chem. Int. Ed.* **2014**, 53, 4603-4607; (b) Uchida, K.; Tsuchida, E.; Aoi, Y.; Nakamura, S.; Irie, M. *Chem. Lett.* **1999**, 28, 63-64.
32. Fihey, A.; Perrier, A.; Browne, W. R.; Jacquemin, D. *Chem. Soc. Rev.* **2015**, 44, 3719-3759.
33. Sumi, T.; Takagi, Y.; Yagi, A.; Morimoto, M.; Irie, M. *Chem. Commun.* **2014**, 50, 3928-3930.
34. Irie, M.; Sakemura, K.; Okinaka, M.; Uchida, K. *J. Org. Chem.* **1995**, 60, 8305-8309.
35. (a) Kellogg, R.M.; Groen, M.B.; Wynberg, H. *J. Org. Chem.* **1967**, 32, 3093-3100; (b) Muszkat, K.A.; Fischer, E. *J. Chem. Soc. (B)* **1967**, 662-678; (c) Muszkat, K.A.; Gegiou, D.; Fischer, E. *Chem. Commun.* **1965**, 447-448; (d) Mallory, F.B.; Wood, C.S.; Gordon, J.T.; *J. Am. Chem. Soc.*, **1964**, 86, 3094-3102.
36. (a) Irie, M.; Mohri, M. *J. Org. Chem.*, **1988**, 53, 803-808; (b) Nakamura, S.; Irie, M. *J. Org. Chem.* **1988**, 53, 6136-6138.
37. Irie, M.; Sayo, K. *J. Phys. Chem.* **1992**, 96, 7671-7674.
38. Uchida, K.; Kido, Y.; Yamaguchi, T.; Irie, M. *Bull. Chem. Soc. Jpn.* **1998**, 71, 1101-1108.
39. Hanazawa, M.; Sumiya, R.; Horikawa, Y.; Irie, M. *J. Chem. Soc.* **1992**, 206-207.
40. de Jong, J.J.D.; Lucas, L.N.; Hania, R.; Pugzlys, A.; Kellogg, R.M.; Feringa, B.L.; Duppen, K.; van Esch, J.H. *Eur. J. Org. Chem.* **2003**, 2003, 1887-1893.
41. (a) Yamaguchi, T.; Kamihashi, Y.; Ozeki, T.; Uyama, A.; Kitai, J.-i.; Kasuno, M.; Sumaru, K.; Kimura, Y.; Yokojima, S.; Nakamura, S.; Morimoto, M.; Uchida, K. *Bull. Chem. Soc. Jpn.* **2014**, 87, 528-538; (b) Takeshita, M.; Mizukami, E.; Murakami, K.;

- Wada, Y.; Matsuda, Y. *Eur. J. Org.Chem.* **2014**, 2014, 3784-3787; (c) Wang, R.; Pu, S.; Liu, G.; Chen, B. *Tetrahedron* **2013**, 69, 5537-5544.
42. (a) Cahová, H.; Jäschke, A. *Angew. Chem. Int. Ed.* **2013**, 52, 3186-3190; (b) Singer, M.; Nierth, A.; Jäschke, A.; *Eur. J. Org. Chem.* **2013**, 2013, 2766-2769.
43. Singer, M.; Jäschke, A. *J. Am. Chem. Soc.* **2010**, 132, 8372-8377.
44. Takami, S.; Kawai, T.; Irie, M. *Eur. J. Org. Chem.* **2002**, 2002, 3796-3800.
45. Shibata, K.; Kobatake, S.; M. Irie, *Chem. Lett.* **2001**, 30, 618-619.
46. Higashiguchi, K. Matsuda, Y. Asano, A. Murakami, S. Nakamura, Irie, M. *Eur. J. Org.Chem.* **2005**, 2005, 91-97
47. Morimitsu, K.; Kobatake, S.; Irie, M. *Mol. Cryst. Liq. Cryst.* **2005**, 431, 451-454.
48. Morimitsu, K.; Kobatake, S.; Nakamura, S.; M. Irie, *Chem. Lett.* **2003**, 32, 858-859.
49. (a) Kobatake, S.; Terakawa, Y.; *Chem. Commun.* **2007**, 1698-1700; (b) Gilat, S.L.; Kawai, S.H.; Lehn, J.-M. *Chem. Eur. J.* **1995**, 1, 275-284.
50. Seefeldt, B.; Altenhoner, K.; Tomic, O.; Geisler, T.; Sauer, M.; Mattay, J. *Photochem. Photobiol. Sci.* **2011**, 10, 1488-1495.
51. Thomas, A.B.; Frewert, D.; Kodatis, K.; Kryschi, C.; Martin, H.-D.; Trommsdorff, H.P. *Eur.J. Org. Chem.* **1998**, 1998, 2333-2338;
52. Irie, M.; Eriguchi, T.; Takada, T.; Uchida, K. *Tetrahedron* **1997**, 53, 12263-12271.
53. Tian, H.; Wang, S. *Chem. Commun.* **2007**, 781-792.
54. Browne, W. R.; de Jong, J. J. D.; Kudernac, T.; Walko, M.; Lucas, L. N.; Uchida, K.; van Esch, J. H.; Feringa, B. L. *Chem. Eur. J.* **2005**, 11, 6414-6429.
55. Zhong, Y.; Vila, N.; Henderson, J. C.; Abruna, H. D. *Inorg. Chem.* **2009**, 48, 7080-7085,
56. Herkstroeter, W. G. *J. Am. Chem. Soc.* **1975**, 97, 4161-4167.
57. Martinez, R.; Ratera, I.; Tarraga, A.; Molina, P.; Veciana, J. *Chem. Rev.* **2000**, 100, 1685-1716.
58. Martínez, R.; Ratera, I.; Tárraga, A.; Molina, P.; Veciana, J. *Chem. Commun.* **2006**, 3809-3811.
59. Takami, S.; Kobatake, T.; Kawai, T.; Irie, M. *Chem. Lett.* **2003**, 32, 892-893.
60. Tanaka, Y.; Inagaki, A.; Akita, M. *Chem. Commun.* **2007**, 1169-1171.
61. Fery-Forgues, S.; Delavaux-Nicot, B. *J. Photochem. Photobiol. A.* **2000**, 132, 137-159.
62. (a) Hiroto, S.; Suzuki, K.; Kamiya, H.; Shinokubo, H. *Chem. Commun.* **2011**, 47, 7149-7151. (b) Yahyaoui, A. E.; Félix, G.; Heynderickx, A.; Moustrou, C.; Samat, A. *Tetrahedron* **2007**, 63, 9482-9487.

63. Herder, M.; Patzel, M.; Grubert, L.; Hecht, S. *Chem. Commun.* **2011**, 47, 460-462.
64. Herder, M.; Diploma thesis, Humboldt-Universität zu Berlin (Berlin), 2010.
65. Ishiyama, T.; Murata, M.; Miyaura, N. *J. Org. Chem.* **1995**, 60, 7508-7510.
66. Murata, M.; Watanabe, S.; Masuda, Y. *J. Org. Chem.* **1997**, 62, 6458-6459.
67. Woodward, R. B.; Hoffmann, R. *J. Am. Chem. Soc.* **1965**, 87, 395-397.
68. Zheng, H.; Zhou, W.; Yuan, M.; Yin, X.; Zuo, Z.; Ouyang, C.; Liu, H.; Li, Y.; Zhu, D. *Tetrahedron Lett.* **2009**, 50, 1588-1592.
69. Lucas, L. N.; Ph.D. Thesis, Rijksuniversiteit Groningen, **2001**.
70. Arnanz, A.; Marcos, M.; Moreno, C.; Farrar, D. H.; Lough, A. J.; Yu, J. O.; Delgado, S.; González-Velasco, J. *J. Organomet. Chem.* **2004**, 689, 3218-3231.
71. Lin, Y.; Yuan, J.; Hu, M.; Cheng, J.; Yin, J.; Jin, S.; Liu, S. H. *Organometallics* **2009**, 28, 6402-6409.
72. Jeong, Y.; Yang, S. I.; Kim, E.; Ahn, K. *Tetrahedron* **2006**, 62, 5855-5861.
73. Jukes, R. T. F.; Adamo, V.; Hartl, F.; Belser, P.; De Cola, L. *Inorg. Chem.* **2004**, 43, 2779-2792.
74. Xue, L.; Lin, Z. *Chem. Soc. Rev.* **2010**, 39, 1692-1705.
75. Franzen, R.; Xu, Y. *Can. J. Chem.* **2005**, 83, 266-272.
76. Fleckenstein, C. A.; Plenio, H. *Chem. Soc. Rev.* **2010**, 39, 694-711.
77. Miyaura, N.; Suzuki, A. *Chem. Rev.* **1995**, 95, 2457-2483.
78. Narayanan, R. *Molecules* **2010**, 15, 2124-2138.
79. Chinchilla, R.; Najera, C. *Chem. Rev.* **2007**, 107, 874-922.
80. Zhang, S.; Zhanga, M.; Shi, M. *Tetrahedron Lett.* **2007**, 48, 8963-8966.
81. Hundertmark, T.; Littke, A. F.; Buchwald, S. L.; Fu, G. C. *Org. Lett.* **2000**, 2, 1729-1731.
82. Batey, R. A.; Shen, M.; Lough, A. J. *Org. Lett.* **2002**, 4, 1411-1414.
83. Uchida, K.; Matsuoka, T.; Kobatake, S.; Yamaguchi, T.; Irie, M. *Tetrahedron* **2001**, 57, 4559-4565.
84. Xiao, S.; Yi, T.; Zhou, Y.; Zhao, Q.; Li, F.; Huang, C. *Tetrahedron* **2006**, 62, 10072-10078.
85. Velema, W. A.; Szymanski, W.; Feringa, B. L. *J. Am. Chem. Soc.* **2014**, 136, 2178-2191.
86. Hill, K.; Morstein, J.; Trauner, D. *Chem. Rev.* **2018**, 118, 10710-10747.
87. Pianowski, Z. L. *Chem. Eur. J.* **2019**, 25, 5128-5144.

88. Zhang, J.; Tian, H. *Adv. Opt. Mater.* **2018**, *6*, 1701278.
89. (a) Wang, Y.; Li, Q. *Adv. Mater.*, **2012**, *24*, 1926; (b) Bisoyi, H. K.; Li, Q. *Acc. Chem. Res.* **2014**, *47*, 3184; (c) Zheng, Z.; Lu, Y.; Li, Q. *Adv. Mater.* **2020**, *32*, 1905318.
90. Intelligent Stimuli Responsive Materials: From Well-defined Nanostructures to Applications, (Ed: Q. Li), John Wiley & Sons, Hoboken **2013**.
91. (a) Yang, W.; Feng, Y.; Si, Q.; Yan, Q.; Long, P.; Dong, L.; Fu, L.; Feng, W. *J. Mater. Chem. A*, **2019**, *7*, (b) Han, G. G. D.; Li, H.; Grossman, J.C. *Nat. Commun.* **2017**, *8*, 1446.
92. (a) Yan, Q.; Zhang, Y.; Dang, Y.; Feng, Y.; Feng, W. *Energy Storage Mater.* **2020**, *24*, 662; (b) Fu, L.; Yang, J.; Dong, L.; Yu, H.; Yan, Q.; Zhao, F.; Zhai, F.; Xu, Y.; Dang, Y.; Hu, W.; Feng, Y.; Feng, W. *Macromolecules* **2019**, *52*, 4222.
93. (a) Kang, M. J.; Santoro, E. G.; Kang, Y. S. *ACS Omega* **2018**, *3*, 9505; (b) Moormann, W.; Tellkamp, T.; Stadler, E.; Rohricht, F.; Nather, C.; Puttreddy, R.; Rissanen, K.; Gescheidt, G.; Herges, R. *Angew. Chem. Int. Ed.* **2020**, *132*, 15081; (c) Moormann, W.; Tellkamp, T.; Stadler, E.; Rohricht, F.; Nather, C.; Puttreddy, R.; Rissanen, K.; Gescheidt, G.; Herges, R. *Angew. Chem.* **2020**, *132*, 15193.
94. Morimoto, M.; Kobatake, S.; Irie, M. *J. Am. Chem. Soc.* **2003**, *125*, 11080-11087.
95. Wigglesworth, T. J.; Myles, A. J.; Branda, N. R. *Eur. J. Org. Chem.* **2005**, 1233-1238.
96. Salazar, E.; Reinink, S.; Faraji, S. *Phys. Chem. Chem. Phys.* **2022**, *24*, 11592-11602.
97. Luo, Q.; Liu, Y.; Tian, H. Photochromic Dithienylethene-Phthalocyanines and Their Analogs, ISBN 1616-8550
98. Tian, H.; Yang, S. *Chem. Soc. Rev.*, **2004**, *33*, 85-97.
99. Yuan, S.-H.; Huang, D.-C.; Tao, Y.-T. *ACS Appl. Mater. Interfaces* **2022**, *14*, 7102-7108.
100. Abdollahi, A.; Roghani-Mamaqani, H.; Razavi, B.; Salami Kalajahi, M. *ACS Nano* **2020**, *14*, 14417-14492.
101. Li, Z., Liu, X., Wang, G.; Li, B.; Chen, H.; Li, H.; Zhao, Y. *Nat Commun* **2021**, 1363.
102. Zacharias, P.; Gather, M. C.; Köhnen, A.; Rehm, N.; Meerholz, K. *Angew. Chem. Int. Ed.* **2009**, *48*, 4038.
103. Shirota, Y. *J. Mater. Chem.* **2005**, *15*, 75-93.
104. Zhang, Z.; Liu, X.; Li, Z.; Chen, Z.; Zhao, F.; Zhang, F.; Tung, C.-H. *Adv. Funct. Mater.* **2008**, *18*, 302-307.
105. Nakatani, K.; Bozec, H. L. *Angew. Chem., Int. Ed.* **2008**, *47*, 577-580.

106. Nitadori, H.; Ordronneau, L.; Boixel, J.; Jacquemin, D.; Boucekkine, A.; Singh, A.; Akita, M.; Ledoux, I.; Guerchais, V.; Bozec, H. L. *Chem. Commun.* **2012**, *48*, 10395-10397.
107. Schweigert, C.; Babii, O.; Afonin, S.; Schober, T.; Leier, J.; Michenfelder, N. C.; Komarov, I. V.; Ulrich, A. S.; Unterreiner, A. N. *ChemPhotoChem* **2019**, *3*, 403-410.
108. Komarov, I. V.; Afonin, S.; Babii, O.; Schober, T.; Ulrich, A. S. *Chem.-Eur. J.* **2018**, *24*, 11245.
109. Afonin, S.; Babii, O.; Reuter, A.; Middel, V.; Ulrich, A. S. *Beilstein J. Org. Chem.* **2020**, *16*, 39-49.
110. Pu, S.; Liu, G.; Li, G.; Wang, R.; Yang, T. *J. Mol. Struct.* **2007**, *833*, 23-29.
111. Alberto, R.; Motterlini, R. *Dalton Trans.*, **2007**, 1651-1660.
112. Guirado, G.; Coudret, C.; Hliwa, M.; Launay, J. P. *J. Phys. Chem. B.*, **2005**, *109*, 17445-17459.
113. Kealy, T. J.; Pauson, P. L. *Nature* **1951**, *168*, 1039-1040.
114. Kowalski, K.; Linseis, M.; Winter, R. F.; Zabel, M.; Zális, S.; Kelm, H.; Krüger, H.-J.; Sarkar, B.; Kaim, W. *Organometallics* **2009**, *28*, 4196-4209.
115. Iordache, A.; Oltean, M.; Milet, A.; Thomas, F.; Baptiste, B.; Saint-Aman, E.; Bucher, C. *J. Am. Chem.Soc.* **2012**, *134*, 2653-2671
116. Fernández, L.; Carrero, H. *Electrochimica Acta* **2005**, *50*, 1233-1240.
117. Fabre, B. *Acc. Chem. Res.* **2010**, *43*, 1509-1518.
118. Heinze, K.; Lang, H. *Organometallics* **2013**, *32*, 5623- 5625.
119. Astruc, D. *Eur. J. Inorg. Chem.* **2017**, 6-29.
120. Sun, R.; Wang, L.; Yu, H.; Abdin, Z.-U.; Chen, Y.; Huang, J.; Tong, R. *Organometallics* **2014**, *33*, 4560-4573.
121. Molina, P.; Tárraga, A.; Caballero, A. *Eur. J. Inorg. Chem.* **2008**, 3401-3417.
122. Beer, P. D.; Chen, Z.; Drew, M. G. B.; Johnson, A. O. M.; Smith, D. K.; Spencer, P. *Inorg. Chim. Acta* **1996**, *246*, 143-150.
123. Beer, P. D.; Wild, K. Y. *Polyhedron* **1996**, *15*, 775-780.
124. Zhang, R.; Wang, Z.; Wu, Y.; Fu, H.; Yao, J. *Org. Lett.* **2008**, *10*, 14, 3065-3068.
125. Bucher, C.; Devillers, C. H.; Moutet, J.-C.; Royal, G.; Saint-Aman, E. *New J. Chem.* **2004**, *28*, 1584-1589.
126. Baryshnikova, S.V.; Poddel'sky, A.I. *Molecules* **2022**, *27*, 3928.
127. Kume, S.; Nishihara, H. *Dalton Trans.* **2011**, *40*, 2299.

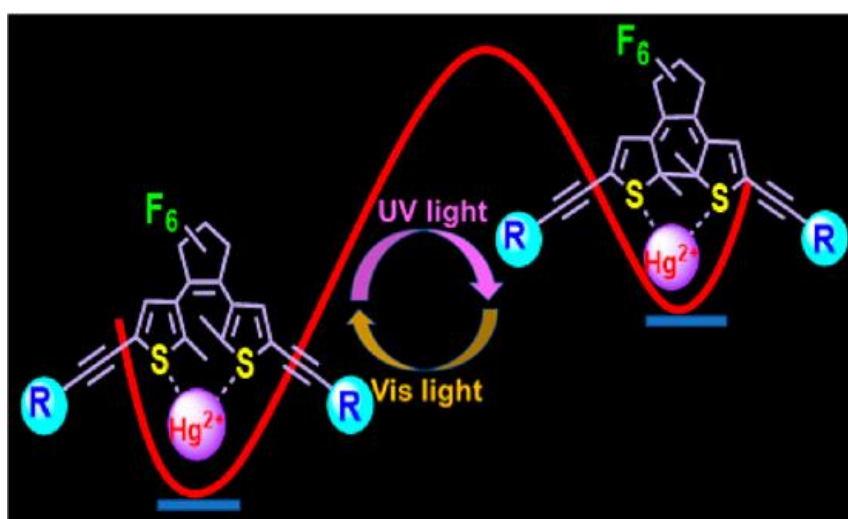
128. Rausch, M. D.; Fischer, E. O.; Grubert, H. *J. Am. Chem. Soc.* **1960**, *82*, 76-82.
129. Maria Mazur, M.; Mrozowicz, M.; Buchowicz, W.; Koszytkowska-Stawińska, M.; Kamiński, R.; Ochal, Z.; Wińska, P.; Bretne, M. *Dalton Trans.* **2020**, *49*, 11504-11511.
130. Tang, J.; Liu, X.-F.; Zhang, L.-Y.; Xu, X.-L.; Zhang, P.-R. *Synthetic Communications* **2000**, *9*, 1657-1660.
131. Al-Allaf, T. A. K. et al *Journal of Organometallic Chemistry* **2003**, *678*, 48-55.
132. Lv, H.; Wang, X.; Hao, Y.; Ma, C.; Li, S.; Li, G.; Zhang, J. *Green Chem.* **2023**, *25*, 554.
133. *Organomet. Chem. Catal., Springer Berlin Heidelberg* **2007**, 251–288.
134. Swarts, J. C.; Neuse, E. W.; Lamprecht, G. J.; *J. Inorg. Organomet. Polym.* **1994**, *4*, 143-153.
135. van Staveren, D. R.; Metzler-Nolte, N. *Chem. Rev.* **2004**, *104*, 5931-5986.
136. Allardyce, C. S.; Dorcier, A.; Scolaro, C.; Dyson, P. J. *Appl. Organomet. Chem.* **2005**, *19*, 1-10.
137. Neuse, E. W. *J. Inorg. Organomet. Polym. Mater.* **2005**, *15*, 3–32.
138. Fouda, M. F. R.; Abd-Elzaher, M. M.; Abdelsamaia, R. A.; Labib, A. A. *Appl. Organomet. Chem.* **2007**, *21*, 613-625.
139. Nguyen, A.; Vessières, A.; Hillard, E. A.; Top, S.; Pigeon, P.; Jaouen, G. *Chimia* **2007**, *61*, 716-724.
140. Hillard, E. A.; Vessières, A.; Jaouen, G.; Top, S. *Organomet. Chem.* **2010**, *32*, 81-117.
141. Biot, C.; Glorian, G.; Maciejewski, L.A.; Brocard, J. S.; Domarle, O.; Blampain, G., Millet, P.; Georges, A. J.; Abessolo, H.; Dive, D.; Lebibi, J. *J. Med. Chem.* **1997**, *40*, 3715-3718.
142. Delhaes, L.; Biot, C.; Berry, L.; Maciejewski, L. A.; Camus, D.; Brocard, J. S.; Dive, D. *Bioorg. Med. Chem.* **2000**, *8*, 2739–2745.
143. Itoh, T.; Shirakami, S.; Ishida, N.; Yamashita, Y.; Yoshida, T.; Kim, H.-S.; Wataya, Y. *Bioorg. Med. Chem. Lett.* **2000**, *10*, 1657–1659.
144. Chavain, N.; Charvet, E. D.; Trivelli, X.; Mbeki, L.; Rottmann, M.; Brun, R.; Biot, C. *Bioorg. Med. Chem.* **2009**, *17*, 8048-8059.
145. Barriere, F.; Geiger, W. E. *J. Am. Chem. Soc.* **2006**, *128*, 3980-3989.
146. Bruce, M. I.; Low, P. J.; Hartl, F.; Humphrey, P. A.; Montigny, P.; Jevric, M.; Lapinte, C.; Perkins, G. J.; Roberts, R. L.; Skelton, B. W.; White, A. H. *Organometallics* **2005**, *24*, 5241-5255.
147. Atkinson, R. C. J.; Gibson, V. C.; Long, N. *J. Chem. Soc. Rev.* **2004**, *33*, 313-328.

148. Wenliang Huang, W.; Diaconescu, P. L. *Inorg. Chem.* **2016**, *55*, 10013–10023.
149. Arrayas, R. G.; Adrido, J.; Carretero, J. C. *Angew. Chem. Int. Ed.* **2006**, *45*, 7674-7715.
150. Gan, K. S.; Hor, T. S. A.; Togni, A.; Hayshi, T. *materials science* **1995**.
151. Sutclie, O. B.; Bryce, M. R. *Tetrahedron Asymm.* **2003**, *14*, 2297-2325.
152. Meric, B.; Kerman, K.; Ozkan, D.; Kara, P.; Erdem, A.; Kucukoglu, O. *J. Pharm. Biomed. Anal.* **2002**, *30*, 1339-1346
153. da Silva, F. M.; Zasloff, M. *Nature* **2002**, *415*, 389-395.
154. Schmitt, M. A.; Weisblum, B.; Gellman, S. H. *J. Am. Chem. Soc.* **2004**, *126*, 6848-6849.
155. Fernandez-Lopez, S.; Kim, H. S.; Choi, E. C.; Delgado, M.; Granja, J. R.; Khasanov, A.; Kraehenbuehl, K.; Long, G.; Weinberger, D. A.; Wilcoxon, K. M.; Ghadiri, M. R. *Nature* **2001**, *412*, 452-455.
156. Moore, A. J.; Skabara, P. J.; Bryce, M. R.; Batsanov, A. S.; Howard, J. A.; Daley, S. T. *J. Chem. Soc.* **1993**, 417-419.
157. Xu, J.; Tian, Y.; Peng, R.; Xian, Y.; Ran, Q.; Jin, L. *Electrochem. Commun.* **2009**, *11*, 1972-1975.
158. Naka, K.; Uemura, T.; Chujo, Y. *Macromolecules* **2000**, *33*, 6965-6969.
159. Salmon, A.; Jutzi, P. *J. Organomet. Chem.* **2001**, *637*, 595-639.
160. Randall, L.; Lee, J. H. *J. Combust. Flame* **2002**, *130*, 27-36.
161. Sun, C.-L.; Gao, Z.; Teng, K.-X.; Niu, L.-Y.; Chen, Y.-Z.; Zhao, Y. S.; Yang, Q.-Z. *ACS Appl. Mater. Interfaces* **2018**, *10*, 26526-26532.
162. (a) Qiu, S.; Cui, S.; Shi, F.; Pu, S. *ACS Omega*, **2019**, *4*, 14841–14848; (b) Feng, E.; Fan, C.; Wang, N.; Liu, G.; Pu, S. *Dyes Pigm.* **2018**, *151*, 22–27.
163. (a) Li, R.-J.; Holstein, J. J.; Hiller, W. G.; Andréasson, J.; Clever, G. H. *J. Am. Chem. Soc.* **2019**, *141*, 2097–2103; (b) Han, M.; Luo, Y.; Damaschke, B.; Gómez, L.; Ribas, X.; Jose, A.; Peretzki, P.; Seibt, M.; Clever, G. H. *Angew. Chem. Int. Ed.* **2016**, *55*, 445-449.
164. (a) Li, R.-J.; Han, M.; Tessarolo, J.; Holstein, J. J.; Lübben, J.; Dittrich, B.; Volkmann, C.; Finze, M.; Jenne, C.; Clever, G. H. *ChemPhotoChem* **2019**, *3*, 378–383; (b) Han, M.; Michel, R.; He, B.; Chen, Y.-S.; Stalke, D.; John, M.; Clever, G. H. *Angew. Chem. Int. Ed.* **2013**, *52*, 1319-1323.
165. Li, C., Yan, H., Zhao, LX. *et al. Nat Commun*, **2014**, *5*, 5709.
166. Weiss, R. G. *J. Am. Chem. Soc.* **2014**, *136*, 7519-7530.

167. Sangeetha, N. M.; Maitra, U. *Chem. Soc. Rev.* **2005**, *34*, 821–836.
168. Verma, P.; Singh, A.; Maji, T.K. *Chem. Sci.* **2021**, *12*, 2674-2682.
169. (a) Zhou, Y. F.; Xu, M.; Yi, T.; Xiao, S. Z.; Zhou, Z. G.; Li, F. Y.; Huang, C. H. *Langmuir* **2007**, *23*, 202-208; (b) Shi, N.; Dong, H.; Yin, G.; Xu, Z.; Li, S. *Adv. Funct. Mater.* **2007**, *17*, 1837-1843.
170. Xia, F.; Zhu, Y.; Feng, L.; Jiang, L. *Soft Matter* **2009**, *5*, 275-281.

Chapter: 2

Light-Triggered Metal Coordination Dynamics in Photoswitchable Dithienylethene–Ferrocene System



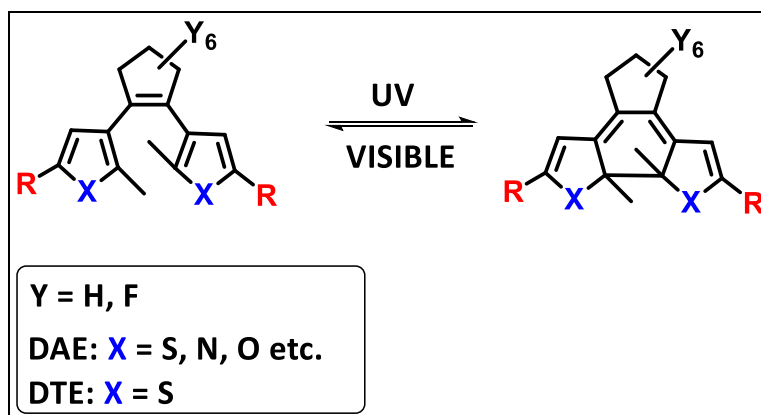
Representative publication

Inorg. Chem. **2021**, *60*, 6086–6098

2.1. Introduction

Stimuli-responsive organic materials with inherent photoswitchable properties is a burgeoning field of research especially in materials science¹ and structural biology.² Starting from the pioneering work of M. Irie in the late 80s and early 90s of the last century photochromic diarylethenes (DAE)³ were primarily associated with dithienylethene (DTE) which undergoes 6π -electrocyclic ring closing or opening to obtain closed and open isomers under irradiation of UV and visible lights respectively (

2.1).⁴ The open (o) and closed (c) forms of DTE exist as two distinctly addressable and thermally stable states. They even respond independently to electrochemical and photochemical stimuli.⁵ Utilizing its open-closed photoswitchable property in presence of light, DTE containing compounds have potential applications in photonic devices *e.g.*, optical memories and display devices, optoelectronic devices such as waveguides, sensors etc.⁶ Various photochromic metal complexes have also been developed by several research groups for the development of organic optical transistors,⁷ NLO switches,⁸ organic light emitting diodes (OLED),⁹ energy storage systems (batteries),¹⁰ and many more. Thus, DTE derivatives have been in the recent trends owing to their wide scope of application.



Scheme 2.1. Photoisomerization in DAE/ DTE systems.

Several research groups have focused on the study of metal-coordinated dithienylethene (DTE) backbones in different fields. Zn^{2+} -bipyridyl complex attached to DTE core has been utilized in reversible switching of NLO response,¹¹ Cu^+ -bipyridyl complex with appended DTE moiety has been employed in monitoring quadratic NLO property.¹² Also, Pt-terpyridine acetylide complexes with pendant DTE moieties has been used in studying the resultant photo-physics where the two components (Pt-complex and DTE) have different intramolecular energy

transfer processes.¹³ Recently, Clever and co-workers have developed coordination cages based on Pd(II) metal ion and DTE unit, that allow modulation of guest uptake and release by irradiation with light of different wavelengths.¹⁴ Furthermore, there are many examples of chemosensors, based on DTE derivatives,¹⁵ where heteroatoms containing fluorophores are attached to the DTE unit and those heteroatom-containing fluorophores assist or participate in metal coordination.¹⁶ All such probes are designed in a way so that the metal ions do not attach to sulphur atoms of the DTE core itself and consequently do not intervene directly in photoisomerization process, rather they bind with a remote binding unit attached to the DTE core.

In order to explore the coordinating capability of the DTE unit towards metal ion, the design of the molecule should be such that there is minimal number of other possible binding sites available for the metal ion. Thus, any additional heteroatom containing fluorophore unit should principally be avoided in the molecular design. In turn, to get access to both of thiophene units at a time, an alkyne moiety (ethynylferrocene) could be attached to the DTE unit as the alkyne group is known to provide linearity in a structure,¹⁷ and therefore can impart rigidity and additional stability to the whole structure. On the other hand, ferrocene is a well-established electrochemically responding unit, which gives a pair of reversible waves in voltammetric studies and it is stable under moist and aerobic conditions. The DTE unit itself is also electrochemically active by producing irreversible waves,¹⁸ but to get to a conclusive electrochemical study, a standard redox moiety with reversible waves is beneficial for a comparative output. Also, there is a negligible scope of binding by the ferrocene unit, such that it does not compete with the binding experiments of the DTE unit.

Unlike the vast majority of DAE or DTE photochromes containing metal complexes,^{14,19,20} our designed compound represents a unique example in which the Hg^{2+} ion directly coordinates to the S atoms of thiophene rings of the photochromic unit, thereby, intervening directly in the dynamics of the photo-isomerization process. Herein, we have designed and synthesized the molecule **3**, devoid of any additional binding site or fluorophore, and it was utilized to evidence the binding activity of the DTE core itself with soft Hg^{2+} ion, in both of its open (**3o**) and closed (**3c**) forms for the first time. In this study we are able to show that the photoisomerization in the DTE core remains unhindered but decelerated upon binding with Hg^{2+} ion in the same unit.

2.2. Results and Discussion

2.2.1. Synthesis and Characterization

The synthesis of target symmetrical ferrocene based DTE moiety connected by *via* alkyne bridge is designed as depicted in Figure 2.1. In the design of our molecular architecture, we wish to combine the photochromic unit (DTE) with redox active ferrocene moiety *via* alkyne (C≡C) bridge, anticipating alkyne (C≡C) bridge may impart rigidity to the molecule. However, Sonogashira coupling between diiodo DTE derivative (I-DTE-I) and ethynylferrocene in presence of Pd(PPh₃)₄ and CuI is known to produce the di-1,4-ferrocenylbutadiyne (“Glaser product”) by homocoupling of ethynylferrocene as a by-product along with the desired product (by Sonogashira coupling).²¹ Therefore, to minimize the self-coupling reaction and to yield the Sonogashira product as the only product, we have introduced the CH₂-O-CH₂ functionality as a spacer between the terminal alkyne group and ferrocene unit. This derivatization was expected not to promote the “Glaser” coupling reaction and indeed it led to the formation of Sonogashira coupling product (**3**) as a sole product in good yield. The compound **3** was obtained as bright yellow solid in 85% yield by the Sonogashira cross coupling reaction between Br-DTE-Br (**1**) and ferrocene-3-ethoxyprop-1-yne (**2**), in presence of Pd(PPh₃)₄ catalyst, CuI co-catalyst and Et₃N base at 65°C (Figure 2.1). The molecule **3** was fully characterized by ¹H, ¹³C, ¹⁹F NMR, HRMS, IR spectra and elemental analysis. Additionally, the molecular structure of compound **3** was unambiguously established by the single crystal diffraction analysis (Figure 2.2a). **3o** crystallizes in triclinic, space group *P* $\bar{1}$. In the crystal structure, the compound undergoes intermolecular hydrogen bonding through C-H of the ferrocene and F atom present in the backbone moiety [C–H...F = 3.248(10)Å, ∠C–H–F = 126.88°] resulting in a two-dimensional hydrogen bonded porous network (Figure 2.2b). The 2D sheets are further assembled on top of each other through various van der Waals interactions (Figure 2.2c).

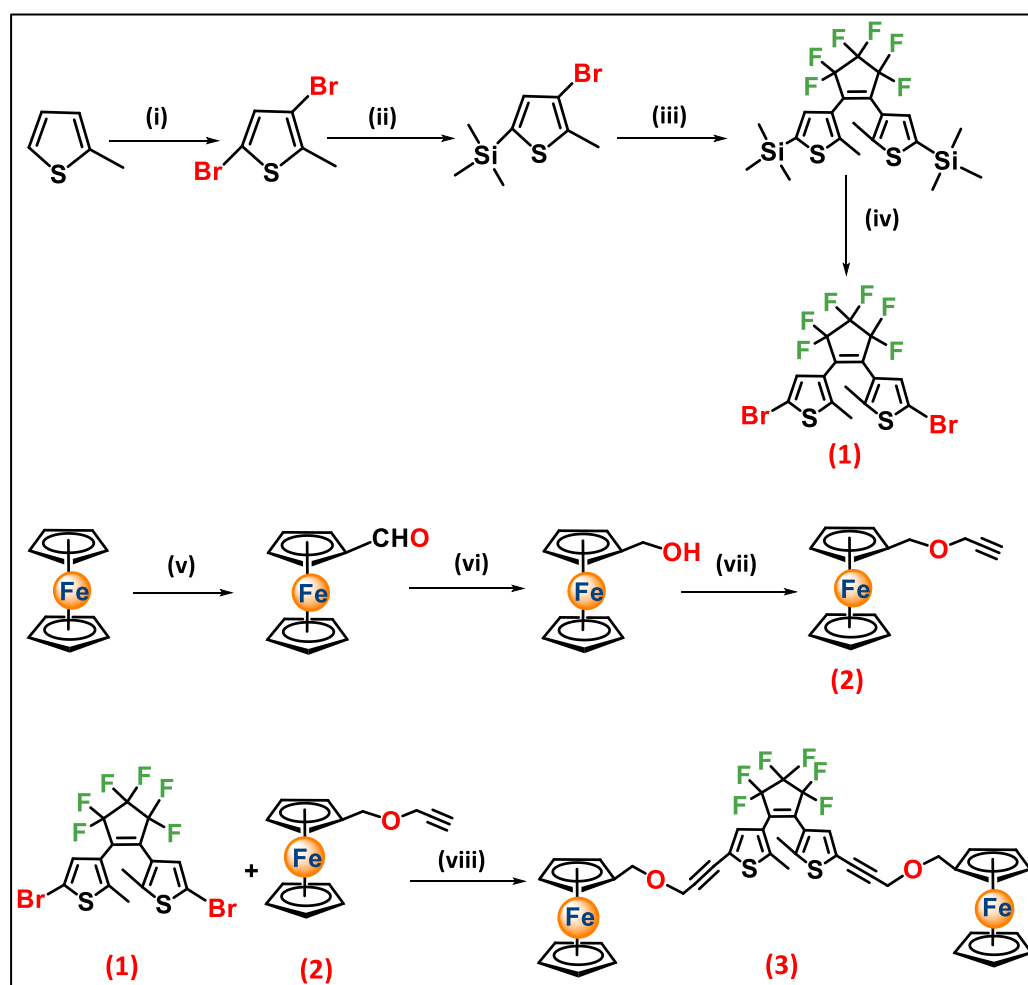


Figure 2.1. Synthetic route of compound 3. i) NBS, glacial AcOH, r.t., 2 h; ii) *n*-BuLi in THF, TMSCl, -78°C to r.t. 12 h; iii) *n*-BuLi in THF, octafluorocyclopentene, -78°C to r.t., 12 h; iv) NBS, glacial AcOH, reflux, overnight; v) POCl_3 in DMF, CCl_4 , reflux; vi) NaBH_4 in MeOH, 0°C to r.t., 2h; (vii) NaH in DMF, propargyl bromide, r.t., overnight; (viii) $\text{Pd}(\text{PPh}_3)_4$, CuI, Et_3N , 65°C , 7 h.

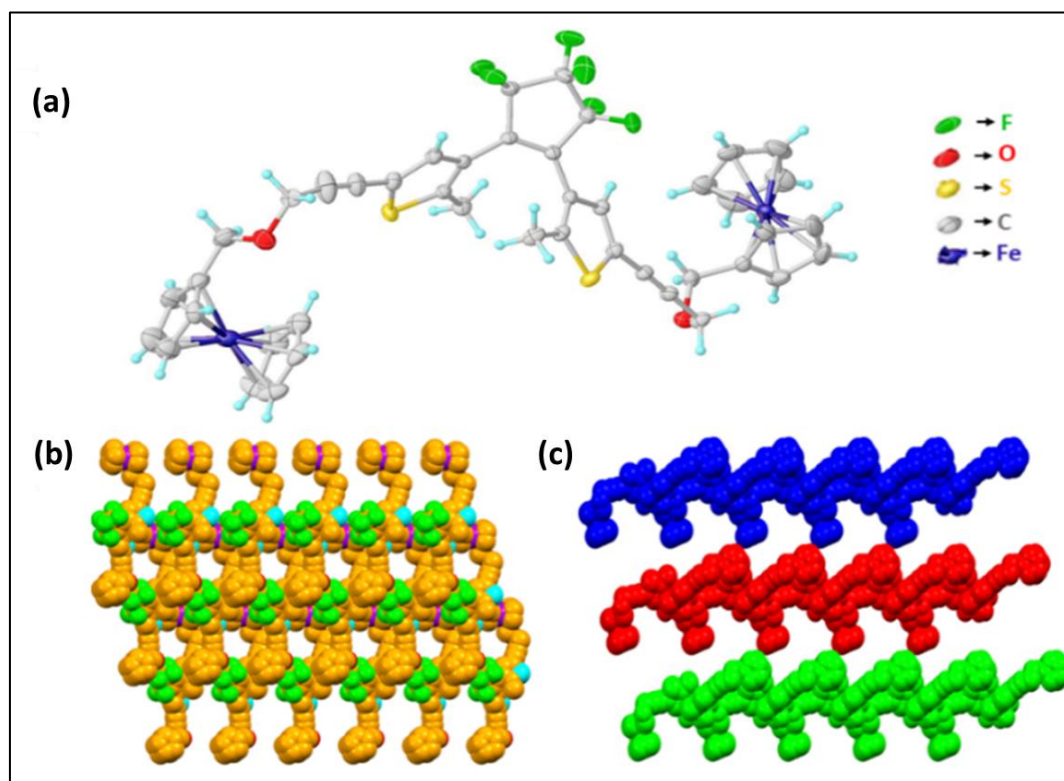


Figure 2.2. (a) X-ray structure of **3o** drawn with thermal ellipsoids at the 50% probability level; (b) porous 2D hydrogen bonded network structure; (c) parallel packing of the 2D networks sustained by van der Waals interactions.

Our objective for synthesizing the compound **3** was not to utilize this molecule as a selective sensing probe for a particular metal ion, rather we were interested to monitor the change of photoswitching efficiency upon coordination of any metal ions to the core DTE unit anticipating some influence on the dynamics of photoswitching if any metal ions coordinate directly to the DTE core. However, we have screened several metal ions (Fe^{3+} , Zn^{2+} , Cu^{2+} , Fe^{2+} , Hg^{2+} , Pb^{2+} , Ag^+ , Co^{2+} , Ni^{2+} , Pd^{2+} , Cu^+ , Cd^{2+}) for checking the binding affinity and coordination behaviour towards the S atoms of the DTE unit and control the chemistry of photoswitching. Addition of all the aforementioned metal ions, even in large excess, in CH_3CN solution to the receptor **3** did not impart any naked eye color changes except for Hg^{2+} , Fe^{3+} and Cu^{2+} ions (Figure 2.3a). Interestingly, for the sake of comparison, we have also screened the compound **1** as a reference, containing the S atoms of DTE, with all the the aforementioned metal ions anticipating the similar kind of interaction like that of compound **3**. However, no color change of the colorless acetonitrile solution of **1** (10^{-3} M) in presence of any of the same series of metal ions (Figure 2.3b) was observed by naked eye (Figure 2.3c), which usually occurs for any kind of interaction between two species. Further, absence of any such interaction was validated by

UV-vis and electrochemical studies which indicate no changes upon interaction with any of the above mentioned metal ions including Hg^{2+} ion with compound **1** (*vide supra*). Therefore, inclusion of ferrocene into the design of molecule **3** is necessary as well as beneficial not only because it serves as an internal standard in voltammetric studies, but also acts as chromogenic unit giving vivid colorimetric response from pale yellow to blue (10^{-3} M CH_3CN solution) upon interaction with Hg^{2+} ion (Figure 2.3d). The perceptible naked eye color change upon metal coordination to DTE moiety is always advantageous to comprehend the photoswitching dynamics of a metal chelated DTE moiety more rapidly. The non-interactive nature of compound **1** may be due to the strong electron-withdrawing property of the two bulky Br atoms, rendering the S atoms of DTE unit less nucleophilic and may generate steric hindrance to accommodate Hg^{2+} ion.

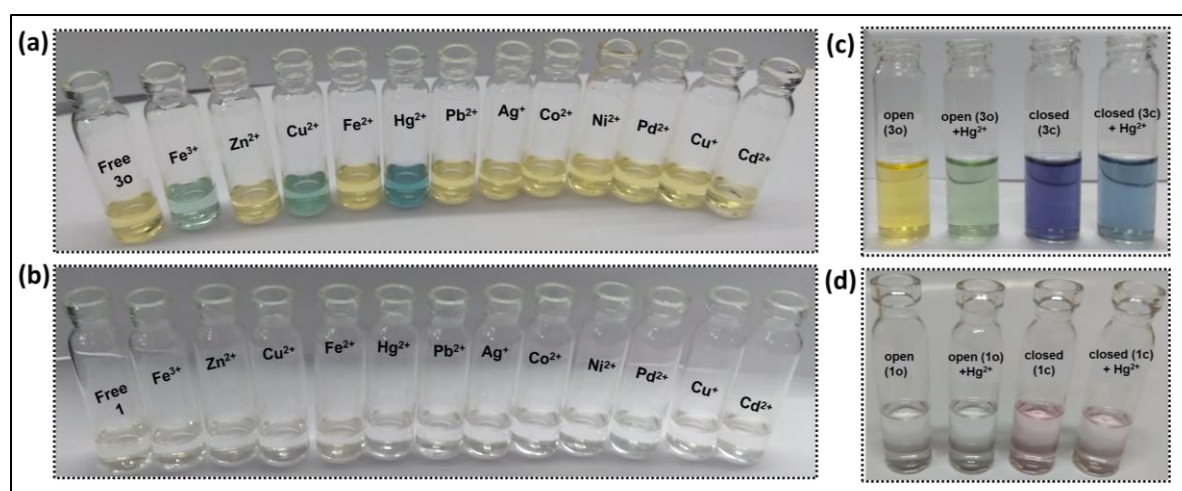


Figure 2.3. Visual color changes observed for free (a) **30** and (b) **1** after addition of several metal ions in 10^{-4} (M) CH_3CN solution. Visible color changes of (c) **1** (open and closed) and (d) **3** (open and closed) in presence of $\text{Hg}(\text{ClO}_4)_2$ in 10^{-3} M CH_3CN solution.

2.2.2. UV-vis Absorption Study

The photochromic DTE unit gives rise to some characteristic undulations in the UV-vis spectra.²¹ The UV-vis spectra of many compounds containing the DTE unit are reported in the literature, however, each new orientation of atoms gives a unique property. The synthesized

molecule **3o** was designed with an intention to investigate the reversible photoswitching behavior of the DTE unit in presence of chelating metal ions. To investigate the behavioral absorption fingerprint in our designed architecture, **3o** was exposed to UV-irradiation having monochromatic wavelength of 365 nm and to visible light.

As shown in Figure 2.4, **3o** displayed an absorption peak at 263 nm ($\epsilon = 3.66 \times 10^3 \text{ M}^{-1} \text{ cm}^{-1}$) due to π - π^* transition in the open form.²² The irradiation of 365 nm UV light for transformation from **3o** to **3c** was done periodically with 5 s of irradiation time and the consequent UV-vis spectra were recorded. When CH₃CN solution of **3o** (3 ml, $5 \times 10^{-5} \text{ M}$) was periodically irradiated by 365 nm UV light for 5 s, the 263 nm peak showed slight increment in intensity, whereas, a new shoulder peak at 581 nm ($\epsilon = 3.01 \times 10^2 \text{ M}^{-1} \text{ cm}^{-1}$), characteristic of the closed DTE unit,²³ appeared. The peak intensified with gradual irradiation and after 5 min (300 s) of irradiation, saturation was obtained signifying almost full conversion from **3o** to **3c**, accompanied by color change to violet from pale yellow (Figure 2.5, *vide infra*).

Upon stepwise addition of Hg²⁺ ion ($5 \times 10^{-5} \text{ M}$) up to 1 equiv in CH₃CN solution of **3o** ($5 \times 10^{-5} \text{ M}$) (Figure 2.4b) and **3c** ($5 \times 10^{-5} \text{ M}$) (Figure 2.4c) separately, the absorption maximum at 263 nm decreased in intensity with the emergence of a new peak at 240 nm (Figure 2.6a and 2.6b, *vide infra*). Two distinct isosbestic points at 211 nm and 259 nm appeared for **3o** along with a color change from pale yellow to blue (Figure 2.5). However, no well-defined isosbestic point was obtained for **3c** and the band at 581 nm diminished slightly by Hg²⁺ addition, along with a change in color of the solution from violet to green (Figure 2.4d). 1:1 binding stoichiometries were determined for both **3o** and **3c** with Hg²⁺ ion from Job's plot (Figure 2.6c and 2.6d) and elemental analysis. Binding constant values of **3o** and **3c** with Hg²⁺ were determined from the equation²⁵ - $1/[A-A_0] = 1/K(A_{\text{max}}-A_0)[\text{Hg}^{2+}]_n + 1/(A_{\text{max}}-A_0)$; where, A_{max} = Maximum absorbance; A_0 = Initial absorbance of free ligand (**3**); A = Absorbance after addition of Hg²⁺. The binding constant (K) values for both the isomers (**3o** and **3c**) are $4.779 \times 10^4 \text{ M}^{-1}$ and $2.149 \times 10^4 \text{ M}^{-1}$ (log K = 4.679 and 4.332 for **3o** and **3c**) respectively (Figure 2.6e and 2.6f), indicating slightly stronger binding (2.22 times) of **3o** with Hg²⁺ as compared to **3c** *i.e.*, it suggests that **3c** is a weaker competitor than **3o** for binding with Hg²⁺.

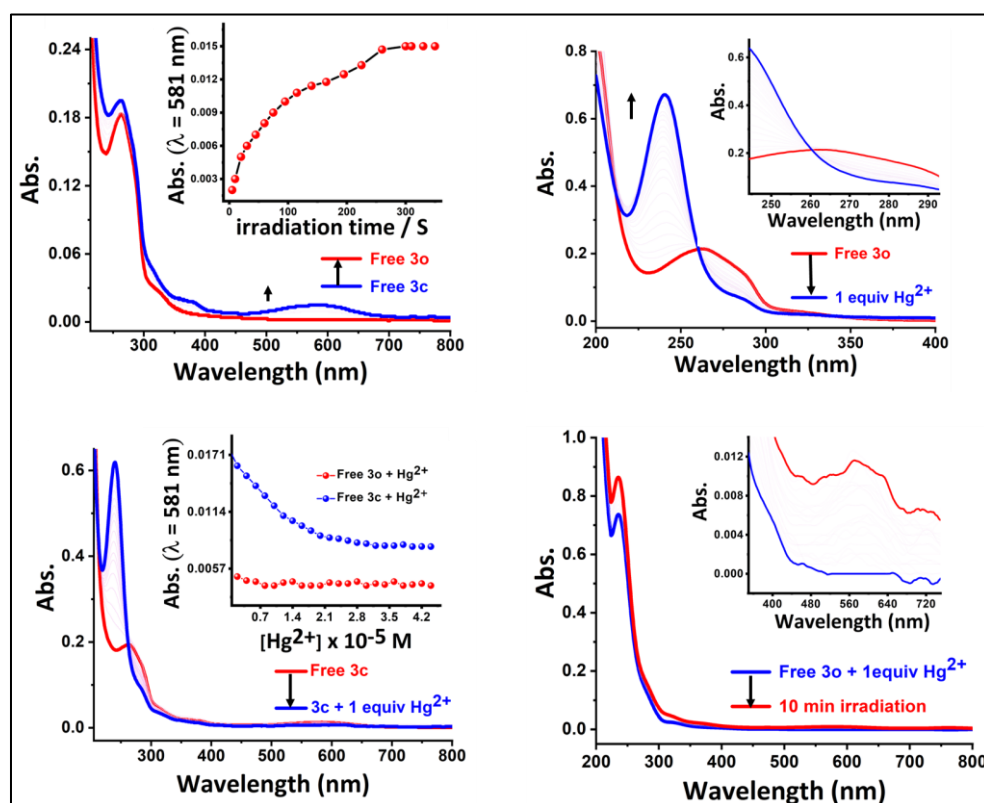


Figure 2.4. (a) Changes in the absorption spectra of **3o** by gradual irradiation at 365 nm UV light in CH₃CN (inset: variation of absorption intensity at 581 nm against irradiation time, upon transforming from **3o** to **3c**); (b) Changes of absorption spectra of **3o** (5×10^{-5} M) upon gradual addition of Hg²⁺ ion up to 1 equiv in CH₃CN solvent (inset: zoomed portion representing the isosbestic point at 259 nm); (c) Changes of absorption spectra of **3c** upon gradual addition of Hg²⁺ up to 1 equiv (inset: variation of absorption intensity of **3c** at 581 nm with [Hg²⁺] and its comparison with **3o** for the same); (d) Changes of absorption spectra of [**3o**·Hg²⁺] upon irradiation with 365 nm UV light (inset: zoomed portion representing the emergence of peak at 581 nm).

To elucidate the efficiency of electrocyclization and cycloreversion, quantum yield calculations were performed. The quantum yields for photocyclization ($\Phi_{o \rightarrow c}$) and cycloreversion ($\Phi_{c \rightarrow o}$) of **3** were found to be 0.56 and 0.007 respectively (Table 2.1) in hexane with 1,2-bis(2-methyl-5-phenyl-3-thienyl)perfluorocyclopentene as a reference.²⁶

Quantum yield was evaluated from the given equation-

$$\Phi(\mathbf{3}) = \left(\frac{\text{slope}(\mathbf{3})}{\text{slope}(\text{ref})} \right) \times \left(\frac{\varepsilon(\text{ref})}{\varepsilon(\mathbf{3})} \right) \times \Phi(\text{ref})$$

where, slope = slope of the linear plot, extracted from A (absorbance) vs t (irradiation time) plot; ε = molar extinction coefficient of concentration 5×10^{-5} M at 574 nm for ref. and at 581 nm for **3** and Φ = quantum yield.

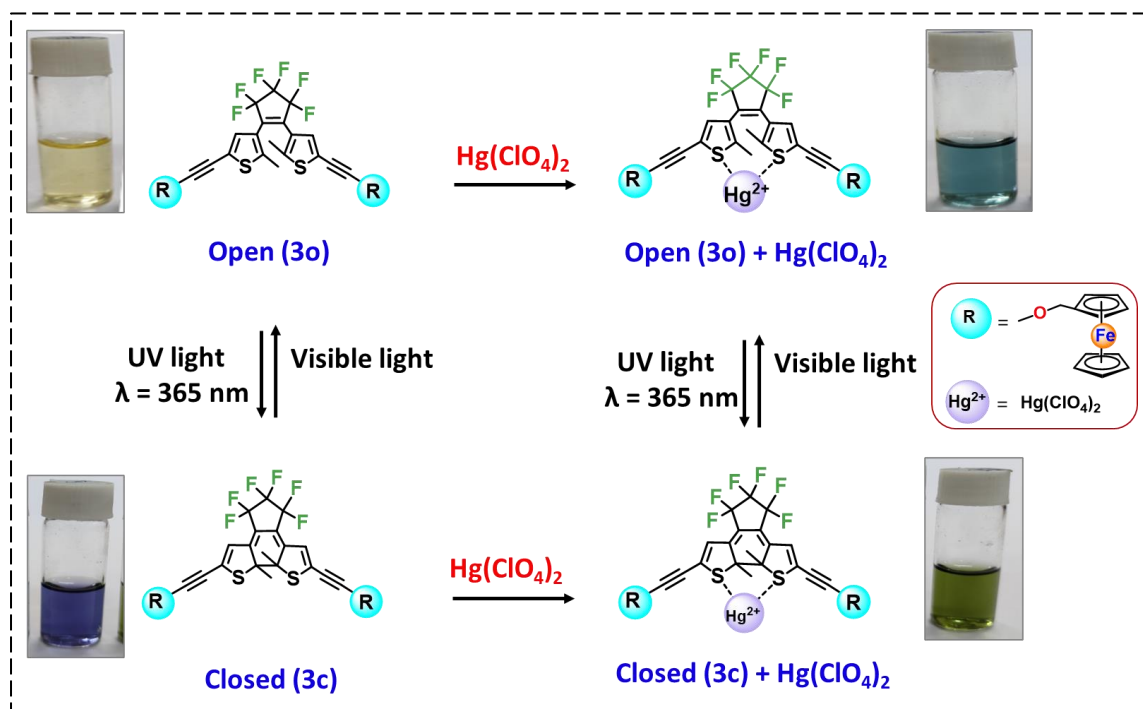


Figure 2.5. Schematic representation of the photoresponsive switching process of **3o** and **3c** in presence of $\text{Hg}(\text{ClO}_4)_2$ and lights of different wavelengths.

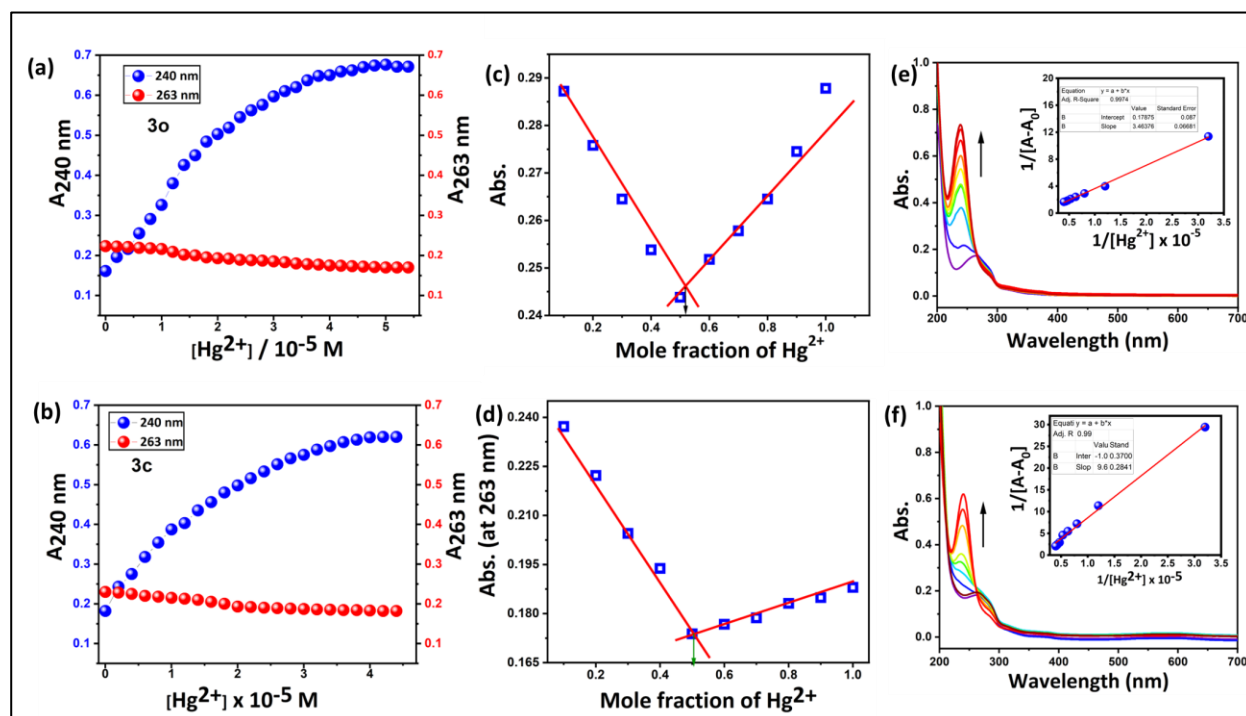


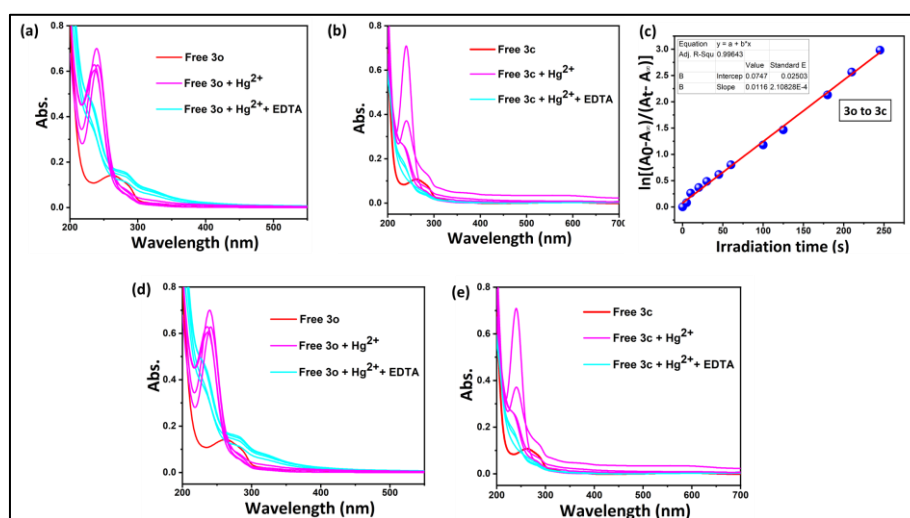
Figure 2.6. Changes of absorption intensities of (a) **3o** and (b) **3c** with Hg^{2+} addition. Job's plot for compound **3** (c) open form and (d) closed form with Hg^{2+} ($5 \times 10^{-5} \text{ M}$) in CH_3CN solution indicating the formation of 1:1 complex. Binding constant for compound **3** (e) open form and (f) closed form with Hg^{2+} ($5 \times 10^{-5} \text{ M}$) in CH_3CN solution.

Moreover, in order to investigate the open to closed isomerization process in metal chelated form, the CH_3CN solution of $[\mathbf{3o} \cdot \text{Hg}^{2+}]$ was subjected to UV irradiation ($\lambda = 365 \text{ nm}$), with 5 s interval (Figure 2.4d). The characteristic band for **3c** at 581 nm ($\epsilon = 4.36 \times 10^2 \text{ M}^{-1} \text{ cm}^{-1}$) appeared after 15 s of irradiation of $[\mathbf{3o} \cdot \text{Hg}^{2+}]$ complex, whereas it appeared after 5 s for free **3o**. The band at 240 nm ($\epsilon = 26.91 \times 10^3 \text{ M}^{-1} \text{ cm}^{-1}$), which appeared due to interaction of **3o** with Hg^{2+} , remained unperturbed even after irradiation of $[\mathbf{3o} \cdot \text{Hg}^{2+}]$ for long time and the formation of peak at 581 nm is very slow for $[\mathbf{3o} \cdot \text{Hg}^{2+}]$ solution. This slower kinetics of ring closing in metal chelated form, $[\mathbf{3o} \cdot \text{Hg}^{2+}]$, was also supported by the lower (8.2 times) quantum yield ($\Phi_{o \rightarrow c}$) of 0.068 (Table 2.1), compared to that of free **3o**. This concludes that although $[\mathbf{3o} \cdot \text{Hg}^{2+}]$ gets converted to $[\mathbf{3c} \cdot \text{Hg}^{2+}]$, the rate of conversion²⁷ of free **3o** to **3c** ($k = 0.01 \text{ s}^{-1}$) is faster than the rate of conversion of $[\mathbf{3o} \cdot \text{Hg}^{2+}]$ to $[\mathbf{3c} \cdot \text{Hg}^{2+}]$ ($k = 0.007 \text{ s}^{-1}$), as confirmed by kinetic studies also, using UV-vis spectra (Figure 2.7a-2.7c). The binding equilibrium in **3c** is not as stable as that for the open isomer, may be due to the formation of strained and puckered 5-membered C-S-Hg-S-C ring, as indicated by DFT calculations (*vide infra*).

Table 2.1. Quantum yields of cyclization ($\Phi_{0\rightarrow c}$) and cycloreversion ($\Phi_{c\rightarrow 0}$) for free **3** and its metal chelated form [**3o**·Hg²⁺] upon irradiation by 365 nm UV light.

Compound	ϵ (M ⁻¹ cm ⁻¹)		Slope		Quantum yield	
	Cyclization	Cycloreversion	Cyclization	Cycloreversion	Cyclization ($\Phi_{0\rightarrow c}$)	Cycloreversion ($\Phi_{c\rightarrow 0}$)
3	0.0184×10^5	0.003×10^5	5.72761×10^{-5}	1.119×10^{-4}	0.56	0.007
[3o +Hg ²⁺]	0.216×10^5	–	7.98726×10^{-5}	–	0.068	–
Ref.	0.2608×10^5	0.0116×10^5	8.5327×10^{-4}	7.94356×10^{-4}	0.59	0.013

In order to assess the kind of interaction (in terms of reversibility) between **3o/3c** and Hg²⁺, aqueous solution of Na₂EDTA (5×10^{-5} M) was employed as a decomplexing agent into the corresponding CH₃CN solution. The nature of interaction of both **3o** and **3c** with Hg²⁺ is reversible, *i.e.*, with every aliquot of Na₂EDTA addition to CH₃CN solution of [**3o/3c**·Hg²⁺] complex, the UV-vis spectrum corresponding to free **3o/3c** got generated, whereas upon Hg²⁺ addition to the same solution, the UV-vis spectrum corresponding to [**3o/3c**·Hg²⁺] got re-generated. This experimental cycle could be repeated two times without much loss of sensitivity; however, in the third cycle the sensitivity decreased slightly (Figure 2.7d and 2.7e).

**Figure 2.7.** $\ln[(A_0-A_\infty)/(A_t-A_\infty)]$ vs irradiation time plot for (a) free **3o** to **3c**; (b) [**3o**·Hg²⁺] to [**3c**·Hg²⁺] for determination of respective rate constants of conversion; (c) comparison of the two linear plots for better comparison of the rates of cyclization. Reversibility test of (d) **3o** and (e) **3c** with Hg²⁺ (5×10^{-5} M, CH₃CN) and EDTA (5×10^{-5} M, H₂O) for 1:1 binding stoichiometry.

In order to investigate the metal-chelation ability of **3o** and **3c** along with dynamics of photo-transformation from **3o** to **3c** in free and in metal-chelated forms, the interactions of **3o** with several metal ions were investigated by UV-vis spectra (Figure 2.8a). Only Hg^{2+} , Fe^{3+} and Cu^{2+} ions displayed positive response, among which, the responses produced by Fe^{3+} and Cu^{2+} ions originate from the oxidation of ferrocene (Fe^{2+}) to ferrocenium ion (Fe^{3+}), formation of which was confirmed by the appearance of a new characteristic absorption peak at around 630 nm^{24} (Figure 2.8b and 2.8c). The back reduction of the oxidized ferrocenium ion (Fe^{3+}) to ferrocene (Fe^{2+}) again was also achieved by employing sodium *L*-ascorbate, a reducing agent, to the acetonitrile solution of oxidized species, indicating reversible oxidation-reduction nature of interaction (Figure 2.8d and 2.8e). On the other hand, Hg^{2+} ion did not promote any such redox interaction; rather it induces the formation of a complex with **3o** and **3c** (Figure 2.8f). Therefore, the interactions of **3o** and **3c** with Hg^{2+} were carefully monitored for executing the study of phototransformation in metal-chelated form.

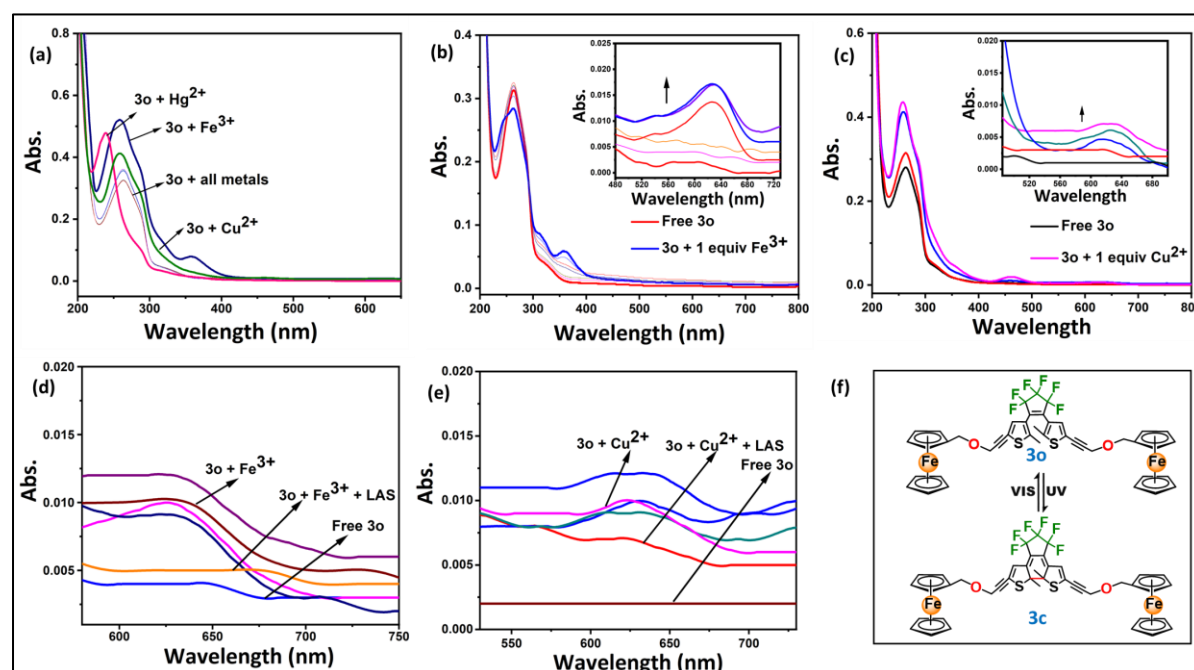


Figure 2.8. (a) UV-vis spectral changes of **3o** upon addition of several metal ions. UV-vis spectral changes of **3o** upon gradual addition of (b) Fe^{3+} and (c) Cu^{2+} in CH_3CN (5×10^{-5} M). UV-vis spectral changes at 630 nm peak of **3o** in CH_3CN (5×10^{-5} M) upon gradual addition of (d) Fe^{3+} /LAS and (e) Cu^{2+} /LAS. (f) Schematic representation of photoisomerization process for **3o** to **3c**.

2.2.3. Electrochemical Studies

To realize the changes occurring in DTE derivatives in presence of metal ion by electrochemical studies was one of the principal objectives of including ferrocene unit within the core of the designed molecule. Electrochemical reversible behavior of ferrocene²⁸ and irreversible nature of dithienylethene²⁹ in **3o** was observed in cyclic voltammetry (CV) and differential pulse voltammetry (DPV) experiments, which were carried out at room temperature in CH₃CN solution (1.25×10^{-4} M) containing 0.1(M) (TBAP) [(n-Bu)₄N]ClO₄ as a supporting electrolyte.

To start with the electrochemical studies, the CV of **3o** was recorded, which displayed a reversible oxidation wave at 0.426 V corresponding to ferrocene/ferrocenium couple³⁰ and an irreversible wave at 1.11 V, characteristic of dithienylethene (DTE) core.³¹ Upon UV irradiation of **3o** by 365 nm light, an increment of the irreversible wave at 1.11V was observed along with a slight anodic shift to 1.16 V ($\Delta E_{1/2} = 50$ mV), which marked the transformation of **3o** to **3c** (Figures 2.9a and 2.9b). The increment of intensity of irreversible wave upon **3o** to **3c** conversion may be attributed to the fact that the closed form is electrochemically more active than the open DTE core.³²

Acetonitrile solution of Hg²⁺ (1.25×10^{-4} M) was added stepwise into CH₃CN solution of **3o** and **3c** separately, to conduct the binding studies using electrochemical method. The oxidation wave at 0.426 V for both **3o** (Figures 2.9c and 2.9d) and **3c** (Figures 2.10a and 2.10b) did not exhibit any shift in potential, whereas, the peaks at 1.11 V and 1.16 V respectively shifted anodically to 1.17 V and 1.19 V ($\Delta E_{1/2} = 60$ mV and 30 mV) respectively and became flattened with gradual addition of Hg²⁺ ion up to 1 equiv. The significant perturbation of the DTE oxidation wave upon Hg²⁺ addition supports the possibility of interaction of **3o** and **3c** with Hg²⁺ by the DTE core. In **3o**, the wave flattened readily after addition of small amount of Hg²⁺ ion, but in **3c**, the restoration of its own property exceeds the effect of Hg²⁺ binding for up to a large quantity of Hg²⁺ ion. The retainment of the nature of oxidation wave of DTE core of **3c** until quantitative addition of Hg²⁺ ion, proved the sluggish interaction of **3c** as compared to **3o** with Hg²⁺ ion.

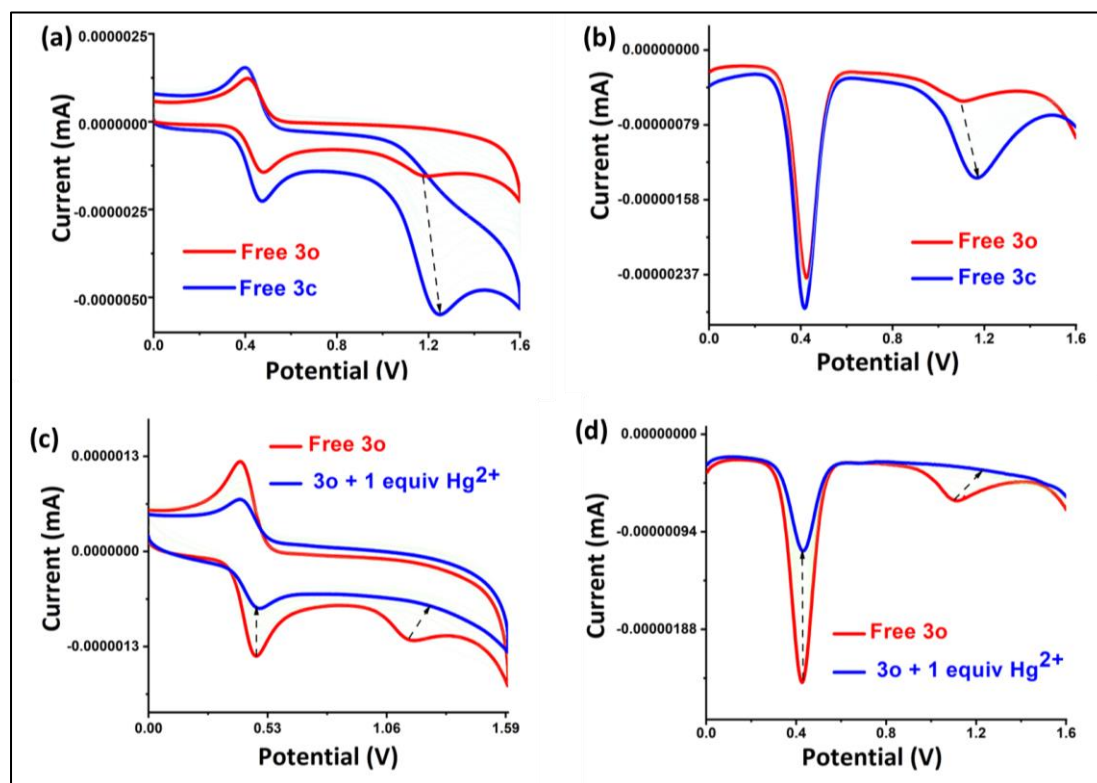


Figure 2.9. (a) Cyclic voltammetry (CV) and (b) differential pulse voltammetry (DPV) of open form (**3o**) to closed form (**3c**) upon irradiation of UV ($\lambda = 365$ nm); (c) Cyclic voltammetry (CV) and (d) differential pulse voltammetry (DPV) of **3o** (open form) upon addition of Hg^{2+} up to 1 equiv in CH_3CN solution with $[(n\text{-Bu})_4\text{N}]\text{ClO}_4$ as supporting electrolyte at 0.06 Vs^{-1} scan rate.

Now upon irradiation of $[\mathbf{3o}\cdot\text{Hg}^{2+}]$ complex with 365 nm UV light (gradually up to total 10 min), substantial difference in the irreversible oxidation wave was observed. The irreversible wave, which had almost flattened due to complexation got regenerated, but in an indistinct way and to a much lesser extent (Figures 2.10c and 2.10d). This clearly signifies the resistance in the conversion of open form to closed one in presence of bounded Hg^{2+} ion which is consistent with other experimental results and DFT calculations. In all the above experiments, the ferrocene/ferrocenium oxidation wave remained almost undisturbed. Tabular depiction of data (Figure 2.11a) and normalized electrochemical measurements (Figure 2.11b) present the changes more clearly, supporting the anticipation of participation of S atoms of the DTE core in both $[\mathbf{3o}\cdot\text{Hg}^{2+}]$ and $[\mathbf{3c}\cdot\text{Hg}^{2+}]$ complexes.

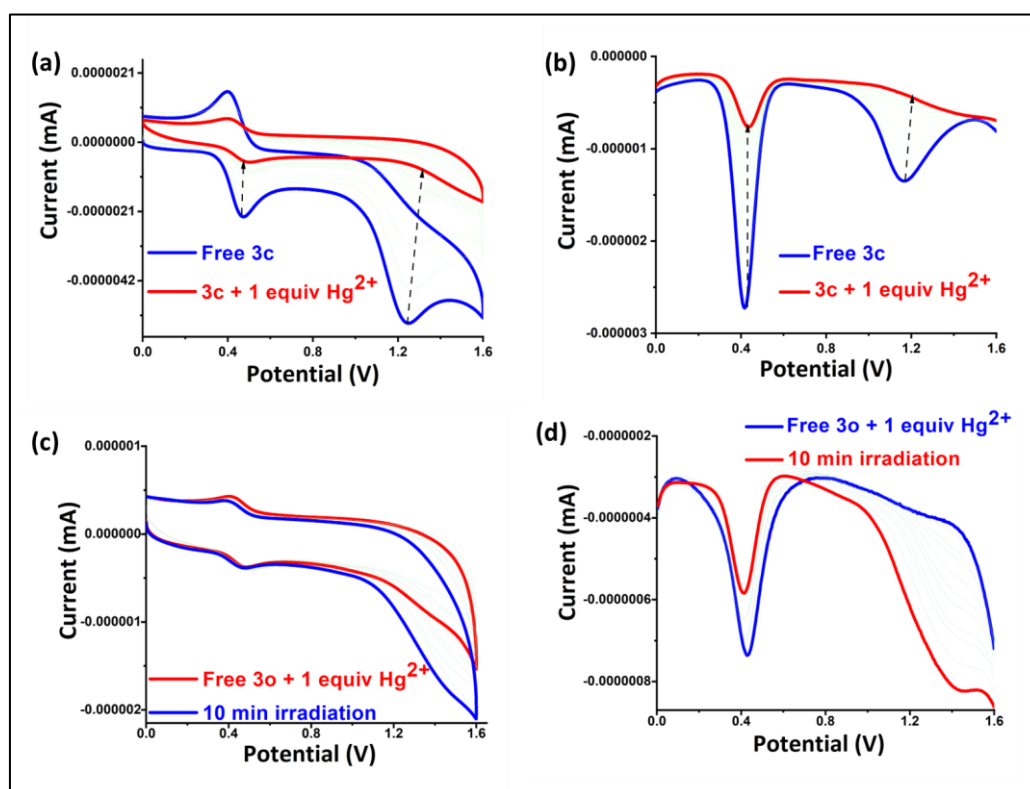


Figure 2.10. (a) Cyclic voltammetry (CV) and (b) differential pulse voltammetry (DPV) of **3c** (closed form) upon addition of Hg²⁺ up to 1 equiv; (c) Cyclic voltammetry (CV) and (d) differential pulse voltammetry (DPV) of [**3o**·Hg²⁺] upon irradiation of UV ($\lambda = 365$ nm) in CH₃CN solution with [(n-Bu)₄N]ClO₄ as supporting electrolyte at 0.06 Vs⁻¹ scan rate.

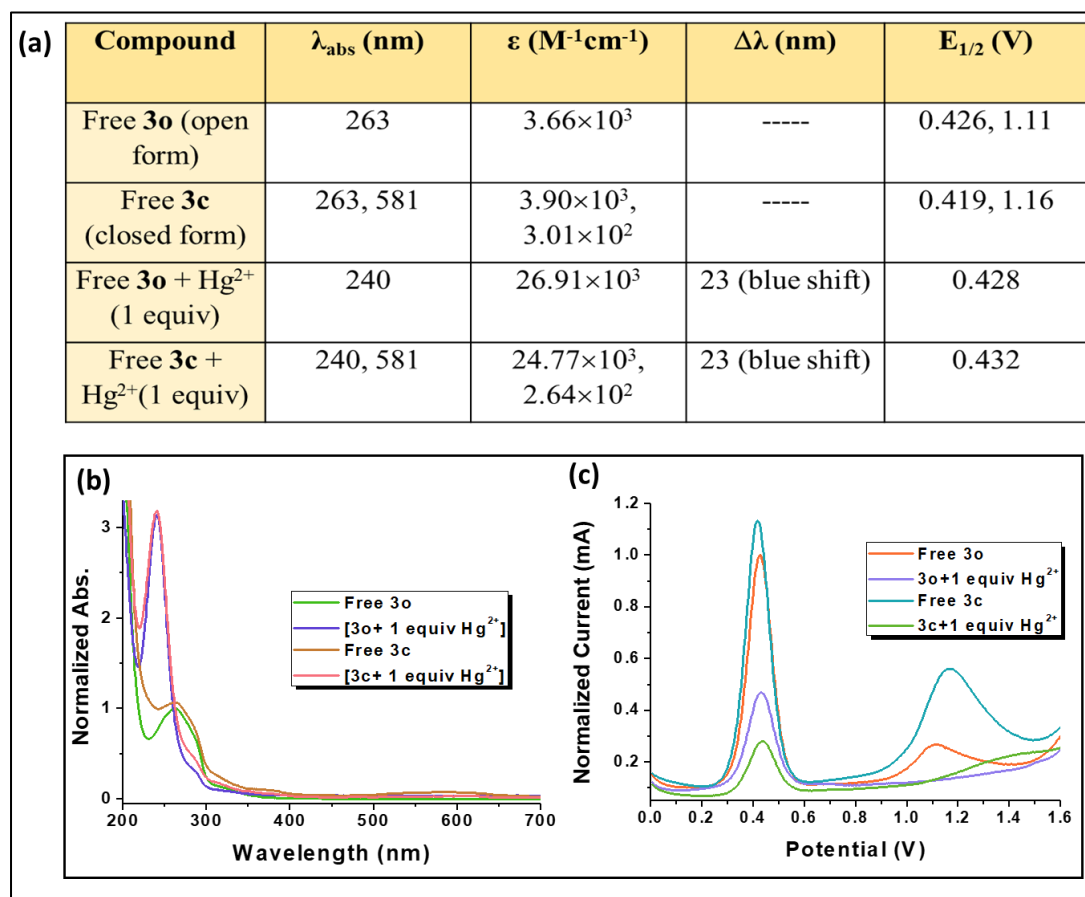


Figure 2.11. (a) Tabular representation of photophysical and electrochemical data for free **3** and $[\mathbf{3} \cdot \text{Hg}^{2+}]$ in both open and closed forms in CH_3CN . Normalized (b) absorption intensity (5×10^{-5} M) and (c) electrochemical changes of compound **3** after Hg^{2+} (1.25×10^{-4} M) binding and after UV irradiation (365 nm) in CH_3CN solution.

2.2.4. Comparative ^1H NMR and IR Studies

The ring-closure process was further monitored by ^1H NMR study which indicates the complete conversion of open form to closed form upon irradiation. ^1H NMR is studied thoroughly to explore the photoisomerization process as well as the chelation phenomenon. Upon conversion of **3o** to **3c**, in CD_3CN , the characteristic singlet peak for methyl protons shifted downfield (from 2.16 to 2.21 ppm) and signal assigned to thienyl protons remained unchanged (Figure 2.24, *vide infra*).

To confirm the plausible binding mode of **3o** with Hg^{2+} , ^1H NMR spectra were recorded in CD_3CN solution. The spectral changes of **3o** and $[\mathbf{3o} + 1 \text{ equiv } \text{Hg}^{2+}]$ are depicted in Figure

2.12. It exhibited a singlet at 2.16 ppm which corresponds to Me protons, the peaks around 4.14 to 4.36 ppm for substituted ferrocene ring protons and OCH_2 respectively, another singlet for the aromatic ring proton of thiophene ring. The Me protons (H_a), close to coordinating S atoms, shifted upfield³³ from 2.16 ppm to 1.96 ppm ($\Delta\delta = 0.20$ ppm), whereas no such displacement was observed for ferrocenyl (Fc), $-\text{OCH}_2$ and thiophene ring (H_b) protons. Hence, the plausible binding mode in **30** for Hg^{2+} (soft acid) is *via* S atoms (soft base) present in DTE unit. After addition of excess Hg^{2+} no further change indicates 1:1 binding stoichiometry. These results suggest that **30** may chelate with Hg^{2+} (soft acid) using S atoms (soft base) present in DTE unit and ferrocene units do not participate in the binding mechanism. This result also corroborates with CV and DPV studies.

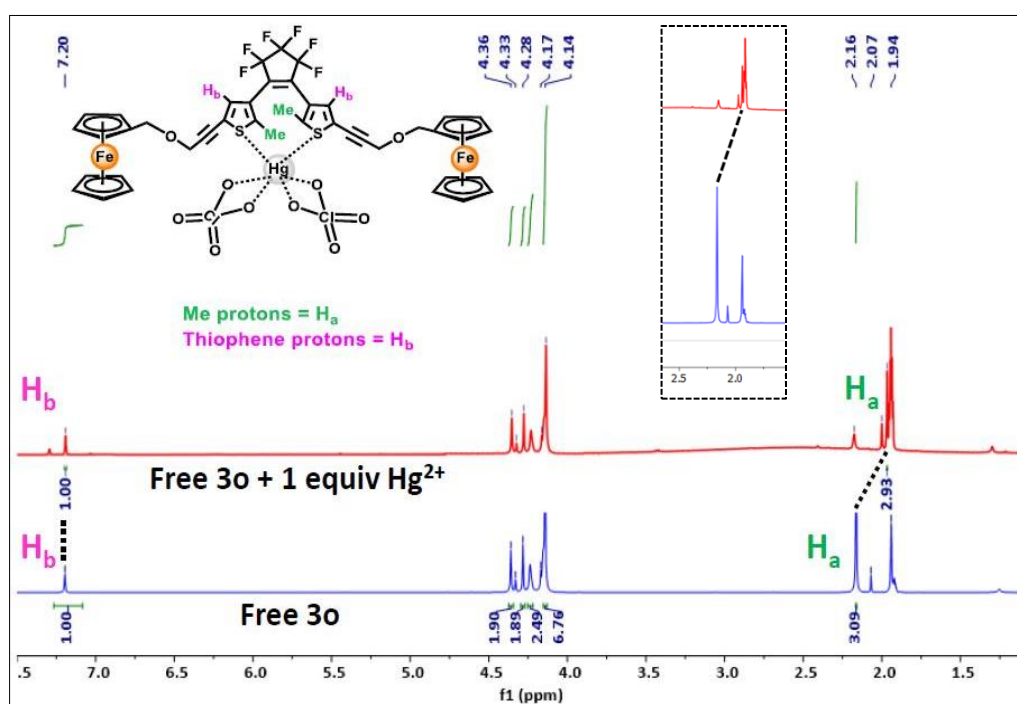


Figure 2.12. Comparative ^1H NMR spectra of **30** in presence of 1 equiv Hg^{2+} in CD_3CN as a solvent.

In order to get further details about the binding behavior, IR spectra was recorded with Hg^{2+} (as its perchlorate salt). The IR spectra of free **30** and [**30** + 1 equiv Hg^{2+}] were measured in solid state, (Figure 2.13a and 2.13b). On addition of $\text{Hg}(\text{ClO}_4)_2$, the peak at 2220 cm^{-1} which is assigned for the $\text{C}\equiv\text{C}$ stretching frequency³⁴ remains unperturbed and a strong band at 1086 cm^{-1} due to $\text{Cl}-\text{O}$ stretching³⁵ appeared, indicating the inclusion of $\text{Hg}(\text{ClO}_4)_2$ unit in **30** (see below the IR sample preparation). The above observation indicates that the alkyne ($\text{C}\equiv\text{C}$) unit does not participate in coordination to Hg^{2+} , probably due to the adjacent OCH_2 groups which

make the alkyne units less susceptible to react with Hg^{2+} ion as compared to the S atoms. Thus, ^1H and IR titrations come in unison to suggest the plausible binding mode where **3o** coordinates Hg^{2+} through the S atoms of DTE core.

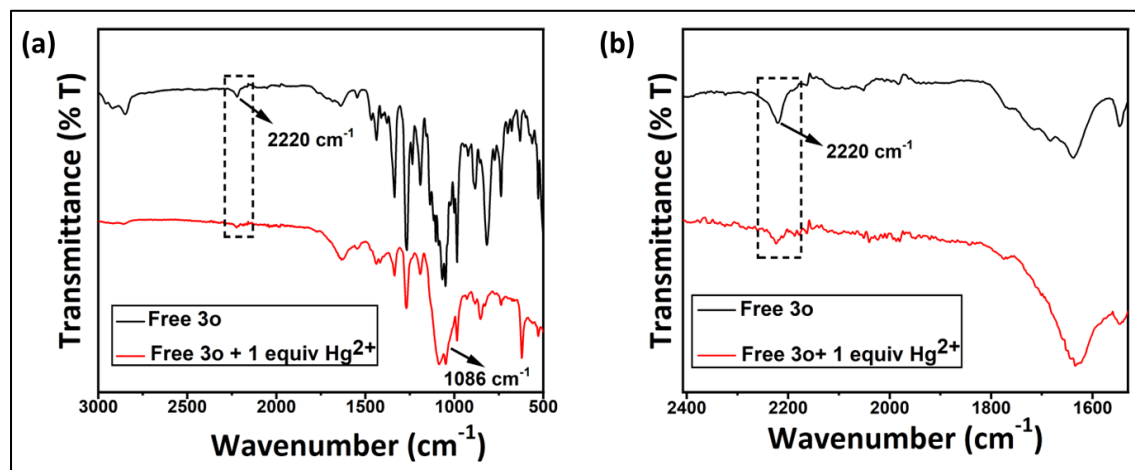


Figure 2.13. (a) Comparative IR spectra of **3o** in presence of 1 equiv Hg^{2+} in solid state at room temperature, (b) zoomed image of IR stretching of alkyne ($-\text{C}\equiv\text{C}-$) peak of **3o** before and after addition of $\text{Hg}(\text{ClO}_4)_2$.

2.3. Theoretical (DFT) Studies

Solution phase theoretical calculations were carried out on the ground of density functional theory (DFT) in order to understand the structural and electronic parameters. The coordinates of the starting geometry of **3o** (Figure 2.14a and 2.14b) was taken from that of the solid-state structure (Figure 2.2a). However, **3c** (Figure 2.14c) was derived from the optimized geometry of **3o**. Various starting points of $[\mathbf{3o}\cdot\text{Hg}(\text{ClO}_4)_2]$ and $[\mathbf{3c}\cdot\text{Hg}(\text{ClO}_4)_2]$ are finally converged which led us to conclude their minimized conformation (Figure 2.14d and Figure 2.14e respectively).

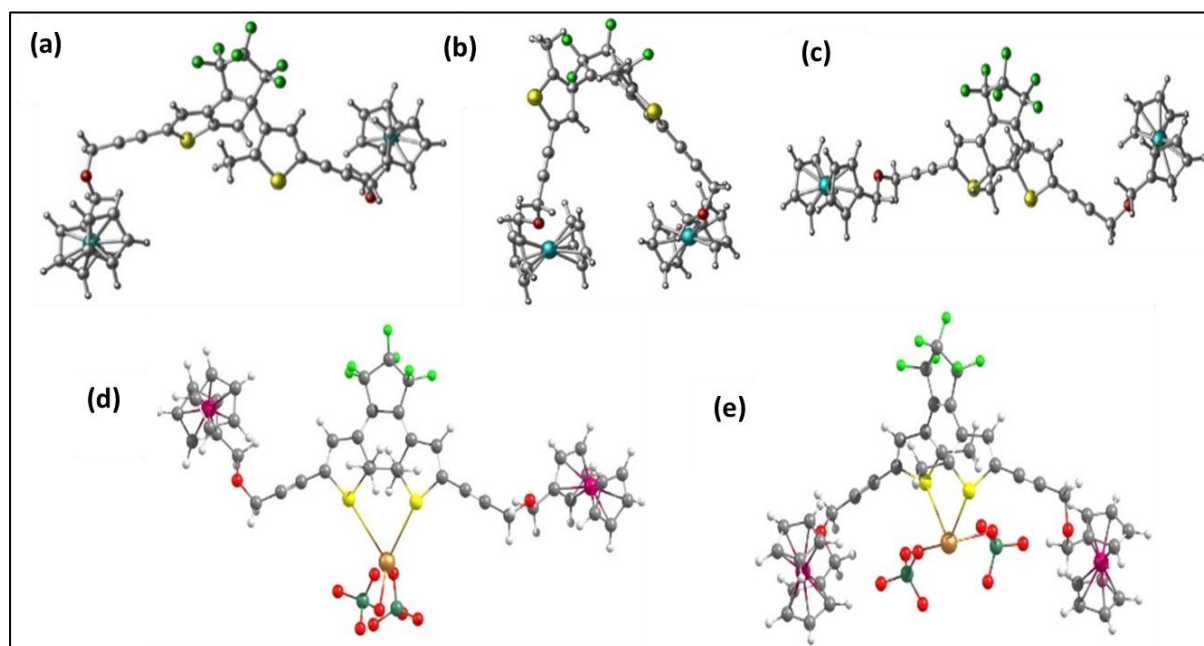


Figure 2.14. Energy minimized structures of **3o** [(a) anti-parallel and (b) parallel], (c) **3c**, (d) [**3o**·Hg(ClO₄)₂], (e) [**3c**·Hg(ClO₄)₂].

In Figure 2.14, we have reported the energy minimized conformers for the parallel, anti-parallel for open form and closed form of the compound **3**. As found out, in the anti-parallel form (Figure 2.14a) the ferrocene containing arms are well separated. The situation is similar in the closed structure **3c** (Figure 2.14c) which is 66.2 kJ/mol less stable than the anti-parallel open form **3o** (Figure 2.16a). The energy values are in consistent with the easy conversion from closed to open conformers. This is also supported by a low energy barrier of 61.6 kJ/mol computed for closed to open process. This energy difference between the anti-parallel open and closed isomers in DTE photochromes are expected.³⁶ Further the newly formed elongated C-C bond of 1.548 Å suggests **3c** to be an unstable product.³⁷ Nevertheless, topology analyses of the frontier orbitals reveal that the LUMO of **3o** has indeed a bonding character between the two reactive C atoms that indicates the possible formation of the closed product **3c**. Notably, the parallel conformer (Figure 2.14b) is nearly isoenergetic to the anti-parallel open form, and is unstable by only 4.06 kJ/mol than the anti-parallel open conformer (this difference, smaller than 4.2 kJ/mol, is negligible at this level of theory). Therefore, in solution, **3o** exists as a blend of parallel and anti-parallel conformers. However, the energy minimized geometry of **3o** shown in Figure 10a, that is the anti-parallel open form corresponds to the SCXRD structure (Figure 2.15).

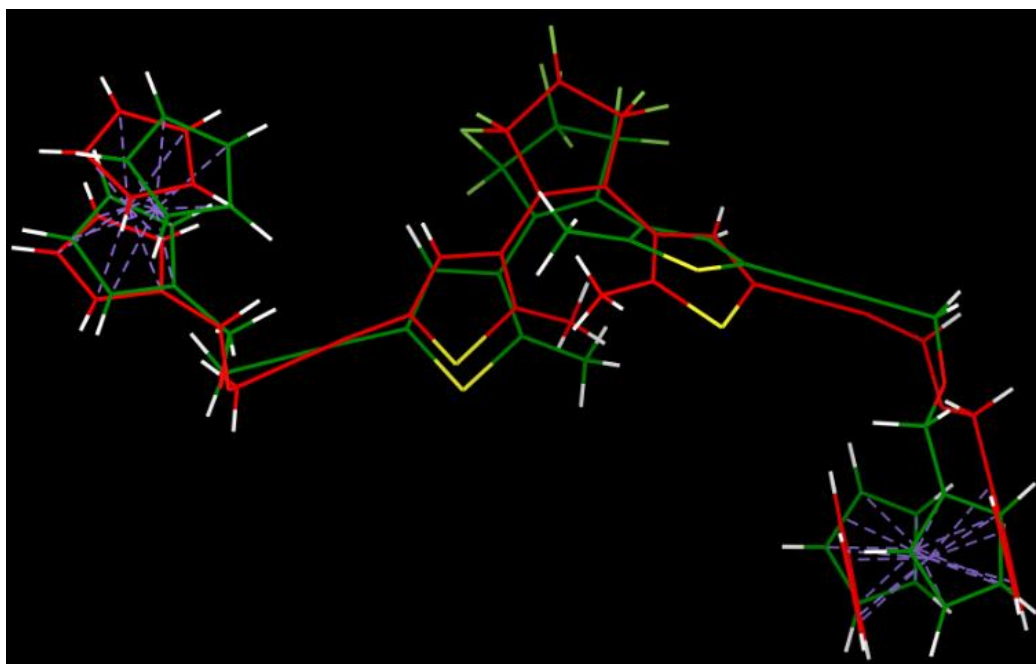


Figure 2.15. Geometry comparison between the starting (red) and optimized (green) geometries.

The optimized geometries reveal that the free ligands maintain their core geometries even after binding with the analyte, Hg^{2+} . The optimized geometries of $[\mathbf{3o}\cdot\text{Hg}(\text{ClO}_4)_2]$ and $[\mathbf{3c}\cdot\text{Hg}(\text{ClO}_4)_2]$ show that, in both cases Hg^{2+} adopts a distorted tetrahedral geometry by connecting it to two S and two O atoms. Although the S atoms of DTE core in the molecule $\mathbf{3o}/\mathbf{3c}$ are taking part in the interactions with Hg^{2+} ion, the Hg-S bonds are relatively weak³⁸ (Wiberg bond index values of ca 0.2), as evidenced from their Hg-S bond lengths (in $[\mathbf{3o}\cdot\text{Hg}(\text{ClO}_4)_2]$: 3.75, 3.69 Å and in $[\mathbf{3c}\cdot\text{Hg}(\text{ClO}_4)_2]$: 3.71, 3.69 Å). Notably, $[\mathbf{3c}\cdot\text{Hg}(\text{ClO}_4)_2]$ is unstable by 79.3 kJ/mol than $[\mathbf{3o}\cdot\text{Hg}(\text{ClO}_4)_2]$. Further, the computed energy of the reaction suggests that complexation of $\mathbf{3o}$ to Hg^{2+} is 4.7 times more exergonic (-22.7 kJ/mol) than the formation of complex, $[\mathbf{3c}\cdot\text{Hg}(\text{ClO}_4)_2]$ (-4.8 kJ/mol). The calculations also suggest a dynamic coordination process that exists in the solution phase (Figure 2.16). The results, suggest that $[\mathbf{3c}\cdot\text{Hg}(\text{ClO}_4)_2]$ may either convert into free $\mathbf{3o}$ by releasing Hg^{2+} (that can further combine into $[\mathbf{3o}\cdot\text{Hg}(\text{ClO}_4)_2]$) or may convert directly into $[\mathbf{3o}\cdot\text{Hg}(\text{ClO}_4)_2]$ complex through intramolecular ring opening. This further shows the instability of the $[\mathbf{3c}\cdot\text{Hg}(\text{ClO}_4)_2]$ suggesting low possibility for the formation of the complex. The DFT calculated MO analyses revealed that due to extension in plane conjugation, the LUMO of $\mathbf{3c}$ is stabilized by 1.11 eV than that of $\mathbf{3o}$ [LUMO: -1.82 eV ($\mathbf{3o}$) and -2.92 eV ($\mathbf{3c}$)]. This causes a decrease in the HOMO-LUMO gap in $\mathbf{3c}$ suggesting a red shift in the absorption spectra (Figure 2.17a-2.17d). Complex formation

between **3o** and Hg^{2+} resulted in destabilization of the HOMO of $[\mathbf{3o}\cdot\text{Hg}(\text{ClO}_4)_2]$ by 0.97 eV that also resulted in decrease of HOMO-LUMO gap in $[\mathbf{3o}\cdot\text{Hg}(\text{ClO}_4)_2]$, whereas, the frontier molecular orbital energies in **3c** and $[\mathbf{3c}\cdot\text{Hg}(\text{ClO}_4)_2]$ are nearly comparable.

To get more information about the electronic transitions, TD-DFT (CAM-B3LYP) calculations have been performed on both the free ligands as well as the complexes in solution phase (acetonitrile). The TD-DFT calculations on **3o** show that the $S_0 \rightarrow S_1$ transitions have large oscillator strength ($f = 1.28$) (Figure 2.18a, Table 2.2) and the excitation wavelength to the S_1 state is calculated to be 267 nm (Table 2.2). This encompasses the transitions between HOMO-5 to LUMO+1 and HOMO-4 to LUMO+2. These are mainly of ligand to ligand charge transfer (LLCT) character that is majorly centered on the ethynyl and thiophene moieties. On the other hand, calculated transition at 288 nm for $[\mathbf{3o}\cdot\text{Hg}(\text{ClO}_4)_2]$ (Figure 2.19a, Table 2.2) involves two major transitions of MLCT ($n(\text{Fe}) \rightarrow \pi^*(\text{C}_5\text{F}_6\text{ ring})$) and LLCT character (π orbital centered on ethynyl and thiophene to π^* of C_5F_6 ring). Calculation on **3c** showed that the excitation wavelengths to the S_1 state are at 302, 344 and 553 nm with oscillator strengths 0.2, 0.17 and 0.49 respectively (Figure 2.18b, Table 2.6). The transition at 344 nm is due to Fe based lone pair to the delocalized π^* orbital of the ligand (MLCT character), and the transition at 302 and 553 are due to $\pi \rightarrow \pi^*$ transition of the central part of the ligand (LLCT character). The TD-DFT calculation on $[\mathbf{3c}\cdot\text{Hg}(\text{ClO}_4)_2]$ showed two major transition to S_1 which are calculated at 697 and 572 nm which are due to ligand based $\pi \rightarrow \pi^*$ transition and ligand based $\pi \rightarrow$ empty orbital centered on Hg, respectively (Figure 2.19b, Table 2.2).

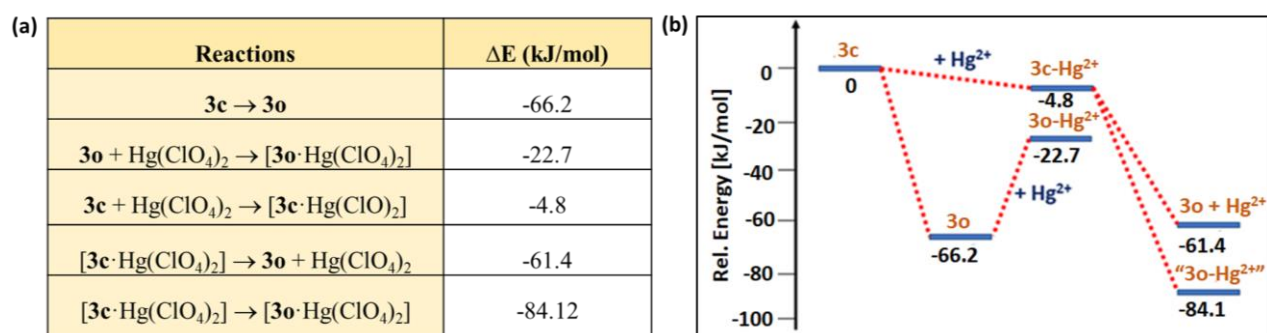


Figure 2.16. (a) Tabular representation of computed energy of the reactions; (b) Energy diagram of the reaction of **3c/3o** with Hg^{2+} , calculated at the B3LYP/6-31(d,p)LANL2DZ level of theory.

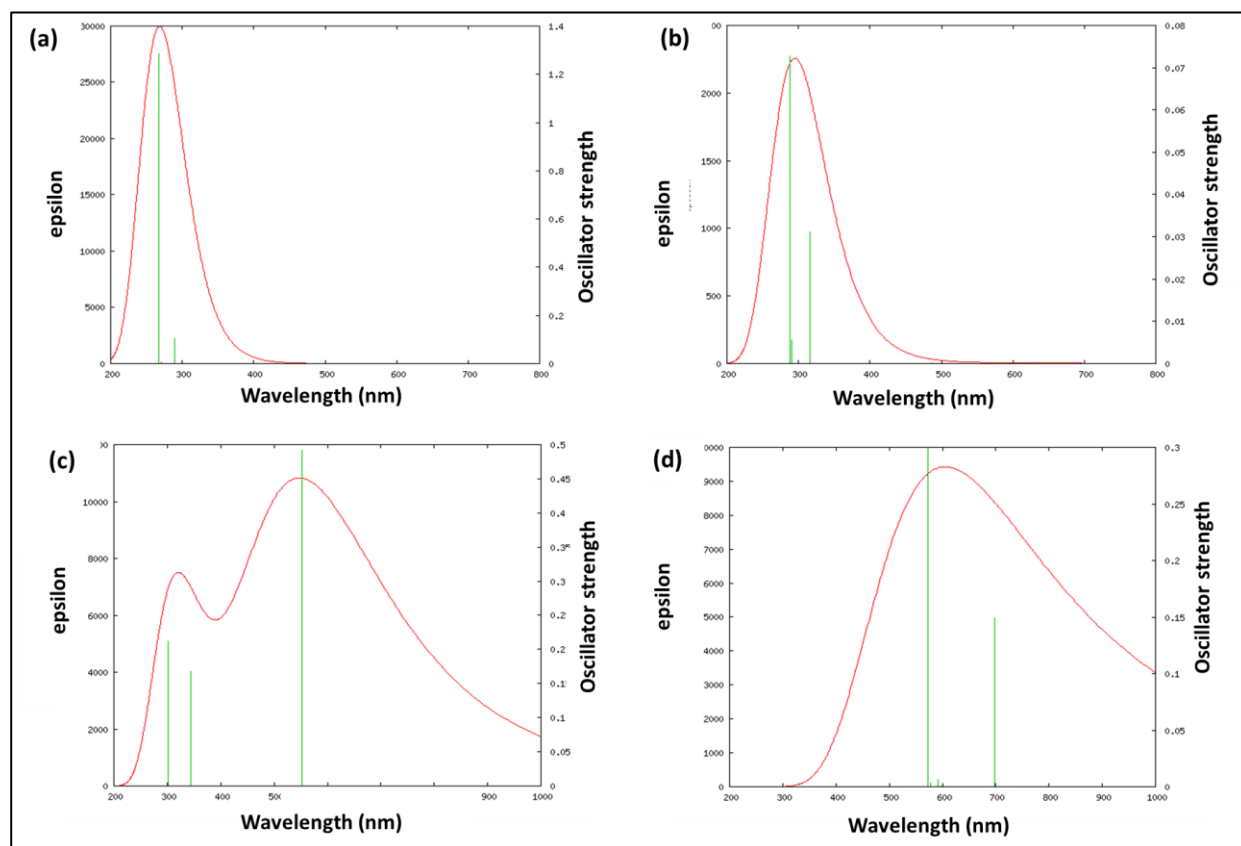


Figure 2.17. Calculated absorption spectra of (a) **3o**, (b) **[3o·Hg(ClO₄)₂]**, (c) **3c**, (d) **[3c·Hg(ClO₄)₂]**.

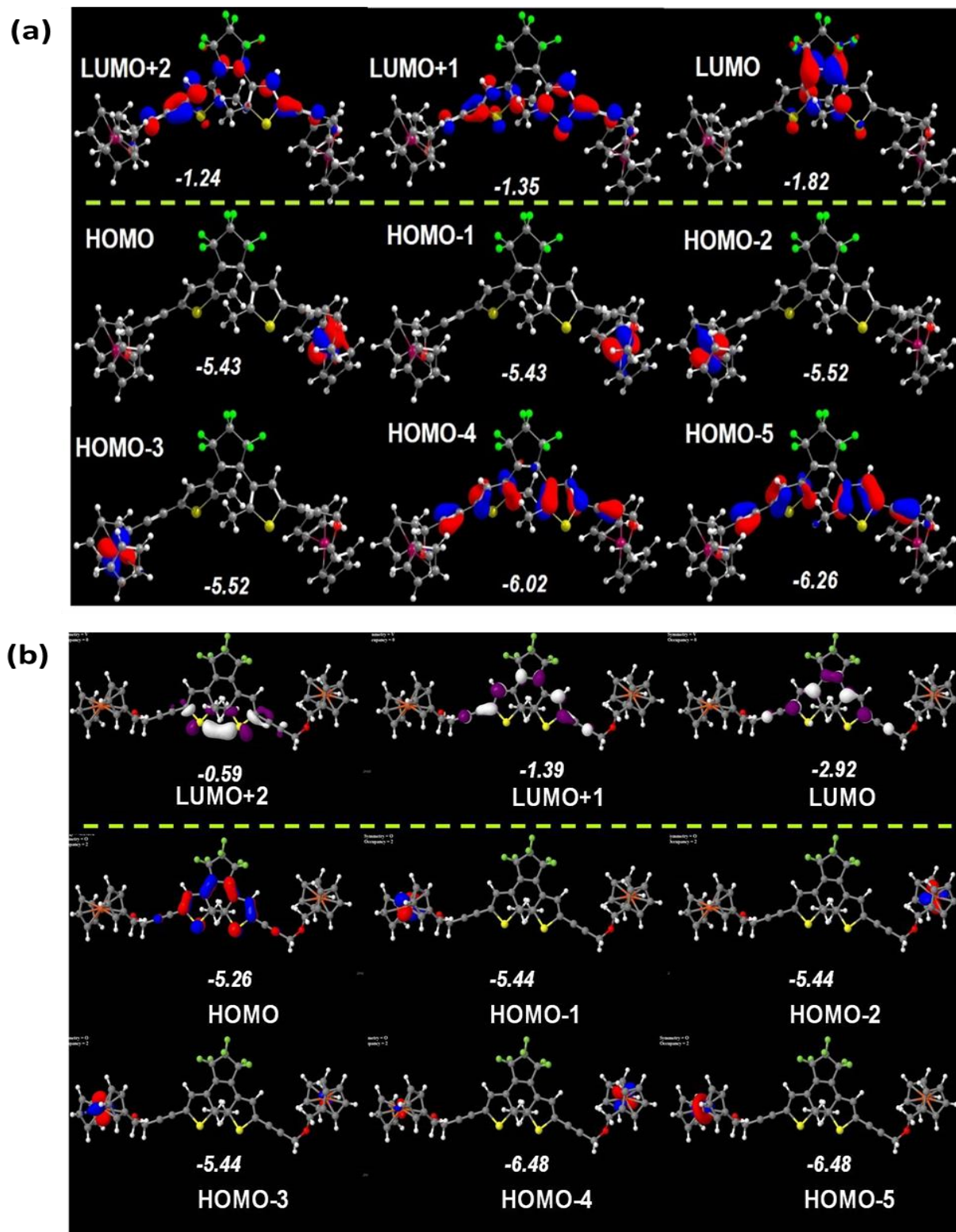


Figure 2.18. FMOs of (a) **3o** (mo cutoff 0.05); (b) **3c** (mo cutoff 0.05).

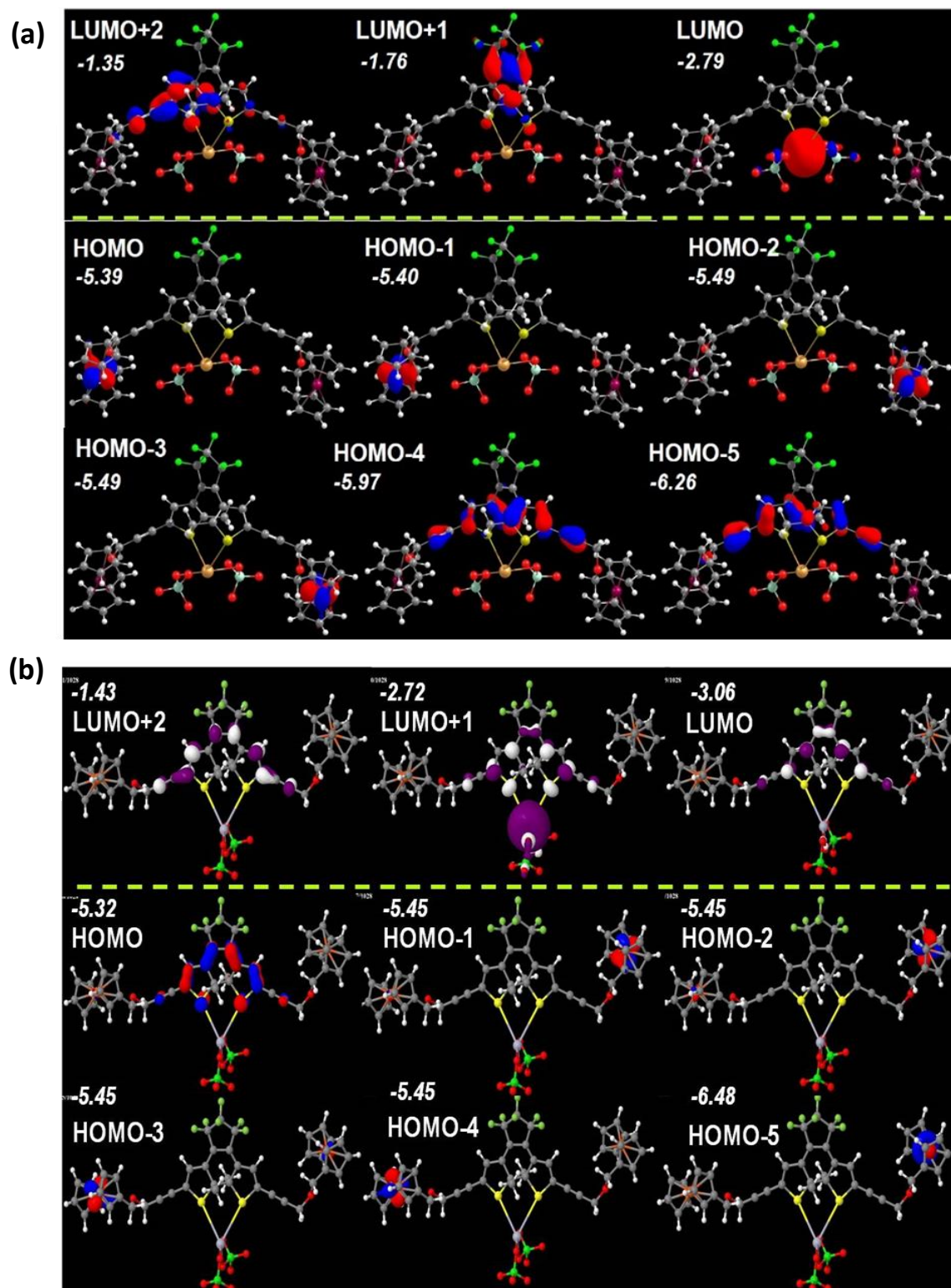


Figure 2.19. FMOs of (a) $[30 \cdot \text{Hg}(\text{ClO}_4)_2]$ (mo cutoff 0.05); (b) $[3c \cdot \text{Hg}(\text{ClO}_4)_2]$ (mo cutoff 0.05).

2.4. Conclusions

In conclusion, we have reported an unprecedented protocol where coordination strength of a metal ion can discriminate the photoswitchable states of DTE unit *via* simple naked-eye color change and electrochemical analysis and all the experimental results were further supported by DFT calculations. Moreover, from the dynamics study in terms of quantum yield and rate constants, it can be established that metal coordination slows down the inherent photoswitchable nature of the DTE core. The electrochemical studies by CV and DPV emphasizes on the differential responses of the open and closed isomers of **3** towards Hg^{2+} , as well as on the effect of metal chelation on photoinduced transformations. The inclusion of rigid alkyne moiety and chromogenic ferrocene unit seems to be very crucial for successful practical application of this type of metal chelated photo-controlled probe. We believe that such fine tuning by metal chelation and the suitable design of DTE based molecular architecture may open up a new avenue for the development of photo-controlled metal coordinating smart molecular switches.

2.5. Experimental Sections

2.5.1. Materials and Measurements

Unless otherwise mentioned, all the analytes used for synthesis were purchased from commercially available suppliers and used without further purification. Perchlorate salts of metals (Zn^{2+} , Fe^{2+} , Fe^{3+} , Pb^{2+} , Hg^{2+} , Ag^+ , Cu^{2+} , Ni^{2+} , Pd^{2+} and Cd^{2+}), $\text{CoCl}_2 \cdot 6\text{H}_2\text{O}$, $[\text{Cu}(\text{CH}_3\text{CN})_4]\text{PF}_6$ were purchased from Sigma Aldrich. K_2CO_3 , NBS, glacial acetic acid, were purchased from local chemicals. DMF, acetonitrile (HPLC), THF were purchased from Merck chemicals. 2-methyl thiophene and 1.6 M *n*-BuLi in hexane were purchased from Alfa aesar. Trimethylchlorosilane, (Trimethylsilyl)acetylene, octafluorocyclopentene were obtained from TCI Chemicals. Tetrakis-(triphenylphosphine)palladium(0) used as catalyst for Sonogashira coupling, was purchased from Sigma Aldrich. All solvents were dried and degassed prior to use and the reactions were performed using Schlenk techniques under nitrogen atmosphere. The dithienylethene derivative (**1**)^{39,40} and ferrocenyl precursor (**2**)⁴¹ were prepared as previously reported. All of the solvents were either HPLC or spectroscopic grade in the optical spectroscopic studies. The reactions were monitored by thin-layer chromatography on silica-gel plates and column chromatography was conducted on the silica gel (mesh 60-120) of 2.5

cm diameter. A conventional three-electrode configuration setup was used to perform cyclic voltammetry (CV) and differential pulse voltammetry (DPV) experiments (10^{-4} M), where glassy carbon, platinum and silver/silver chloride (Ag/Ag^+) were used as working electrode, auxiliary electrode and reference electrode respectively. Tetrabutylammoniumperchlorate, $[\text{n-Bu}_4\text{N}]\text{ClO}_4$, was employed as supporting electrolyte at scan rate 0.06 Vs^{-1} for carrying out the experiments.

2.5.2. Instrumentation

^1H and ^{13}C NMR spectroscopic measurements were recorded with Bruker 400 MHz FT-NMR spectrometer using TMS (SiMe_4) as an internal reference at room temperature and the chemical shifts are reported in ppm. The shifts were referenced to the residual solvents as follows: $\text{DMSO-d}_6 = 2.49$ (^1H), $\text{CD}_3\text{CN} = 1.94$ (^1H) and $\text{CDCl}_3 = 77.15$ (^{13}C). HRMS were collected from a water HRMS model XEVO-G2QTOF#YCA351 spectrometer. FT-IR spectra were obtained with a PerkinElmer LX-1 FT-IR spectrophotometer. UV and visible light irradiations were performed with lamp of wavelength 365 nm. SHIMADZU-UV-1900i UV-vis spectrophotometer was used for the study of absorption spectra at room temperature. The cyclic voltammetry (CV) performed on a CH Instruments electrochemical workstation. CHN analysis was performed on a Vario EL elemental CHNS analyzer.

Caution! Metal perchlorate salts are potentially explosive in certain conditions. All due precautions should be taken while handling perchlorate salts!

2.5.3. Preparation of sample for IR and elemental analysis of $[\mathbf{30}\cdot\text{Hg}^{2+}]$ complex

The pure compound **30** was dissolved in minimum amount of CH_3CN , in which 1 molar equiv CH_3CN solution of $\text{Hg}(\text{ClO}_4)_2$ was added. The two solutions were mixed up progressively and solvent mixture was evaporated under reduced pressure. The resulting blue solid compound was washed with H_2O to remove free perchlorate anion, followed by filtration

by suction and was dried under vacuum for several hours. The dry solid complex was directly used for IR and elemental analysis.

2.5.4. Synthesis of Compound 3

An oven dried Schlenk flask was charged with compound **1** (0.271 g, 0.5156 mmol) in distilled Et₃N solvent under nitrogen atmosphere. It was further degassed by bubbling nitrogen for 45 min to remove dissolved O₂. Then the catalyst Pd(PPh₃)₄ (0.029 g, 0.0258 mmol), CuI (0.006 g, 0.0361 mmol) were added under N₂ stream. Pre-dried solid compound **2** (0.327 g, 1.289 mmol) was added to the solution and the reaction mixture was stirred for 7 h at 65 °C. After 7 h stirring, the solution was cooled to room temperature and poured onto H₂O. The organic layer was extracted by DCM and dried over Na₂SO₄. The residue was purified by column chromatography on silica gel (ethyl acetate:hexane = 5:95) to afford a pure compound **3** (85%, yellow solid). The synthesized compound **3** was fully characterized by ¹H NMR, ¹³C NMR, ¹⁹F NMR, HRMS, IR spectroscopy and elemental analysis.

¹H NMR (400 MHz, DMSO-d₆): δ 7.31 (s, 1H, *H*_{thiophene}), 4.34 (s, 2H, OCH₂), 4.32 (s, 2H, OCH₂), 4.25 (s, 2H, *H*_{Cp}), 4.15 (s, 7H, *H*_{Cp}), 1.94 (s, 3H, CH₃); **¹³C NMR** (100 MHz, CDCl₃): δ 143.29 (C_{DTE}), 136.44 (C_{DTE}), 131.98 (C_{DTE}), 124.72 (C_{DTE}), 121.08 (C_{DTE}), 115.74 (C_{DTE}), 113.70 (C_{DTE}), 90.75 (C_{alkyne}), 82.21 (C_{alkyne}), 69.67 (C_{Cp}), 68.83 (C_{Cp}), 68.63 (C_{Cp}), 68.32 (C_{Cp}), 57.42 (OCH₂), 57.08 (OCH₂), 14.54 (CH₃). **¹⁹F NMR** (376 MHz, CDCl₃): δ -110.29 (s, 4F), -131.87 (s, 2F). **HRMS**: *m/z* [M+H]⁺ Calcd. for C₄₃H₃₄O₂S₂F₆Fe₂ 873.0681; found 873.1068; **Elemental analysis**: Anal. Calcd. for C₄₃H₃₄O₂S₂F₆Fe₂C, 59.19; H, 3.93; found C, 60.8; H, 4.25. C₄₃H₃₄O₂S₂F₆Fe₂Hg (for [**3o**+Hg²⁺]) C, 48.12; H, 3.19; found C, 50.62; H, 5.07. **FT-IR**: ν = 2220.84 cm⁻¹ (C≡C).

2.5.5. X-ray crystallographic analysis

Single crystals of compound **3** were grown by slow diffusion of EtOAc/hexane (7:3 v/v) solution. Single crystal X-ray data of compound **3o** was collected using Mo Kα (λ = 0.71069 Å) radiation at room temperature on a Microfocal D8 venture Bruker APEX 3 diffractometer equipped with CCD area detector. The unit cell parameters were refined using all the collected spots after the integration process. The structure was solved by direct methods and refined by

full-matrix least-squares on F^2 using SHELXL97.⁴² All the non-hydrogen atoms were refined with anisotropic temperature factors. Hydrogen atoms were calculated and refined in riding mode.

2.6. Computational Details

All the calculations (DFT and TD-DFT) were carried out utilizing Gaussian 09 (Rev. E. 01)⁴³ package and were performed on a parallel cluster system. The ground-state geometries were optimized without symmetry constraints employing B3LYP functional,⁴⁴⁻⁴⁶ in combination with the mixed basis sets: 6-31g(d)^{47,48} for all non-metallic atoms (C, H, O, F, S and Cl) and double- ξ quality basis set (LANL2DZ)^{49,50} for the metal atoms (Fe and Hg). The optimized geometries were confirmed to be local minima by performing frequency calculations and obtaining only positive (real) frequencies. The zero-point corrected energy values are reported herein. Based on the optimized structures, the lowest-energy vertical transitions were calculated (singlets, fifteen states) by TD-DFT, using the Coulomb-attenuated functional CAM-B3LYP⁵¹ at the aforementioned level of calculation. All the calculations (geometry optimizations and frequency calculations, MO calculations, TDDFT) have been performed including the solvent effect through Polarizable Continuum Model (PCM) that use the integral equation formalism variant (IEFPCM).

2.7. References

1. Wigglesworth, T. J.; Branda, N. R. *Chem. Mater.* **2005**, *17*, 5473-5480.
2. Baggaley, E.; Botchway, S. W.; Haycock, J. W.; Morris, H.; Sazanovich, I. V.; Williams, J. A. G.; Weinstein, J. *Chem. Sci.* **2014**, *5*, 879-886.
3. (a) Kobatake, S.; Yamada, T.; Uchida, K.; Kato, N.; Irie, M. *J. Am. Chem. Soc.* **1999**, *121*, 2380-2386. (b) Irie, M.; Mohri, M. *J. Org. Chem.* **1988**, *53*, 803-808. (c) Irie, M.; Sakemura, K.; Okinaka, M.; Uchida, K. *J. Org. Chem.* **1995**, *60*, 8305-8309.
4. Li, R.; Nakashima, T.; Galangau, O.; Iijima, S.; Kanazawa, R.; Kawai, T. *Chem. Asian J.* **2015**, *10*, 1725-1730.
5. (a) Guerchais, V.; Ordronneau, L.; Bozec, H. L. *Coord. Chem. Rev.* **2010**, *254*, 2533-2545. (b) Shen, C.; He, X.; Toupet, L.; Norel, L.; Rigaut, S.; Crassous, J.

- Organometallics* **2018**, *37*, 697-705. (c) Ordronneau, L.; Aubert, V.; Guerchais, V.; Boucekkine, A.; Bozec, H. L.; Singh, A.; Ledoux, I.; Jacquemin, D. *Chem. Eur. J.* **2013**, *19*, 5845-5849.
6. (a) Sun, C.-L.; Gao, Z.; Teng, K.-X.; Niu, L.-Y.; Chen, Y.-Z.; Zhao, Y. S.; Yang, Q.-Z. *ACS Appl. Mater. Interfaces* **2018**, *10*, 26526-26532. (b) Wigglesworth, T. J.; Myles, A. J.; Branda, N. R. *Eur. J. Org. Chem.* **2005**, 1233-1238.
7. Pärss, M.; Hofmann, C. C.; Willinger, K.; Bauer, P.; Thelakkat, M.; Köhler, J. *Angew. Chem. Int. Ed.* **2011**, *50*, 11405-11408.
8. (a) Boixel, J.; Guerchais, V.; Bozec, H. L.; Jacquemin, D.; Amar, A.; Boucekkine, A.; Colombo, C.; Dragonetti, A.; Marinotto, D.; Roberto, D.; Righetto, S.; Angelis, R. D. *J. Am. Chem. Soc.* **2014**, *136*, 5367-5375. (b) Ordronneau, L.; Nitadori, H.; Ledoux, I.; Singh, A.; Williams, J. A. G.; Akita, M.; Guerchais, V.; Bozec, H. L. *Inorg. Chem.* **2012**, *51*, 5627-5636. (c) Ma, T. Y.; Ma, N. N.; Yan, L. K.; Zhang, T.; Su, Z. M. *J. Phys. Chem. A* **2013**, *117*, 10783-10789.
9. Monaco, S.; Semeraro, M.; Tan, W.; Tian, H.; Ceroni, P.; Credi, A. *Chem. Commun.* **2012**, *48*, 8652-8654.
10. Green, K. A.; Cifuentes, M. P.; Corkery, T. C.; Samoc, M.; Humphrey, M. G. *Angew. Chem. Int. Ed.* **2009**, *48*, 7867-7870.
11. Aubert, V.; Guerchais, V.; Ishow, E.; Hoang-Thi, K.; Ledoux, I.; Nakatani, K.; Bozec, H. L. *Angew. Chem. Int. Ed.* **2008**, *47*, 577-580.
12. Nitadori, H.; Ordronneau, L.; Boixel, J.; Jacquemin, D.; Boucekkine, A.; Singh, A.; Akita, M.; Ledoux, I.; Guerchais, V.; Bozec, H. L. *Chem. Commun.* **2012**, *48*, 10395-10397.
13. Roberts, M. N.; Nagle, J. K.; Majewski, M. B.; Finden, J. G.; Branda, N. R.; Wolf, M. O. *Inorg. Chem.* **2011**, *50*, 4956-4966.
14. (a) Li, R. -J.; Holstein, J. J.; Hiller, W. G.; Andréasson, J.; Clever, G. H. *J. Am. Chem. Soc.* **2019**, *141*, 2097-2103. (b) Han, M.; Luo, Y.; Damaschke, B.; Gómez, L.; Ribas, X.; Jose, A.; Peretzki, P.; Seibt, M.; Clever, G. H. *Angew. Chem. Int. Ed.* **2016**, *55*, 445-449. (c) Li, R. -J.; Han, M.; Tessarolo, J.; Holstein, J. J.; Lübben, J.; Dittrich, B.; Volkmann, C.; Finze, M.; Jenne, C.; Jenne, F.; Clever, G. H. *ChemPhotoChem* **2019**, *3*, 378-383. (d)

- Han, M.; Michel, R.; He, B.; Stalke, D.; John, M.; Clever, G. H. *Angew. Chem. Int. Ed.* **2013**, *52*, 1319-1323.
15. Piao, X.; Zou, Y.; Wu, J.; Li, C.; Yi, T. *Org. Lett.* **2009**, *11*, 3818-3821.
16. (a) Qiu, S.; Cui, S.; Shi, F.; Pu, S. *ACS Omega* **2019**, *4*, 14841-14848. (b) Feng, E.; Fan, C.; Wang, N.; Liu, G.; Pu, S. *Dyes and Pigments* **2018**, *151*, 22-27. (c) Jing, S.; Zheng, C.; Pu, S.; Fan, C.; Liu, G. *Dyes and Pigments* **2014**, *107*, 38-44.
17. Wang, Q.; Yu, C.; Zhang, C.; Long, H.; Azarnoush, S.; Jin, Y.; Zhang, W. *Chem. Sci.* **2016**, *7*, 3370-3376.
18. Sánchez, R. S.; Gras-Charles, R.; Bourdelande, J. L.; Guirado, G.; Hernando, J. *J. Phys. Chem. C* **2012**, *116*, 7164-7172.
19. (a) Motoyama, K.; Li, H.; Koike, T.; Hatakeyama, M.; Yokojima, S.; Nakamura, S.; Akita, M. *Dalton Trans.* **2011**, *40*, 10643-10657. (b) Li, B.; Wang, J. -Y.; Wen, H. -M.; Shi, L. -X.; Chen, Z. -N. *J. Am. Chem. Soc.* **2012**, *134*, 16059-16067.
20. (a) Li, B.; Wen, H. -M.; Wang, J. -Y.; Shi, L. -X.; Chen, Z. -N. *Inorg. Chem.* **2013**, *52*, 12511-12520. (b) Matsuda, K.; Takayama, K.; Irie, M. *Chem. Commun.* **2001**, 363-364.
21. Guirado, G.; Coudret, C.; Launay, J. -P. *J. Phys. Chem. C* **2007**, *111*, 2770-2776.
22. Zhao, H.; Garoni, E.; Roisnel, T.; Colombo, A.; Dragonetti, C.; Marinotto, D.; Righetto, S.; Roberto, D.; Jacquemin, D.; Boixel, J.; Guerchais, V. *Inorg. Chem.* **2018**, *57*, 7051-7063.
23. Boixel, J.; Guerchais, V.; Bozec, H. L.; Chantzis, A.; Jacquemin, D.; Colombo, A.; Dragonetti, C.; Marinottoe, D.; Roberto, D. *Chem. Commun.* **2015**, *51*, 7805-7808.
24. (a) Lloveras, V.; Caballero, A.; Tárraga, A.; Velasco, M. D.; Espinosa, A.; Wurst, K.; Evans, D. J.; Vidal-Gancedo, J.; Rovira, C.; Molina, P.; Veciana, J. *Eur. J. Inorg. Chem.* **2005**, 2436-2450. (b) Zhao, L.; Ling, Q.; Liu, X.; Hang, C.; Zhao, Q.; Liu, F.; Gu, H. *Appl. Organomet. Chem.* **2018**, *32*, 4000-4012.
25. Remón, P.; González, D.; Li, S.; Basílio, N.; Andréasson, J.; Pischel, U. *Chem. Commun.* **2019**, *55*, 4335-4338.
26. (a) Irie, M.; Lifka, T.; Kobatake, S.; Kato, N. *J. Am. Chem. Soc.* **2000**, *122*, 4871-4876. (b) Tanaka, Y.; Ishisaka, T.; Inagaki, A.; Koike, T.; Lapinte, C.; Akita, M. *Chem. Eur. J.* **2010**, *16*, 4762-4776.
27. Wan, H.; Xue, H.; Ling, Y.; Qiao, Y.; Chen, Y.; Zhou, G. *Phys. Chem. Chem. Phys.* **2018**, *20*, 14348-14356.
28. Karmakar, M.; Bhatta, S. R.; Giri, S.; Thakur, A. *Inorg. Chem.* **2020**, *59*, 4493-4507.

29. Harvey, E. C.; Areephong, J.; Cafolla, A. A.; Long, C.; Browne, W. R.; Feringa, B. L.; Pryce, M. T. *Organometallics* **2014**, *33*, 3309-3319.
30. Otón, F.; Tárraga, A.; Molina, P. *Org. Lett.* **2006**, *8*, 2107-2110.
31. Zhong, Y. -W.; Vila, N.; Henderson, J. C.; Abruña, H. D. *Inorg. Chem.* **2009**, *48*, 991-999.
32. Liu, Y.; Ndiaye, C. M.; Lagrost, C.; Costuas, K.; Choua, S.; Turek, P.; Norel, L.; Rigaut, S. *Inorg. Chem.* **2014**, *53*, 8172-8188.
33. The upfield shift of methyl protons is due to the close proximity to the coordination site as reported in the following literature: Hatai, J.; Pal, S.; Jose, G. P.; Bandyopadhyay, S. *Dyes and Pigments* **2013**, *99*, 995-1003.
34. Chen, Y.; Zhang, Y. -H.; Zhao, L. -J. *Phys. Chem. Chem. Phys.* **2004**, *6*, 537-542.
35. (a) Perrier, A.; Maurel, F.; Aubard, J. *J. PhotoChem. PhotoBiol. A* **2007**, *189*, 167-176.
(b) Perrier, A.; Maurel, F.; Jacquemin, D. *J. Phys. Chem. C* **2011**, *115*, 9193-9203.
36. (a) Previous report showed that a distance of 1.53 Å is required for the molecule to be thermodynamically stable. See. Maurel, F.; Perrier, A.; Perpète, E. A.; Jacquemin, D. *J. Photochem. Photobiol. A: Chem.* **2008**, *199*, 211-223. (b) Perrier, A.; Maurel, F.; Jacquemin, D. *Acc. Chem. Res.* **2012**, *45*, 1173-1182. (c) Boixel, J.; Zhu, Y.; Bozec, H. L.; Benmensour, M. A.; Boucekkine, A.; Wong, K. M. -C.; Colombo, A.; Roberto, D.; Guerchais, V.; Jacquemin, D. *Chem. Commun.* **2016**, *52*, 9833-9836.
37. (a) Manceau, A.; Lemouchi, C.; Rovezzi, M.; Lanson, M.; Glatzel, P.; Nagy, K. L.; Gautier-Luneau, I.; Joly, Y.; Enescu, M. *Inorg. Chem.* **2015**, *54*, 11776-11791. (b) Li, X.; Liao, R. -Z.; Zhou, W.; Chen, G. *Phys. Chem. Chem. Phys.* **2010**, *12*, 3961-3971.
38. Zhang, N.; Lo, W. -Y.; Jose, A.; Cai, Z.; Li, L.; Yu, L. *Adv. Mater.* **2017**, *29*, 1701248.
39. Fredrich, S.; Bonasera, A.; Valderrey, V.; Hecht, S. *J. Am. Chem. Soc.* **2018**, *140*, 6432-6440.
40. Bhatta, S. R.; Bheemireddy, V.; Thakur, A. *Organometallics* **2017**, *36*, 829-838.
41. Sheldrick, G. M. *Acta Crystallogr. Sect. A* **2008**, *64*, 112 -122.
42. Frisch, M. J.; Trucks, G. W.; Schlegel, H. B.; Scuseria, G. E.; Robb, M. A.; Cheeseman, J. R.; Scalmani, G.; Barone, V.; Mennucci, B.; Petersson, G. A.; Nakatsuji, H.; Caricato, M.; Li, X.; Hratchian, H. P.; Izmaylov, A. F.; Bloino, J.; Zheng, G.; Sonnenberg, J. L.; Hada, M.; Ehara, M.; Toyota, K.; Fukuda, R.; Hasegawa, J.; Ishida, M.; Nakajima, T.; Honda, Y.; Kitao, O.; Nakai, H.; Vreven, T.; Montgomery, J. A.; Peralta, J. E.; Ogliaro, F.; Bearpark, M.; Heyd, J. J.; Brothers, E.; Kudin, K. N.; Staroverov, V. N.; Keith, T.;

Kobayashi, R.; Normand, J.; Raghavachari, K.; Rendell, A.; Burant, J. C.; Iyengar, S. S.; Tomasi, J.; Cossi, M.; Rega, N.; Millam, J. M.; Klene, M.; Knox, J. E.; Cross, J. B.; Bakken, V.; Adamo, C.; Jaramillo, J.; Gomperts, R.; Stratmann, R. E.; Yazyev, O.; Austin, A. J.; Cammi, R.; Pomelli, C.; Ochterski, J. W.; Martin, R. L.; Morokuma, K.; Zakrzewski, V. G.; Voth, G. A.; Salvador, P.; Dannenberg, J. J.; Dapprich, S.; Daniels, A. D.; Farkas, O.; Foresman, J. B.; Ortiz, J. V.; Cioslowski, J.; Fox, D. J. Gaussian, Inc., Wallingford CT, **2013**.

43. Becke, A. D. *J. Chem. Phys.* **1993**, *98*, 5648-5652.
44. Lee, C.; Yang, W.; Parr, R. G. *Phys. Rev. B* **1988**, *37*, 785-789.
45. Stephens, P. J.; Devlin, F. J.; Chabalowski, C. F.; Frisch, M. J. *J. Phys. Chem.* **1994**, *98*, 11623-11627.
46. Petersson, G. A.; Al-Laham, M. A. *J. Chem. Phys.* **1991**, *94*, 6081-6090.
47. Petersson, G. A.; Bennett, A.; Tensfeldt, T. G.; Al-Laham, M. A.; Shirley, W. A.; Mantzaris, J. *J. Chem. Phys.* **1988**, *89*, 2193-2218.
48. Wadt, W. R.; Hay, P. J. *J. Chem. Phys.* **1985**, *82*, 284-298.
49. Hay, P. J.; Wadt, W. R. *J. Chem. Phys.* **1985**, *82*, 299-310.
50. Yanai, T.; Tew, D. P.; Handy, N. C. *Chem. Phys. Lett.* **2004**, *393*, 51-57.

Spectroscopic and Computational Details

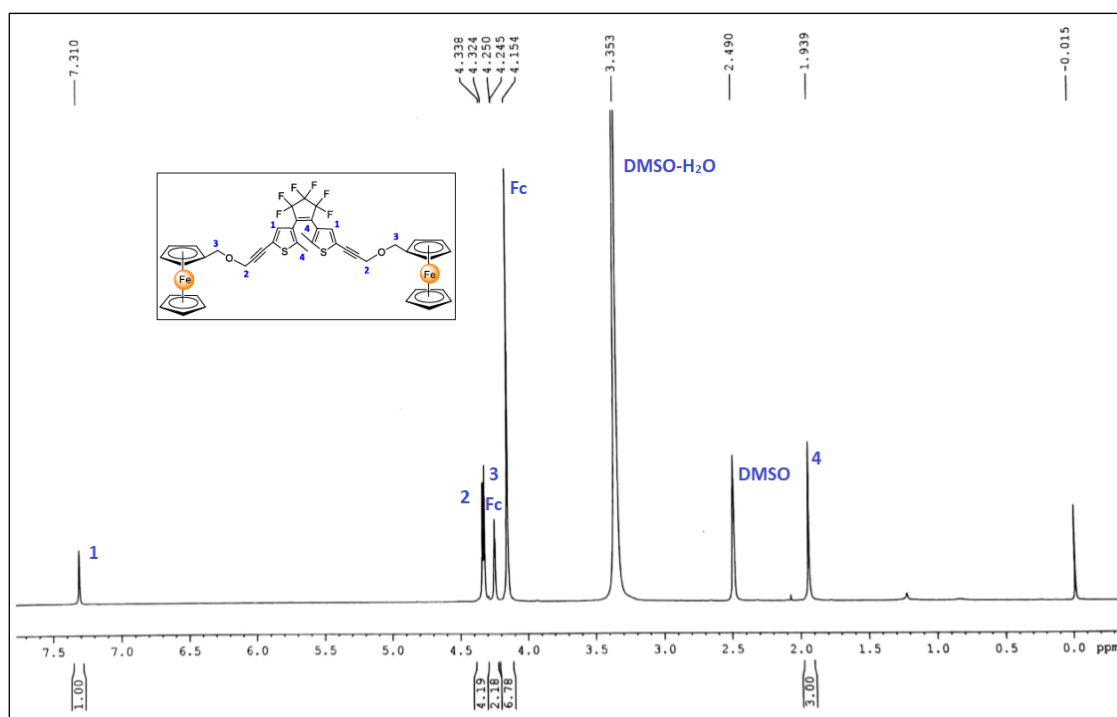


Figure 2.20. ^1H NMR spectra of compound **3o** in DMSO-d_6 as a solvent.

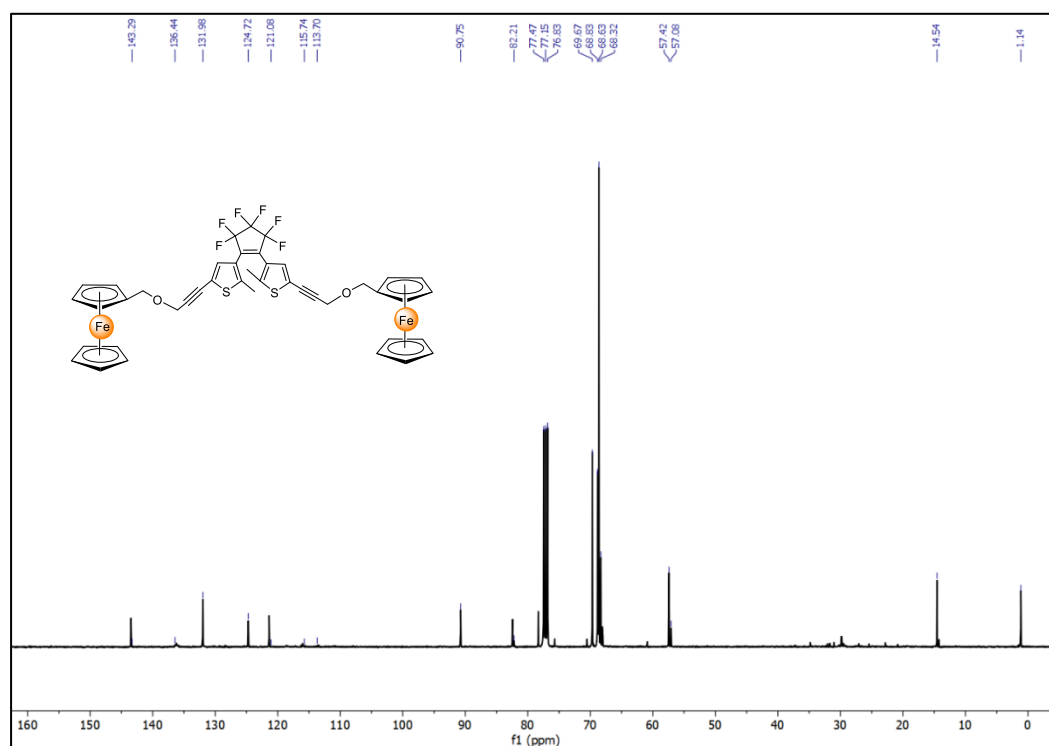


Figure 2.21. ^{13}C NMR spectra of compound **3o** in CDCl_3 as a solvent.

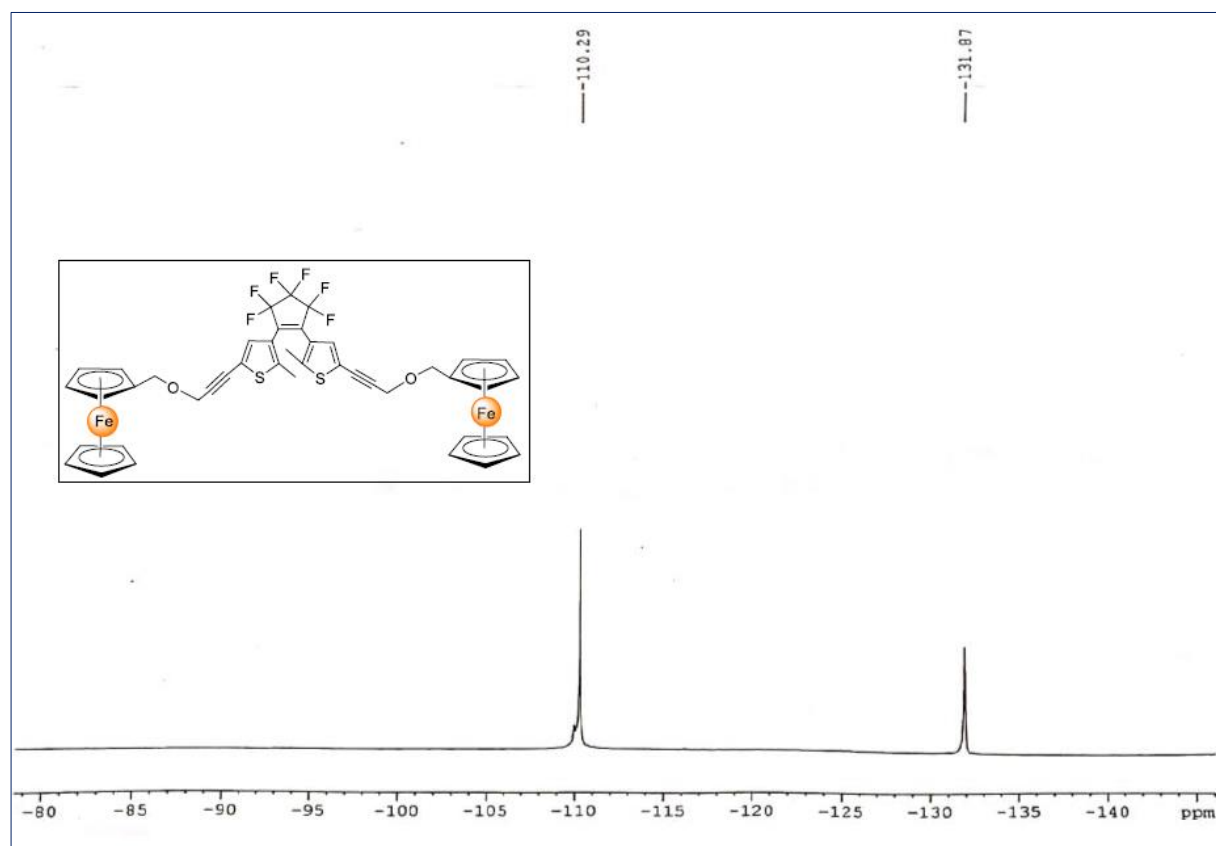


Figure 2.22. ^{19}F NMR spectra of compound **30** in CDCl_3 as a solvent.

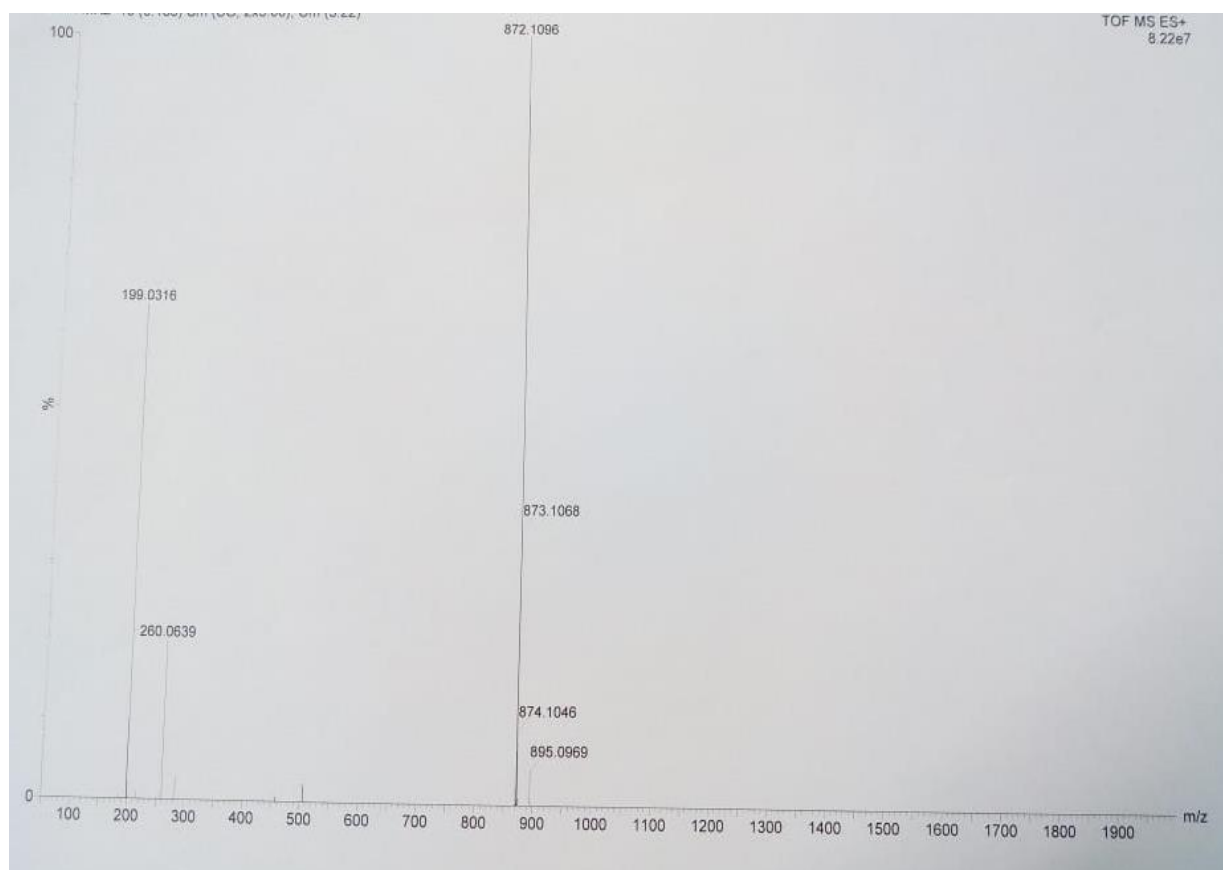
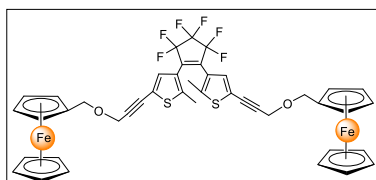


Figure 2.23. HRMS spectrum of compound 3.

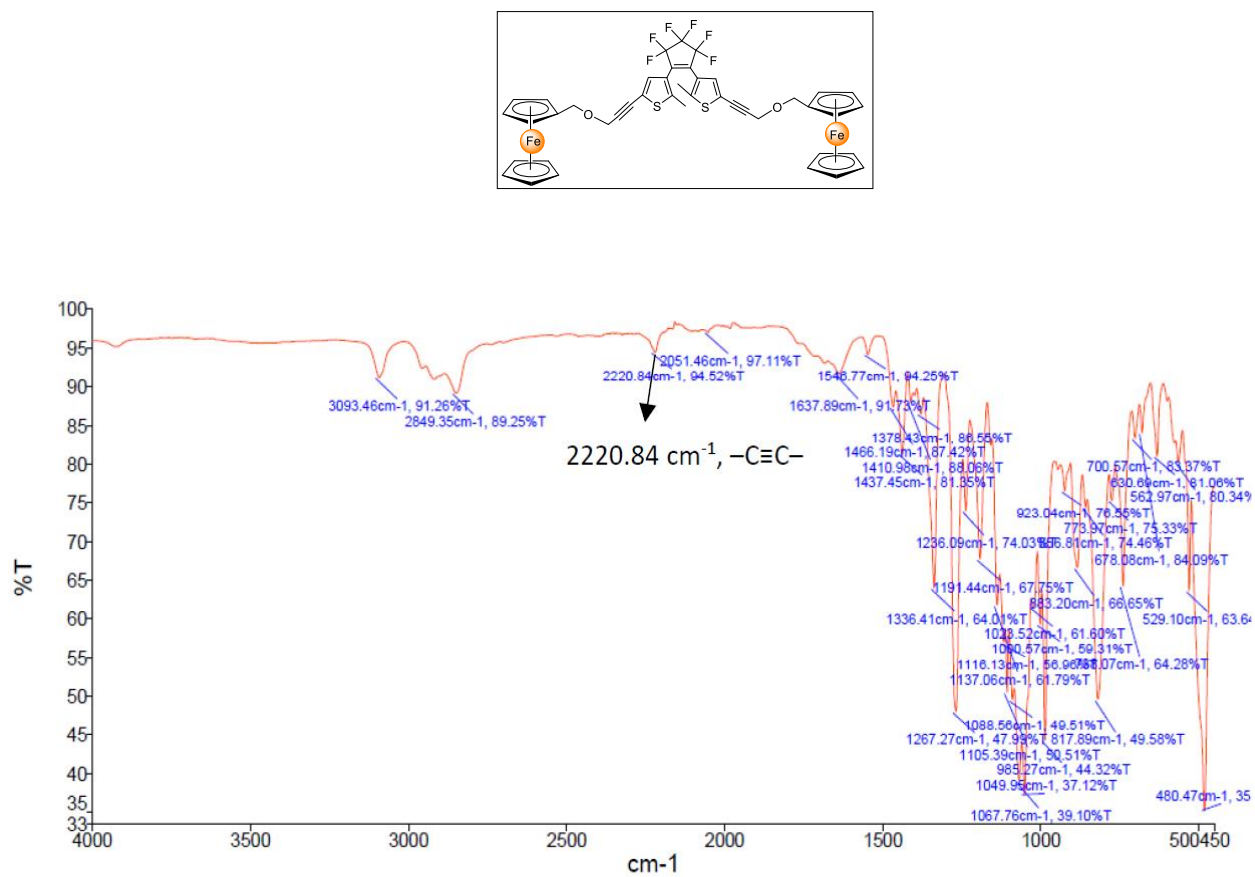


Figure 2.24. FT-IR spectra of compound **3o**.

Crystallographic data for **3o**

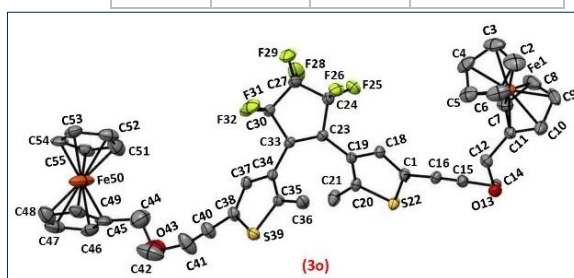
Empirical Formula $C_{43}H_{34}F_6Fe_2O_2S_2$, $M_r = 872.52 \text{ g mol}^{-1}$, Crystal size (mm) 0.3 X 0.2 X 0.2, triclinic, space group $P\bar{1}$, $a = 10.1067(3)\text{\AA}$, $b = 13.3869(4)\text{\AA}$, $c = 15.3025(5)\text{\AA}$, $\alpha = 73.5830(10)^\circ$, $\beta = 79.4690(10)^\circ$, $\gamma = 68.8940(10)^\circ$, $V = 1845.15(10)\text{\AA}^3$, $Z = 2$, $\rho = 1.570 \text{ g cm}^{-3}$, $\mu(\text{Mo-K}\alpha) = 0.968 \text{ mm}^{-1}$, $F(0\ 0\ 0) = 892$, $T (\text{K}) = 140(2)$, $\theta_{\text{min/max}} = 2.421/ 27.256$, reflections: 21904 collected, 8112 unique, 6990 observed, Goodness-of-Fit (GOF) on $F^2 = 1.053$, $R_{\text{int}} = 0.0592$, $R_1(\text{all}) = 0.0743$, $wR_2(\text{all}) = 0.1578$. Final R indices [$I > 2\sigma(I)$]: $R_1 = 0.0647$, $wR_2 = 0.1505$.

Interatomic distances (\AA) for **3o**

Atom	Atom	Distance (\AA)
C35	C36	1.500(4)
C35	S39	1.719(3)
C38	S39	1.732(4)
C38	C40	1.427(4)
C40	C41	1.187(5)
C41	O43	1.500(4)
C44	O43	1.44(2)
C44	C45	1.50(1)
C20	C21	1.495(4)
C20	S22	1.717(3)
C30	F32	1.354(4)

Bond angles (deg) for **3o**

Atom	Atom	Atom	Angle (deg)
C36	C35	S39	119.4(2)
C35	S39	C38	92.9(2)
C38	C40	C41	179.3(5)
C41	C42	O43	104.0(1)
C36	C35	C34	130.0(3)
C34	C33	C23	129.5(3)
C23	C19	C20	125.1(3)
C21	C20	S22	118.9(2)
C27	C30	F32	109.2(3)



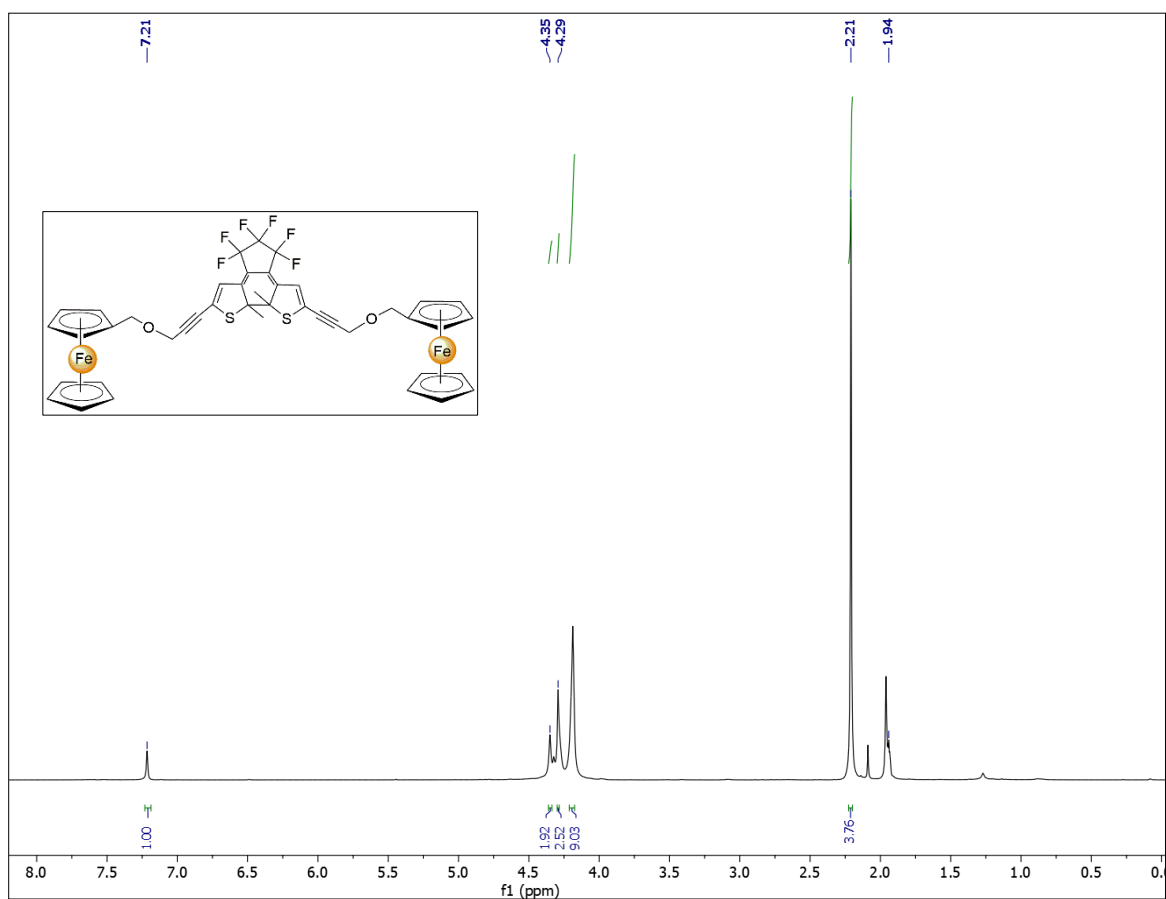


Figure 2.25. ^1H NMR spectra of compound **3c** in CD_3CN as a solvent.

Table 2.2. TD-DFT calculated photophysical data for **3o**, **3c**, [**3o**·Hg(ClO₄)₂] and [**3c**·Hg(ClO₄)₂].

Absorption	Transition (<i>f</i>)	E ^a /eV	λ ^a /nm	Dominant components ^b (%)
3o	S ₁ ← S ₀ (1.28)	4.64(4.26)	267 (263)	H-5->L+1 (34%), H-4->L+2 (37%), H-2->L+2 (18%)
3c	S ₁ ← S ₀ (0.49)	2.24 (1.16)	553 (581)	HOMO->LUMO (97%)
	S ₁ ← S ₀ (0.16)	3.60	344	H-5->LUMO (87%)
	S ₁ ← S ₀ (0.21)	4.10 (4.19)	302 (263)	HOMO->L+1 (84%)
[3o ·Hg(ClO ₄) ₂]	S ₁ ← S ₀ (0.07)	4.32 (4.28)	288 (240)	H-4->L+1 (30%), H-2->L+1 (55%)
[3c ·Hg(ClO ₄) ₂]	S ₁ ← S ₀ (0.15)	1.77	697	HOMO->LUMO (90%)
	S ₁ ← S ₀ (0.29)	2.16 (4.32)	572 (581)	HOMO->L+1 (89%)

^aValues in parentheses are experimental longest-wavelength absorption or emission maxima in acetonitrile. ^bComponents with greater than 10% contribution shown. Percentage contribution approximated by $2 \times (c_i)^2 \times 100\%$, where c_i is the coefficient for the particular 'orbital rotation'. ^cTaken as the reverse of excitation to S₁ from S₀ at the optimised S₁ geometry.

Table 2.3. Energy, wavelength, oscillator strength and major contributions for each of the 15 mono-excitations calculated by TD-DFT methods at cam-B3LYP/6-31g(d)/LANL2DZ//B3LYP/6-31g(d)/LANL2DZ for **3o**.^a [a] Components with greater than 10 % contribution shown.

No.	Energy (cm ⁻¹)	Wavelength (nm)	Osc. Strengths	Symmetry	Major contributions
1	16176.36736	618.185763061	0.0	Singlet-A	H-1->L+8 (12%), H-1->L+10 (24%), H-1->L+12 (12%), HOMO->L+10 (26%), HOMO->L+12 (14%)
2	16183.6264	617.908480636	0.0	Singlet-A	H-1->L+10 (26%), H-1->L+12 (14%), HOMO->L+8 (12%), HOMO->L+10 (24%), HOMO->L+12 (12%)
3	16189.27232	617.692988439	0.0	Singlet-A	H-3->L+6 (21%), H-3->L+9 (28%), H-2->L+6 (15%), H-2->L+9 (13%)
4	16192.49856	617.569917511	0.0	Singlet-A	H-3->L+6 (24%), H-3->L+9 (19%), H-2->L+6 (15%), H-2->L+9 (18%)
5	20430.97136	489.452988984	0.0	Singlet-A	H-12->L+6 (13%), H-12->L+9 (25%),

					H-3->L+6 (21%), H-2->L+9 (19%)
6	20434.1976	489.375712017	0.0	Singlet-A	H-11->L+10 (34%), H-1->L+8 (12%), H-1->L+12 (16%), HOMO->L+10 (28%)
7	20516.46672	487.413361008	0.0001	Singlet-A	H-12->L+6 (21%), H-12->L+9 (11%), H-3->L+9 (26%), H-2->L+6 (16%)
8	20522.11264	487.27926678	0.0	Singlet-A	H-11->L+8 (13%), H-11->L+12 (19%), H-1->L+10 (29%), HOMO->L+8 (12%), HOMO->L+12 (16%)
9	28198.14416	354.633267468	0.0	Singlet-A	H-12->L+6 (49%), H-3->L+6 (12%)
10	28320.74128	353.09810224	0.0	Singlet-A	H-11->L+10 (58%), H-1->L+12 (11%), HOMO->L+10 (20%)
11	28345.74464	352.786639653	0.0	Singlet-A	H-11->L+8 (23%), H-11->L+12 (32%), H-1->L+10 (20%), HOMO->L+12 (11%)

12	28440.11216	351.616053542	0.0	Singlet-A	H-12->L+9 (56%), H-3->L+9 (13%)
13	34619.97488	288.850585093	0.1058	Singlet-A	H-4->LUMO (60%), H-2->LUMO (28%)
14	36991.26128	270.334118221	0.0059	Singlet-A	H-5->LUMO (52%), H-4->L+1 (22%), H-2->L+1 (10%)
15	37422.77088	267.216984869	1.2871	Singlet-A	H-5->L+1 (34%), H-4->L+2 (37%), H-2->L+2 (18%)

Table 2.4. Energy, wavelength, oscillator strength and major contributions for each of the 15 mono-excitations calculated by TD-DFT methods at cam-B3LYP/6-31g(d)/LANL2DZ//B3LYP/6-31g(d)/LANL2DZ for **3c**.^a[a] Components with greater than 10 % contribution shown.

No.	Energy (cm ⁻¹)	Wavelength (nm)	Osc. Strengths	Symmtry	Major contributions
1	16179.5936	618.062495711	0.0	Singlet-A	H-3->L+9 (12%), H-3->L+11 (10%), H-3->L+13 (11%), H-1->L+11 (39%)
2	16190.88544	617.631446844	0.0002	Singlet-A	H-3->L+11 (39%), H-1->L+9 (12%), H-1->L+11 (11%), H-1->L+13 (11%)
3	16204.59696	617.108837985	0.0	Singlet-A	H-4->L+12 (21%), H-2->L+10 (47%)
4	16207.8232	616.985999699	0.0001	Singlet-A	H-4->L+10 (47%), H-2->L+12 (21%)
5	18098.39984	552.535035606	0.4916	Singlet-A	HOMO->LUMO (97%)

6	20438.2304	489.279150117	0.0	Singlet-A	H-10->L+11 (34%), H-1->L+11 (27%)
7	20450.3288	488.989692919	0.0	Singlet-A	H-11->L+10 (32%), H-4->L+12 (13%), H-2->L+10 (28%)
8	20527.75856	487.145246315	0.0	Singlet-A	H-10->L+13 (11%), H-3->L+11 (27%)
9	20554.37504	486.514427247	0.0	Singlet-A	H-11->L+12 (13%), H-4->L+10 (28%), H-2->L+12 (13%)
10	28328.00032	353.007620977	0.0	Singlet-A	H-10->L+11 (51%), H-1->L+11 (20%)
11	28345.74464	352.786639653	0.0	Singlet-A	H-10->L+9 (14%), H-10->L+13 (17%), H-3->L+11 (19%)
12	28346.5512	352.776601621	0.0	Singlet-A	H-11->L+10 (52%), H-2->L+10 (20%)
13	28362.6824	352.575960869	0.0	Singlet-A	H-11->L+12 (23%), H-11- >L+13 (10%), H- 4->L+10 (20%)
14	29082.94048	343.844186143	0.1681	Singlet-A	H-5->LUMO (87%)
15	33075.41248	302.339388996	0.2125	Singlet-A	HOMO->L+1 (84%)

Table 2.5. Energy, wavelength, oscillator strength and major contributions for each of the 15 mono-excitations calculated by TD-DFT methods at cam-B3LYP/6-31g(d)/LANL2DZ//

B3LYP/6-31g(d)/LANL2DZ for [30·Hg(ClO₄)₂].^a

[a] Components with greater than 10 % contribution shown.

No.	Energy (cm ⁻¹)	Wavelength (nm)	Osc. Strengths	Symmetry	Major contributions
1	16205.40352	617.078123828	0.0001	Singlet-A	H-4->L+6 (26%), H-3->L+9 (15%), H-3->L+10 (29%), H-2->L+6 (12%)
2	16210.24288	616.893903073	0.0	Singlet-A	H-4->L+9 (10%), H-4->L+10 (21%), H-3->L+6 (37%), H-2->L+10 (10%)
3	16213.46912	616.771150331	0.0	Singlet-A	H-1->L+12 (40%), HOMO->L+8 (10%), HOMO->L+13 (25%)
4	16223.9544	616.372541087	0.0	Singlet-A	H-1->L+8 (10%), H-1->L+13 (24%), HOMO->L+12 (40%)
5	20439.84352	489.240536025	0.0	Singlet-A	H-12->L+9 (10%), H-12->L+10 (18%), H-3->L+6 (18%)
6	20464.04032	488.662055177	0.0	Singlet-A	H-10->L+12 (37%), H-1->L+13 (16%), HOMO->L+12 (24%)
7	20535.82416	486.953916341	0.0001	Singlet-A	H-12->L+6 (22%), H-4->L+6 (11%), H-3->L+10 (16%)
8	20550.34224	486.609900858	0.0	Singlet-A	H-10->L+8 (10%), H-10->L+13 (23%), H-1->L+12 (25%), HOMO->L+13 (16%)
9	28202.17696	354.582556311	0.0	Singlet-A	H-12->L+6 (45%), H-3->L+6 (13%)
10	28352.19712	352.706351387	0.0	Singlet-A	H-10->L+8 (15%), H-10->L+13 (34%), H-1->L+12 (18%), HOMO->L+13 (11%)
11	28364.29552	352.555909346	0.0	Singlet-A	H-10->L+12 (54%), H-1-

					>L+13 (11%), HOMO->L+12 (18%)
12	28450.59744	351.486467765	0.0	Singlet-A	H-12->L+9 (17%), H-12- >L+10 (38%), H-3->L+10 (11%)
13	31596.988	316.485862513	0.0312	Singlet-A	H-4->LUMO (32%), H-2- >LUMO (61%)
14	34377.20032	290.890471211	0.0056	Singlet-A	H-5->LUMO (90%)
15	34724.02112	287.985079995	0.0727	Singlet-A	H-4->L+1 (30%), H-2- >L+1 (55%)

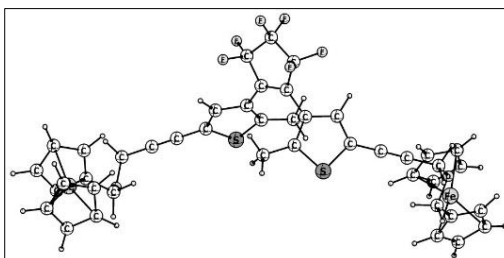
Table 2.6. Energy, wavelength, oscillator strength and major contributions for each of the 15 mono-excitations calculated by TD-DFT methods at cam-B3LYP/6-31g(d)/LANL2DZ//B3LYP/6-31g(d)/LANL2DZ for [3c·Hg(ClO₄)₂].^a

[a] Components with greater than 10 % contribution shown.

No.	Energy (cm ⁻¹)	Wavelength (nm)	Osc. Strengths	Symmetry	Major contributions
1	14337.41056	697.476016199	0.1488	Singlet-A	HOMO->LUMO (90%)
2	16753.05776	596.905958498	0.0004	Singlet-A	H-1->LUMO (89%)
3	16790.15952	595.586956043	0.0001	Singlet-A	H-2->LUMO (88%)
4	16896.62544	591.834152654	0.0066	Singlet-A	H-4->L+7 (11%), H-3->LUMO (61%), H-3->L+6 (10%)
5	16923.24192	590.903329709	0.0	Singlet-A	H-4->LUMO (60%), H-4->L+6 (13%), H-3->L+7 (13%)
6	17163.5968	582.628461652	0.0001	Singlet-A	H-2->L+5 (33%), H-1->L+8 (42%)

7	17171.6624	582.354798683	0.0001	Singlet-A	H-2->L+8 (42%), H-1->L+5 (33%)
8	17317.64976	577.445562105	0.0035	Singlet-A	H-4->L+6 (10%), H-4->L+7 (22%), H-3->LUMO (30%), H-3->L+6 (17%)
9	17329.74816	577.042430604	0.0004	Singlet-A	H-4->LUMO (38%), H-4->L+6 (16%), H-3->L+7 (19%)
10	17482.188	572.010780344	0.2997	Singlet-A	HOMO->L+1 (89%)
11	19805.88736	504.900377258	0.0	Singlet-A	H-1->L+1 (94%)
12	19837.3432	504.099762714	0.0	Singlet-A	H-2->L+1 (93%)
13	19877.6712	503.077040534	0.0	Singlet-A	H-3->L+1 (94%)
14	19920.41888	501.997476069	0.0	Singlet-A	H-4->L+1 (98%)
15	21024.59952	475.633316605	0.0	Singlet-A	H-6->L+6 (30%), H-4->L+6 (23%), H-3->L+7 (23%)

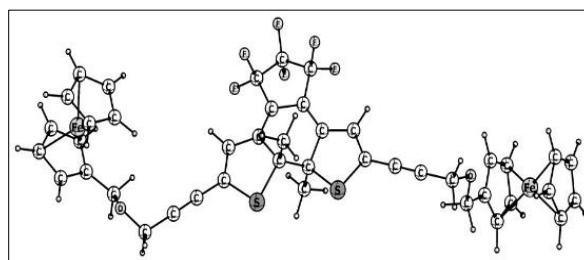
Table 2.7. Cartesian coordinates (Å) of **3o**.



26	-9.162625000	-1.697218000	0.943081000	6	0.417300000	3.016155000	0.158535000
16	-0.969647000	-0.834101000	-2.527631000	6	1.251385000	2.105136000	0.955926000
16	2.023072000	0.242118000	2.563527000	6	0.748111000	1.053406000	1.707691000
9	-1.551561000	4.052045000	-2.472958000	6	-0.671136000	0.599366000	1.874793000
9	-2.519829000	4.062998000	-0.507481000	1	-1.359080000	1.437226000	1.730113000
9	0.340083000	5.588365000	-1.716839000	1	-0.840691000	0.186270000	2.873533000
9	-1.113312000	6.187350000	-0.180416000	1	-0.932603000	-0.174942000	1.143438000
9	1.791814000	4.979114000	0.272424000	6	2.669880000	2.257660000	1.090339000
9	0.090313000	4.845804000	1.644066000	1	3.241964000	3.023830000	0.583782000
8	-6.292168000	-3.177642000	-2.114127000	6	3.250835000	1.321987000	1.913932000
6	-9.290636000	-2.798619000	-0.813578000	6	4.611185000	1.172160000	2.253873000
1	-9.425440000	-3.872394000	-0.851094000	6	5.777384000	1.038504000	2.568963000
6	-10.329392000	-1.822309000	-0.779396000	6	-9.349533000	-2.996606000	2.557554000
1	-11.392763000	-2.023880000	-0.780000000	1	-9.471812000	-4.068361000	2.469087000
6	-9.720481000	-0.532401000	-0.691234000	6	-10.402213000	-2.030546000	2.580554000
1	-10.241409000	0.413282000	-0.616125000	1	-11.461209000	-2.242135000	2.508562000
6	-8.305691000	-0.714142000	-0.676463000	6	-9.809495000	-0.733676000	2.670461000
1	-7.562415000	0.068440000	-0.587758000	1	-10.340935000	0.209235000	2.678601000
6	-8.028875000	-2.120007000	-0.742911000	6	-8.390604000	-0.897730000	2.702243000
6	-6.676481000	-2.770451000	-0.789365000	1	-7.659001000	-0.101201000	2.742873000
1	-5.913746000	-2.102269000	-0.366752000	6	-8.106446000	-2.296476000	2.632722000
1	-6.674403000	-3.697984000	-0.211124000	1	-7.121748000	-2.745267000	2.613100000
6	-5.998408000	-2.103880000	-3.003151000	26	8.749023000	-2.290477000	-0.568023000
1	-6.833622000	-1.390053000	-3.047415000	8	7.899297000	-0.027857000	2.086391000
1	-5.907874000	-2.561404000	-3.994338000	6	7.193346000	0.879214000	2.925547000
6	-4.758919000	-1.386565000	-2.674484000	1	7.708947000	1.840168000	2.825504000
6	-3.732454000	-0.798811000	-2.394895000	1	7.274188000	0.567523000	3.979186000
6	-2.525812000	-0.131687000	-2.099258000	6	7.519490000	-1.388605000	2.283191000
6	-2.340516000	1.083489000	-1.484047000	1	6.470461000	-1.543505000	1.994130000
1	-3.163733000	1.696053000	-1.137669000	1	7.603269000	-1.630846000	3.356741000
6	-0.962910000	1.449540000	-1.331907000	6	8.413032000	-2.286519000	1.484531000
6	-0.092345000	0.510080000	-1.863836000	6	9.806638000	-2.100405000	1.218396000
6	1.403308000	0.546088000	-1.959815000	1	10.386850000	-1.229435000	1.491419000
1	1.758369000	1.580169000	-1.984620000	6	10.277237000	-3.231642000	0.485137000
1	1.754574000	0.041573000	-2.864917000	1	11.281246000	-3.369226000	0.104903000
1	1.872841000	0.054498000	-1.099226000	6	9.181049000	-4.129389000	0.305493000
6	-0.559581000	2.730065000	-0.740331000	1	9.206354000	-5.067516000	-0.233534000
6	-1.305083000	3.981733000	-1.139237000	6	8.031267000	-3.546154000	0.919208000
6	-0.403416000	5.150093000	-0.672794000	1	7.033530000	-3.966767000	0.933616000
6	0.517221000	4.505858000	0.393381000	6	9.484001000	-1.725822000	-2.434437000

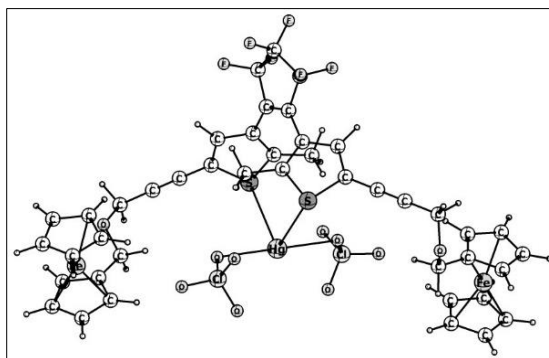
1	10.492917000	-1.916479000	-2.776850000	6	7.657133000	-0.738015000	-1.417279000
6	8.365473000	-2.600798000	-2.590223000	1	7.046970000	-0.055672000	-0.840815000
1	8.378505000	-3.569877000	-3.072169000	6	9.046356000	-0.575422000	-1.708979000
6	7.236335000	-1.990067000	-1.962166000	1	9.666082000	0.259384000	-1.407948000
1	6.244425000	-2.416497000	-1.885473000				

Table 2.8. Cartesian coordinates (Å) of **3c**.



6	-1.081235000	0.643676000	-0.460364000	9	0.964449000	5.035457000	0.078058000
6	-2.470144000	0.641208000	-0.780086000	9	0.358981000	3.768292000	1.772177000
6	-2.980965000	-0.599783000	-1.055296000	9	2.700558000	2.757776000	1.288097000
16	-1.784950000	-1.918912000	-0.951916000	9	2.601270000	3.251489000	-0.844617000
6	-0.532575000	-0.766212000	-0.168134000	9	-1.702939000	3.501680000	0.194906000
6	3.088576000	-0.172008000	0.143359000	9	-0.478157000	3.679669000	-1.617893000
6	1.766473000	0.246542000	-0.179056000	6	-0.599027000	-0.984516000	1.365973000
6	0.896305000	-0.886552000	-0.753296000	6	-4.309168000	-0.903409000	-1.411308000
16	1.796479000	-2.455961000	-0.264543000	6	4.453220000	-2.226820000	0.429614000
6	3.264818000	-1.531129000	0.136872000	6	-5.443468000	-1.202445000	-1.730397000
6	-0.214583000	1.689092000	-0.326613000	6	5.457326000	-2.862873000	0.684838000
6	1.195377000	1.483191000	-0.085364000	1	-3.067694000	1.542412000	-0.844127000
6	-0.504092000	3.158354000	-0.349794000	1	3.879349000	0.514422000	0.421341000
6	0.678078000	3.771694000	0.452849000	1	-0.307737000	-2.001921000	1.633518000
6	1.861774000	2.791480000	0.213746000	1	0.063593000	-0.283119000	1.882317000

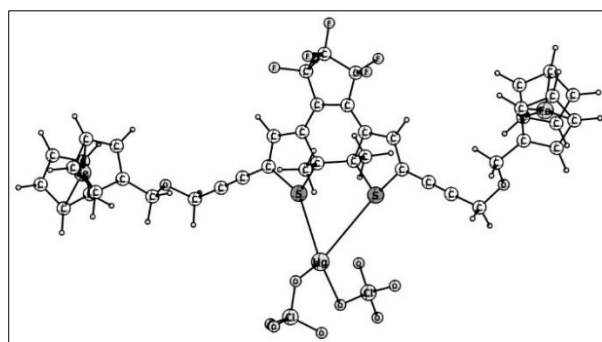
1	-1.621272000	-0.810223000	1.710755000	6	-12.558319000	0.555442000	-0.174887000
6	0.949984000	-0.783460000	-2.299503000	6	-12.862553000	-0.657702000	0.515871000
1	0.424069000	-1.616352000	-2.770093000	1	-12.145796000	-2.757354000	0.185735000
1	0.494758000	0.152879000	-2.636425000	1	-12.922179000	1.541914000	0.081881000
1	1.992741000	-0.797920000	-2.626273000	1	-13.497918000	-0.751454000	1.387119000
6	-6.828142000	-1.530353000	-2.101508000	6	8.043212000	-1.820922000	1.809353000
1	-6.957203000	-2.624010000	-2.101581000	6	9.352936000	-1.123137000	1.609184000
1	-7.029220000	-1.175180000	-3.118023000	1	8.019058000	-2.306737000	2.799613000
6	6.695068000	-3.598457000	0.982099000	6	9.618528000	0.246302000	1.936125000
1	6.787099000	-4.450464000	0.299940000	6	10.578435000	-1.701379000	1.149465000
1	6.643922000	-4.000530000	2.006974000	6	10.997363000	0.510075000	1.675423000
8	7.867144000	-2.819519000	0.803472000	1	8.888088000	0.961529000	2.293309000
8	-7.798413000	-0.908040000	-1.271263000	6	11.588937000	-0.693114000	1.183045000
6	-7.844876000	-1.456507000	0.046436000	1	10.700832000	-2.717329000	0.799022000
6	-8.793201000	-0.667125000	0.893822000	1	11.494817000	1.464010000	1.792897000
1	-6.836171000	-1.424987000	0.488436000	1	12.615230000	-0.812005000	0.860310000
6	-9.566195000	-1.191970000	1.979556000	26	10.034379000	-0.096742000	-0.065494000
6	-9.022619000	0.744537000	0.844780000	6	8.575718000	-0.203968000	-1.542554000
6	-10.270142000	-0.111153000	2.592094000	6	9.794431000	-0.779702000	-2.016357000
1	-9.623500000	-2.234705000	2.265703000	1	7.635537000	-0.724015000	-1.417126000
6	-9.938767000	1.085034000	1.885661000	6	8.834489000	1.160496000	-1.206797000
1	-8.603392000	1.424048000	0.115125000	1	9.935065000	-1.807802000	-2.323912000
1	-10.962992000	-0.191897000	3.419562000	6	10.805980000	0.228228000	-1.973514000
1	-10.336421000	2.072132000	2.083174000	6	10.213036000	1.427446000	-1.472348000
26	-10.816334000	-0.289094000	0.592890000	1	8.119457000	1.860874000	-0.794592000
6	-11.400886000	-1.161835000	-1.203291000	1	11.845842000	0.097444000	-2.244042000
6	-11.654492000	0.243754000	-1.236631000	1	10.724983000	2.364416000	-1.294777000
1	-10.727776000	-1.700026000	-1.857230000	1	-8.153646000	-2.511970000	0.005710000
6	-12.147054000	-1.718982000	-0.119784000	1	7.219225000	-1.094385000	1.780311000
1	-11.217045000	0.952980000	-1.927443000				

Table 2.9. Cartesian coordinates (Å) of [3o·Hg(ClO₄)₂].

26	-8.177597000	-2.099947000	0.238415000	6	-4.922426000	1.216830000	-2.944515000
16	-1.119469000	0.975416000	-2.495835000	6	-3.822305000	1.558558000	-2.558555000
16	1.243389000	1.070080000	2.894907000	6	-2.536909000	1.953483000	-2.131444000
9	-0.566505000	5.887309000	-2.186354000	6	-2.169981000	3.077692000	-1.431165000
9	-1.772149000	6.033686000	-0.361626000	1	-2.881114000	3.827296000	-1.106447000
9	1.501904000	6.896834000	-1.080324000	6	-0.763731000	3.152872000	-1.161961000
9	0.025685000	7.741120000	0.312935000	6	-0.051131000	2.086597000	-1.685386000
9	2.490542000	5.842136000	1.015832000	6	1.426999000	1.834810000	-1.679665000
9	0.631438000	6.062932000	2.153208000	1	1.970295000	2.778186000	-1.575867000
8	-6.411604000	-0.595851000	-3.548564000	1	1.747506000	1.346635000	-2.603909000
6	-8.887995000	-1.385050000	-1.576477000	1	1.724052000	1.181208000	-0.851102000
1	-9.265063000	-2.013360000	-2.373684000	6	-0.160495000	4.287495000	-0.451569000
6	-9.654218000	-0.833487000	-0.507604000	6	-0.532657000	5.697308000	-0.842317000
1	-10.715075000	-0.975494000	-0.346332000	6	0.542095000	6.593049000	-0.174292000
6	-8.766484000	-0.104387000	0.342630000	6	1.136580000	5.693976000	0.940139000
1	-9.037620000	0.405521000	1.257977000	6	0.724463000	4.289798000	0.574578000
6	-7.453715000	-0.200805000	-0.206981000	6	1.197455000	3.151554000	1.376824000
1	-6.551157000	0.223251000	0.215311000	6	0.342200000	2.294511000	2.049207000
6	-7.517364000	-1.003321000	-1.393980000	6	-1.153426000	2.344173000	2.148032000
6	-6.378545000	-1.334142000	-2.314777000	1	-1.507202000	3.365796000	1.983050000
1	-5.418599000	-1.171198000	-1.805669000	1	-1.495433000	2.010939000	3.131553000
1	-6.424037000	-2.379386000	-2.630712000	1	-1.628038000	1.693159000	1.405446000
6	-6.256974000	0.811456000	-3.410927000	6	2.580620000	2.836604000	1.569580000
1	-7.018509000	1.228709000	-2.735950000	1	3.391710000	3.400955000	1.126715000
1	-6.444840000	1.223070000	-4.408868000	6	2.785946000	1.722400000	2.349724000

6	4.002007000	1.100248000	2.698902000	6	7.508183000	-4.272564000	-0.785538000
6	5.035640000	0.544914000	3.015907000	1	7.436622000	-4.904846000	-1.661086000
6	-8.363373000	-4.170979000	0.239790000	6	6.428151000	-3.573561000	-0.165645000
1	-8.756059000	-4.748832000	-0.586877000	1	5.396840000	-3.573595000	-0.495309000
6	-9.126913000	-3.607479000	1.308269000	6	9.194202000	-1.326265000	-2.161341000
1	-10.199773000	-3.681705000	1.430777000	1	10.181838000	-1.711374000	-2.380330000
6	-8.231127000	-2.891988000	2.161025000	6	7.989878000	-1.659810000	-2.853964000
1	-8.508047000	-2.328668000	3.042797000	1	7.905823000	-2.344330000	-3.688320000
6	-6.913530000	-3.012659000	1.621869000	6	6.910382000	-0.965397000	-2.225405000
1	-6.014915000	-2.562844000	2.024893000	1	5.864254000	-1.046257000	-2.491041000
6	-6.996779000	-3.802224000	0.433404000	6	7.448301000	-0.203184000	-1.143036000
1	-6.171091000	-4.057284000	-0.218560000	1	6.883074000	0.394954000	-0.441294000
26	7.841011000	-2.222834000	-0.855348000	6	8.859257000	-0.426011000	-1.103692000
8	6.884664000	-0.843636000	2.288031000	1	9.549294000	-0.010715000	-0.380529000
6	6.290370000	-0.132420000	3.367767000	80	-0.004310000	-1.233918000	0.309455000
1	7.036761000	0.605020000	3.681763000	8	-2.078263000	-2.938780000	2.596654000
1	6.112032000	-0.807275000	4.220343000	8	1.423881000	-3.549937000	-1.908429000
6	6.146075000	-1.998721000	1.890803000	17	-2.540642000	-1.525126000	2.678719000
1	5.189690000	-1.709275000	1.432878000	17	2.251440000	-2.321660000	-2.068136000
1	5.911501000	-2.597613000	2.787576000	8	-1.747867000	-0.777489000	3.694260000
6	6.954864000	-2.814681000	0.929647000	8	-2.349239000	-0.866046000	1.309556000
6	8.364602000	-3.056682000	0.983323000	8	-3.992695000	-1.459094000	3.002035000
1	9.053355000	-2.605646000	1.685123000	8	1.636337000	-1.407792000	-3.071101000
6	8.706136000	-3.948973000	-0.077584000	8	3.643993000	-2.672283000	-2.465426000
1	9.703012000	-4.292146000	-0.322829000	8	2.331358000	-1.602475000	-0.717934000

Table 2.10. Cartesian coordinates (Å) of $[3c \cdot \text{Hg}(\text{ClO}_4)_2]$.

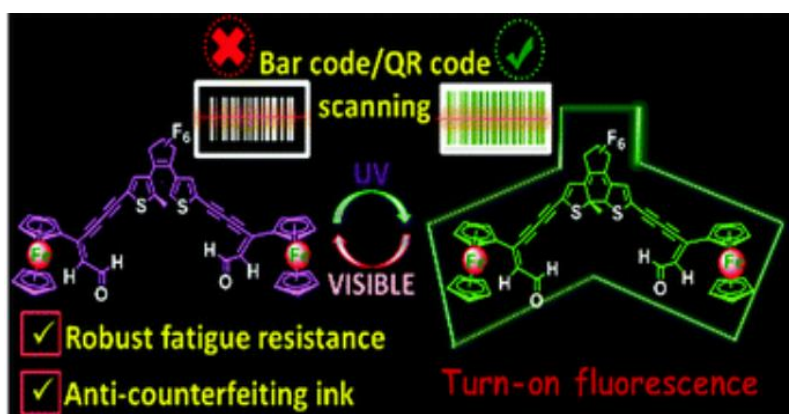


6	-0.873525000	-2.284025000	0.252263000	1	7.029046000	2.812886000	0.445006000
6	-2.270640000	-2.318824000	0.532811000	1	6.902965000	2.673159000	-1.316074000
6	-2.787907000	-1.126601000	0.965628000	8	8.091672000	1.277205000	-0.326299000
16	-1.581695000	0.184517000	1.088433000	8	-7.614414000	-1.034390000	1.337781000
6	-0.314732000	-0.849949000	0.176423000	6	-7.793698000	-0.434850000	0.053684000
6	3.304777000	-1.396731000	-0.146194000	6	-8.764608000	-1.236990000	-0.755523000
6	1.979514000	-1.859155000	0.092859000	1	-6.822417000	-0.390381000	-0.464806000
6	1.096710000	-0.824680000	0.813925000	6	-9.691051000	-0.699216000	-1.707044000
16	2.011738000	0.797067000	0.608581000	6	-8.874377000	-2.662922000	-0.807182000
6	3.481629000	-0.055316000	0.070983000	6	-10.369418000	-1.786497000	-2.336610000
6	-0.004330000	-3.302527000	-0.009109000	1	-9.862855000	0.353553000	-1.892823000
6	1.410822000	-3.067875000	-0.190065000	6	-9.867582000	-3.000496000	-1.775865000
6	-0.294168000	-4.758990000	-0.204159000	1	-8.323540000	-3.358903000	-0.188848000
6	0.902723000	-5.252472000	-1.065551000	1	-11.152494000	-1.702238000	-3.078883000
6	2.082151000	-4.320546000	-0.665478000	1	-10.204255000	-4.000365000	-2.017726000
9	1.182196000	-6.557783000	-0.873039000	26	-10.706609000	-1.814472000	-0.285516000
9	0.607762000	-5.056951000	-2.375886000	6	-11.154990000	-1.154045000	1.635629000
9	2.939424000	-4.132254000	-1.708585000	6	-11.295662000	-2.573651000	1.557923000
9	2.802454000	-4.931810000	0.327056000	1	-10.455160000	-0.619951000	2.264067000
9	-1.482552000	-5.016122000	-0.814800000	6	-12.056171000	-0.569481000	0.693705000
9	-0.291506000	-5.457715000	0.975370000	1	-10.729748000	-3.300737000	2.125806000
6	-0.338552000	-0.429998000	-1.316849000	6	-12.284952000	-2.866719000	0.569390000
6	-4.120508000	-0.872439000	1.340407000	6	-12.754614000	-1.627899000	0.034740000
6	4.673981000	0.674399000	-0.092275000	1	-12.169317000	0.488217000	0.493324000
6	-5.257837000	-0.626305000	1.692401000	1	-12.599725000	-3.854032000	0.256943000
6	5.683681000	1.338092000	-0.226910000	1	-13.487585000	-1.512074000	-0.753299000
1	-2.870513000	-3.217615000	0.456975000	6	8.265686000	0.471651000	-1.492859000
1	4.099725000	-2.033464000	-0.515599000	6	9.538060000	-0.309738000	-1.384754000
1	-0.007594000	0.601654000	-1.451369000	1	8.296688000	1.130372000	-2.377374000
1	0.313379000	-1.082146000	-1.906040000	6	9.766085000	-1.599623000	-1.964556000
1	-1.357072000	-0.523832000	-1.701467000	6	10.762599000	0.111694000	-0.776278000
6	1.106472000	-1.162830000	2.327254000	6	11.120672000	-1.972247000	-1.710397000
1	0.569622000	-0.406934000	2.903877000	1	9.025882000	-2.197304000	-2.481645000
1	0.641892000	-2.136873000	2.507542000	6	11.734792000	-0.916263000	-0.970345000
1	2.139970000	-1.202955000	2.680157000	1	10.907856000	1.033192000	-0.228795000
6	-6.638745000	-0.375071000	2.130882000	1	11.586779000	-2.906563000	-1.995279000
1	-6.823998000	0.710033000	2.158649000	1	12.749186000	-0.910449000	-0.592839000
1	-6.769427000	-0.756252000	3.149755000	26	10.105610000	-1.671616000	0.080773000
6	6.934550000	2.096075000	-0.377783000	6	8.611194000	-1.754451000	1.523765000

6	9.851610000	-1.375935000	2.123536000	80	-0.428636000	3.421562000	-0.298424000
1	7.714231000	-1.150883000	1.487423000	8	-0.783256000	4.435633000	-2.640880000
6	8.786084000	-3.039697000	0.924707000	8	-0.429203000	5.068064000	1.742653000
1	10.052311000	-0.442874000	2.634075000	17	-1.218246000	5.898790000	-2.503615000
6	10.792376000	-2.426844000	1.895963000	17	0.490766000	4.553096000	2.850240000
6	10.134105000	-3.454967000	1.154238000	8	-1.510258000	6.404785000	-3.870238000
1	8.037991000	-3.589690000	0.368339000	8	-2.436460000	5.955307000	-1.646923000
1	11.830219000	-2.429323000	2.203288000	8	-0.108241000	6.671103000	-1.879547000
1	10.585455000	-4.373386000	0.801590000	8	0.390258000	5.499017000	3.993273000
1	-8.153542000	0.598840000	0.167492000	8	1.886308000	4.500878000	2.329189000
1	7.413670000	-0.210437000	-1.621529000	8	0.038908000	3.189534000	3.253166000

Chapter: 3

A Conjugated Photoresponsive Dithienylethene-Ferrocene System: Application in Secret Writing and Decoding Information



Representative publication

J. Mater. Chem. C. 2022, 10, 8860-8873

3.1. Introduction

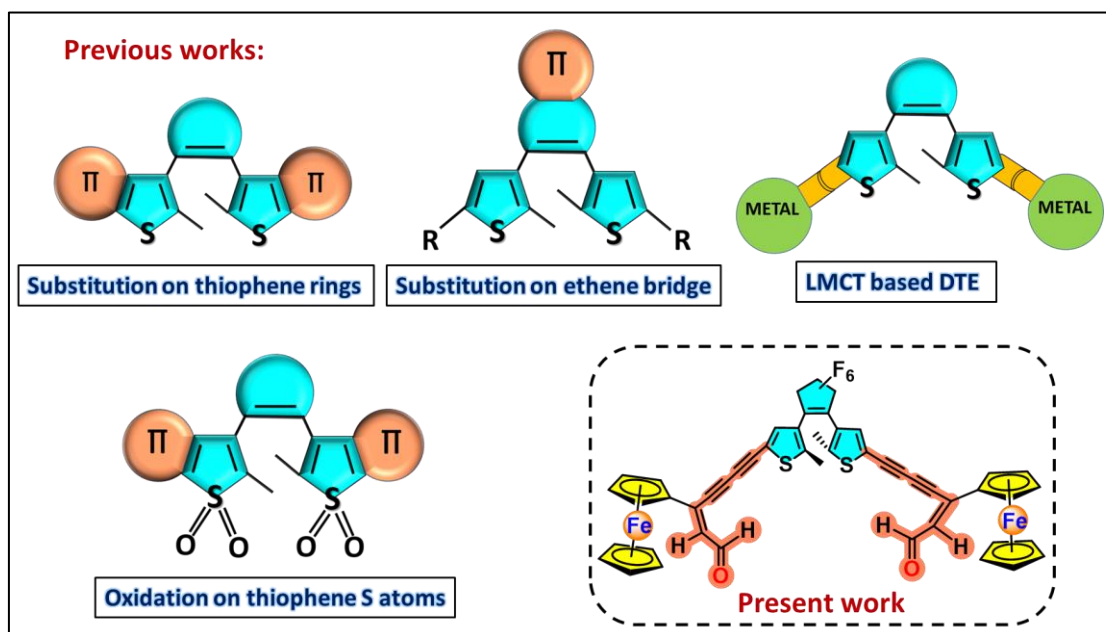
The fluorescent photochromic molecules are the most promising class of organic materials because of their notable fluorescent properties and inherent photochromic behavior.¹ Nonetheless, most of the photochromic molecules are non or weakly fluorescent. Combining a fluorescent unit with the photochromic molecule is the most convenient and widely used practice to impart the fluorescent property into the molecule.² The fluorescence intensities of such materials are triggered by various external stimuli such as lights, chemicals, electrons, or photons.³ Among different classes of photochromic compounds, the family of diarylethene derivatives (DAEs) is the best performing photochrome due to high thermal stability,⁴ rapid response,⁵ robust fatigue resistance,⁶ and permitting non-damaging readout for optical memories.⁷ Further, fluorescent-photochromic DAE-based materials have widely been applied in the field of optoelectronics, logic operations, sensing devices, optical data storage, photoresistors,⁸⁻¹² fluorescent biological markers, security code (anticounterfeiting materials), and many more.^{13,14}

Recently, the most demanding and challenging application of DAE based photochromic smart materials is in secret writing and decoding information technology. Photochromic smart materials are widely explored in secret writing and decoding information technology by several research groups,¹⁵⁻¹⁸ however, utilization of ferrocene based DTE materials as anti-counterfeiting agents remains relatively unexplored. Several stimuli-responsive substances (such as heat, chemicals like hydrogen peroxide) have been developed as innovative anticounterfeiting materials with more reliable characteristics that are capable to provide a constricted security system, however, in an invasive manner. On the other hand, compared to other chemical stimuli, light being a fascinating external stimulus, it often offers clean and unrestrictive regulation¹⁹ of the operation with high accuracy and superior convenience in activating or erasing the secret encoded information.²⁰ Therefore, for reversible information encryption and decryption, the development of stimuli responsive photochromic fluorescent materials, works in a non-invasive manner, could be an ideal entry to the field of security technology and for the development of more portable erasable ink (rewritable paper).²¹ In most of the cases it was observed that, photoswitchable fluorescence and photochromism were measured at low concentration in the polymer matrix or in solution phase when photoluminescence is treated as a detection or readout signal.^{22,23} However, the optoelectronic applications of such materials are usually investigated in the solid state.²⁴ Nonetheless, the solid

state luminescence often encountered some limitations for the application in high-density optical systems due to concentration-caused fluorescence quenching, or aggregation caused quenching (ACQ).^{25,26} Therefore, the design and innovation of turn-on fluorescent photochromic system, that operates in solution as well as in solid state, are very crucial to overcome this problem.

Over the last few years, great progress has been made in the development of fluorescent photoswitching molecules by introducing DAE substituents as a photochromic unit which can confer photocyclization and photocycloreversion between two differently colored isomeric open and closed forms.²⁷ Conventional “turn-off” mode fluorescent DAEs in which the open-ring isomer is fluorescent, and the closed-ring isomer is non-fluorescent, are great in number.²⁸ On the other hand, “turn-on” mode fluorescent DAEs, in which the weak fluorescent ring-open form is triggered to a fluorescent state upon photoisomerization reaction (A, Scheme 3.1), have recently been developed, however, with low quantum yield.²⁹⁻³¹ Development of “turn-on” mode fluorescent DAEs with high photoelectron quantum yield are extremely demanding due to its bioimaging applications, including super resolution microscopies.³² “Turn-on” mode fluorescent DAEs with good quantum yield have been developed in recent years by various research groups *via* different strategies *e.g.*, by oxidizing the sulfur atoms of thiophene units to sulfones³³ (B, Scheme 3.1) and by substituting the 6,6'-positions with suitable aryl groups^{30,31} or by replacing the ethene moiety itself to other heterocyclic units instead of the perfluoro- or perhydro-cyclopentene unit³⁴ (C, Scheme 3.1) or by introducing some metal atoms into the π -conjugated skeleton (D, Scheme 3.1).³⁵ However, the example of perfluoro DTE-based “turn-on” fluorescence probes with high quantum yield (Φ) are not well developed without oxidizing ‘S’ atoms of thiophene unit to electron acceptor sulfones.

Herein, we have designed a ferrocenyl DTE-based extended π -conjugated system, attached to the reactive carbon atom of the DTE unit, in which the open-ring isomer is non/weak-fluorescent and closed one is fluorescent. An unprecedented “turn-on” fluorescent material with good quantum yield and anti-fatigue property is achieved without oxidation of sulphur atoms to sulfones and devoid of any conventional fluorophore unit. Further, our designed material is found to be a highly proficient anti-counterfeiting agent that operates in non-invasive manner both in solution as well as in solid state.



Scheme 3.1. Strategies for designing UV-light triggered “turn-on” mode fluorescent DAEs.

3.2. Results and Discussion

3.2.1. Synthesis and Characterization

Very few ferrocene based DTE systems are reported in the literature.^{36,37} Keeping this idea in mind, we have successfully designed and developed a π -conjugated ferrocene appended dithienylethene (DTE-Fc) system as shown in Figure 3.1. The ferrocene moiety has been judiciously introduced to conjugated DTE unit to offer a reversible redox system and as a source of transferable electron, to an extended DTE unit. Moreover, it is expected to contribute a substantial ionization potential (Ip) difference during the conversion of the open state to the closed state upon irradiation.³⁷ On the other hand, ferrocene exhibits a pair of reversible waves in voltammetric studies under both moist and aerobic conditions. Although, the DTE unit is electrochemically active however, it provides irreversible waves³⁸ which is sometime bit difficult to explain. Therefore, to get a conclusive electrochemical study, a redox moiety with reversible waves (e.g ferrocene) is always beneficial to comprehend the photoswitching properties of the isomeric states (open and closed). On the other hand, our motivation for choosing bis-enediyne systems was not only to study their various photophysical properties but also this enediyne moiety can offer a bridge system that could lead to cross electronic communication between peripheral ferrocene and central DTE units.³⁹

The synthesis of the new ferrocenyl-DTE based photochromic compound, **40** with extended π -conjugation, is mainly promoted by an alkyne-alkyne coupling in one step. The

precursors, (2-formyl-1-chlorovinyl)ferrocene (**P1**) and dithienylethene derivative 1,2-Bis(5-(4-ethynyl)-2-methylthiophen-3-yl)perfluorocyclopentene (**3**) were prepared according to the respective literature reports.^{40,41} “Sonogashira” coupling between (2-formyl-1-chlorovinyl)ferrocene, **P1** and trimethylsilylacetylene afforded compound **1** (yield: 74%) which was readily converted to compound **2** by treating with K_2CO_3 in MeOH. The target molecule (**4o**) was obtained *via* Cu(I) catalyzed Glaser–Hay coupling between (2-formyl-1-en-1-yne)ferrocene (**2**) and 1,2-Bis(5-(4-ethynyl)-2-methylthiophen-3-yl)perfluorocyclopentene (**3**) as pale violet solid in 53% yield (Figure 3.1).⁴² Both the intermediate compounds, **1** and **2** are well characterized based on 1H NMR, ^{13}C NMR, and mass spectrometry. Additionally, the molecular structure of **2** is established by single-crystal X-ray diffraction measurement. Compound **4o** is also fully characterized by 1H , ^{13}C , ^{19}F NMR, HRMS, IR spectra, elemental analysis and HRTEM.

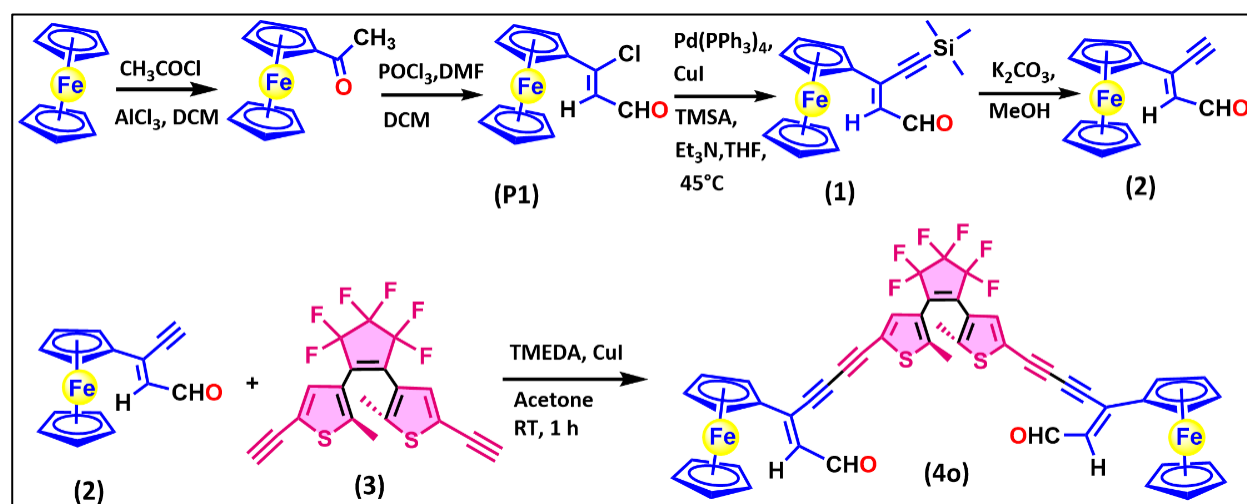


Figure 3.1. Synthetic route of compounds **1**, **2**, and **4o**.

3.2.2. Photophysical studies

Encouraged by the known photochromic capability of common dithienylethene derivatives, our synthesized molecule **4o/4c**, was also subjected to investigation for the photoinduced isomerisation process. The photoresponsive DTE unit gives rise to two isomeric photochromes: open form (**4o**) and ring closed form (**4c**) in presence of different wavelengths of light (UV or visible) and each isomer has a unique spectral signature that opens up a window for us to investigate the reversible photoswitching behavior of the DTE unit. The photochromic behavior of **4o** was investigated by UV-vis absorption spectroscopic measurements in CH_3CN

(5×10^{-5} M) upon alternating irradiation with UV (365 nm) and visible (>450 nm) light. As shown in Figure 3.2a, **4o** displayed three intense absorption bands centered at 262 nm ($\epsilon = 8.58 \times 10^3 \text{ M}^{-1} \text{ cm}^{-1}$) attributed to the π - π^* transition of DTE unit,⁴³ 315 nm ($\epsilon = 8.05 \times 10^3 \text{ M}^{-1} \text{ cm}^{-1}$) and a weak absorption band at 550 nm ($\epsilon = 0.625 \times 10^3 \text{ M}^{-1} \text{ cm}^{-1}$) due to the extended π -conjugated ferrocene unit.⁴⁴ Upon irradiation of **4o** (3 ml, 5×10^{-5} M) by UV light (365 nm) for ~ 300 s, a new low energy characteristic absorption band of the closed DTE unit arises at 630 nm ($\epsilon = 1.44 \times 10^3 \text{ M}^{-1} \text{ cm}^{-1}$, 80 nm red shift) with concomitant reduction of absorption maxima at 262 nm and 315 nm with an isosbestic point at 376 nm. The red shifted broad absorption feature between 550–650 nm indicates the formation of more extended π -conjugated structure **4c**.⁴⁵ A decrease in HOMO-LUMO gap has been observed for **4o** to **4c** ($\Delta E_{\text{HOMO-LUMO}} = 3.04$ eV (**4o**) and 1.86 eV (**4c**)) (see theoretical studies, *vide infra*) which is in agreement with the experimentally observed red shift in the absorption spectra. Irradiation beyond ~ 300 s led to no further significant changes, signifying almost full conversion from **4o** to **4c**, which was accompanied by a change in color from pale violet to green. Notably, the conversion of **4c** to **4o** (cycloreversion) was also accomplished by irradiation with visible light for ~ 420 s that showed a diminution in absorption intensity at 630 nm along with 80 nm blue shift (Figure 3.2b).

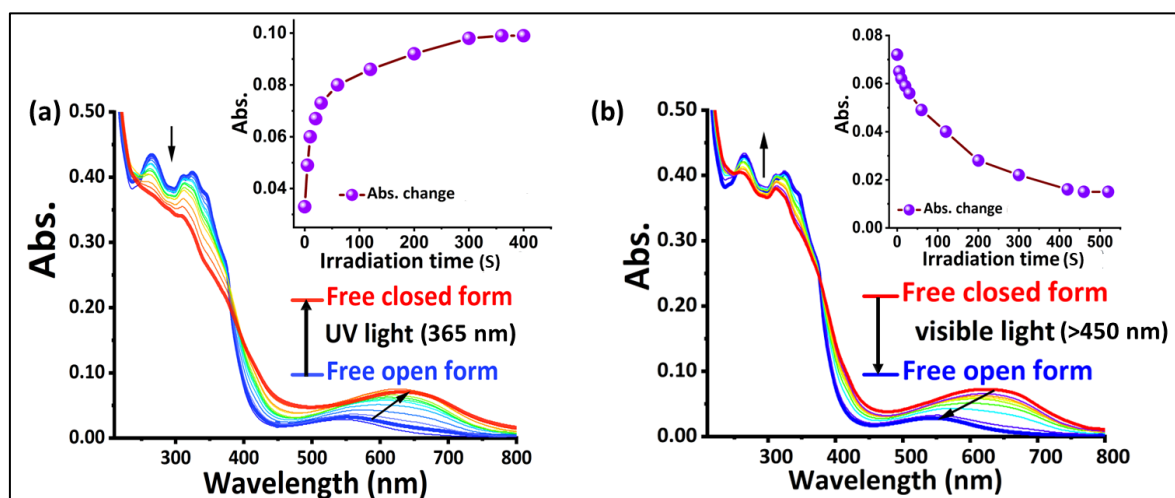


Figure 3.2. Absorption spectral changes of (a) **4o** by gradual irradiation of 365 nm UV light (inset: variation of absorption intensities of **4o** with irradiation time); (b) **4c** by gradual irradiation of >450 nm visible light (inset: variation of absorption intensities of **4c** with irradiation time) in CH_3CN (5×10^{-5} M) solvent.

Further, the photoreaction (**4o**→**4c** and **4c**→**4o**) quantum yields were calculated from UV-vis absorption spectra using the following equation-

$$\Phi(\mathbf{4o/4c}) = \left(\frac{\text{slope}(\mathbf{4o/4c})}{\text{slope}(\text{ref})} \right) \times \left(\frac{\varepsilon(\text{ref})}{\varepsilon(\mathbf{4o/4c})} \right) \times \Phi(\text{ref})$$

where, slope = slope of the linear plot, extracted from A (absorbance) vs t (irradiation time) plot; ε = molar extinction coefficient of concentration 5×10^{-5} M at 574 nm for ref. and at 630 nm for **4o** and Φ = quantum yield. The photocyclization and cycloreversion quantum yields were determined to be 0.83 ($\Phi_{\text{o} \rightarrow \text{c}}$) and 0.021 ($\Phi_{\text{c} \rightarrow \text{o}}$) respectively (Table 3.1 and Figure 3.3) in hexane with 1,2-bis(2-methyl-5-phenyl-3-thienyl)-perfluorocyclopentene as a reference.⁴⁶ The photocyclization and cycloreversion quantum yields of the present probe are comparable or even greater than those obtained with other reported DTEs.⁴⁷

For the sake of legibility, we have compared the photocyclization and cycloreversion quantum yields values of **4o/4c** with other reported DTE systems in tabular form (Table 3.2).

Table 3.1. Quantum yields of cyclization ($\Phi_{\text{o} \rightarrow \text{c}}$) and cycloreversion ($\Phi_{\text{c} \rightarrow \text{o}}$) for **4o** and **4c** upon irradiation by 365 nm UV light and visible light (>450 nm) respectively.

Compound	ε ($\text{M}^{-1}\text{cm}^{-1}$)		Slope		Quantum yield	
	cyclization	cycloreversion	cyclization	cycloreversion	cyclization ($\Phi_{\text{o} \rightarrow \text{c}}$)	cycloreversion ($\Phi_{\text{c} \rightarrow \text{o}}$)
4o/4c	1.420×10^3	0.015×10^5	6.56726×10^{-5}	4.78×10^{-5}	0.83	0.0215
Ref. 1,2-bis(2-methyl-5-phenyl-3-thienyl)perfluorocyclopentene	0.2608×10^5	0.0413×10^5	8.5327×10^{-4}	7.94356×10^{-4}	0.59	0.013

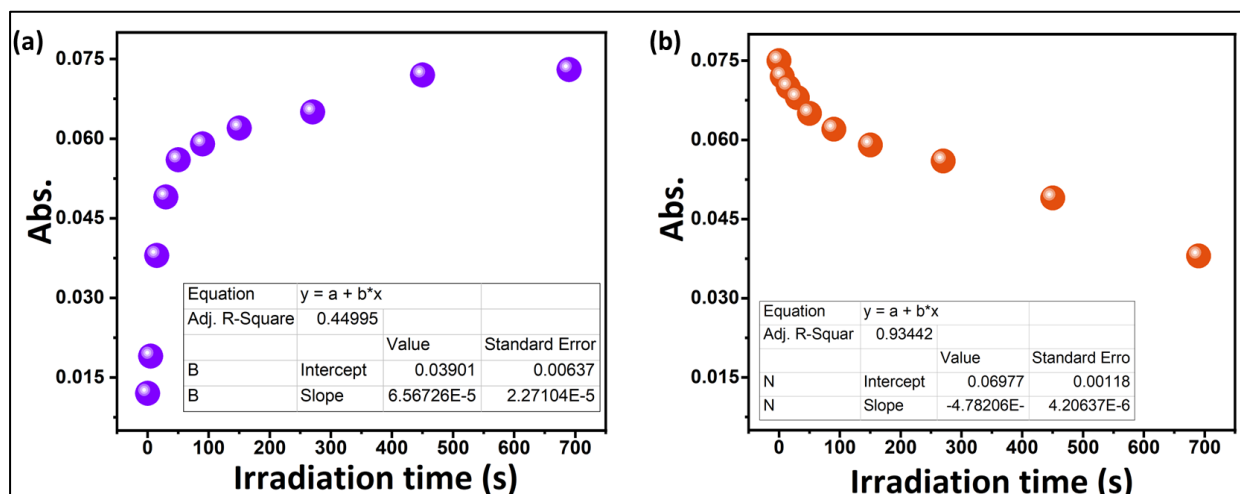
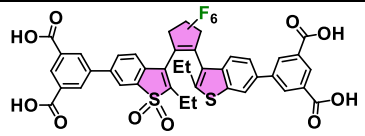
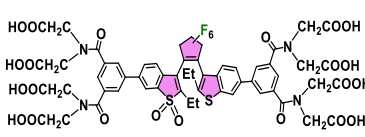
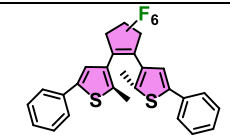
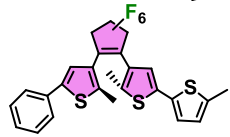
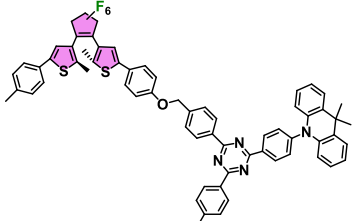
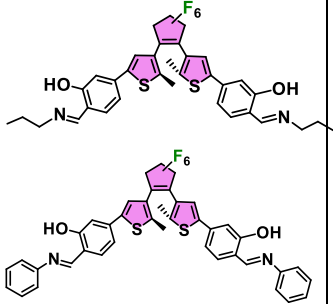
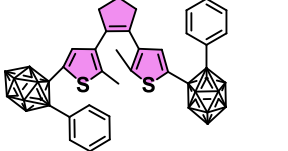
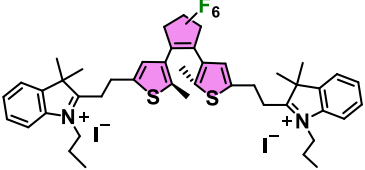
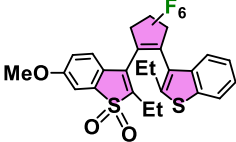
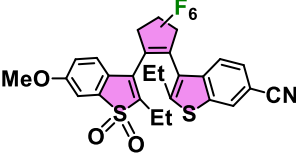
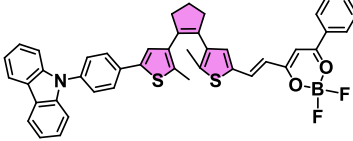
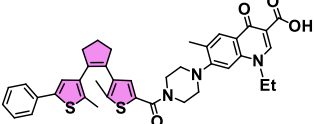
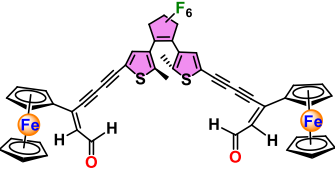


Figure 3.3. Plot of Absorbance vs irradiation time (s) for the (a) cyclization (**4o** to **4c**), (b) cycloreversion (**4c** to **4o**) for the calculations of respective quantum yields.

Table 3.2. Comparative quantum yield values for photocyclization and cycloreversion.

Compound	Solvent	Photocyclisation quantum yield ($\Phi_{o \rightarrow c}$)	Photocycloreversion quantum yield ($\Phi_{c \rightarrow o}$)	Ref.
	H ₂ O	0.19±0.04	0.0012 ±0.0003	48
		0.23±0.04	0.002±0.0003	
	Hexane	0.63	0.010	49
		0.65	0.015	

	Toluene	0.37	0.006	50
	MeOH	0.46	0.070	51
	Toluene	1.00	0.055	52
	CH ₃ CN	0.15	0.029	53
 	CH ₃ CN	0.50	0.020	54
	Toluene	0.55	0.009	55
	DMSO	0.21	0.001	56

	CH ₃ CN	0.83	0.021	Present work
---	--------------------	------	-------	---------------------

In order to understand the rate of photocyclization and cycloreversion, the photoisomerization rate constant for photocyclization and cycloreversion (k) for **4o**→**4c** and **4c**→**4o** were measured by the plot of $\ln[(A_0-A_\infty)/(A_t-A_\infty)]$ vs irradiation time (s).⁵⁷ The conversion of pale violet, **4o** to green color **4c** is associated with a slightly higher rate constant ($k = 0.007 \text{ s}^{-1}$) than the conversion of **4c** to **4o** ($k = 0.004 \text{ s}^{-1}$) (Figure 3.4) indicating the photocyclization occurs at a higher rate than cycloreversion.

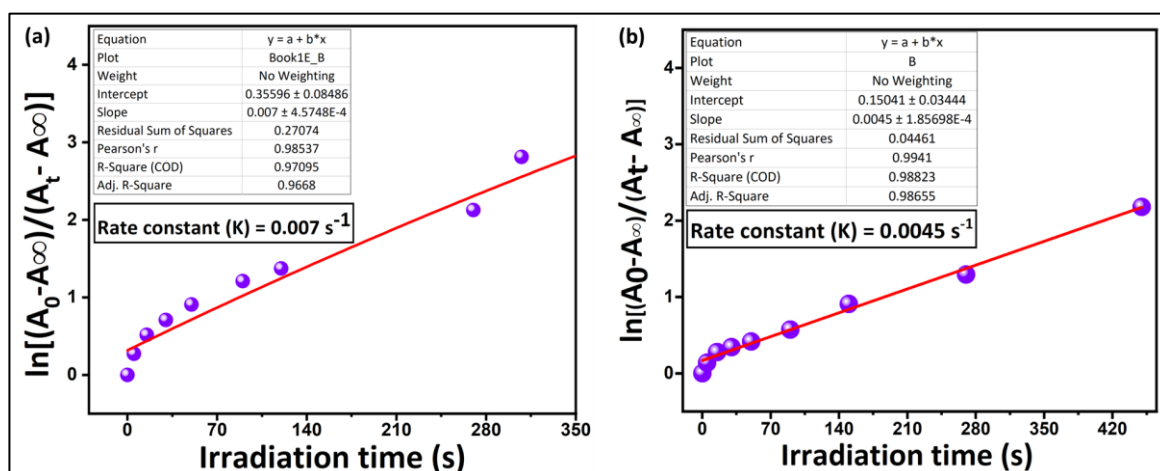


Figure 3.4. Plot of $\ln[(A_0-A_\infty)/(A_t-A_\infty)]$ vs irradiation time (s) for determination of rate constant (K) for conversion of (a) free **4o** to **4c**, and (b) free **4c** to **4o** in CH₃CN solution.

To analyze the purity of DTE-Fc (**4o/4c**) and to determine the ratio of **4o:4c** at photostationary state (PSS) HPLC analysis was performed. The quantitative HPLC method for analysis was validated by setting UV detector at 365 nm. The photoconversion ratio of open ring isomer (**4o**) to closed isomer (**4c**) at photostationary state (PSS) was determined by reverse phase HPLC method using CH₃CN:H₂O (80:20) as an eluent where **4c** was formed upon exposure of 365 nm UV light of the corresponding **4o** solution. Therefore, the extended π -

conjugated DTE-Fc (**4o/4c**) is treated herein as a quantitative two-state system. The single peak at 1.15 min indicates the purity level of DTE-Fc (**4o/4c**). As shown in Figure 3.5a, the PSS of DTE-Fc was achieved after saturated irradiation with UV light (365 nm) with 89.5% ring-closing yield. We determined the retention time (R_f) 1.15 and 3.72 min for **4o** and **4c** respectively. Therefore, from HPLC spectra both open and closed isomers (**4o** and **4c**) can be distinguished, and importantly the distinction can also be performed *via* the naked eye color change (pale violet, **4o** to green color **4c**) (Figure 3.5b).

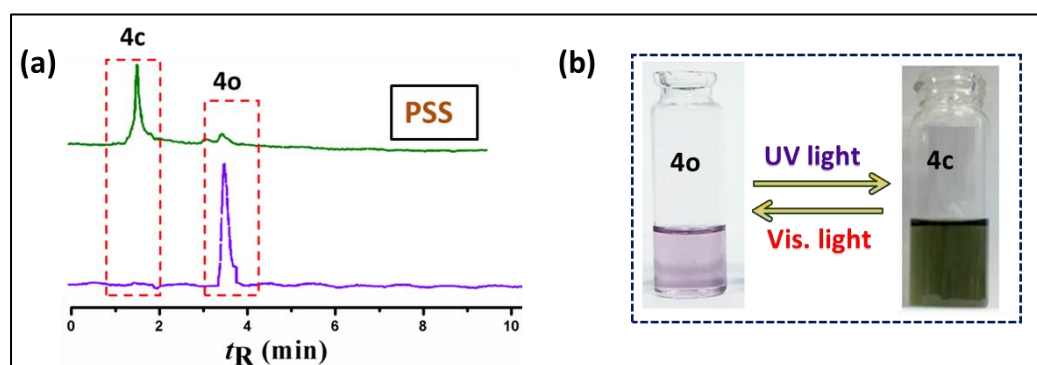


Figure 3.5. (a) HPLC chromatograms of **4o** and **4c**; (b) reversible color changes of **4o** and **4c** with UV and visible light irradiation respectively in CH_3CN solution.

Further, the photoswitching behavior of DTE-Fc (**4o/4c**) is studied by fluorescence emission spectroscopic analysis in CH_3CN solution. As shown in Figure 3.6a, the progressive UV light irradiation of CH_3CN (1.5×10^{-7} M) solution of **4o** yielded gradual enhancement of two fluorescence emission bands at 595 nm and 623 nm ($\lambda_{\text{ex}} = 550$ nm, $\Phi_{\text{F}} = 0.299$; Table 3.3) and attains a saturation level after ~ 300 s (Figures. 3.6b and 3.6d). Cycloreversion from **4c** to **4o** was achieved by irradiation with visible light (>450 nm), displaying diminution of the fluorescence intensity to the initial state ($\Phi_{\text{F}} = 0.071$, Table 3.3) (Figure 3.6c). The repeating conversion from **4o** to **4c** and **4c** to **4o** using UV and visible light respectively can complete at least 10 cycles without losing any recovery efficiency, demonstrating high photostability and robust fatigue resistance property of DTE-Fc material (Figure 3.6e).⁵⁸ Further, to investigate photoswitching properties at excited state, fluorescence lifetimes were measured for **4o** upon irradiation by 365 nm light using time-resolved techniques. Initially, the ring open isomer present in the solution shows a lifetime 2.22 ns. However, a mixture of isomer presents in the solution (ring open isomer, **4o** and ring closed isomer, **4c**) by UV irradiation with variable time. During time variation the solution implies an exponential decay in nature and reached ring

closed isomer after ~ 300 s irradiation with lifetime 8.82 ns (Figure 3.6f). Therefore, with increasing time of irradiation both the amplitude of (“turn-on”) fluorescence intensity and life time increases which corroborated with the result of the significant enhancement of fluorescence intensity upon ring closing.⁵⁹ The enhancement of fluorescence may be ascribed to the formation of a more rigid π -conjugated closed isomer (**4c**) compared to its flexible ring open isomer.⁶⁰

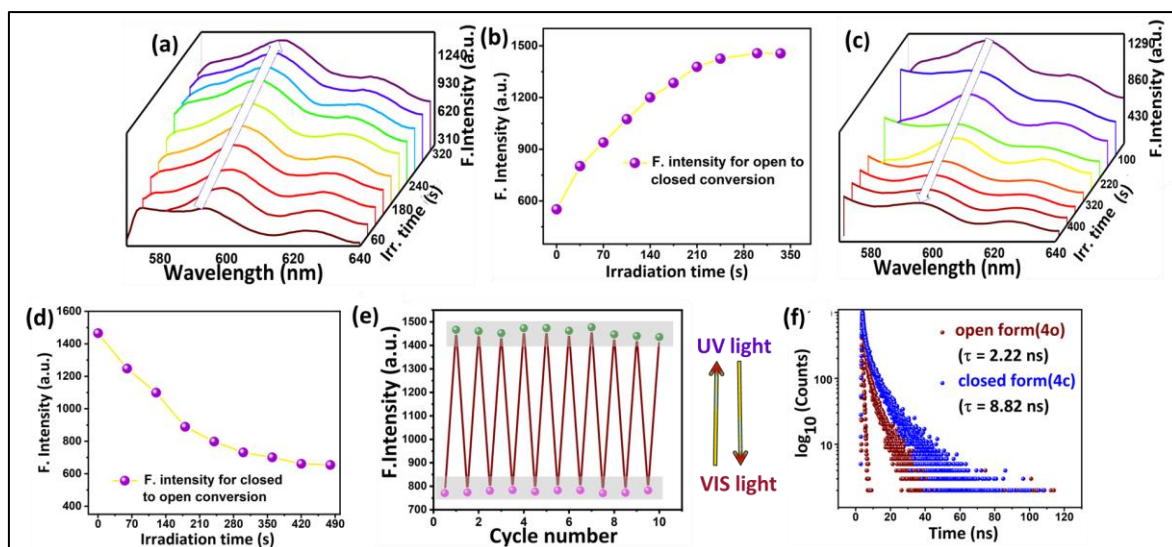


Figure 3.6. Changes of fluorescence emission spectra upon gradual irradiation of (a) UV light (365 nm) ($\lambda_{\text{ex}} = 550$ nm) for **4o**; (b) Linear plot of fluorescence emission intensity vs irradiation time (s) of compound **4o** CH_3CN solution. Changes of fluorescence emission spectra upon gradual irradiation of (c) visible light (>450 nm) ($\lambda_{\text{ex}} = 630$ nm) for **4c** in CH_3CN (1.5×10^{-7} M) solution; (d) Linear plot of fluorescence emission intensity vs irradiation time (s) of compound **4c** CH_3CN solution. (e) 10 consecutive photoswitching cycles of fluorescence intensity of **4o** and **4c** ($\lambda_{\text{em}} = 595$ nm) upon alternating irradiation of UV and visible light; (f) fluorescence lifetime spectra of **4o** (1.5×10^{-7} M) and **4c** (1.5×10^{-7} M) at room temperature.

Table 3.3. Fluorescence quantum yields of open (**4o**) and closed (**4c**) isomers.

Compound	Area under the curve from fluorescence emission spectra (S)	Abs. at excitation wavelength (Abs.)	Refractive index (η)	Fluorescence quantum yield (Φ_f)
4o	245894.5	0.0245	1.3441(CH_3CN)	0.071
4c	957890.5	0.07414	1.3441(CH_3CN)	0.299
Standard ref. (Congo red)	125708.1	0.08718	1.333 (Water)	0.011

The aforementioned photochromic change in the solution state due to structural isomerisation of stimuli responsive material encouraged us to examine the photoswitching ability of **4o/4c** in solid state as well to develop a potentially useful smart material with real life applications. Similar to the studies in solution phase, we have examined the UV-vis absorption spectra of solid **4o** and **4c** by irradiation with UV and visible light respectively (Figures 3.7a and 3.7b). During photoirradiation, the growth of absorption band at 630 nm indicates the formation of ring closed isomer (**4c**). Furthermore, upon irradiation of **4c** by visible light (>450 nm), the peak at 630 nm decreased to the initial state. Similar to the solution phase, photocyclization ($k = 0.005 \text{ s}^{-1}$) occurs at slightly higher rate than photocycloreversion ($k = 0.003 \text{ s}^{-1}$) in solid powder state also (Figures 3.7c and 3.7d). However, the rate of photocyclization and cycloreversion in the solid state occurs at a marginally slower rate than that of solution phase.

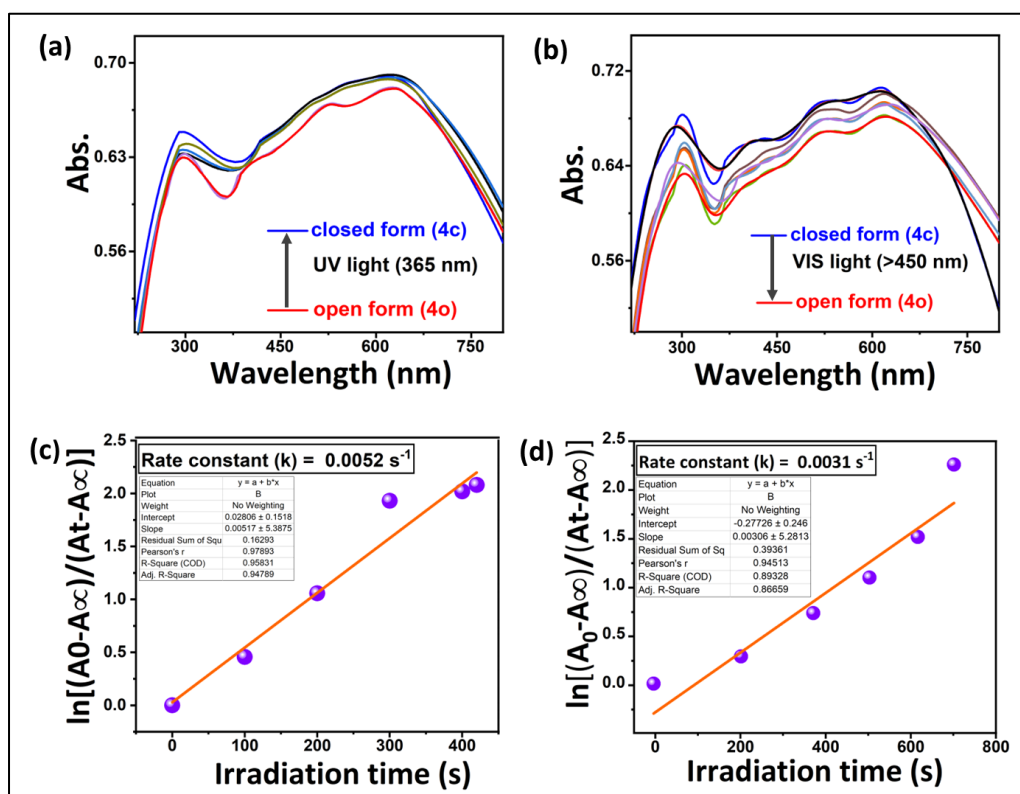


Figure 3.7. Changes in the (a,b) absorption spectra of **4o** and **4c** by gradual irradiation of UV light (365 nm) and visible light (>450 nm) in solid state respectively. Plot of $\ln[(A_0 - A_\infty)/(A_t - A_\infty)]$ vs irradiation time (s) for determination of rate constant of (c) free **4o** to **4c**, (d) free **4c** to **4o** in solid state.

For the sake of comparison of the emissive nature for **4o/4c** in solution with that of in solid state, we have recorded fluorescence emission spectra of solid **4o/4c** upon exposure of UV ($\lambda_{\text{ex}} = 550 \text{ nm}$) and visible ($\lambda_{\text{ex}} = 630 \text{ nm}$) light. Interestingly, like solution phase, a similar kind of double-humped fluorescence emission spectra (590 and 601 nm) suggests that DTE-Fc material **4o/4c** retains its photochromic behavior in the solid state as well (Figures 3.8).

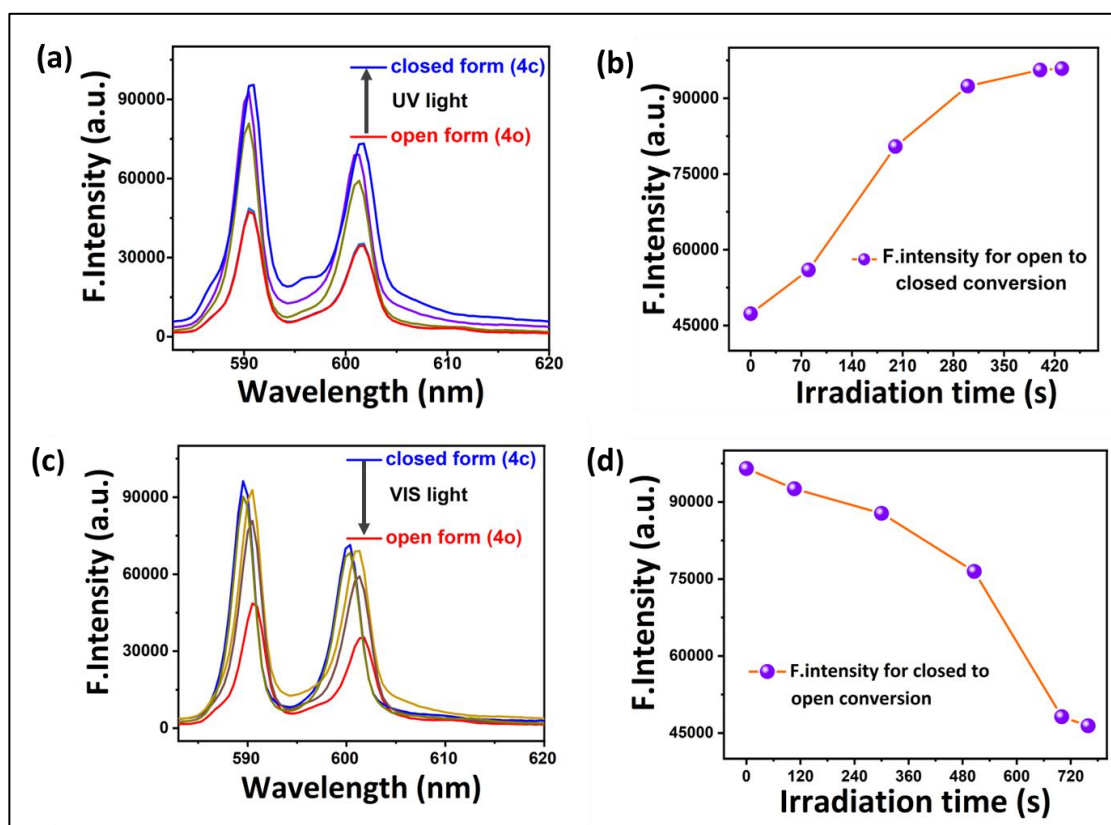


Figure 3.8. Changes in the (a,c) absorption spectra of **4o** and **4c** by gradual irradiation of UV light (365 nm) and visible light (>450 nm) in solid state respectively. Linear plot of fluorescence emission intensity vs irradiation time (s) of compound (b) **4o** and (d) **4c** in solid state.

The UV-vis absorption and fluorescence emission properties (photoswitching behaviors) of DTE-Fc were also investigated in PMMA (Poly methyl methacrylate) thin film with embedded DTE-Fc. The film is developed by liquefying **4o** (1 mg) and PMMA (15 mg) in 4 ml CHCl_3 , the homogeneous mixture was spread on FTO glass ($3 \times 1 \text{ cm}^2$) and dried overnight. Interestingly, **4o** and **4c** in PMMA embedded solid film displayed almost similar photophysical behavior (Figure 3.9) as observed in solid powder state as well as in solution phase. However, compared to the solution phase, the solid state emission spectrum of **4o** showed slight blue-

shift. An increase of dipole moment of **4o** in the S_1 -state as compared to the S_0 was observed (*vide infra*) and this induces strong solvent relaxation in the S_1 -state. However, in solid polymeric films (in our case PMMA), due to extremely high viscosity excited-state relaxation got restricted due to unavailability of freely moving liquid solvent. So a relative "blue-shift" was observed in the solid state may be due to inefficient solvent relaxation in the S_1 -state.

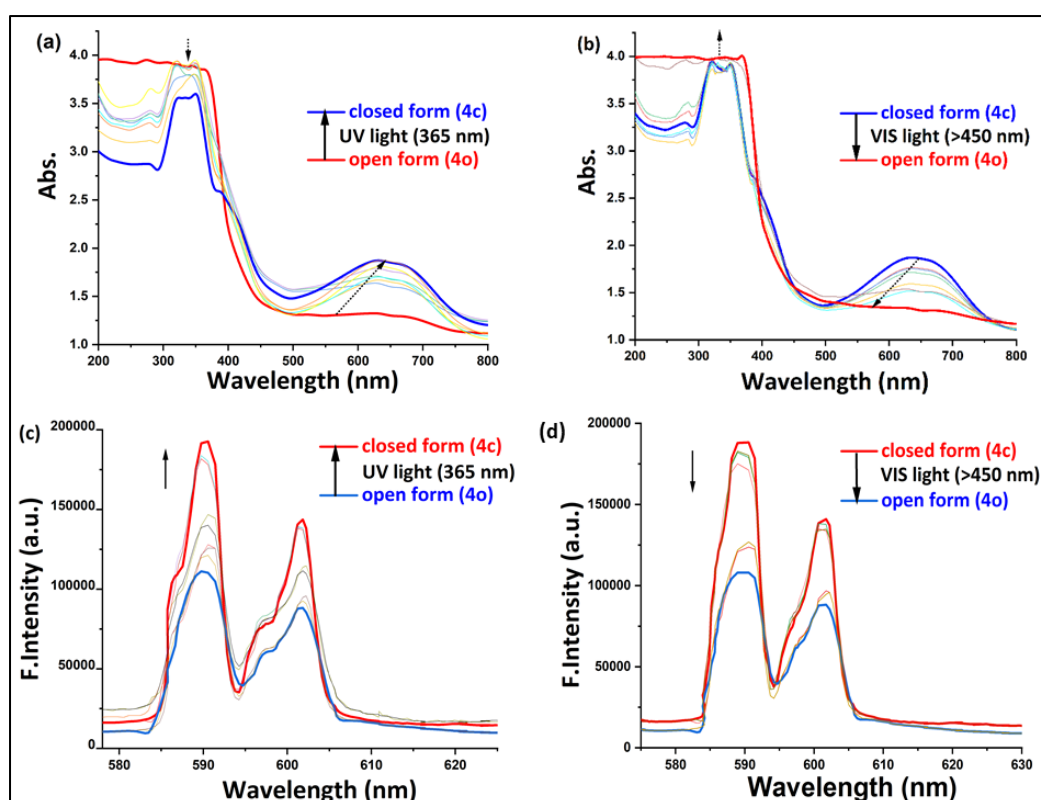


Figure 3.9. Changes in the (a,b) absorption spectra and (c,d) fluorescence emission spectra of **4o** and **4c** by gradual irradiation of UV light (365 nm) and visible light (>450 nm) in PMMA film respectively.

Upon irradiation with 365 nm UV light for 500 s, the deep violet solid **4o** gradually changes to dark green color solid **4c** (Figure 3.10a) as well as in PMMA thin film with embedded DTE-Fc (Figure 3.10b). To check the solid state photochromic reversibility and morphological change upon UV/visible light irradiation of solid **4o/4c** (both open and closed isomers separately), we have performed the high-resolution transmission electron microscopy (HRTEM). The HRTEM image of open form (**4o**) depicts the crystalline long-range array whereas the closed form (**4c**) shows the non-crystalline nature. Interestingly, upon irradiation with visible light (>450 nm), the original crystalline long-range array of open form was regained indicating a reversible change in morphology of open and closed form can also be

achieved in solid state upon UV/visible light irradiation (Figure 3.10c), making them promising materials for possible applications in light-driven actuators and molecular pumps.⁶¹

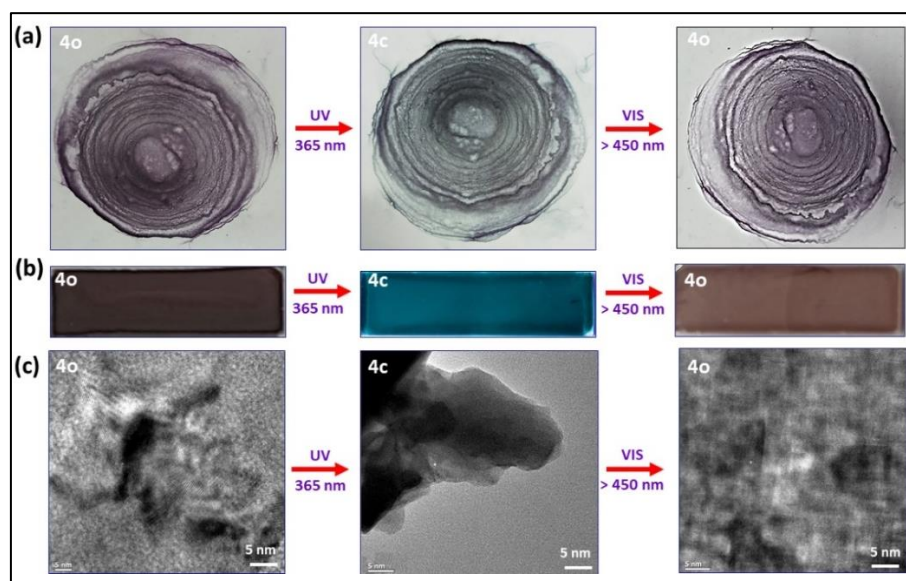


Figure 3.10. (a) Solid state color change of DTE-Fc and (b) color change in PMMA thin film with embedded DTE-Fc, (c) HRTEM images of DTE-Fc upon irradiation with UV (365 nm) and visible (>450 nm) light respectively.

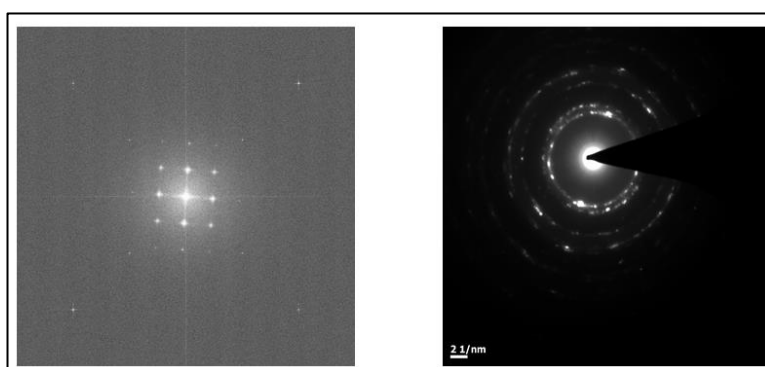


Figure 3.11. SAED image of **4o**.

Further, the reversible photocyclization property of DTE-Fc (Figure 3.12a) is also dependent on solvents polarity. To investigate the wide application of DTE-Fc in various (polar/protic) solvents, we have performed the solvatochromism experiment of **4o** and **4c** in different solvents (Figure 3.12b). Fluorescence emission spectra with increasing polarity (hexane, CHCl₃, DCM, ethanol) indicate a trend of red shift for the open isomer, whereas it was blue shift for the closed isomer (Figures 3.12c and 3.12d). This contrasting phenomenon

is attributed to the difference in dipole moment values calculated from the DFT studies (*vide infra*). The results reveal a drastic change in the dipole moment after closing the ring ($\mu = 13.46$ Debye (**4c**) vs 8.72 Debye (**4o**)), this rationalizes the blue shift in **4c** as the ground state becomes more stable due to profound solvent interaction.

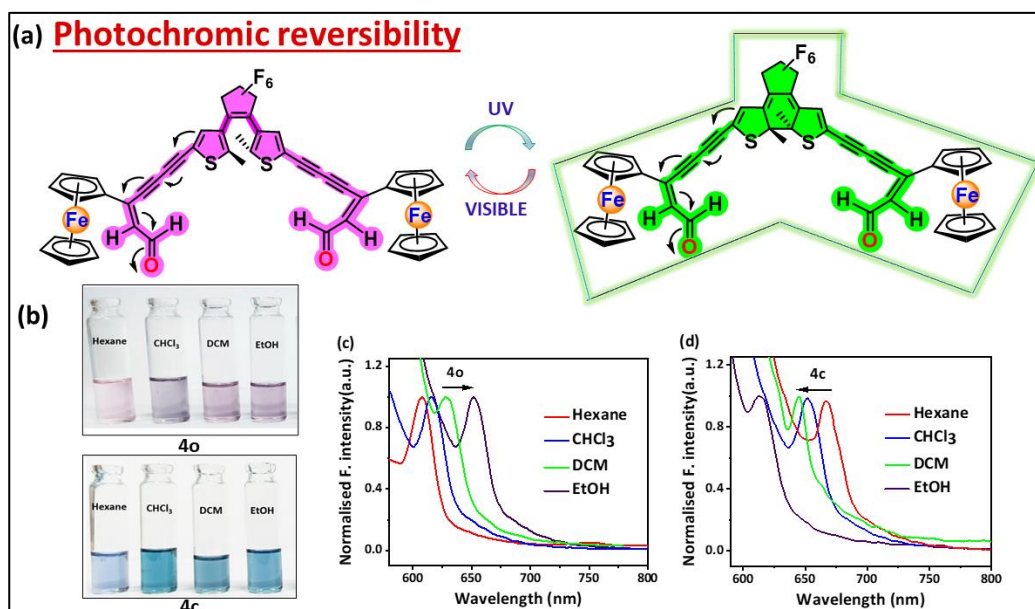


Figure 3.12. (a) Schematic representation of the photo-responsive fluorescent switching process of **4o** and **4c** in presence of UV and visible light respectively; colorimetric picture of (b) **4o** and **4c** in different solvents; normalized fluorescence emission spectra of (c) **4o** and (d) **4c** ($\lambda_{\text{ex}} = 550\text{-}583$ nm) in different solvents.

3.2.3. Electrochemical Studies

To understand the cross electronic communication between ferrocene and enediene π -conjugated central DTE derivative, the electrochemical study was performed. The molecule contains two electrochemically active units, reversible behavior of ferrocene and irreversible nature of dithienylethene which were observed in cyclic voltammetry (CV) and differential pulse voltammetry (DPV) experiments. The cyclic voltammogram of compound **4o** revealed that two well-defined consecutive redox waves at $E_{1/2} = 0.543$ V and 1.25 V were formed due to the ferrocene/ferrocenium redox couple, and irreversible redox wave of DTE fragment respectively (Figure 3.13a).⁶² After the conversion of **4o** to **4c**, anodic shifts in half-wave potentials by 0.021 V and 0.08 V were observed for ferrocene and DTE unit respectively. The

anodic shift in the conversion of **4o** to **4c** indicates the possibility of enhanced electronic communication between the photoactive DTE core and Cp ring of the redox switching ferrocene unit through π -conjugated system in case of closed form (Figure 3.13b). The increment of the intensity of the peak at 1.25 V may be accredited to the fact that the closed form is electrochemically more active than the open DTE core.⁶³ The differential pulse voltammetry (DPV) also corroborated the results obtained from the CV experiment (Figures 3.13c and 3.13d). The results obtained from UV-vis and fluorescence studies were also corroborated by electrochemical studies. Our original motive for incorporation of ferrocene unit to obtain the difference in I_p values between **4o** and **4c** was also verified by quantum chemical calculations which provided I_p_v (vertical ionization potential) values of 4.8 and 5.24 eV respectively for **4o** and **4c** (adiabatic ionization potentials, $I_{p_{ad}}$: 4.59 and 5.075 eV). Indeed, this large ionization potential difference ($\Delta I_{p_v} = 0.44$ eV and $\Delta I_{p_{ad}} = 0.48$ eV) between open and closed isomer indicates **4o/4c** could be utilized in organic light-emitting device (OLED).

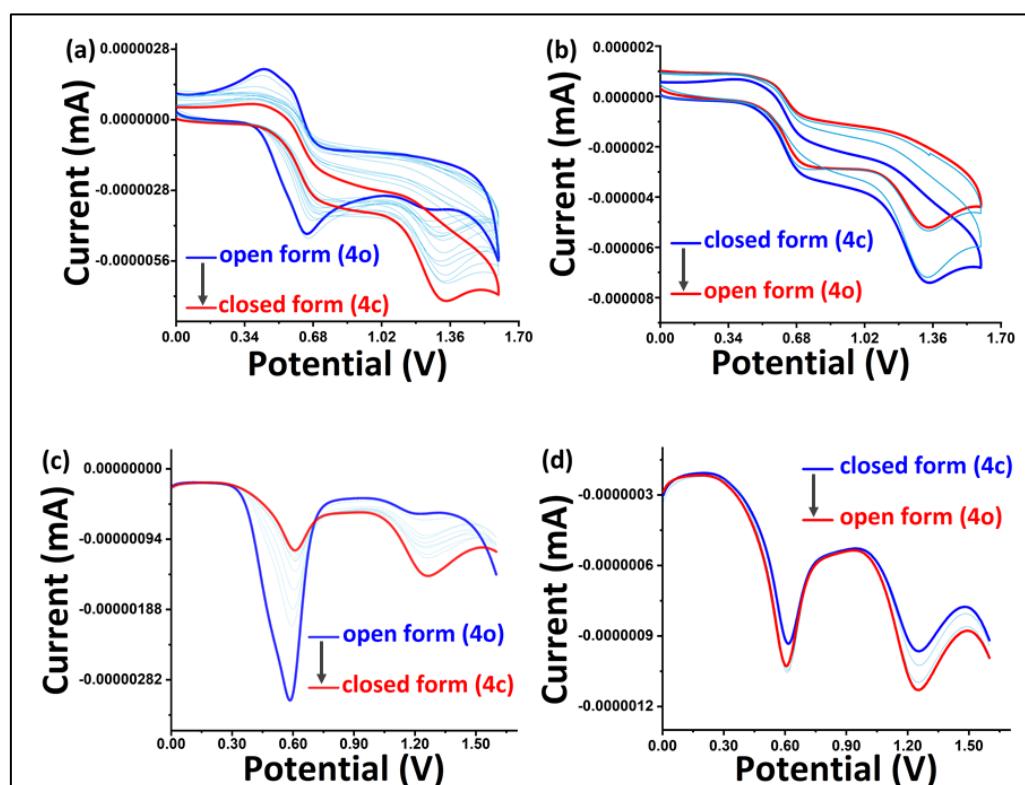


Figure 3.13. Cyclic voltammetry for (a) open to closed (**4o** to **4c**); (b) closed to open (**4c** to **4o**) conversion; differential pulse voltammetry (DPV) for (c) open (**4o**) to closed (**4c**) and (d) closed (**4c**) to open (**4o**) by irradiation of UV ($\lambda = 365$ nm) and visible light (>450 nm) respectively.

3.3. Application

Our designed and synthesized DTE-Fc demonstrated various important characteristics such as rapid photo-responsive property, prominent anti-fatigue capability, and excellent photo-switching emission with good quantum yield. Therefore, all these properties of DTE-Fc encourage us to explore its real-time application in lithography, photo-writable and erasable materials, anticounterfeiting smart material, and security ink. In recent years, the use of the quick response (QR) code is increasing dramatically due to its low-cost production, high capacity of storage and robustness. QR code is mainly utilized in various commercial purposes, such as identification of patients in the medical field, monitoring/manufacturing process for industrial spare parts, digital identification of solar panels etc. Since the colored form of DTE-Fc can be reversibly observed or bleached upon UV and visible light irradiations respectively in both solution and solid state, we envisioned utilizing DTE-Fc as a photochromic ink (Figure 3.14a) and its application in smart security technology. We have exploited our DTE-Fc for writing applications by coating over an ordinary paper and few designs have been made through UV-masking upon irradiation with UV-light for a very short period of time, demonstrating the potential of the material to be utilized in the lithographic technique.[‡] Further, DTE-Fc (**4o**, 2 mg) in CH₃CN (3 ml) solution was coated on white printing paper which gives an almost colorless (due to dilute solution) platform under daylight. The reverse quick response (RQR) code/barcode was pasted on the platform that acted as a mask of UV light. Remarkably, when the reverse QR and bar code is used, it would be impossible to counterfeit the original information. In this condition, the total system was irradiated by UV light (~400 s) which develops the original QR/bar code as green color to retrieve the encoded information quickly (Figures 3.14b and 3.14c) and accurately by scanning through a smartphone (See video VS1, and VS2). Notably, with visible light irradiation (~700 s), the code was disappeared. This process can be repeated many times without much loss in sensitivity. Thus, DTE-Fc, **4o/4c** shows potential material for cryptography and is highly efficient for confidential information encryption in a more secure manner without applying invasive stimulus *e.g.*, thermal, chemical, and mechanical means.

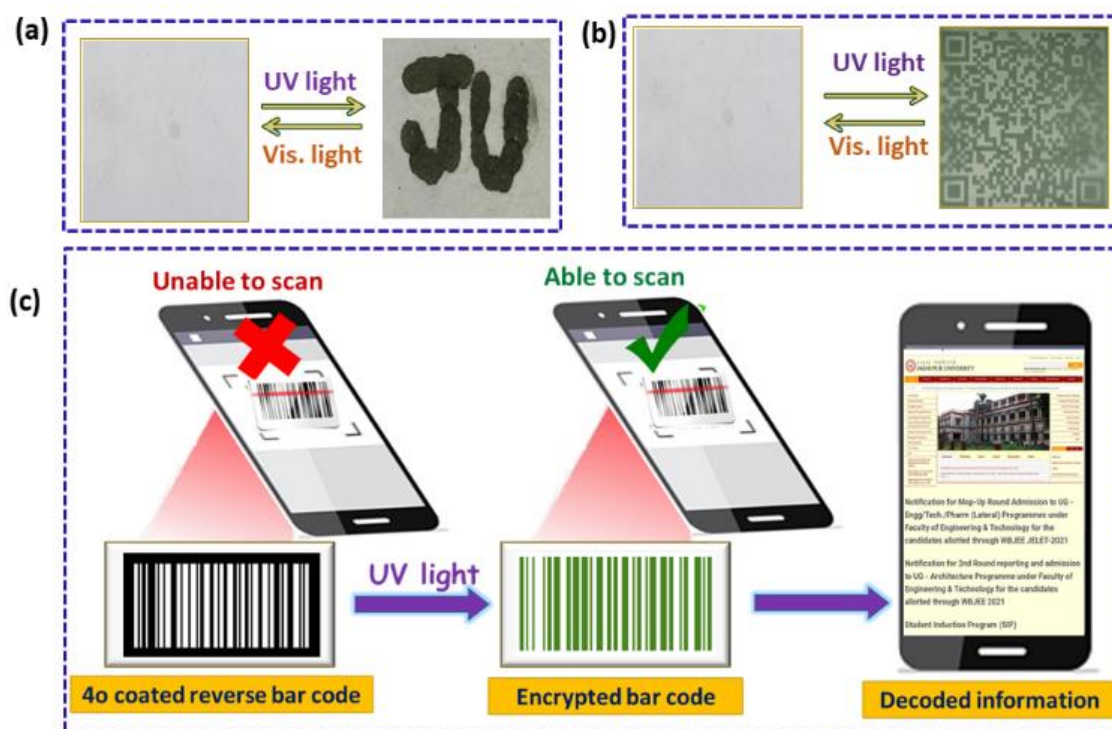


Figure 3.14. (a) Writing patterns obtained by masking of **4o** (2 mg in 3 ml CH_3CN) as photochromic ink on white coated paper; (b) QR code with visible/invisible transformation behavior was achieved by using **4o**; (c) decoding information *via* bar code scanning through a smartphone.

3.4. Theoretical (DFT) Studies

Theoretical calculations were performed on the ground of density functional theory (DFT) in order to explain the electronic structures and the optical behavior. The ligand geometries were modeled by DFT calculations considering the solvent effect (PCM, acetonitrile) using Gaussian 09 package at the B3LYP level as explained in the computational details. Both the optimized geometries apparently look similar except in the orientation of the ferrocene moieties in **4o**. However, the formation of C-C bond in **4c** increased strain within the molecule that caused **4c** to be unstable by 68.79 kJ/mol.

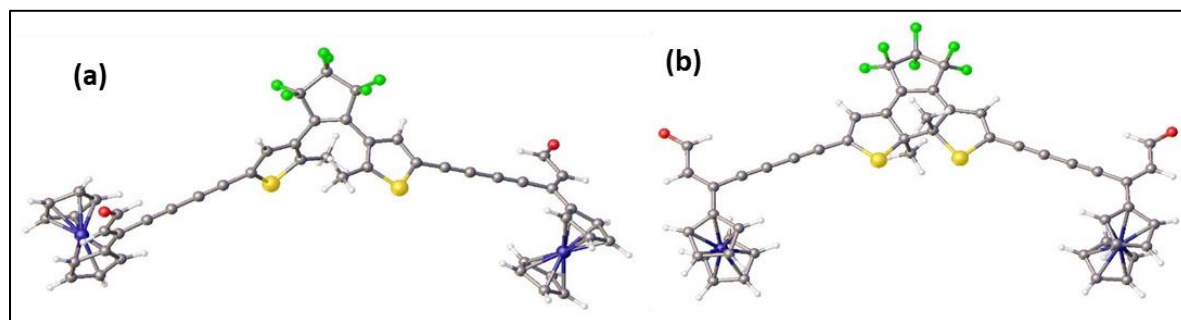


Figure 3.15. Ground state DFT optimized structure of **4o** and **4c**.

The molecular orbital analyses of **4o** revealed that the HOMO is ferrocene centered (Fe centered lone pair) and the LUMO majorly centered on the alkyne and aldehyde moieties (Figure 3.16). In contrast, both the HOMO and LUMO of **4c** are delocalized over the molecule (Figure 3.17). Similar frontier molecular orbital arrangements were observed, albeit less π -conjugation, in our previous account.^{36(b)} Extended in plane conjugation led to the stabilization of LUMO of **4c** that resulted into a decreased HOMO-LUMO gap compared to **4o** ($\Delta E_{\text{HOMO-LUMO}} = 3.04$ eV (**4o**) and 1.86 eV (**4c**)) (Figure 3.18a). This agrees with the experimentally observed red shift in the absorption spectra.

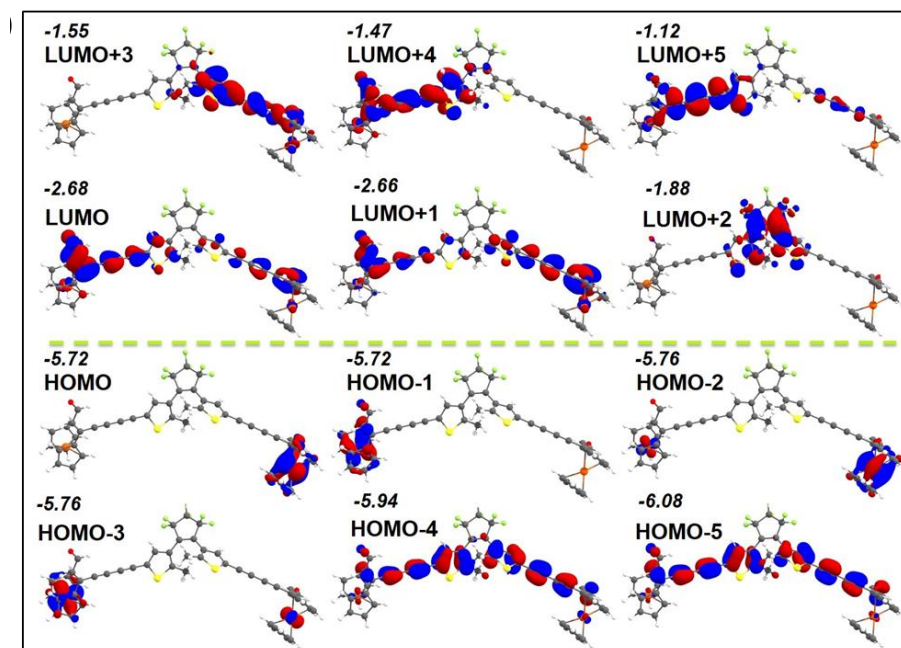


Figure 3.16. FMOs of open (**4o**) B3LYP/6-31G*/LANL2DZ (Solvent: Acetonitrile) (m cutoff 0.03).

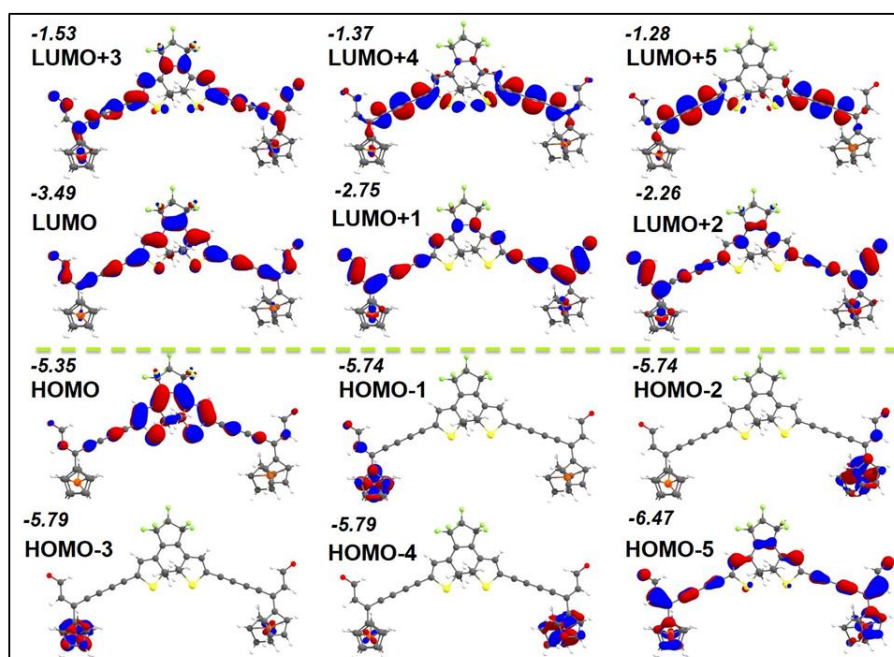


Figure 3.17. FMOs of closed (**4c**) B3LYP/6-31G*/LANL2DZ (Solvent: Acetonitrile) (mo cutoff 0.03).

Solution-phase TD-DFT (CAM-B3LYP or WB97XD) calculations were carried out to shed more light into the optical behavior of **4o** and **4c** (Figures 3.19a and 3.19b and Tables 3.4–3.7). The theoretical UV/vis plots are in close agreement with the experimental results accompanied by two UV/vis absorption bands. The transition occurring at 286 nm of **4o** accounts for the nFe (HOMO, centered on ferrocene)– π^* (LUMO+2, centered on DTE core) transition (Figure 3.16 and Table 3.4 and 3.5). The results show that the major transition at 379 nm of **4o** is assigned to (HOMO, HOMO-1) \rightarrow (LUMO, LUMO+1) transitions with high oscillator strength ($f = 1.04\%$). Note that, the HOMO (-5.72 eV) and HOMO-1 (-5.72 eV) are degenerate ferrocene centered molecular orbitals whereas, LUMO, LUMO+1 are largely located on the π -conjugated part (alkyne and aldehyde moieties). These are of mainly of metal to ligand charge transfer (MLCT) types. Therefore, an intrinsic electron transfer from ferrocene to π -conjugated fragments attached to the DTE moiety (nFe to π^* transition) may lead **4o** to be non-fluorescent. On the other hand, after UV light irradiation, an intense transition at 653 nm was observed (for **4c**) due to the transition involving HOMO to LUMO ($f = 0.98\%$) (Table 3.6–3.7). Note that the nFe orbitals in **4c** are lower in energy (HOMO-2 to HOMO-4), hence electronic transition involving nFe orbitals is not facile, leading to fluorescence enhancement. The HOMO of **4c** is mainly localized on the DTE moiety (π -type), and the LUMO is

delocalized over the complete π -conjugated framework, indicating of ligand to ligand (LLCT) type of charge transfer.[†] This is further verified from the ESP scale (electrostatic potential surfaces) which show charge depletion on alkynes and aldehyde moieties and charge concentration on S and Fe centers (Figures 3.18b and 3.18c). The natural charge analysis satisfactorily corroborated with this. The NPA charge showed an intrinsic oxidation of Fe centers from **4o** (0.23e) to **4c** (0.24e).

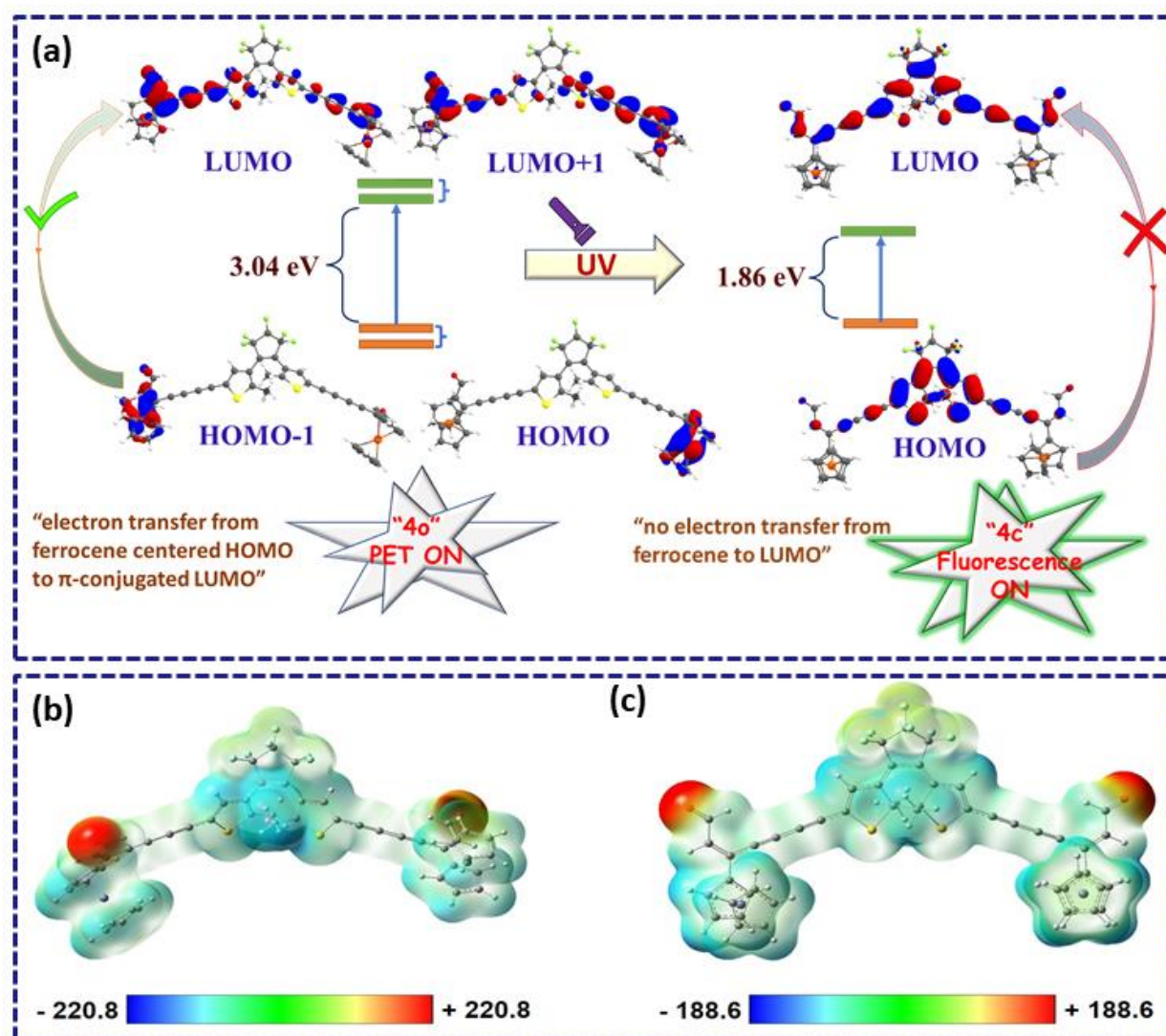


Figure 3.18. (a) Illustration of the probable fluorescence “turn-on” mechanism for **4o/4c** before and after UV light exposure; molecular electrostatic potential (ESP) energy (kJ/mol) map of (b) **4o** and (c) **4c** calculated at B3LYP/6-31g*/LANL2DZ (isovalues = 0.002).

This consequences of the electronic properties of **4o** and **4c** are also reflected in solvent-dependent bathochromic shifts as observed in their PL spectra. The dipole moment (μ) value

for the excited states (S_1) for **4c** is greater than that of **4o** (Figure 3.20). However, the change in dipole moment from S_0 to S_1 state is more in **4o** (2.02 Debye) than **4c** (1.04 Debye). Therefore, absorption spectra of **4c** should be more red shifted compared to **4o** as the polarity of the solvents is increased.

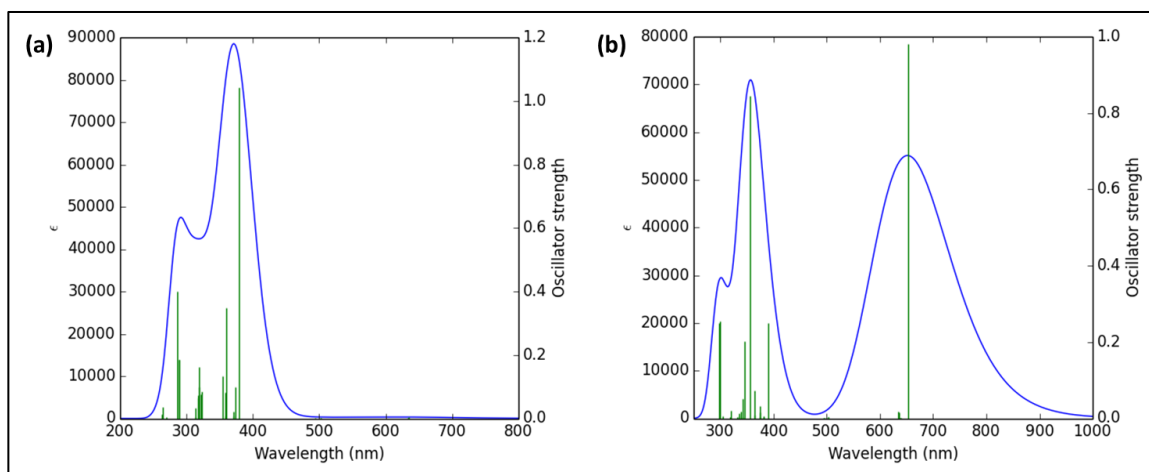


Figure 3.19. TD CAM-B3LYP computed absorption spectrum of (a) **4o** and (b) **4c**.

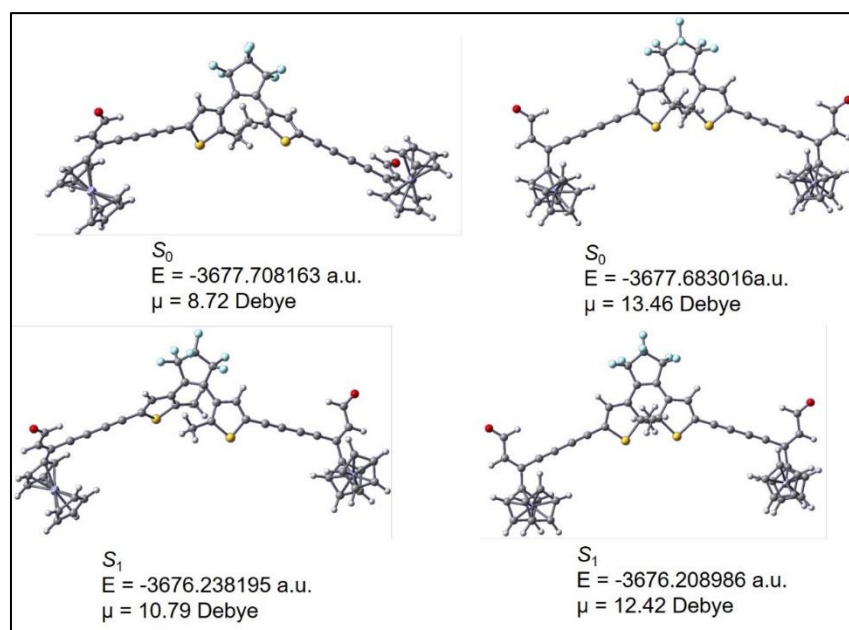


Figure 3.20. Ground state (S_0) and Excited state (S_1) geometries of **4o** (left) and **4c** (right) with energies and dipole moments.

3.5. Conclusions

In summary, we have achieved a unique molecular system, devoid of any conventional fluorophore, S,S-dioxide moiety, that displayed “turn-on” fluorescence upon irradiation with UV light. To our delight, it is an unprecedented example with highly conjugated O=CH–C=C–C≡C–C≡C– unit at the reactive carbon centre of DTE, that contributes interesting practical application for the erasable ink, based on “write-erase-write” concept on daily usable paper. Owing to the high photochromic and prominent anti-fatigue capability in solution as well as in solid state, the DTE-Fc derivative **4o/4c**, has been utilized as anti-counterfeiting ink for securing QR/bar code which could be operated in a non-invasive manner with an advanced level of security in the field of authenticating food and medicine. This result will be helpful to develop photoactive DTE derivatives as multifunctional material in the solid state with turn-on fluorescent feature. Further, this work demonstrates the opportunity of developing a new class of ferrocene appended conjugated DTEs/DAEs as smart optical encryption materials and as potential OLED.

3.6. Experimental Sections

3.6.1. Materials and Measurements

All the starting analytes used in synthesis were purchased from commercial suppliers and used with no further purification. Tetrahydrofuran was dried with sodium and benzophenone under N₂ atmosphere. K₂CO₃, NBS, TMEDA, glacial acetic acid, were purchased from local brands. DMF, acetonitrile (HPLC), THF were purchased from Merck chemicals. 2-methyl thiophene and 1.6 M *n*-BuLi in hexane were purchased from Alfa aesar. Trimethylchlorosilane, (Trimethylsilyl)acetylene, octafluorocyclopentene were obtained from TCI Chemicals. Tetrakis-(triphenylphosphine)palladium(0) used as catalyst for Sonogashira coupling, was purchased from Sigma Aldrich. The melting point of (2-formyl-1-chlorovinyl)ferrocene (**P1**) was measured at 56°C. All of the solvents were either HPLC or spectroscopic grade in the optical spectroscopic studies. Thin-layer chromatography (TLC) with Merck silica gel 60 F254 coated (layer thickness: 0.2 mm) was performed for monitoring the reaction. Silica gel (mesh 100-200 of 2.5 cm diameter) column chromatography was performed and analyzed under UV light (254 nm). The experiment was carried out using a glassy carbon electrode as a working electrode, the platinum electrode as a counter electrode,

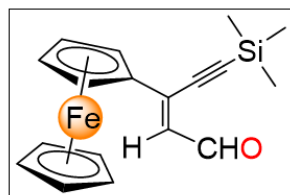
and Ag/Ag⁺ act as a reference electrode at room temperature in CH₃CN solution (1.25×10^{-4} M) containing 0.1(M) (TBAP) [(*n*-Bu)₄N]ClO₄ as a supporting electrolyte at scan rate 0.06 V.

3.6.2. Instrumentation

¹H NMR, ¹³C NMR, and ¹⁹F NMR spectra were recorded with Bruker 300 MHz FT-NMR and Bruker 400 MHz FT-NMR spectrometer using TMS (SiMe₄) as an internal reference by using CDCl₃ as a solvent. The chemical shifts (δ) of the residual solvents are as follows: CDCl₃ = 7.26 (¹H) and CDCl₃ = 77.16 (¹³C) are reported in ppm and coupling constants (J) are given in Hz. HRMS spectra were recorded on a water HRMS model XEVO-G2QTOF#YCA351 spectrometer. A Perkin Elmer LX-1 FT-IR spectrophotometer is used for FT-IR spectra characterization of materials in KBr. The YL9100 HPLC system was fitted with a Venusil XPB C18 (4.8×250 mm), 100A ns. UV-vis absorption spectra were recorded on a SHIMADZU-UV-1900i spectrophotometer at room temperature. Fluorescence emission spectra were measured with a Horiba Scientific Fluoromax-4 spectrophotometer. Solid state UV-vis and fluorescence emission spectra were measured with a PerkinElmer UV/VIS spectrometer Lambda 35 and Horiba Scientific Duetta fluorescence spectrometer respectively. CH Instruments electrochemical workstation was used for cyclic voltammetry (CV) and differential pulse voltammetry (DPV) experiments. Elemental analysis was performed by Vario EL elemental CHNS analyzer. In the photochromic experiments, the UV light irradiation experiment is carried out using a monochromatic 365 nm lamp. Luminescence lifetime measurements in nanosecond was carried out by using time-correlated single photon counting set up from Horiba Jobin-Yvon. The morphology was investigated using a high-resolution transmission electron microscope (HRTEM, FEI-TECNAIG2 20ST, energy ~200 keV). Single crystals of C₁₅H₁₂FeO were grown by slow evaporation of EtOAc/Hexane solution. A suitable crystal was selected and recorded on Microfocal D8 venture Bruker APEX 3 diffractometer. The crystal was kept at 293.00 K during data collection. Using OLEX2,⁶⁴ the structure was solved with the olex2.solve⁶⁵ structure solution program using Flipping and refined with the SHELXL⁶⁶ refinement package using Least Squares minimisation.

3.6.3.A. Synthesis of Compound 1

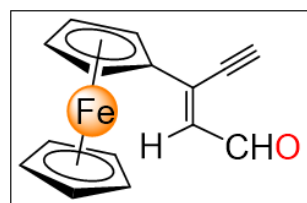
Under N₂ atmosphere, an oven-dried Schlenk RB was charged with (2-formyl-1-chlorovinyl)ferrocene (**P1**) (1.27 g, 4.65 mmol) in THF (20 mL), and then Pd(PPh₃)₄ (53.81 mg, 0.046 mmol), CuI (14.19 mg, 0.074 mmol) were added successively. Trimethylsilylacetylene (TMSA) (0.64 mL, 4.65 mmol) followed by triethylamine (1.5 ml) was added to the reaction mixture slowly. The reaction mixture was stirred at 45 °C for 7 h. After completion of the reaction (monitored by TLC), the solution was cooled to room temperature (RT) and poured into water. The reaction mixture then was washed with water and extracted with DCM (2×30 mL). The organic layer was dried over anhydrous Na₂SO₄. The solvent was evaporated under reduced pressure. The obtained residue was purified by column chromatography (silica gel, 100-200 mesh size, hexane/ethyl acetate, 99:1, v/v) to afford the pure compound **1** as a deep brown color solid (1.15 g, yield: 74 %). The synthesised compound **1** was fully characterised by ¹H NMR, ¹³C NMR, spectroscopy, and HRMS analysis.



¹H NMR (300 MHz, CDCl₃, ppm) δ 10.10 (d, 1H, J = 6.0, CHO), 6.40 (d, 1H, J = 6.0, CH), 4.66 (s, 2H, H_{Cp}), 4.48 (s, 2H, H_{Cp}), 4.15 (s, 5H, H_{Cp}), 0.30 (s, 9H, Si(CH₃)₃). ¹³C NMR (100 MHz, CDCl₃, ppm) δ 192.5 (-CHO), 145.4 (-C=C-), 128.2 (-C=C-), 99.2 (-C≡C-), 80.7 (-C≡C-), 71.9 (C_{cp}), 70.8 (C_{cp}), 70.7 (C_{cp}), 68.6 (C_{cp}), -0.1 (-Si(CH₃)₃). HRMS: m/z [M+Na]⁺ Calcd. for C₁₈H₂₀OFeSi 359.0530; found 359.0533.

3.6.3.B. Synthesis of Compound 2

To a methanolic solution of **1** (1.2 g, 3.571 mmol), K₂CO₃ (180 mg, 3 mol%) was added and the mixture was stirred at room temperature for 45 min. Upon completion (monitored by TLC), the resulting solution was poured into water and organic layer was extracted with DCM (2×30 ml), and dried over anhydrous Na₂SO₄. The solvent was evaporated under reduced pressure and the crude product was purified by column chromatography (silica gel, 100-200 mesh size, hexane/ethyl acetate, 99:1, v/v) to give a dark violet color solid (0.70 g, yield: 74.2%). mp 96-98°C. The synthesised compound **2** was fully characterised by ¹H NMR, ¹³C NMR spectroscopy, HRMS and elemental analysis.

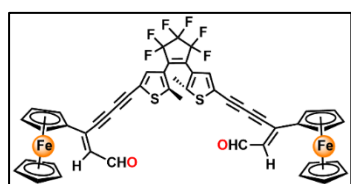


¹H NMR (400 MHz, CDCl₃, ppm) δ 10.13 (d, 1H, J = 8.0, CHO), 6.50 (d, 1H, J = 8.0, CH), 4.73 (s, 2H, H_{Cp}), 4.54 (s, 2H, H_{Cp}), 4.21 (s, 5H, H_{Cp}), 3.63 (s, 1H, -C≡C-H). ¹³C NMR

(100 MHz, CDCl₃, ppm) δ 192.2 (-CHO), 144.5 (-C=C-), 129.1 (-C=C-), 87.3 (-C \equiv C-), 80.2 (-C \equiv C-), 78.2 (C_{cp}), 72.0 (C_{cp}), 70.7 (C_{cp}), 68.5 (C_{cp}). **HRMS:** m/z [M+K]⁺ Calcd. for C₁₅H₁₂OFe 302.9874; found 302.9867. **Elemental analysis:** Anal. Calcd. for C₁₅H₁₂OFe: C 68.21; H, 4.58. Found: C 68.33; H 4.69.

3.6.3. C. Synthesis of Compound 4o

(2-formyl-1-en-1-yne)ferrocene (**2**) (0.126 g, 0.4807 mmol) and 1,2-Bis(5-(4-ethynyl)-2-



methylthiophen-3-yl)perfluorocyclopentene (**3**) (0.100 g, 0.240 mmol) were dissolved in acetone, and then N,N,N',N'-tetramethyl ethylenediamine (TMEDA) (0.02 mL, 0.012 mmol) and CuI (0.002 g, 0.012 mmol) were added respectively. The

mixture was stirred at room temperature for 1 hr. The reaction mixture was diluted with DCM (50 ml). The organic phase was washed with water and brine several times. The organic layer was dried over anhydrous Na₂SO₄. The solvent was evaporated under reduced pressure and crude product was purified by chromatography on silica gel (100-200 mesh, hexane/ethyl acetate, 85:15, v/v) afforded **4o** (yield: 53%) as a pale violet solid. mp 99-100°C. The synthesised compound **4o** was fully characterised by ¹H NMR, ¹³C NMR, ¹⁹F NMR, IR spectroscopy, HRMS and elemental analysis.

¹H NMR (400 MHz, CDCl₃, ppm) δ 10.10 (d, 1H, J = 8.0 Hz, CHO), 7.28 (s, 1H, $H_{\text{thiophene}}$), 6.57 (d, 1H, J = 8.0 Hz, CH), 4.73 (s, 2H, H_{cp}), 4.57 (s, 2H, H_{cp}), 4.24 (s, 5H, H_{cp}), 1.97 (s, 3H, CH₃). **¹³C NMR** (100 MHz, CDCl₃, ppm) δ 191.4 (-CHO), 145.8 (C_{DTE}), 145.2 (C_{DTE}), 144.0 (C_{DTE}), 134.7 (-C=C-), 134.0 (C_{DTE}), 130.1 (C_{DTE}), 125.1 (C_{DTE}), 119.9 (-C=C-), 114.1 (C_{DTE}), 82.7 (-C \equiv C-), 80.2 (-C \equiv C-), 78.7 (-C \equiv C-), 78.2 (-C \equiv C-), 72.2 (C_{cp}), 70.8 (C_{cp}), 69.4 (C_{cp}), 68.6 (C_{cp}), 14.1 (-CH₃). **¹⁹F NMR** (376 MHz, CDCl₃, ppm) δ -113.23 (s, 4F), -134.74 (s, 2F). **HRMS:** m/z [M+H]⁺ Calcd. for C₄₉H₃₀O₂S₂F₆Fe₂ 941.0368; found 941.0364. **Elemental analysis:** Anal. Calcd. for C₄₉H₃₀O₂S₂F₆Fe₂: C 62.57; H, 3.21. Found: C 62.43; H 3.52.

3.7. Computational Details

The calculations (DFT and TD-DFT) were carried out utilizing the Gaussian 09 (Rev. E. 01)⁶⁷ package and were performed on a parallel cluster system. All of the calculations

(geometry optimizations and frequency calculations, molecular orbitals, TDDFT etc.) have been performed including the solvent effects through the polarizable continuum model (PCM) that uses the integral equation formalism variant (IEFPCM). The ground-state geometries were optimized without symmetry constraints by employing the B3LYP functional,⁶⁸⁻⁷⁰ in combination with the basis set 6-31g(d)^{71,72} for all non-metallic atoms (C, H, O, F and S) and the double- ξ -quality basis set LANL2DZ^{73,74} for the metal atoms (Fe). The optimized geometries were confirmed to be local minima by performing frequency calculations and obtaining only positive (real) frequencies. The zero-point-corrected energy values are reported herein. The geometries were also reoptimized at WB97XD⁶³ level using cc-pVDZ⁷⁶ basis set. On the basis of the optimized structures, the lowest-energy vertical transitions were calculated (singlets, 60 states) by TD-DFT, using the Coulomb-attenuated functional CAM-B3LYP⁷⁷ at the aforementioned level of calculation or at WB97XD level using cc-pVDZ basis set. The TDDFT calculations were further TDDFT results were extracted using GaussSum 3.0 program.⁷⁸

†Note that, the calculations do not show any transition around this range for **4o**, even when we verified the calculation at higher level.

3.8.1. Preparation of DTE-Fc containing photochromic ink for generation of QR/bar code.

In a standard procedure, a photochromic ink containing DTE-Fc in CH₃CN was coated on white paper and dried the paper for few times. The thickness of the DTE-Fc (**4o**) coated layer was approximately 0.5 μm . Finally, a reverse QR/bar code was pasted on it which was irradiated by UV light and generated the original QR/bar code. The QR/bar code was scanned by a commercially available smartphone APP.

3.8.2. Preparation of DTE-Fc containing PMMA film.

The films are obtained by a homogeneous solution of DTE-Fc which is spread on the quartz plate (thickness 1 μm). The films are dried in air and recorded the photophysical behavior.

3.9. References

1. (a) Su, J.; Fukaminato, T.; Placial, J.-P.; Onodera, T.; Suzuki, R.; Oikawa, H.; Brosseau, A.; Brisset, F.; Pansu, R.; Nakatani, K.; Métivier, R. *Angew. Chem.* **2016**, *128*, 3726-3730; (b) Irie, M.; Fukaminato, T.; Sasaki, T.; Tamai, N.; Kawai, T. *Nature* **2002**, *420*, 759-760; (c) Fukaminato, T. *J. Photochem. Photobiol. C: Photochem. Rev.* **2011**, *12*, 177-208.
2. Sumi, T.; Kaburagi, T.; Morimoto, M.; Une, K.; Sotome, H.; Ito, S.; Miyasaka, H.; Irie, M. *Org. Lett.* **2015**, *17*, 4802-4805.
3. Uno, K.; Niikura, H.; Morimoto, M.; Ishibashi, Y.; Miyasaka, H.; Irie, M. *J. Am. Chem. Soc.* **2011**, *133*, 13558-13564.
4. Fukushima, T.; Tamaki, K.; Isobe, A.; Hirose, T.; Shimizu, N.; Takagi, H.; Haruki, R.; Adachi, S. I.; Hollamby, M. J.; Yagai, S.; *J. Am. Chem. Soc.* **2021**, *143*, 5845-5854.
5. Tian, H.; Yang, S. *Chem. Soc. Rev.* **2004**, *33*, 85-97.
6. Li, C.; Aldred, M. P.; Harder, R. A.; Chen, Y.; Yufit, D. S.; Zhu, M. Q.; Fox, M. A. *Chem. Commun.* **2021**, *57*, 9466-9469.
7. Taguchi, M.; Nakagawa, T.; Nakashima, T.; Kawai, T. *J. Mater. Chem.* **2011**, *21*, 17425-17432.
8. (a) Chan, J. C.-H.; Lam, W. H.; Yam, V. W.-W.; *J. Am. Chem. Soc.* **2014**, *136*, 16994-16997; (b) Andreasson, J.; Pischel, U.; Straight, S. D.; Moore, T. A.; Moore, A. L.; Gust, D. *J. Am. Chem. Soc.* **2011**, *133*, 11641-11648; (c) Tian, H.; Wang, S. *Chem. Commun.*, **2007**, 781-792.
9. Yun, C.; You, J.; Kim, J.; Huh, J.; Kim, E. *J. Photochem. Photobiol. C: Photochem. Rev.*, **2009**, *10*, 111-129.
10. Klajn, R. *Chem. Soc. Rev.* **2014**, *43*, 148-184.
11. Feringa, B. L. *J. Org. Chem.* **2007**, *72*, 6635-6652.
12. Sreejith, S.; Divya, K. P.; Manojkumar, T. K.; Ajayaghosh, A.; *Chem. Asian J.* **2011**, *6*, 430-437.
13. (a) Cheng, H. B.; Hu, G. F.; Zhang, Z. H.; Gao, L.; Gao, X.; Wu, H. C. *Inorg. Chem.* **2016**, *55*, 7962-7968; (b) Fukaminato, T.; Sasaki, T.; Kawai, T.; Tamai, N.; Irie, M. *J. Am. Chem. Soc.* **2004**, *126*, 14843-14849; (c) Meng, X.; Zhu, W.; Zhang, Q.; Feng, Y.; Tan, W.; Tian, H.; *J. Phys. Chem. B* **2008**, *112*, 15636-15645; (d) Lv, G.; Cui, B.; Lan, H.; Wen, Y.; Sun, A.; Yi, T. *Chem. Commun.* **2015**, *51*, 125-128; (e) Piao, X.; Zou, Y.;

- Wu, J.; Li, C.; Yi, T. *Org. Lett.* **2009**, *11*, 3818-3821; (f) Hu, F.; Jiang, L.; Cao, M.; Xu, Z.; Huang, J.; Wu, D.; Yang, W.; Liu, S. H.; Yin, J. *RSC Adv.* **2015**, *5*, 5982-5987.
14. Wang, J.; Gao, Y.; Zhang, J.; Tian, H. *J. Mater. Chem. C* **2017**, *5*, 4571-4577.
15. Fu, H.-G.; Chen, Y.; Dai, X. Y.; Liu, Y. *Adv. Optical Mater.* **2020**, *8*, 2000220.
16. (a) Verma, P.; Singh, A.; Maji, T. K. *Chem. Sci.* **2021**, *12*, 2674-2682; (b) Hsu, C.-W.; Sauvée, C.; Sundén, H.; Andreasson, J. *Chem. Sci.* **2018**, *9*, 8019-8023.
17. (a) Yu, M.; Zhang, P.; Krishnan, B. P.; Wang, H.; Gao, Y.; Chen, S.; Zeng, R.; Cui, J.; Chen, J. *Adv. Funct. Mater.* **2018**, *28*, 1804759; (b) Yu, M.; Zhang, P.; Liu, L.; Wang, H.; Wang, H.; Zhang, C.; Gao, Y.; Yang, C.; Cui, J.; Chen, J. *Adv. Opt. Mater.* **2021**, *9*, 2101227.
18. (a) Yoon, B.; Lee, J.; Park, I. S.; Jeon, S.; Lee, J.; Kim, J.-M. *J. Mater. Chem. C* **2013**, *1*, 2388-2403; (b) Lin, S.; Gutierrez-Cuevas, K. G.; Zhang, X.; Guo, J.; Li, Q. *Adv. Funct. Mater.* **2021**, *31*, 2007957; (c) Li, Z.; Wang, G.; Ye, Y.; Li, B.; Li, H.; Chen, B. *Angew. Chem.* **2019**, *131*, 18193-18199.
19. Gu, Y.; Alt, E. A.; Wang, H.; Li, X.; Willard, A. P.; Johnson, J. A. *Nature*, **2018**, *560*, 65-69.
20. Li, C.; Xiong, K.; Chen, Y.; Fan, C.; Wang, Y. L.; Ye, H.; Zhu, M. Q. *ACS Appl. Mater. Interfaces*, **2020**, *12*, 27651-27662.
21. (a) Li, B.; Lin, C.; Lu, C.; Zhang, J.; He, T.; Qiu, H.; Yin, S. *Mater. Chem. Front.*, **2020**, *4*, 869-874; (b) Li, Z.; Liu, X.; Wang, G.; Li, B.; Chen, H.; Li, H.; Zhao, Y. *Nat. Commun.* **2021**, *12*, 1363.
22. (a) Fukaminato, T.; Doi, T.; Tamaoki, N.; Okuno, K.; Ishibashi, Y.; Miyasaka, H.; Irie, M. *J. Am. Chem. Soc.* **2011**, *133*, 4984-4990; (b) Fukaminato, T.; Hirose, T.; Doi, T.; Hazama, M.; Matsuda, K.; Irie, M. *J. Am. Chem. Soc.* **2014**, *136*, 17145-17154.
23. (a) Tan, W.; Zhou, J.; Li, F.; Yi, T.; Tian, H. *Chem. Asian J.* **2011**, *6*, 1263-1268; (b) Zhang, J.; Zou, Q.; Tian, H. *Adv. Mater.* **2013**, *25*, 378-399.
24. (a) Li, C.; Yan, H.; Zhao, L. X.; Zhang, G. F.; Hu, Z.; Huang, Z. L.; Zhu, M. Q. *Nat. Commun.* **2014**, *5*, 5709; (b) Wang, Q.; Frisch, J.; Herder, M.; Hecht, S.; Koch, N. *ChemPhysChem*, **2017**, *18*, 722-727; (c) Mei, J.; Leung, N. L. C.; Kwok, R. T. K.; Lam, J. W. Y.; Tang, B. Z. *Chem. Rev.* **2015**, *115*, 11718-11940.
25. Li, C.; Gong, W. L.; Hu, Z.; Aldred, M. P.; Zhang, G. F.; Chen, T.; Huang, Z. L.; Zhu, M. Q. *RSC Adv.* **2013**, *3*, 8967-8972.
26. Sharnoff, M. J. *Lumin.*, **1971**, *4*, 69-71.

27. Nakashima, R. Li, T.; Galangau, O.; Iijima, S.; Kanazawa, R.; Kawai, T. *Chem. Asian J.* **2015**, *10*, 1725-1730.
28. (a) Irie, M.; Fukaminato, T.; Matsuda, K.; Kobatake, S. *Chem. Rev.* **2014**, *114*, 12174-12277; (b) Xu, K.; Zhao, J.; Cui, X.; Ma, J. *Chem. Commun.* **2015**, *51*, 1803-1806.
29. Jeong, Y.-C.; Yang, S. I.; Ahn, K.-H.; Kim, E. *Chem. Commun.* 2005, 2503-2505.
30. Uno, K.; Aktalay, A.; Bossi, M. L.; Irie, M.; Belov, V. N.; Hell, S. W.; *Proc. Nat. Acad. of Sci. U.S.A.*, **2021**, *118*, e2100165118.
31. Irie, M.; Morimoto, M. *Bull. Chem. Soc. Jpn.* **2018**, *91*, 237-250.
32. (a) Mi, Y.; Cheng, H.-B.; Chu, H.; Zhao, J.; Yu, M.; Gu, Z.; Zhao, Y.; Li, L. *Chem. Sci.* **2019**, *10*, 10231-10239; (b) Qiang, Z.; Shebek, K. M.; Irie, M.; Wang, M. *ACS Macro Lett.* **2018**, *7*, 1432-1437.
33. Barrez, E.; Laurent, G.; Pavageau, C.; Sliwa, M.; Métivier, R. *Phys. Chem. Chem. Phys.*, **2018**, *20*, 2470-2479.
34. Li, Z.; Xia, J.; Liang, J.; Yuan, J.; Jin, G.; Yin, J.; Yu, G.-A.; Liu, S. H. *Dyes and Pigments.* **2011**, *90*, 290-296.
35. Wong, C.-L.; Cheng, Y.-H.; Poon, C.-T.; Yam, V. W.-W.; *Inorg. Chem.* **2020**, *59*, 14785-14795.
36. (a) Guirado, G.; Coudret, C.; Launay, J. P.; *J. Phys. Chem. C* **2007**, *111*, 2770-2776; (b) Karmakar, M.; Pal, A.; Mondal, B.; Adarsh, N. N.; Thakur, A. *Inorg. Chem.* **2021**, *60*, 6086-6098.
37. Zhang, Z.; Liu, X.; Li, Z.; Chen, Z.; Zhao, F.; Zhang F.; Tung, C.-H. *Adv. Funct. Mater.* **2008**, *18*, 302-307.
38. Sánchez, R. S.; Gras-Charles, R.; Bourdelande, J. L.; Guirado, G.; Hernando, J. *J. Phys. Chem. C* **2012**, *116*, 7164-7172.
39. Singh, A.; Pati, A. K.; Mishra, A. K. *Phys. Chem. Chem. Phys.* **2018**, *20*, 14889-14898.
40. Han, W.; Shi, Y.; Xue, T.; Wang, T. *Dyes and Pigments.* **2019**, *166*, 140-148.
41. Ma, J.; Cui, X.; Wang, F.; Wu, X.; Zhao, J.; Li, X. *J. Org. Chem.* **2014**, *79*, 10855-10866.
42. Su, L.; Dong, J.; Liu, L.; Sun, M.; Qiu, R.; Zhou, Y.; Yin, S.-F. *J. Am. Chem. Soc.* **2016**, *138*, 12348-12351.
43. Zhao, H.; Garoni, E.; Roisnel, T.; Colombo, A.; Dragonetti, C.; Marinotto, D.; Righetto, S.; Roberto, D.; Jacquemin, D.; Boixel, J.; Guerchais, V. *Inorg. Chem.* 2018, **57**, 7051-7063.

-
44. Prabu, S.; David, E.; Viswanathan, T.; Angelin Jinisha, J. S.; Malik, R.; Rudharachari Maiyelvaganan, K.; Prakash, M.; Palanisami, N. *J. Mol. Struct.* **2020**, *1202*, 127302.
 45. Zhang, M.-Y.; Wang, C.-H.; Wang, W.-Y.; Ma, N.-N.; Sun, S.-L.; Qiu, Y.-Q. *J. Phys. Chem. A*, **2013**, *117*, 12497-12510.
 46. (a) Irie, M.; Lifka, T.; Kobatake, S.; Kato, N. *J. Am. Chem. Soc.* **2000**, *122*, 4871-4876; (b) Tanaka, Y.; Ishisaka, T.; Inagaki, A.; Koike, T.; Lapinte, C.; Akita, M. *Chem. Eur. J.* **2010**, *16*, 4762-4776.
 47. (a) Jeong, W.; Khazi, M. I.; Park, D.-H.; Jung, Y.-S.; Kim, J.-M. *Adv. Funct Mater* **2016**, *26*, 5230-5238; (b) Fredrich, S.; Bonasera, A.; Valderrey, V.; Hech, S. *J. Am. Chem. Soc.* **2018**, *140*, 6432-6440.
 48. Roubinet, B.; Bossi, M. L.; Alt, P.; Leutenegger, M.; Shojaei, H.; Schnorrenberg, S.; Nizamov, S.; Irie, M.; Belov, V. N.; Hell, S. W. *Angew. Chem. Int. Ed.* **2016**, *55*, 15429.
 49. Pariani, G.; Quintavalla, M.; Colella, L.; Oggioni, L.; Castagna, R.; Ortica, F. ; Bertarelli, C.; Bianco, A. *J. Phys. Chem. C* **2017**, *121*, 23592-23598.
 50. Zhang, Z.; Wang, W.; Jin, P.; Xue, J.; Sun, L.; Huang, J.; Zhang, J.; Tian, H. *Nat. Commun.* **2019**, *10*, 4232.
 51. Xi, H.; Zhang, Z.; Zhang, W.; Li, M.; Lian, C.; Luo, Q.; Tian, H.; Zhu, W.-H.; *J. Am. Chem. Soc.* **2019**, *141*, 18467-18474.
 52. Li, C.; Aldred, M. P.; Harder, R. A.; Chen, Y.; Yufit, D. S.; Zhu, M.-Q.; Fox, M. A.; *Chem. Commun.* **2021**, *57*, 9466-9469.
 53. Hu, F.; Cao, M.; Ma, X.; Liu, S. H.; Yin, J. *J. Org. Chem.* **2015**, *80*, 7830-7835.
 54. Uno, K.; Bossi, M. L.; Belov, V. N.; Irie, M.; Hell, S. W.; *Chem. Commun.* **2020**, *56*, 2198.
 55. Li, Z.; Pei, Y.; Wang, Y.; Lu, Z.; Dai, Y.; Duan, Y.; Ma, Y.; Guo, H. *J. Org. Chem.* **2019**, *84*, 13364-13373.
 56. Li, Z.; Wang, Y.; Li, M.; Zhang, H.; Guo, H.; Ya, H.; Yin, J. *Org. Biomol. Chem.* **2018**, *16*, 6988-6997.
 57. Wan, H.; Xue, H.; Ling, Y.; Qiao, Y.; Chen, Y.; Zhou, G. *Phys. Chem. Chem. Phys.* **2018**, *20*, 14348-14356.
 58. Herder, M.; Schmidt, B. M.; Grubert, L.; Pätzelt, M.; Schwarz, J.; Hecht, S. *J. Am. Chem. Soc.* **2015**, *137*, 2738-2747.
 59. Cui, X.; Zhao, J.; Zhou, Y.; Ma, J.; Zhao, Y. *J. Am. Chem. Soc.* **2014**, *136*, 9256-9259.
-

60. (a) Zhao, H.; Al-Atar, U.; Pace, T. C.S.; Bohne, C.; Branda, N. R. *J. Photochem. Photobiol. C: Photochem. Rev.* **2008**, *200*, 74-82. (b) Xu, Z.; Liu, Q. T.; Wang, X.; Liu, Q.; Hean, D.; Chou, K. C.; Wolf, M. O. *Chem. Sci.* **2020**, *11*, 2729-2734.
61. Cao, X.; Zhou, J.; Zou, Y.; Zhang, M.; Yu, X.; Zhang, S.; Yi, T.; Huang, C. *Langmuir* **2011**, *27*, 5090-5097; (b) Kobatake, S.; Takami, S.; Muto, H.; Ishikawa, T.; Irie, M. *Nature* **2007**, *446*, 778-781.
62. (a) Harvey, E. C.; Areephong, J.; Cafolla, A. A.; Long, C.; Browne, W. R.; Feringa, B. L.; Pryce, M. T. *Organometallics* **2014**, *33*, 3309-3319; (b) Romero, T.; Caballero, A.; Tárraga, A.; Molina, P. *Org. Lett.* **2009**, *11*, 3466-3469.
63. Liu, Y.; Ndiaye, C. M.; Lagrost, C.; Costuas, K.; Choua, S.; Turek, P.; Norel, L.; Rigaut, S. *Inorg. Chem.* **2014**, *53*, 8172-8188.
64. Dolomanov, O. V.; Bourhis, L. J.; Gildea, R. J.; Howard, J. A. K.; Puschmann, H. *J. Appl. Cryst.* **2009**, *42*, 339-341.
65. Bourhis, L. J.; Dolomanov, O. V.; Gildea, R. J.; Howard, J. A. K.; Puschmann, H. *Acta Cryst.* **2015**, *A71*, 59-75.
66. Sheldrick, G. M. *Acta Cryst.* **2015**, *C71*, 3-8.
67. Frisch, M. J.; Trucks, G. W.; Schlegel, H. B.; Scuseria, G. E.; Robb, M. A.; Cheeseman, J. R.; Scalmani, G.; Barone, V.; Mennucci, B.; Petersson, G. A.; Nakatsuji, H.; Caricato, M.; Li, X.; Hratchian, H. P.; Izmaylov, A. F.; Bloino, J.; Zheng, G.; Sonnenberg, J. L.; Hada, M.; Ehara, M.; Toyota, K.; Fukuda, R.; Hasegawa, J.; Ishida, M.; Nakajima, T.; Honda, Y.; Kitao, O.; Nakai, H.; Vreven, T.; Montgomery, J. A.; Peralta, J. E.; Ogliaro, F.; Bearpark, M.; Heyd, J. J.; Brothers, E.; Kudin, K. N.; Staroverov, V. N.; Keith, T.; Kobayashi, R.; Normand, J.; Raghavachari, K.; Rendell, A.; Burant, J. C.; Iyengar, S. S.; Tomasi, J.; Cossi, M.; Rega, N.; Millam, J. M.; Klene, M.; Knox, J. E.; Cross, J. B.; Bakken, V.; Adamo, C.; Jaramillo, J.; Gomperts, R.; Stratmann, R. E.; Yazyev, O.; Austin, A. J.; Cammi, R.; Pomelli, C.; Ochterski, J. W.; Martin, R. L.; Morokuma, K.; Zakrzewski, V. G.; Voth, G. A.; Salvador, P.; Dannenberg, J. J.; Dapprich, S.; Daniels, A. D.; Farkas, O.; Foresman, J. B.; Ortiz, J. V.; Cioslowski, J.; Fox, D. J. *Gaussian 09, Rev. E.01*; Gaussian, Inc.: Wallingford, CT, **2013**.
68. Becke, A. D. *J. Chem. Phys.* **1993**, *98*, 5648-5652.
69. Lee, C.; Yang, W.; Parr, R. G.; *Phys. Rev. B: Condens. Matter Mater. Phys.* **1988**, *37*, 785-789.

70. Stephens, P. J.; Devlin, F. J.; Chabalowski, C. F.; Frisch, M. J. *J. Phys. Chem.* **1994**, *98*, 11623-11627.
71. Petersson, G. A.; Al-Laham, M. A. *J. Chem. Phys.* **1991**, *94*, 6081-6090.
72. Petersson, G. A.; Bennett, A.; Tensfeldt, T. G.; Al-Laham, M. A.; Shirley, W. A.; Mantzaris, J. *J. Chem. Phys.* **1988**, *89*, 2193-2218.
73. Wadt, W. R.; Hay, P. J. *J. Chem. Phys.* **1985**, *82*, 284-298.
74. Hay, P. J.; Wadt, W. R. *J. Chem. Phys.* **1985**, *82*, 299-310.
75. Chai, J.-D.; Head-Gordon, M. *Phys. Chem. Chem. Phys.* **2008**, *10*, 6615-6620.
76. Dunning, Jr. T. H. *J. Chem. Phys.* **1989**, *90*, 1007-1023.
77. Yanai, T.; Tew, D. P.; Handy, N. C. *Phys. Lett.* **2004**, *393*, 51-57.
78. O'Boyle, M.; Tenderholt, A. L.; Langner, K. M. *J. Comp. Chem.* **2008**, *29*, 839-845.

Spectroscopic and Computational Details

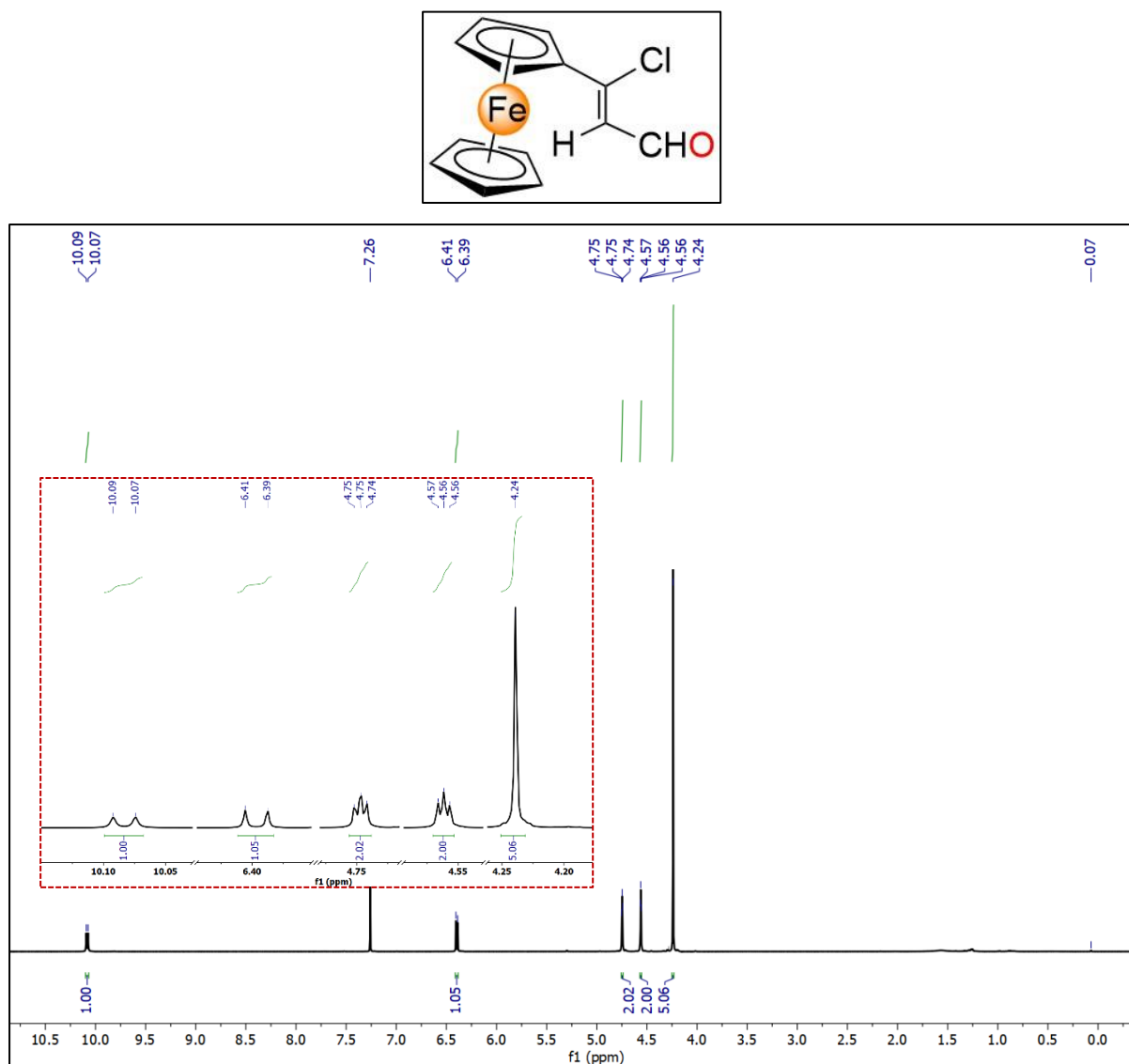


Figure 3.21. ^1H NMR spectrum of compound P1 in CDCl_3 as a solvent.

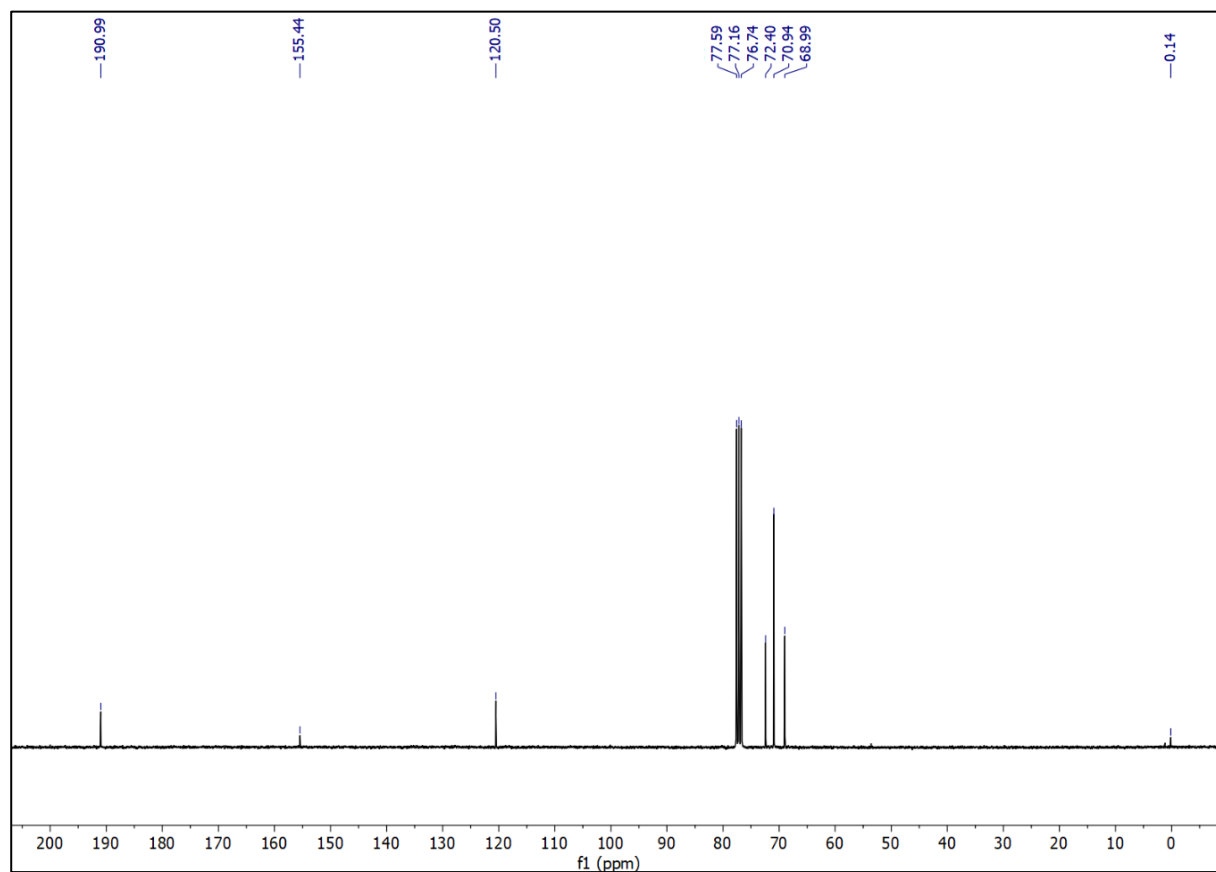
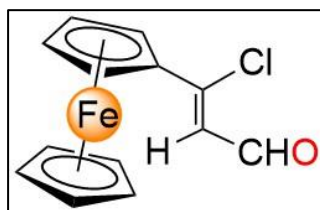


Figure 3.22. ^{13}C NMR spectrum of compound P1 in CDCl_3 as a solvent.

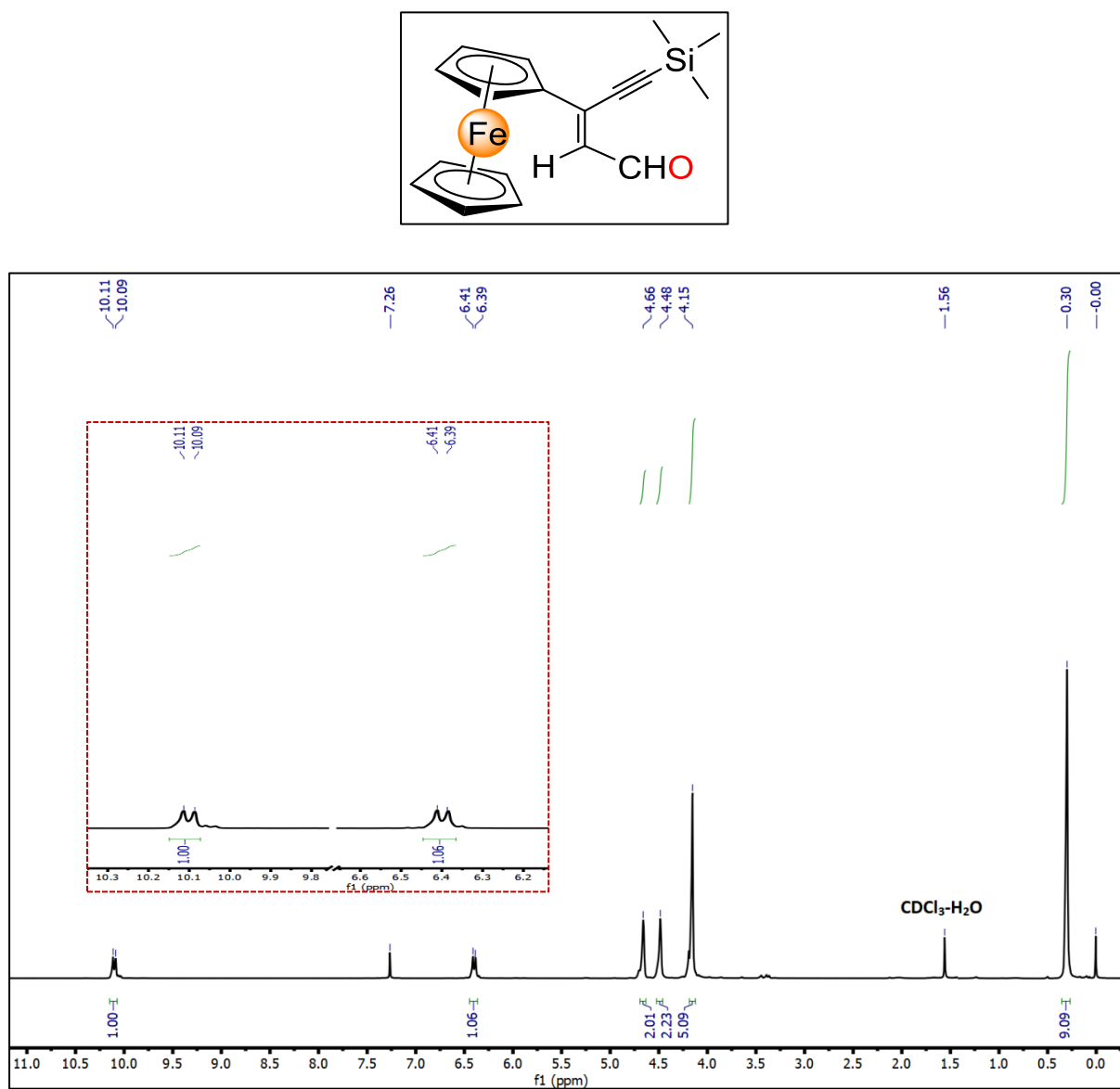


Figure 3.23. ^1H NMR spectrum of compound **1** in CDCl_3 as a solvent.

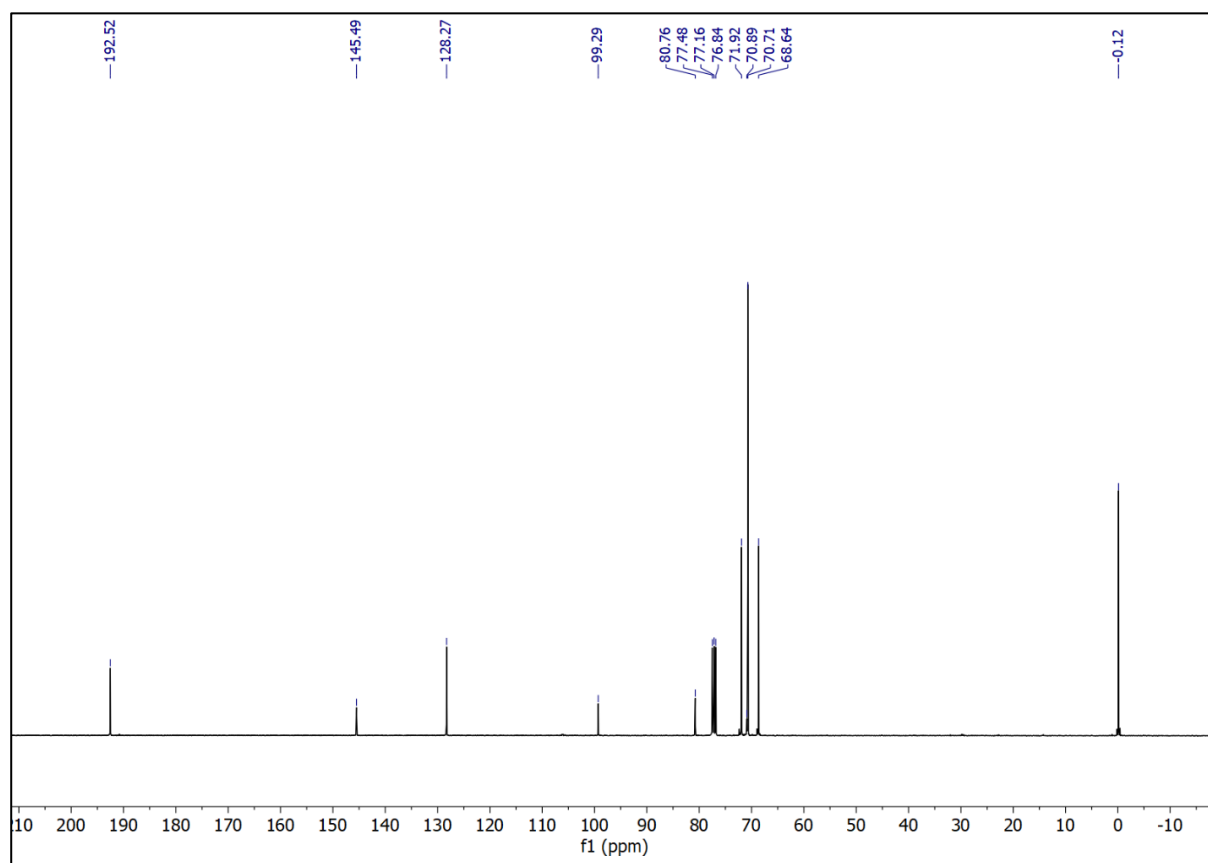
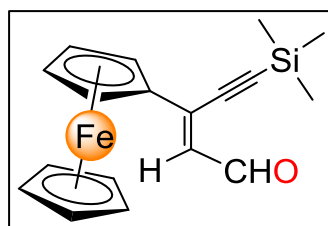


Figure 3.24. ^{13}C NMR spectrum of compound **1** in CDCl_3 as a solvent.

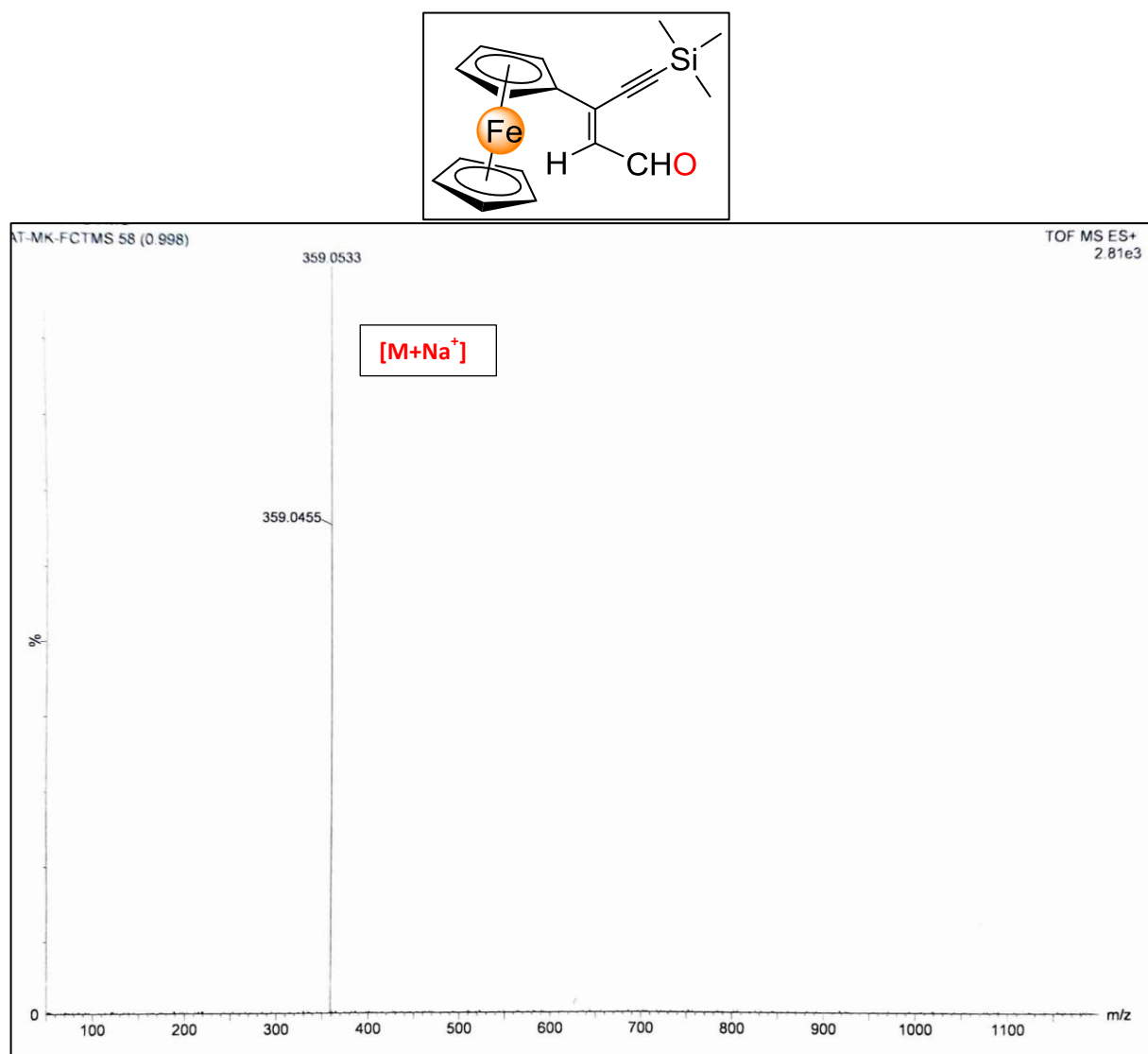


Figure 3.25. HRMS spectra of compound 1.

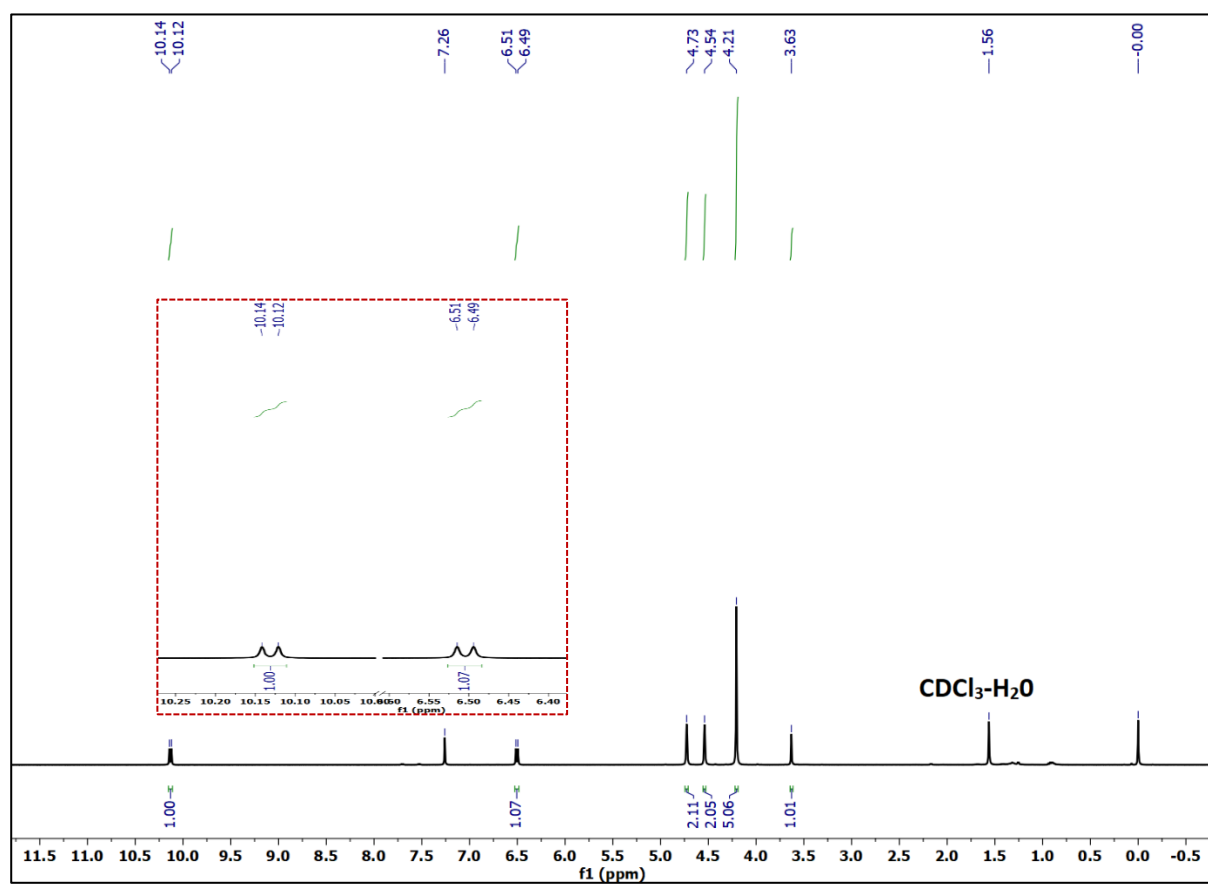
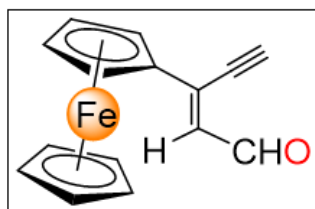


Figure 3.26. ¹H NMR spectrum of compound **2** in CDCl₃ as a solvent.

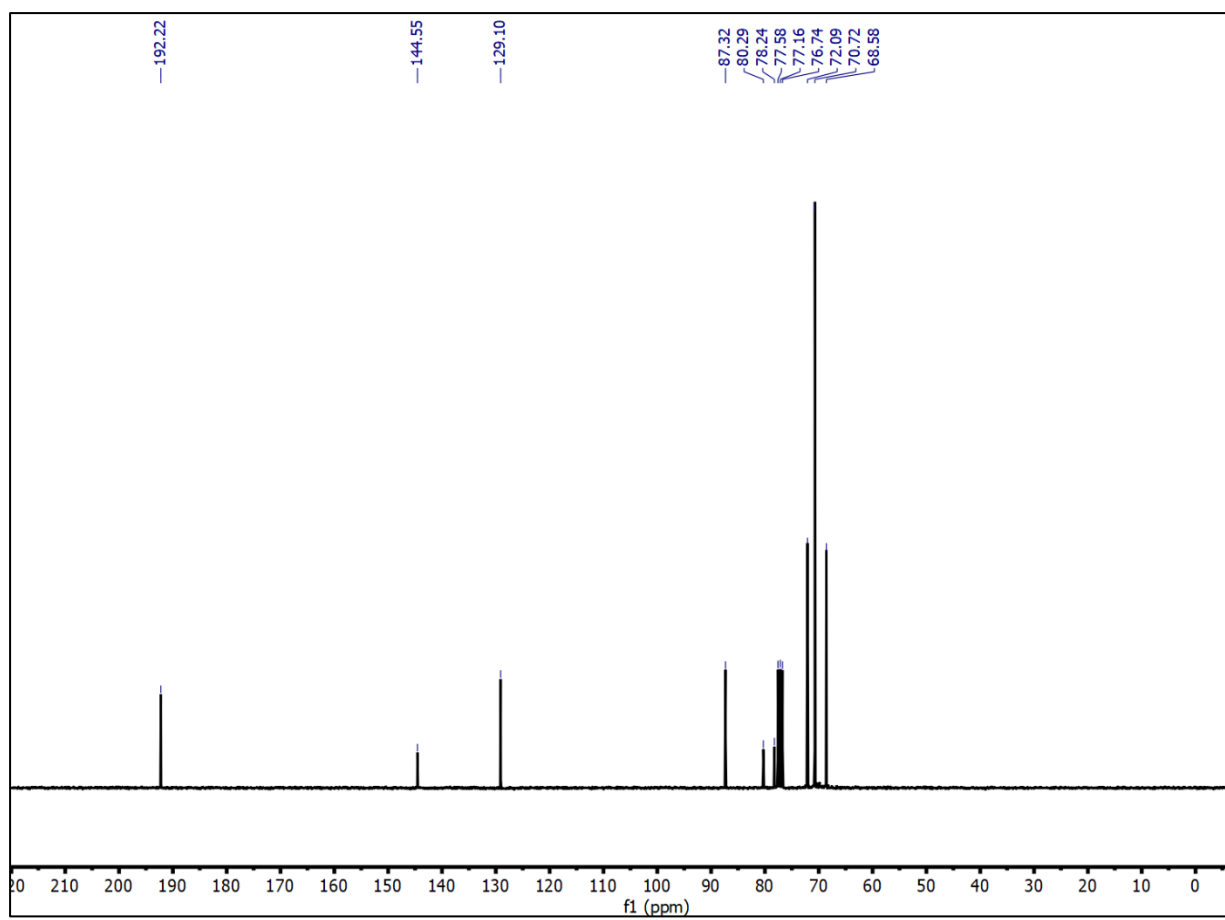
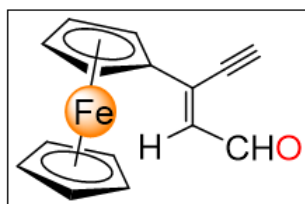


Figure 3.27. ^{13}C NMR spectrum of compound **2** in CDCl_3 as a solvent.

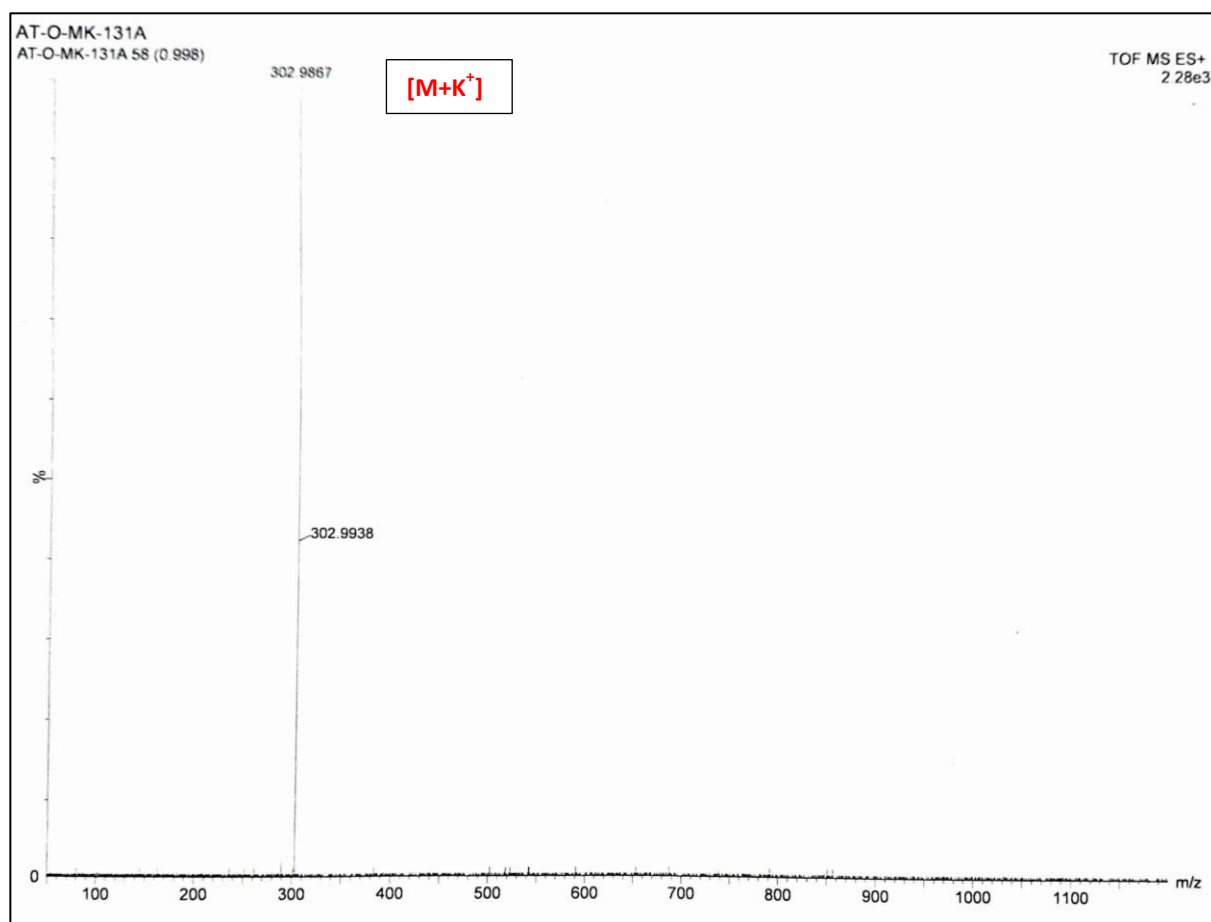
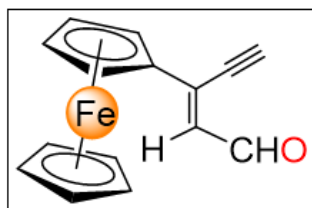


Figure 3.28. HRMS spectra of compound 2.

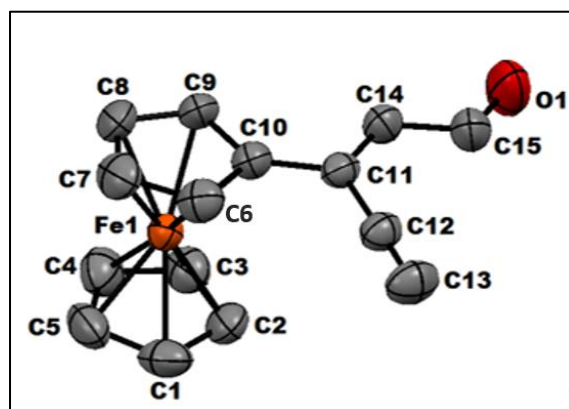


Figure 3.29. ORTEP representation of the molecular structure of **2** with thermal ellipsoids drawn at the 50% probability level.

Crystallographic data for 2:

Empirical Formula $C_{15}H_{12}FeO$, $M_r = 264.10 \text{ g mol}^{-1}$, Crystal size (mm) $0.2 \times 0.15 \times 0.12$, monoclinic, space group $P 2_1/c$, $a = 10.0806(8) \text{ \AA}$, $b = 9.2146(7) \text{ \AA}$, $c = 13.0917(10) \text{ \AA}$, $\beta = 96.363(2)^\circ$, $V = 1213.98(16) \text{ \AA}^3$, $Z = 4$, $T = 293.00 \text{ K}$, $\mu(\text{Mo-K}\alpha) = 1.220 \text{ mm}^{-1}$, $F(0 0 0) = 544.0$, $D_{\text{calc}} = 1.445 \text{ g/cm}^3$, $R_{\text{int}} = 0.0333$, $R_{\text{sigma}} = 0.0119$, Final R indices $[I > 2\sigma(I)]$: $R_1 = 0.0238$, $wR_2(\text{all}) = 0.0654$.

Selected bond lengths (\AA) and angles (deg) for **2**: C2-C3 1.421(3), C12-C13 1.177(3), C14-C15 1.445(3); O1-C15-C14 123.7 (2), O1-C15-H15 118.2.

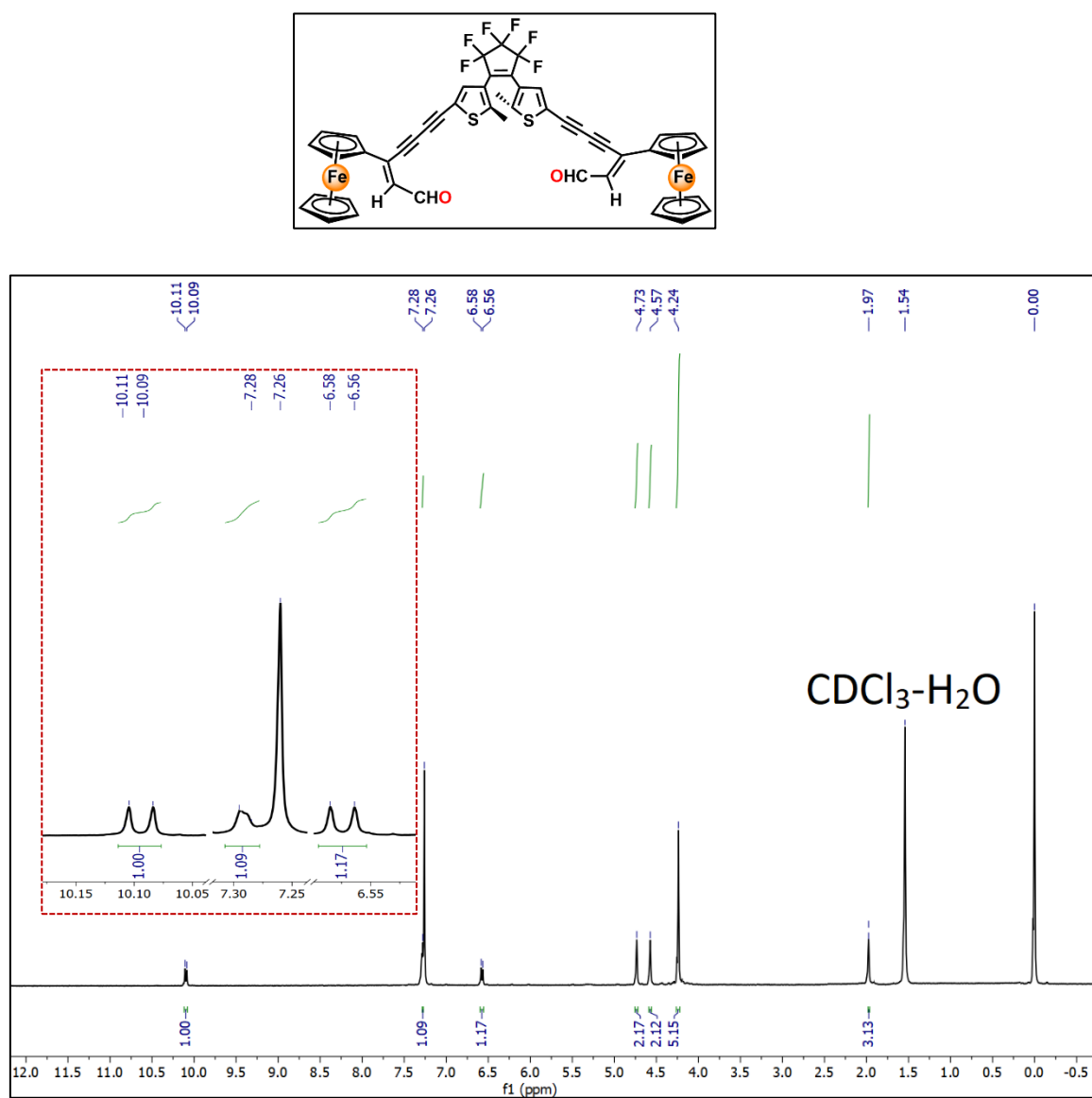


Figure 3.30. ^1H NMR spectrum of compound **4o** in CDCl_3 as a solvent.

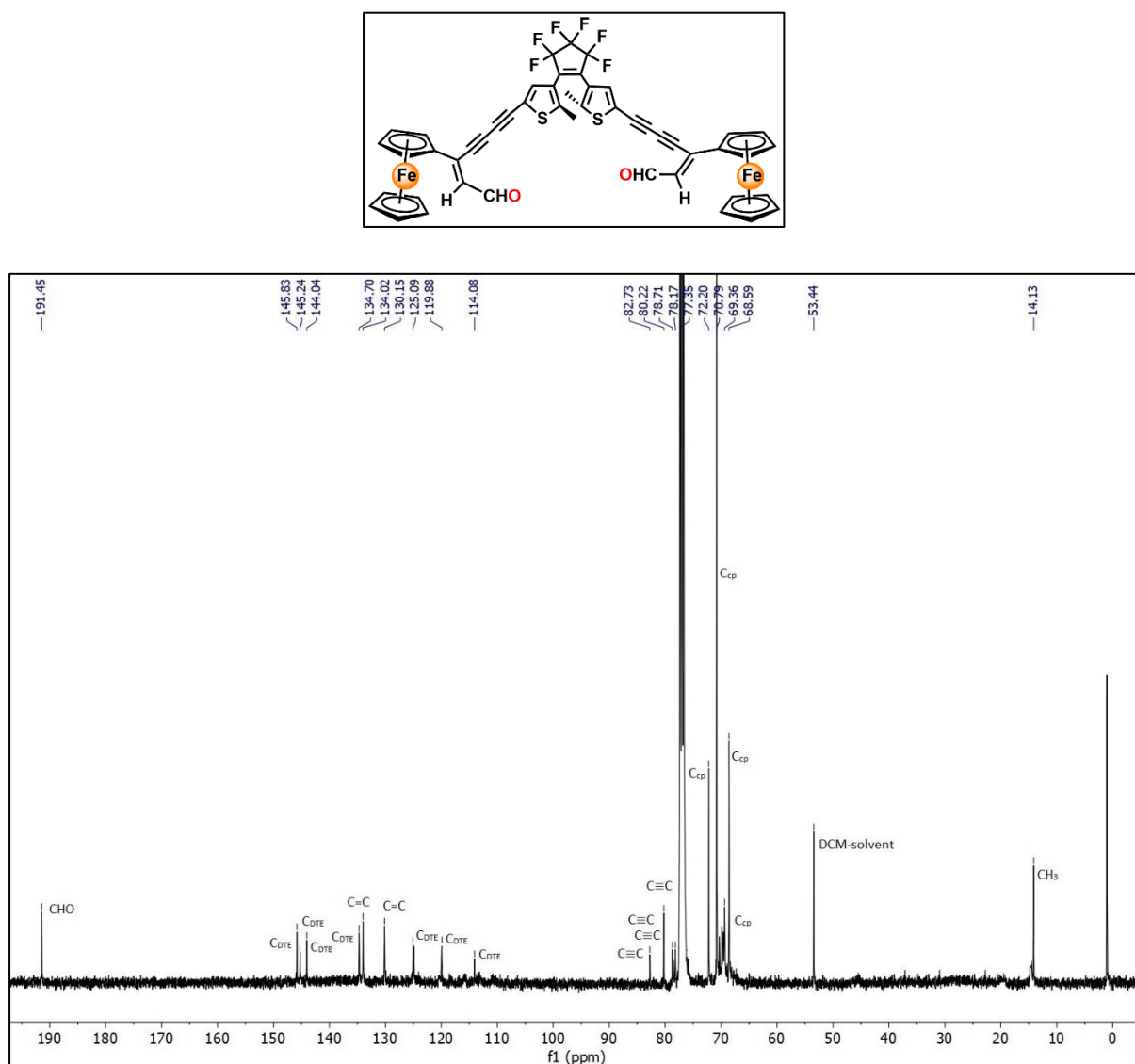


Figure 3.31. ^{13}C NMR spectrum of compound **4o** in CDCl_3 as a solvent.

NOTE: We have surveyed several literatures till date and came to know that the nature of the ^{13}C NMR spectra of diarylethene (DTE) unit are similar kind as obtained in our case even at high concentration (*J. Am. Chem. Soc.*, 2019, **141**, 2097-2103).

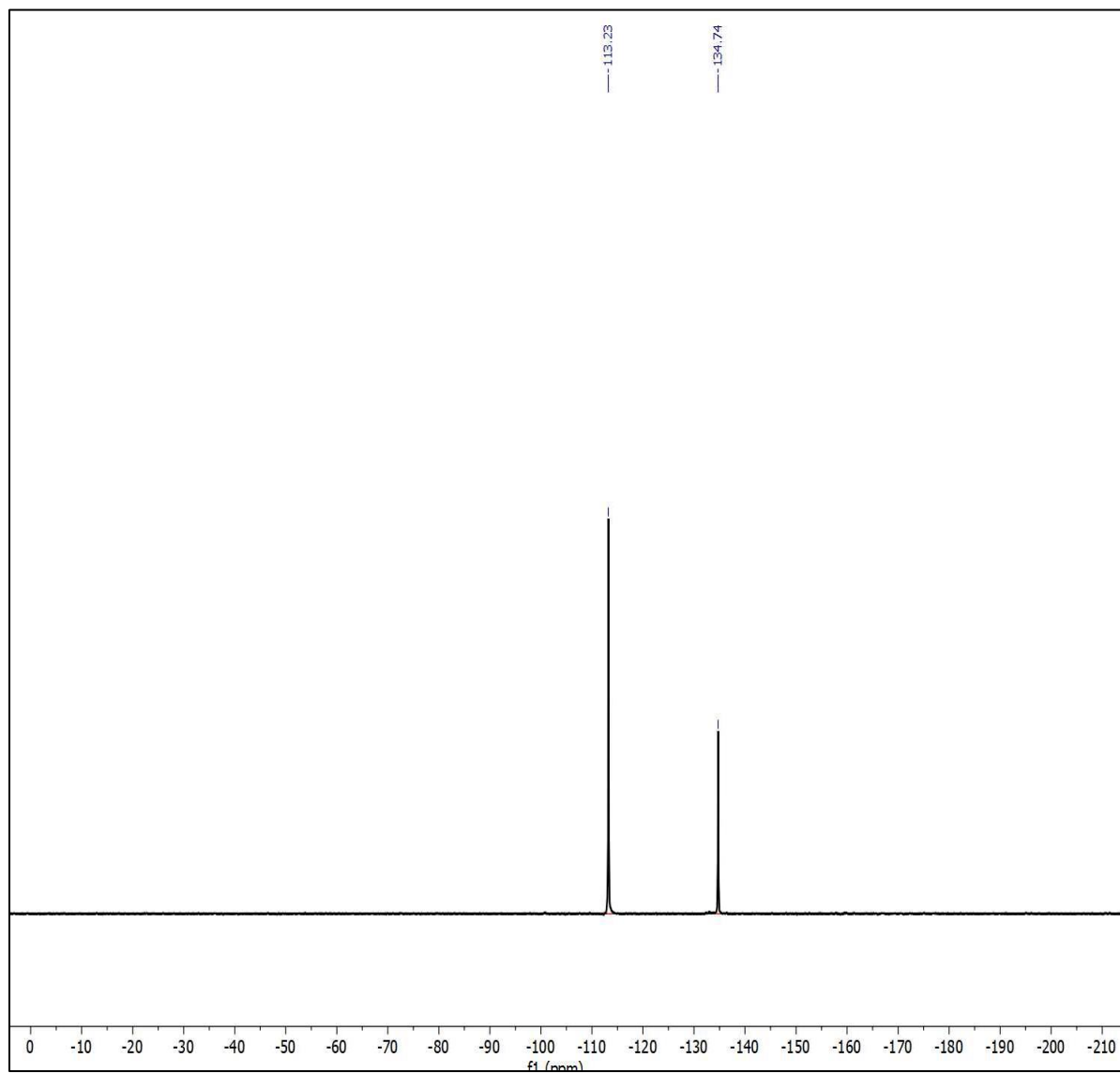
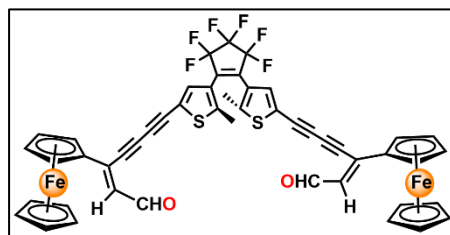


Figure 3.32. ^{19}F NMR spectrum of compound **40** in CDCl_3 as a solvent.

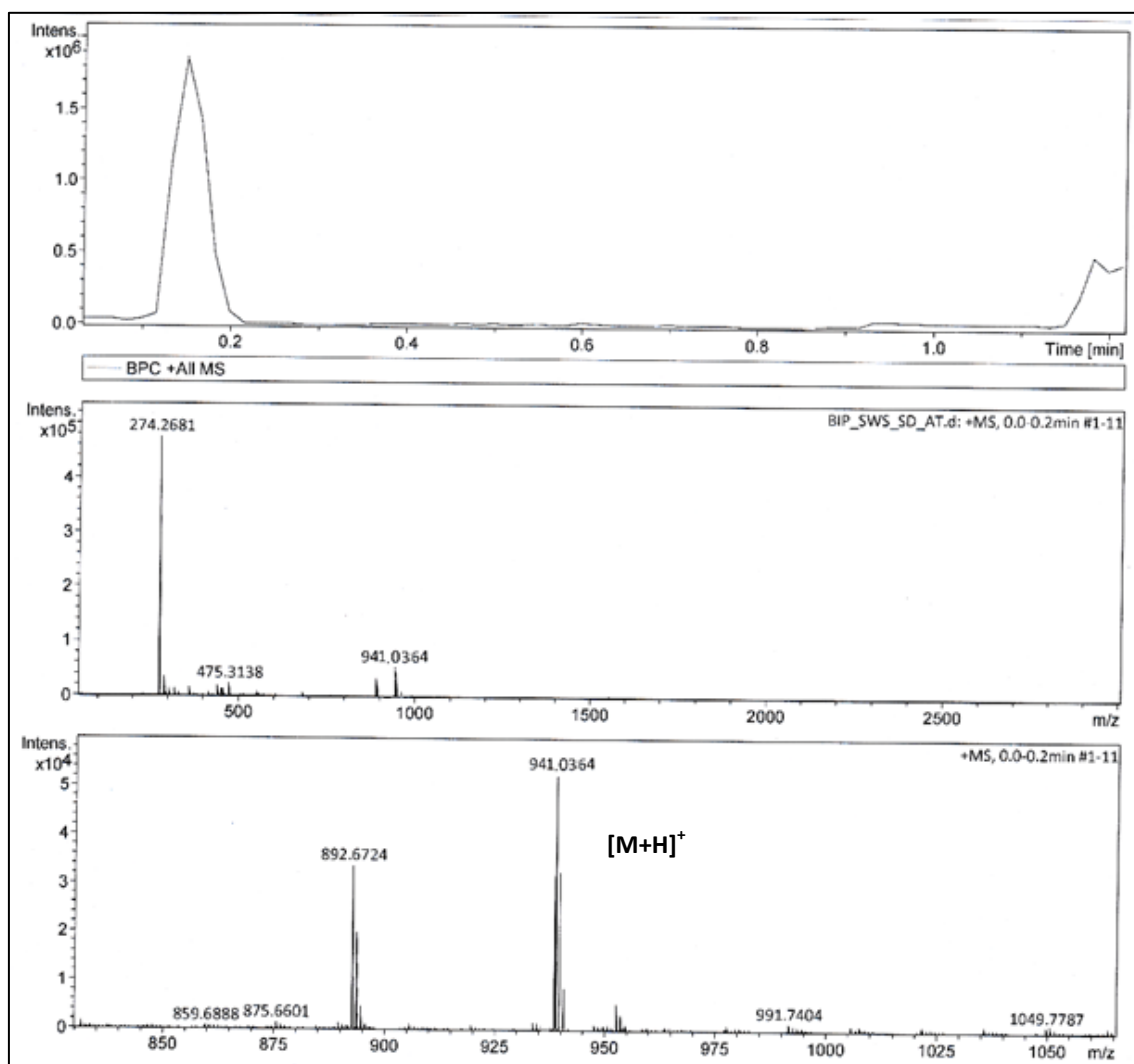
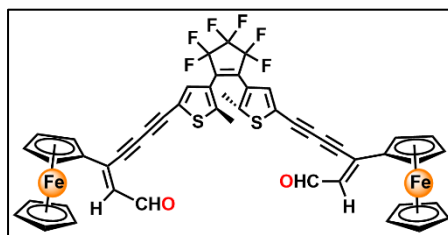


Figure 3.33. HRMS spectra of compound **4o**.

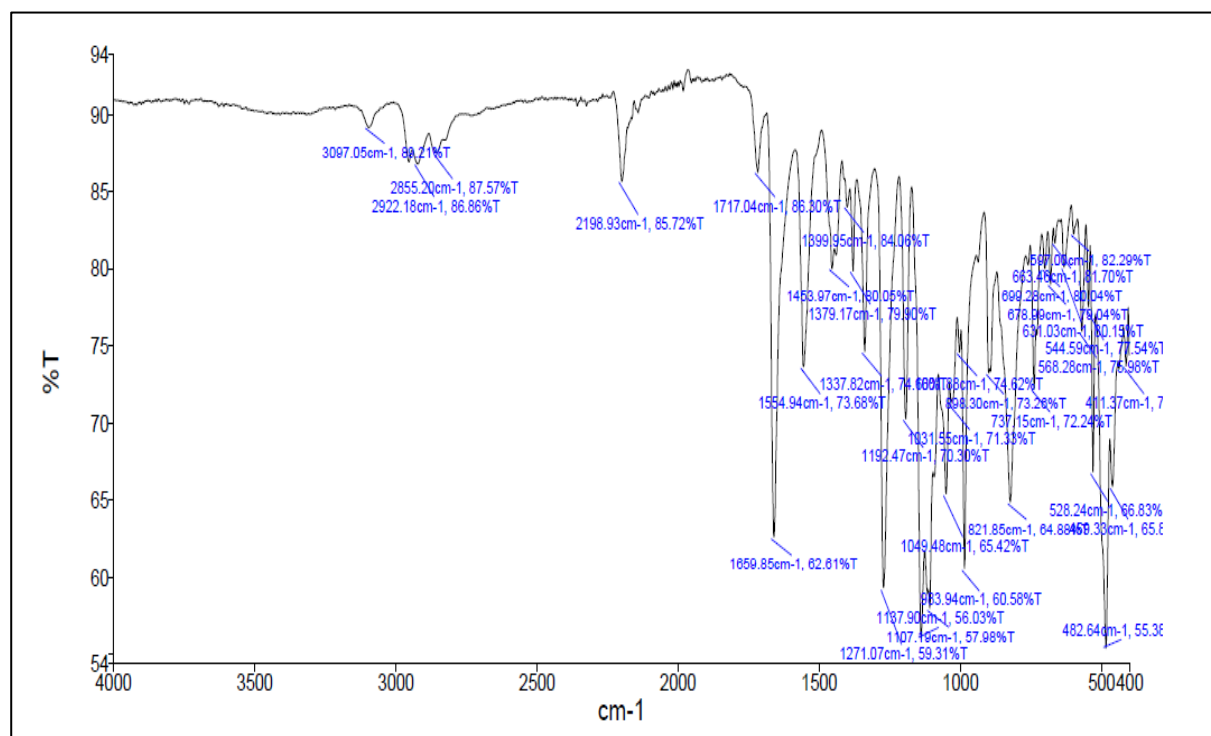
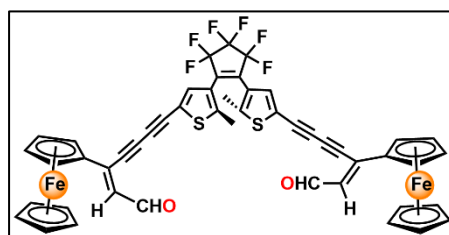


Figure 3.34. FT-IR spectra of compound **4o** at room temperature in solid state.

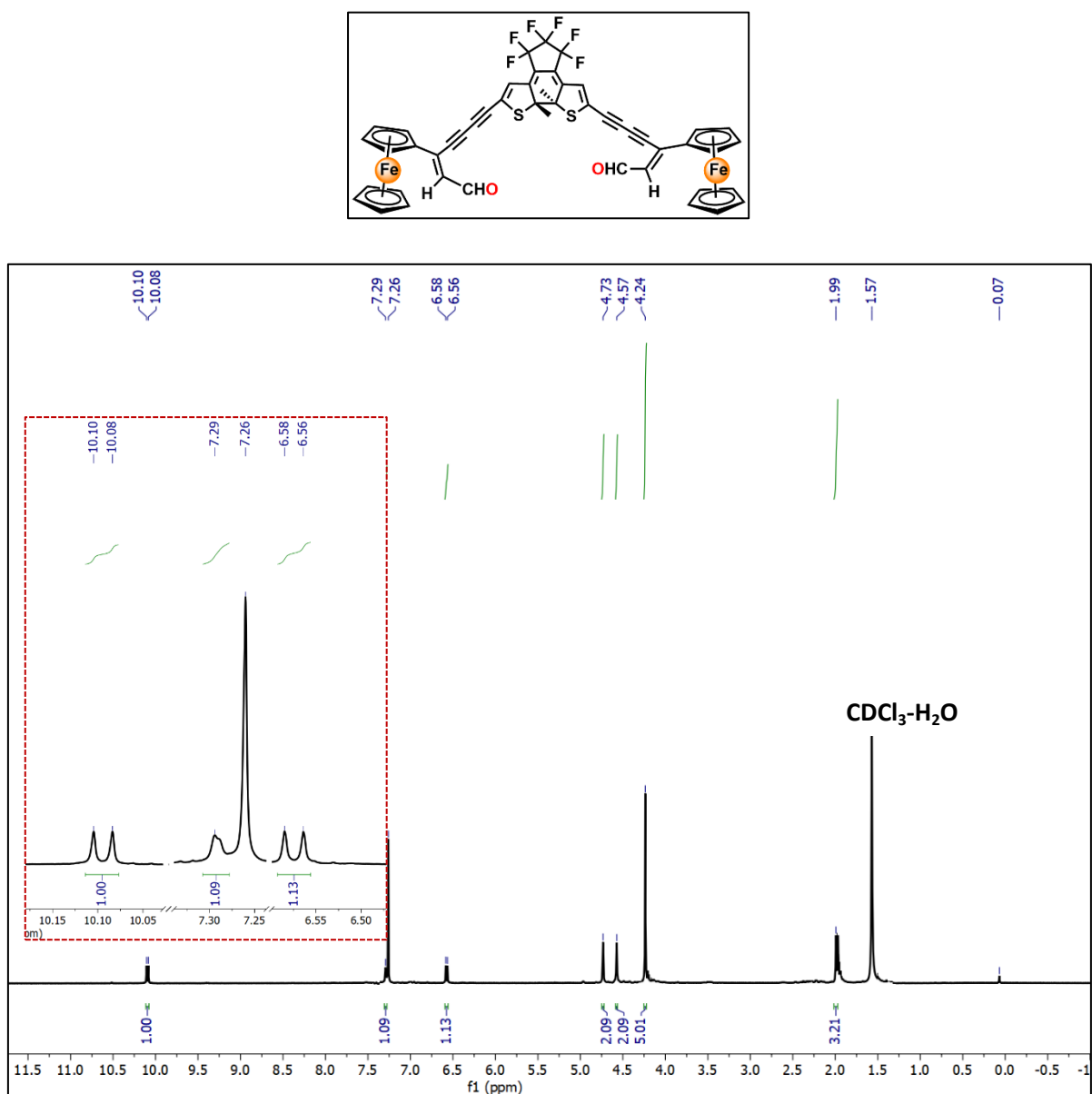


Figure 3.35. ^1H NMR spectrum of compound **4c** in CDCl_3 as a solvent.

Procedure of HPLC study:

The YL9100 HPLC system was fitted with a Venusil XPB C18 (4.8×250 mm), 100Å. The separation was performed by employing a mobile phase with 80% CH₃CN and 20% water (v/v). The injection volume was 20.0 μL and the detection of eluted samples was performed at the wavelength of 365 nm. The flow rate was maintained at 1.0 mL/min for 10 min at room temperature.

Table 3.4. HPLC data for **4o** and **4c** at PSS.

	RT	Area	%Area	%Height
4o	3.733	29.195	10.5	10.9
4c	1.637	150.796	89.5	89.1

Theoretical Details**Table 3.5.** Energy, wavelength, oscillator strength and major contributions for each of the 30 mono-excitations calculated by TD-DFT methods at CAM-B3LYP/6-31g(d)/LANL2DZ//B3LYP/6-31g(d)/LANL2DZ for Open-Solvent-opt (**4o**).^a

[a] Components with greater than 10 % contribution shown.

No.	Energy (cm ⁻¹)	Wavelength (nm)	Osc. Strengths	Symmetry	Major contributions
1	15706.8409503	636.665261437	0.0	Singlet-A	H-5->L+9 (11%), H-5->L+12 (22%), H-3->L+7 (19%)
2	15745.5555629	635.099851512	0.0	Singlet-A	H-4->L+9 (20%), H-4->L+12 (13%), H-2->L+8 (23%)
3	15768.139087	634.190245587	0.003	Singlet-A	H-5->L+7 (28%), H-3->L+12 (16%)
4	15799.5947097	632.927627813	0.0028	Singlet-A	H-4->L+8 (31%), H-2->L+9 (16%), H-2->L+12 (10%)
5	19907.3764166	502.326363391	0.0024	Singlet-A	H-13->L+12 (15%), H-5->L+7 (27%)
6	19939.6385937	501.513603318	0.0024	Singlet-A	H-14->L+9 (17%), H-14->L+12 (11%), H-4->L+8 (27%)
7	20217.0933173	494.630946351	0.0	Singlet-A	H-13->L+7 (26%), H-3->L+7 (23%), H-2->L+7 (11%)

8	20244.5161679	493.960928336	0.0001	Singlet-A	H-14->L+8 (31%), H-2->L+8 (24%)
9	26392.0740257	378.901635023	1.0411	Singlet-A	H-1->L+1 (24%), HOMO->LUMO (29%)
10	26732.4399948	374.077338318	0.0985	Singlet-A	H-1->LUMO (17%), HOMO->L+1 (20%)
11	26910.6885236	371.599559455	0.0218	Singlet-A	H-13->L+12 (18%), H-5->L+7 (16%)
12	26956.662126	370.965809982	0.0064	Singlet-A	H-14->L+9 (19%), H-14->L+12 (12%), H-4->L+8 (17%)
13	27736.6002589	360.534452913	0.3485	Singlet-A	H-14->L+8 (16%), H-9->LUMO (10%)
14	27831.7736815	359.301570731	0.0816	Singlet-A	H-14->L+8 (21%), H-9->LUMO (12%)
15	27860.0030865	358.937505102	0.006	Singlet-A	H-13->L+7 (41%), H-5->LUMO (10%), H-3->L+7 (10%)
16	28179.3986404	354.869176863	0.1344	Singlet-A	H-14->L+8 (16%), H-8->L+1 (10%), HOMO->L+1 (10%)
17	30921.683699	323.3976551	0.0835	Singlet-A	H-19->LUMO (13%)
18	31079.7683671	321.752719708	0.0768	Singlet-A	H-17->L+1 (17%)
19	31354.8034274	318.930400031	0.1621	Singlet-A	H-4->L+1 (15%), H- 2->LUMO (12%)

20	31385.4524957	318.618952567	0.0991	Singlet-A	H-3->LUMO (23%)
21	31437.8785336	318.087621254	0.0642	Singlet-A	H-5->LUMO (11%), H-4->L+1 (20%)
22	31474.9800373	317.712671721	0.0725	Singlet-A	H-2->L+1 (11%)
23	31808.0870165	314.38545785	0.0317	Singlet-A	H-1->L+3 (11%), HOMO->L+3 (14%), HOMO->L+6 (11%)
24	31885.5162417	313.62201961	0.0049	Singlet-A	HOMO->L+5 (18%)
25	34535.0475409	289.560915998	0.1864	Singlet-A	H-7->L+1 (29%), H- 6->LUMO (20%), HOMO->L+2 (18%)
26	34647.965161	288.617237796	0.1844	Singlet-A	H-7->LUMO (24%), H-6->LUMO (11%), H-6->L+1 (25%)
27	34943.164082	286.179007045	0.4003	Singlet-A	HOMO->L+2 (51%)
28	37081.3398733	269.677418189	0.0034	Singlet-A	H-1->L+2 (44%), HOMO->L+1 (12%)
29	37850.7927985	264.195258821	0.0372	Singlet-A	H-10->LUMO (32%), H-10->L+1 (10%)
30	38001.6184768	263.146686926	0.0121	Singlet-A	H-1->L+1 (19%), HOMO->LUMO (23%)
31	38037.9134261	262.895598084	0.0115	Singlet-A	H-11->LUMO (11%), H-11->L+1

					(30%), H-8->L+1 (19%)
32	38283.9125269	261.206322446	0.0188	Singlet-A	H-1->LUMO (15%), H-1->L+2 (12%), HOMO->L+1 (17%)
33	39450.9967857	253.479019917	0.0567	Singlet-A	H-1->L+4 (13%), HOMO->L+4 (16%)
34	39664.7337094	252.113125813	0.0352	Singlet-A	H-1->L+6 (11%), HOMO->L+1 (10%)
35	40053.4929441	249.666115611	0.0096	Singlet-A	H-16->LUMO (16%), H-13- >LUMO (28%), H- 13->L+1 (10%)
36	40217.2234932	248.649686165	0.313	Singlet-A	H-14->L+1 (17%), H-12->L+2 (11%)
37	40328.5280044	247.963426756	0.2487	Singlet-A	H-14->L+1 (16%), H-12->L+2 (13%)
38	40573.7205508	246.46494983	0.6252	Singlet-A	H-8->L+3 (14%), H- 1->L+1 (10%)
39 ^a	40923.765173	244.356792629	0.5321	Singlet-A	
40	41105.2399196	243.277986446	0.0016	Singlet-A	H-21->LUMO (40%), H-21->L+1 (15%), H-21->L+12 (12%)
41	41202.026451	242.706508911	0.0106	Singlet-A	H-20->LUMO (15%), H-20->L+1

					(40%), H-20->L+9 (11%)
42	41843.2372221	238.987245344	0.0411	Singlet-A	H-16->LUMO (19%), H-13->LUMO (25%), H-13->L+1 (10%)
43	41948.0892979	238.389880621	0.0439	Singlet-A	H-17->L+1 (11%), H-15->LUMO (10%), H-15->L+1 (23%)
44	42065.8462445	237.722544362	0.2446	Singlet-A	H-12->L+1 (11%)
45	43078.8786073	232.132319208	0.0068	Singlet-A	H-3->LUMO (17%), H-2->LUMO (45%), H-2->L+1 (15%)
46	43374.8840828	230.548166559	0.0038	Singlet-A	H-3->LUMO (13%), H-3->L+1 (40%), H-2->LUMO (11%), H-2->L+1 (12%)
47	43463.60507	230.077555323	0.0265	Singlet-A	H-3->L+3 (11%), H-2->L+3 (35%)
48	43714.4434974	228.757344254	0.0104	Singlet-A	H-3->L+4 (23%), H-2->L+4 (11%)
49	43821.7152364	228.197366216	0.0001	Singlet-A	H-5->LUMO (12%), H-4->LUMO (58%), H-4->L+1 (18%)
50 ^a	43937.8590742	227.594157082	0.0206	Singlet-A	

51	44097.5568511	226.769932714	0.0615	Singlet-A	H-23->L+1 (10%), H-12->L+2 (11%)
52	44129.0124739	226.608288729	0.0007	Singlet-A	H-5->LUMO (23%), H-5->L+1 (50%), H- 4->L+1 (11%)
53	44272.5791622	225.873445578	0.0218	Singlet-A	H-22->LUMO (11%), H-6->L+7 (10%)
54	44287.9036964	225.795288676	0.0039	Singlet-A	H-7->L+8 (30%), H- 6->L+8 (12%)
55	44324.1986457	225.610395801	0.014	Singlet-A	H-7->L+7 (12%), H- 6->L+7 (30%)
56	44566.9715288	224.381411995	0.1254	Singlet-A	H-3->L+4 (10%)
57	44605.6861414	224.186664639	0.0037	Singlet-A	H-5->L+3 (10%), H- 4->L+3 (49%)
58 ^a	44871.0425486	222.860879356	0.1019	Singlet-A	
59	44937.9865662	222.528884005	0.0153	Singlet-A	H-16->L+7 (16%), H-5->L+4 (31%)
60	45069.4549381	221.879763439	0.0079	Singlet-A	H-17->L+8 (28%), H-15->L+8 (34%)

Table 3.6. Energy, wavelength, oscillator strength and major contributions for each of the 60 mono-excitations calculated by TD-DFT methods at WB97XD/cc-pVDZ//B3LYP/6-31g(d)/LANL2DZ for Open-Solvent-opt (**4o**).^a

[a] Components with greater than 10 % contribution shown.

No.	Energy (cm ⁻¹)	Wavelength (nm)	Osc. Strengths	Symmetry	Major contributions
1	16264.1700608	614.848465223	0.0	Singlet-A	H-4->L+10 (13%), H-3->L+10 (11%)
2	16309.3371088	613.145705021	0.0	Singlet-A	H-4->L+10 (10%), H-2->L+8 (12%)
3	16364.9893644	611.060586556	0.004	Singlet-A	H-3->L+7 (11%), H- 2->L+10 (11%)
4	16402.8974226	609.648389695	0.0037	Singlet-A	H-4->L+8 (15%)
5	19036.2976333	525.312232066	0.0021	Singlet-A	H-8->L+10 (17%)
6	19076.6253547	524.201729292	0.0021	Singlet-A	H-4->L+8 (14%)
7	19521.8433995	512.246707206	0.0	Singlet-A	H-8->L+7 (10%), H- 8->L+9 (14%)
8	19525.8761717	512.140910456	0.0	Singlet-A	H-10->L+8 (11%), H-9->L+8 (17%), H- 2->L+8 (16%), H-1- >L+8 (11%)
9	25762.1550167	388.166284751	0.0061	Singlet-A	H-8->L+10 (13%)
10	25814.5810546	387.377969794	0.0052	Singlet-A	H-4->L+8 (13%)
11	26456.5983801	377.977541041	0.4655	Singlet-A	HOMO->LUMO (17%)
12 ^a	26588.8733064	376.097169848	0.1479	Singlet-A	
13	26667.9156405	374.982437129	0.05	Singlet-A	H-10->L+8 (13%), H-9->L+8 (20%)

14 ^a	26919.5606223	371.477088364	0.1176	Singlet-A	
15	27680.1414489	361.269830159	0.8579	Singlet-A	HOMO->LUMO (18%)
16	28079.3858912	356.133144747	0.1147	Singlet-A	HOMO->L+1 (22%)
17	30053.024579	332.745210843	0.0297	Singlet-A	H-5->LUMO (11%), H-4->LUMO (14%)
18	30216.7551281	330.94221923	0.0218	Singlet-A	H-4->L+1 (22%)
19	30335.3186291	329.648754386	0.1571	Singlet-A	H-3->LUMO (11%), H-2->LUMO (19%), H-1->LUMO (10%)
20	30370.0004696	329.272303108	0.1406	Singlet-A	H-2->L+1 (25%), H- 1->L+1 (13%)
21	31244.3054706	320.058322609	0.1432	Singlet-A	H-17->L+1 (14%)
22	31305.6036072	319.431630371	0.0141	Singlet-A	H-18->LUMO (18%)
23	31892.7752315	313.550637328	0.0557	Singlet-A	HOMO->L+3 (14%)
24	31976.6568921	312.72812645	0.0149	Singlet-A	HOMO->L+4 (10%), HOMO->L+5 (17%)
25	34661.6765863	288.503066928	0.2401	Singlet-A	H-7->L+1 (27%), H- 6->LUMO (23%), HOMO->L+2 (11%)
26	34756.8500089	287.713069436	0.2079	Singlet-A	H-7->LUMO (26%), H-6->L+1 (26%)
27	35160.1272234	284.413077816	0.4122	Singlet-A	HOMO->L+2 (46%)

28	37229.7458882	268.602424256	0.0072	Singlet-A	H-11->LUMO (10%), H-8->LUMO (25%), H-8->L+1 (11%)
29	37257.1687388	268.404721521	0.02	Singlet-A	H-10->L+1 (18%), H-9->L+1 (24%)
30	37855.6321251	264.161485059	0.0209	Singlet-A	H-5->L+2 (33%), H-3->L+2 (12%), H-1->L+2 (15%)
31	38575.0786758	259.234727272	0.0288	Singlet-A	H-12->LUMO (17%), H-11->LUMO (27%), H-11->L+1 (11%)
32	38721.0650274	258.257359216	0.0056	Singlet-A	H-13->LUMO (12%), H-13->L+1 (30%), H-10->L+1 (13%)
33	39382.4396592	253.920277325	0.0379	Singlet-A	H-14->LUMO (14%), HOMO->L+4 (12%)
34 ^a	39612.3076715	252.446792117	0.1062	Singlet-A	
35	40380.9540423	247.641499245	0.7791	Singlet-A	H-14->L+2 (18%)
36 ^a	40941.5093705	244.250887516	0.601	Singlet-A	
37 ^a	41314.9440711	242.043169241	0.3779	Singlet-A	
38	41694.8312072	239.83788183	0.003	Singlet-A	H-20->LUMO (36%), H-20->L+1

					(15%), H-20->L+10 (11%)
39	41819.0405892	239.125524142	0.0044	Singlet-A	H-21->LUMO (14%), H-21->L+1 (36%)
40	42320.7174441	236.290890229	0.2993	Singlet-A	H-19->LUMO (11%)
41	42564.2968816	234.938686473	0.0144	Singlet-A	H-16->LUMO (32%), H-16->L+1 (12%)
42	42733.6733117	234.007498655	0.0154	Singlet-A	H-17->L+1 (17%), H-15->L+1 (22%)
43	42933.6988101	232.917271913	0.0573	Singlet-A	H-5->L+1 (12%)
44	43004.6755999	232.532855103	0.0327	Singlet-A	H-5->LUMO (15%), HOMO->L+1 (11%)
45	43338.5891335	230.741244695	0.0291	Singlet-A	H-2->L+3 (28%), H- 1->L+3 (20%)
46	43593.460333	229.392205244	0.0194	Singlet-A	H-2->L+4 (19%), H- 1->L+4 (15%)
47	44345.1690608	225.503706757	0.0027	Singlet-A	H-4->L+3 (35%), H- 3->L+3 (18%)
48	44536.3224605	224.535827108	0.0417	Singlet-A	H-3->L+4 (14%)
49	44658.1121793	223.923482476	0.0913	Singlet-A	H-19->L+1 (11%), H-14->L+2 (21%)
50 ^a	44861.3638954	222.908960666	0.0505	Singlet-A	

51	16264.1700608	614.848465223	0.0	Singlet-A	H-4->L+10 (13%), H-3->L+10 (11%)
52	16309.3371088	613.145705021	0.0	Singlet-A	H-4->L+10 (10%), H-2->L+8 (12%)
53	16364.9893644	611.060586556	0.004	Singlet-A	H-3->L+7 (11%), H- 2->L+10 (11%)
54	16402.8974226	609.648389695	0.0037	Singlet-A	H-4->L+8 (15%)
55	19036.2976333	525.312232066	0.0021	Singlet-A	H-8->L+10 (17%)
56	19076.6253547	524.201729292	0.0021	Singlet-A	H-4->L+8 (14%)
57	19521.8433995	512.246707206	0.0	Singlet-A	H-8->L+7 (10%), H- 8->L+9 (14%)
58	19525.8761717	512.140910456	0.0	Singlet-A	H-10->L+8 (11%), H-9->L+8 (17%), H- 2->L+8 (16%), H-1- >L+8 (11%)
59	25762.1550167	388.166284751	0.0061	Singlet-A	H-8->L+10 (13%)
60	25814.5810546	387.377969794	0.0052	Singlet-A	H-4->L+8 (13%)

Table 3.7. Energy, wavelength, oscillator strength and major contributions for each of the 60 mono-excitations calculated by TD-DFT methods at CAM-B3LYP/6-31g(d)/ LANL2DZ// B3LYP/6-31g(d)/LANL2DZ for closed-Solvent-opt (**4c**).^a

No.	Energy (cm ⁻¹)	Wavelength (nm)	Osc. Strengths	Symmetry	Major contributions
1	15321.3079333	652.68579181	0.98	Singlet-A	HOMO->LUMO (90%)
2	15655.2214669	638.764518353	0.0009	Singlet-A	H-4->L+10 (24%), H-2->L+8 (13%), H-1->L+8 (16%)
3	15685.0639808	637.549200454	0.0013	Singlet-A	H-3->L+10 (18%), H-3->L+11 (10%), H-2->L+9 (18%), H-1->L+9 (12%)
4	15727.0048111	635.848982062	0.0149	Singlet-A	H-4->L+8 (32%), H-2->L+10 (12%)
5	15756.8473249	634.644722626	0.0173	Singlet-A	H-3->L+9 (32%)
6	19858.1765964	503.570906999	0.0031	Singlet-A	H-15->L+10 (16%), H-4->L+8 (33%)
7	19895.2781001	502.631827998	0.0028	Singlet-A	H-14->L+10 (12%), H-3->L+9 (32%)
8	20172.7328237	495.71865584	0.0001	Singlet-A	H-15->L+8 (28%), H-2->L+8

					(15%), H-1->L+8 (19%)
9	20204.9950009	494.927120723	0.0001	Singlet-A	H-14->L+9 (29%), H-2->L+9 (21%), H-1->L+9 (14%)
10	25589.5523689	390.784483286	0.2499	Singlet-A	H-5->LUMO (16%), HOMO->L+1 (57%)
11	26179.9502109	381.97169664	0.0041	Singlet-A	H-12->LUMO (10%), H-10->LUMO (20%), H-10->L+1 (17%)
12	26218.6648235	381.407675308	0.0056	Singlet-A	H-11->LUMO (25%), H-11->L+1 (23%)
13	26606.6175039	375.846347194	0.004	Singlet-A	H-7->LUMO (13%), H-4->L+8 (10%), H-1->LUMO (10%)
14 ^a	26650.171443	375.232107658	0.0148	Singlet-A	
15	26677.5942936	374.846393192	0.0331	Singlet-A	H-5->LUMO (11%), H-3->L+9 (13%)
16	27401.8801708	364.938461801	0.0721	Singlet-A	H-15->L+8 (28%), H-4->LUMO (17%)

17	27472.0504062	364.006321048	0.0092	Singlet-A	H-14->L+9 (30%), H-3->LUMO (16%)
18	28030.186071	356.758245367	0.8453	Singlet-A	H-6->LUMO (20%), HOMO->L+2 (13%)
19	28914.9762797	345.841542572	0.2008	Singlet-A	H-7->LUMO (10%), H-1->LUMO (30%)
20	29154.5229451	342.999953004	0.0026	Singlet-A	H-18->LUMO (19%), H-18->L+1 (17%)
21	29222.2735171	342.204722509	0.0514	Singlet-A	H-19->L+1 (10%), H-1->LUMO (10%)
22	29437.6235496	339.701334353	0.0182	Singlet-A	H-2->LUMO (32%)
23	29778.7960731	335.809412021	0.0061	Singlet-A	H-4->LUMO (14%), H-4->L+10 (10%), H-3->LUMO (18%)
24	29836.0614376	335.164881629	0.0141	Singlet-A	H-4->LUMO (18%), H-3->LUMO (14%)
25	30123.1948143	331.970100172	0.0036	Singlet-A	H-13->LUMO (16%), H-5->LUMO (19%)

26	31183.007334	320.687478693	0.0201	Singlet-A	HOMO->L+2 (20%), HOMO->L+4 (22%), HOMO->L+5 (13%)
27	31433.8457614	318.12842997	0.0038	Singlet-A	HOMO->L+2 (14%), HOMO->L+4 (33%), HOMO->L+5 (11%)
28	32825.9587059	304.636951798	0.0056	Singlet-A	H-6->LUMO (17%), HOMO->L+2 (17%), HOMO->L+5 (24%)
29	33382.4812619	299.558319873	0.2539	Singlet-A	H-13->LUMO (11%), H-10->LUMO (10%)
30 ^a	33440.5531808	299.038115367	0.2491	Singlet-A	
31	35110.1208488	284.818159501	0.0654	Singlet-A	HOMO->L+7 (48%)
32	35344.0216332	282.933280875	0.1249	Singlet-A	H-2->L+1 (17%), H-1->LUMO (17%), H-1->L+2 (12%)
33	35458.5523621	282.019409531	0.0546	Singlet-A	H-2->LUMO (22%), H-2->L+2

					(14%), H-1->L+1 (22%)
34	35803.7576577	279.30029288	0.002	Singlet-A	H-3->LUMO (40%), H-3->L+1 (18%), H-3->L+2 (18%)
35	35923.1277132	278.372197427	0.0063	Singlet-A	H-4->LUMO (37%), H-4->L+1 (16%), H-4->L+2 (17%)
36	36162.6743786	276.528220654	0.0132	Singlet-A	H-9->LUMO (27%), H-9->L+1 (18%)
37	36197.3562191	276.263270154	0.0081	Singlet-A	H-8->LUMO (23%), H-8->L+1 (17%)
38	36656.2856892	272.804508476	0.1017	Singlet-A	H-22->LUMO (36%), H-5->L+1 (14%)
39	36714.3576081	272.373007496	0.1934	Singlet-A	HOMO->L+3 (36%), HOMO- >L+4 (10%)
40	37886.2811934	263.947784924	0.0798	Singlet-A	H-22->LUMO (11%), H-6- >LUMO (17%), H-6->L+2 (14%)

41	38162.9293626	262.034392198	0.0216	Singlet-A	H-15->LUMO (16%)
42	38412.1546811	260.334263543	0.0115	Singlet-A	HOMO->L+6 (20%), HOMO->L+18 (14%)
43	38434.7382051	260.181296062	0.0	Singlet-A	H-15->LUMO (10%), H-14->LUMO (16%)
44	38682.3504148	258.515831969	0.0353	Singlet-A	H-15->LUMO (10%), H-6->L+1 (10%), HOMO->L+3 (10%)
45 ^a	38903.3463284	257.047296538	0.1007	Singlet-A	
46 ^a	39086.4341838	255.843240982	0.0111	Singlet-A	
47	39857.5002179	250.893807824	0.0206	Singlet-A	H-16->LUMO (12%)
48	40102.6927643	249.359813785	0.0056	Singlet-A	H-21->LUMO (17%), H-20->L+1 (10%)
49	40122.856625	249.234497271	0.0239	Singlet-A	H-21->L+1 (17%), H-20->LUMO (16%)
50	40159.9581288	249.004243678	0.0069	Singlet-A	H-20->LUMO (11%), H-20->L+1 (14%)

51	40260.7774324	248.380697983	0.0114	Singlet-A	H-17->LUMO (10%)
52 ^a	40272.8757488	248.306082296	0.0304	Singlet-A	
53	40768.9067227	245.284968469	0.016	Singlet-A	H-22->LUMO (11%), H-7->L+1 (29%)
54 ^a	41417.3764836	241.444554171	0.0188	Singlet-A	
55	41685.152554	239.893568508	0.1131	Singlet-A	H-13->L+1 (14%)
56	42202.9604974	236.950201648	0.0294	Singlet-A	H-8->LUMO (21%), H-8->L+2 (10%)
57	42275.550396	236.543342578	0.0118	Singlet-A	H-9->LUMO (24%), H-9->L+2 (11%)
58	42576.3951981	234.871927355	0.0316	Singlet-A	H-24->LUMO (31%)
59	42600.5918309	234.738522875	0.0429	Singlet-A	H-24->LUMO (25%), H-2->L+1 (17%), H-1->L+2 (16%)
60 ^a	42654.6309777	234.441132669	0.0991	Singlet-A	

Table 3.8. Energy, wavelength, oscillator strength and major contributions for each of the 60 mono-excitations calculated by TD-DFT methods at WB97XD/cc-pVDZ//B3LYP/6-31g(d)/LANL2DZ for closed-Solvent-opt (**4c**).^a

No.	Energy (cm ⁻¹)	Wavelength (nm)	Osc. Strengths	Symmetry	Major contributions
1	17053.7868468	586.380027489	0.7883	Singlet-A	HOMO->LUMO (88%)
2	18382.9885458	543.981190822	0.0001	Singlet-A	H-3->L+10 (22%), H-3->L+11 (22%), H-1->L+9 (23%)
3	18384.6016546	543.933460613	0.0002	Singlet-A	H-4->L+10 (20%), H-4->L+11 (25%), H-2->L+8 (21%)
4	18470.9029785	541.392048436	0.0061	Singlet-A	H-3->L+9 (30%), H-1->L+10 (20%), H-1->L+11 (19%)
5	18479.7750772	541.132127323	0.0056	Singlet-A	H-4->L+8 (29%), H-2->L+10 (18%), H-2->L+11 (21%)
6	20869.5958504	479.165963332	0.0025	Singlet-A	H-8->L+10 (17%), H-8->L+11 (16%), H-3->L+9 (25%)

7	20871.2089592	479.128929212	0.0019	Singlet-A	H-9->L+10 (15%), H-9->L+11 (18%), H-4->L+8 (24%)
8	21307.5549053	469.317105807	0.0001	Singlet-A	H-8->L+9 (32%), H-1->L+9 (29%)
9	21323.6859939	468.962073577	0.0001	Singlet-A	H-9->L+8 (32%), H-2->L+8 (29%)
10	27039.7372322	369.826079082	0.1449	Singlet-A	H-7->LUMO (11%), H-5->LUMO (15%), HOMO->L+1 (11%)
11	27178.464594	367.938371405	0.0033	Singlet-A	H-13->L+1 (12%)
12	27260.7331458	366.827991989	0.0425	Singlet-A	H-9->L+11 (11%), H-4->L+8 (19%), H-2->L+1 (10%)
13	27276.8642344	366.611055951	0.0053	Singlet-A	H-3->L+9 (18%)
14	27297.8346495	366.329422403	0.1931	Singlet-A	H-5->LUMO (20%), HOMO->L+1 (11%)
15	27844.6785524	359.135049133	0.0036	Singlet-A	H-9->L+8 (20%), H-4->LUMO (13%), H-4->L+1 (13%), H-2->L+8 (10%)

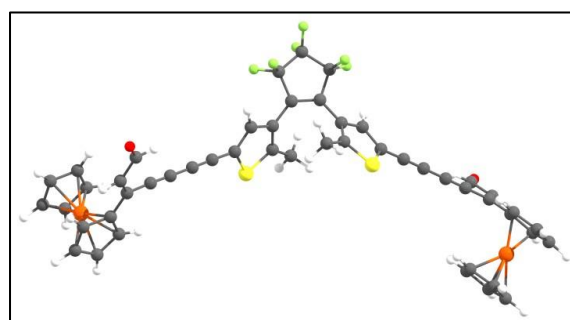
16	27889.8456004	358.553437093	0.0053	Singlet-A	H-8->L+9 (20%), H-3->LUMO (11%), H-3->L+1 (13%), H-1->L+9 (11%)
17	29322.2862663	341.037527196	0.0023	Singlet-A	H-7->LUMO (22%), HOMO- >L+1 (34%)
18	29757.0191035	336.055166185	0.8601	Singlet-A	H-6->LUMO (16%), H-5->L+1 (11%)
19	30104.6440624	332.174663127	0.1579	Singlet-A	H-1->LUMO (16%)
20	30315.1547684	329.868017379	0.109	Singlet-A	H-2->LUMO (12%)
21	30383.7118949	329.123710579	0.0183	Singlet-A	H-4->L+10 (11%)
22	30410.328191	328.83564877	0.1372	Singlet-A	H-3->L+10 (10%)
23	30568.4128591	327.135073911	0.016	Singlet-A	H-20->LUMO (16%), H-20- >L+1 (12%)
24	30654.714183	326.214100066	0.0226	Singlet-A	H-21->LUMO (16%), H-21- >L+1 (11%)
25	32153.2923121	311.010141759	0.0407	Singlet-A	H-6->L+1 (12%), H-5->LUMO (19%), HOMO- >L+1 (15%),

					HOMO->L+3 (10%)
26	33476.8481301	298.713904043	0.0091	Singlet-A	H-5->L+5 (15%), HOMO->L+4 (49%)
27	33998.6888456	294.128989662	0.0043	Singlet-A	H-5->L+4 (20%), HOMO->L+5 (38%)
28	35206.1008259	284.041679295	0.0337	Singlet-A	H-7->L+1 (13%), H-6->LUMO (12%), H-6->L+2 (16%)
29	35406.9328787	282.430563366	0.4587	Singlet-A	H-6->L+1 (17%)
30	36054.5960852	277.357149596	0.056	Singlet-A	HOMO->L+2 (35%), HOMO- >L+6 (10%)
31	36507.0731198	273.91952149	0.0168	Singlet-A	H-9->LUMO (23%), H-9->L+1 (19%), H-9->L+2 (11%)
32	36540.9484058	273.6655844	0.0433	Singlet-A	H-8->LUMO (22%), H-8->L+1 (21%), H-8->L+2 (11%)
33	37028.107281	270.065113621	0.0015	Singlet-A	HOMO->L+7 (62%)

34	38416.9940077	260.301469657	0.1423	Singlet-A	H-22->LUMO (31%)
35	38552.4951518	259.386583427	0.0856	Singlet-A	H-1->LUMO (37%), H-1->L+2 (17%)
36	38626.6981592	258.888294277	0.0016	Singlet-A	H-2->LUMO (15%)
37	38686.383187	258.488883586	0.0408	Singlet-A	H-2->LUMO (16%)
38	38772.6845109	257.913531811	0.0084	Singlet-A	H-14->LUMO (10%)
39	38883.1824677	257.180594935	0.0044	Singlet-A	H-3->LUMO (46%), H-3->L+2 (16%)
40	38938.8347233	256.813026663	0.0038	Singlet-A	H-4->LUMO (45%), H-4->L+2 (16%)
41	39868.7919799	250.822748907	0.1523	Singlet-A	H-5->L+2 (11%), HOMO->L+3 (30%)
42	40252.7118881	248.430466692	0.043	Singlet-A	HOMO->L+6 (11%), HOMO- >L+13 (11%)
43 ^a	41193.1543523	242.758782551	0.0054	Singlet-A	
44 ^a	41414.9568203	241.458660536	0.1129	Singlet-A	
45 ^a	41617.401982	240.284100491	0.0006	Singlet-A	

46	41911.7943486	238.596322478	0.0451	Singlet-A	HOMO->L+4 (10%)
47	42173.924538	237.113337437	0.002	Singlet-A	H-19->LUMO (23%), H-19->L+1 (27%), H-19->L+2 (17%)
48	42220.7046949	236.850618015	0.0017	Singlet-A	H-18->LUMO (22%), H-18->L+1 (29%), H-18->L+2 (16%)
49	42369.1107098	236.02100286	0.0033	Singlet-A	H-17->LUMO (13%)
50	42509.4511804	235.241804406	0.0243	Singlet-A	H-16->LUMO (15%)
51	42963.541324	232.75548737	0.0053	Singlet-A	H-22->LUMO (11%), H-7->L+1 (12%), H-5->L+1 (22%)
52 ^a	43346.6546777	230.6983105	0.0622	Singlet-A	
53	43513.6114445	229.813147381	0.0892	Singlet-A	H-24->LUMO (26%)
54	43662.8240139	229.02778796	0.0278	Singlet-A	H-24->LUMO (38%)
55	44027.3866158	227.131355473	0.0089	Singlet-A	H-2->L+4 (43%), H-2->L+5 (16%), H-1->L+5 (17%)

56	44087.0716436	226.823865301	0.1686	Singlet-A	H-1->L+4 (19%), H-1->L+5 (16%)
57 ^a	44433.890048	225.053444323	0.7135	Singlet-A	
58 ^a	44567.7780833	224.377351308	0.0798	Singlet-A	
59 ^a	44918.6292599	222.62478096	0.0129	Singlet-A	H-3->L+4 (30%), H-3->L+5 (40%)
60 ^a	44948.4717737	222.476974308	0.0604	Singlet-A	



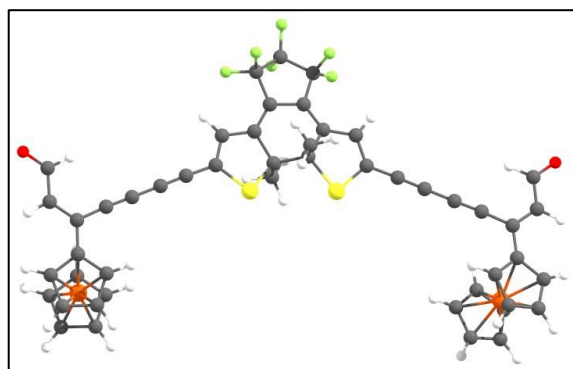
Open solvent opt **4o**

E = -3677.062017

6	-1.645492000	2.489554000	-0.593540000	6	1.097672000	1.097262000	1.105680000
6	-2.938764000	2.414914000	0.008793000	16	2.335762000	-0.116744000	1.154377000
6	-3.731005000	1.410843000	-0.508781000	6	3.367438000	0.787025000	0.048298000
16	-2.871572000	0.556244000	-1.787065000	6	-0.647918000	3.508356000	-0.233696000
6	-1.460700000	1.546943000	-1.597513000	6	0.669270000	3.360829000	0.053414000
6	2.755837000	1.969476000	-0.311951000	6	-1.032313000	4.970028000	-0.277280000
6	1.463243000	2.145852000	0.271259000	6	0.199666000	5.728622000	0.276037000

6	1.353352000	4.705445000	0.139952000	6	-7.426630000	0.335770000	0.497582000
9	0.441771000	6.875958000	-0.391642000	6	-8.558627000	0.000945000	0.819560000
9	0.009127000	6.017111000	1.585521000	6	-9.887981000	-0.419311000	1.101751000
9	2.067997000	4.971529000	-0.999494000	6	-10.477317000	-0.172353000	2.315150000
9	2.220247000	4.796473000	1.180119000	1	-11.508216000	-0.468981000	2.482233000
9	-2.143311000	5.248568000	0.463116000	6	-9.802787000	0.479910000	3.423707000
9	-1.295001000	5.378563000	-1.551924000	1	-8.751053000	0.777568000	3.241635000
6	-0.273100000	1.334494000	-2.487405000	8	-10.334184000	0.703215000	4.508562000
6	-0.138405000	0.934595000	1.937583000	6	6.913647000	-0.657437000	-1.030557000
6	-5.031558000	1.050438000	-0.139884000	6	8.006406000	-1.093673000	-1.366055000
6	4.616529000	0.295643000	-0.346403000	6	9.268760000	-1.665585000	-1.686716000
6	-6.168933000	0.709438000	0.159286000	6	9.619039000	-0.099948000	-3.592877000
6	5.705675000	-0.160672000	-0.670068000	1	8.645216000	0.370594000	-3.351684000
1	-3.270957000	3.068248000	0.804725000	8	10.293280000	0.312191000	-4.533685000
1	3.214769000	2.685671000	-0.982125000	6	-10.600208000	-1.107787000	0.016138000
1	-0.576230000	0.981827000	-3.477520000	6	-11.801715000	-1.892962000	0.132924000
1	0.281653000	2.268747000	-2.611445000	6	-10.215574000	-1.120536000	-1.372254000
1	0.414269000	0.591914000	-2.064252000	6	-12.153146000	-2.359356000	-1.164391000
1	-0.916858000	0.387231000	1.392714000	1	-12.330397000	-2.117701000	1.049165000
6	-11.176982000	-1.881519000	-2.092208000	6	-8.728810000	-3.908300000	0.498663000
1	-9.342424000	-0.634257000	-1.784884000	6	-9.931059000	-4.663802000	0.650705000
26	-10.255907000	-3.053256000	-0.628379000	6	-9.362500000	-4.665663000	-1.590308000
1	-12.991174000	-3.002326000	-1.398979000	1	-11.209986000	-5.709172000	-0.866882000
1	-11.150824000	-2.092814000	-3.152975000	6	-8.377683000	-3.906653000	-0.886148000
6	-10.322494000	-5.132274000	-0.641439000	1	-8.200391000	-3.389867000	1.288153000

1	-10.466313000	-4.829101000	1.576659000	1	11.872308000	-5.007161000	0.461423000
1	-9.396820000	-4.825561000	-2.660080000	6	10.560071000	-2.287004000	3.129144000
1	-7.532289000	-3.395388000	-1.327385000	6	10.609439000	-0.573802000	1.579640000
1	0.072913000	0.384266000	2.859038000	6	9.772859000	-1.271488000	2.504253000
1	-0.546821000	1.912365000	2.208183000	6	11.879947000	-2.218676000	2.588112000
6	9.713014000	-2.780627000	-0.838704000	1	10.208067000	-3.007150000	3.856187000
6	8.901379000	-3.490588000	0.116913000	6	11.910984000	-1.158746000	1.630018000
6	11.033218000	-3.354074000	-0.784932000	1	10.298951000	0.229104000	0.923582000
6	9.706201000	-4.490838000	0.727497000	1	8.721566000	-1.083244000	2.677809000
1	7.861395000	-3.286060000	0.330346000	1	12.703392000	-2.875287000	2.837115000
6	11.020284000	-4.405774000	0.172896000	1	12.761957000	-0.871148000	1.026437000
1	11.894996000	-3.029185000	-1.351500000	6	10.017265000	-1.205482000	-2.739895000
26	10.504473000	-2.589778000	1.071677000	1	10.964990000	-1.679681000	-2.975364000
1	9.387350000	-5.172305000	1.504933000				

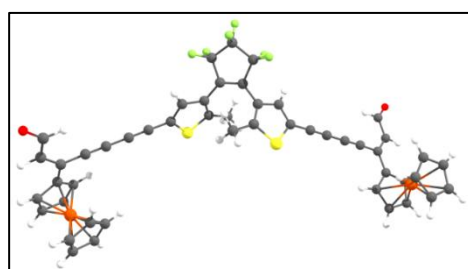


Closed solvent opt **4c**

E = -3677.035813

6	-1.421963000	3.163544000	-0.251671000	6	-5.657132000	0.720394000	-0.534137000
6	-2.825784000	2.960657000	-0.230494000	6	5.646736000	0.639843000	-0.604594000
6	-3.210401000	1.659290000	-0.459740000	1	-3.540638000	3.744592000	-0.011241000
16	-1.850180000	0.531164000	-0.702225000	1	3.578006000	3.660099000	0.127051000
6	-0.639892000	1.958286000	-0.806125000	1	0.116506000	1.362402000	-2.778451000
6	2.850420000	2.873396000	-0.030657000	1	-1.307991000	2.420686000	-2.820747000
6	1.447507000	3.080332000	0.032228000	1	0.285474000	3.095699000	-2.432687000
6	0.642802000	1.767122000	0.041773000	1	-0.272284000	2.151178000	1.994021000
16	1.834662000	0.491310000	-0.640248000	6	-6.916573000	0.227641000	-0.578355000
6	3.214782000	1.587065000	-0.355779000	6	-8.062756000	-0.199126000	-0.613944000
6	-0.696520000	4.268426000	0.105379000	6	-9.363567000	-0.770166000	-0.690005000
6	0.741552000	4.246901000	0.146601000	6	-10.483069000	-0.023890000	-0.425004000
6	-1.202139000	5.636497000	0.458710000	1	-11.465720000	-0.475008000	-0.521531000
6	0.050735000	6.366379000	1.023616000	6	-10.450920000	1.370637000	-0.015716000
6	1.254405000	5.638978000	0.360890000	1	-9.445786000	1.827438000	0.074009000
9	0.037659000	7.690646000	0.771514000	8	-11.458888000	2.030547000	0.221417000
9	0.109437000	6.175592000	2.365397000	6	6.896671000	0.135934000	-0.725772000
9	1.542832000	6.273869000	-0.818435000	6	8.033950000	-0.304309000	-0.825834000
9	2.369108000	5.711290000	1.136101000	6	9.318078000	-0.903348000	-0.952460000
9	-2.221072000	5.631535000	1.362873000	6	10.478553000	1.289746000	-0.705459000
9	-1.650867000	6.321732000	-0.637653000	1	9.489744000	1.772612000	-0.577957000
6	-0.363102000	2.223124000	-2.308641000	8	11.507919000	1.958103000	-0.670420000
6	0.364408000	1.396683000	1.522122000	6	-9.436055000	-2.182884000	-1.084952000
6	-4.521605000	1.179005000	-0.494719000	6	-10.583694000	-3.047925000	-0.991123000
6	4.518874000	1.103742000	-0.485781000	6	-8.355396000	-2.965484000	-1.629882000

6	-10.213771000	-4.328229000	-1.488207000	6	10.484137000	-3.227616000	-1.002653000
1	-11.551987000	-2.783751000	-0.588948000	6	8.667231000	-4.533720000	-1.580169000
6	-8.841614000	-4.277174000	-1.883173000	1	7.205678000	-2.838915000	-1.647043000
1	-7.350551000	-2.608476000	-1.808497000	6	10.063591000	-4.558228000	-1.278240000
26	-9.017912000	-3.804056000	0.145153000	1	11.481221000	-2.928737000	-0.710343000
1	-10.851449000	-5.201820000	-1.518733000	26	8.994104000	-3.772834000	0.338905000
1	-8.260913000	-5.103141000	-2.271544000	1	8.049828000	-5.393737000	-1.803208000
6	-9.331451000	-5.230069000	1.626459000	1	10.686670000	-5.441169000	-1.224389000
6	-8.449546000	-3.133887000	2.033291000	6	7.963070000	-4.984100000	1.679251000
6	-9.633276000	-3.927118000	2.129971000	6	8.601617000	-2.813085000	2.144723000
6	-7.962546000	-5.240524000	1.219562000	6	7.495077000	-3.637597000	1.775083000
1	-10.027938000	-6.053063000	1.533667000	6	9.357730000	-4.990276000	1.986743000
6	-7.417059000	-3.943889000	1.469205000	1	7.372935000	-5.842848000	1.386752000
1	-8.360940000	-2.089194000	2.301986000	6	9.753185000	-3.647439000	2.274505000
1	-10.596381000	-3.592373000	2.492425000	1	8.580178000	-1.737564000	2.263578000
1	-7.441268000	-6.072985000	0.765174000	1	6.487820000	-3.297736000	1.573010000
1	-6.408211000	-3.623511000	1.244558000	1	10.008034000	-5.855205000	1.970197000
1	-0.128541000	0.425960000	1.599825000	1	10.754157000	-3.316908000	2.519046000
1	1.310188000	1.354184000	2.067702000	6	10.462500000	-0.149142000	-0.912594000
6	9.343582000	-2.359661000	-1.142845000	1	11.427593000	-0.628567000	-1.04430000
6	8.216600000	-3.188363000	-1.488963000				

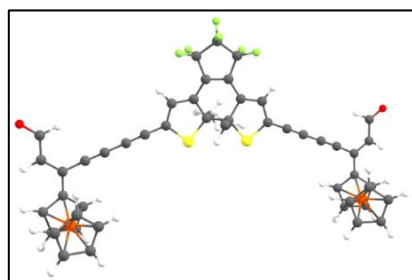


Open opt **4o** (S1) excited state

E = -3676.238195

6	-1.692813000	2.676480000	-0.614479000	6	-6.197212000	0.787496000	-0.245776000
6	-3.019489000	2.545206000	-0.104159000	6	5.649856000	0.170776000	-0.565423000
6	-3.739869000	1.560826000	-0.725304000	1	-3.417980000	3.147925000	0.700335000
16	-2.790111000	0.798936000	-1.973572000	1	3.167561000	2.997733000	-0.662887000
6	-1.425803000	1.800098000	-1.644236000	1	-0.411222000	1.381869000	-3.490482000
6	2.675278000	2.204126000	-0.116182000	1	0.377854000	2.594780000	-2.470727000
6	1.346856000	2.301362000	0.397432000	1	0.476625000	0.882193000	-2.045601000
6	0.946204000	1.165490000	1.066731000	1	-1.060362000	0.394731000	1.124516000
16	2.186704000	-0.032371000	1.046136000	6	-7.476373000	0.378825000	0.002463000
6	3.264492000	0.995736000	0.139092000	6	-8.612340000	0.024367000	0.235690000
6	-0.740183000	3.675773000	-0.114946000	6	-9.946082000	-0.440671000	0.446987000
6	0.545921000	3.520799000	0.251478000	6	-10.734853000	0.083613000	1.416975000
6	-1.150144000	5.123181000	-0.060489000	1	-11.754370000	-0.266612000	1.536922000
6	0.029157000	5.855462000	0.611480000	6	-10.294738000	1.123207000	2.337640000
6	1.194649000	4.850421000	0.524942000	1	-9.256820000	1.481061000	2.207348000
9	0.313962000	7.017832000	0.003997000	8	-11.007606000	1.590805000	3.209888000
9	-0.260287000	6.096583000	1.903603000	6	6.890618000	-0.259787000	-0.940216000
9	2.032176000	5.209647000	-0.486276000	6	7.993720000	-0.627376000	-1.284038000
9	1.924134000	4.850906000	1.660847000	6	9.277965000	-1.126441000	-1.663587000
9	-2.292860000	5.315851000	0.643859000	6	9.845989000	0.986943000	-2.828189000
9	-1.361295000	5.625972000	-1.300463000	1	8.860908000	1.391748000	-2.531353000
6	-0.179381000	1.655604000	-2.458447000	8	10.622747000	1.664066000	-3.482595000
6	-0.340468000	0.895812000	1.779886000	6	-10.409963000	-1.504878000	-0.452997000
6	-5.060888000	1.155530000	-0.458506000	6	-11.543054000	-2.357321000	-0.257135000
6	4.548267000	0.562311000	-0.241536000	6	-9.795248000	-1.885029000	-1.689247000

6	-11.624078000	-3.240011000	-1.362444000	6	10.853540000	-3.152588000	-1.325845000
1	-12.199904000	-2.357579000	0.601011000	6	9.362959000	-4.613957000	-0.373376000
6	-10.547759000	-2.947955000	-2.246143000	1	7.643497000	-3.195006000	-0.394413000
1	-8.902722000	-1.442181000	-2.107489000	6	10.703862000	-4.460467000	-0.812049000
26	-9.812694000	-3.469596000	-0.381646000	1	11.766797000	-2.735273000	-1.726916000
1	-12.353062000	-4.028394000	-1.488753000	26	10.328761000	-2.998472000	0.819342000
1	-10.320476000	-3.470475000	-3.164817000	1	8.938632000	-5.498575000	0.081807000
6	-9.699676000	-5.421763000	0.272849000	1	11.484979000	-5.205670000	-0.744870000
6	-8.465181000	-3.695203000	1.161071000	6	10.469408000	-3.442681000	2.989651000
6	-9.598081000	-4.527691000	1.375089000	6	10.461207000	-1.284850000	2.194649000
6	-8.629651000	-5.141424000	-0.620952000	6	9.660465000	-2.292723000	2.794395000
1	-10.476209000	-6.159176000	0.122365000	6	11.765996000	-3.154221000	2.495881000
6	-7.866693000	-4.073077000	-0.072920000	1	10.144978000	-4.382088000	3.417185000
1	-8.140793000	-2.886759000	1.802123000	6	11.759408000	-1.822663000	1.999510000
1	-10.280857000	-4.469367000	2.211503000	1	10.133531000	-0.291965000	1.916939000
1	-8.451489000	-5.627860000	-1.570165000	1	8.614937000	-2.200555000	3.057407000
1	-7.004209000	-3.607602000	-0.529698000	1	12.609297000	-3.831946000	2.485178000
1	-0.182243000	0.258331000	2.653010000	1	12.599270000	-1.309556000	1.549927000
1	-0.791173000	1.831676000	2.117009000	6	10.137092000	-0.370581000	-2.395248000
6	9.592171000	-2.489848000	-1.229195000	1	11.099615000	-0.772811000	-2.691793000
6	8.681370000	-3.400899000	-0.616523000				



Closed solvent opt **4c** (S1) excited state

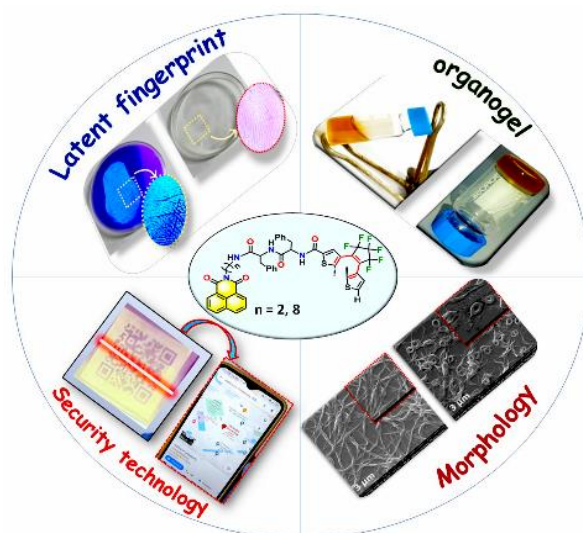
E = -3676.208986

6	-1.413103000	3.121400000	-0.376112000	1	0.617737000	3.068639000	-2.279554000
6	-2.777198000	2.910341000	-0.338577000	1	-0.634879000	2.162744000	1.908001000
6	-3.166093000	1.599498000	-0.632040000	6	-6.864108000	0.179364000	-0.661581000
16	-1.802541000	0.549877000	-0.974796000	6	-8.005768000	-0.241254000	-0.671276000
6	-0.598952000	1.939294000	-0.872177000	6	-9.314468000	-0.797139000	-0.716454000
6	2.761455000	2.794965000	0.114654000	6	-10.416022000	-0.040645000	-0.470233000
6	1.396073000	2.985757000	0.197961000	1	-11.404422000	-0.481262000	-0.542996000
6	0.572202000	1.711915000	0.153807000	6	-10.361391000	1.367422000	-0.107375000
16	1.769260000	0.397813000	-0.328302000	1	-9.352361000	1.814368000	-0.040276000
6	3.142159000	1.478513000	-0.161283000	8	-11.354230000	2.041324000	0.114996000
6	-0.683065000	4.256806000	0.040731000	6	6.835031000	0.120050000	-0.623318000
6	0.679055000	4.198306000	0.273533000	6	7.972997000	-0.289063000	-0.756933000
6	-1.203811000	5.638449000	0.258294000	6	9.271972000	-0.844956000	-0.923875000
6	-0.031822000	6.374415000	0.949379000	6	10.364566000	1.363045000	-0.639370000
6	1.224087000	5.554385000	0.572677000	1	9.366714000	1.814744000	-0.488454000
9	0.061031000	7.656569000	0.564438000	8	11.370209000	2.053063000	-0.600655000
9	-0.202447000	6.330643000	2.285705000	6	-9.401770000	-2.223318000	-1.060037000
9	1.823137000	6.125908000	-0.506883000	6	-10.542319000	-3.073781000	-0.901270000
9	2.134213000	5.560834000	1.573790000	6	-8.346092000	-3.019884000	-1.609270000
9	-2.324897000	5.679233000	1.020867000	6	-10.190429000	-4.369010000	-1.355331000
9	-1.501393000	6.269161000	-0.907688000	1	-11.494774000	-2.791570000	-0.475805000
6	-0.070341000	2.219511000	-2.292119000	6	-8.836730000	-4.335863000	-1.792262000
6	0.043799000	1.378876000	1.562683000	1	-7.346552000	-2.671925000	-1.827309000
6	-4.462699000	1.114758000	-0.636986000	26	-8.953398000	-3.783303000	0.200385000
6	4.438249000	1.018962000	-0.323338000	1	-10.828787000	-5.241301000	-1.331135000
6	-5.599182000	0.666206000	-0.648106000	1	-8.268443000	-5.176813000	-2.164306000
6	5.573021000	0.590165000	-0.468083000	6	-9.189116000	-5.147773000	1.727767000
1	-3.496087000	3.668388000	-0.053958000	6	-8.371591000	-3.017752000	2.024043000
1	3.489395000	3.592136000	0.204454000	6	-9.520403000	-3.840794000	2.182295000
1	0.457047000	1.348482000	-2.686106000	6	-7.836330000	-5.131654000	1.289784000
1	-0.902169000	2.456086000	-2.958167000	1	-9.859262000	-5.995508000	1.687479000
6	-7.330630000	-3.814503000	1.471611000	1	-7.299420000	-5.964430000	0.856718000
1	-8.312182000	-1.960773000	2.245462000	1	-6.340401000	-3.470868000	1.206026000
1	-10.485483000	-3.521517000	2.551012000	1	-0.492313000	0.427667000	1.558275000

1	0.877286000	1.307677000	2.263933000	6	8.557330000	-2.796784000	2.061934000
6	9.330446000	-2.296103000	-1.150165000	6	7.463313000	-3.614851000	1.665093000
6	8.233278000	-3.129276000	-1.540658000	6	9.314367000	-4.963121000	1.896503000
6	10.479038000	-3.138181000	-1.007295000	1	7.348451000	-5.809178000	1.250415000
6	8.706722000	-4.460221000	-1.644533000	6	9.701498000	-3.629033000	2.204737000
1	7.219791000	-2.794042000	-1.708716000	1	8.533036000	-1.723093000	2.189672000
6	10.090584000	-4.465916000	-1.313970000	1	6.461499000	-3.272771000	1.444830000
1	11.461747000	-2.826356000	-0.683324000	1	9.965530000	-5.826357000	1.881599000
26	8.980030000	-3.732928000	0.275507000	1	10.697416000	-3.300793000	2.468733000
1	8.109879000	-5.325960000	-1.895589000	6	10.388170000	-0.071739000	-0.882474000
1	10.727448000	-5.338035000	-1.261755000	1	11.363906000	-0.518585000	-1.040061000
6	7.931703000	-4.954295000	1.564093000				

Chapter: 4

A Peptide Bridged Naphthalimide-Dithienylethene Diad with Aggregation Induced Emission Activity: Application in Forensic Fingerprint Technology



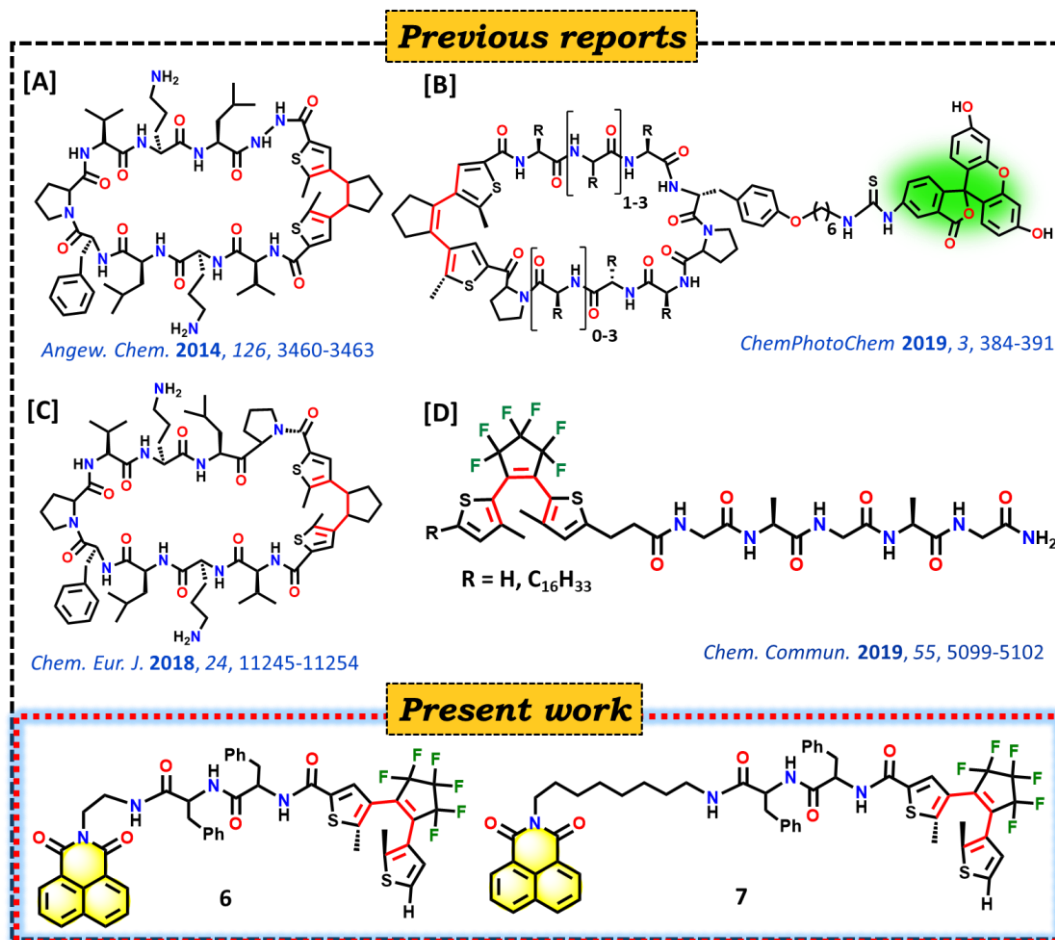
Representative publication

Under revision.....(Chemphotochem)

4.1. Introduction

Photoswitchable fluorescent materials constitute a rapidly growing area of chemistry that has granted access to monitor the dynamic processes in various fields ranging from biology to material science.^{1,2} Among all the numerous types of photochromic families documented earlier (e.g. azobenzene, stilbene, spiropyran, spirooxazine etc.), dithienylethene (DTE) derivatives are one of the best performing class of photochromic entity for its superior thermal stability, strong fatigue resistance, and efficient photo-reversibility between open and closed isomer by 6π electrons, upon alternate UV and visible light irradiation.³⁻⁸ Recently, a very few photo-controllable compounds of dithienylethene (DTE) covalently coupled with peptide scaffolds are developed (A-D, Scheme 4.1).⁹⁻¹⁴ Most of these materials displayed many biological activities such as light triggered activity of enzyme,¹² anti-cancer agent,¹³ medicine for microbial infection,¹⁴ and so on. Moreover, this peptide based DTE molecules provide a supramolecular system in which peptide unit majorly contributes to construct self-assembly via hydrogen-bonding, and van der Waals interactions.¹⁵ Interestingly, the two different photo isomeric forms of DTE can exhibits distinct morphological feature.¹⁶ Though DTE-coupled- peptide molecules have been investigated in the field of biology,¹²⁻¹⁴ its application as smart optoelectronic materials and security agent in forensic science have not been explored so far. Therefore, in order to explore the DTE based peptide molecule as smart optoelectronic materials, inclusion of fluorophore in the design is too crucial to gain advantages of monitoring the optoelectronic properties and photo-dynamic processes through fluorescence modulation.

Naphthalimide (NI), is widely used as an adjustable fluorescent core, which can tune not only the intriguing supramolecular systems through π -system but also alters the photophysical behavior in aggregated state.¹⁷ Furthermore, it is known that DTE molecules connected to the conventional AIEgen (tetraphenylethenes (TPE), hexaphenylsilole (HPS), salicyladazine (SA) etc.) generally exhibit enhanced fluorescence emission with aggregation.¹⁸ However, a number of DTE based molecules are also reported¹⁹⁻²⁵ that exhibit AIE phenomena with any non-AIEgen like NI unit. Knowing these properties, we have included the NI unit in our design to obtain a supramolecular self-assembled system along with probable AIE activity.



Scheme 4.1. Schematic illustration for designing of peptide based photoswitchable dithienylethene molecule.

Further, in order to tune the AIE activity *via* self-assembly and to monitor the fluorescence photoswitching performance we have introduced spacer of varying length in between NI moiety and peptide unit. The spacers incorporated in the system may contribute to offer flexibility between photochromic DTE unit and fluorophore moiety that may control the self-assembly, and photophysical properties.²⁶

Here, in the present work we have designed and successfully synthesized photochromic and fluorescent DTE based materials **6** and **7**. In this system, unsymmetrical DTE unit and fluorescent chromophore (NI) are covalently connected by a di-peptide (phe-phe) unit linked via variable (2, 8) alkyl chain length. Both the molecules (**6** and **7**) displayed excellent reversible photochromic as well as fluorescence properties in solution as well as in solid state. Due to suitable overlapping of absorption and emission bands, **7** showed effective fluorescence quenching behavior via Förster resonance energy transfer (FRET) mechanism. Interestingly, **7** showed formation of organic gel in ethanol which was confirmed by

frequency sweep study. Furthermore, the material **7** is found to be highly efficient and rapid responsive in fingerprint visualization process, which is reversible in nature. We have also applied this material in security technology (encryption/decryption of QR code) and as erasable ink. To the best of our knowledge, this is the first report where DTE is asymmetrically connected with peptide along with NI and it is capable for fingerprint generator under UV light (365 nm) as well as under visible light.

4.2. Results and Discussion

4.2.1. Synthesis and Characterization

The designed fluorescent photo-switchable compounds (**6** and **7**) are basically composed of four units: [1] naphthalimide (NI), [2] alkyl $(\text{CH}_2)_n$ [$n = 2,8$] chain (C_n), [3] dipeptide of phe-phe scaffold, and [4] unsymmetrical dithienylethene (DTE) moiety. It is well established that the fluorophore naphthalimide unit shows a strong London dispersion force to promote the self-assembly process²⁷ and the peptide unit also triggers the supramolecular self-assembly process *via* H-bonding/Vander Wall interactions.²⁸ Further, taking advantage of the excellent reversible photochromic properties of DTE,²⁹ we have attached DTE unit with NI- C_n -pep (**4C₂**/ **4C₈**) conjugates, to tune the self-assembly behavior upon reversible photoisomerization. Interestingly, knowing the fact that the length of alkyl chain variation may affect the photoconversions speed of DTE,³⁰ we have purposefully introduced alkyl chain connected with the naphthalimide having shorter (C_2) and longer (C_8) distance from di-peptide unit where the short alkyl chain resulted more rigid structure and the long alkyl chain produces more flexibility.³¹ As a result, the designed NI- C_n -pep-DTE (**6/7**) conjugates may exhibit photo controllable property with self-assembly behavior.

The intermediates (**P1**, **1C₂**, **1C₈**, **2** and **5**) were synthesized by adapting previously reported procedures (details of the synthetic scheme is given in the Figure 4.1)³² and the general synthetic route for designing of **6/7** is depicted in Figure 4.2. The N-terminally Boc protected dipeptide (**2**) unit was reacted with NI- C_n -NH₂ (**1C₂** or **1C₈**) to afford protected NI- C_n -PepBoc (**3C₂** and **3C₈**) which were readily deprotected to form precursor **4C₂** or **4C₈** by treating with TFA/DCM. The final compounds **6** and **7** (yield: 37% and 38%) were obtained *via* coupling reaction between NI- C_n -pep-NH₂ (**4C₂** or **4C₈**) and unsymmetrical DTE acid, 4-[3,3,4,4,5,5-Hexafluoro-2-(2-methyl-3-thienyl)-1-cyclopenten-1-yl]-5-methyl-2-thiophenecarboxylic acid (**5**). All the newly synthesized precursor compounds (**3C₂**, **3C₈**, **4C₂**, and **4C₈**) were fully characterized by ¹H, ¹³C NMR, HRMS and the final compounds **6**

and **7** are fully characterized by ^1H , ^{13}C , ^{19}F NMR, HRMS, and elemental analysis.

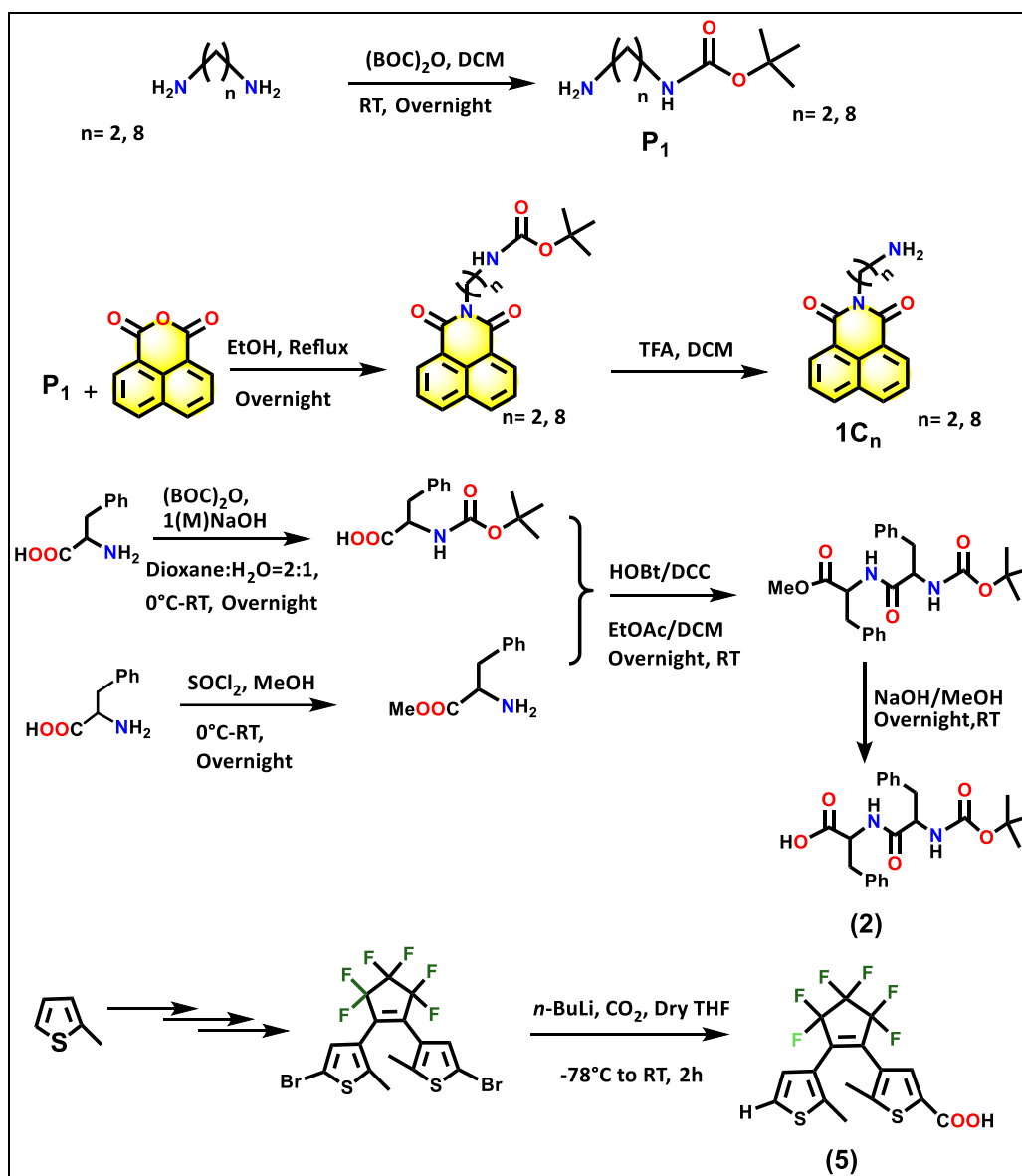


Figure 4.1. Stepwise synthesis of precursor compounds **P₁**, **1C_n**, **2** and **5**.

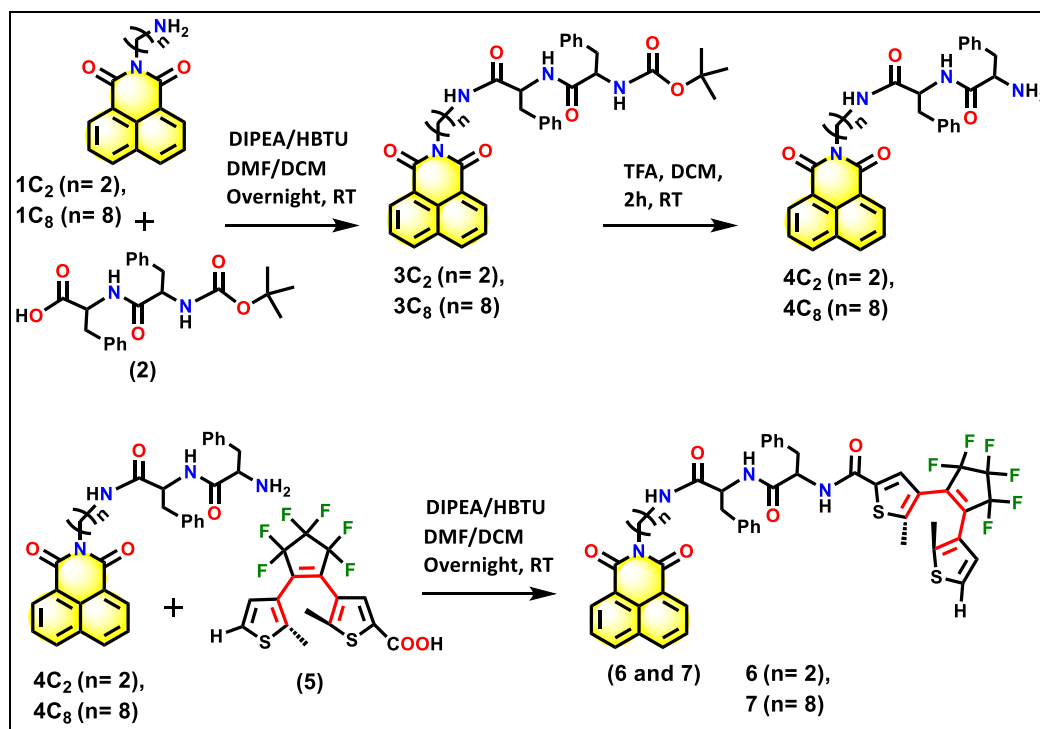


Figure 4.2. Synthetic procedure of compounds **3C₂**, **3C₈**, **4C₂**, **4C₈**, **6** and **7**.

4.2.2. Photophysical studies

As our synthesized compounds, **6/7** comprise both photochromic DTE unit and naphthalimide (NI) fluorophore, it was expected to provide fluorescent photoswitching performance in presence of external light source. The photochromic behavior of our synthesised compounds (**6** and **7**) was triggered by photoirradiation (254 nm, UV/>450 nm, visible light) and examined in CH₃CN (1.25×10⁻⁵ M) solution at room temperature. The UV-vis absorption spectrum of **6o/7o** showed maximum absorption located at 232 nm ($\epsilon = 7.83 \times 10^4 \text{ M}^{-1} \text{ cm}^{-1}$) for DTE unit ($\pi\text{-}\pi^*$ transition)³³ and two other characteristic absorption peaks at 330 nm ($\epsilon = 1.94 \times 10^4 \text{ M}^{-1} \text{ cm}^{-1}$) and 343 nm ($\epsilon = 1.66 \times 10^4 \text{ M}^{-1} \text{ cm}^{-1}$) for naphthalimide subunit (Figure 4.3a and 4.3b).³⁴ Intriguingly, upon exposure of UV light (254 nm), the generation of visible region absorption band at 550 nm ($\epsilon = 9.76 \times 10^3 \text{ M}^{-1} \text{ cm}^{-1}$), indicated the formation of respective ring closed isomer (**6c/7c**). Although the nature of absorption spectrum is quite similar, the speed of photocyclization for **6** and **7** were slightly different. Complete conversion of open isomer to the closed isomer took 95 s and 85 s for **6** and **7** respectively (Figure 4.3a, 4.3b, inset), where the alkyl group may play a pivotal role in photoisomerization speed. Notably, the photocycloreversion process of **6/7** was also accomplished by gradual irradiation with visible light (>450 nm) that showed the complete

restoration of the initial state with diminution of visible region absorption band at 550 nm ($\epsilon = 9.76 \times 10^3 \text{ M}^{-1} \text{ cm}^{-1}$) and emergence of the absorption bands at 232 nm and 330 nm for **6o/7o** (Figure 4.3c, 4.3d). Complete cycloreversion process takes 105 s (for **6**) and 100 s (for **7**) and beyond the saturation level no noticeable changes were observed (Figure 4.3c, 4.3d, inset).

More importantly, presence of the most promising photochromic DTE unit in our synthesized compounds **6/7** encouraged us to test their capabilities to stand against consecutive irradiation of UV and visible light. Both **6** and **7** displayed excellent fatigue resistance properties and the robust photo-reversibility remain unaltered even after 45 cycles without loss of efficiency (Figure 4.3e, 4.3f).

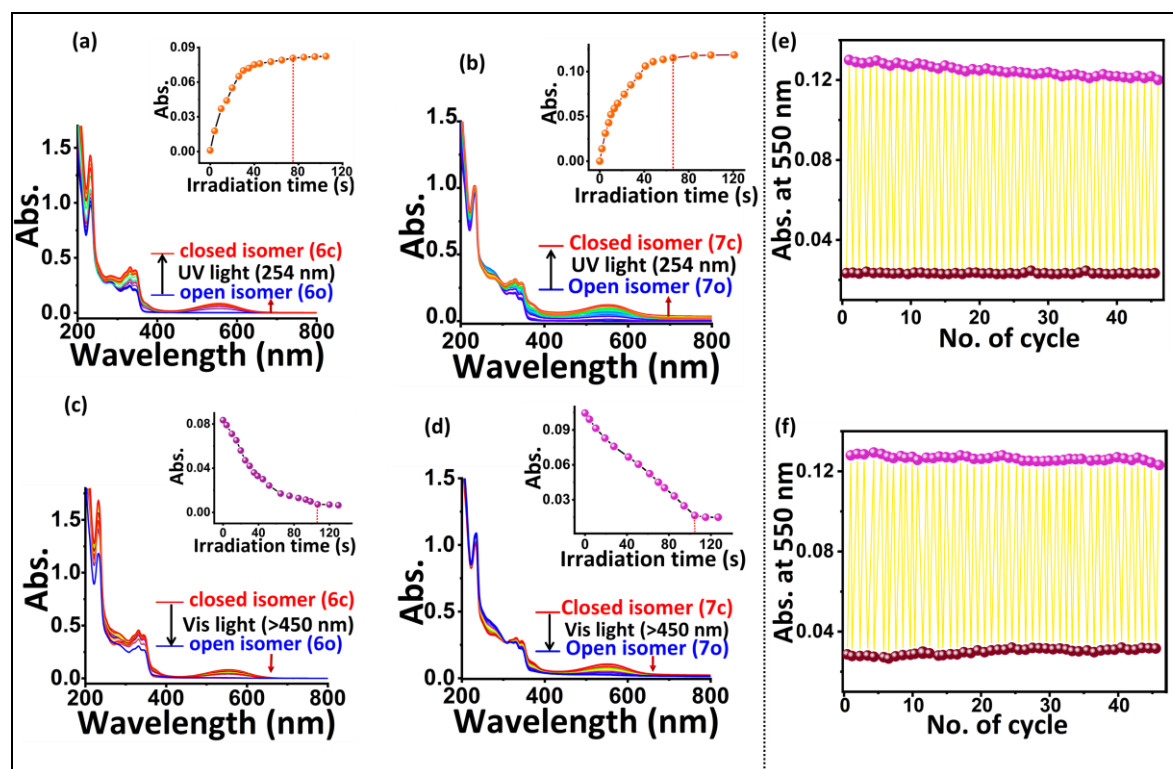


Figure 4.3. The absorption spectra of (a) **6o** (inset: absorbance at 550 nm vs exposure time); (b) **7o** (inset: absorbance at 550 nm vs exposure time) upon gradual irradiation of 254 nm UV ($310 \mu\text{W}/\text{cm}^2$); (c) **6c** (inset: absorbance at 550 nm vs exposure time); (d) **7c** (inset: absorbance at 550 nm vs exposure time) upon gradual irradiation of >450 nm visible light in CH_3CN ($1.25 \times 10^{-5} \text{ M}$) solution respectively. Fatigue resistance (at least 45 cycles) for (e) **6** and (f) **7** measured at 550 nm monitored by alternating irradiation of UV ($\lambda = 254 \text{ nm}$) and visible ($\lambda = >450 \text{ nm}$) light respectively.

In order to isolate the open and closed isomer for obtaining photoisomerization quantum yield and to evaluate the purity of photo-isomeric open and closed isomer at photostationary state (PSS), high-performance liquid chromatography (HPLC) was performed by adjusting the detector wavelength at 210 nm. The pale-yellow photo isomeric respective open form (**6o/7o**) was almost converted to the purple closed form (**6c/7c**) (Figure 4.4a, 4.4b) at photostationary state (PSS), which were measured by eluting with CH₃CN: H₂O (90:10) in reverse phase HPLC procedure. We also detected the retention time (t_R) at 3.00 min and 2.60 min for open and closed ring isomer of **6** while it was 7.58 min and 6.81 min for open and closed ring isomer of **7** respectively (Figure 4.4c, 4.4d). The broad spectrum appeared in the HPLC chromatogram might be attributed to the amide linkage found in peptide-based compounds (**6** and **7**).³⁵

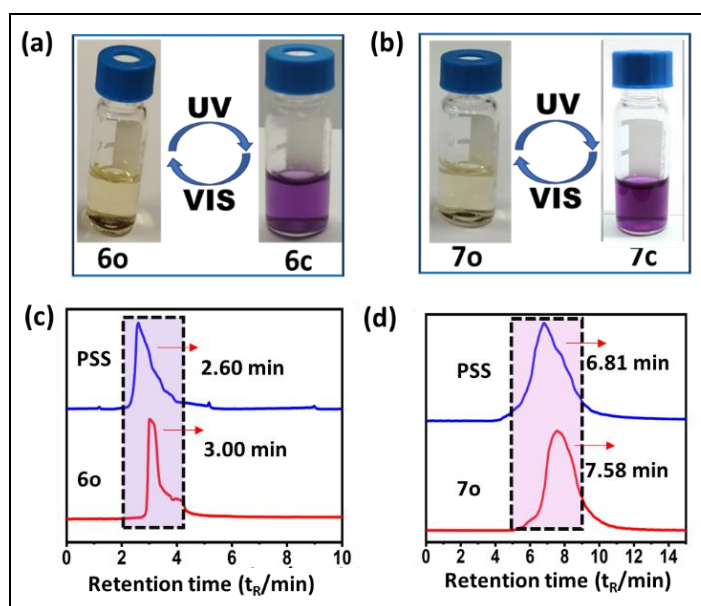


Figure 4.4. Naked eye color changes of open and closed isomer for (a) **6** and (b) **7** in CH₃CN (10⁻³ M) under UV light/visible light; HPLC chromatogram of (c) **6** and (d) **7** before and after UV light irradiation (310 μ W/cm²) (eluted with CH₃CN: H₂O = 90:10).

To better understand the photoisomerization efficiency, photoreaction quantum yields were determined. After isolating two isomers from HPLC, the photoreaction quantum yields are recorded with 1,2-bis(2-methyl-5-phenyl-3-thienyl)-perfluorocyclopentene as a

reference using the well-established procedure³⁶ and the corresponding values were reported in tabular form in Table 4.1 (Figure 4.5).

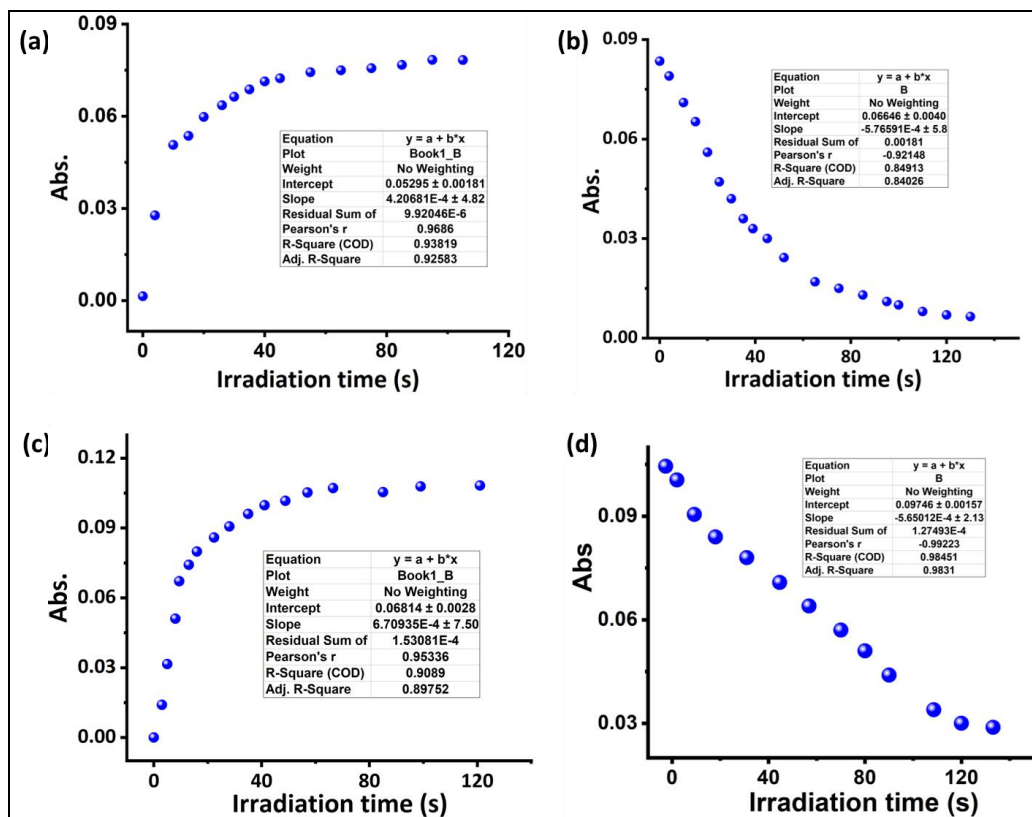


Figure 4.5. Calculation of photoreaction quantum yields for cyclization ($\Phi_{o \rightarrow c}$) and cycloreversion ($\Phi_{c \rightarrow o}$) of (a) **6o** and (b) **7o** by 254 nm UV light and (c) **6c** and (d) **7c** by >450 nm visible light irradiation.

On the other hand, the photocyclization and photocycloreversion rate constants (K) were also calculated by plotting of $\ln[(A_0 - A_\infty)/(A_t - A_\infty)]$ vs irradiation time (s) (Figure 4.6).³⁷ The obtained results clearly indicated that with increasing the alkyl chain length both photocyclization quantum yields (Φ) and rate constants (K) are increased while for the cycloreversion process both the values were slightly reversed in order.³⁸

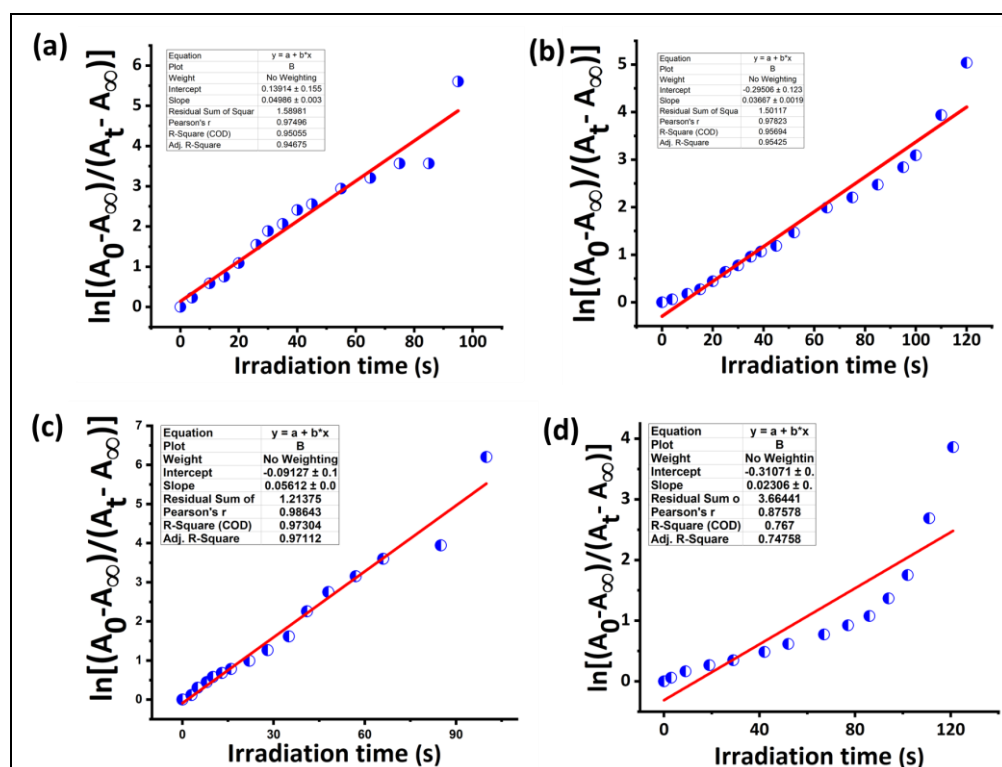


Figure 4.6. Plot of $\ln[(A_0 - A_\infty)/(A_t - A_\infty)]$ vs irradiation time (s) for determination of rate constant (K) of (a) **6o** to **6c**, (b) **6c** to **6o** and (c) **7o** to **7c**, (b) **7c** to **7o** in CH_3CN solution.

Table 4.1. Summary of photoreaction quantum yields [$(\Phi_{o \rightarrow c})$ and $(\Phi_{c \rightarrow o})$] and rate constants (K) data for **6** and **7** upon exposure of UV light (254 nm) and visible light (>450 nm) respectively.

Compounds	ϵ ($\text{M}^{-1}\text{cm}^{-1}$)		Slope		Quantum yield		Rate constant	
	Cyclization	Cycloreversion	Cyclization	Cycloreversion	Cyclization ($\Phi_{o \rightarrow c}$)	Cycloreversion ($\Phi_{c \rightarrow o}$)	Cyclization ($K_{o \rightarrow c}$)	Cycloreversion ($K_{c \rightarrow o}$)
6	6.584×10^3	1.3×10^2	4.2×10^{-4}	5.76×10^{-4}	0.81	0.283	0.049	0.037
7	9.484×10^3	2.408×10^2	6.7×10^{-4}	5.650×10^{-4}	0.89	0.17	0.056	0.023
Ref.	7.2×10^3	1.2×10^3	3.35×10^{-4}	2.44×10^{-4}	0.59	0.013	-	-

Considering excellent optical properties of naphthalimide (NI), present in materials (**6/7**), fluorescence emission ($\lambda_{\text{ex}} = 330 \text{ nm}$) spectral changes were monitored by exposure of light (UV/ visible) in acetonitrile ($7.8 \times 10^{-7} \text{ M}$) solution. Both the compounds (**6** and **7**)

displayed almost similar type of single humped strong emission band at 381 nm (for **6o**) and 392 nm (for **7o**) respectively, which correspond to the characteristic emission of NI unit.³⁹ Upon UV light (254 nm) irradiation, the fluorescence emission band was quenched (Figure 4.7a) with the change in fluorescence quantum yield (Φ_F) from 0.32 to 0.10 for **6** (Table 4.2), which was quite less effective than that of **7** (Figure 4b), where the fluorescence quantum yield (Φ_F) was significantly decreased from 0.27 to 0.04 (Table 4.2). Notably, fluorescence quenching process was very rapid and reached the saturation level at about 75 s for **6** and 65 s for **7** with 8 nm red shift (Figure 4.7a, 4.7b, inset). Visible light triggered the cycloreversion process resulted to (**6o/7o**) from (**6c/7c**) that also led to the restoration of the original emission spectra for open isomer (Figure 4.7c, 4.7d). The closed isomer was completely converted to open isomer after visible light irradiation for 105 s and 100 s for **6** and **7** respectively (Figure 4.7c, 4.7d, inset). However, the fluorescence quenching phenomena upon UV light irradiation of **7** can be explained by the possible Förster resonance energy transfer (FRET) process where NI unit exhibited unperturbed strong fluorescence emission in **7o** and after conversion to the closed isomer **7c**, the fluorescence intensity was significantly quenched due to the energy transfer process from the donor NI fluorophore to the acceptor, ring-closed form of DTE moiety (Figure 4.7e). The spectral overlap in **7c** between normalised absorption band of the acceptor (DTE_{closed}) and normalised emission band of the donor (NI) further corroborated with the FRET process leading to fluorescence quenching phenomenon of **7** (Figure 4.7f).⁴⁰ It was presumed that the flexibility of the long alkyl chain containing **7**, bring the FRET donor and acceptor closer proximity than the shorter alkyl chain containing **6**, which accounts for the relatively stronger fluorescence quenching efficiency of **7** comparing to **6**.⁴¹

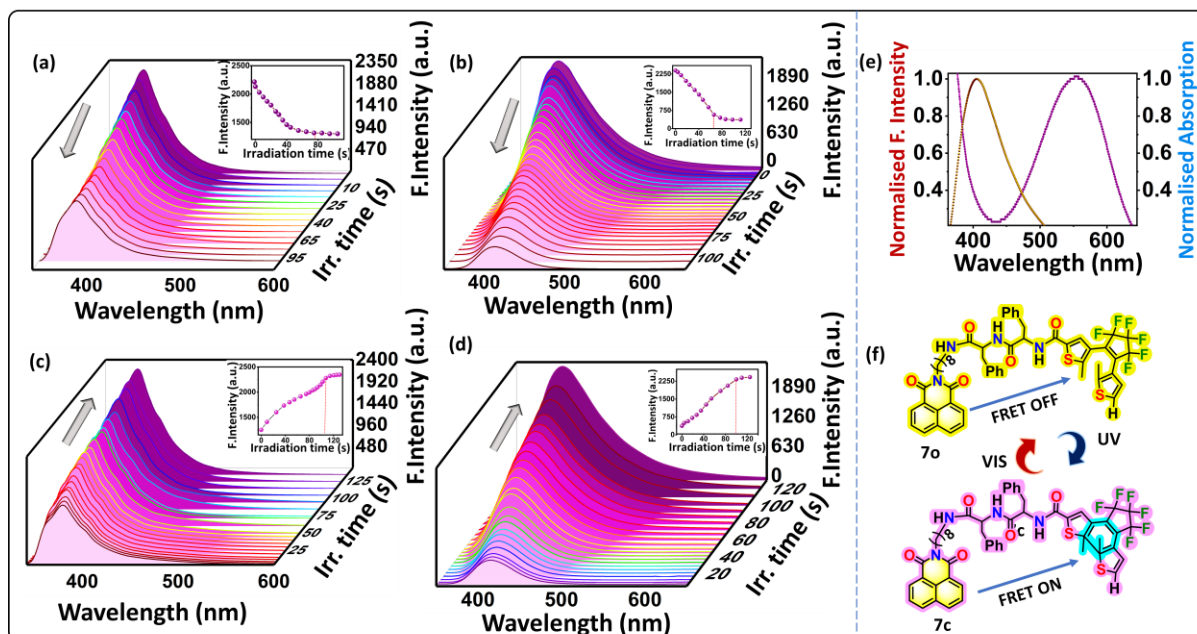


Figure 4.7. Fluorescence emission spectra ($\lambda_{\text{ex}} = 330 \text{ nm}$) of (a) **6o** (inset: fluorescence intensities vs exposure time); (b) **7o** (inset: fluorescence intensities vs exposure time) upon gradual irradiation of 254 nm UV ($310 \mu\text{W}/\text{cm}^2$); (c) **6c** (inset: fluorescence intensities vs exposure time); (d) **7c** (inset: fluorescence intensities vs exposure time) upon gradual irradiation of >450 nm visible light in acetonitrile ($7.8 \times 10^{-7} \text{ M}$) solution respectively; (e) spectral overlap of normalised absorption and emission spectra of **7** for FRET process; (f) schematic representation of **7** for reversible fluorescence switching (OFF-ON) via FRET process.

Table 4.2. Data for fluorescence quantum yields for open (**7o**) and closed (**7c**) isomers in normal and aggregated state.

Compound	Area under the curve from fluorescence emission spectra (S)	Abs. at excitation wavelength (Abs.)	Refractive index (η)	Fluorescence quantum yield (Φ_F)
6o	69523600	0.100	1.407 (THF)	0.32
6c	40221000	0.193	1.407 (THF)	0.10
7	78872000	0.140	1.407 (THF)	0.27
7c	14858800	0.170	1.407 (THF)	0.04
7o (aggregated)	146559000	0.218	1.407 (THF)	0.38
7c (aggregated)	106340000	0.251	1.407 (THF)	0.28
Standard ref. (Quinine sulphate)	190868000	0.141	1.333 (Water)	0.59

Considering the excellent robust fatigue resistance and rapid photoresponsive properties in solution, we have investigated the photoswitching performance of **6/7**, dispersed in PMMA (polymethyl methacrylate) films in order to make a potentially valuable smart material with practical applications. For this reason, PMMA embedded thin film was prepared by combining PMMA (15 mg), compound **6/7** (1 mg) and chloroform (2 ml, as a solvent) to form a homogeneous mixture, then it was spread on FTO glass ($3 \times 1 \text{ cm}^2$). The **6/7** coated PMMA film was directly used to record the UV-vis absorption and fluorescence emission spectra. Interestingly, in solid PMMA film, the compounds (**6/7**) showed similar photophysical behavior as obtained in solution phase (Figure 4.8). However, it takes little bit more time to reach saturation level for cyclization (125 s, for **6** and 110 s, for **7**) and cycloreversion process (170 s, for **6** and 150 s, for **7**) as compared to CH_3CN solution.

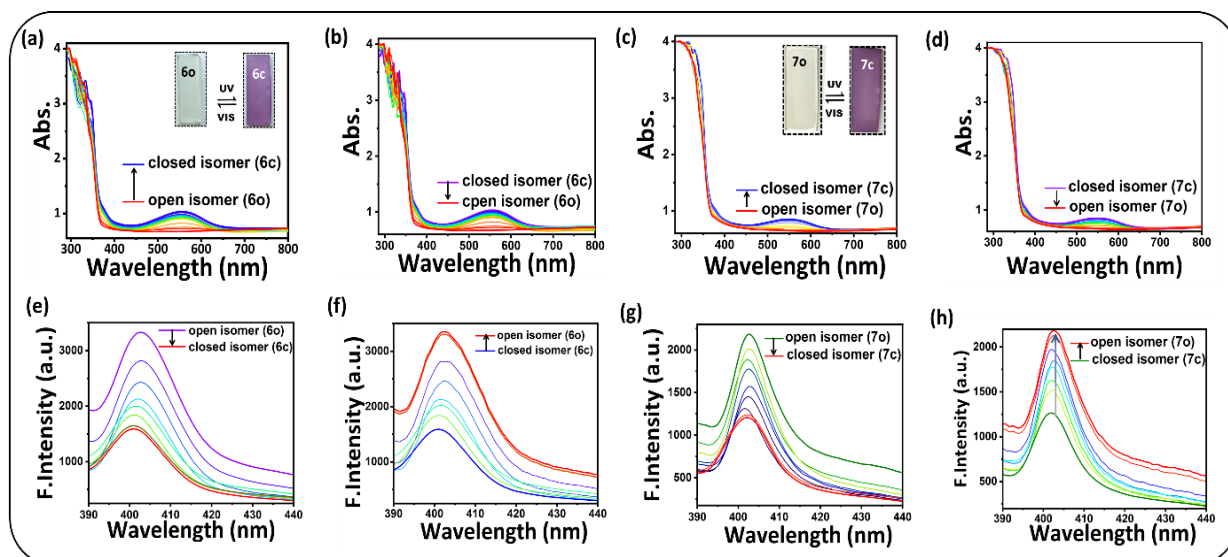


Figure 4.8. Absorption spectra of (a) **6o** (b) **6c** by gradual irradiation of 254 nm UV light and (c) **7o** (d) **7c** by gradual irradiation of >450 nm visible light respectively. Fluorescence emission spectra of (e) **6o** (f) **6c** by gradual irradiation of 254 nm UV light and (g) **7o** (h) **7c** by gradual irradiation of >450 nm visible light respectively in PMMA embedded thin film.

4.2.3. AIE Property studies

Aromatic luminophores generally show aggregation behavior for their intrinsic hydrophobicity and π - π interactions.⁴² In this regard designing of molecule with freely rotating bonds, bended flexures, opens a way to impose AIE behavior to the molecule, where the rigid structural orientation in aggregated state triggered the stronger emission spectra.⁴³ As our synthesised compounds (**6/7**) contain an aliphatic alkyl chain, an aromatic naphthalimide unit and a simple dipeptide moiety, we were interested to begin studies in aggregated state anticipating the formation of self-assembly *via* hydrophobicity, aromatic π - π stacking.⁴⁴ Both the compounds **6** and **7** were subjected to photophysical studies to characterize the aggregation phenomenon upon increasing percentage of water in THF system. Interestingly, the UV-vis absorption spectra of compound **7o/7c** demonstrated an increase of absorption bands with increasing percentage of water from 0% to 90% (Figure 4.9a, 4.9b). Further fluorescence spectra of both open and closed isomer of **7** unveiled the aggregation induced emission phenomenon, where weak emission was observed for 0% of water in THF and progressive enhancement fluorescence intensity was observed upon increasing percentage of water (Figure 4.9c, 4.9d).

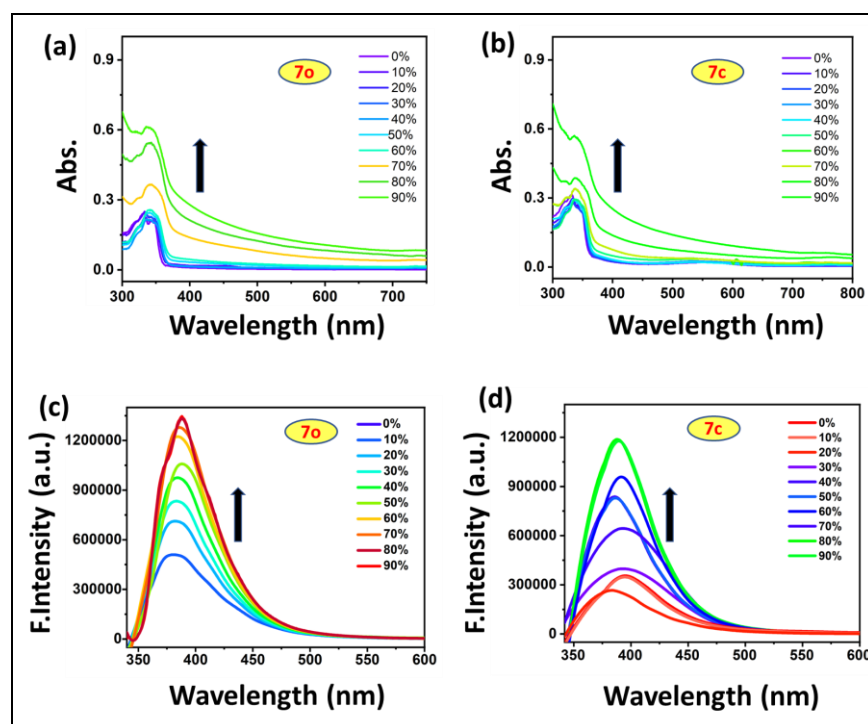


Figure 4.9. Changes in the absorption spectra of (a) **7o** and (b) **7c** in THF/water binary solvents with increasing water fractions ranging from 0 to 90%. Fluorescence emission spectra of (c) **7o** and (d) **7c** in THF/water binary solvents with increasing water fractions ranging from 0 to 90%.

After reaching 70%, fluorescence intensity increased significantly that achieved maxima after 90% water in THF with 8 nm bathochromic shift, which in turn refer to the formation of *J*-type aggregation (Figure 4.10a, 4.10b).^{42,45} The fluorescence photographs of **7o/7c** in THF with increasing percentage of water under 365 nm UV light is shown in Figure 4.10c, 4.10d. Further, to get more insight, we have investigated the morphological features of the compound **7o/7c**. However, the material **6** did not show any significant change in absorption and emission spectra upon aggregation. Therefore, morphological studies of **6** was not performed. The influence of alkyl chain length on AIE behavior can be correlated to the well-established fact that long alkyl chains increase the tendency to self-assemble by zigzag packing in polar media, especially in water.⁴⁶ Also, the use of long alkyl chain effectively optimized the dispersive and van der Waals interactions, which results in well-ordered self-assembled structures.⁴⁷ To capture the FESEM images of compound **7**, diluted THF (0% water in THF) solution and THF-water mixture (70% water in THF) were drop-casted on a mica foil, after evaporation of solvent the FESEM images were captured. In normal state (0% water in THF), Figure 4.10e shows “nanofibers” like morphology in

open isomeric form of **7** which further combined each other to form thicker ones in their aggregated state. It provided a significant sign of nanofibers having been wrapped up by the ribbons or films during aggregation (70% water in THF) (Figure 4.10f).⁴⁸ The peptide and naphthalimide (NI) scaffolds may help to stabilize supramolecular self-assemblies to form the fibrillar morphology *via* intermolecular interaction such as hydrogen bonding of peptide and π - π stacking of NI scaffold.⁴⁸ Though the ring-open isomer formed fibrillar self-assembly, the closed isomer (**7c**) was unable to form long fibrillar structure due to the increased rigidity, rather it formed doughnuts (toroids) like structures in normal state (0% water in THF) (Figure 4.10g).⁴⁹ During aggregation the rigid **7c** molecules are in close vicinity that helps to provide intermolecular hydrogen bonding and displayed rigid circular doughnuts (toroids) structures which in turn stabilized with smaller aggregated form (Figure 4.10h).

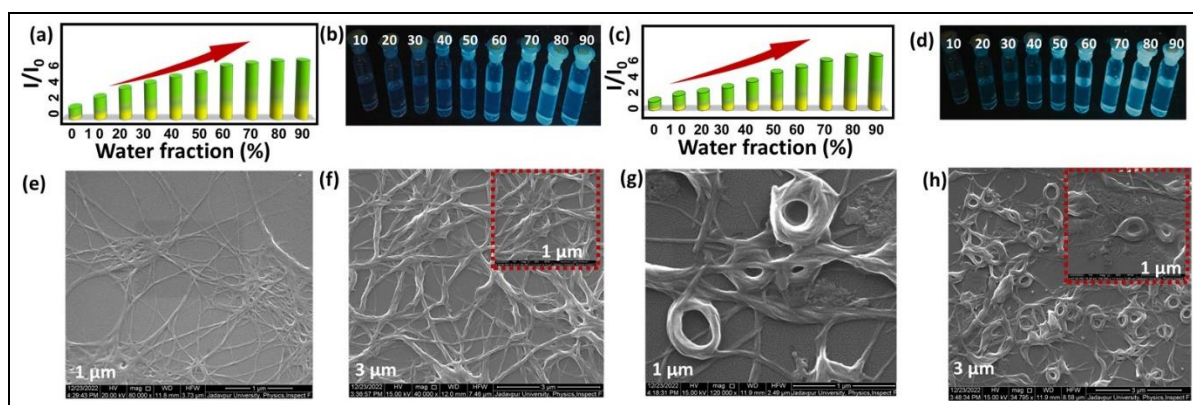


Figure 4.10. Bar plot from fluorescence emission spectra of (a) **7o** and (b) **7c** with different percentage of water (0 and 90% H₂O) in THF. Fluorescence photograph of (c) **7o** and (d) **7c** at different water contents (0 and 90% H₂O) under illumination of 365 nm UV light. FESEM images of **7o** in (e) 0% THF, (f) aggregated state (THF: H₂O=30:70); FESEM images of **7c** in (g) 0% THF, (h) aggregated state (THF: H₂O=30:70).

4.2.4. Organogelation Study

The organogels are types of soft materials which formed solely through multiple weak noncovalent interactions such as π - π stacking, H-bonding, van der Waals interactions, hydrophobic interaction etc.⁵⁰ The potential application of gel material is not only limited to pollutant removal, excess metal ion removal, also widely used the gel in real-life usage.⁵¹⁻⁵³ Taking advantages of all the structural features in our materials (**6/7**), we were fascinated in

the investigation of gelation ability of the materials in a simple and reproducible way. The gelation protocol of **6** and **7** were preliminary examined at a concentration of 6 mg/mL with various solvents such as DCM, EtOAc, THF, CH₃CN, H₂O, EtOH, MeOH. The Figure 4.11a depicted the summarization of gelation ability of **6** and **7** in different solvents. The compounds **6** and **7** were taken in a septum capped vial, heated until it formed a clear solution and kept standing to room temperature. It was observed that the compound **6** led to form no gelation at any conditions while **7** form successfully turned up to gel in EtOH (Figure 4.11b). In case of **6**, gelation was not occurred may be due to the imbalance of hydrophobicity and hydrophilicity of short alkyl chain in the medium. On contrary, compound **7** with longer and flexible eight-carbon alkyl chain fulfilled the balanced condition to form gel.⁵⁴ The photoisomerization process was also investigated in gel state where the reversible color change from pale yellow (**7o**) to purple (**7c**) was observed upon consecutive irradiation of UV light (254 nm) and visible light (>450 nm) (Figure 7b). Further, to characterize the gelation behavior, sample at same concentration (6 mg/mL) was prepared and the rheological experiment was performed. In the frequency sweep, the value of storage modulus (G') was roughly 10 times to than the respective loss modulus (G'') value which demonstrate its semi-solid like feature (Figure 4.11c). The high G' values also suggested that the gel was resistant to elastic deformation. As confirmed from rheological study the inherently photochromic material (**7**) can be considered for photophysical study in gel state. Based on the literature procedure,¹⁶ we have recorded the gel state UV-vis absorption spectra. Although the increase of absorption intensity demonstrated high compound concentration in gel state, the compound gel-**7o** displayed almost similar absorption bands as obtained in solution state. The characteristic absorption bands at 230 nm, 332 nm and, 350 nm were found increased with concomitant generation of new hump at 552 nm upon UV light irradiation (Figure 4.11d). These spectral changes were consistent with those of dithienylethene derivatives and the absorption bands are reverse back to initial open isomeric state by visible light irradiation (>450 nm) (Figure 4.11e). Furthermore, the fluorescence emission spectra was recorded in gel state which resulted in reversible fluorescence modulation in presence of light (UV/vis) (Figure 4.11f, 4.11g).

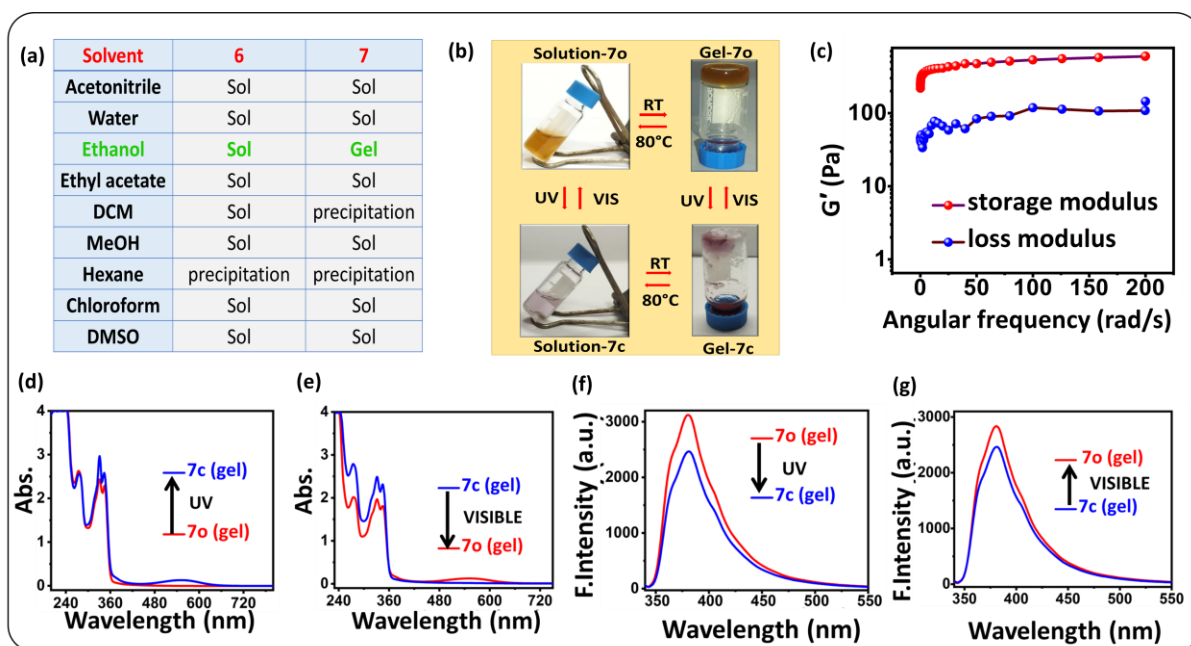


Figure 4.11. (a) Optimization table for gelation experiment; (b) preparation of the organogel from 7_o (sol) to 7_o (gel) and photoisomerisation; (c) strain sweep tests for 7 (gel). Absorption spectra of 7(gel) for (d) cyclization and (e) cycloreversion; Fluorescence emission spectra of 7 (gel) for (f) cyclization and (g) cycloreversion.

4.3. Applications

4.3.1. Fingerprint technology

In view of rapid photo-response rate, distinct photo-generated color with high fluorescent and robust anti-fatigue capability of compound 7, it was expected to deliver potential application in photo erasable ink, security marking, information encryption and anticounterfeiting technology on various substrates in solution as well as solid state powder form.⁴⁹ However, in security market several techniques have been used to develop and improve the visualisation quality of latent fingerprints (LFP) where it is used as various dusting agents for authentication of individual identity.⁵⁵ In the traditional techniques, there are few difficulties because of inadequate sensitivity, irreversibility, background noise, high toxicity and other factors.⁵⁶ To tackle this challenge the development of rapid responsive latent fingerprints visualisation techniques is highly demanding. Moreover, our synthesized compound 7 is both fluorescent and photochromic in nature which displayed dual behavior: (i) blue fluorescent color (under 365 nm UV light) and (ii) reversible visible color change

from pale yellow to purple conducted by irradiation of UV (254 nm) and visible (>450 nm) light. At first, a bare finger was impressed on glass petri dish (also applicable in any daily used material like steel, iron materials, wooden/fibre handle of knives) that could not be recognised through any pattern in UV/visible light. Then, we have directly used fine powdered **7o** as a fluorescent photochromic material to develop proper LFPs on a glass petri dish, which resulted in two types (fluorescent and photochromic) of latent fingerprint images. Due to the presence of lipid in finger which was pasted on the petri dish, the fine dust powder was adsorbed on that particular surface which was visible only in 365 nm UV light and permanently visualized in naked eye after exposure of UV (254 nm) light for 110 s (Figure 4.12). Interestingly, rapid responsive fingerprint visualization process was reversible in nature that was completely vanished in 150 s after visible light (>450 nm) irradiation (See video, 4VS1). After successful visualization process, the latent fingerprint powder (**7o**) can be recovered completely and it could be utilized again for another identification process. This is the first example of DTE based photochromic fluorescent material which is successfully used as latent fingerprints (LFPs) powder in a non-invasive manner. Therefore, we believe that the present material **7** could be utilized as a smart material for LFP imaging applications in forensic sciences.

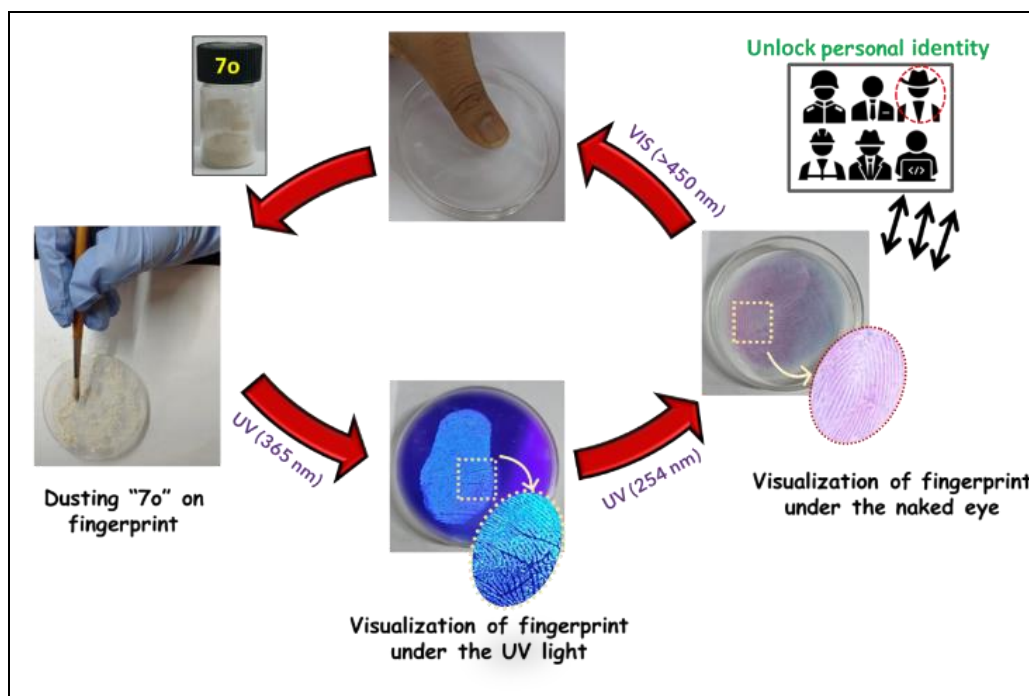


Figure 4.12. Schematic representation of the overall methodology used for the generation of latent fingerprints using compound **7**. *All the pictures (except cartoon personal identity) are captured during the experiment in the laboratory.*

4.3.2. Light controlled security technology

As our designed and synthesized compound **7** has the decent reversible photoswitching speed and anti-fatigue behavior, we have further explored its application for quick response (QR) code generation and the fabrication of a reversible “write-erase-write” process by erasable security ink. First, to keep the secret information, the DCM solution of **7o** (10^{-2} M) was evenly coated onto the normal white paper, dried, and covered the reverse QR code ($10\text{ mm} \times 10\text{ mm}$) on the coated paper (Figure 4.13a). After 110 s exposure to UV light (254 nm), the masked QR pattern was removed and an encrypted QR code was generated which was scanned quickly using a smartphone to browse the linked location in Google Maps (See video, 4VS2). After successful decryption, the information may be easily vanished by converting it back to the original white paper using visible light ($>450\text{ nm}$, 150 s) and this reversible encryption and decryption process can be repeated over several cycles. In addition, the light-triggered compound **7**, has been used as a potential material for erasable secret writing. For this purpose, an ethanolic solution (10^{-4} M) of colorless compound **7o** was inserted in a fountain pen and written secret information such as signatures, future property wills, and so on. Interestingly, the written content become visible after 150s UV light irradiation and it completely bleached upon visible light exposure (Figure 4.13b). Thus, the repeated “write-erase-write” function revealed good reusable application of **7** as an erasable ink (See video, 4VS3).

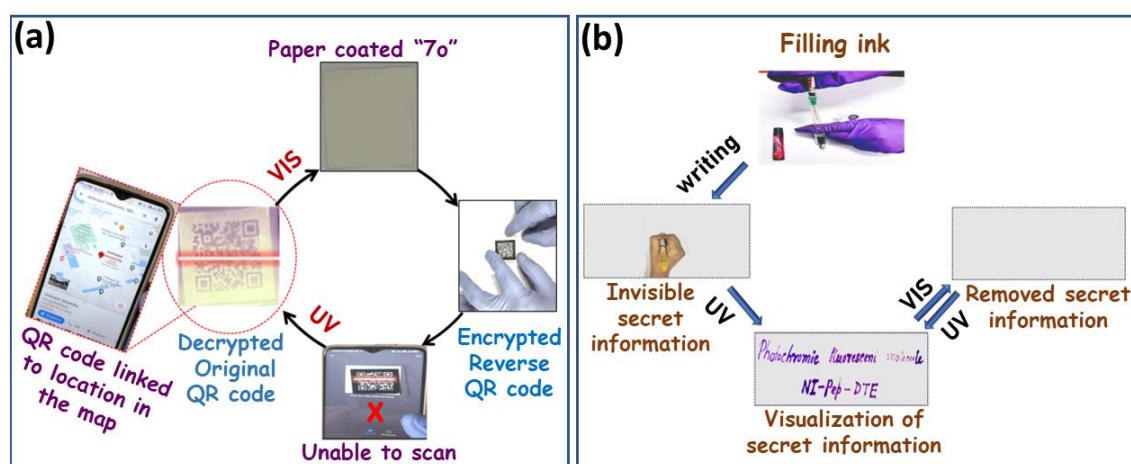


Figure 4.13. Schematic representation of the overall methodology (developed in laboratory) used for the generation of (a) QR code and (b) erasable writing pattern using compound **7**. *All the pictures are captured during the experiment in the laboratory.*

4.4. Conclusion

In conclusion, we have designed and synthesized an unusual kind of high-performance of peptide bridged dithienylethene with AIE activity without an AIE-gen. Furthermore, we have also demonstrated that how the only chain length of alkyl group can tune the AIE activity as well as the morphological properties based of supramolecular self-assembly. The designed strategy of the molecule offers a vital concept to construct peptide bridged photochromic fluorescent materials based on unsymmetrical DTE unit. To our delight, our designed and synthesized materials are unique examples that can retain their fluorescence photoswitching performance in solution, solid state, as well as in gel form. More remarkably, **6** and **7** could be conveniently implanted into PMMA polymeric matrix to fabricate photowritable and erasable materials with good reproducibility and easier operability. Benefiting from the satisfactory photochromic and prominent anti-fatigue capability in solution as well as in solid state, compound **7**, have been utilized as anti-counterfeiting ink for securing QR/bar code and as a invisible security ink based on “write-erase-write” concept in a non-invasive manner. To the best of our knowledge, this is the first example of DTE-peptide based photochromic materials which have been utilized in latent fingerprints imaging application in forensic sciences as well. We also envision that our work will encourage more scientists in developing many such peptide bridged photochromic fluorescent DTE smart materials for real forensic laboratory investigation in near future.

4.5. Experimental Sections

4.5.1. Materials and Measurements

All the starting analytes used in synthesis were purchased from commercial suppliers and used with no further purification. Tetrahydrofuran was dried with sodium and benzophenone under N₂ atmosphere. K₂CO₃, NBS, glacial acetic acid, were purchased from local chemicals. DMF, acetonitrile (HPLC), MeOH, THF were purchased from Merck chemicals. 2-methyl thiophene and 1.6 M *n*-BuLi in hexane were purchased from Alfa aesar. Octafluorocyclopentene were obtained from TCI Chemicals. HOBt, DCC, HBTU were purchased from SRL. DIPEA, Boc anhydride, SOCl₂ were purchased from Merck chemicals. All the solvents were either HPLC or spectroscopic grade in the optical spectroscopic studies. Thin-layer chromatography (TLC) with Merck silica gel 60 F254

coated (layer thickness: 0.2 mm) was performed for monitoring the reaction and silica gel (mesh 60-120 of 2.5 cm diameter) was used for column chromatography.

4.5.2. Instrumentation

^1H NMR, ^{13}C NMR, and ^{19}F NMR spectra were recorded with Bruker 300 MHz FT-NMR and Bruker 400 MHz FT-NMR spectrometer using TMS (SiMe_4) as an internal reference by using CDCl_3 and $\text{DMSO-}d_6$ as a solvent. The chemical shifts (δ) of the residual solvents are as follows: $\text{CDCl}_3 = 7.26$ (^1H) and $\text{CDCl}_3 = 77.16$ (^{13}C) $\text{DMSO-}d_6 = 2.13$ (^1H) and $\text{DMSO-}d_6 = 39.5$ (^{13}C) are reported in ppm and coupling constants (J) are given in Hz. HRMS spectra were recorded on a water HRMS model XEVO-G2QTOF#YCA351 spectrometer. A Perkin Elmer LX-1 FT-IR spectrophotometer is used for FT-IR spectra characterization. UV-vis absorption spectra were recorded on a SHIMADZU-UV-1900i spectrophotometer at room temperature. Fluorescence emission spectra were measured with a Horiba Scientific Fluoromax-4 spectrophotometer. Solid-state UV-vis and fluorescence emission spectra were measured with a SHIMADZU-UV-1900i spectrophotometer and Horiba Scientific Duetta fluorescence spectrometer respectively. Elemental analysis was performed by Vario EL elemental CHNS analyzer. HPLC was recorded in Agilent Infinity G7161B HPLC system, fitted with a Venusil XPB C18 (4.8×250 mm), 100Å. In the photochromic experiments, the UV light irradiation experiment is carried out using a monochromatic 254 nm lamp (310 $\mu\text{W}/\text{cm}^2$). Scanning electron microscopic (SEM) images are captured in BRUKER INSPECT F50SEM. The rheology experiment is carried out using an AR 2000 advanced rheometer (TA Instruments) using cone-plate geometry in a Peltier plate.

4.5.3. Synthesis and Characterization

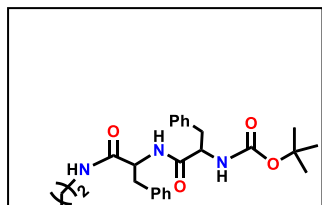
4.5.3.1. General procedure for synthesis of compound 3C_2 and 3C_8

NI-Cn-amine ($n=2,8$) (1 equiv) was dissolved in dry DMF (10 mL) and compound **2** (1 equiv) was added. To this mixture, HBTU (1.5 equiv) and DIPEA (1.5 equiv) were added successively. The reaction mixture was stirred for overnight at room temperature and completion of the reaction was monitored by TLC. After removal of the solvent, the residue was dissolved in water and extracted with EtOAc. The EtOAc extract was concentrated with a rotary evaporator and the crude product was purified by column chromatography (silica

gel, 100-200 ms) to give **3C₂** or **3C₈**. The synthesised compounds **3C₂** and **3C₈** were fully characterised by ¹H NMR, ¹³C NMR and HRMS.

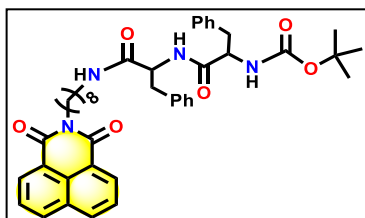
4.5.3.1.A. Synthesis of compound **3C₂**

Utilizing the same method as described above compound **3C₂** was obtained from the reaction of NI-Cn-amine(n=2), **1C₂** (481 mg, 2.004 mmol) and **2** (826.6 mg, 2.004 mmol) in presence of HBTU (1.13 g, 2.98 mmol) and DIPEA (0.55 ml, 2.98 mmol) and the crude product was purified by column chromatography (silica gel; eluent, MeOH:CH₂Cl₂ = 10:90) to give pure product as a pale white solid (597 mg, 47%). ¹H NMR (400 MHz, CDCl₃, ppm) δ 8.60 (d, *J*= 6 Hz, 2H, naphthalimide CH), 8.25 (d, *J*= 9 Hz, 2H, naphthalimide CH), 7.77 (t, *J*= 6 Hz, 2H, naphthalimide CH), 7.28-7.01 (m, 10H, aryl CH), 6.81 (t, *J*= 6 Hz, 1H, amide NH), 6.50 (d, *J*= 6 Hz, 1H, amide NH), 6.41 (t, *J*= 6 Hz, 1H, amide NH), 4.90 (d, *J*= 6 Hz, 1H, αCH), 4.58 (d, *J*= 6 Hz, 1H, αCH), 4.27 (t, *J*= 6 Hz, 2H, CH), 3.63-3.44 (m, 2H, CH), 3.01-2.97 (m, 2H, βCH), 2.83 (s, 1H, βCH), 2.58 (s, 1H, βCH), 1.36 (s, 9H, BOC CH₃). ¹³C NMR (100 MHz, CDCl₃, ppm) δ 170.9 (C_{CO}), 170.6 (C_{CO}), 164.7 (C_{CO}), 155.4 (C_{CO}), 136.5 (Aryl), 136.4 (Aryl), 134.2 (C_{NI}), 131.6 (C_{NI}), 129.4 (Aryl), 129.3 (C_{NI}), 129.3 (C_{NI}), 129.2 (Aryl), 128.7(Aryl), 128.3 (C_{NI}), 127.0 (Aryl), 126.9 (Aryl), 126.6 (C_{NI}), 122.4 (C_{NI}), 55.8 (αC), 54.2 (αC), 39.3 (CH₂), 37.9 (CH₂), 36.8 (βC), 35.5 (βC), 29.7 (tert butyl-C), 28.2 (boc CH₃). HRMS: *m/z* [M+Na]⁺Calcd. for C₃₇H₃₈N₄O₆Na 657.2689; found 657.2684.



Utilizing the same method as described above compound **3C₈** was obtained from the reaction of NI-Cn-amine(n=8), **1C₈** (481 mg, 1.483 mmol) and **2** (611.707 mg, 1.48 mmol) in presence of HBTU (843.08 mg, 2.22 mmol) and DIPEA (0.410 ml, 2.22 mmol) and the crude product was purified by column chromatography (silica gel; eluent, MeOH:CH₂Cl₂ = 10:90) to give pure product as a white solid (520 mg, 49%). ¹H NMR (400 MHz, CDCl₃, ppm) δ 8.63 (d, *J*= 12 Hz, 2H, naphthalimide CH), 8.24 (d, *J*= 12 Hz, 2H, naphthalimide CH), 7.78 (t, *J*= 12 Hz, 2H, naphthalimide CH), 7.36-7.20 (m, 10H, aryl CH), 7.06 (s, 3H, amide NH), 4.90-4.85 (m, 1H, αCH), 4.62 (t, *J*= 8 Hz, 1H, αCH), 4.29 (d, *J*= 12 Hz, 2H, CH), 4.19 (t, *J*= 8 Hz, 2H,

4.5.3.1.B. Synthesis of compound **3C₈**



Employing the same method as described above, compound **3C₈** was obtained from the reaction of NI-Cn-amine (n=8) **1C₈** (481 mg, 1.483 mmol) and **2** (611.707 mg, 1.48 mmol) in presence of HBTU (843.08 mg, 2.22 mmol) and DIPEA (0.410 ml, 2.22 mmol) and the crude product was purified by column chromatography (silica gel; eluent, MeOH:CH₂Cl₂ = 10:90) to give pure product as a white solid (520 mg, 49%). ¹H NMR (400 MHz, CDCl₃, ppm) δ 8.63 (d, *J*= 12 Hz, 2H, naphthalimide CH), 8.24 (d, *J*= 12 Hz, 2H, naphthalimide CH), 7.78 (t, *J*= 12 Hz, 2H, naphthalimide CH), 7.36-7.20 (m, 10H, aryl CH), 7.06 (s, 3H, amide NH), 4.90-4.85 (m, 1H, αCH), 4.62 (t, *J*= 8 Hz, 1H, αCH), 4.29 (d, *J*= 12 Hz, 2H, CH), 4.19 (t, *J*= 8 Hz, 2H,

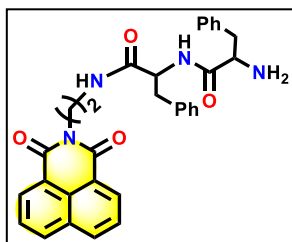
CH), 3.11-2.82 (m, 8H, CH), 1.79-1.69 (m, 2H, CH), 1.34 (s, 9H, BOC CH₃), 1.31-1.21(m, 6H, CH). ¹³C NMR (100 MHz, CDCl₃, ppm) δ 170.8 (C_{CO}), 170.0 (C_{CO}), 165.9 (C_{CO}), 164.2 (C_{CO}), 136.4 (Aryl), 136.1 (Aryl), 133.9 (C_{NI}), 131.6 (C_{NI}), 131.2 (C_{NI}), 129.3 (Aryl), 129.2 (Aryl), 128.8 (Aryl), 128.7 (C_{NI}), 128.6 (Aryl), 128.2 (Aryl), 127.3 (Aryl), 127.1 (Aryl), 126.9 (Aryl), 122.8 (C_{NI}), 56.2 (αC), 53.9 (αC), 40.5 (βC), 39.6 (βC), 37.7 (CH₂), 29.2 (CH₂), 29.1 (CH₂), 29.0 (tert butyl-C), 28.3 (CH₂), 28.1 (CH₂), 28.0 (boc CH₃), 27.0 (CH₂), 26.7 (CH₂), 26.4 (CH₂). HRMS: m/z [M+H]⁺Calcd. for C₄₃H₅₀N₄O₆ 719.3808; found 719.3807.

4.5.3.2. General procedure for synthesis of compound 4C₂ and 4C₈

To a solution of 3C₂ or 3C₈ (1 equiv) in CH₂Cl₂ (10 mL) was stirred with tri-fluoroacetic acid (TFA) (1 mL) for 4h at room temperature. After removal of the solvent with a rotary evaporator, the residue was washed several times with diethyl ether and to give solid 4C₂ or 4C₈. The synthesised compounds 4C₂ and 4C₈ were fully charecterised by ¹H NMR, ¹³C NMR and HRMS.

4.5.3.2.A. Synthesis of compound 4C₂

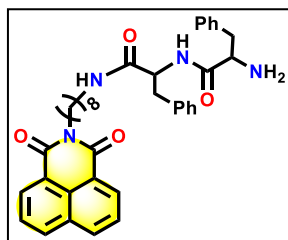
Following the above-described method compound 4C₂ was obtained as pale-yellow solid



(300 mg, 60%) from 3C₂ (597 mg, 0.941 mmol). ¹H NMR (400 MHz, DMSO-*d*₆, ppm) δ 9.01 (d, *J*= 12 Hz, 2H, NH₂), 8.55 (t, *J*= 8 Hz, 2H, naphthalimide CH), 8.14 (s, 4H, naphthalimide CH), 7.93 (t, *J*= 12 Hz, 1H, NH), 7.36-7.24 (m, 10H, aryl CH), 7.21 (s, 1H, NH), 4.57 (q, *J*= 8 Hz, 2H, CH₂), 4.04 (t, *J*= 8 Hz, 2H, CH₂), 3.09-3.04 (m, 2H, α CH), 3.00-2.92 (m, 4H, beta CH₂). ¹³C NMR (100 MHz, DMSO-*d*₆, ppm) δ 171.1, 168.7, 164.2, 138.0, 135.5, 135.1, 134.9, 134.8, 134.7, 131.8, 131.3, 131.2, 131.1, 129.8, 129.0, 128.0, 127.7, 122.7, 122.6, 65.4, 54.0, 42.3, 37.2, 37.0, 31.2. HRMS: m/z [M+H]⁺Calcd. for C₃₂H₃₁N₄O₄ 535.2345; found 535.2361.

4.5.3.2.B. Synthesis of compound 4C₈

Following the above-described method compound **4C₈** was obtained as white solid (280 mg, 63 %) from **3C₈** (597 mg, 0.724 mmol). ¹H NMR (400 MHz, CDCl₃, ppm) δ 8.70 (d, *J*= 12 Hz, 2H, naphthalimide CH), 8.32 (d, *J*= 12 Hz, 2H, naphthalimide CH), 7.85 (t, *J*= 12 Hz, 2H, naphthalimide CH), 7.55 (br s, 2H, NH₂), 7.39 (s, 2H, NH), 7.34-7.18 (m, 10H, aryl CH), 4.67 (s, 2H, CH₂), 4.25 (t, *J*= 12 Hz, 2H, CH₂), 3.24-2.94 (m, 6H, CH), 1.38-1.31 (m, 12H, CH₂). ¹³C NMR (100 MHz, DMSO-*d*₆, ppm) δ 170.3, 168.2, 163.8, 137.8, 135.2, 134.6, 131.7, 131.1, 130.0, 129.6, 128.9, 128.6, 127.8, 127.7, 122.5, 119.2, 116.2, 54.9, 54.7, 53.9, 53.7, 38.6, 37.4, 34.7, 29.3, 29.1, 27.9, 27.0, 26.7. HRMS: *m/z* [M+Na]⁺ Calcd. for C₃₈H₄₂N₄O₄Na 641.3103; found 641.3106.

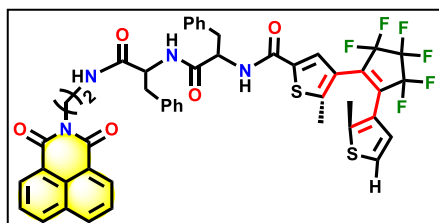


4.5.3.3. General procedure for synthesis of compound 6 and 7

To a solution of **4C₂** or **4C₈** (1 equiv) in dry DMF (10 mL) was added **5** (1 equiv), HBTU (1.5 equiv) and DIPEA (1.5 equiv) at 0°C. The reaction mixture was stirred for overnight at room temperature and completion of the reaction was monitored by TLC. After removal of the solvent, the residue was dissolved in water and extracted with EtOAc and washed several times by brine solution. The EtOAc extract was concentrated with a rotary evaporator and crude product was purified by column chromatography (silica gel) to give **6** or **7** as solid product.

4.5.3.3.A. Synthesis of compound 6

Utilizing the same method as described above compound **6** was obtained from the reaction of **4C₂** (200 mg, 0.3743 mmol) and **5** (170.78 mg, 0.3743 mmol) in presence of HBTU (212.79, 0.5614 mmol) and DIPEA (0.1 mL, 0.5614 mmol). After removal of the solvent, the residue was dissolved in water and extracted with EtOAc and washed several times by brine solution. The EtOAc extract was concentrated with a rotary evaporator and crude product was purified by column chromatography (silica gel, eluent, EtOAc:Hexane =

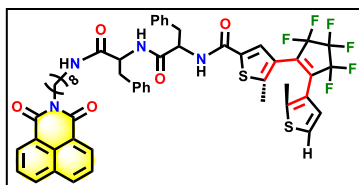


40:60) to give **6** as a pale yellow solid (128 mg, 37 %). The synthesised compound **6** was fully characterised by ^1H NMR, ^{13}C NMR, ^{19}F NMR, HRMS and elemental analysis.

^1H NMR (400 MHz, CDCl_3 , ppm) δ 8.59 (d, $J=8$ Hz, 2H, naphthalimide CH), 8.23 (d, $J=8$ Hz, 2H, naphthalimide CH), 7.76 (t, $J=8$ Hz, 2H, naphthalimide CH), 7.20-6.92 (m, 13H, aryl CH), 6.74 (t, $J=8$ Hz, 1H, NH), 6.67-6.60 (m, 1H, NH), 6.41-6.34 (m, 1H, NH), 4.81-4.74 (m, 1H, CH), 4.60-4.56 (m, 1H, CH), 4.34-4.19 (m, 3H, CH), 3.70-3.63 (m, 1H, CH), 3.46-3.40 (m, 1H, CH), 3.07-3.01 (m, 2H, CH), 2.86-2.81 (m, 1H, CH), 1.91 (s, 6H, CH_3). ^{13}C NMR (100 MHz, CDCl_3 , ppm) δ 170.5, 164.9, 160.9, 160.8, 147.3, 142.0, 136.6, 136.4, 136.3, 134.5, 132.2, 131.7, 129.5, 129.4, 129.4, 129.3, 129.3, 129.1, 128.8, 128.4, 128.3, 128.1, 127.2, 127.1, 126.6, 125.7, 124.7, 124.2, 122.4, 120.2, 54.9, 54.7, 39.6, 38.2, 31.5, 29.8, 14.5, 13.7. ^{19}F NMR (376 MHz, CDCl_3 , ppm) δ -110.03 (s, 2F), -110.33 (s, 2F), -131.87 (t, 2F). HRMS: m/z $[\text{M}+\text{H}]^+$ Calcd. for $\text{C}_{48}\text{H}_{39}\text{F}_6\text{N}_4\text{O}_5\text{S}_2$ 929.2266; found 929.2263. Elemental analysis: Anal. Calcd. for $\text{C}_{47}\text{H}_{39}\text{F}_6\text{N}_4\text{O}_5\text{S}_2$: C 61.49; H 4.28; N 6.10; Found: C 68.33; H 4.39; N 6.03.

4.5.3.3.B. Synthesis of compound 7

Utilizing the same method as described above compound **7** was obtained from the reaction



of **4C8** (200 mg, 0.6169 mmol) and **5** (254.4735 mg, 0.6169 mmol) in presence of HBTU (350.70, 0.9253 mmol) and DIPEA (0.17 mL, 0.9253 mmol). After removal of the solvent, the residue was dissolved in water and extracted with EtOAc

and washed several times by brine solution. The EtOAc extract was concentrated with a rotary evaporator and crude product was purified by column chromatography (silica gel, eluent, EtOAc:Hexane = 40:60) to give **7** as a pale yellow solid (235 mg, 38%). The synthesised compound **7** was fully characterised by ^1H NMR, ^{13}C NMR, ^{19}F NMR, HRMS, IR spectra and elemental analysis.

^1H NMR (400 MHz, CDCl_3) 8.59 (2H, d, $J=8$ Hz, naphthalimide CH), 8.21 (d, $J=8$ Hz, 2H, naphthalimide CH), 7.75 (t, $J=8$ Hz, 2H, naphthalimide CH), 7.42 (s, 1H, NH), 7.21-7.11 (m, 10H, aryl H), 7.08-7.06 (m, 3H, aryl H), 7.01 (d, $J=8$ Hz, 2H, NH), 7.94-7.81 (m, 2H, alpha CH), 4.60-4.57 (m, 2H, CH_2), 4.18-4.15 (m, 2H, CH_2), 3.10-2.96 (m, 10H, CH_2), 1.90 (s, 3H, CH_3), 1.86 (s, 3H, CH_3), 1.74-1.68 (m, 6H, CH_2). ^{13}C NMR (100 MHz, CDCl_3 , ppm) δ 170.5, 170.0, 164.3, 160.8, 147.1, 141.9, 136.4, 136.2, 136.2, 136.1, 133.9, 133.9,

131.6, 131.3, 131.2, 129.4, 129.3, 128.8, 128.7, 128.6, 128.2, 128.0, 127.2, 127.0, 125.6, 124.5, 124.1, 124.0, 122.7, 54.9, 54.8, 40.4, 39.6, 38.5, 38.2, 29.7, 29.2, 28.0, 27.0, 26.7, 22.7, 14.6, 14.4. ^{19}F NMR (376 MHz, CDCl_3 , ppm) δ -110.05, -110.31, -131.90. HRMS: m/z $[\text{M}+\text{H}]^+$ Calcd. for $\text{C}_{54}\text{H}_{51}\text{F}_6\text{N}_4\text{O}_5\text{S}_2$ 1013.3205; found 1013.3208. Elemental analysis: Anal. Calcd. for $\text{C}_{54}\text{H}_{50}\text{F}_6\text{N}_4\text{O}_5\text{S}_2$: C 66.11; H 5.14; N 5.71; Found: C 66.75; H 5.69; N 5.02.

4.6. References

1. (a) Velema, W. A.; Szymanski, W.; Feringa, B. L. *J. Am. Chem. Soc.* **2014**, *136*, 2178-2191; (b) Hüll, K.; Morstein, J.; Trauner, D. *Chem. Rev.* **2018**, *118*, 10710-10747.
2. (a) Pianowski, Z. L. *Chem. Eur. J.* **2019**, *25*, 5128-5144; (b) J. Zhang, H. Tian, *Adv. Opt. Mater.* **2018**, *6*, 1701278.
3. Poon, C.-T. Lam, W. H.; Wong, H.-L.; Yam, V. W.-W.; *J. Am. Chem. Soc.* **2010**, *132*, 13992-13993.
4. Büllmann, S. M.; Kolmar, T.; Zorn, N. F.; Zaumseil, J.; Jäschke, A. *Angew. Chem. Int. Ed.* **2022**, *61*, e202117735.
5. Irie, M.; Uchida, K. *Bull. Chem. Soc. Jpn.* **1998**, *71*, 985-996.
6. Irie, M.; Lifka, T.; Kobatake, S.; Kato, N. *J. Am. Chem. Soc.* **2000**, *122*, 4871-4876.
7. Jia, C.; Migliore, A.; Xin, N.; Huang, S.; Wang, J.; Yang, Q.; Wang, S.; Chen, H.; Wang, D.; Feng, B.; Liu, Z.; Zhang, G.; Qu, D. H.; Tian, H.; Ratner, M. A.; Xu, H. Q.; Nitzan, A.; Guo, X. *Science* **2016**, *352*, 1443-1445.
8. Wesenhagen, P.; Areephong, J.; Landaluce, T. F.; Heures, N.; Katsoni, N.; Hjelm, J.; Rudolf, P.; Browne, W. R.; Feringa, B. L. *Langmuir* **2008**, *12*, 6334-6342.
9. Babii, O.; Afonin, S.; Diel, C.; Huhn, M.; Dommermuth, J.; Schober, T.; Koniev, S.; Hrebonkin, A.; Nesterov-Mueller, A.; Komarov, I.V.; Ulrich, A. S. *Angew. Chem. Int. Ed.* **2021**, *60*, 21789-21794.
10. (a) Komarov, I. V.; Afonin, S.; Babii, O.; Schober, T.; Ulrich, A. S. *Chem. Eur. J.* **2018**, *24*, 11245-11254; (b) Nishitani, N.; Hirose, T.; Matsuda, K. *Commun.* **2019**, *55*, 5099-5102
11. Schober, T.; Wehl, I.; Afonin, S.; Babii, O.; Iampolska, A.; Schepers, U.; Komarov, I. V.; Ulrich, A. S. *ChemPhotoChem* **2019**, *3*, 384-391.
12. Szymański, W.; Beierle, J. M.; Kistemaker, H. A.; Velema, W. A.; Feringa, B. L. *Chem. Rev.* **2013**, *113*, 6114- 6178.

13. (a) Afonin, S.; Babii, O.; Reuter, A.; Middel, V.; Takamiya, M.; Strähle, U.; Komarov, I. V.; Ulrich, A. S.; *Beilstein J. Org. Chem.* **2020**, *16*, 39-49, b) Babii, O.; Afonin, S.; Garmanchuk, L. V.; Nikulina, V. V.; Nikolaienko, T. V.; Storozhuk, O. V.; Shelest, D. V.; Dasyukevich, O. I.; Ostapchenko, L. I.; Iurchenko, V.; Zozulya, S.; Ulrich, A. S.; Komarov, I. V. *Angew. Chem., Int. Ed.* **2016**, *55*, 5493-5496.
14. Babii, O.; Afonin, S.; Berditsch, M.; Reiber, S.; Mykhailiuk, P. K.; Kubyshkin, V. S.; Steinbrecher, T.; Ulrich, A. S.; Komarov, I. V. *Angew. Chem.* **2014**, *126*, 3460-3463.
15. Jiang, Y.; Zeng, F.; Gong, R.; Guo, Z.; Chen, C.-F.; Wan, X. *Soft Matter*, **2013**, *9*, 7538-7544.
16. Cao, X.; Zhou, J.; Zou, Y.; Zhang, M.; Yu, X.; Zhang, S.; Yi, T.; Huang, C. *Langmuir* **2011**, *27*, 5090-5097.
17. Li, C.; Xiong, K.; Chen, Y.; Fan, C.; Wang, Y.-L.; Ye, H.; Zhu, M.-Q. *ACS Appl. Mater. Interfaces* **2020**, *12*, 27651-27662.
18. Wang, Z.; Zhou, Y.; Xu, R.; Xu, Y.; Dang, D.; Shen, Q.; Meng, L.; Tang, B. Z. *Coord. Chem. Rev.* **2022**, *451*, 214279.
19. Chen, S.; Li, W.; Li, X.; Zhu, W.-H. *J. Mater. Chem. C* **2017**, *5*, 2717-2722.
20. Chen, L.; Zhang, J.; Wang, Q.; Zou, L. *Dyes Pigments* **2015**, *123*, 112-115.
21. Lim, S.-J.; An, B.-K.; Park, S. Y. *Macromolecules* **2005**, *38*, 6236-6239.
22. Li, Z.; Liu, Y.; Yang, X.-G.; Gao, X.; Zhang, Y.; Zhang, H.; Kang, G.; Wang, M.; Guo, H. *J. Lumin.* **2022**, *250*, 119061.
23. Liu, G.; Zhang, Y.-M.; Zhang, L.; Wang, C.; Liu, Y. *ACS Appl. Mater. Interfaces* **2018**, *10*, 12135-12140.
24. Gong, S.-S.; Zheng, C.-H.; Chen, Z.-Z.; Yang, D.-Z.; Chi, M.; Pu, S.-Z.; Sun, Q.; *Molecules* **2021**, *26*, 5382.
25. Kono, L.; Nakagawa, Y.; Fujimoto, A.; Nishimura, R.; Hattori, Y.; Mutai, T.; Yasuda, N.; Koizumi, K.; Yokojima, S.; Nakamura, S.; Uchida, K. *Beilstein J. Org. Chem.* **2019**, *15*, 2204-2212.
26. Rossos, A. K.; Katsiaflaka, M.; Cai, J.; Myers, S. M.; Koenig, E.; Bückner, R.; Keskin, S.; Kassier, G.; Gengler, R. Y. N.; Miller, R. J. D.; Murphy, R. S. *Langmuir* **2018**, *34*, 10905-10912.
27. Hsu, S.-M.; Chakravarthy, R. D.; Cheng, H.; Wu, F.-Y.; Lai, T.-S.; Lin, H.-C. *New J. Chem.* **2018**, *42*, 4443-4449.
28. Chakravarthy, R. D.; Mohammed, M.; Lin, H. C. *Chem. - An Asian J.* **2020**, *15*, 2696-2705.

-
29. Irie, M.; Fukaminato, T.; Matsuda, K.; Kobatake, S. *Chem. Rev.* **2014**, *114*, 12174-12277.
 30. Kandasamy, Y. S.; Cai, J.; Beler, A.; Jemeli Sang, M.-S.; Andrews, P. D.; Murphy, R. S.; *Org. Biomol. Chem.* **2015**, *13*, 2652-2663.
 31. Wu, J.; T. Yi, Q. Xia, Y. Zou, F. Liu, J. Dong, T. Shu, F. Li, C. Huang, *Chem. Eur. J.* **2009**, *15*, 6234-6243.
 32. (a) Devi, K.; Sarma, R. J. *ChemPhotoChem* **2017**, *1*, 524-531; (b) Ghosh, S.; Adler-Abramovich, L.; Gazit, E.; Verma, S. *Tetrahedron* **2013**, *69*, 2004-2009; (c) Fujimoto, K.; Maruyama, T.; Okada, Y.; Itou, T.; Inouye, M. *Tetrahedron* **2013**, *69*, 6170-6175; (d) Liu, D.; Sponza, A. D.; Yang, D.; Chiu, M.; *Angew. Chem. Int. Ed.* **2019**, *58*, 16210-16216.
 33. Kinashi, K.; Kotake, T.; Ono, Y.; Ishida, K.; Ueda, Y. *Opt. Mater.* **2009**, *31*, 1711-1714.
 34. Ventura, B.; Bertocco, A.; Braga, D.; Catalano, L.; d'Agostino, S.; Grepioni, F.; Taddei, P. *J. Phys. Chem. C* **2014**, *118*, 18646-18658.
 35. Kakwere, H.; Payne, R. J.; Jolliffe, K. A.; Perrier, S. *Soft Matter* **2011**, *7*, 3754-3757.
 36. Tanaka, Y.; Ishisaka, T.; Inagaki, A.; Koike, T.; Lapinte, C.; Akita, M. *Chem. Eur. J.* **2010**, *16*, 4762-4776.
 37. Wan, H.; Xue, H.; Ling, Y.; Qiao, Y.; Chen, Y.; Zhou, G. *Phys. Chem. Chem. Phys.* **2018**, *20*, 14348-14356.
 38. Irie, M.; Sakemura, K.; Okinaka, M.; Uchida, K. *J. Org. Chem.* **1995**, *60*, 8305-8309.
 39. Gopikrishna, P.; Meher, N.; Iyer, P. K. *ACS Appl. Mater. Interfaces* **2018**, *10*, 12081-12111.
 40. Giordano, L.; Macareno, J.; Song, L.; Jovin, T. M.; Irie, M.; Jares-Erijman, E. A. *Molecules* **2000**, *5*, 591-593.
 41. Liu, B.; Gaylord, B. S.; Wang, S.; Bazan, G. C. *J. Am. Chem. Soc.* **2003**, *125*, 6705-6714.
 42. Felip-León, C.; Galindo, F.; Miravet, J. F. *Nanoscale* **2018**, *10*, 17060-17069.
 43. (a) Shi, H.; Kwok, R. T. K.; Liu, J.; Xing, B.; Tang, B. Z.; Liu, B. *J. Am. Chem. Soc.* **2012**, *134*, 17972-17981; (b) Wang, E.; Lam, J. W. Y.; Hu, R.; Zhang, C.; Zhao, Y. S.; Tang, B. Z. *J. Mater. Chem. C* **2014**, *2*, 1801-1807.
 44. (a) Shen, X. Y.; Wang, Y. J.; Zhao, E.; Yuan, W. Z.; Liu, Y.; Lu, P.; Qin, A.; Ma, Y.; Sun, J. Z.; Tang, B. Z. *J. Phys. Chem. C* **2013**, *117*, 7334-7347; (b) Mei, J.; Hong, Y.; Lam, J. W. Y.; Qin, A.; Tang, Y.; Tang, B. Z. *Adv. Mater.* **2014**, *26*, 5429.
-

45. Würthner, F.; Kaiser, T. E.; Saha-Möller, C. R. *Angew. Chem. Int. Ed.* **2011**, *50*, 3376-3410.
46. (a) De, S.; Das, G. *Langmuir* **2022**, *38*, 6158-6163; (b) Soni, M.; Das, S. K.; Sahu, P. K.; Kar, U. P.; Rahaman, A.; Sarkar, M. *J. Phys. Chem. C* **2013**, *117*, 14338-14347.
47. Wu, T.; Huang, J.; Yan, Y. *Chem. Asian J.* **2019**, *14*, 730.
48. Li, H.; Cheng, J.; Zhao, Y.; Lam, J. W. Y.; Wong, K. S.; Wu, H.; Li, B. S.; Tang, B. Z. *Mater. Horizons* **2014**, *1*, 518-521.
49. Podder, D.; Bera, S.; Debnath, M.; Das, T.; Haldar, D. *J. Mater. Chem. B* **2017**, *5*, 7583-7590.
50. Duan, P.; Cao, H.; Zhang, L.; Liu, M. *Soft Matter* **2014**, *10*, 5428-5448.
51. Chen, S.; Slattum, P.; Wang, C.; Zang, L. *Chem. Rev.* **2015**, *115*, 11967-11998.
52. (a) Singh, A.; Verma, P.; Samanta, D.; Dey, A.; Dey, J., Majhi, T. K. *J. Mater. Chem. A* **2021**, *9*, 5780-5786; (b) Verma, P.; Singh, A.; Rahimi, F. A.; Majhi, T. K. *J. Mater. Chem. A* **2021**, *9*, 13608-13614.
53. (a) Garain, S.; Garain, B. C.; Eswaramoorthy, M.; Pati, S. K.; George, S. J. *Angew. Chem. Int. Ed.* **2021**, *60*, 19720; (b) Pradhan, B.; Gupta, M.; Pal, S. K.; Achalkumar, A. *S. J. Mater. Chem. C* **2016**, *4*, 9669-9673.
54. Pramanik, A.; Karimadom, B. R.; Kornweitz, H.; Levine, M. *ACS Omega* **2021**, *6*, 32722-32729.
55. (a) Abdollahi, A.; Roghani-Mamaqani, H.; Razavi, B.; Salami-Kalajahi, M. *ACS Nano* **2020**, *14*, 14417-14492; (b) Karmakar, M.; Bag, S. K.; Mondal, B.; Thakur, A. *J. Mater. Chem. C* **2022**, *10*, 8860-8873.
56. Singla, N.; Kaur, M.; Sofat, S. *Forensic Sci. Int.* **2020**, *309*, 110187.
57. Li, B.; Li, Y.; Tomkiewicz-Raulet, C.; Dao, P.; Lietha, D.; Yen-Pon, E.; Du, Z.; Coumoul, X.; Garbay, C.; Etheve-Quellejeu, M.; Chen, H. *J. Med. Chem.* **2020**, *63*, 12707-12724.

Spectroscopic Details

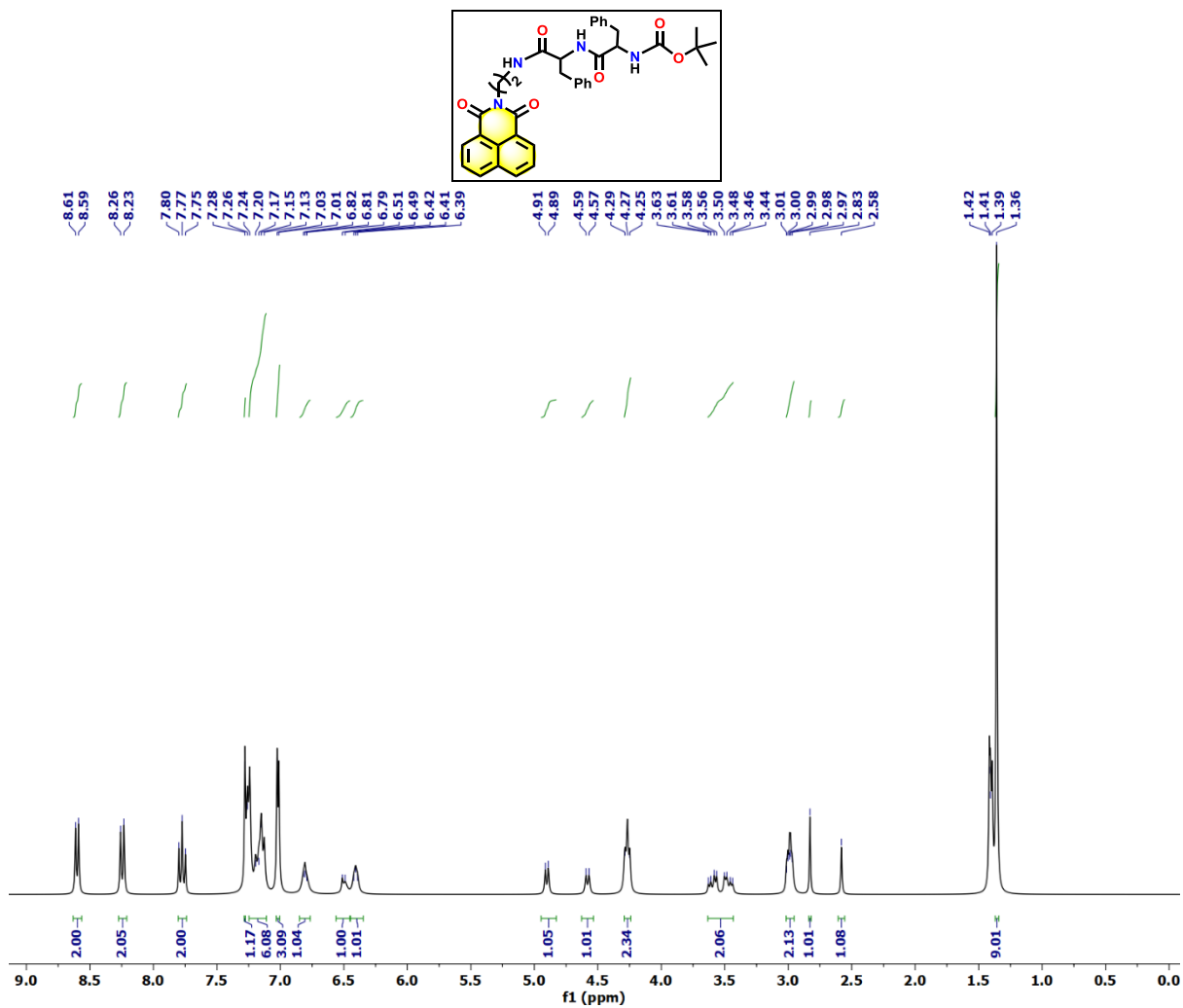


Figure 4.14. ¹H NMR spectra of compound **3C₂** in CDCl₃ as a solvent.

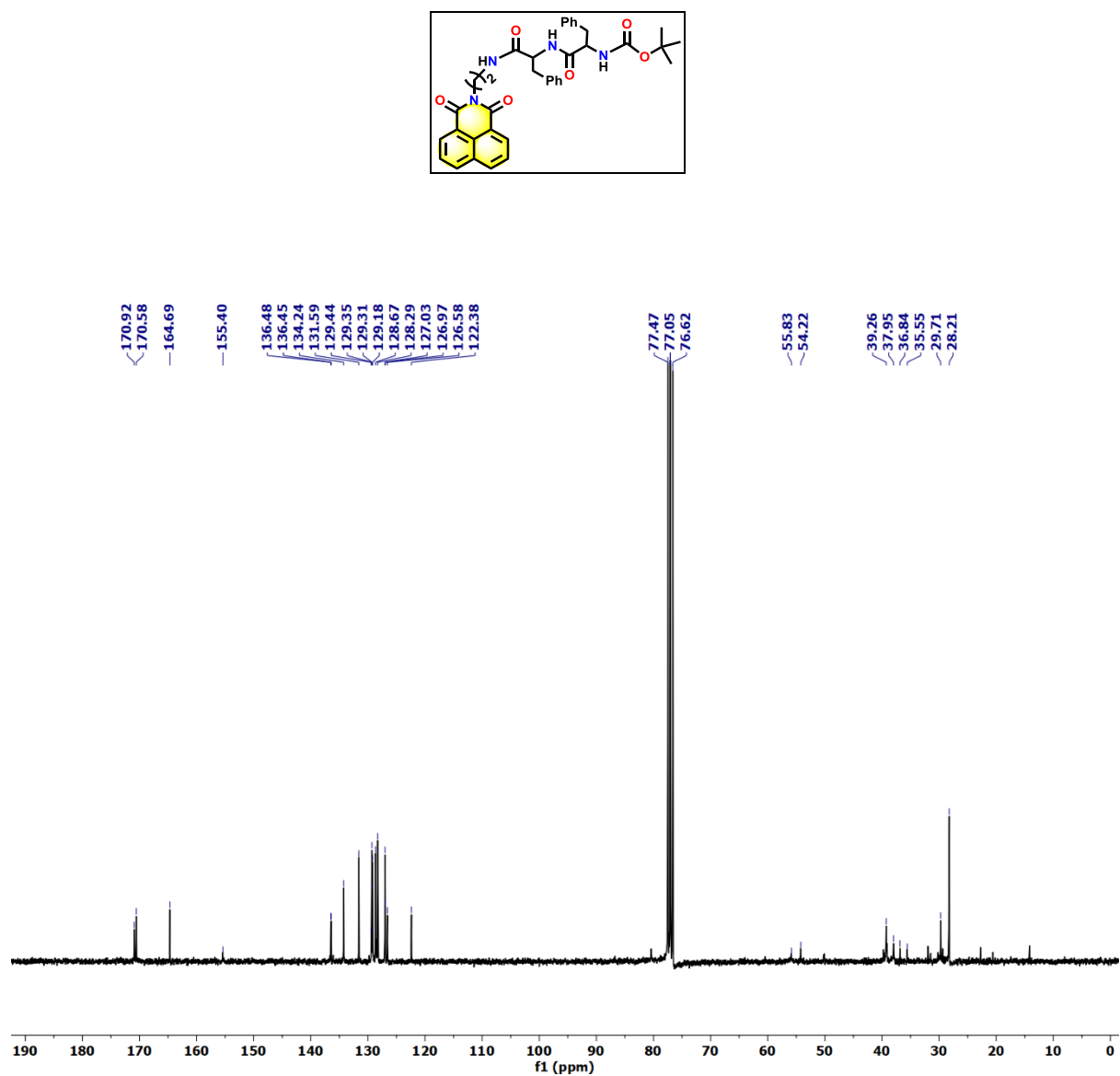


Figure 4.15. ^{13}C NMR spectra of compound 3C_2 in CDCl_3 as a solvent.

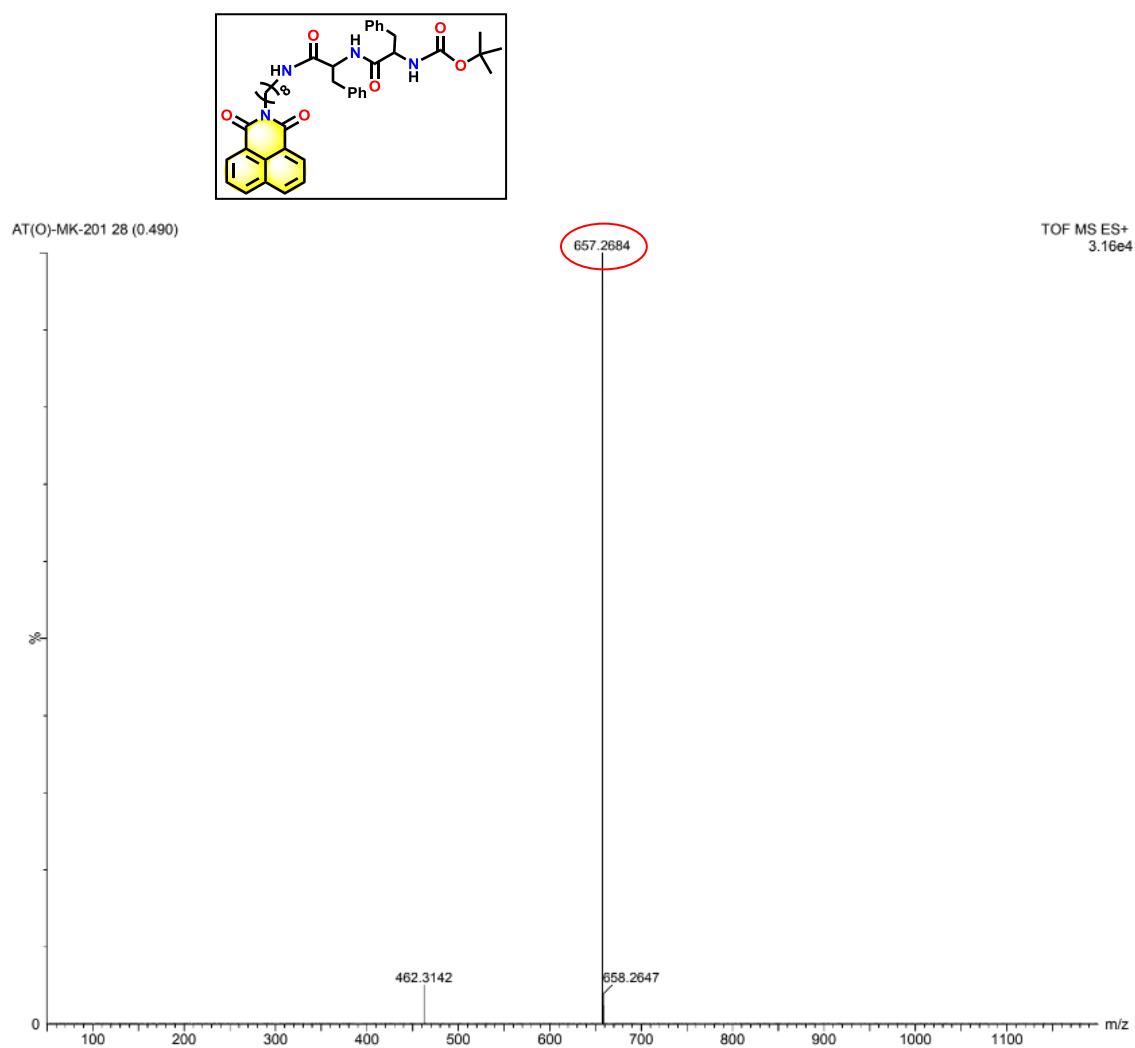


Figure 4.16. HRMS spectra of compound 3C₂.

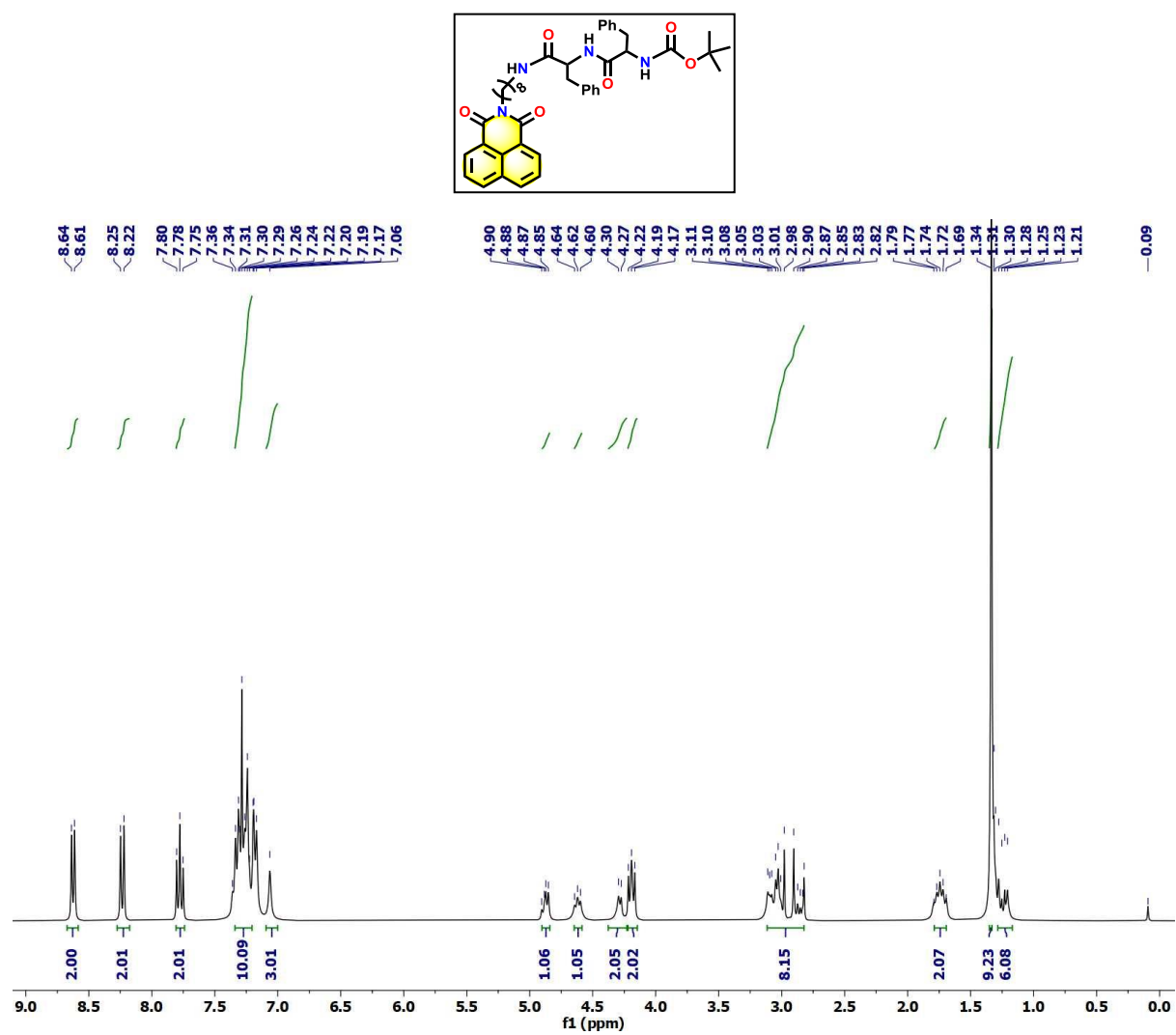


Figure 4.17. ^1H NMR spectra of compound 3C_8 in CDCl_3 as a solvent.

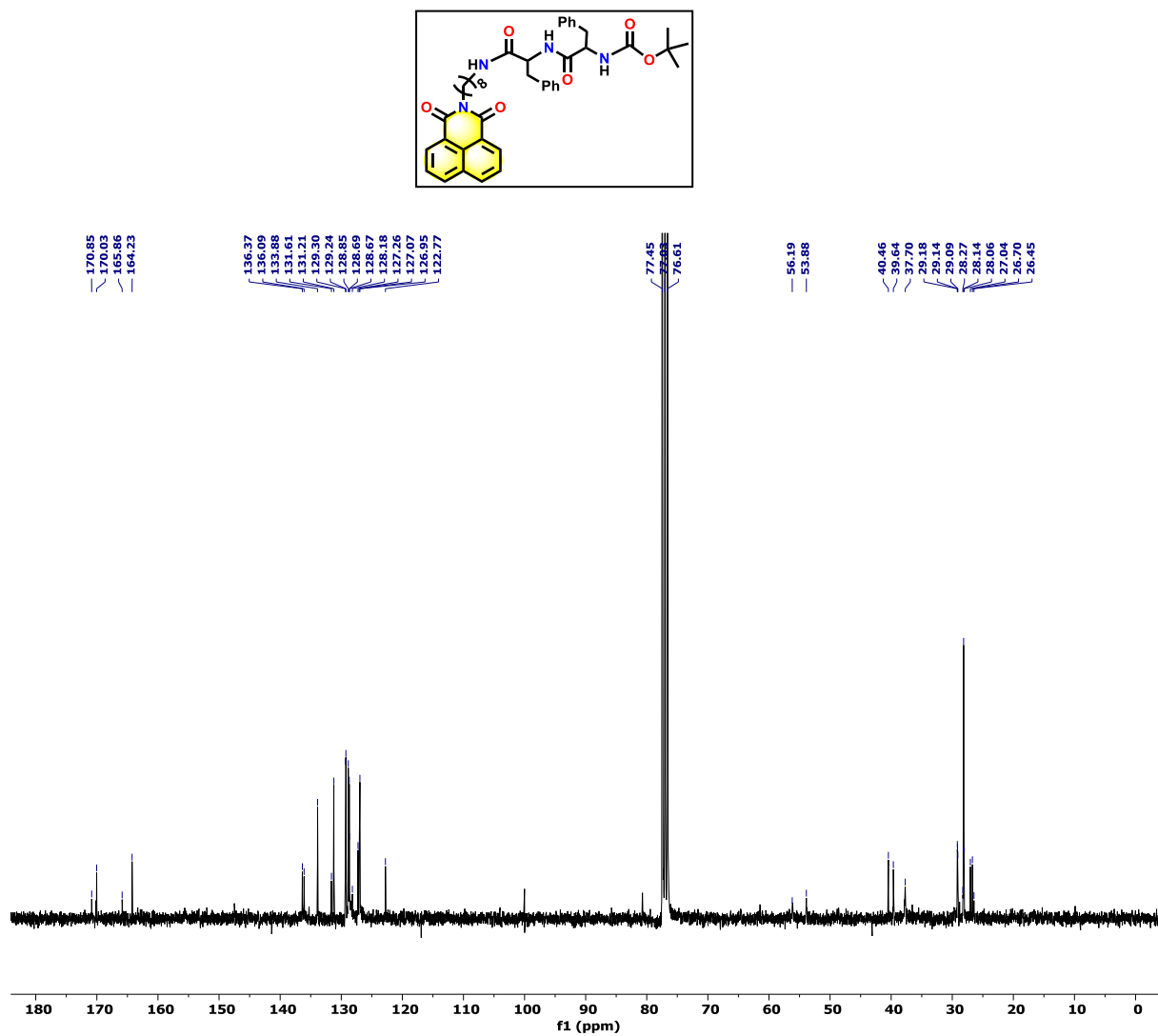


Figure 4.18. ^{13}C NMR spectra of compound 3C₈ in CDCl₃ as a solvent.

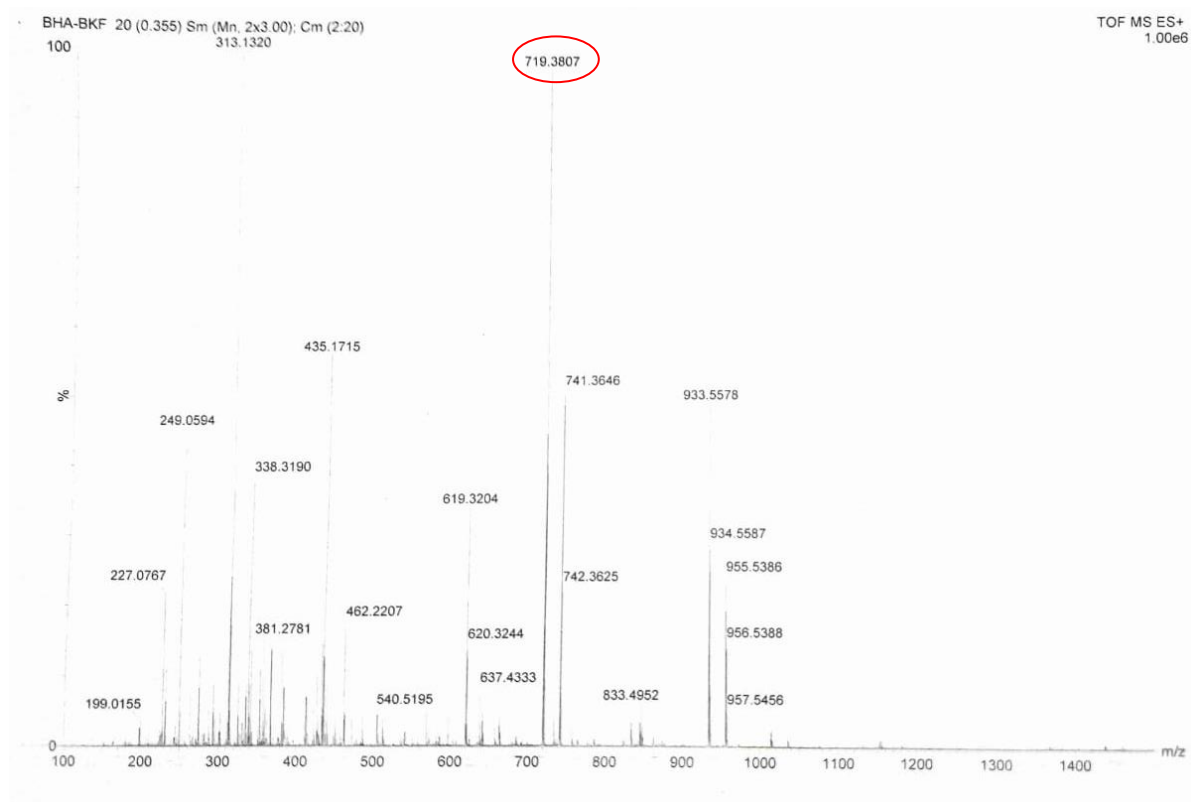
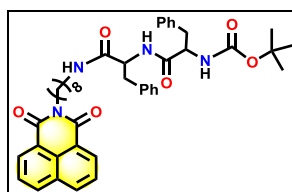


Figure 4.19. HRMS spectra of compound 3C₈.

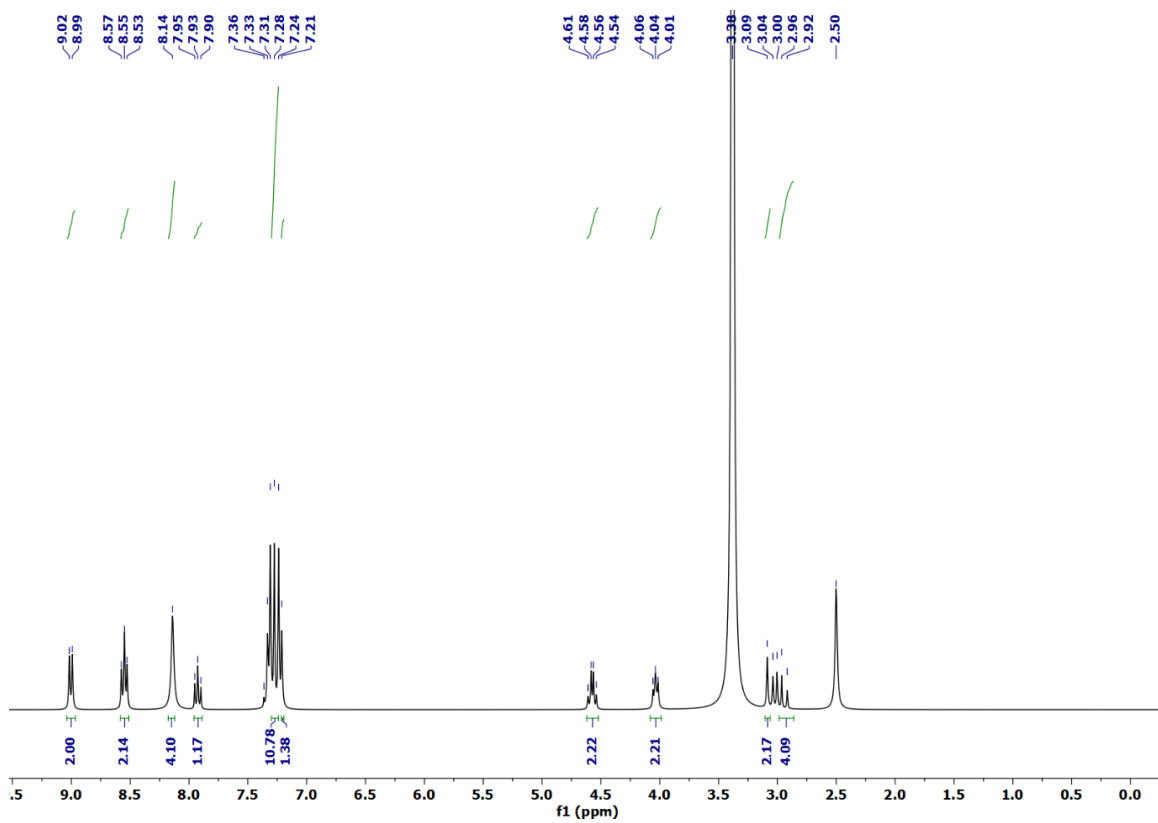
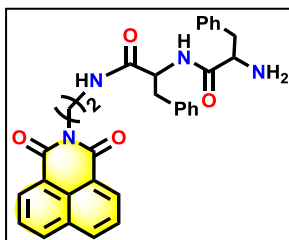


Figure 4.20. ^1H NMR spectra of compound 4C_2 in DMSO-d_6 as a solvent.

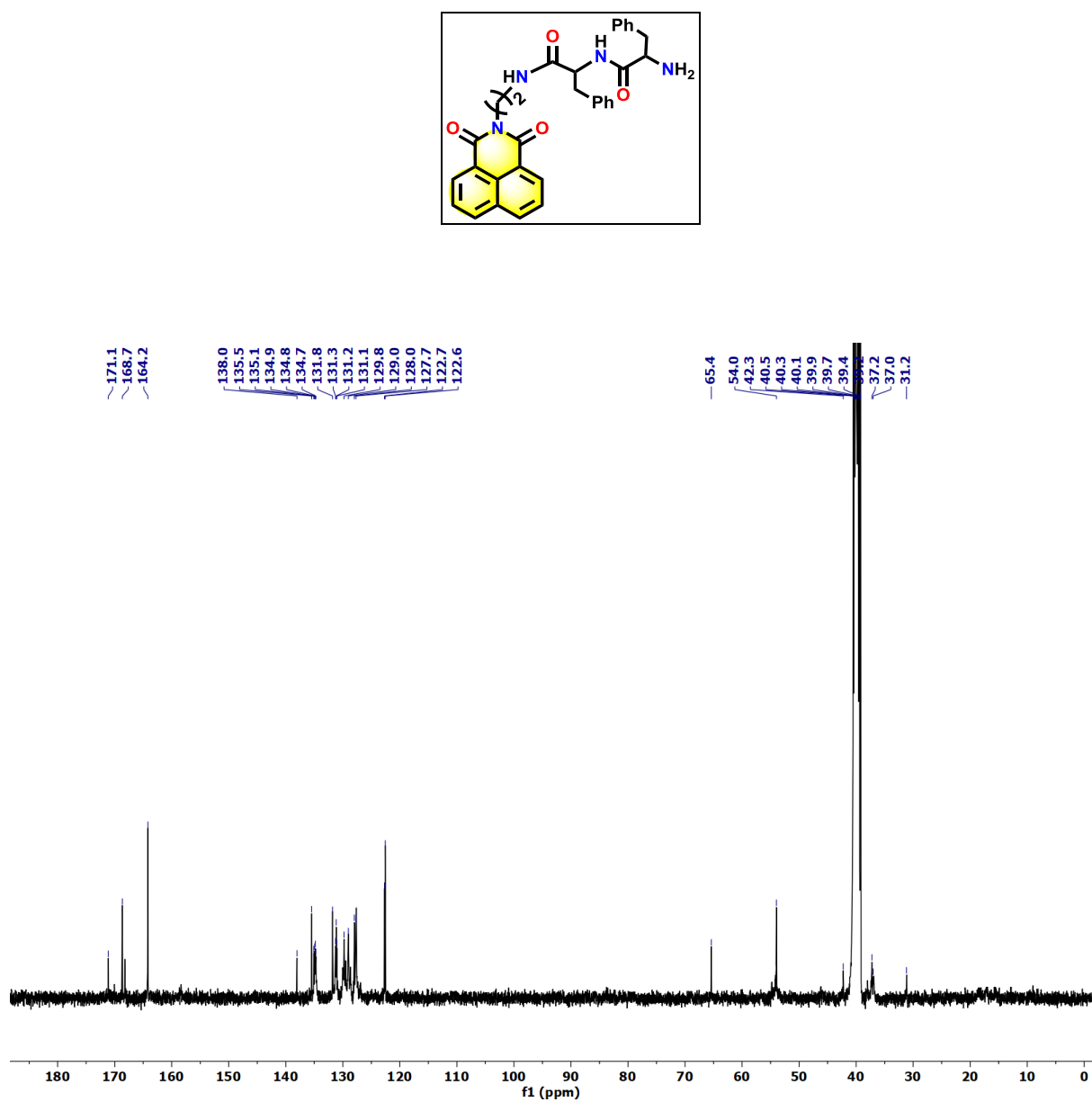


Figure 4.21. ^{13}C NMR spectra of compound 4C₂ in DMSO-d₆ as a solvent.

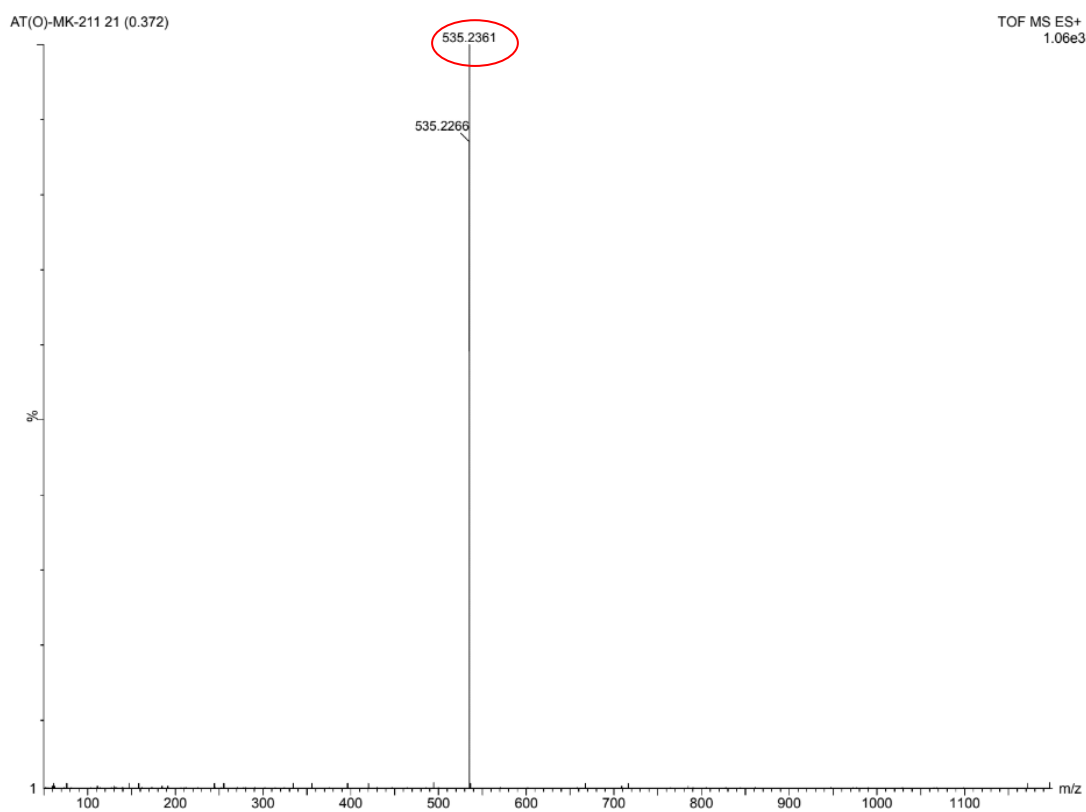
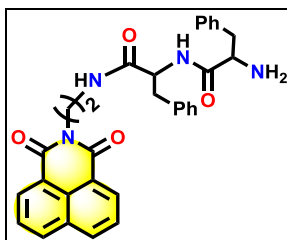


Figure 4.22. HRMS spectra of compound **4C₂**.

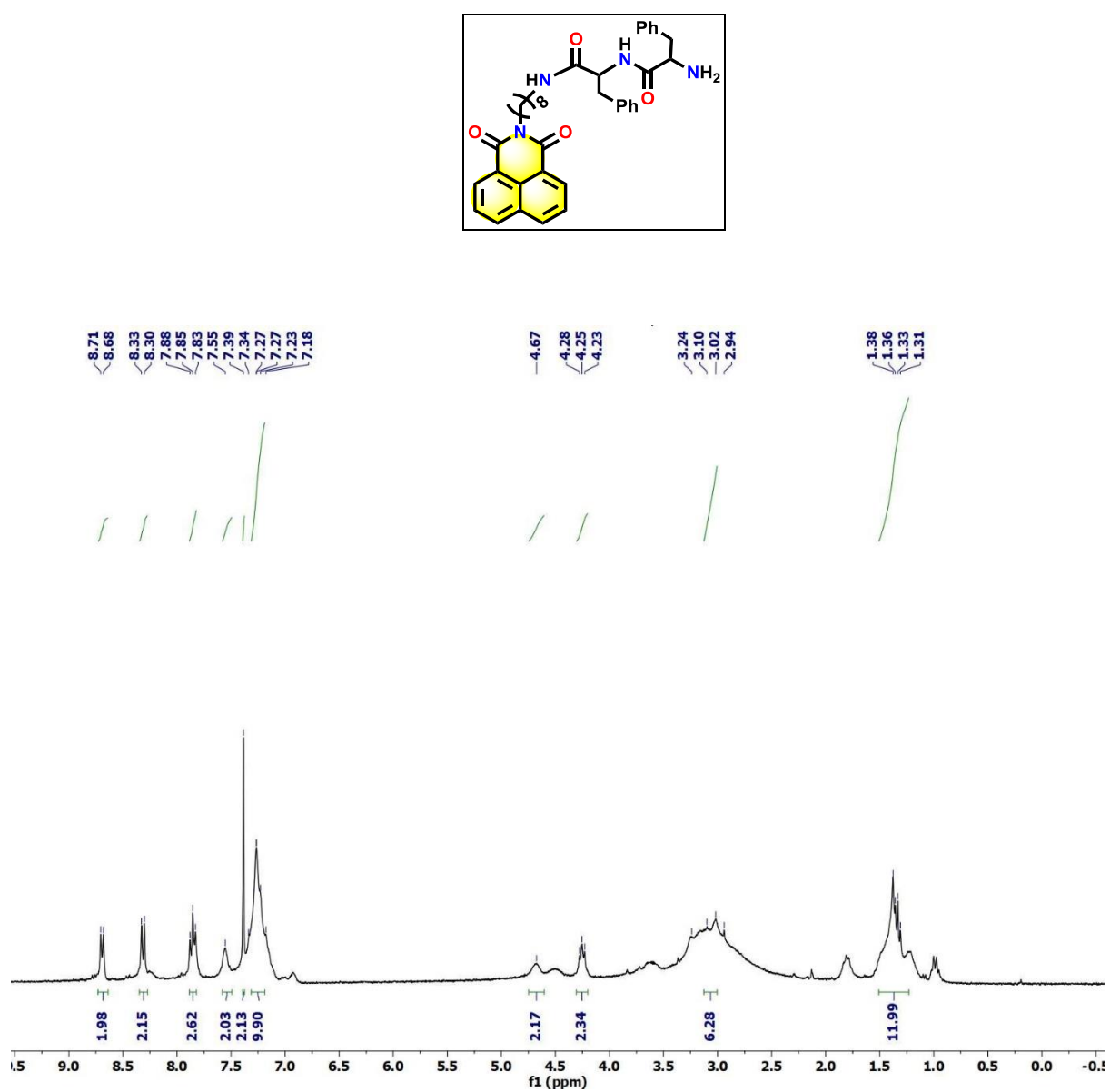


Figure 4.23. ¹H NMR spectra of compound **4C₈** in CDCl₃ as a solvent.

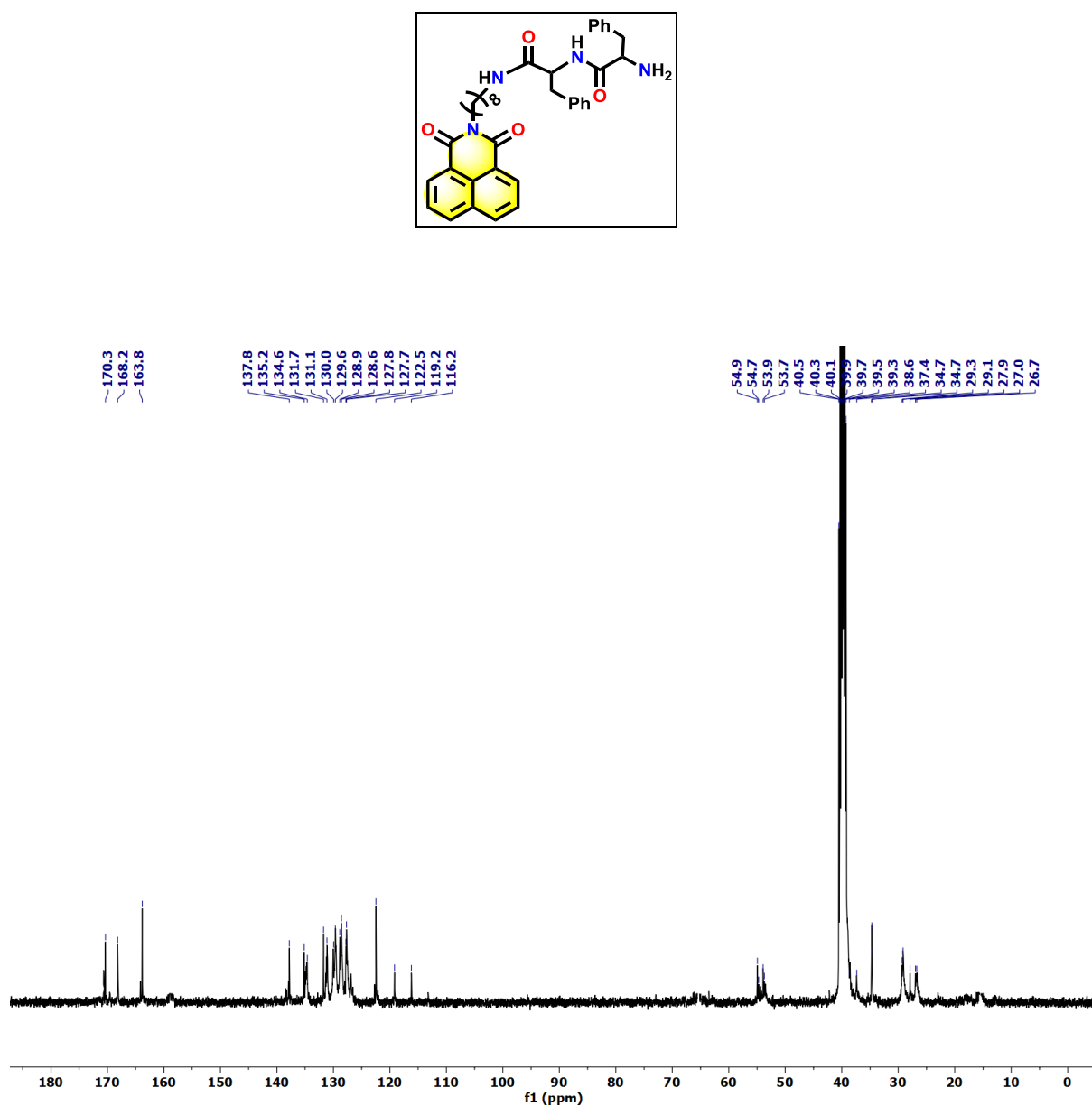


Figure 4.24. ¹³C NMR spectra of compound **4C₈** in DMSO-d₆ as a solvent.

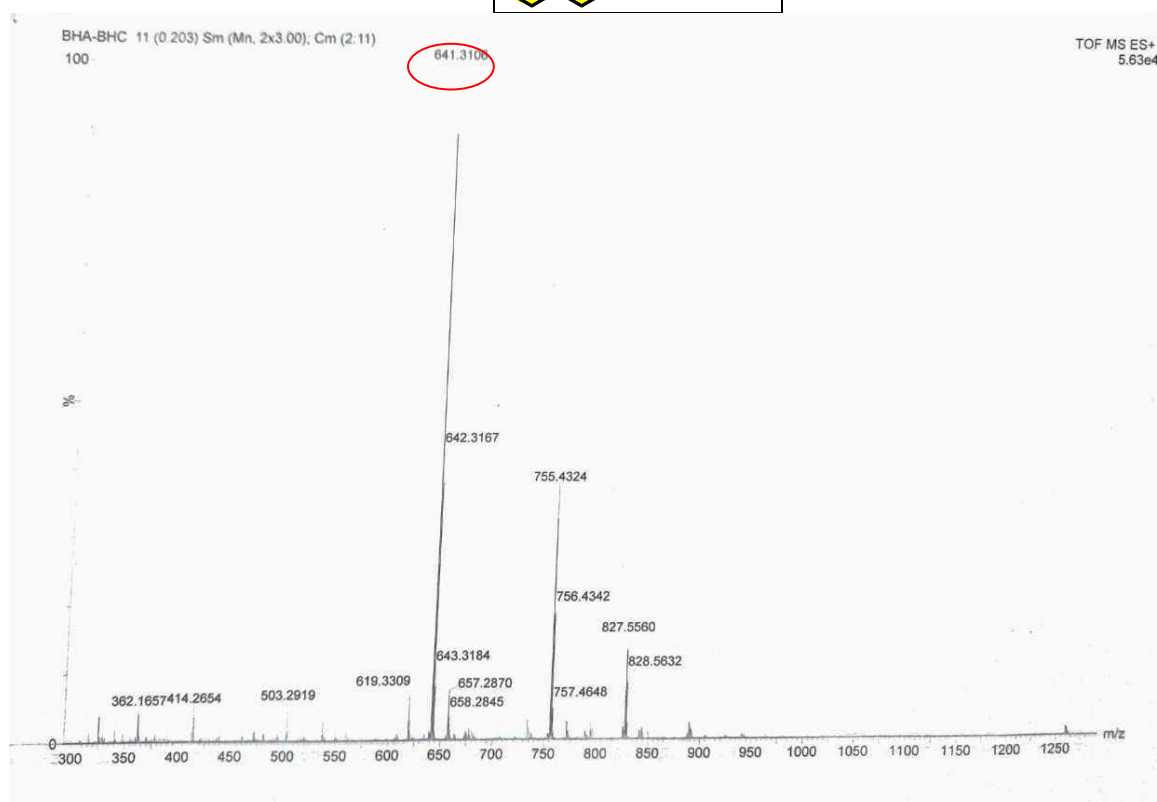
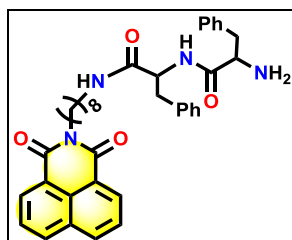


Figure 4.25. HRMS spectra of compound **4C₈**.

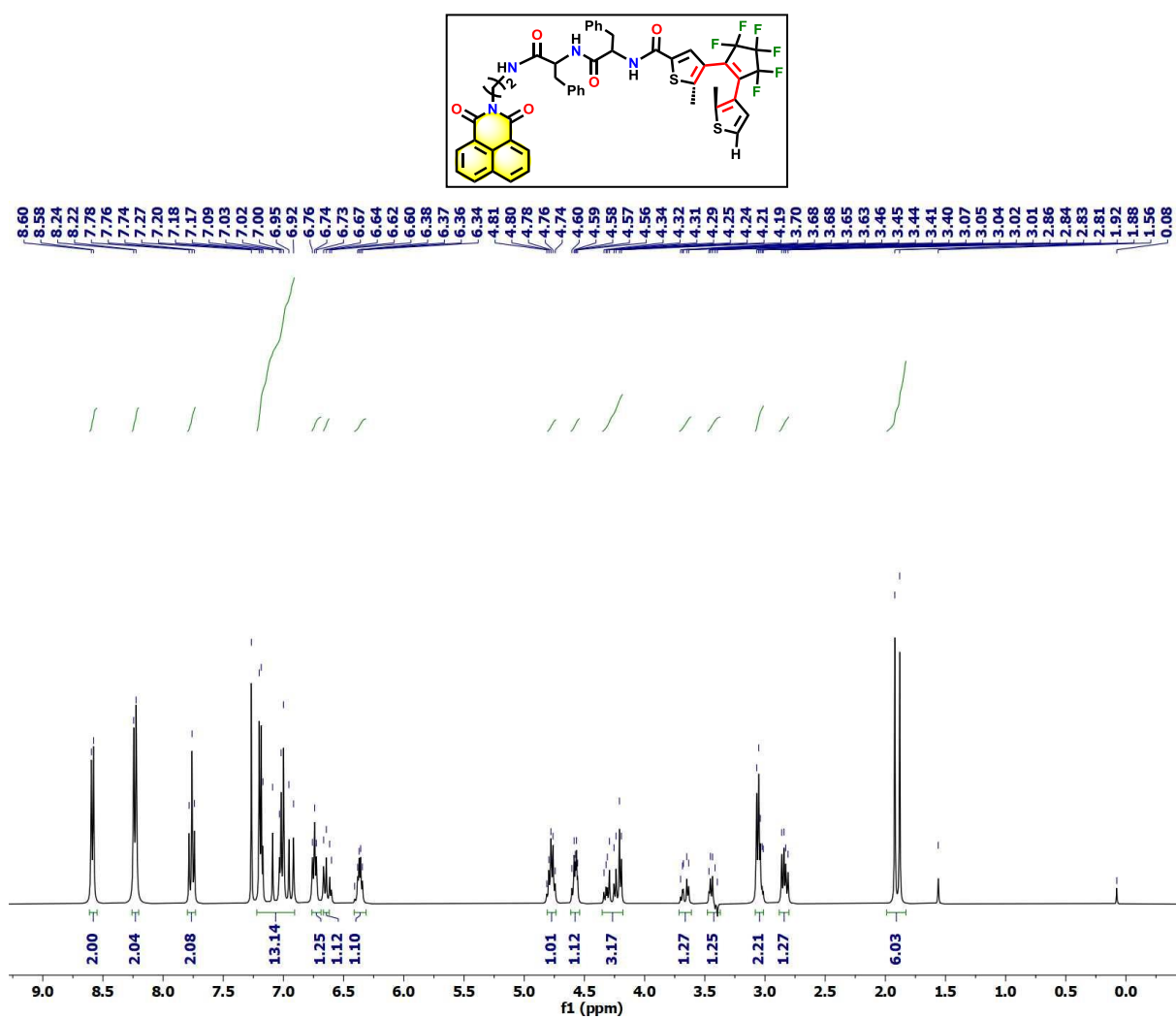


Figure 4.26. ¹H NMR spectra of compound 6 in CDCl₃ as a solvent.

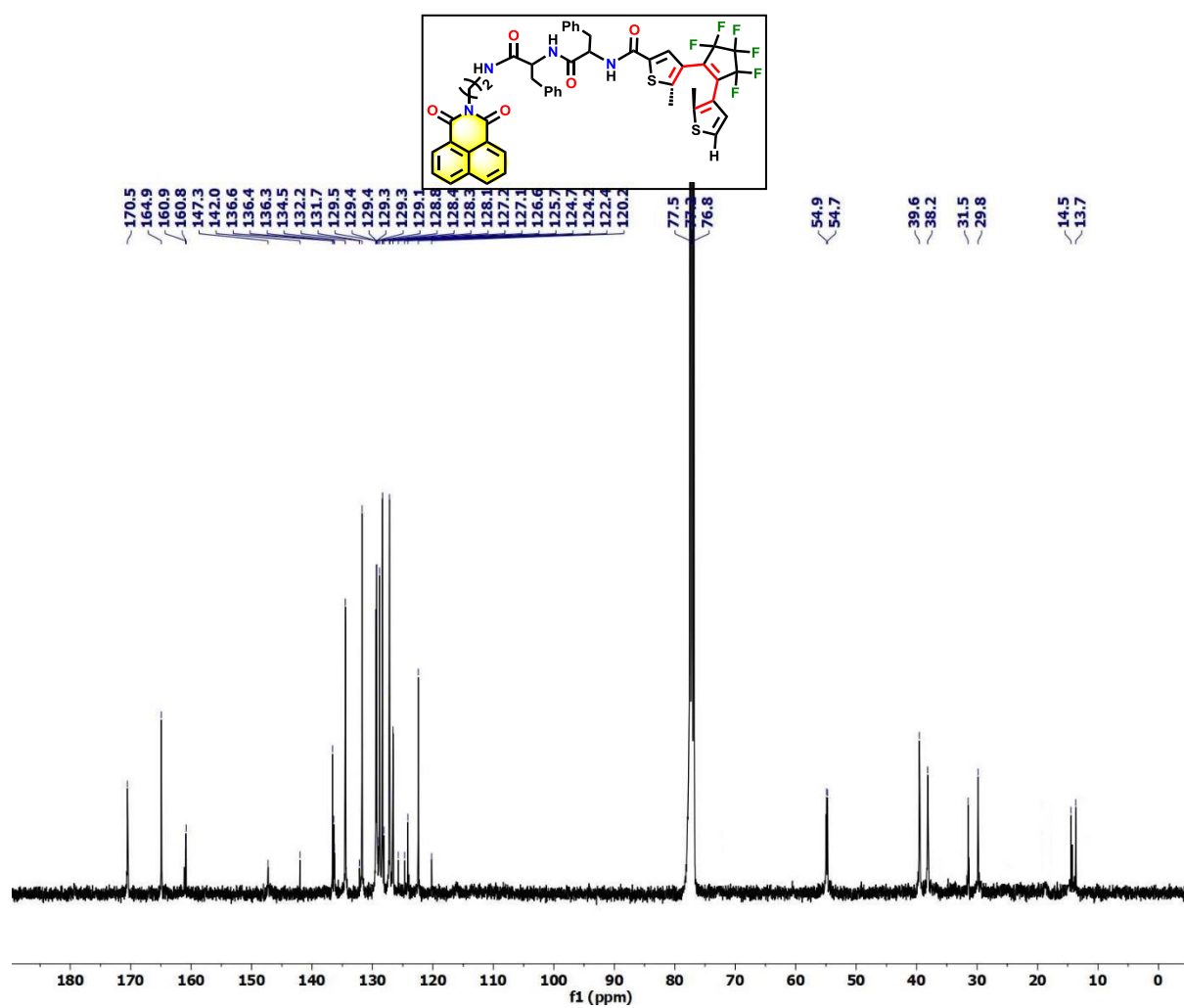


Figure 4.27. ^{13}C NMR spectra of compound 6.

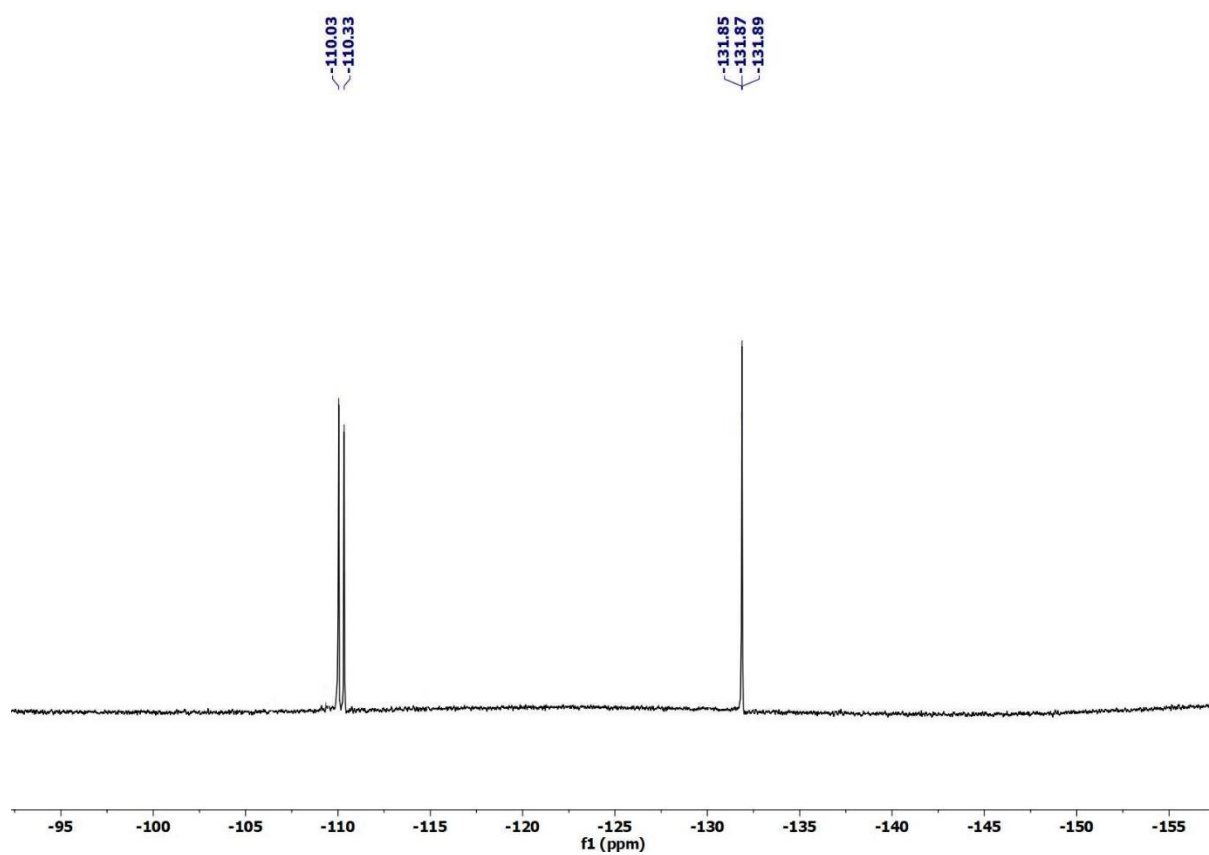


Figure 4.28. ^{19}F NMR spectra of compound **6** in CDCl_3 as a solvent.

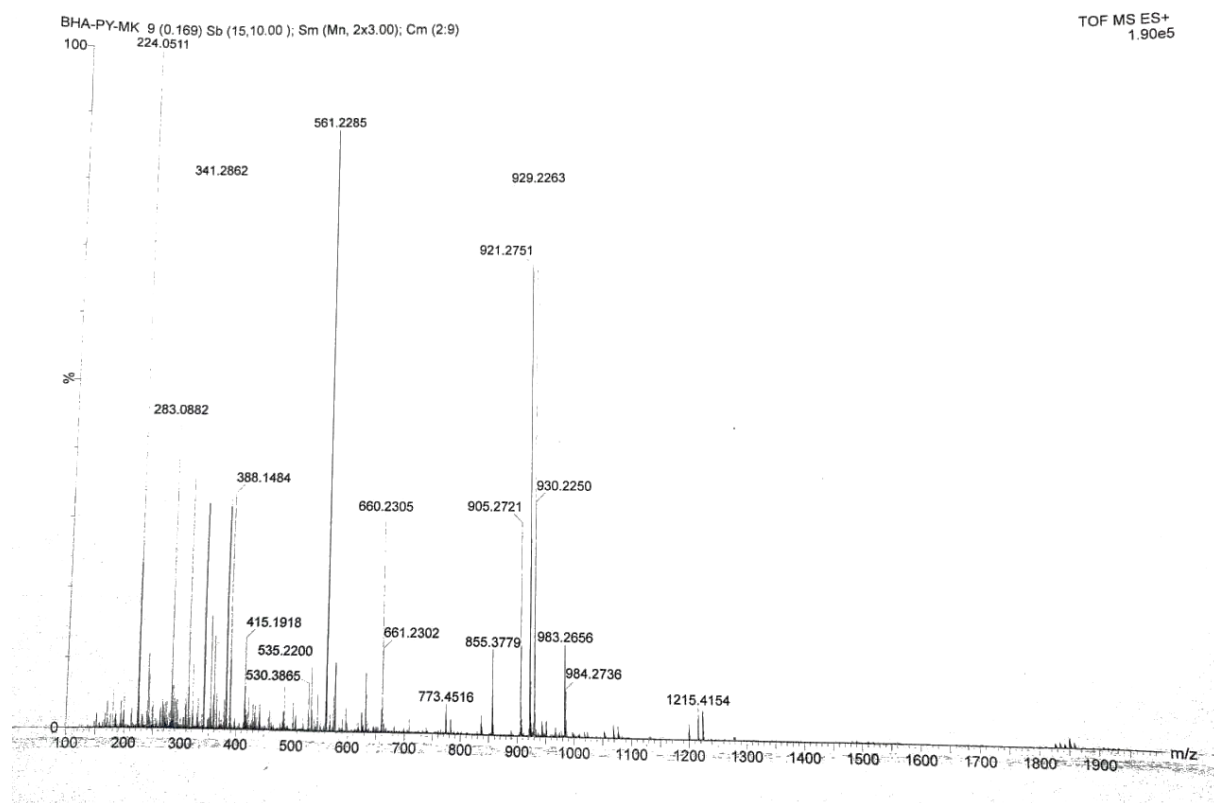


Figure 4.29. HRMS spectra of compound **6**.

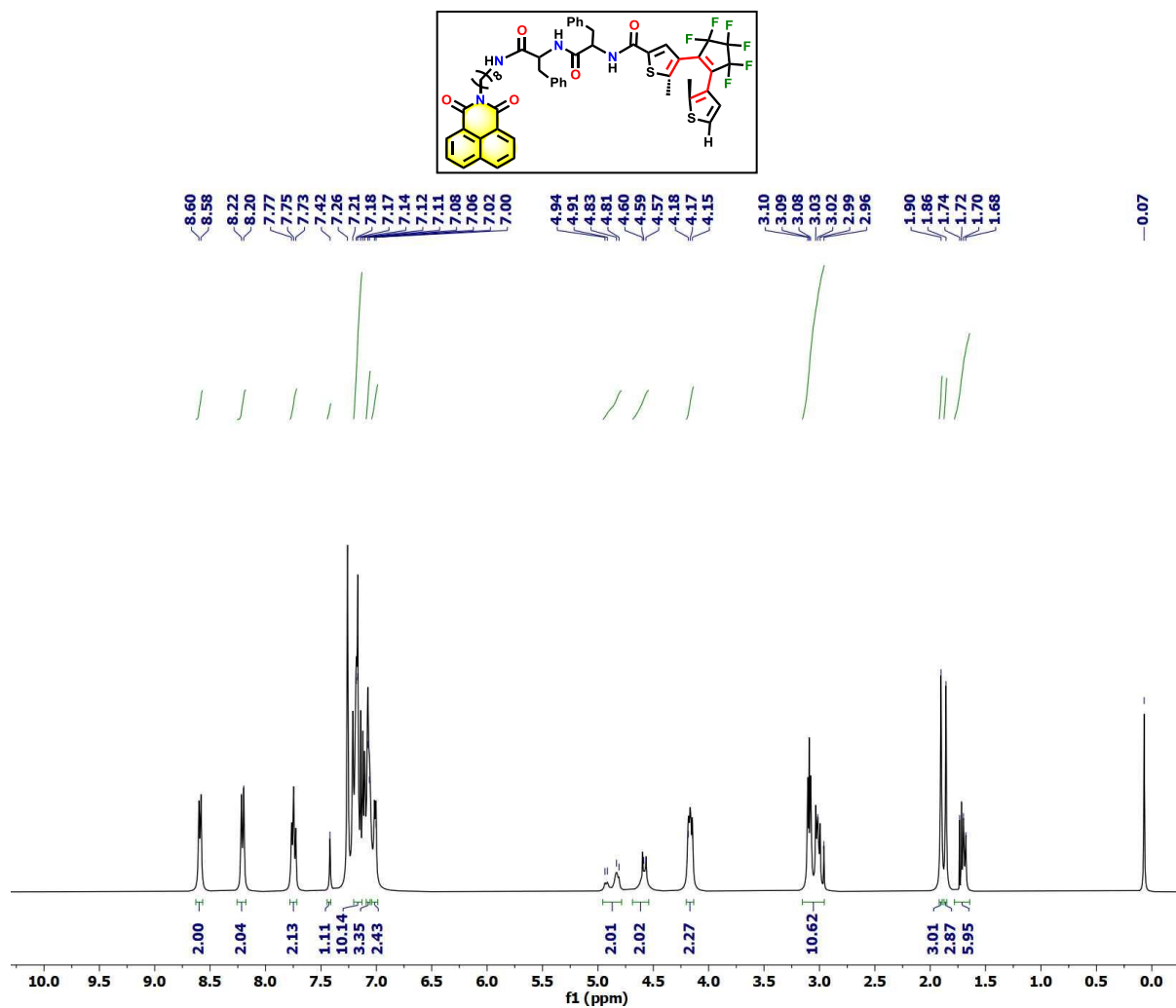


Figure 4.30. ¹H NMR spectra of compound 7 in CDCl₃ as a solvent.

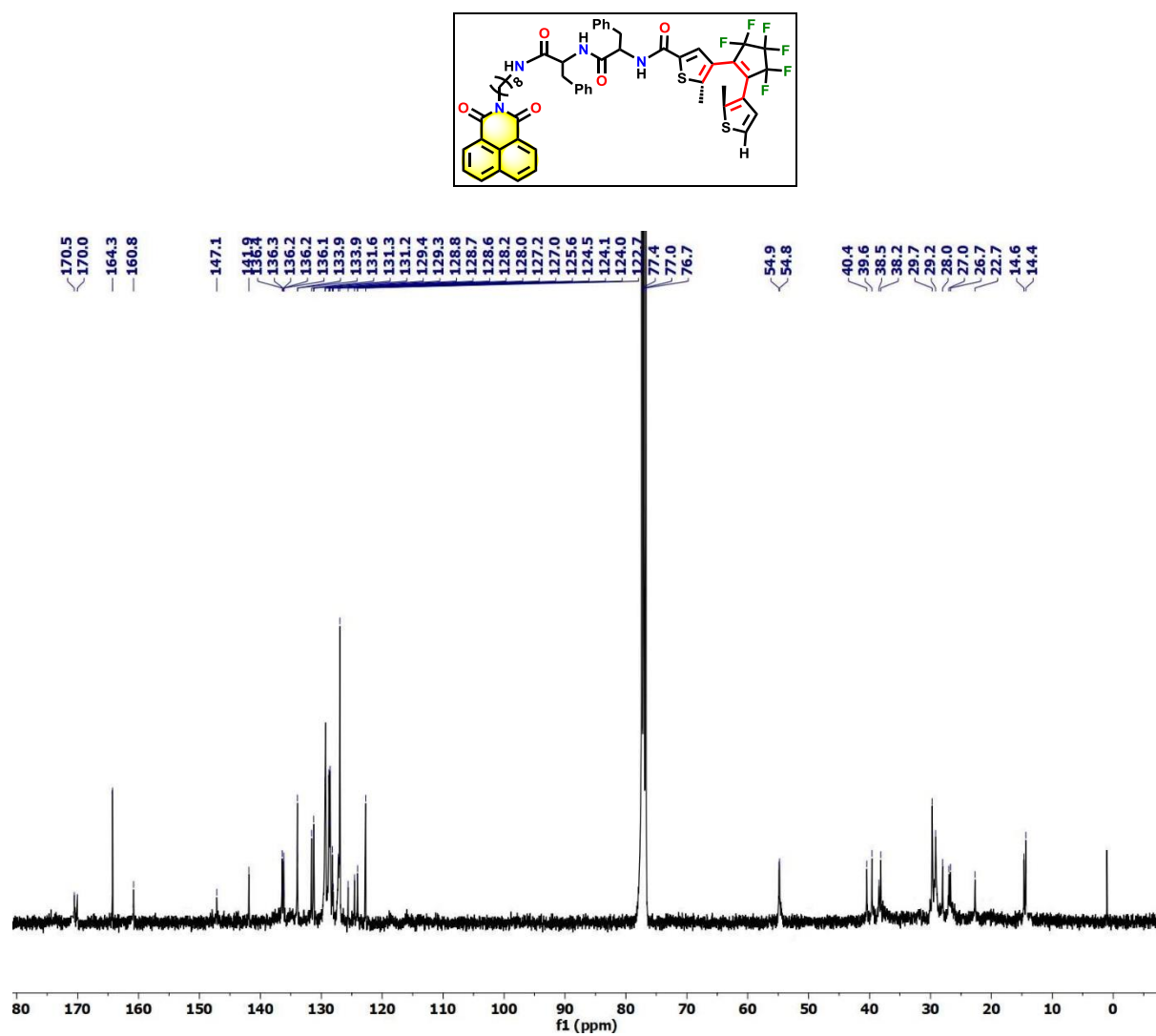


Figure 4.31. ^{13}C NMR spectra of compound 7.

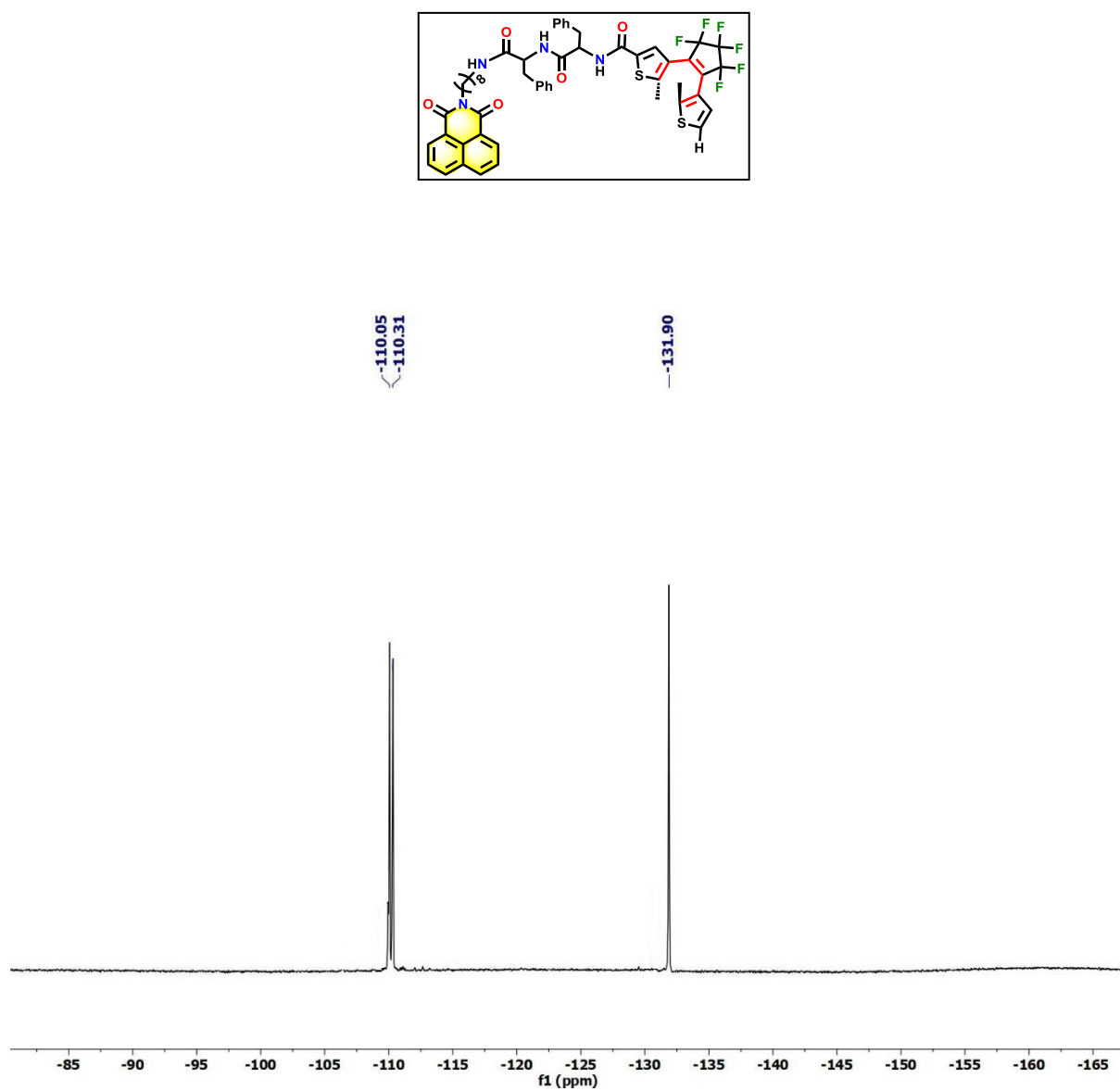


Figure 4.32. ^{19}F NMR spectra of compound 7 in CDCl_3 as a solvent.

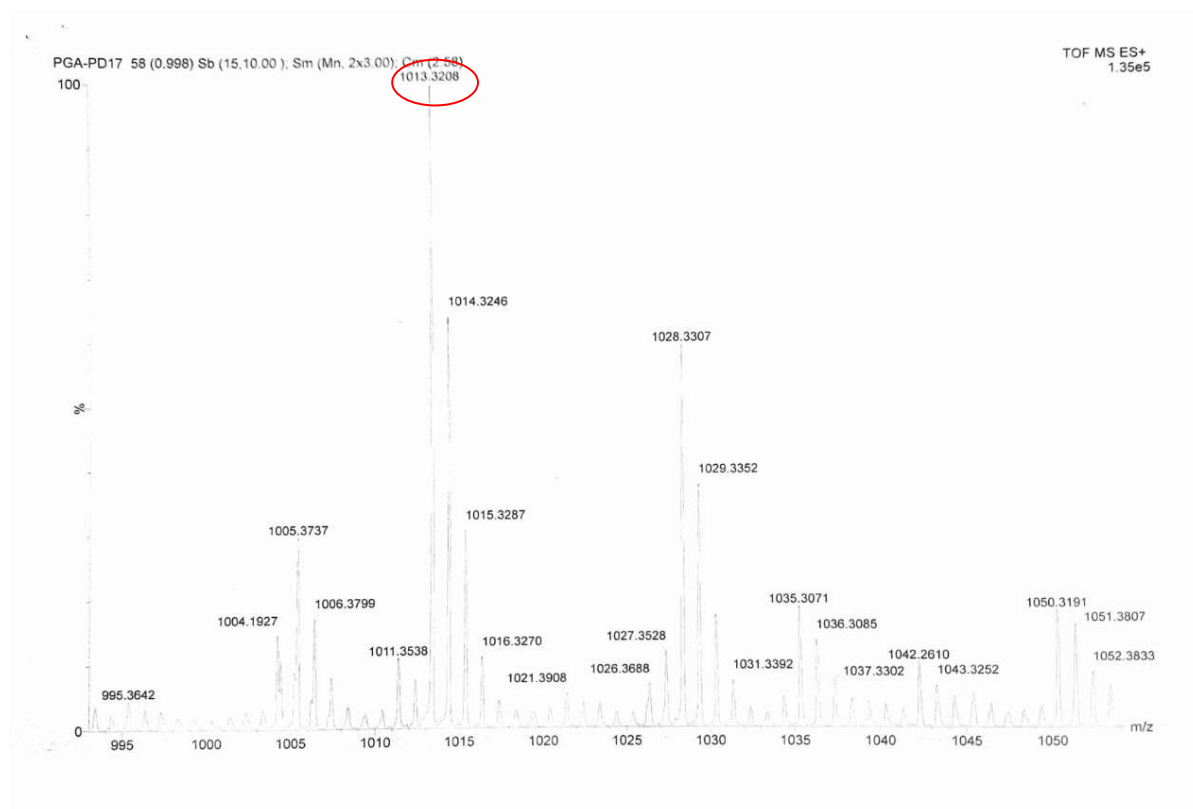
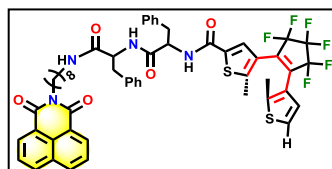


Figure 4.33. HRMS of compound 7.

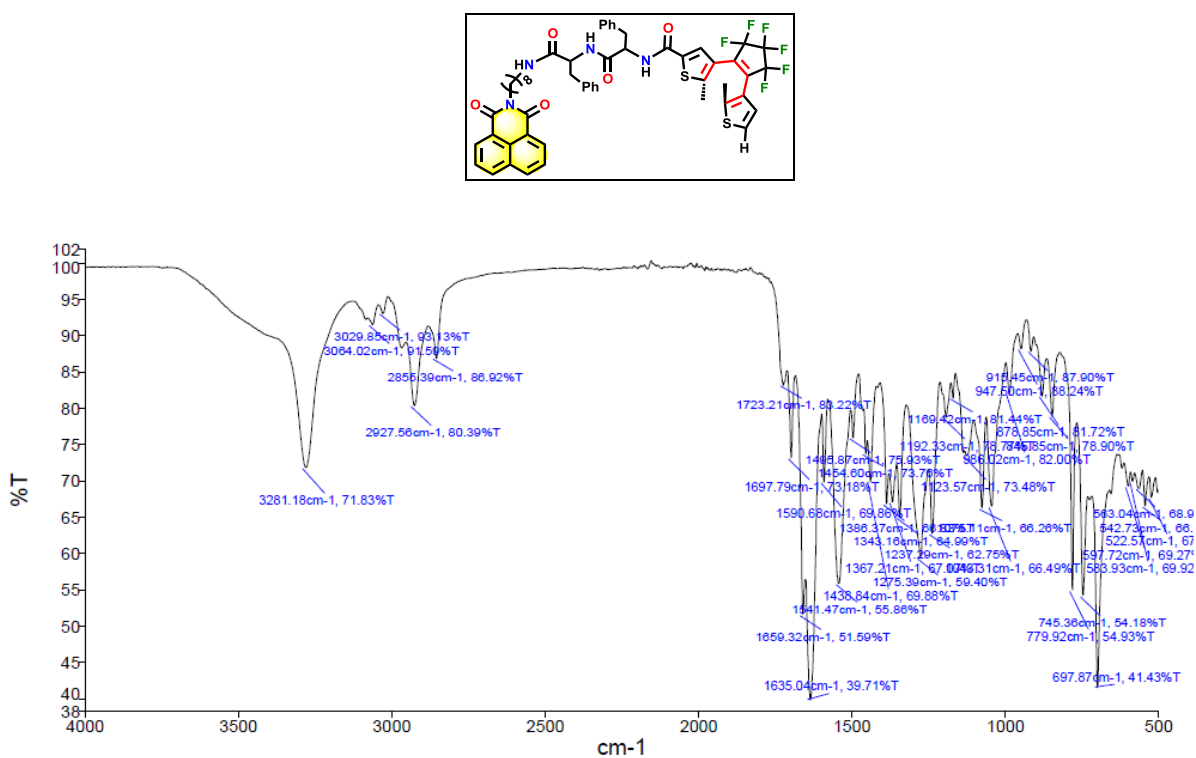
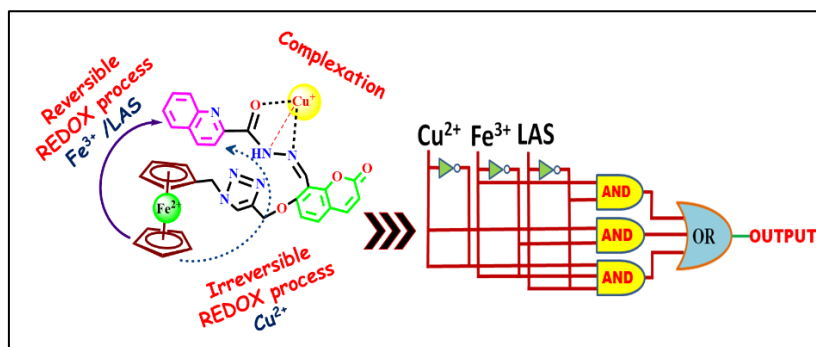


Figure 4.34. FT-IR spectra of compound 7.

Chapter: 5

*Oxidation Induced Differentially
Selective Turn-On Fluorescence via PET
Based on Ferrocene Appended
Coumarin-Quinoline Platform:
Application in Cascaded Molecular Logic*



Representative publication

Inorg. Chem. **2020**, *59*, 4493–4507

5.1. Introduction

This chapter describes the “Host-guest Chemistry” and more specifically it defines the molecular recognition of ferrocene based redox active “host” molecules triggered by specific metal ions as “guest” molecules. The content of this section, however, does not include any photochromic organic molecules and their specific applications in security technology (photochromic ink or photo-erasable writing of confidential information, light triggered generation of QR/bar code, latent fingerprint genitor, and so on), rather, it is comprised of ferrocene and two fluorophores (quinoline and coumarin) and applied in cascaded molecular logic gates. Therefore, this chapter of thesis deals with the manufacture of ferrocene based organometallic sensor molecule with specific functions, which have a pivotal role to detect biologically relevant metal ions.

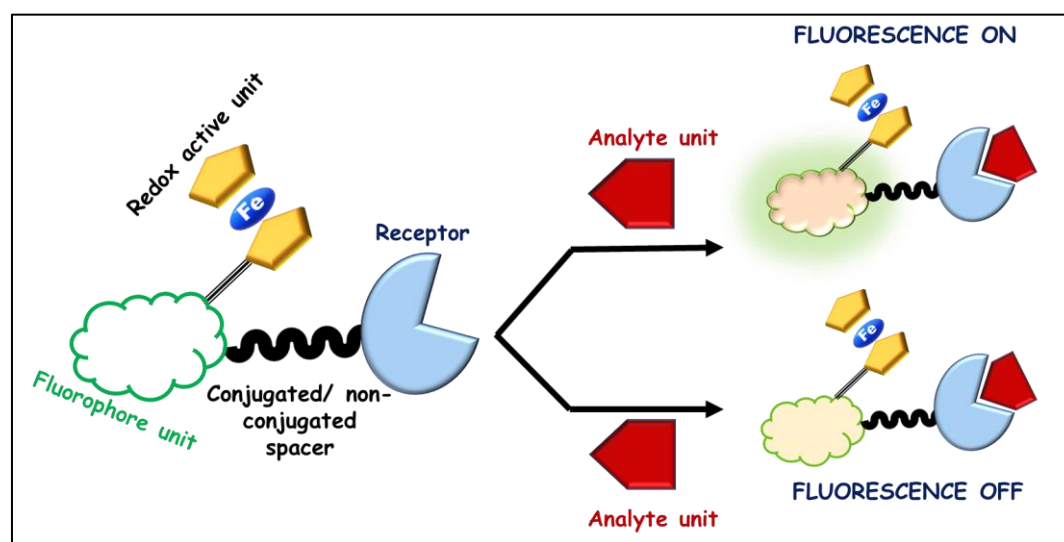
Supramolecular chemistry with macrocyclic hosts is a broadly applicable and rapidly growing study area in chemistry, biology, and material science. These host-guest based supramolecular assemblies are built by non-covalent interactions, thus rendering them highly dynamic in nature and easily tunable through their responses to many different external stimuli like biologically active several metal ions. Additionally, the host molecule also has a "signalling unit" like a fluorophore or chromophore, a redox-active center with a "binding site" to facilitate host-guest interaction with biologically relevant metal ions. To recognize metal cations, we have planned to combine a well-organized system comprising of a redox active center, and/or a chromophore, and a fluorophore moiety (Scheme 5.1) to understand the binding phenomena through multiple channels.

- **Molecular recognition phenomena for the development of chemosensor molecules**

The term "molecular recognition" refers to a specific interaction that takes place between a host molecule and a guest molecule, which results in the formation of a host-guest complex *via* non-covalent interaction. Generally, “host” and “guest” interactions are typically random in nature. Chemosensors played an important role for the sensing of various metal ions *via* molecular recognition because they can bind with analyte in a selective and reversible

manner, resulting in a change in photophysical properties of the system, such as absorption or emission spectra or redox potential.

For the detection of metal ions by host molecules by numerous analytical tools have been reported. Among the common spectroscopic techniques one of the most important technique is fluorescence spectroscopy which offers an excellent sensitivity due to its ability to measure very small quantity of samples. For the qualitative identification and quantitative estimation of cations, anions, and molecules, fluorescence-based sensing techniques and fluorescence-related parameters, such as emission and excitation spectra, fluorescence intensity, Stokes shift and anisotropy, and fluorescence lifetime, offer a great deal of flexibility (Scheme 5.1). Therefore, to synthesize the host molecule, a judicious choice of the fluorophore subunit is essential, which is favored by the inclusion of quinoline and coumarin. On the other hand, we have incorporated chromogenic and redox active ferrocene molecule to modulate electron transport from itself to the fluorophore unit. Also, ferrocene acts as a classical quencher at excited state that helps to transport electron/ energy which is becoming more important for molecular switches. Therefore, utilizing this strategy fulfilled the objective of developing chemosensor molecules based on a redox-active unit and a fluorophore moiety (as illustrated in Scheme 5.1).



Scheme 5.1. Schematic representation of chemosensor towards interaction with an analyte unit.

Electron transfer reactions are of fundamental importance to both chemistry and biology. Particularly, the photo induced electron transfer (PET) process, a state-of-the-art technology, has widely been utilized in several fields for example, catalytic reactions,^{1,2} detecting chemical warfare agents,^{3,4} and measuring glucose⁵ levels in blood etc. Therefore, the development of PET based sensors and switches is becoming a great deal of interest to the scientists. Different design strategies are being employed in the development of PET based sensor molecules with most commonly exploited approach of a ‘fluorophore–spacer–receptor’ configuration in which a donor (mostly nitrogen containing groups) and an acceptor units are present.⁶⁻¹⁰ On contrary, relatively less number of examples are known where the PET is triggered by the oxidation of the donor unit (ferrocene moiety)¹¹⁻¹⁵ and the process can be modulated between fluorescence “on” and “off” states by controlling the redox property of the donor unit.

Fluorescent sensors have been widely reconnoitered due to fast and reliable sensing of chemical species, especially biologically and environmentally important metal ions, with high sensitivity and selectivity in a non-destructive manner.^{16,17} Although, various fluorescent “turn-on” probes are reported for the detection of closed-shell metal cations, including Zn^{2+} ,^{18,19} Cd^{2+} ^{20,21} and Hg^{2+} ^{22,23} but, the detection of redox-active transition metals such as Cu^{+2} ²⁴⁻²⁶ and $Fe^{2+/3+}$ ^{27,28} has received comparatively less attention. In the past few decades, a great effort has been devoted towards the development of “turn-on” fluorescent probe especially for the paramagnetic metal ions like, Fe^{3+} and Cu^{2+} ions, which are potential quencher of excited state fluorophores.^{29,30} Among all the fluorophores developed, the coumarin and quinoline dyes have been extensively used as fluorophores due to their suitable photophysical properties and biocompatibility.^{31,32} Due to the excellent photophysical properties³³ and a large Stokes shift of coumarin dyes, very significant class of fluorescent compounds, have been extensively used to build a variety of chemosensors. Quinoline and its derivatives are well known for its strong coordination ability with metals^{34,35} and quinoline moiety could easily be modified to get the probe with functional group like $-OH$, $-NH$, $-C=N$, $-C=O$, $-N=$ ³⁶ which not only imparts an additional binding site to the metal ions but also increase the water solubility of the probe. Therefore, anticipating a fluorescent probe based on two or more fluorophore units may be more valuable because it can provide multiple signals and improve selectivity, a novel Schiff’s base fluorescent probe based on coumarin-quinoline platform has been designed and synthesized in our laboratory. Although fluorescence “OFF-ON” switches *via* PET/FRET

mechanism based on coumarin-quinoline platforms are reported³⁷⁻³⁹ such switches fabricated on ferrocene-based redox systems are still not explored.

Keeping this idea in mind, we have incorporated ferrocene unit to our designed probe as ferrocene displays excellent reversible redox properties and its stability under aerobic conditions.⁴⁰⁻⁴² Therefore, combination of quinoline-coumarin fluorophores with ferrocene as a redox active unit result in a system where fluorescence can be modulated *via* control of the photo induced electron transfer (PET) process from donor ferrocene to excited state fluorophore.

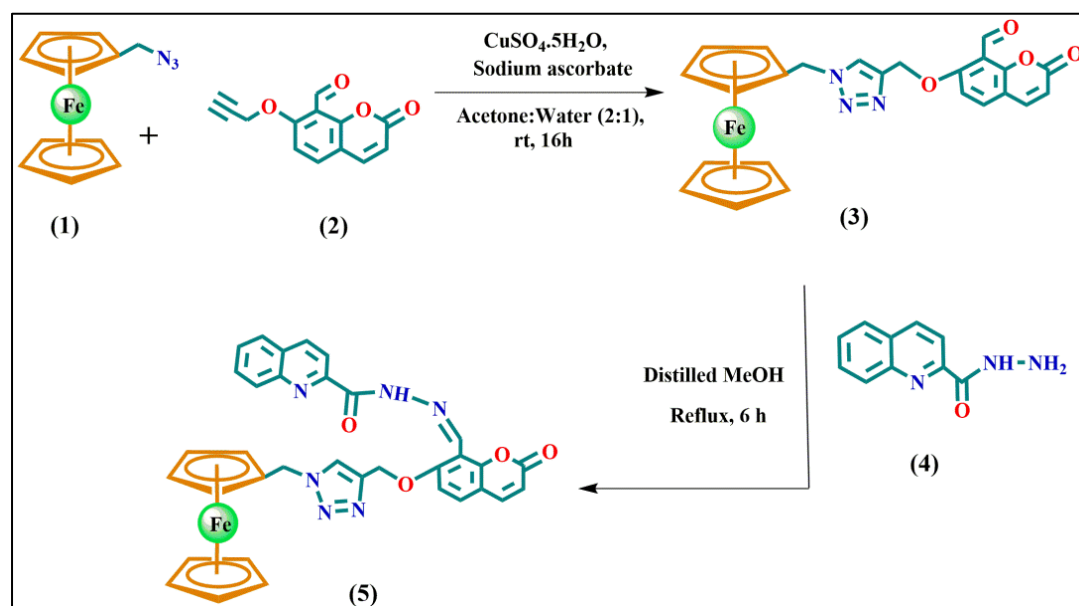
Our continuous pursuit to synthesize an economical, easy to handle, electrochemical and turn-on fluorescent probe for the recognition of selective biological metal ions led us to explore an unprecedented ferrocene based differentially selective PET sensor. To the best of our knowledge, the present probe is the 1st example of ferrocene appended coumarin-quinoline based PET sensor, which is differentially selective towards Fe³⁺, Cu²⁺ and Cu⁺ ions. As it is a great challenge to develop new functional materials based next-generation molecular logic gates with superior applicability, taking the advantage of differentially selective property of present probe, we could mimic a simple “AND-OR” combinational logic circuits which monitored the “OFF-ON -OFF” fluorescent molecular switch.

5.2. Results and Discussion

5.2.1. Synthesis and Characterization

Our synthetic strategy to design a ferrocene appended coumarin-quinoline receptor **5** has been depicted in Scheme 5.2. Mono(azidomethyl) ferrocene, **1** undergoes [2+3] cyclo addition reaction with 2-oxo-7-(prop-2-ynyloxy)-2*H*-chromene-8-carbaldehyde, **2** to afford compound **3**, which was characterized by ¹H NMR, ¹³C NMR, and HRMS study. Further, condensation of compound **3** with quinoline-2-carbohydrazide, **4** afforded our desired aldimine compound, **5** in good yield. Although molecular structure of compound **3** was unambiguously established by single crystal XRD analysis (Figure 5.1, *vide infra*), our several attempts to isolate X-ray quality single crystal for compound **5** were unsuccessful. However, compound **5** was fully characterized by using ¹H NMR, HRMS, IR spectra and elemental analysis. The HRMS spectrum shows the major peak at *m/z* 639.1445 [M+H]⁺, which perfectly matches with the calculated molecular weight *m/z* 639.1443 of desired compound **5**. The advantages of incorporation of quinoline-2-carbohydrazide are multifaceted; a) to prevent oxidation of -CHO

to –COOH in presence of perchlorate salt which is a potential oxidant.⁴³ Sometime –COOH group is unwanted as it may impart the pH dependence into the probe; b) hetero atoms present in quinoline-2-carbohydrazide moiety may furnish an additional binding site and could improve the selectivity of the receptor; c) it is a fluorophore unit which displays outstanding photophysical properties and easy modification.⁴⁴⁻⁴⁶ After having the compound **5** in good amount in hand, the metal sensing properties have been investigated as metals are absolute requirement for all life and plays vital roles in osmotic regulation, enzymatic catalysis, metabolism and signaling.⁴⁷ The designed probe **5** shows an excellent selectivity and sensitivity towards Fe³⁺, Cu²⁺ and Cu⁺ ions. Fe³⁺ and Cu²⁺ are known as efficient quencher of excited state fluorophores due to their paramagnetic nature.^{29,30} Consequently, a plethora of “turn-off” fluorescent probes are known to date for Fe³⁺⁴⁸⁻⁵⁰ and Cu²⁺^{51,52} ions. Therefore, the development of “turn-on” fluorescent chemosensors for Fe³⁺ and Cu²⁺ is still a challenging task. Keeping this idea in mind, we have introduced ferrocene moiety in our designed probe so that it can easily be oxidized to ferrocenium ion by suitable metal oxidant, Fe³⁺ and Cu²⁺. Thus, we have tactfully avoided the quenching issue by treating Fe³⁺ and Cu²⁺ as an oxidant rather than a binding agent. However, the Cu⁺ causes quenching of weak fluorescence of **5** *via* chelation induced quenching effect and electron transfer.⁵³⁻⁵⁵ Interestingly, oxidation of ferrocene unit to ferrocenium ion in probe **5** by Cu²⁺ ion followed by complexation with resulting Cu⁺ ion was also observed. The formation of [**5**⁺·Cu⁺] complex was confirmed by the HRMS, which shows a peak at *m/z* 701.09 (M+Cu⁺) which is also corroborated with calculated molecular weight of *m/z* 701.06 (Figure 5.2, *vide infra*).



Scheme 5.2. Synthesis of ligands **3** and **5**.

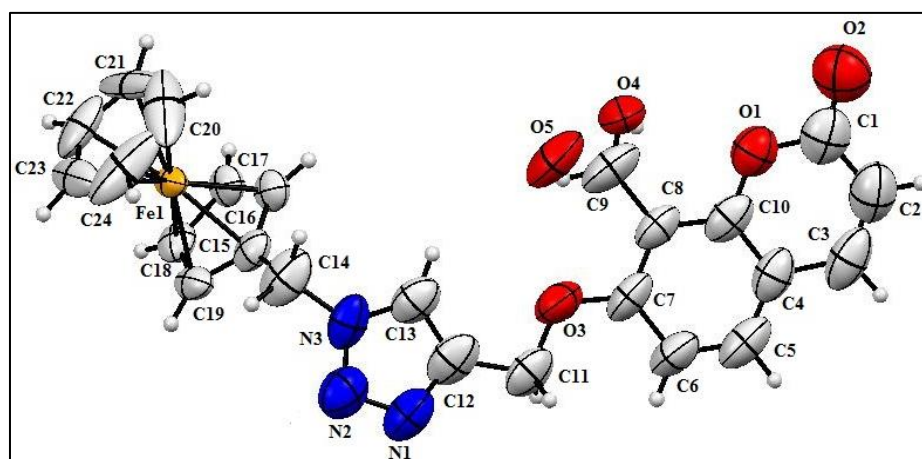


Figure 5.1. Single crystal structure of compound **3**.

Figure 5.1 shows the molecular structure of **3** with thermal ellipsoids drawn at the 50% probability level. Selected bond lengths (\AA) and angles (deg): C1-O2 1.230(16), C1-O11.386(14), C7-O3 1.365(11), N3-C14 1.472(11), C8-C9 1.467(13), [Triazole ring: C12-C13 1.350(13), C12-N1 1.351(15), N1-N2 1.338(12), N2-N3 1.343(12), N3-C13 1.363(12)]; O1-C1-O2 116.3(12), C7-O3-C11 117.8(7), C12-C11-O3 103.5(8), [Triazole ring: N1-C12-C13 106.6(0), C12-C13-N3 106.2(10), N2-N3-C13 111.1(8), N3-N2-N1 104.3(9), C12-N1-N2 111.7(9)].

Crystal data for 3. Formula, $C_{24}H_{19}FeN_3O_4$; crystal system, monoclinic; space group, P21/c; unit cell dimensions, $a = 26.306(5) \text{ \AA}$, $b = 7.6453(12) \text{ \AA}$, $c = 10.4673(17) \text{ \AA}$, $\beta = 92.035(5)$; $Z = 4$; density (calcd) = 1.482 g/cm^3 ; $R_{\text{int}} = 0.0826$; final R indices [$I \geq 2\sigma(I)$], $R1 = 0.1128$; $wR2 = 0.3002$; θ range (deg), $4.648\text{--}55.108$; total reflection collected, 25692; independent reflections, 4780; goodness of fit on $F^2 = 1.034$.

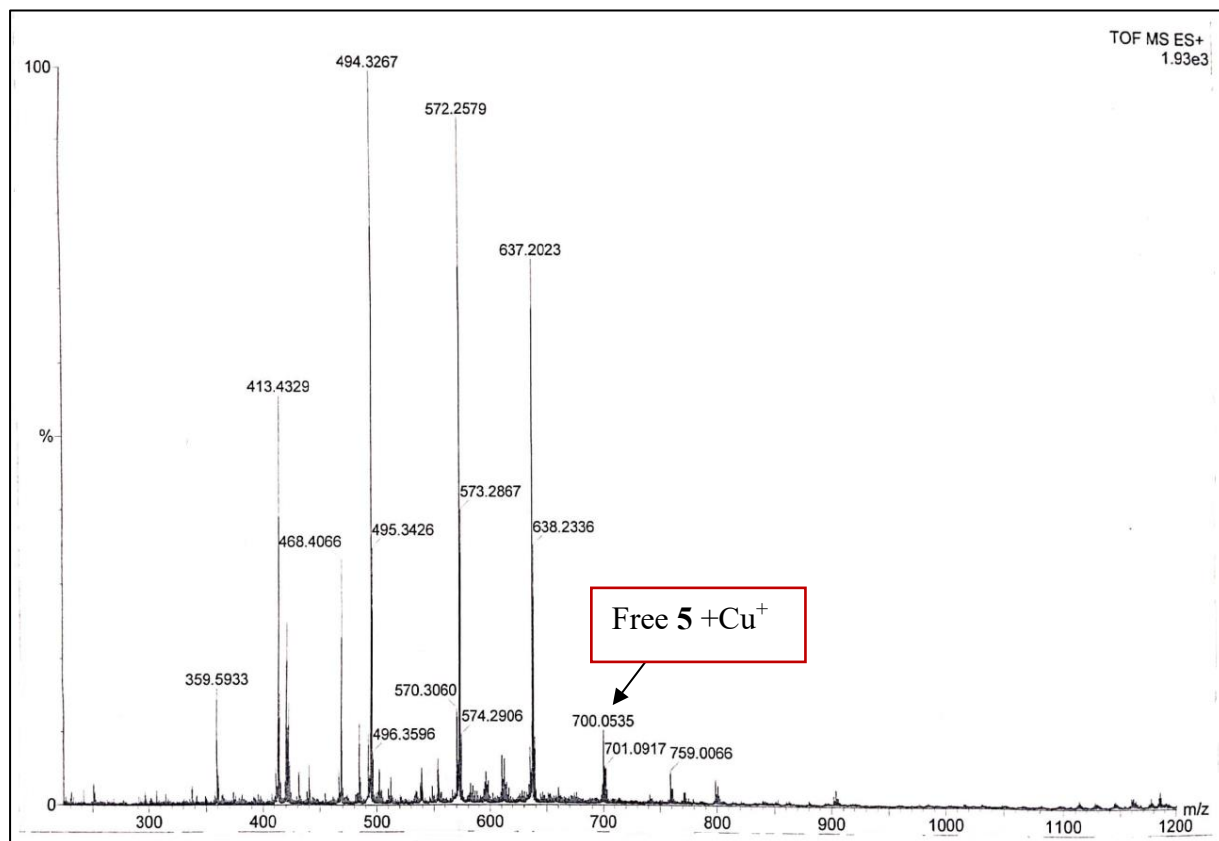


Figure 5.2. HRMS of compound $[5 \cdot Cu^+]$.

5.2.2. UV-vis Absorption Study

Cation recognition properties and optical sensitivities of ferrocene-appended quinoline-coumarin derivative **5**, were investigated by spectrophotometric study. Thus, to obtain more quantitative information regarding photophysical property, UV-vis experiment was carried out in presence of various biologically relevant metal ions, such as K^+ , Ag^+ , Cu^+ , Ni^{2+} , Mg^{2+} , Hg^{2+} , Cu^{2+} , Cd^{2+} , Fe^{2+} , Fe^{3+} , Al^{3+} , Cr^{3+} , Mn^{2+} , Pb^{2+} , Co^{2+} and Zn^{2+} in CH_3CN ($2.5 \times 10^{-5} \text{ M}$) medium (Figure 5.3a). All the absorption spectra showed no significant changes except Fe^{3+} , Cu^{2+} and Cu^+ ions. The receptor **5** exhibited two main absorption bands with the absorption maxima

located at $\lambda_{\max} = 237$ ($\epsilon = 31511 \text{ M}^{-1} \text{ cm}^{-1}$) and 318 nm ($\epsilon = 23873 \text{ M}^{-1} \text{ cm}^{-1}$). These two bands are attributed for the substituted quinoline and the typical coumarin dye respectively.^{56,57}

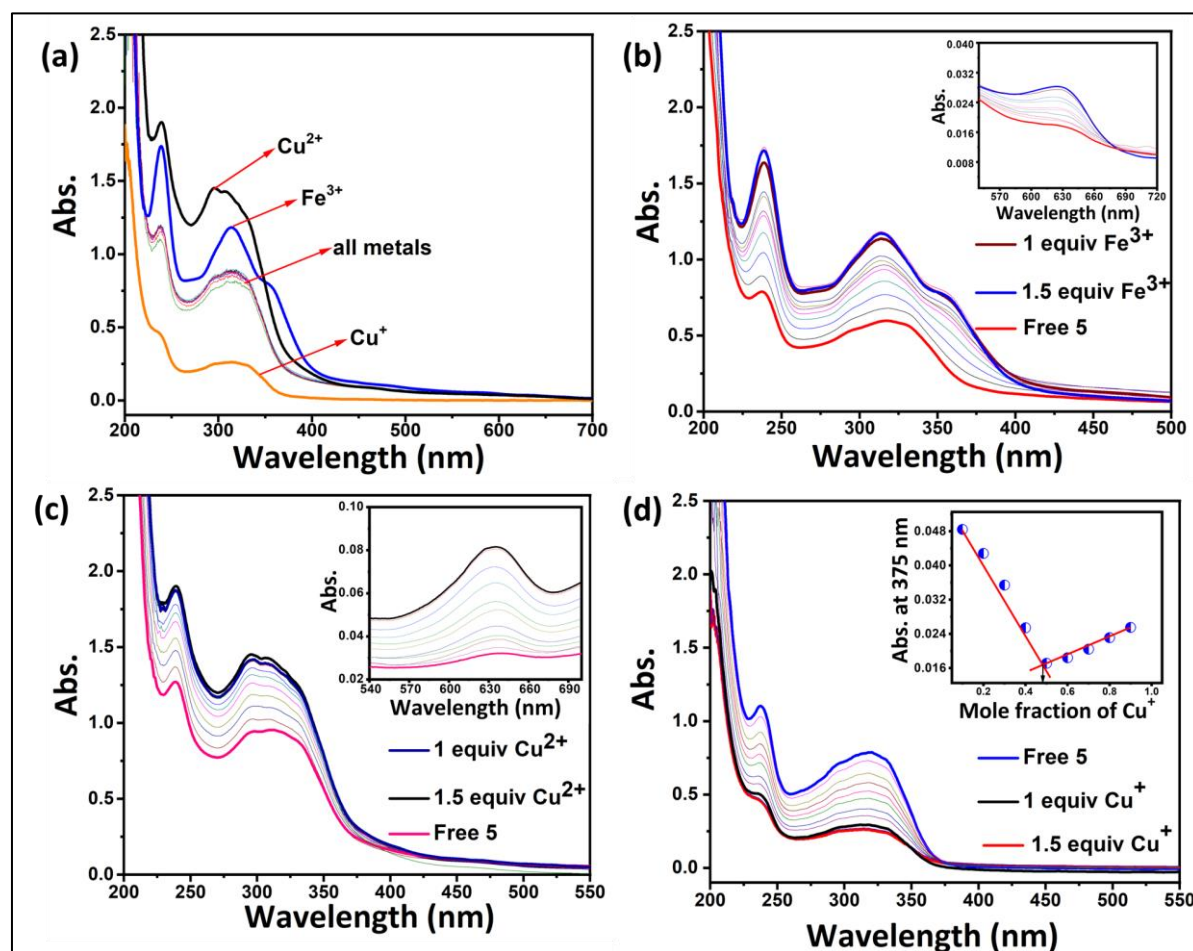


Figure 5.3. (a) Changes in the absorption spectra of **5** (10^{-5} M) in CH_3CN upon addition of several cations. Variation in absorption spectra of **5** in CH_3CN ($2.5 \times 10^{-5} \text{ M}$) upon addition of increasing amount of (b) Fe^{3+} , (c) Cu^{2+} , (d) Cu^+ up to 1.5 equiv; The inset in (d): Job's plot of receptor **5** with Cu^+ .

Upon drop wise addition of Fe^{3+} and Cu^{2+} ions to the ligand solution, the absorption band at 237 nm ($\epsilon = 68810 \text{ M}^{-1} \text{ cm}^{-1}$ for Fe^{3+} ; $76054 \text{ M}^{-1} \text{ cm}^{-1}$ for Cu^{2+}) and at 318 nm ($\epsilon = 46676 \text{ M}^{-1} \text{ cm}^{-1}$ for Fe^{3+} ; $57225 \text{ M}^{-1} \text{ cm}^{-1}$ for Cu^{2+}) were gradually increased (Figures 5.3b and 5.3c) up to 1 equiv of metal ions and beyond that no significant changes were observed. No distinct isosbestic point was found in case of Fe^{3+} and Cu^{2+} ions indicating Fe^{3+} and Cu^{2+} ions did not form any complex with ligand **5**. Although reduced Cu^+ ion formed a complex with the oxidized ligand (*vide infra*), no isosbestic point was observed in the UV-vis spectra may be due to the fact that oxidation by Cu^{2+} ion predominated over complexation with Cu^+ ion.

Furthermore, a new weak band arises at 634 nm for Cu^{2+} and 626 nm for Fe^{3+} , which are the characteristic for the formation of ferrocenium ion.⁵⁸⁻⁶¹ The formation of ferrocenium ion can further be perceived from change of color from yellow to greenish blue, which can be used for the “naked eye” detection of these metal ions. On contrary, upon gradual addition of Cu^+ ion to the receptor **5**, both the peaks around 237 nm and 318 nm concurrently decreased along with an isosbestic point at 375 nm, which indicates the formation of a complex with ligand **5** (Figure 5.3d). The binding ratio of the receptor **5** with Cu^+ ion was calculated from Job’s plot analysis, which indicates the formation of 1:1 complex (Figure 5.3d, inset). The formation of $[\mathbf{5}\cdot\text{Cu}^+]$ complex was also confirmed by the HRMS (Figure 5.2).

5.2.3. Fluorescence Study

To investigate the efficiency of the receptor **5** as a potential chemosensor, we have carried out fluorescence emission experiments in CH_3CN (1×10^{-6} M) as solvent in presence of all different metal ion as their perchlorate salts (K^+ , Ag^+ , Ni^{2+} , Mg^{2+} , Hg^{2+} , Cd^{2+} , Fe^{2+} , Fe^{3+} , Cu^{2+} , Al^{3+} , Cr^{3+} , Mn^{2+} , Pb^{2+} , Co^{2+} and Zn^{2+}) and tetrakis(acetonitrile) hexafluorophosphate salt of Cu^+ . No substantial change was observed in the fluorescence spectra of receptor **5**, however, the only significant response appeared when Fe^{3+} , Cu^{2+} and Cu^+ were added (Figure 5.4).

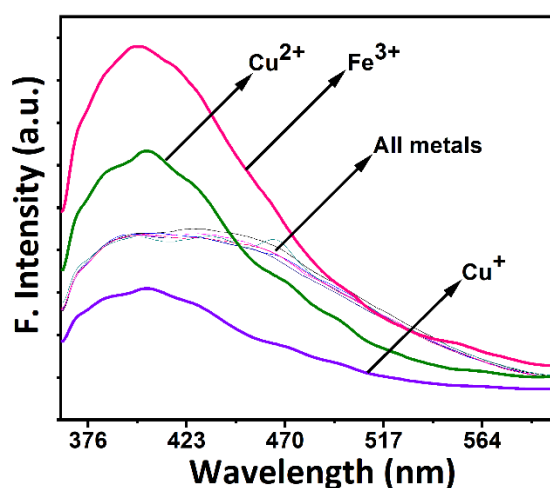


Figure 5.4. Effect of addition of various metal ions in fluorescence emission spectra of **5** (10^{-6} M).

Upon exciting at $\lambda_{\text{ex}} = 318$ nm, the receptor **5** displayed two weak bands at 406 and 465 nm for quinoline and coumarin moiety respectively.³⁷ Gradual addition of increasing amounts of Fe^{3+} and Cu^{2+} ions to the solution of receptor **5** led to a dramatic enhancement of fluorescence emission at 406 nm, corresponding to the quinoline unit, whereas the intensity of small plateau at 465 nm, corresponding to coumarin unit, changed very insignificantly (Figures 5.5a and 5.5c). The fluorescence intensity at 406 nm gradually increased and reached a plateau when the Fe^{3+} and Cu^{2+} were added up to 1 equiv and remained almost unchanged beyond further addition of Fe^{3+} and Cu^{2+} ions indicating no ferrocene unit (Fe^{2+}) left to be oxidized to ferrocenium ion (Fe^{3+}). Fluorescence of receptor **5** was initially turned-off probably due to photo-induced electron transfer (PET) from well-known donor ferrocene unit to excited state fluorophores.⁶²⁻⁶⁴ Oxidation of ferrocene unit by $\text{Fe}(\text{ClO}_4)_3$ and $\text{Cu}(\text{ClO}_4)_2$ to ferrocenium ion inhibited the electron transfer process (PET) which resulted a significant enhancement of fluorescence emission. In order to understand this PET process and enhancement mechanism, sodium L-ascorbate (LAS) was added as a reducing agent which induced gradual diminishing of the fluorescence spectra and remained unchanged after addition of 1 equiv of LAS in case of Fe^{3+} ion (Figure 5.5b). However, mere addition of LAS to a CH_3CN solution of **5** did not produce any changes in fluorescence emission. It is evident from these experiments that Fe^{3+} and LAS can be used to control the fluorescence “OFF-ON-OFF” switching of molecule **5**. However, the “turn-on” response with Cu^{2+} did not reverse back to its original state through fluorescence quenching upon addition of LAS. This phenomenon may be attributed to the fact that upon oxidation of ferrocene to ferrocenium ion, Cu^{2+} ion got simultaneously reduced to Cu^+ , which in turn formed a complex with the oxidized receptor and this produced a “off-set” effect of fluorescence enhancement. In order to understand our hypothesis, the binding interaction of Cu^+ with receptor **5** was also investigated with fluorescence spectra using $[\text{Cu}(\text{CH}_3\text{CN})_4]\text{PF}_6$ as a Cu^+ ion source. Indeed, Cu^+ ion causes chelation induced fluorescence quenching⁵⁵ of the receptor **5** (Figure 5.5d).

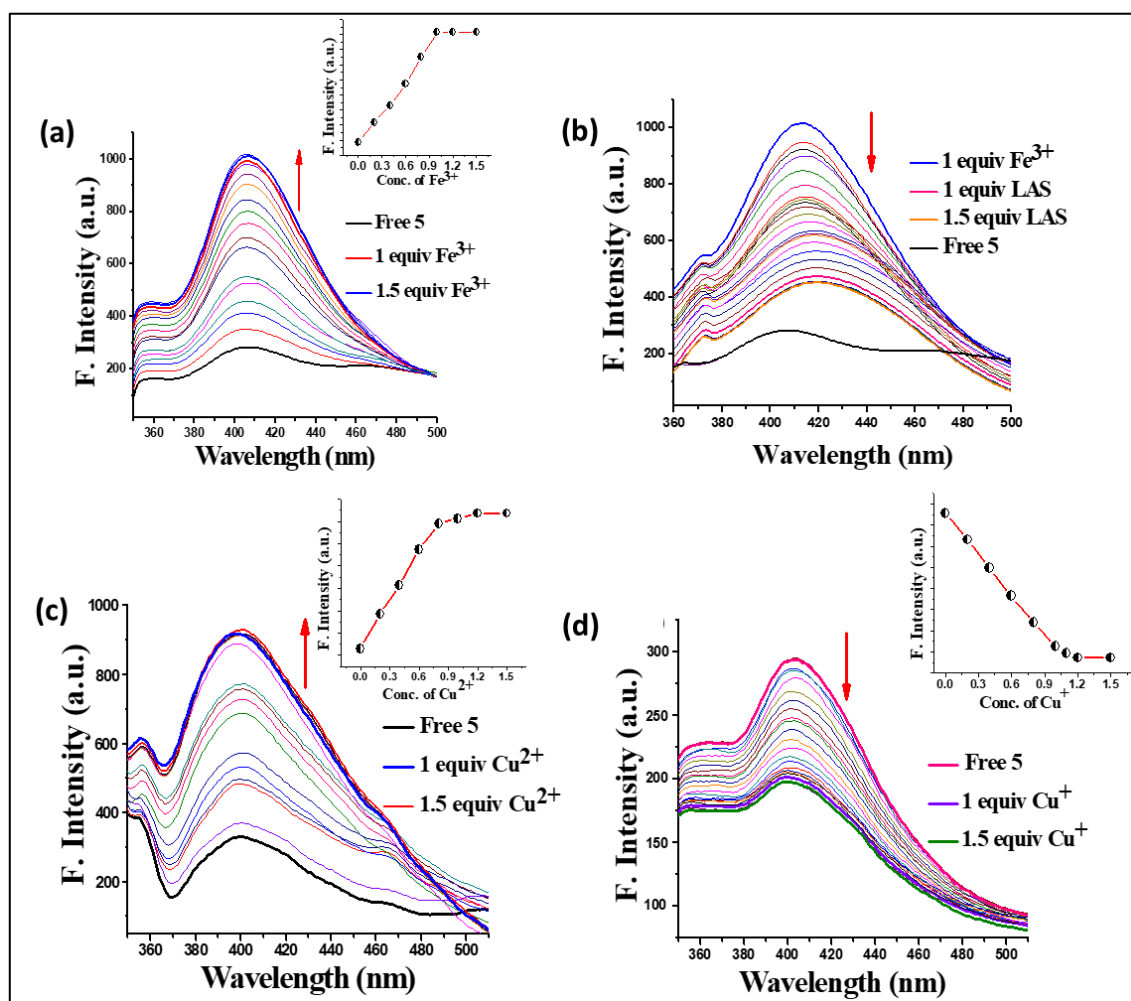


Figure 5.5. Fluorescence emission spectra ($\lambda_{\text{ex}} = 318 \text{ nm}$) of compound **5** ($1 \times 10^{-6} \text{ M}$) upon addition of various concentrations of (a) Fe^{3+} ion up to 1.5 equiv, (b) back reduction by LAS, (c) Cu^{2+} and (d) Cu^{+} ions up to 1.5 equiv in CH_3CN solution.

Interestingly, addition of 1 equiv of EDTA, led to the re-enhancement of fluorescence emission due to ratiometrically displacement of Cu^{+} ion from $[\mathbf{5}\cdot\text{Cu}^{+}]$ complex (Figure 5.6a). The activation and deactivation pathways are described in Figure 3a. In order to understand the situation better, we have captured the pictures of the solutions (Free ligand, Fe^{3+} , Cu^{2+} and Cu^{+}) under an illumination with 365 nm light in dark. Weak fluorescence of free ligand turned into bright bluish green color in case of Fe^{3+} and Cu^{2+} , but the weak fluorescence of free ligand completely turned off in presence of Cu^{+} ion (Figure 5.6b). The 1:1 binding ratio of **5** with Cu^{+} ion was confirmed from Job's plot analysis. Further, a peak at m/z 701.09 ($\text{M}+\text{Cu}^{+}$) in HRMS confirms the formation of $[\mathbf{5}\cdot\text{Cu}^{+}]$ complex (Figure 5.2). It is noteworthy that, upon oxidation

of ferrocene unit to ferrocenium ion by Fe^{3+} or Cu^{2+} , the fluorescence intensity at 406 nm drastically increased, whereas the intensity at 465 nm changed very insignificantly. This result suggested that quinoline moiety is involved in PET process with ferrocene unit, not the coumarin moiety. This observation can be further validated based on thermodynamic calculations employing Weller equation^{65,66} as, ($\Delta G_{\text{PET}} = E_{\text{OX}} - E_{\text{RED}} - E_{\text{S}} - e^2/\epsilon r$), where E_{OX} is the oxidation potential of ferrocene (0.45 V),^{67,68} E_{RED} is the reduction potential of coumarin (-1.60 V)⁶⁹ and quinoline (-1.40 V),⁷⁰ E_{S} is the singlet excited state energy of coumarin (3.9 eV) and quinoline (4.07 eV), and $e^2/\epsilon r$ is the columbic term (0.10 eV) (all values are versus SCE). ΔG_{PET} from ferrocene to excited state fluorophore quinoline is -2.32 eV and ΔG_{PET} from ferrocene to another fluorophore center coumarin is -1.95 eV. These values suggested that PET from ferrocene to quinoline is highly favorable compared to ferrocene to coumarin unit (Figure 5.6a). This result was further supported *via* quantum chemical calculations using DFT method (*vide infra*).

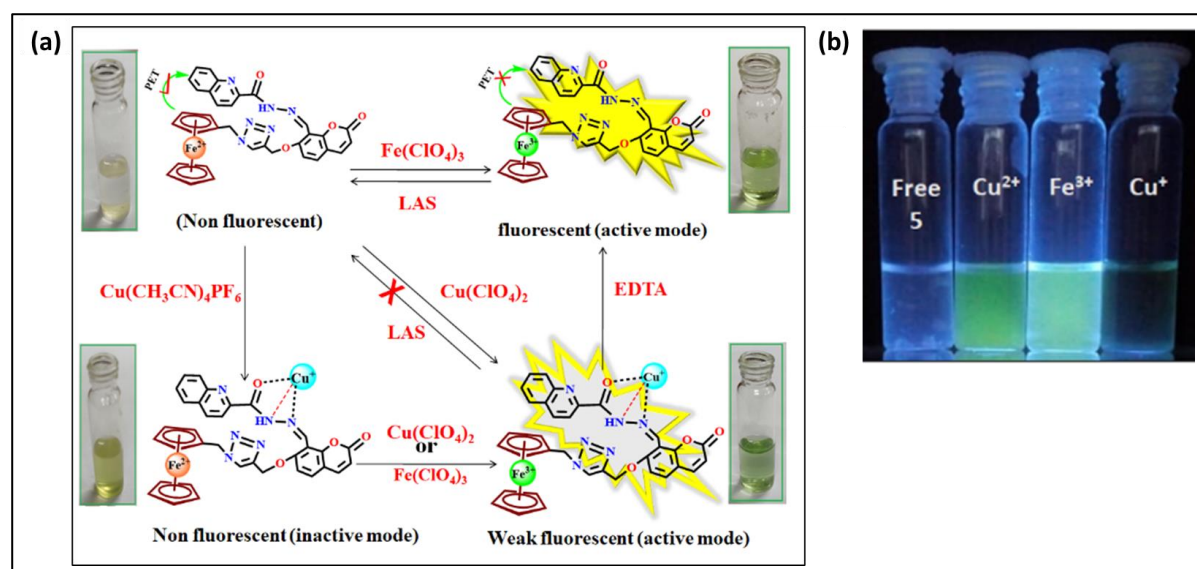


Figure 5.6. (a) Schematic representation of active and inactive mode due to interaction of different metal ions *via* PET process, (b) color changes of receptor **5** with Cu^{2+} , Fe^{3+} and Cu^+ ions under illumination of light 365 nm.

The limit of detection (LOD) was calculated on the basis of fluorescence titration (data extracted from Figure 5.5d). The fluorescence emission spectrum of **5** was measured 3 times, and the standard deviation of the blank measurement was achieved. The LOD, calculated using the equation $3.3\sigma/S^{71}$ (where “ σ ” is the standard deviation of the blank and “S” is the slope of the calibration curve) was found to be 9.08×10^{-7} M for the Cu^+ ion (Figure 5.7a). In order to

compare the LOD of our present probe with other reported probes, we have prepared a comparative table for Cu^+ ion (Table 5.1). The LOD of present probe is comparable or even lower than those obtained with other molecular sensors for Cu^+ ion. The binding constant value of Cu^+ ion with receptor **5** was determined from the fluorescence emission intensity data following the modified Benesi-Hildebrand equation,⁷² $[1/F-F_0]$ versus $[\text{C}]^{-1}$, where F and F_0 are the emission intensities of **5** measured in an intermediate value of Cu^+ concentration and in the absence of Cu^+ , respectively. From the plot of $[1/F-F_0]$ vs $[\text{C}]^{-1}$, the value of “K” was extracted and it is found to be $1.10 \times 10^5 \text{ M}^{-1}$ (Figure 5.7b).

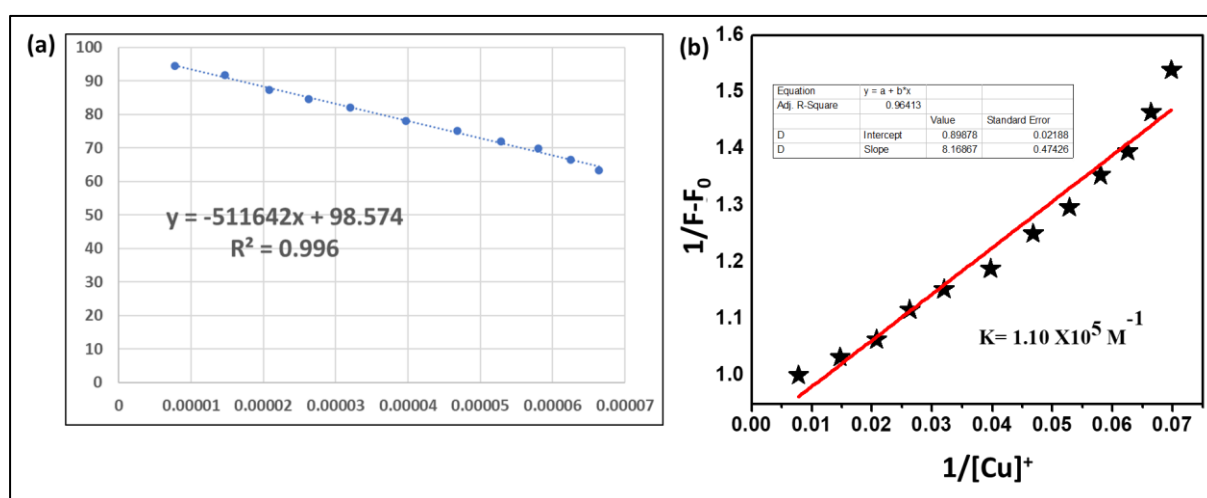


Figure 5.7. (a) Limit of Detection (LOD) calculation for **5** with Cu^+ ion by $3.3\sigma/S$ method; (b) Quantitative binding data (Benesi-Hildebrand plot) for **5** with Cu^+ ion. (b) Quantitative binding data (Benesi-Hildebrand plot) for **5** with Cu^+ ion.

Table 5.1. Comparison of LOD of present probe with various other reported Cu⁺ ion sensors.

Sl. No.	Probe	LOD	References
1.	C ₅₆ H ₄₁ CuN ₇ O ₁₃ S ₅ Zn ³⁺	8.2 nM	73
2.	C ₂₆ H ₁₈ N ₂ O ₆ S ₂	60.9 μM	74
3.	C ₃₃ H ₃₃ N ₇ O	10.8 nM	75
4.	C ₂₇ C ₃₅ S ₄ NO	5 × 10 ⁻⁷ M	76
5.	C ₁₃ H ₁₀ I ₂ N ₂ O	4.64 × 10 ⁻⁶ M	77
6.	C ₃₂ H ₂₆ N ₅ OS	20 μM	78
7.	C ₁₈ H ₂₁ N ₅ O ₃	0.20 μM	79
8.	C ₃₃ H ₂₃ O ₁₀ S ₃	1.02 × 10 ⁻⁶ M	80
9.	C ₃₄ H ₂₆ N ₆ O ₄ Fe	9.08 × 10 ⁻⁷ M	Present work

5.2.4. Electrochemical Study

Taking advantages of well-behaved electrochemically reversible nature of ferrocene derivatives,^{81,82} cation recognition process of receptor **5** was carried out using cyclic voltammetry (CV) and differential pulse voltammetry (DPV) experiments in CH₃CN solution (1.25 × 10⁻⁴ M) containing 0.1(M) [*n*-Bu₄N]ClO₄ as supporting electrolyte. Except Fe³⁺, Cu²⁺ and Cu⁺ ions, no perturbation of the cyclic voltammograms of **5** was observed for any other metal ions such as K⁺, Ag⁺, Zn²⁺, Ni²⁺, Mg²⁺, Hg²⁺, Cd²⁺, Fe²⁺, Al³⁺, Cr³⁺, Mn²⁺, Pb²⁺ and Co²⁺ even in large excess in CH₃CN solution (Figure 5.8). The receptor **5** displays a reversible one electron oxidation process with a clear evolution of redox wave at $E_{1/2} = 0.492$ V due to the ferrocene/ferrocenium redox couple.

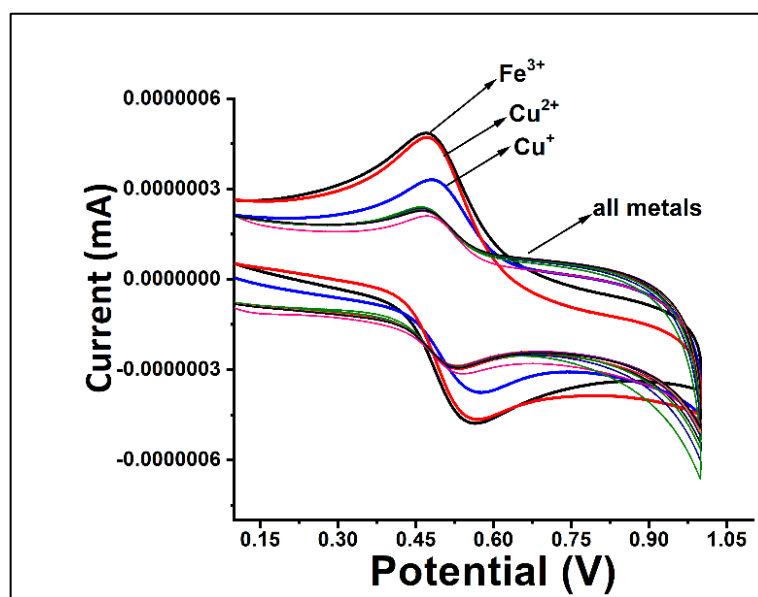


Figure 5.8. Evolution of Electrochemical study (CV) observed for **5** in CH_3CN (10^{-4} M) after addition of 1 equiv of several metal cations.

As shown in Figure 5.9a, gradual addition of Fe^{3+} ion led to the voltammetric wave shifted towards more cathodic current with insignificant change in potential. On the other hand, after addition of Cu^{2+} to the solution of receptor **5**, the voltammetric wave shifted towards a more cathodic current along with a slight shift towards anodic potential ($\Delta E_{1/2} = 12$ mV) (Figure 5.9b). This result demonstrated that Fe^{3+} ion promoted the mere oxidation of the Fc unit to Fc^+ ion, whereas Cu^{2+} metal cation promoted the oxidation of the Fc unit to Fc^+ ion, along with concomitant reduction to Cu^+ ion, which in turn formed a chelate complex with the oxidized ligand. The formation of $[\mathbf{5}^+\cdot\text{Cu}^+]$ complex led to a slight anodic shift. Beyond 1 equiv of Fe^{3+} and Cu^{2+} , the voltammograms did not show any alteration, which indicated no ferrocene unit remained to be oxidized to ferrocenium ion. Further, as shown in Figure 5.9c, upon stepwise addition of Cu^+ ion to the receptor **5** led to a significant voltammetric shift towards anodic potential $\Delta E_{1/2} = 30$ mV, which is due to the formation of a new complex species between the receptor **5** and Cu^+ ion. DPV experiments were also corroborated to the results obtained from CV experiments (Figures 5.9d, 5.9e, 5.9f). Interestingly, both CV and DPV experimental results are along the same line with that of the results obtained from spectrophotometric studies.

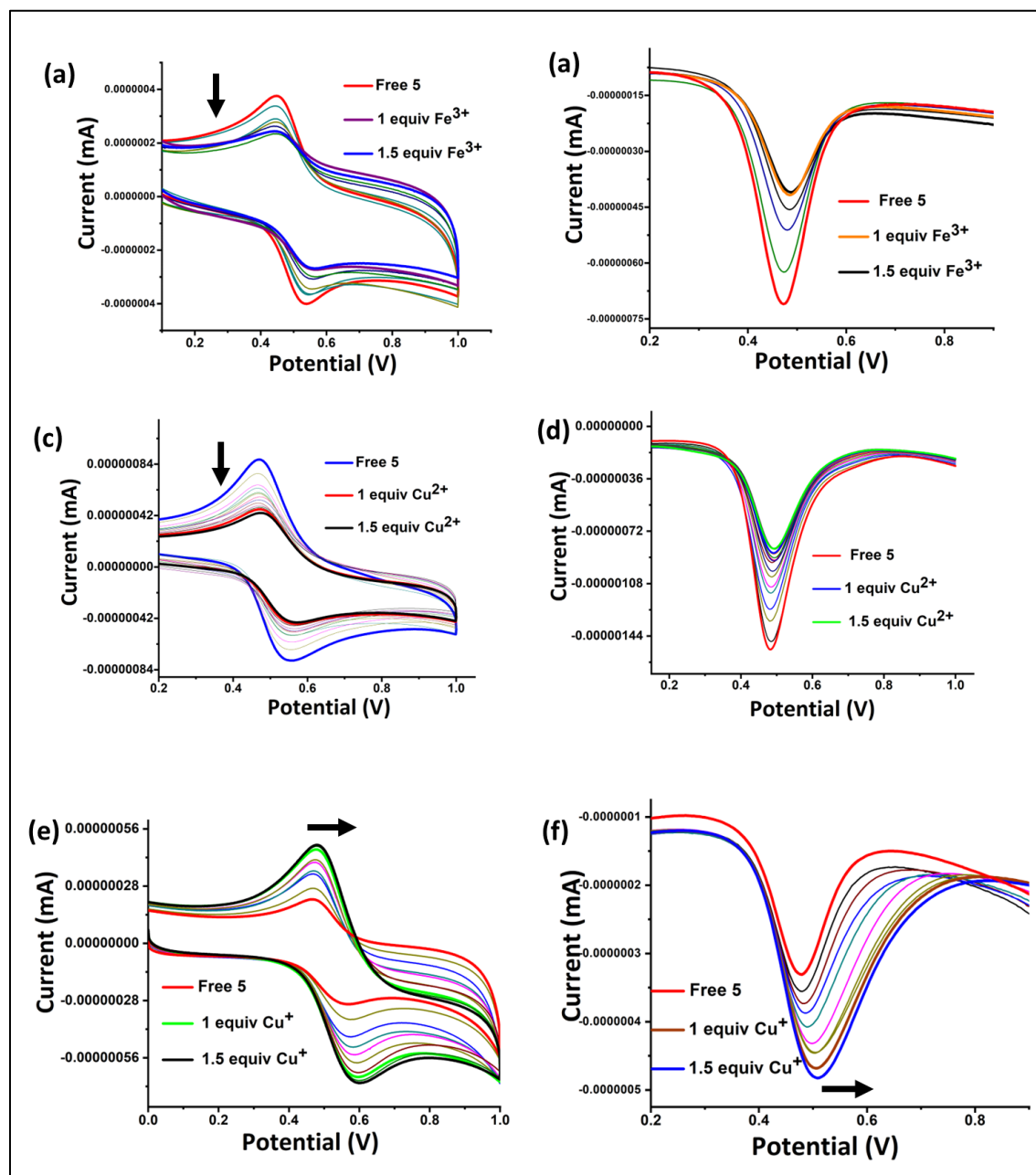


Figure 5.9. Cyclic voltammetry (CV) and (b) differential pulse voltammetry (DPV) of **5** (1.25×10^{-4} M) upon addition of (a) Fe^{3+} , (b) Cu^{2+} , (c) Cu^{+} up to 1.5 equiv in CH_3CN solution with $[\text{n-Bu}_4\text{N}]\text{ClO}_4$ as supporting electrolyte in the presence of ferrocene (Fc/Fc^+) as an internal standard. Differential pulse voltammetry (DPV) of **5** (1.25×10^{-4} M) upon addition of (d) Fe^{3+} , (e) Cu^{2+} , (f) Cu^{+} up to 1.5 equiv in CH_3CN solution with $[\text{n-Bu}_4\text{N}]\text{ClO}_4$ as supporting electrolyte in the presence of ferrocene (Fc/Fc^+) as an internal standard.

5.2.5. Reversibility Test

The reversibility test is one of the basic experiments to represent the practical application of a sensor. We have performed the reversibility experiment by treating $[5 \cdot \text{Cu}^+]$ complex with EDTA as a chelating agent. Upon addition of EDTA, Cu^+ ion came out from its binding site of the complex to form a more stable complex with EDTA, hence free ligand, **5** was obtained. This complexation and decomplexation phenomena can be monitored by fluorescence emission spectra (Figure 5.10). Addition of Cu^+ ion led to the diminution of fluorescence intensity and upon subsequent addition of EDTA as a chelating agent to the $[5 \cdot \text{Cu}^+]$ complex, the fluorescence emission was further increased to its original form. This experimental cycle could be repeated 3 times without much loss in sensitivity (Figure 5.10) and it indicated that the complexation and decomplexation process is indeed reversible. Similarly, oxidation of free ligand by Fe^{3+} and its back reduction to its original form by using LAS was described earlier.

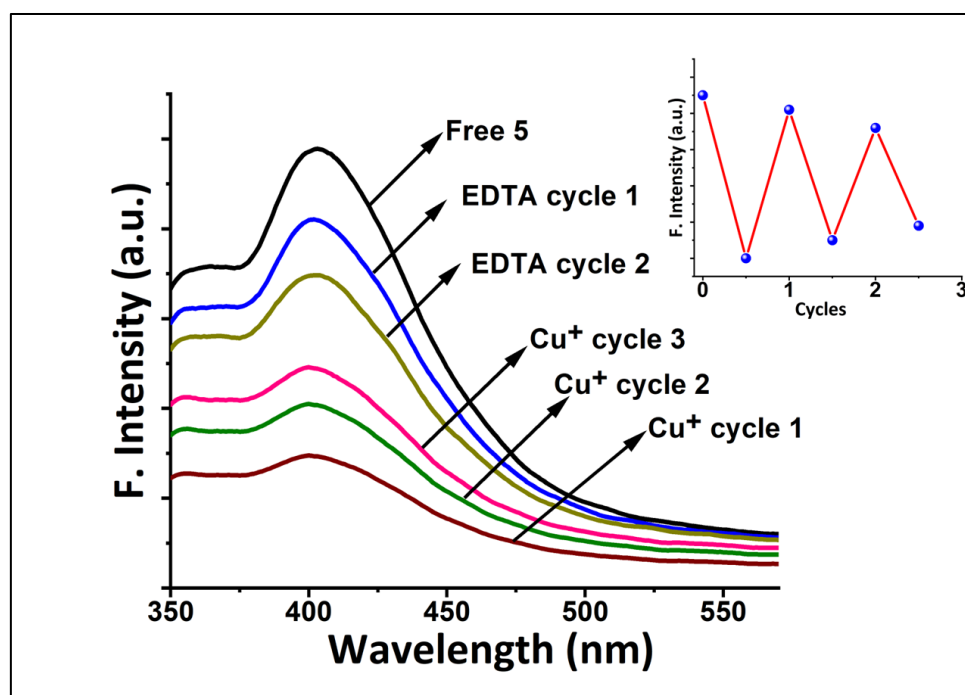


Figure 5.10. Reversible interaction of **5** with Cu^+ , introduction of EDTA to the system; Inset: Stepwise complexation/decomplexation cycles carried out in CH_3CN .

5.2.6. Binary Logic Gates

We observed that significant modulation of optical properties of probe **5** is possible upon interaction with different external agents such Fe^{3+} , Cu^{2+} , LAS and Cu^+ . Further, as molecular logic gates have been widely employed for mimicking the functions of chemical circuits, herein we will use emission spectral responses as function of a suitable combination of ionic inputs to mimic the binary logic operation. The output fluorescent signal (I/I_0 at 406 nm) above and below the threshold levels defines the “1” and “0” states respectively. Here the threshold value has been set at 30 for all of the logic operations. The values of I/I_0 at 406 nm for **5** with different combinations of varying concentration of Fe^{3+} (0 to 1 equiv) and LAS (0 to 1 equiv) resemble to an “INHIBIT” logic gate (Figure 5.11a). As shown in Figure 7a, the presence of only Fe^{3+} ion led to the maximum output value of I/I_0 at 406 nm ($I/I_0 = 70$) whereas in any other combination value of I/I_0 is below threshold level ($I/I_0 < 30$). This behavior is the well characteristic of an “INHIBIT” logic gate.⁷⁵ The normalized emission intensity in the form of column bars and the corresponding truth table for the developed “INHIBIT” logic gate were shown in Figure 5.11a.

Probe **5** has also the ability to mimic the function of an “OR” gate using Fe^{3+} and Cu^{2+} as inputs. A classical “OR” logic gate, having two inputs and one output port, should provide an enhanced signal in the presence of either one or both inputs. The values of I/I_0 at 406 nm for **5** with all possible combinations of varying concentration of Fe^{3+} (0 to 1 equiv) and Cu^{2+} (0 to 1 equiv) correspond to an “OR” logic gate (Figure 5.11b). The emission at 406 nm is low in the absence of both inputs, indicating the off state (0) of the system. On the other hand, output value of I/I_0 at 406 nm has a maximum ($I/I_0 = 70$) in the presence of either one or both of the inputs, indicating the on state (1) of the system. Thus, the present probe, **5** well mimics the function of a two-input “OR” logic gate (Figure 5.11b).

In order to make a single molecule to process complex operations, simple molecular Boolean logic gates need to be cascaded to obtain more complicated combinational molecular gates.⁷⁶ Keeping this idea in mind, we have tried to ensemble all the logic circuits utilizing all the inputs simultaneously and the fluorescence emission intensity is an output. By considering the output result from the three inputs combinational truth table (Figure 5.11c), a simple “AND-OR” combinational logic circuit can be achieved.

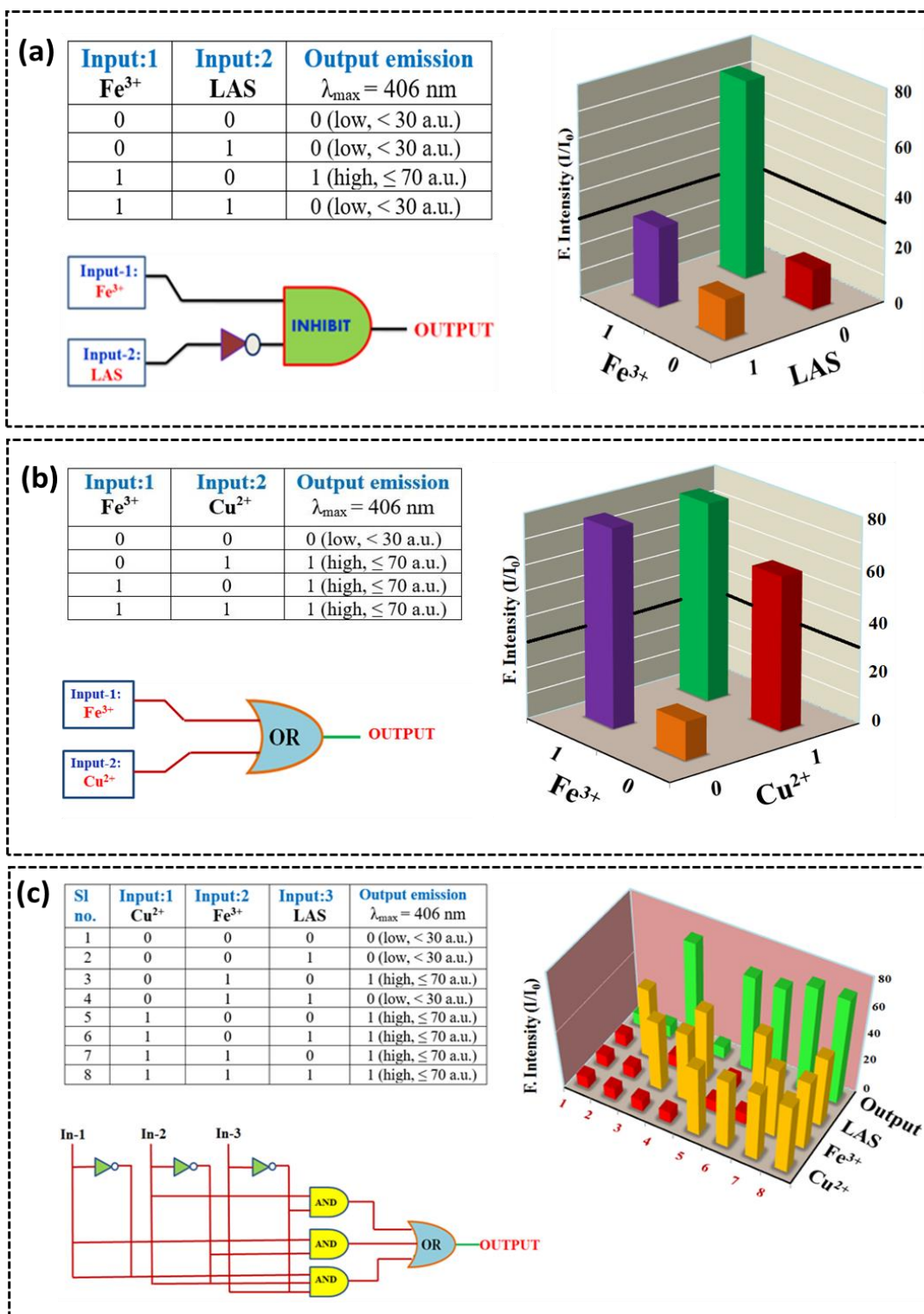


Figure 5.11. Truth table, logic circuit and bar diagram representation of (a) INHIBIT logic gate constructed with Fe^{3+} and LAS as inputs; (b) OR logic gate constructed with Fe^{3+} and Cu^{2+} as inputs and (c) combinational logic gate (red bar indicates input 0; yellow bar indicates input 1 and green bar is for output) constructed with Cu^{2+} , Fe^{3+} and LAS as inputs respectively.

5.2.7. Colorimetric Detection by Naked Eye

In order to obtain the naked eye perception for the color change of the probe **5** upon interaction with various metal ions, colorimetric test, one of the fundamental and preliminary investigations, was carried out. To elucidate the sensitivity and selectivity of probe **5** by colorimetric experiment, receptor **5** (1.25×10^{-4} M) was treated with perchlorate salts of various biologically active cations such as K^+ , Ag^+ , Ni^{2+} , Mg^{2+} , Hg^{2+} , Cd^{2+} , Fe^{2+} , Fe^{3+} , Cu^{2+} , Cu^+ , Al^{3+} , Cr^{3+} , Mn^{2+} , Pb^{2+} , Co^{2+} , Zn^{2+} and tetrakis(acetonitrile) hexafluorophosphate salt of Cu^+ in equimolar concentration (1.25×10^{-4} M) in CH_3CN (Figure 5.12). An instantaneous color change of receptor **5** from colorless to greenish blue was observed in the presence of Fe^{3+} and Cu^{2+} ion within 10 s, and light yellow for the Cu^+ ion within 60-80 s. Whereas other competing cations are completely non-responsive.

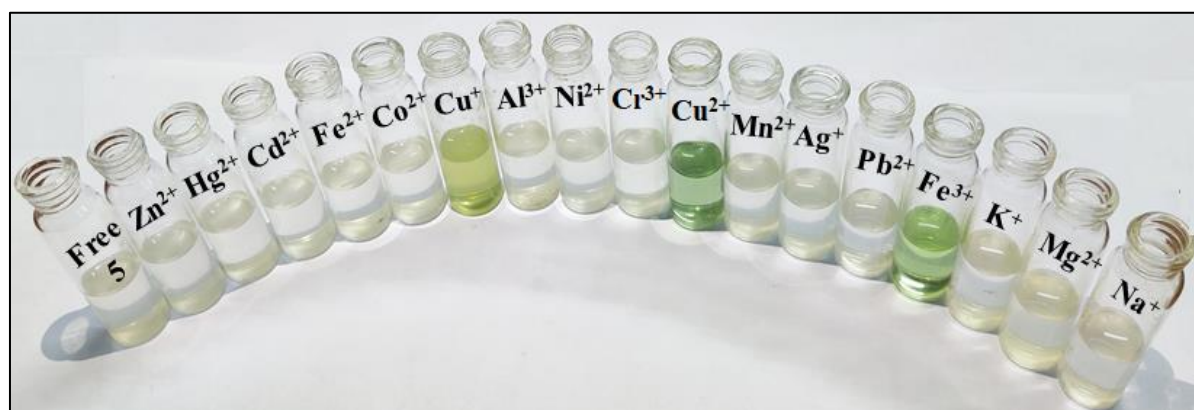


Figure 5.12. Visual color changes observed for receptor **5** in CH_3CN (1.25×10^{-4} M) after addition of 1 equiv of several metal cations.

5.2.8. Competitive Experiment

To further investigate the utility of probe **5** as a highly selective sensing probe towards Fe^{3+} , Cu^{2+} and Cu^+ ions over the other competitive metal ions, interference experiment was carried out. A solution of **5** in CH_3CN was treated separately with 1 equiv of Fe^{3+} ion in the presence of 10.0 equiv of each of interfering metal ions (Hg^{2+} , Cu^{2+} , Cu^+ , Al^{3+} , K^+ , Mg^{2+} , Cd^{2+} , Fe^{2+} , Cr^{3+} , Ni^{2+} , Zn^{2+} , Mn^{2+} , Ag^+ and Co^{2+}). As shown in Figure 5.13a, there is small or no

obvious interference with the detection of Fe^{3+} could be observed in the fluorescence emission spectra.

In a similar fashion, a solution of **5** was treated separately with 1 equiv of Cu^{2+} in the presence of 10.0 equiv of each of interfering metal ions (Fe^{3+} , Cu^+ , Hg^{2+} , Al^{3+} , K^+ , Mg^{2+} , Cd^{2+} , Fe^{2+} , Cr^{3+} , Ni^{2+} , Zn^{2+} , Mn^{2+} , Ag^+ and Co^{2+}) and the resulting titration showed small increase in the fluorescence intensity in presence of Fe^{3+} ion and a very little decrease in intensity in case of Cu^+ ion (Figure 5.13b). As shown in Figures 5.13c and 5.13d, on addition of Fe^{3+} and Cu^{2+} ions into CH_3CN solution of $[\mathbf{5}\cdot\text{Cu}^+]$ complex fluorescence intensity was found to be increased steadily. Therefore, **5** could be used for the detection of Fe^{3+} in the presence of other competing metal ions, including Cu^{2+} and Cu^+ ions and the present sensor could be utilized as Cu^{2+} selective probe in the presence of other competing ions, except Fe^{3+} ion. These results evidently demonstrate the high selectivity of **5** towards Fe^{3+} ion over other metal ions.

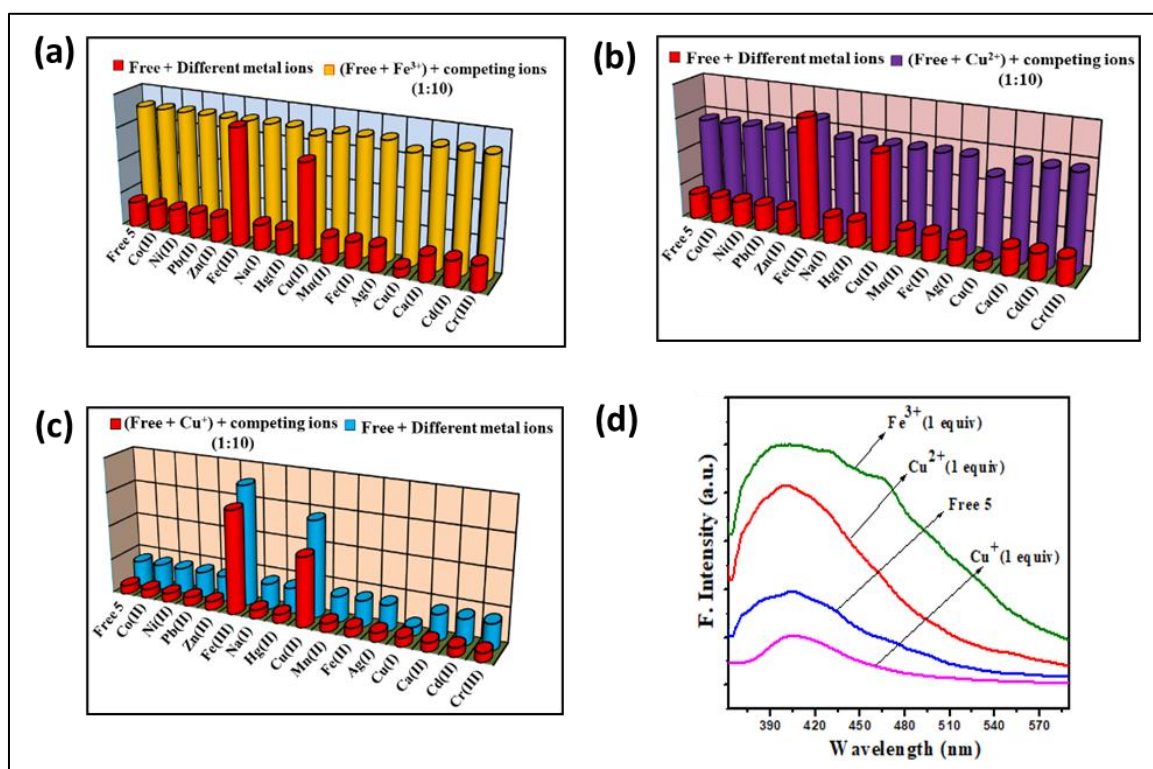


Figure 5.13. Bar plot representation of the fluorescence emission intensity of **5** upon the addition of (a) Fe^{3+} , (b) Cu^{2+} , (c) Cu^+ upon several competitive metal cations in CH_3CN medium and (d) fluorescence emission spectra upon addition of Fe^{3+} , Cu^{2+} , Cu^+ up to 1 equiv.

5.2.9. ^1H NMR and FT-IR Titration

In order to understand the binding sites of ligand **5** with Cu^+ , ^1H NMR titration was performed in CDCl_3 . As shown in Figure 5.14, the following changes in ^1H NMR spectrum of ligand **5** were observed upon addition of 1 equiv Cu^+ ion; (i) $-\text{NH}$ proton of amide linkage at 11.42 ppm was shifted downfield by 0.24 ppm, (ii) interestingly, signal corresponding to the $\text{N}=\text{CH}$ proton at $\delta = 9.33$ ppm merged together with the triazole proton at 8.98 ppm. This was confirmed from the integral value of the new merged peak at 8.97 ppm; (iii) there is no significant shift in ferrocene region (4.08 - 4.51 ppm), however, slight shift in aromatic region (7.08 - 8.52 ppm) was observed due to close proximity of coumarin and quinoline unit to the binding site of Cu^+ ion. It is noteworthy that, significant shifts were observed only in the case of $-\text{NH}$ and $-\text{N}=\text{CH}$ protons. Therefore, the overall significant changes in the chemical shift value suggested that the ligand **5** may bind with Cu^+ using either oxygen ($-\text{C}=\text{O}$) or nitrogen atom ($-\text{NH}$) of amide moiety (or with both oxygen and nitrogen) and 'N' atom of imine moiety (Inset, Figure 5.14).

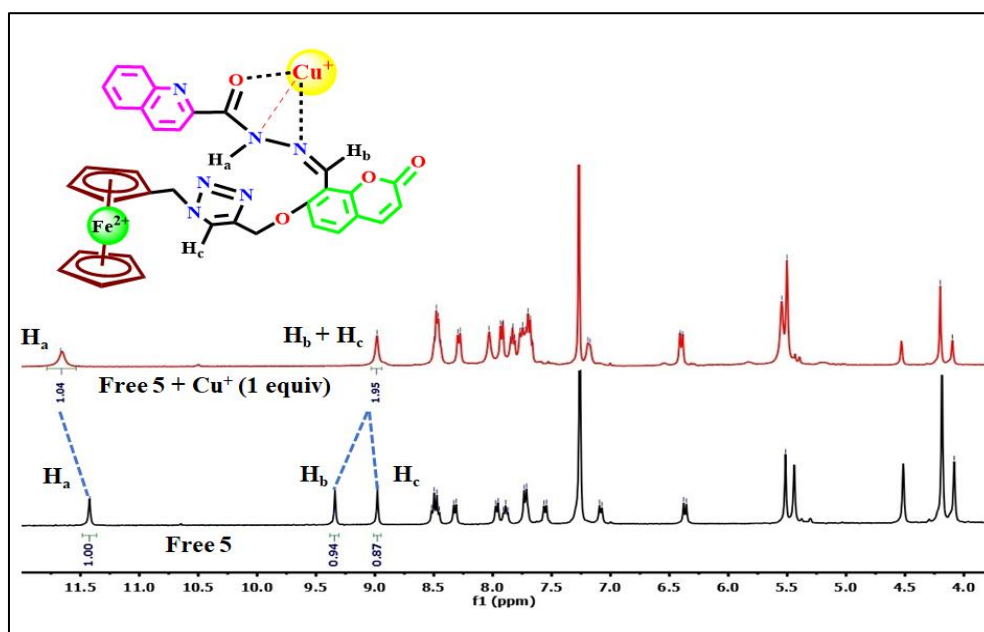


Figure 5.14. ^1H NMR spectral changes of probes **5** upon the addition of 1 equiv of Cu^+ ion in CDCl_3 as a solvent.

Further, to support the proposed binding mode of the ligand **5** with Cu^+ , FT-IR was carried out as presented in Figure 5.15. The probe **5** exhibits two bands at 1730 and 1678 cm^{-1} which can be assigned to the $\text{C}=\text{O}$ stretching vibration of the lactone moiety of the coumarin unit⁵⁷ and the amide carbonyl group of quinoline moiety⁴⁶ respectively. After addition of 1

equiv Cu^+ ion, C=O stretching frequency at 1678 cm^{-1} , corresponding to the amide ($-\text{CONH}_2$) group of quinoline subunit, significantly shifted (80 cm^{-1}) to 1598 cm^{-1} , whereas an insignificant shift of 8 cm^{-1} for C=O unit of coumarin moiety was observed. Moreover, the peak at 3285 cm^{-1} corresponding to secondary amine ($-\text{CO-NH-N-}$) got almost diminished, indicating the involvement of $-\text{NH}$ unit in complexation of the probe with Cu^+ ion. Combining the results, obtained from ^1H NMR and IR titration, it can be concluded that the plausible binding mode of Cu^+ is the oxygen ($-\text{CONH}_2$) and nitrogen ($-\text{CONH}_2$) atom of amide unit attached to quinoline moiety and N atom of imine moiety ($\text{N}=\text{CH}$) (Inset, Figure 5.14).

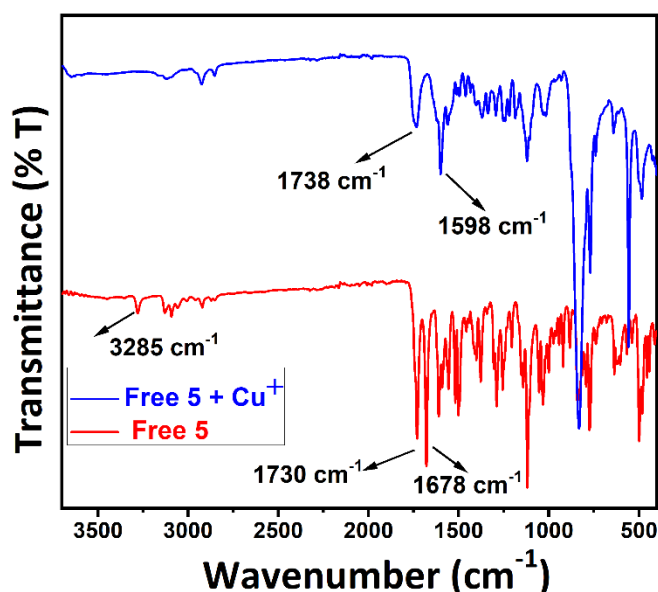


Figure 5.15. FT-IR spectra of receptor **5** and its binding effect on addition of Cu^+ metal ion.

5.3. Theoretical (DFT) Studies

Quantum chemical calculations were performed in order to obtain the detailed theoretical aspects of structural and electronic parameters of probe **5** before and after of its oxidation and complexation with corresponding metal ions. Many different starting geometries were used to obtain the optimized geometry which corresponds to the global minima and geometry optimization of **5**, oxidized **5** and $[\mathbf{5}\cdot\text{Cu}^+]$ was done by DFT calculations at the CAM-B3LYP/LanL2DZ(CPCM) level in acetonitrile (Figures 5.16 and 5.17) and their corresponding molecular orbital pictures are shown in Supporting Information (Figures 5.18, 5.19 and 5.20).

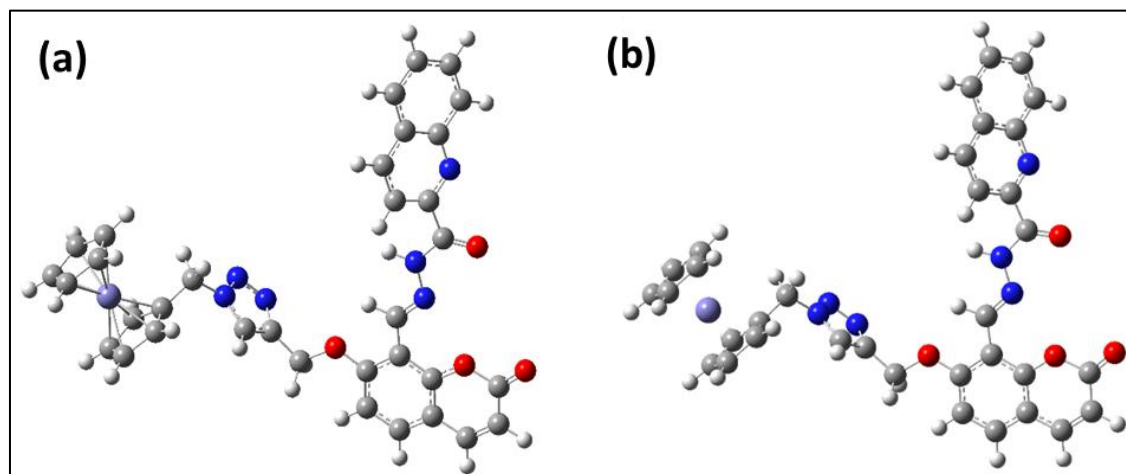


Figure 5.16. (a) The most stable optimized structure of receptor **5** and (b) after oxidation of ligand, calculated at the CAM-B3LYP/LanL2DZ/CPCM (acetonitrile) level.

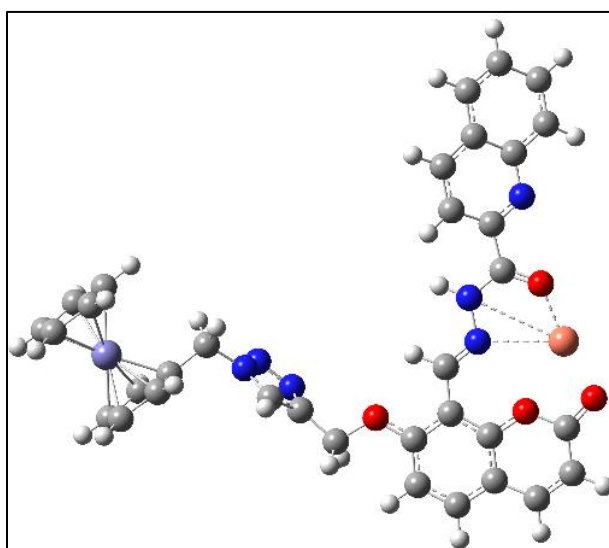


Figure 5.17. The most stable optimized geometry of [5·Cu⁺] calculated at the CAM-B3LYP/LanL2DZ/CPCM (acetonitrile) level (Cu–O = 1.93 Å, Cu–N = 2.72 Å and Cu–NH = 3.20 Å distances).

Further, to rationalize the UV-vis and emission spectra, time-dependent DFT (TD-DFT) calculations at the CAM-B3LYP/LanL2DZ(CPCM) (acetonitrile) level were performed on **5**, oxidized **5** and on [5·Cu⁺] complex. A major strong highest occupied molecular orbital

(HOMO)-2 (coumarin π type) to lowest unoccupied molecular orbital (LUMO; coumarin π^* type) transition with oscillator strength of $f = 0.8424$ (Table 5.2) was observed in case of ligand **5** from TD-DFT vertical excited state calculations, whereas, a transition between HOMO (coumarin π type) to LUMO+3 (coumarin π^* type) (oscillator strength $f = 0.8394$) (Table 5.3) dominates in the case of the oxidized product. Both the cases, HOMO-LUMO gap remains almost the same (in the range of 6.34-6.66 eV), which indicates the insignificant shifts in UV-vis absorption bands. This is in close agreement with the experimental UV-vis results. Similarly, TD-DFT calculations at the CAM-B3LYP/LanL2DZ(CPCM) (acetonitrile) level on [5·Cu⁺] predict a strong HOMO-3 (coumarin π type) to LUMO transition with oscillator strength of $f = 0.8337$ (Table 5.4), with almost similar HOMO-LUMO gap, which is an agreement with the experimental evidence.

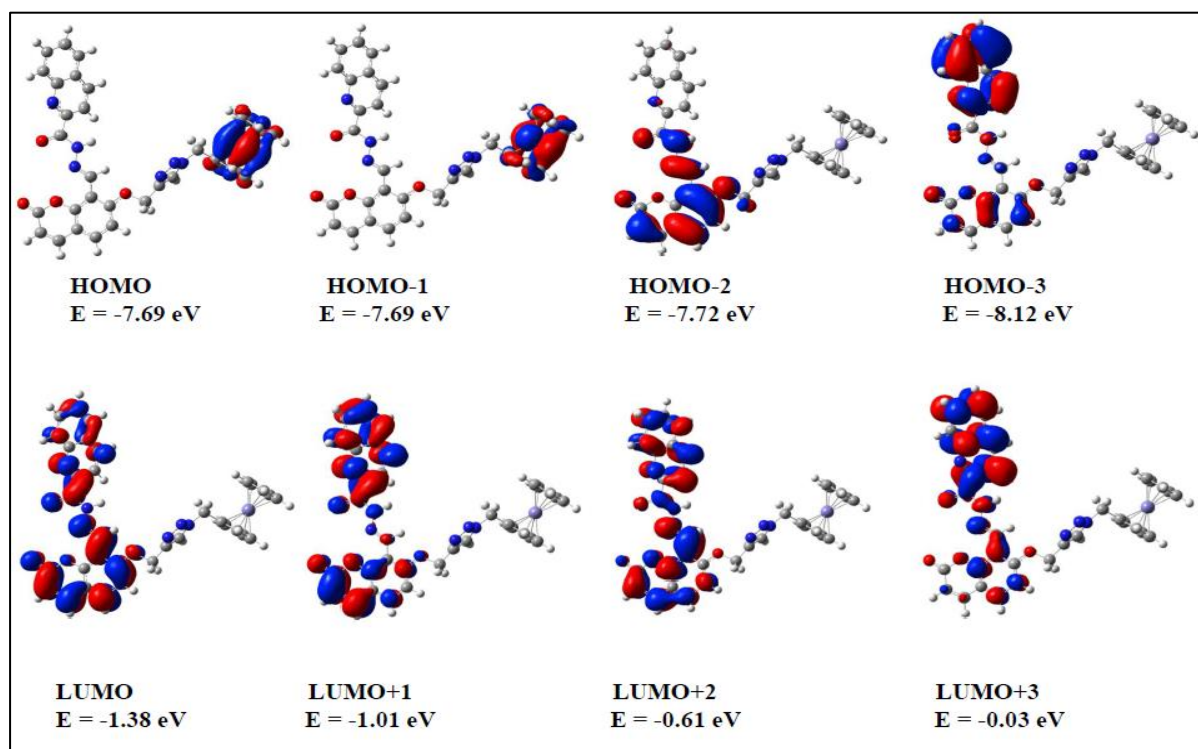


Figure 5.18. Frontier Molecular Orbitals of free ligand with energy calculated at the CAM-B3LYP/LanL2DZ/CPCM (acetonitrile) level.

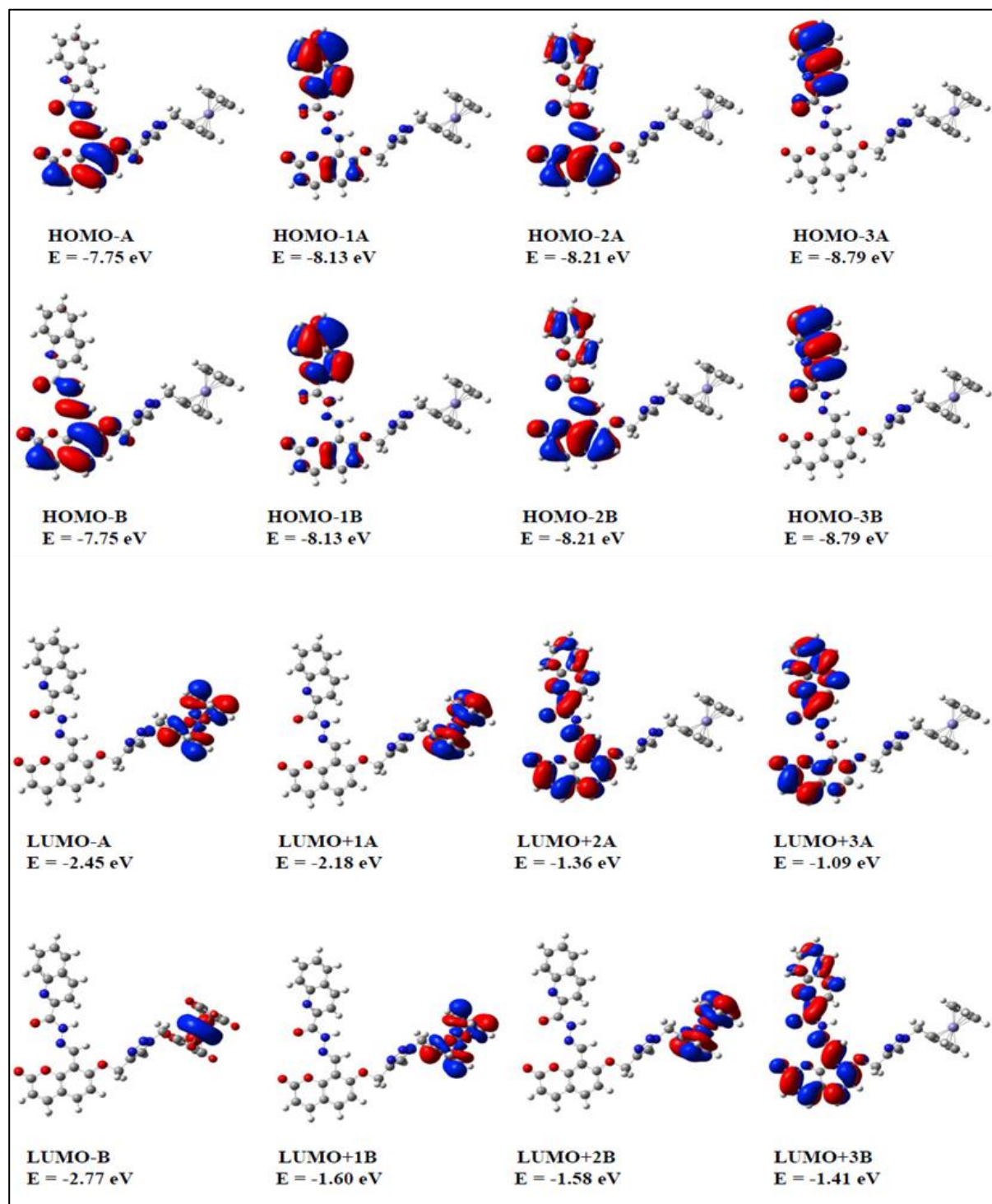


Figure 5.19. Frontier molecular orbitals of oxidized ligand with energy calculated at the CAM-B3LYP/LanL2DZ/CPCM (acetonitrile) level.

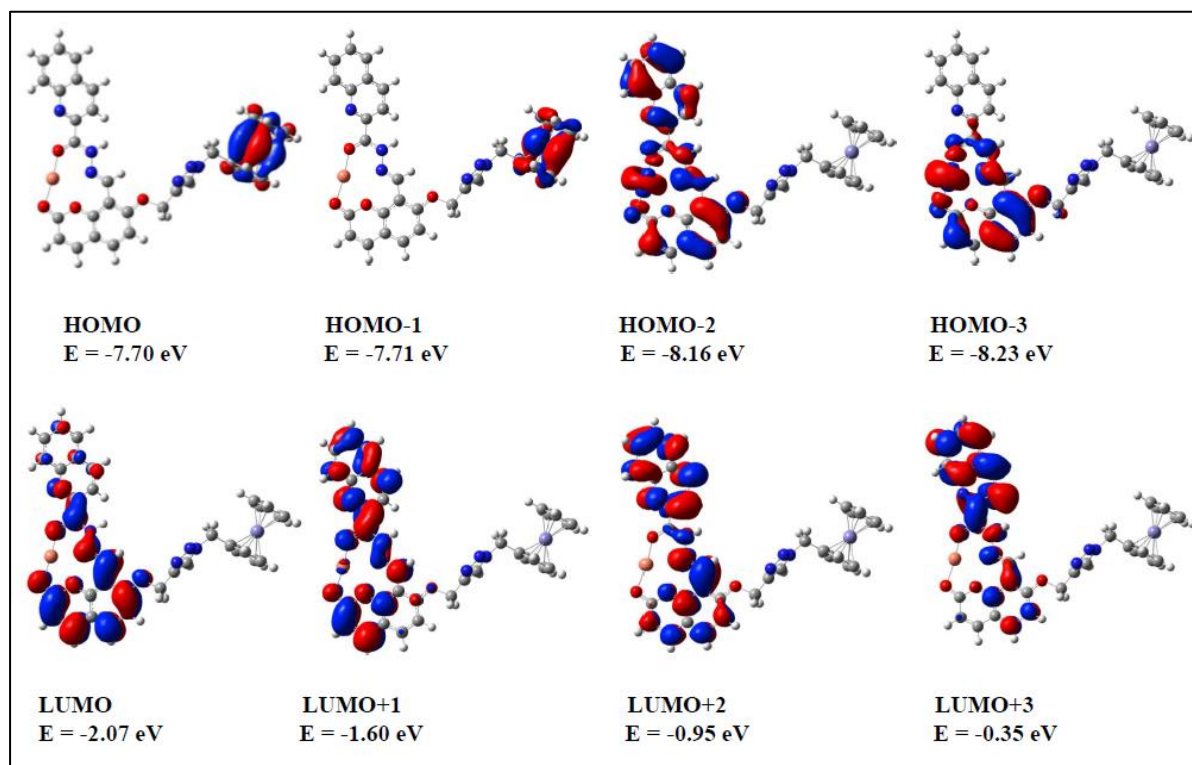


Figure 5.20. Frontier Molecular Orbitals of [5·Cu⁺] with energy calculated at the CAM-B3LYP/LanL2DZ/CPCM (acetonitrile) level.

Table 5.2. The major transitions with Osc. strength and λ_{exc} of free ligand.

Molecule	λ_{exc} (nm)	Osc. strength (f)	Major transition
Free Ligand (5)	301.958580156	0.8424	H-2->LUMO (74%), H-2->L+2 (10%)
	294.681259239	0.5809	H-4->LUMO (58%), H-3->LUMO (12%)
	288.154398429	0.1667	H-2->L+1 (41%), H-2->L+2 (31%)
	280.774022855	0.0465	H-3->LUMO (21%), H-3->L+1 (26%)

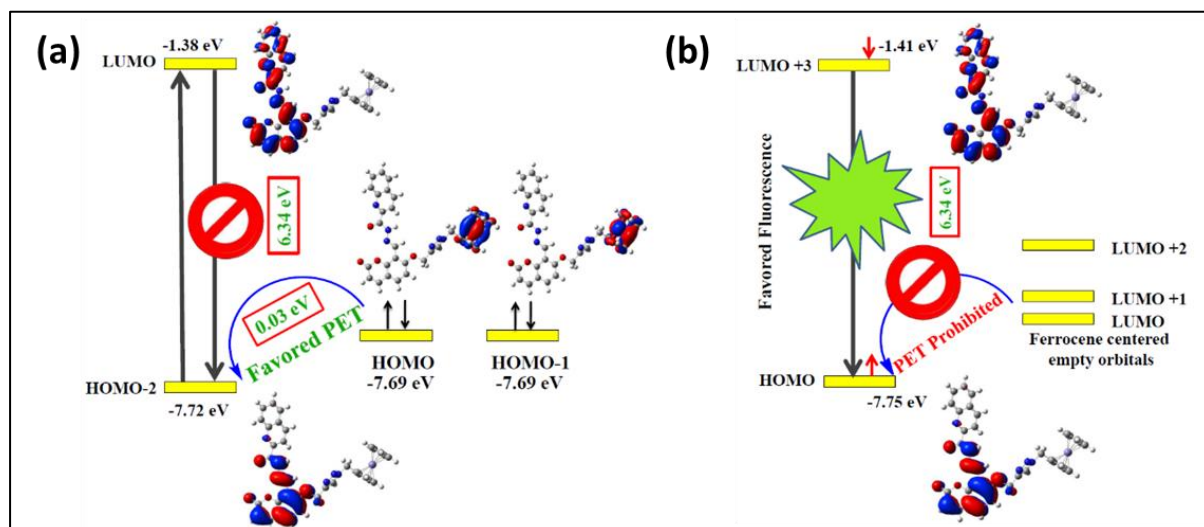
Table 5.3. The major transitions with Osc. strength and λ_{exc} of oxidized ligand.

Molecule	λ_{exc} (nm)	Osc. strength (f)	Major transition
Oxidized Ligand	301.63	0.8394	HOMO(A)->L+2(A) (37%), HOMO(B)->L+3(B) (37%)
	301.20	0.0047	HOMO(B)->LUMO(B) (99%)
	294.67	0.5693	H-2(A)->L+2(A) (30%), H-2(B)->L+3(B) (30%)

Table 5.4. The major transitions with Osc.strength and λ_{exc} of $[5\cdot\text{Cu}^+]$.

Molecule	λ_{exc} (nm)	Osc. strength (f)	Major transition
$[5\cdot\text{Cu}^+]$	321.836239778	0.2339	H-7->LUMO (68%)
	319.152061914	0.0191	H-3->L+1 (40%), H-2->L+1 (36%)
	316.181350604	0.8337	H-7->LUMO (14%), H-3->LUMO (39%), H-2->LUMO (30%)
	297.602537174	0.1378	H-3->L+1 (29%), H-2->L+1 (25%)
	296.634191478	0.0353	H-4->LUMO (19%), H-4->L+1 (36%)

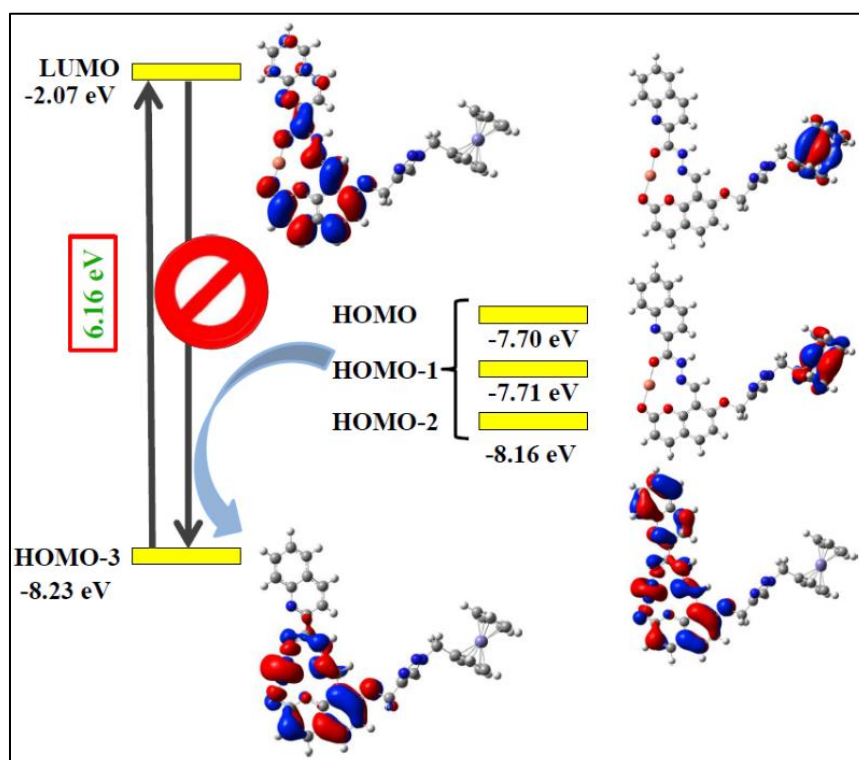
TD-DFT calculations revealed that for the free ligand, the major fluorophore transition involves HOMO-2 and LUMO orbitals. The HOMO/HOMO-1 are degenerate molecular orbitals of free ligand with energy -7.69 eV and they lie in between the fluorophore transition orbitals, HOMO-2 (-7.72 eV) and LUMO (-1.38 eV). As a result, an energetically favorable electron transfer from HOMO/HOMO-1 to HOMO-2 occurs and it inhibits excited electron to come back from LUMO to HOMO-2 (Scheme 5.3a). Therefore, the fluorescence is efficiently quenched in the case of free ligand. Moreover, it is evident from molecular orbital pictures of fluorophore transition orbitals (Scheme 5.3a) that electron density in quinoline unit is less than that of coumarin moiety, and hence the quinoline unit took part in PET process by accepting electron more easily compared to coumarin unit from donor ferrocene unit. This phenomenon was further supported by thermodynamic calculation using Weller equation (*vide supra*).



Scheme 5.3. Illustration of probable PET based mechanism for **5**, (a) before oxidation (b) after oxidation at the CAM-B3LYP/LanL2DZ/CPCM (acetonitrile) level.

On the other hand, upon oxidation of **5** by Fe^{3+} or Cu^{2+} , the population of electron density on ferrocene got diminished due to the formation of ferrocenium ion (Fe^{3+}). Thus, the electron transfer from ferrocene to quinoline is no more facile. Furthermore, all the orbitals, (LUMO, LUMO+1, LUMO+2) lie in between fluorophore centered orbitals [HOMO (-7.75 eV) and LUMO+3 (-1.41 eV)] are ferrocene centered empty orbitals and thus the PET process is forbidden and re-emergence of fluorescence is observed upon oxidation (Scheme 5.3b).

Furthermore, the formation of [**5**· Cu^+] complex was examined by DFT calculation using CAM-B3LYP/LanL2DZ/CPCM level (Figure 13). WBI and bond distance in [**5**· Cu^+] complex are follows: $\text{WBI}_{\text{Cu-O}} = 0.233$, $d = 1.93 \text{ \AA}$; $\text{WBI}_{\text{Cu-N}} = 0.050$, $d = 2.72 \text{ \AA}$ and $\text{WBI}_{\text{Cu-NH}} = 0.010$, $d = 3.20 \text{ \AA}$ (weak interaction). We have performed natural population analysis (NPA) on [**5**· Cu^+] complex and calculation suggests the charge on Cu, N (of imine), O (amide linkage) and NH as 0.732, -0.292, -0.686 and -0.434 respectively. Further, TD-DFT calculations, performed on [**5**· Cu^+] predict a major HOMO-3 to LUMO transition (oscillator strength $f = 0.8337$) (Table S4). Incidentally, the HOMO-2 (-8.16 eV), HOMO-1 (-7.71 eV) and HOMO (-7.70 eV) are situated in between the major transition orbitals, HOMO-3 (-8.23 eV) and LUMO (-2.07 eV). Consequently, an energetically favorable electron transfer from HOMO (Cu centered orbital) to HOMO-3 (fluorophore centered orbital) occurs and it inhibits excited electron to come back from LUMO to HOMO-3 (Scheme 5.4), leading to the fluorescence quenching.



Scheme 5.4. Schematic representation of fluorescence quenching for $[5 \cdot \text{Cu}^+]$ complex calculated at the CAM-B3LYP/LanL2DZ/CPCM (acetonitrile) level.

5.4. Conclusions

In summary, we have developed an “OFF-ON-OFF” molecular device which exhibits oxidation induced turn-on fluorescence emission *via* PET process in presence of paramagnetic transition metal ions (Fe^{3+} and Cu^{2+}), which are potential quencher of the excited state fluorophores. We have circumvented the quenching issues of Fe^{3+} and Cu^{2+} ion by treating them as an oxidizing agent rather than binding agents. The viability of the PET process was authenticated by Weller equation and DFT calculations. Moreover, we have successfully designed an attractive probe, **5** that can exhibit different fluorescence responses for different metal ions, therefore, it can be used to distinguish multi-ions at a time, which would ultimately diminish the cost of the sensing processes and analytical time. To the best of our knowledge, the present probe, **5** is the 1st example of ferrocene appended coumarin-quinoline based PET sensor, which is differentially selective towards Fe^{3+} , Cu^{2+} and Cu^+ ions. Taking advantage of this differentially selective properties of the present probe two basic logic circuits, “INHIBIT” and “OR” have been constructed. These basic binary logic gates were further cascaded to form

an “AND-OR” combinational gate, which could be a useful prototype from which other bioanalyte detection systems can be constructed.

5.5. Experimental Sections

5.5.1. Materials and Measurements

Unless otherwise stated, all the analytes used for synthesis were purchased from commercial suppliers and used without further purification. Perchlorate salt of metals (Ag^+ , K^+ , Cr^{3+} , Ca^{2+} , Co^{2+} , Hg^{2+} , Cu^{2+}) and (Mn^{2+} , Pb^{2+} , Fe^{3+} , Mg^{2+} , Cd^{2+} , Zn^{2+} , Fe^{2+}) were purchased from Alfa Aesar and Sigma Aldrich respectively. Tetrakis(acetonitrile)copper(I) hexafluorophosphate is the source of Cu^+ , purchased from sigma Aldrich. Ferrocene, 7-hydroxy coumarin, hexamethylenetetramine and quinaldic acid were purchased from Sigma Aldrich. POCl_3 , SOCl_2 , propargyl bromide, hydrazine monohydrate, NaN_3 , Na_2SO_4 , $\text{CuSO}_4 \cdot 5\text{H}_2\text{O}$, sodium L-ascorbate, K_2CO_3 , glacialacetic acid, ethanol were purchased from local chemicals. DMF, methanol and acetonitrile (HPLC) were purchased from Merck, all the solvents were of the spectroscopic grade for the optical spectroscopic studies, and they were dried according to the standard procedures prior to use. Mono (azidomethyl) ferrocene **1**, receptor **2** and **4** were synthesized according to the literature procedure.⁸⁵⁻⁸⁷ The reactions were monitored by thin-layer chromatography on silica-gel plates and column chromatography was conducted on the silica gel (mesh 60-120) in a column of 2.5 cm diameter. A conventional three-electrode configuration setup was used to perform cyclic voltammetry (CV) and differential pulse voltammetry (DPV) experiments (1.25×10^{-4} M), where glassy carbon, platinum and silver/silver chloride (Ag/Ag^+) were used as working electrode, auxiliary electrode and reference electrode respectively. Deoxygenation of the solutions was achieved by bubbling nitrogen for at least 10 min, and the working electrode was cleaned after each run. Tetrabutylammonium perchlorate, $[\text{n-Bu}_4\text{N}]\text{ClO}_4$, was employed as supporting electrolyte for carry out the experiments. Receptor **5** (1.25×10^{-4} M) was dissolved in CH_3CN containing 0.1 M $[\text{n-Bu}_4\text{N}]\text{ClO}_4$ and the resulting solution was subjected to cyclic voltammetric experiments at a scan rate 0.05 Vs^{-1} . Ferrocene (Fc/Fc^+) is the level of the internal standard. All the cycles were demonstrated at a scan rate of 0.05 Vs^{-1} . UV-vis and fluorescence spectra were recorded at $C = 2.5 \times 10^{-5}$ M and 1×10^{-6} M respectively and were stated in the corresponding figure captions.

5.5.2. Instrumentation

^1H and ^{13}C NMR spectroscopic measurements were carried out with a BRUKER 400 MHz FT-NMR spectrometer using TMS (SiMe_4) as an internal reference at room temperature and the chemical shifts are reported in ppm. FT-IR spectra obtained from a Perkin Elmer LX-1 FTIR spectrophotometer. HRMS were collected from a water HRMS model XEVO-G2QTOF#YCA351 spectrometer. SHIMADZU-TCC-240A UV-vis spectrophotometer was used for the study of absorption spectra at room temperature. Fluorescence emission spectra were obtained using SHIMADZU RF-5301PC spectrophotometer. The cyclic voltammetry (CV) and differential pulse voltammetry (DPV) performed on a CH Instruments electrochemical workstation. CHN analysis was performed on a Vario EL elemental CHNS analyzer.

Caution! Metal perchlorate salts are potentially explosive in certain conditions. All due precautions should be taken while handling perchlorate salts!

5.5.3.A. Synthesis of Compound 3

In a typical procedure, the mixture of alkyne of (2-oxo) chromene carbaldehyde (0.100 g, 0.438 mmol) and mono (azidomethyl) ferrocene (0.105 g, 0.438 mmol) were dissolved in 10 ml of solvent comprised of acetone and water (2:1). Subsequently, $\text{CuSO}_4 \cdot 5\text{H}_2\text{O}$ (0.175 mmol) and sodium L-ascorbate (0.219 mmol) were added by dissolving in water successively to the reaction mixture and stirred for overnight at room temperature. The reaction mixture was diluted with ethyl acetate (100 ml). The organic phase was washed with water and brine several times and dried over Na_2SO_4 . The crude product was purified by column chromatography (silica gel, EtOAc: hexane, 8:2, v/v) to obtain the pure product, **3** as yellow solid (0.069 g, 33.56 %).

^1H NMR (CDCl_3 , 400 MHz) δ = 10.64 (s, 1H, $\text{CHO}_{\text{coumarin}}$), 7.72 (s, 1H, H_{triazole}), 7.66-7.60 (m, 2H, H_{coumarin}), 7.19 (d, 1H, H_{coumarin} , J = 12 Hz), 6.34 (d, 1H, H_{coumarin} , J = 12.8 Hz), 5.38 (s, 2H, OCH_2), 5.31 (s, 2H, NCH_2), 4.28 (t, 2H, H_{Cp}), 4.23 (t, 2H, H_{Cp}), 4.18 (s, 5H, H_{Cp}); ^{13}C NMR (CDCl_3 , 100 MHz) δ = 186.71, 161.62, 159.35, 156.26, 142.98, 134.09, 122.69,

114.31, 113.09, 112.96, 109.83, 80.56, 69.21, 68.96, 63.68, 50.33. **HRMS** (ESI) m/z calcd for $C_{24}H_{19}FeN_3O_4$ $[M + Na]^+$ 492.0622; found 492.0624.

5.5.3.B. Synthesis of Compound 5

Compound **3** (0.106 g, 0.226 mmol) and quinaldic acid hydrazide (0.042 g, 0.226 mmol) were dissolved in 10 ml of distilled methanol and the resulting reaction mixture was refluxed for 6 h. Then the solution was cooled to room temperature to obtain a precipitate. The precipitate was filtered, washed several times with cold methanol and dried under vacuum. The crude product was further recrystallized from acetonitrile at room temperature to obtain pure compound **5** (0.045 g, 31.2 %) as a pale yellow powder.

1H NMR ($CDCl_3$, 400 MHz) δ = 11.42 (s, 1H, NH), 9.33 (s, 1H, CH), 8.98 (s, 1H, $H_{triazole}$), 8.52-8.45 (m, 2H, $H_{quinoline}$), 8.32 (d, 1H, $H_{quinoline}$, J = 8 Hz), 7.96 (d, 1H, $H_{quinoline}$, J = 8 Hz), 7.89 (t, 1H, $H_{quinoline}$, J = 8 Hz), 7.72 (d, 2H, $H_{quinoline}$, J = 8 Hz), 7.55 (d, 1H, $H_{coumarin}$, J = 8 Hz), 7.08 (d, 1H, $H_{coumarin}$, J = 8 Hz), 6.37 (d, 1H, $H_{coumarin}$, J = 8 Hz), 5.51 (s, 2H, OCH_2), 5.44 (s, 2H, NCH_2), 4.51 (s, 2H, H_{c_p}), 4.19 (s, 5H, H_{c_p}), 4.08 (s, 2H, H_{c_p}). **FT-IR** (cm^{-1}) 3279.67, 1730.74, 1678.72, 1610.49, 1591.08, 1556.52, 1119.19, 775.94; **HRMS** (ESI) m/z calcd for $C_{34}H_{26}FeN_6O_4$ $[M + H]^+$ 639.1443; found 639.1445; Anal. Calcd for $C_{34}H_{26}FeN_6O_4$, C, 63.94; H, 4.11; N, 13.17. Found: C, 63.25, H, 4.17; N, 12.94.

5.6. Computational Details

The energy of the optimized geometries of free ligand and oxidized ligand are performed in solvent (acetonitrile) phase by using the density functional theory method with the Becke, 3-parameter, CAM-B3LYP⁸⁸ hybrid functional for exchange–correlation and LanL2DZ in the form of basis set. The optimized geometry of free ligand and oxidized ligand are shown in Figure 10. All the calculations were performed using the Gaussian 09⁸⁹ and Gauss Sum⁹⁰ software's.

5.7. References

1. Yan, P.; Holman, M. W.; Robustelli, P.; Chowdhury, A.; Ishak, F. I.; Adams, D. M. *J. Phys. Chem. B* **2005**, *109*, 130-137.
2. Roeffaers, M. B. J.; De Cremer, G.; Uji-i, H.; Muls, B.; Sels, B. F.; Jacobs, P. A.; De Schryver, F. C.; De Vos, D. E.; Hofkens, J. *Proc. Natl. Acad. Sci. U. S. A.* **2007**, *104*, 12603-12609.
3. Dale, T. J.; Rebek, J. Jr. *J. Am. Chem. Soc.* **2006**, *128*, 4500-4501.
4. Nagale, S. B.; Sternfeld, T.; Walt, D. R. *J. Am. Chem. Soc.* **2006**, *128*, 5041-5048.
5. Sun, X.; James, T. D. *Chem. Rev.* **2015**, *115*, 8001-8037.
6. Johnson, A. D.; Paterson, K. A.; Spiteri, J. C.; Denisov, S. A.; Jonusauskas, G.; Tron, A.; McClenaghan, N. D.; Magri, D. C. *New J. Chem.* **2016**, *40*, 9917-9922.
7. Kumar, A.; Chae, P. S. *Anal. Chimica Acta* **2017**, *958*, 38-50.
8. Kumar, A.; Vanitab, V.; Waliab, A.; Kumar, S. *Sens. Actuators, B* **2013**, *177*, 904-912.
9. Veale, E. B.; Gunnlaugsson, T. *J. Org. Chem.* **2008**, *73*, 8073-8076.
10. de Silva, A. P.; Moody, T. S.; Wright, G. D. *Analyst* **2009**, *134*, 2385-2393.
11. Spiteri, J. C.; Denisov, S. A.; Jonusauskas, G.; Klejna, S.; Szaciłowski, K.; McClenaghan, N. D.; Magri, D. C. *Org. Biomol. Chem.* **2018**, *16*, 6195-6201.
12. Bhatta, S. R.; Bheemireddy, V.; Thakur, A. *Organometallics* **2017**, *36*, 829-838.
13. Alfonso, M.; Tárraga, A.; Molina, P. *Inorg. Chem.* **2013**, *52*, 7487-7496.
14. Qu, J.; Song, Y.; Ji, W.; Jing, S.; Zhu, D.; Huang, W.; Zheng, M.; Lie, Y.; Ma, J. *Dalton Trans.* **2016**, *45*, 3417-3428.
15. Martínez, R.; Ratera, I.; Tárraga, A.; Molina, P.; Veciana, J. *Chem. Commun.* **2006**, 3809-3811.
16. Huang, Y.-Q.; Chen, H.-Y.; Wang, Y.; Ren, Y.-H.; Li, Z.-G.; Li, L.-C.; Wang, Y. *RSC Adv.* **2018**, *8*, 21444-21450.
17. Carter, K. P.; Young, Al. M.; Palmer, A. E. *Chem. Rev.* **2014**, *114*, 4564-4601.
18. Hosseini, M.; Ghafarloo, A.; Ganjali, M. R.; Faridbod, F.; Norouzi, P.; Niasari, M. S. *Sens. Actuators, B* **2014**, *198*, 411-415.
19. Sohrabi, M.; Amirnasr, M.; Meghdadi, S.; Lutz, M.; Torbati, M. B.; Farrokhpour, H. *New J. Chem.* **2018**, *42*, 12595-12606.
20. Aich, K.; Goswami, S.; Das, S.; Mukhopadhyay, C. D.; Quah, C. K.; Fun, H. K. *Inorg. Chem.* **2017**, *56*, 7404-7415.

21. Wang, J.; Xia, T.; Zhang, X.; Zhang, Q.; Cui, Y.; Yang, Y.; Qian, G. *RSC Adv.* **2017**, *7*, 54892-54897.
22. Li, J.; Zhang, C. F.; Yang, S. H.; Yang, W. C.; Yang, G. F. *Anal. Chem.* **2014**, *86*, 8693-8699.
23. Huang, L.; Zhu, Q.; Zhu, J.; Luo, L.; Pu, S.; Zhang, W.; Zhu, W.; Sun, J.; Wang, J. *Inorg. Chem.* **2019**, *58*, 1638-1646.
24. Fahrni, C. J. *Current Opinion in Chemical Biology* **2013**, *17*, 656-662.
25. Wu, X.; Guo, Z.; Wu, Y.; Zhu, S.; James, T. D.; Zhu, W. *ACS Appl. Mater. Interfaces* **2013**, *5*, 12215-12220.
26. Kumar, A.; Chae, P. S.; Kumar, S. *Dyes Pigm.* **2020**, *174*, 108092-108103.
27. Kim, Y. S.; Park, G. J.; Lee, J. J.; Lee, S. Y.; Lee, S. Y.; Kim, C. *RSC Adv.* **2015**, *5*, 11229-11239.
28. Sen, S.; Sarkar, S.; Chattopadhyay, B.; Moirangthem, A.; Basu, A.; Dhara, K.; Chattopadhyay, P. *Analyst* **2012**, *137*, 3335-3342.
29. Kumar, M.; Kumar, R.; Bhalla, V. *Tetrahedron Lett.* **2010**, *51*, 5559-5562.
30. Narayanaswamy, N.; Govindaraju, T. *Sens. Actuators, B* **2012**, *161*, 304-310.
31. Nuñez, C.; Bastida, R.; Macais, A.; Bertolo, E.; Fernandes, L.; Capelo, J. L.; Lodeiro, C. *Tetrahedron* **2009**, *65*, 6179-6188.
32. Oliveira, E.; Capelo, J. L.; Lima, J. C.; Lodeiro, C. *Amino Acids* **2012**, *43*, 1779-1790.
33. Wang, W.; Wu, J.; Liu, Q.; Gao, Y.; Liu, H.; Zhao, B. *Tetrahedron Lett.* **2018**, *59*, 1860-1865.
34. Zhang, B.; Liu, H.; Wu, F.; Hao, G.; Chen, Y.; Tan, C.; Tan, Y.; Jiang, Y. *Sens. Actuators, B* **2017**, *243*, 765-774.
35. Chebrolu, L. D.; Thurakkal, S.; Balaraman, H. S.; Danaboyina, R. *Sens. Actuators, B* **2014**, *204*, 480-488.
36. Li, G.; Zhu, D.; Xue, L.; Jiang, H. *Org. Lett.* **2013**, *15*, 5020-5023.
37. Zhu, Q.; Li, L.; Mu, L.; Zeng, X.; Redshaw, C.; Wei, G. *J. Photochem. Photobiol. A: Chem.* **2016**, *328*, 217-224.
38. Wu, G.; Li, M.; Zhu, J.; Lai, K. W. C.; Tong, Q.; Lu, F. *RSC Adv.* **2016**, *6*, 100696-100699.
39. Qin, J.-C.; Li, T.-R.; Wang, B.-D.; Yang, Z.-Y.; Fan, L. *Spectrochim. Acta A Mol. Biomol. Spectroscopy.* **2014**, *133*, 38-43.
40. Bhatta, S. R.; Mondal, B.; Vijaykumar, G.; Thakur, A. *Inorg. Chem.* **2017**, *56*, 11577-11590.

-
41. Romero, T.; Orenes, R. A.; Tárraga, A.; Molina, P. *Organometallics* **2014**, *33*, 2837-2852.
42. Otón, F.; González, M. D. C.; Espinosa, A.; de Arellano, C. R.; Tárraga, A.; Molina, P. *J. Org. Chem.* **2012**, *77*, 10083-10092.
43. Wu, X.-F.; Darcel, C. *Eur. J. Org. Chem.* **2009**, *8*, 1144-1147.
44. Samanta, S.; Datta, B. K.; Boral, M.; Nandan, A.; Das, G. *Analyst* **2016**, *141*, 4388-4393.
45. Datta, B. K.; Thiyagarajan, D.; Ramesh, A.; Das, G. *Dalton Trans.* **2015**, *44*, 13093-13099.
46. Purkait, R.; Patra, C.; Mahapatra, A. D.; Chattapadhyay, D.; Sinha, C. *Sens. Actuators, B* **2018**, *257*, 545-552.
47. Hu, Y.; Wang, J.; Long, L.; Xiao, X. *Luminescence* **2016**, *31*, 16-21.
48. Zhao, B.; Liu, T.; Fang, Y.; Wang, L.; Song, B.; Deng, Q. *Tetrahedron Lett.* **2016**, *57*, 4417-4423.
49. Pan, C.; Wang, K.; Ji, S.; Wang, H.; Li, Z.; Heb, H.; Huo, Y. *RSC Adv.* **2017**, *7*, 36007-36014.
50. Chena, Z.; Lu, D.; Zhang, G.; Yang, J.; Dong, C.; Shuang, S. *Sens. Actuators, B* **2014**, *202*, 631-637.
51. Ekmekci, Z. *Tetrahedron Lett.* **2015**, *56*, 1878-1881.
52. Zhong, L.; Xing, F.; Bai, Y.; Zhao, Y.; Zhu, S. *Spectrochim. Acta A Mol. Biomol. Spectrosc.* **2013**, *115*, 370-375.
53. Chen, X. L.; Zeng, W. F.; Yang, X. D.; Lu, X. W.; Qu, J. Q.; Liu, R. Y. *Chinese Journal of Polymer Science* **2016**, *34*, 324-331.
54. Buruiana, E. C.; Stroea, L.; Buruiana, T. *Polymer Journal* **2009**, *41*, 694-701.
55. Rapisarda, V. A.; Volentini, S. I.; Farias, R. N.; Massa, E. M. *Anal. Biochem.* **2002**, *307*, 105-109.
56. Lin, W.; Yuan, L.; Cao, Z.; Feng, J.; Feng, Y. *Dyes Pigm.* **2009**, *83*, 14-20.
57. Bazzicalupi, C.; Caltagirone, C.; Cao, Z.; Chen, Q.; Natale, C. D.; Garau, A.; Lippolis, V.; Lvova, L.; Liu, H.; Lundström, I.; Mostallino, M. C.; Nieddu, M.; Paolesse, R.; Prodi, L.; Sgarzi, M.; Zaccheroni, N. *Chem. Eur. J.* **2013**, *19*, 14639-14653.
58. Otón, F.; González, M. del C.; Espinosa, A.; Tárraga, A.; Molina, P. *Organometallics* **2012**, *31*, 2085-2096.
59. Lloveras, V.; Caballero, A.; Tárraga, A.; Velasco, M. D.; Espinosa, A.; Wurst, K.; Evans, D. J.; Vidal-Gancedo, J.; Rovira, C.; Molina, Veciana, J. *Eur. J. Inorg. Chem.* **2005**, 2436-2450.
60. Mu, S.; Ling, Q.; Liu, X.; Ruiz, J.; Astruc, D.; Gu, H. *J. Inorg. Biochem.* **2019**, *193*, 31-41.
-

61. Zhao, L.; Ling, Q.; Liu, X.; Hang, C.; Zhao, Q.; Liu, F.; Gu, H. *Appl. Organometal. Chem.* **2018**, *32*, 4000-4012.
62. Li, M.; Guo, Z.; Zhu, W.; Marken, F.; James, T. D. *Chem. Commun.* **2015**, *51*, 1293-1296.
63. Mohandoss, S.; Stalin, T. *RSC Adv.* **2017**, *7*, 16581- 16593.
64. Scerri, G. J.; Spiteri, J. C.; Mallia, C. J.; Magri, D. C. *Chem. Commun.* **2019**, *55*, 4961-4964.
65. Weller, A. *Pure Appl. Chem.* **1968**, *16*, 115-123.
66. Aigner, D.; Freunberger, S. A.; Wilkening, M.; Saf, R.; Borisov, S. M.; Klimant, I. *Anal. Chem.* **2014**, *86*, 9293-9300.
67. Xiao, P.; Dumur, F.; Frigoli, M.; Tehfe, M.-A.; Graff, B.; Fouassier, J. P.; Gigmes, D.; Lalevée, J. *Polym. Chem.* **2013**, *4*, 5440-5448.
68. Farrugia, T. J.; Magri, D. C. *New J. Chem.* **2013**, *37*, 148-151.
69. Seidel, C. A. M. *J. Phys. Chem.* **1996**, *100*, 5541-5553.
70. Crawford, P. W.; Foye, W. O.; Ryan, M. D.; Kovacic, P. *J. Pharm. Sci.* **1987**, *76*, 481-484.
71. Yi, X. Q.; He, Y. F.; Cao, Y. S.; Shen, W. X.; Lv, Y. Y. *ACS Sens.* **2019**, *4*, 856-864.
72. Benesi, H. A.; Hildebrand, J. H. *J. Am. Chem. Soc.* **1949**, *71*, 2703–2707.
73. Yi, X.-Q.; He, Y.-F.; Cao, Y.-S.; Shen, W.-X.; Lv, Y.-Y. *ACS Sens.* **2019**, *4*, 856-864.
74. Dong, M.; Zheng, W.; Chen, Y.; Ran, B.; Qian, Z.; Jiang X. *Anal. Chem.* **2018**, *90*, 2833-2838.
75. Hu, Z.; Hu, J.; Wang, H.; Zhang, Q.; Zhao, M.; Brommesson, C.; Tian, Y.; Gao, H.; Zhang, X.; Uvdal, K. *Anal. Chim. Acta* **2016**, *933*, 189-195.
76. Liu, W.; Dong, H.; Zhang, L.; Tian, Y. *Angew. Chem. Int. Ed.* **2017**, *56*, 16328 -16332.
77. Chenb, X.-li.; Zengb, W.-F.; Yangb, X.-D, Lua, X.-W.; Qub, J,-Q.; Liua, R,-Y. *Chinese Journal of Polymer Science* **2016**, *34*,324-331.
78. Maity, D.; Kumar, V.; Govindaraju, T. *Org. Lett.* **2012**, *14*, 6008-6011.
79. Park, S.; Kim, H.-Jo. *Tetrahedron Lett.* **2012**, *53*, 4473-4475.
80. Saha, T.; Sengupta, A.; Hazra, P.; Talukdar, P. *Photochem. Photobiol. Sci.* **2014**, *13*, 1427-1433.
81. Mukhopadhyay, S.; Gupta, R. K.; Paitandi, R. P.; Rana, N. K.; Sharma, G.; Koch, B.; Rana, L. K.; Hundal, M. S.; Pandey, D. S. *Organometallics* **2015**, *34*, 918-925.
82. Alfonso, M.; Ferao, A. E.; Tárraga, A.; Molina, P.; *Inorg. Chem.* **2015**, *54*, 7461–747.
83. Zhang, L.; Zhang, H.; Liu, M.; Dong, B. *ACS Appl. Mater. Interfaces* **2016**, *8*, 15654-15660.

84. Cakmak, E. S.; Kolemen, S.; Sedgwick, A. C.; Gunnlaugsson, T.; James, T. D.; Yoon, J.; Akkaya, E. U. *Chem. Soc. Rev.* **2018**, *47*, 2228-2248.
85. Casas-Solvas, J. M.; Vargas-Berenguel, A.; Capitán-Vallvey, L. F.; Santoyo-González, F. *Org. Lett.* **2004**, *6*, 3687-3690.
86. Singh, R.; Samanta, S.; Mullick, P.; Ramesh, A.; Das, G. *Anal. Chimica Acta* **2018**, *1025*, 172-180.
87. Sree, K. U.; Ramana Reddy, A. L. V.; Reddy, B. T. *European Journal of Biomedical and Pharmaceutical Sciences* **2017**, *4*, 812-816.
88. Yanai, T; Tew, D. P; Handy, N. C. *Chemical Physics Letters* **2004**, *393*, 51-57.
89. Frisch, M. J.; Trucks, G. W.; Schlegel, H. B.; Scuseria, G. E.; Robb, M. A.; Cheeseman Jr, S. G.; Barone, V.; Mennucci, B.; Petersson, G. A. *Gaussian 09, revision B.01*. Gaussian, Inc., Wallingford, **2010**.
90. Boyle, N. M. O.; Tenderholt, A. L.; Langner, K. M. *J. Comput. Chem.* **2008**, *29*, 839-845.

Spectroscopic Details

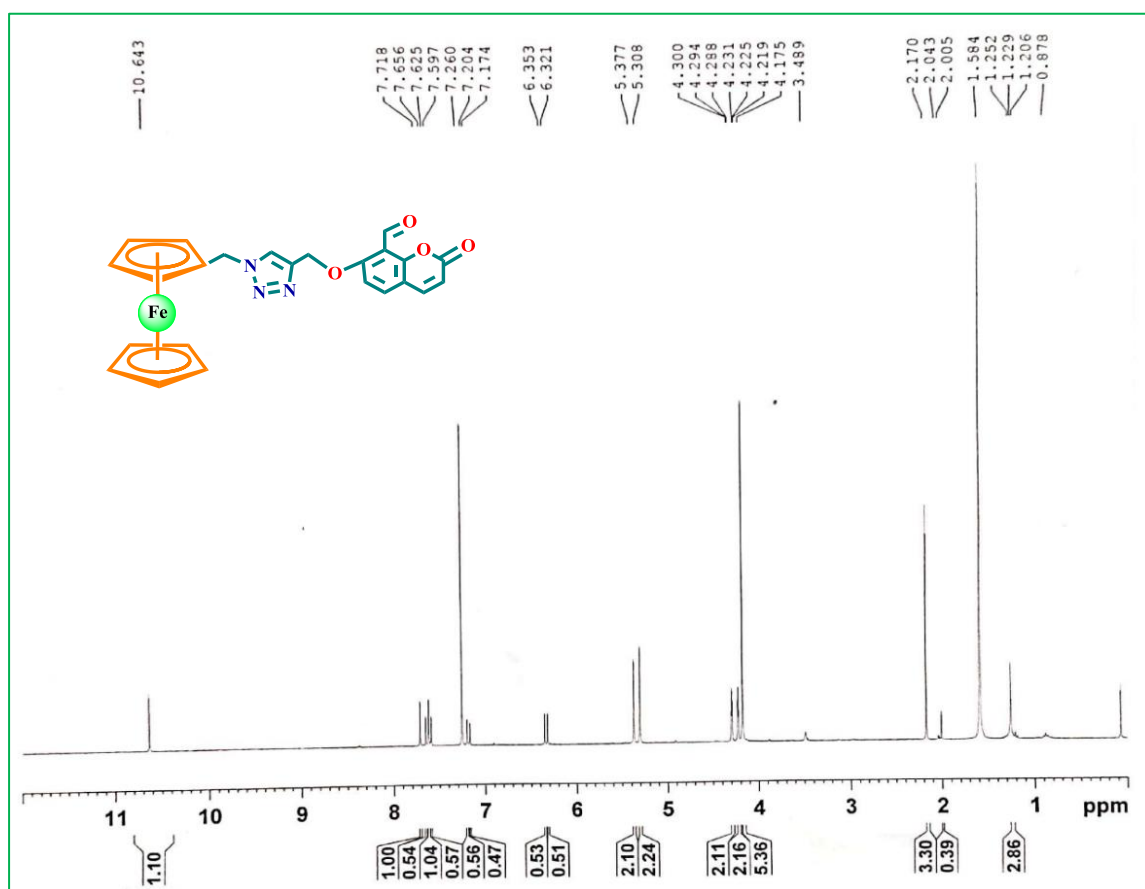


Figure 5.21. ^1H NMR spectrum of compound **3** in CDCl_3 as a solvent.

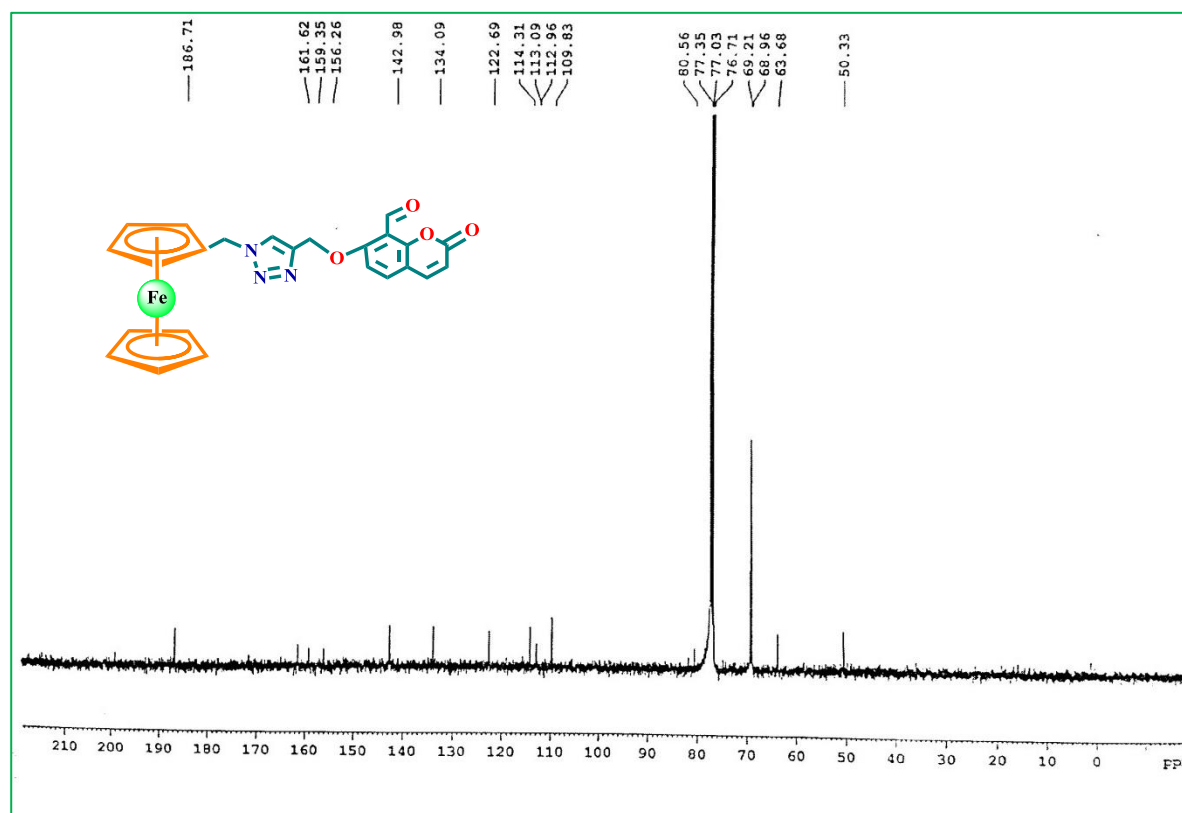


Figure 5.22. ^{13}C NMR spectrum of compound **3** in CDCl_3 as a solvent.

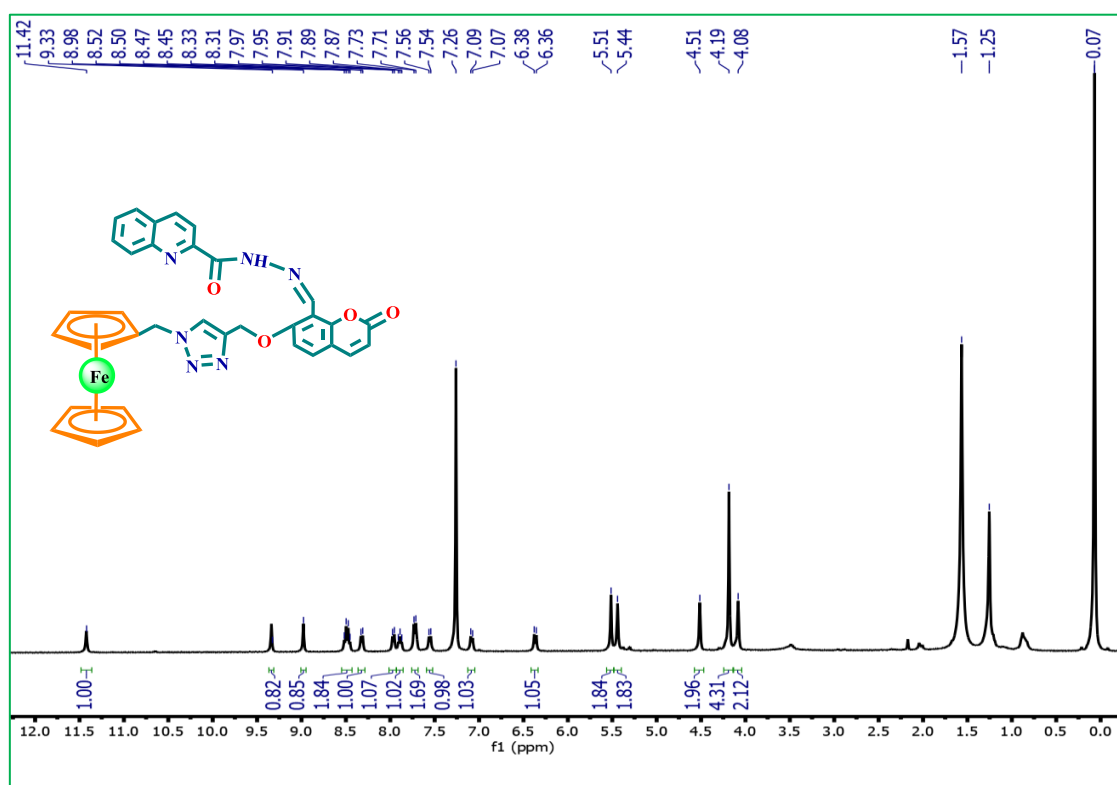


Figure 5.23. ^1H NMR spectrum of compound **5** in CDCl_3 as a solvent.

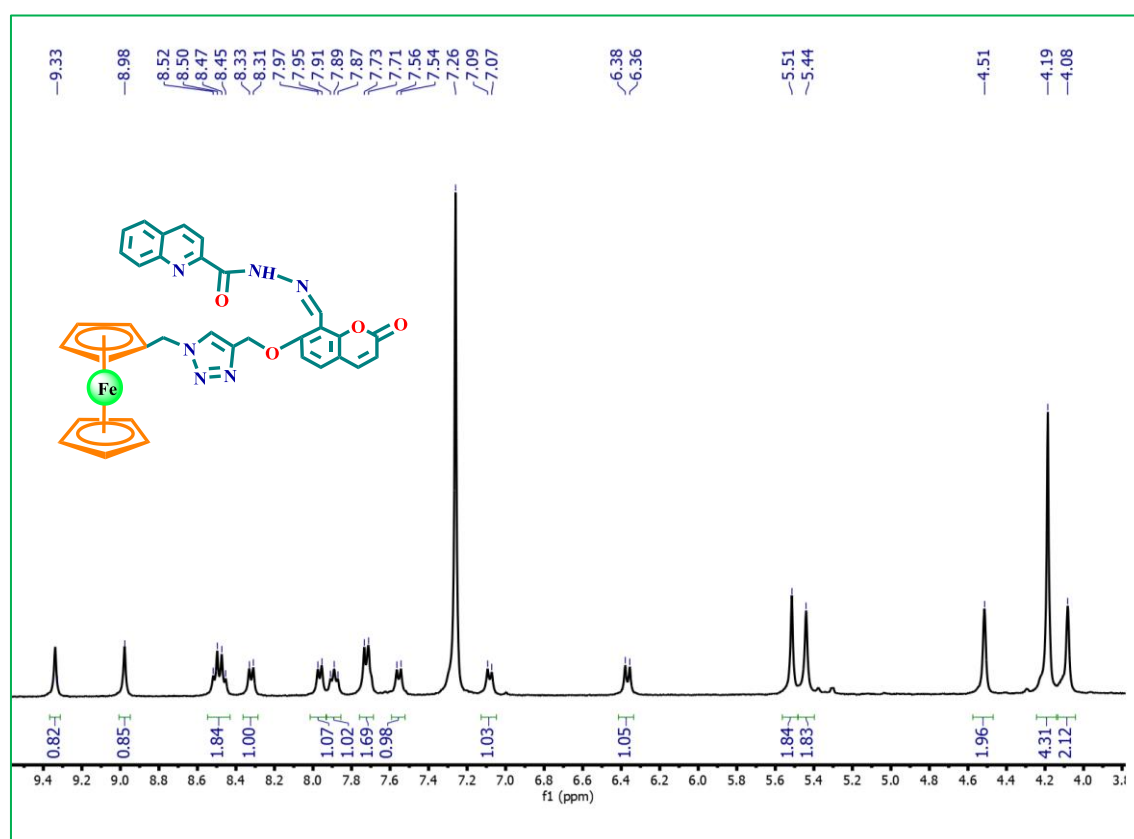


Figure 5.24. Expanded ^1H NMR spectrum of compound **5** in CDCl_3 as a solvent.

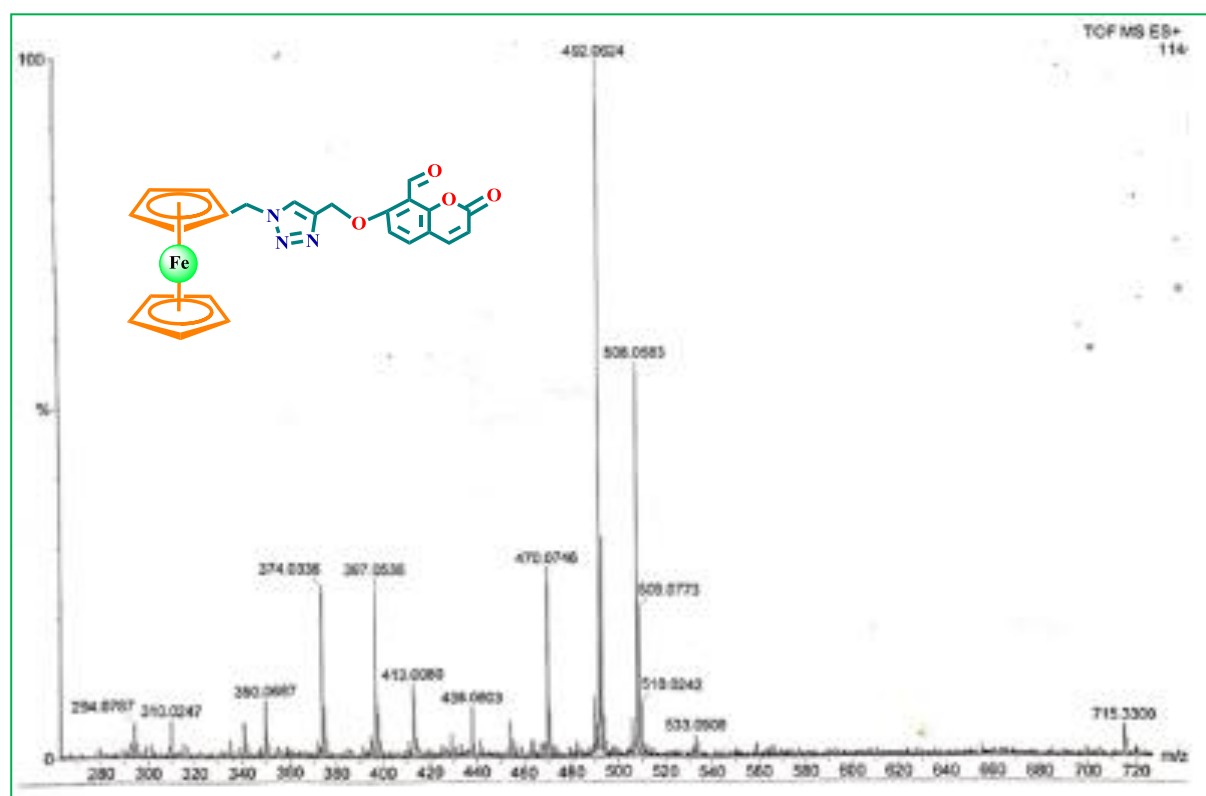


Figure 5.26. HRMS of compound 3.

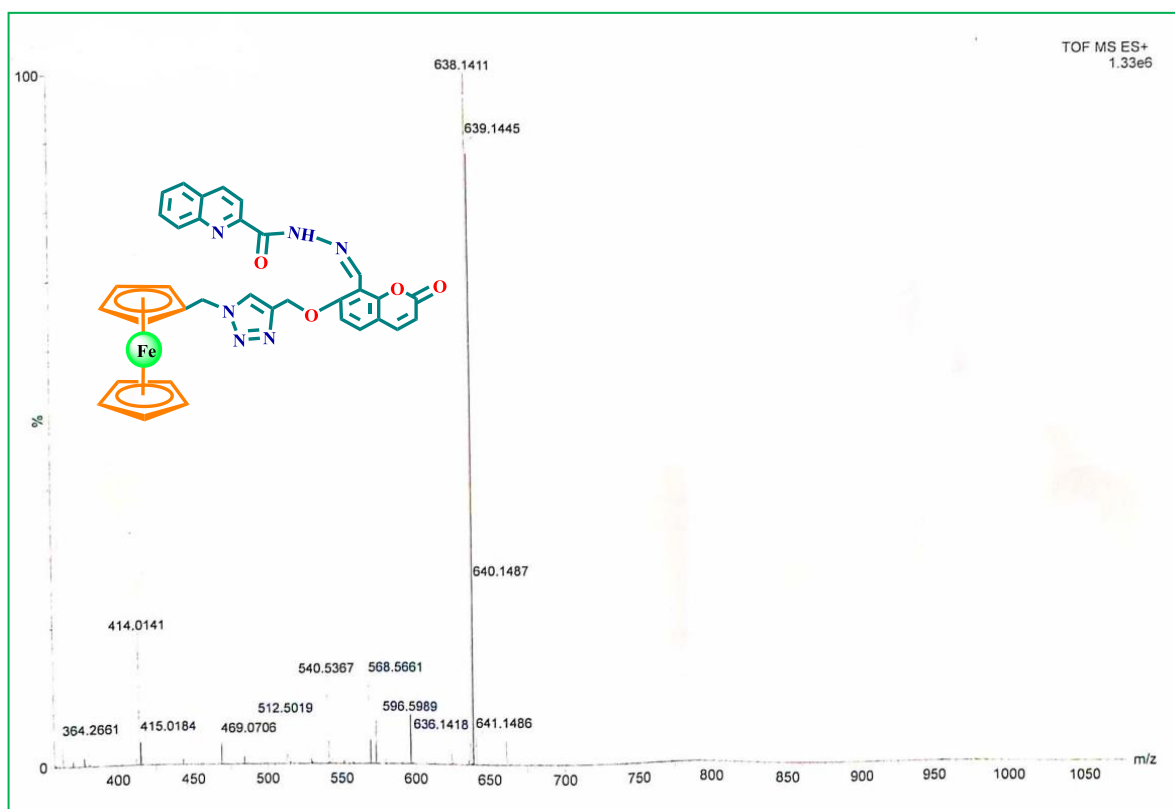


Figure 5.27. HRMS of compound 5.

Summary and Future scope:

The entire PhD works are described and summarized within the five chapters in this dissertation. This cumulative doctoral dissertation explores the synthesis and characterisation of photo-responsive organic compounds coupled with redox active (ferrocene) unit or different fluorophore (coumarin, quinoline, naphthalimide) in a conjugated or non-conjugated manner. Therefore, the synthesis of perfluoro dithienylethene (DTE) derivatives is successfully established by introducing wide variety of functional groups. The main aim of this thesis is the design, synthesis and investigation of photophysical and electrochemical performance of DTE derivatives in solution and in solid state upon exposure of UV/vis light and further explore its practical applications in material science.

Chapter 1 is the general introduction which provides the comprehensive literature survey on perfluoro dithienylethene (DTE) based photochromic organic molecules and their structural versatility. This chapter highlights on the structural aspects of how to tune the photochemical properties of DTEs, and these stimuli responsive work has been done by isomerization reaction using UV/visible light. On the other hand, ferrocene being an interesting redox active molecule may be attached to the thiophene rings of dithienylethene compounds that can significantly perturb on electrochemical and photophysical behavior of photochromic molecules. At the end of this chapter, the different applications of DTE derivatives have been reviewed briefly which provides an idea for designing the multi-responsive DTE based molecules.

Chapter 2 describes, an unprecedented protocol and light triggered metal co-ordination dynamics that uses to distinguish the photoswitchable states of a DTE unit based on metal ion coordination strength *via* simple naked-eye color change and electrochemical analysis. Moreover, from the dynamics study in terms of quantum yield and rate constants, it can be established that metal coordination slows down the inherent photoswitchable nature of the DTE core. Also, the electrochemical experiments highlight the differential responses of the open and closed isomers towards the Hg^{2+} ion. All the photochemical and electrochemical results were further supported by theoretical studies. The incorporation of both a chromogenic ferrocene unit and a rigid alkyne moiety is required for the successful practical application of this sort of metal-chelated photocontrolled probe. Metal chelation and DTE-based molecular architecture may open up a new avenue in photocontrolled metal-coordinating smart molecular switches.

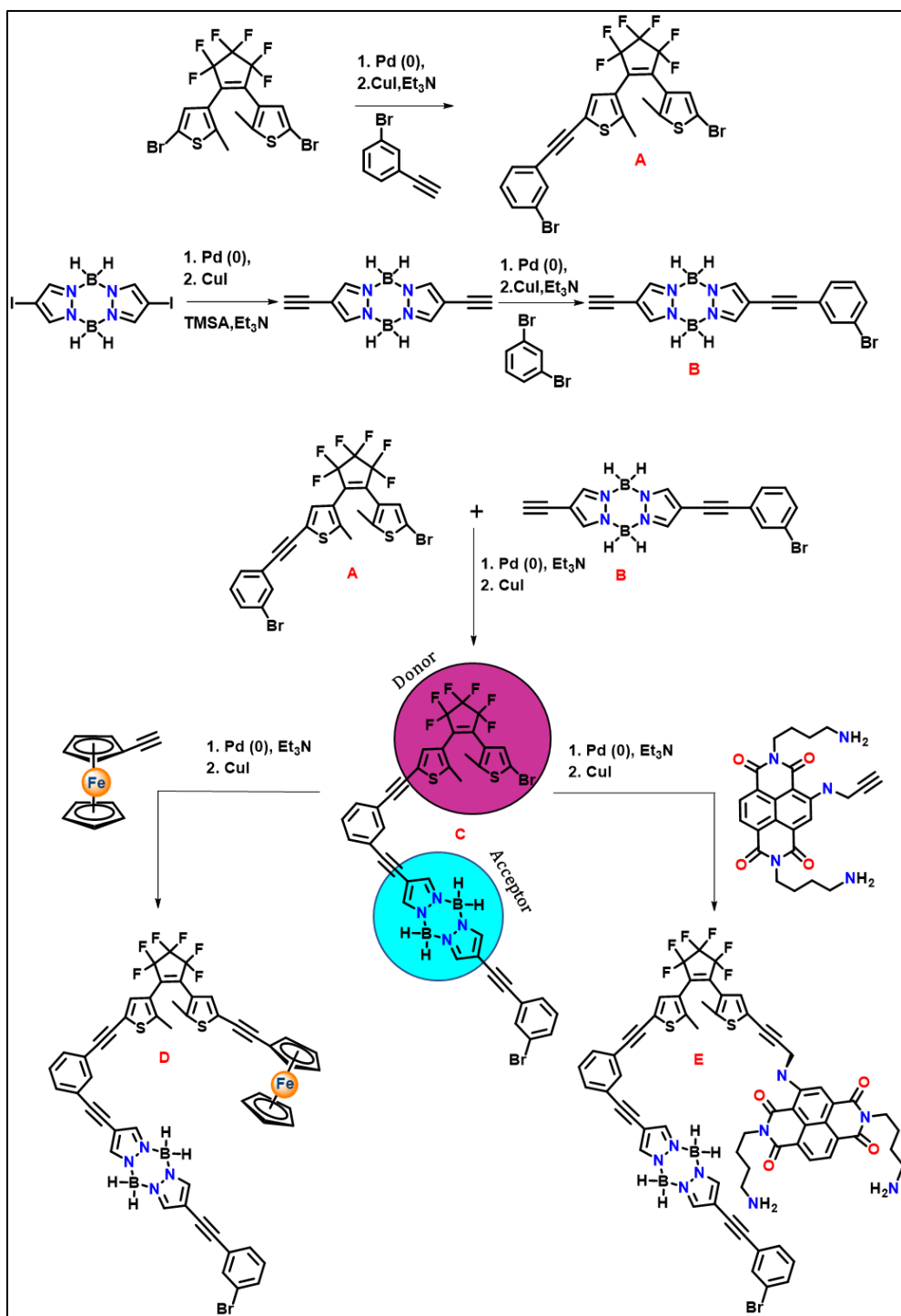
Chapter 3 presents an unique molecular system, devoid of any conventional fluorophore, S,S-dioxide moiety, that displayed “turn-on” fluorescence upon irradiation with UV light. It is completely conjugated DTE-ferrocene system, not only to switch the photochemical, morphological, and electrochemical properties by means of light, but also to induce the “turn-on” fluorescence property upon photocyclization without incorporating any fluorophore to the system in solution as well as solid state. The highly conjugated O=CH-C=C-C-C-C- unit in the reactive carbon centre of the DTE is an unprecedented example, and it contributes to interesting practical applications like anti-counterfeiting ink and secret code encryption and decryption technique.

In **Chapter 4**, a novel type of high-performance peptide bridged dithienylethene with AIE activity without an AIE-gen is described. Furthermore, we have also demonstrated that how the only chain length of alkyl group can tune the AIE activity as well as the morphological properties based of supramolecular self-assembly. To our delight, the designed and synthesized materials retain fluorescence photoswitching performance in solution, solid, and gel form. Moreover, the synthesized molecules were easily implanted into a PMMA polymeric matrix to create photowritable and erasable materials with high repeatability and operability. Benefiting from the satisfactory photochromic and prominent anti-fatigue capability in solution as well as in solid state, it has been utilized as anti-counterfeiting ink for securing QR/bar code and latent fingerprints imaging application in forensic sciences as well. We also envision that our finding will inspire other scientists to create new fluorescent photochromic DTE based materials for real forensic laboratory investigations in the near future.

Chapter 5 describes, little different class of organometallic molecules without any photochromic unit, rather, it is comprised of ferrocene and two fluorophores (quinoline and coumarin) and applied in cascaded molecular logic gates. This chapter describes an “OFF–ON–OFF” molecular device that exhibits oxidation-induced turn-on fluorescence emission *via* the photo-induced electron transfer (PET) process in the presence of paramagnetic transition-metal ions (Fe^{3+} and Cu^{2+}), where Fe^{3+} and Cu^{2+} ions are treated as oxidizing agents rather than binding agents. The viability of the PET process was authenticated by the Weller equation and DFT calculations. The newly synthesized probe is differentially selective toward Fe^{3+} , Cu^{2+} , and Cu^+ ions. Two logic circuits, "INHIBIT" and "OR," were built using differentially selective features of the probe. These basic binary logic gates were further cascaded to form an “AND–OR” combinational gate.

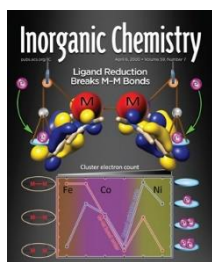
Based on the results obtained from the photochemical, electrochemical and morphological studies for the photochromic DTE and redox active ferrocene-based molecules, it can be concluded that these types of molecules are potential candidates for application in light triggered security technology. We have designed and synthesized a variety of photochromic molecules by tuning different system (like redox active ferrocene or fluorophore), attached to the reactive C atom of DTE. It has been observed that DTE molecules with high π -conjugation preferentially transport electrons from electron rich to electron deficient centres with high photoreaction quantum yield and fatigue resistance property, however photoisomerization speed is slow. The aforementioned issue has been solved by the incorporation of non-conjugated spacer in between DTE and fluorophore moieties. However, in order to achieve the high photoreaction quantum yield as well as a rapid photoisomerization speed in the conjugated system upon exposure of light, we can design a donor-acceptor type photochromic system as described in the below scheme.

Following the entire study in the present thesis and to develop a route map for future scope, it will be interesting to link a organic π -systems (conjugated DTE unit) with electron-deficient elements such as boron anticipating the smooth electron flow. This strategy may lead to the development of a wide range of new materials (A-E) with exciting properties that could contain electron rich and/or deficient species (C), redox active moieties (D) and fluorophore (E) (Proposed Scheme). Electronic communication in such hybrid system will be achieved through the vacant p-orbital of the boron atom. Such light triggered switchable materials would be of great interest not only in anticounterfeiting applications like forensic science and security technology, but also for development of smart materials having π -conjugation that are promising for example in memory devices, optoelectronic material and so on. Therefore, this type of proposed π -conjugated donor-acceptor DTE systems may be applicable as optoelectronic material. Additionally, the photoswitchable DTE could lead to applications in the new area of boron containing responsive materials in a significant way.

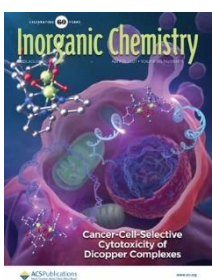


Proposed Scheme . Desining of donor-acceptor type photochromic system.

List of publications



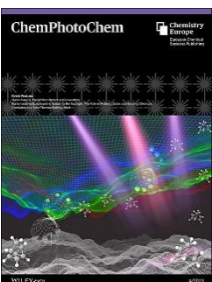
1. **Karmakar, M.**; Bhatta, S. R.; Giri, S.; Thakur, A.* Oxidation-induced differentially selective turn-on fluorescence *via* photoinduced electron transfer based on a ferrocene-appended coumarin-quinoline platform: Application in cascaded molecular logic. *Inorg. Chem.* 2020, *59*, 16091-16094.



2. **Karmakar, M.**; Pal, A.; Mondal, B.; Adarsh, N. N.; Thakur, A.* Light-Triggered Metal Coordination Dynamics in Photoswitchable Dithienylethene–Ferrocene System. *Inorg. Chem.* 2021, *60*, 6086-6098.



3. **Karmakar, M.**; Bag, S. K.; Mondal, B.; Thakur, A.* A Conjugated Photoresponsive Dithienylethene-Ferrocene System: Application in Secret Writing and Decoding. *J. Mater. Chem. C.* 2022, *10*, 8860-8873.



4. **Karmakar, M.**; Bag, S. K.; Thakur, A.* Peptide Bridged Naphthalimide-Dithienylethene Diad with Aggregation Induced Emission Activity: Application in Forensic Fingerprint Technology. (*ChemPhotoChem Accepted for publication.*)



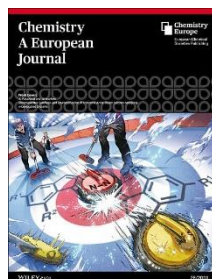
5. Bhatta, S. R.; **Karmakar, M.**; Thakur, A.* Naphthol based positional isomers of ferrocene appended benzochromene: Differential selectivity towards Hg (II) ion. *J. Organomet. Chem.* 2021, *949*, 121958.



6. Pal, A.; **Karmakar, M.**; Bhatta, S. R.; Thakur, A.* A detailed insight into anion sensing based on intramolecular charge transfer (ICT) mechanism: A comprehensive review of the years 2016 to 2021. *Coord. Chem. Rev.* 2021, 448, 214167.



7. Bhat, N. S.; Yadav, A. K. **Karmakar, M.**; Thakur, A.; Mal, S.S.; Dutta, S.; Straightforward and scalable preparation of 5-(acyloxymethyl)furfurals directly from carbohydrates as stable, hydrophobic congeners of 5-(hydroxymethyl)furfural. *ACS Omega* 2023, 8, 8119-8124.



8. Bag, S. K.; **Karmakar, M.**; Mondal, B.; Thakur, A.* Non-conjugated Bis-(dithienylethene)-naphthalenediimide as a Dynamic Anti-counterfeiting Agent: Driving the Wheel of Photoswitching Enactment. (*Chem.Eur.J.* Under revision.).

List of scientific conference attended and poster presentations

- Emerging Trends in Chemical Science (ETCS-2018), 28th march **2018**, Department of Chemistry, University of Calcutta, Kolkata, India.
- National Seminar on Chemical Sciences: Today and Tomorrow (CSTT-2019), 14th March **2019**, Department of Chemistry, Jadavpur University, Kolkata, India.
- National Seminar on Celebration of the International Year of the Periodic Table (CIYPT), Department of Chemistry Jadavpur University, Kolkata, India, Date: 13 & 14th August **2019**.
- BRICS Workshops-2020, Indian Institute of Science Education and Research, Kolkata, Date: 3rd January, **2020**.
- Virtual Chemistry Course “Developments in Boron Chemistry: from Fundamental Studies to Applications,” October, **2021**.
- 27th CRSI National Symposium in Chemistry, Indian Institute of Science Education and Research, Kolkata, Date: 26-29th September, **2021**.
- 28th CRSI National Symposium in Chemistry, Indian Association for the Cultivation of Science. Date: 4th June, **2022**.